SAKARYA ÜNİVERSİTESİ

FEN BİLİMLERİ ENSTİTÜSÜ DERGİSİ

Sakarya University Journal of Science (SAUJS)

SAKARYA ÜNİVERSİTESİ

e-issn: 2147-835X

SAÜ Fen Bil Der/SAUJS

Cilt/Volume: 25

Sayı/Issue: 3

Haziran/June 2021

Sakarya Üniversitesi Fen Bilimleri Enstitüsü Dergisi
(Sakarya University Journal of Science)
Cilt/Volume: 25 No/ Issue: 3 Haziran/June 2021
Editör Kurulu/Editorial Boards

Editor-in-Chief

Editors

Editorial Board

English Language Editor

SAKARYA ÜNİVERSİTESİ FEN BİLİMLERİ ENSTİTÜSÜ DERGİSİ
(SAKARYA UNIVERSITY JOURNAL OF SCIENCE)
İÇİNDEKİLER/CONTENTS
Cilt/Volume: 25 – No/Issue: 3 (HAZİRAN/JUNE-2021)

RESEARCH ARTICLES

SAKARYA ÜNİVERSİTESİ
FEN BİLİMLERİ ENSTİTÜSÜ DERGİSİ

Sakarya University Journal of Science
SAUJS

e-ISSN 2147-835X | Period Bimonthly | Founded: 1997 | Publisher Sakarya University |
http://www.saujs.sakarya.edu.tr/en/

Title: Comparison of Two Different Circular Diaphragm Models with Central Mass for MEMS Based FPI Pressure Sensor Performance Based on Sensitivity and Frequency Response

Authors: Fikret YILDIZ

Recieved: 2020-05-15 16:28:37

Accepted: 2021-04-01 11:55:19

Article Type: Research Article

Volume: 25
Issue: 3
Month: June
Year: 2021
Pages: 619-628

How to cite
Fikret YILDIZ; (2021), Comparison of Two Different Circular Diaphragm Models with Central Mass for MEMS Based FPI Pressure Sensor Performance Based on Sensitivity and Frequency Response. Sakarya University Journal of Science, 25(3), 619-628, DOI: https://doi.org/10.16984/saufenbilder.737982
Access link
http://www.saujs.sakarya.edu.tr/en/pub/issue/62736/737982

Sakarya University Journal of Science 25(3), 619-628, 2021

Comparison of Two Different Circular Diaphragm Models with Central Mass for MEMS Based FPI Pressure Sensor Performance Based on Sensitivity and Frequency Response

Fikret YILDIZ*[1]

Abstract

The sensitivity and the fundamental frequency of circular membrane with a central mass (embossment) were analytically evaluated for Fabry- Pérot interferometers (FPI) based pressure sensor. Two different previously developed model (named as M1 and M2, respectively in this study), which includes a diaphragm with center embossment, were considered to obtain results and performance of models were compared. Thickness of diaphragms were 5 µm and 10 µm with the radius of 300 µm, 500 µm,600 µm and 700 µm, respectively. According to the results, it was noted that diaphragm considering M1 model shows higher sensitivity and displacement compared to diaphragm considering M2 model. 155.15-102.87 nm/kPa and 149.5-39.7 nm/kPa sensitivity range were calculated for the diaphragm based on the M1and M2 model, respectively when 300 µm in radius and 5 µm thick diaphragm was used. Moreover, frequency response of diaphragm considering two different model is slightly different for thinner embossment; however, same frequency response was calculated for thicker embossment. For example, frequency range of 700 µm in radius and 10 µm was changes between 42-22.7 kHz and 42.2-22.7 kHz when M1 and M2 model was considered. It was understand that compared with the conventional circular diaphragm (CD) model, non-uniform diaphragm with a central mass provides more geometrical parameters to tune the device performance (sensitivity) and it provides design flexibility on the sensor structure.

Keywords: central embossment, FPI pressure sensor, MEMS, sensitivity analyze

1. INTRODUCTION

Pressure is a fundamental parameter and significance for different applications [1-4]. It has studied intensively for years [5]. Pressure sensors based on piezo resistive/piezoelectric effects have dominantly used in this field. However, electromagnetic interference still is an issue such type of devices [6,7]. Fiber optic pressure sensors are the alternative to the conventional piezo resistive/piezoelectric based sensors [8]. Some of them are Mach-Zehnder interferometers and Fabry-Pérot interferometers (FPI) [9-14]. FPI-

*Corresponding author: fikretyildiz@hakkari.edu.tr
[1]Hakkari University, Faculty of Engineering, Electrical and Electronics Engineering Department, 30000, Hakkari,Turkey
ORCID: https://orcid.org/0000-0003-4846-3998

based sensors have various superiorities among the other fiber optic sensors [14-17]. Reflecting parallel mirrors separated by a gap (cavity) are the main component of the FPI-based pressure sensor [3]. Extrinsic cavity with a diaphragm is commonly used for variety applications [5], [18,19]. An extrinsic Fabry-Pérot interferometer is placed between a fiber end face and a reflective membrane [20]. Thus, the choice of diaphragm material and geometry is a key factor for pressure sensor design [21]. Some of the studies related to MEMS based FPI pressure sensors are summarized below.

Rectangular, square or circular shape flat diaphragm have extensively used in the MEMS based pressure sensor technology. In one study, the design guidelines of pressure sensors with a square shape diaphragm have presented by considering the relationships between diaphragm thickness, side length, sensitivity and resonant frequency [22]. Another study of different research group used a piezoresistive pressure sensor with polysilicon piezoresistors and a square shape diaphragm for high temperature applications in the desired operation range (0–30 Bar). Fabricated sensor results show good sensitivity and linearity [23]. In the different work, a micro piezoresistive pressure sensor was designed, fabricated using wet etching technology and tested for Tire Pressure Measurement System (TPMS) [24]. Another previous study designed, fabricated, and tested the micro pressure sensor with a square diagram made of silicon and bossed diaphragm. 11.098 μV/V/Pa sensitivity was measured in the operating range of 500 Pa and it was confirmed that the sensor enables to measure the absolute micro pressure lower than 500 Pa [25]. More studies are available and can be found in literature [26].

Square diaphragm as a pressure sensor commonly used due to better sensitivity than rectangular diaphragm or circular diaphragm under same conditions [23]. However, advantages of compatibility with standard fiber components make circular geometries more use in literature for numerical and analytical modeling [27-30]. Moreover, the sensitivity and the frequency response of the circular diaphragm are tuned by less geometric parameters compared to square or rectangular shape geometry [22-28]. However, one of the disadvantage of flat diaphragms is pressure induced large deflections and thus, undesired volatility effects to the output of the sensor [21]. Hence, many innovative sensor designs have been widely explored in the past decades with the aim of fabrication of high performance pressure sensors. Placing a center mass on diaphragm is an effective method to improve sensor characteristics by increase the stiffness of the diaphragm and reduce the nonlinear effects [21].

In this paper, two different model of center-embossed circular diaphragm, which were previously developed and available in literature [26,33], were used to determine performance and behaviors of the circular diaphragm with a center embossment (mass). These two models explained in the following section of study. The sensitivity and frequency response as a function of embossment thickness and radius at a given pressure were obtained. Then performance of pressure sensors based on embossed diaphragm results were compared and discussed considering the two different circular diaphragm models with a central mass.

2. SENSOR DESIGN

In general, a fiber optic EFPI (Extrinsic Fabry-Pérot Interferometer) system composed of a sensor probe, a fiber optic coupler, a light source, and a detector [31,32] as illustrated in Figure 1. Membrane is the main part of the sensing probe, which sense the acoustic signal. In this system, the light emitted by the source passing through the fiber optic coupler is reflected from two different surface: fiber optic coupler and diaphragm. Detection of incoming pressure waves is measured by comparison of light intensity of reflected light from first and second surface (membrane). The membrane structure is deformed under pressure and, thus, change the cavity length, which results in the phase differences between collected light from the consecutive surfaces [28,31]. Therefore, the membrane deflection due to the acoustic pressure determines the performance of FPI system in

terms of the sensitivity and linear range. Frequency response also an important parameter to evaluate sensor characteristic. Two of FPI sensor designs, (a) conventional circular diaphragm and (b) center embossment diaphragm, are illustrated in Figure 2.

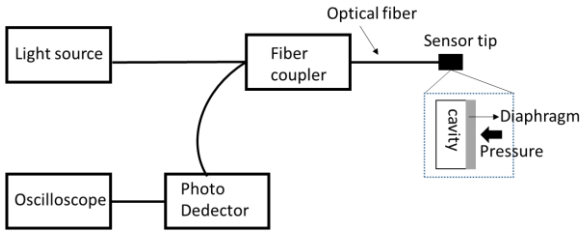

Figure 1 Schematic of a FPI pressure sensor components

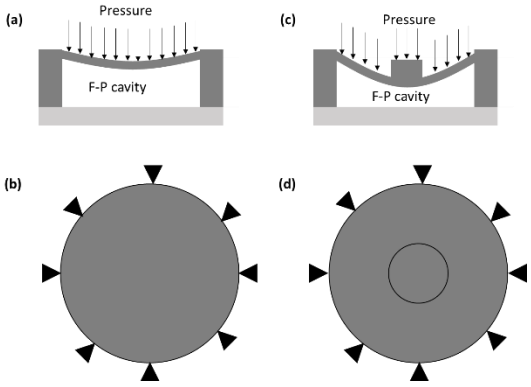

Figure 2 Schematic of FPI pressure sensor. (a) Cross-sectional and (b) top view of conventional circular diaphragm sensor. (c) Cross-sectional and (d) top view of embossed diaphragm

Analysis of FPI pressure sensor, thus, can be initiated by considering its diaphragm geometry. Different kind of diaphragms have been designed in literature [22,23], [27-29]. One approaches is the use of non-uniform membrane by adding a mass on the geometrical center of vibrating membrane [26,33,34]. Under the small deflection approximation, the equation governing deflection, w(r), of a thin flexible circular plate with radius, *R*, under a uniform loading, P, is given as [35-37]

$$\nabla^2 w \nabla^2 D = \mathrm{P} \tag{1}$$

$$D = \frac{Eh^3}{12(1-v^2)} \tag{2}$$

Here, P is the applied pressure, D is the flexural rigidity of the plate, E is the Young's modulus, h is the diaphragm thickness, and ν is the Poisson's ratio. The differential operator (∇) in cylindrical coordinates is given by Eq.3. When substitution Eq.3 into Eq.1 and considering D is constant through the plate, Eq.4 is obtained.

$$\nabla^2 = \frac{\partial}{\partial r^2} + \frac{1}{r^2}\frac{\partial^2}{\partial \emptyset^2} + \frac{1}{r}\frac{\partial}{\partial r} \tag{3}$$

$$\nabla^2 w = \mathrm{P/D}$$

The vertical deflection w (r) is obtained as

$$w(r) = \frac{Pr^4}{64D}\left\{1 - \left(\frac{r}{R}\right)^2\right\}^2 \tag{4}$$

$$w(r=0) = w_{max} = \frac{Pr^4}{64D}$$

Eq.4 describes the deflection of clamped circular diaphragm (CD) (Figure 2 (a-b)). Deflection profile of non-uniform membrane as illustrated in Figure 2 (c-d), can be re-established using above equation of clamped thin circular membrane [33]. In this study, two different model of central embossment membrane were considered for calculation of frequency response and sensitivity.

In the first model named as M1 in this study, deflection of center embossment membrane (Y_0) is analytically expressed as in Eq.5 as described previously in [26]:

$$Y_0 = \frac{A_p a^4 P}{EH^3} \tag{5}$$

$$A_p = \frac{3(1-v^2)}{16}\left(1 - \frac{b^4}{a^4} - 4\frac{b^2}{a^2}\log\frac{a}{b}\right) \quad (6)$$

where H is the thickness of membrane, b is the radius of embossment and a is the radius of membrane.

To obtain simplified analytical model of the center-embossed diaphragm, it is divided into two parts [33], which is named as as M2 in this study. First part is referring to a thin round plates expect that there is a circular hole in the center. Second part defines the circular plates with a sum of thickness of a central mass and diaphragms. More details can be found about analytical model of center-embossed membrane in [33]. Center deflection and structural sensitivity of embossed membrane under constant pressure is expressed as Eq.7-8 [33];

$$w_0 = \left(\frac{[D_0 r_1^4 + D_1(r_0^4 - r_1^4)]}{64 D_0 D_1} + \frac{(D_1 - D_0)(r_0^2 - r_1^2) r_0^2 r_1^2 \ln\frac{r_1}{r_0}}{16 D_0\left[D_1(r_0^2 - r_1^2) + D_0\left(\frac{1-v}{1+v}r_0^2 + r_1^2\right)\right]}\right) P \quad (7)$$

$$S = \frac{w_0}{P} = \frac{[D_0 r_1^4 + D_1(r_0^4 - r_1^4)]}{64 D_0 D_1} + \frac{(D_1 - D_0)(r_0^2 - r_1^2) r_0^2 r_1^2 \ln\frac{r_1}{r_0}}{16 D_0\left[D_1(r_0^2 - r_1^2) + D_0\left(\frac{1-v}{1+v}r_0^2 + r_1^2\right)\right]} \quad (8)$$

where D0 and D1 denote the flexural rigidities of first and second part, respectively, which can be expressed as below and H is the thickness of central mass, r0 is the radius of the membrane and r1 is the radius of embossment.

$$D_0 = \frac{Eh^3}{12(1-v^2)} \; and \quad D_1 = \frac{E(h+H)^3}{12(1-v^2)} \quad (9)$$

When the central embossment ignored, in other word H = 0 or $r_0 = r_1$, sensitivity equals to $r_0/64D_0$ same as the clamped round shape plate [33]. The resonance frequency of a circular and fixed diaphragm is expressed as Eq.10 [38];

$$f = \frac{1}{2\pi}\sqrt{\frac{k_m}{m_m + m_a}} \quad (10)$$

here, k_m is elastic coefficient of the membrane, m_m is mass of the membrane, m_a any additional mass on the surface of the membrane. The elastic coefficient, k_m, of the membrane depends on its shape and can be calculated using Hooke's law, having a circular shaped membrane with a radius of a_m

$$k_m = \frac{188D}{a_m^2} \quad (11)$$

where D is the flexural rigidity of membrane. In this study, FPI diaphragm with a central mass was analytically evaluated using the previously developed two different models and these models are available in literature [26,33]. Sensitivity and frequency response were calculated and results of diaphragm with a central mass considering two different models were compared.

3. RESULTS AND DISCUSSION

Two different model of center-embossed membranes were used to obtain analytical results in terms of sensitivity and frequency response. Displacement profile of first model (M1) is not include effect of embossment thickness [26]. On the other hand, thickness of embossment is considered for analytical results for second model(M2) [33]. Performance of these two model

was evaluated in terms of sensitivity and frequency response of center embossed diaphragm. Moreover, results were also compared with the conventional circular design (CD).

3.1. Frequency Response

Different geometrical values were selected for frequency response analysis; membrane radius (r_0), embossment radius (r_{em}) and thickness of embossment (t_{em}). Calculations were performed for the 5 µm and 10 µm thick membranes, respectively. SiO_2 was selected as diaphragm and embossment material (E=73 GPa, υ=0.17 and ρ=2200 kg/m^3 [39]). The fundamental frequency of diaphragm considering the M1 model and M2 model was calculated using Eq.10 and the results were presented in Table 1. Figure 3 shows the fundamental frequency of diaphragm considering M1 and M2 model as a function of thickness of central embossment (t_{em}) and radius (r_{em}) when the thickness of diaphragm is 5 µm. Maximum thickness of embossment was selected up to 10 times of membrane thickness. Similarly, embossment radius (r_i in Fig.3) was selected as 10%, 30% and 50% of membrane radius. It has been observed that as the embossment thickness increases fundamental frequency of structures as expected based on the Eq.10. Comparatively, the embossment radius has an obviously impact on the fundamental frequency.

Table 1
Frequency (kHz) response of diaphragm considering CD, M1 and M2 model for different membrane thicknesses

r_0 (µm)	**t_m (µm)=5**			**t_m (µm)=10**		
	CD	**M1**	**M2**	**CD**	**M1**	**M2**
		t_{em}=5-50 (µm) r_{em}= r_0 /2 (max.)	**t_{em}=5-50 (µm) r_{em}= r_0 /2 (max.)**		**t_{em}=10-100 (µm) r_{em}= r_0 /2 (max.)**	**t_{em}=10-100 (µm) r_{em}= r_0 /2 (max.)**
300	152.34	114.3-61.7	114.8-61.7	304.67	228.6-123.4	229.5-123.4
500	54.84	41.1-22.2	41.3-22.2	109.68	82.3-44.4	82.6-44.4
600	38.08	28.6-15.4	28.7-15.4	76.17	57.1-30.8	57.4-30.8
700	27.98	21-11.3	21.1-11.3	55.96	42-22.7	42.2-22.7

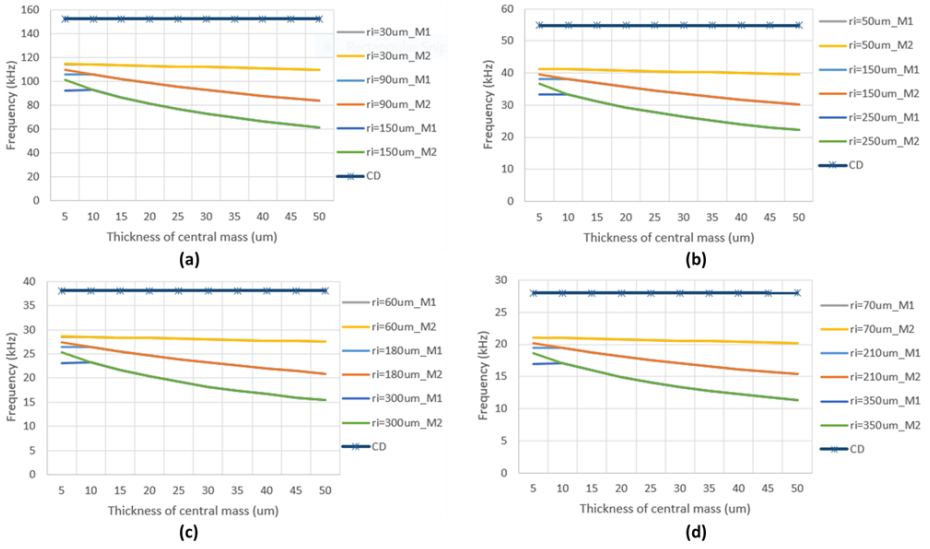

Figure 3 Comparison of frequency response for the diaphragm using M1 and M2 model, respectively. (a) t_m=5 µm and r_0=300 µm, (b) t_m=5 µm and r_0=500 µm,(c) t_m=5 µm and r_0=600 µm and (d) t_m=5 µm and r_0=700 µm

Fundamental frequency results of diaphragm with a central mass was very close when both the M1 and M2 model were considered. It was seen form the Figure 3 that the diaphragm with same

embossment thickness and radius have almost same frequency response when M1 and M2 models were considered separately. For example, fundamental frequency of diaphragm based on M1 and M2 models are 105.9 kHz and 109.9 kHz, respectively with a 5 µm thick embossment and radius of 90 µm (30%xr_0). However, when thicker embossment selected, this differences is vanished as shown in Fig.3. From the Table 1 and Fig.3, the fundamental frequency of CD is constant and higher than M1 model and M2 model. This is the results of increased membrane mass due to embossment as in Eq.10. It can be concluded that pressure sensor diaphragm with a central embossment is suitable for low frequency and wide frequency bandwidth applications compared to CD structure.

3.2. Sensitivity

As mentioned in the design section, the sensitivity, S, of pressure sensor is defined as ratio of center displacement to pressure. To obtain the sensitivity values of diaphragm, first membrane deformation was calculated under acoustic pressure ranging from 1 Pa to 10 kPa [20]. Then, the sensitivities for different cases depending on the embossment thickness and radius were obtained for the CD, M1 and M2 model. The results are listed in Table 2. Figure 4 shows the sensitivity of diaphragm with a thickness of 10 µm. From these results, diaphragm considering M1 model has higher sensitivity than its M2 model based diaphragm counterparts.

Table 2
Sensitivity (nm/kPa) performance of CD, M1 and M2 models for different membrane thicknesses

r_0 (µm)	**t_m (µm)=5**			**t_m (µm)=10**		
	CD	**M1**	**M2**	**CD**	**M1**	**M2**
		t_{em}=5-50 (µm) $r_{em=}$ r_0/2 (max.)	**t_{em}=5-50 (µm) $r_{em=}$ r_0/2 (max.)**		**t_{em}=10-100 (µm) $r_{em=}$ r_0/2 (max.)**	**t_{em}=10-100 (µm) $r_{em=}$ r_0/2 (max.)**
300	161.63	155.15-102.87	149.5-39.7	20.20	19.39-12.86	18.7-5
500	1247.13	1197.12-793.76	1153.4-306.2	155.89	149.64-99.22	144.2-38.3
600	2586.05	2482.35-1645.94	2391.7-634.9	323.26	310.29-205.74	299-79.4
700	4790.98	4598.86-3049.32	4431-1176.1.	598.87	574.86-381.16	553.9-147

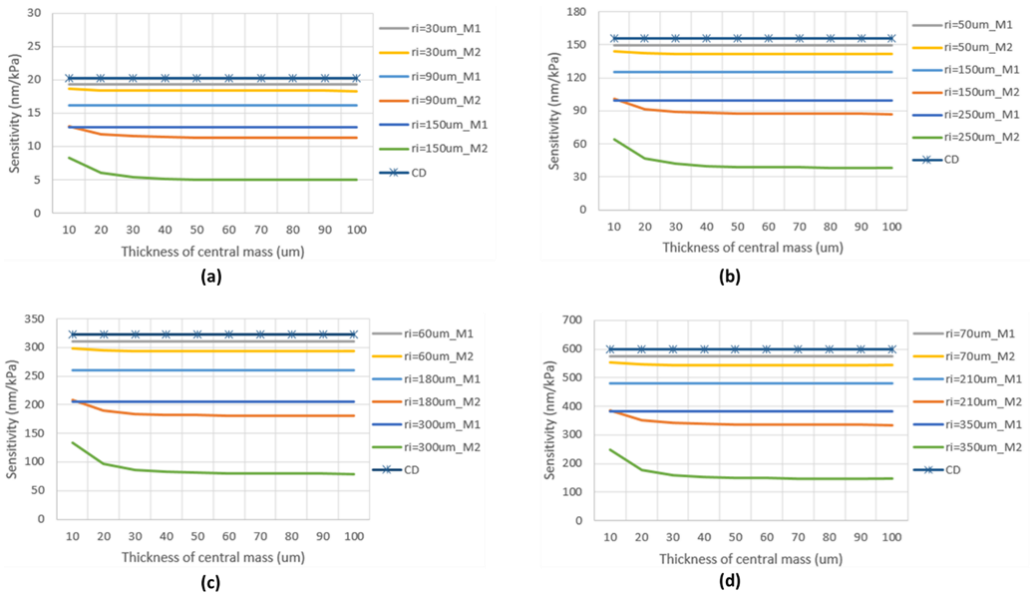

Figure 4 Comparison of diaphragm sensitivity (nm/kPa) considering the M1 model and M2 model. (a) t_m=10 µm and r_0=300 µm, (b) t_m=10 µm and r_0=500 µm, (c) t_m=10 µm and r_0=600 µm and (d) t_m=10 µm and r_0=700 µm

Moreover, sensitivity of diaphragm considering M1 model changes only with radius of embossment. This results can be explained when considering Eq.5-6. The narrower the width of embossment is, the larger the sensitivity. On the other hand, diaphragm sensitivity based on M2 model changes with both embossment thickness and radius. Analytical results of central displacement and sensitivity of diaphragm based on M2 model showed lower values compared to CD and M1 model based diaphragm. Sensitivity of M2 model based diaphragm is decreases, when the embossment thickness increases. Therefore, it was founded that sensitivity values of FPI diaphragm based on M1 and M2 models are not agrees well and there is discrepancy between these two models in terms of sensitivity. It is suggested that more experimental and numerical studies are required to find best model of embossment membrane and eliminate the differences between two models in terms of sensitivity.

4. CONCLUSION

The frequency response and sensitivity of MEMS based fiber optic pressure sensor diaphragm with a central embossment were analytically investigated and compared using two different models. These models were developed previously and available in literature [26,33]. As a result of these analyses, the following conclusions are reached. M1 model based diaphragm structure show better sensitivity than M2 model based diaphragm structure and however, this model ignores the effect of embossment thickness on sensor performance. From these results, differences between diaphragm sensitivities were calculated. For example, 149.64-99.22 nm/kPa and 144.2-38.3 nm/kPa sensitivity range were calculated for the diaphragm based on the M1 and M2 model, respectively when 500 μm in radius and 10 μm thick diaphragm was used for calculations. On the other hand, these two diaphragm model show very close frequency values. For example, frequency range of 600 μm in radius and 5 μm thick diaphragm was changes between 28.6-15.4 kHz and 28.7-15.4 kHz when M1 and M2 model was considered, respectively.

M2 model based diaphragm not only includes more geometrical parameters for determination of sensitivity and but also provides stiffer membrane compared to M1 model based diaphragm due to lower membrane deformation under same pressure conditions. This provides more flexibility to tune sensitivity response of sensor. From the point of view of frequency response, both of M1 and M2 model based diaphragm show slight differences between the fundamental frequencies for thinner and wider embossment.

As a conclusion, we hoped that the results obtained from this study will be used as a comparative study and help the obtain more accurate theoretical and practical models of embossed diaphragm for the future studies.

Acknowledgments

The authors would like to acknowledge the reviwers and editors of Sakarya University Journal of Science.

Funding

The author (s) has no received any financial support for the research, authorship or publication of this study.

The Declaration of Conflict of Interest/ Common Interest

No conflict of interest or common interest has been declared by the authors.

The Declaration of Ethics Committee Approval

This study does not require ethics committee permission or any special permission.

The Declaration of Research and Publication Ethics

The authors of the paper declare that they comply with the scientific, ethical and quotation rules of SAUJS in all processes of the paper and that they do not make any falsification on the data collected. In addition, they declare that Sakarya

University Journal of Science and its editorial board have no responsibility for any ethical violations that may be encountered, and that this study has not been evaluated in any academic publication environment other than Sakarya University Journal of Science.

REFERENCES

[1] A. P. Jathoul et al., "Deep in vivo photoacoustic imaging of mammalian tissues using a tyrosinase-based genetic reporter," Nat. Photonics, vol. 9, no. 4, pp. 239–246, 2015.

[2] J. Zhu, L. Ren, S. C. Ho, Z. Jia, and G. Song, "Gas pipeline leakage detection based on PZT sensors," Smart Mater. Struct., vol. 26, no. 2, 2017.

[3] X. Qi et al., "Fiber Optic Fabry-Perot Pressure Sensor with Embedded MEMS Micro-Cavity for Ultra-High Pressure Detection," J. Light. Technol., vol. 37, no. 11, pp. 2719–2725, 2019.

[4] H. F. Zhang, K. Maslov, G. Stoica, and L. V. Wang, "Functional photoacoustic microscopy for high-resolution and noninvasive in vivo imaging," Nat. Biotechnol., vol. 24, no. 7, pp. 848–851, 2006.

[5] W. Ni et al., "Ultrathin graphene diaphragm-based extrinsic Fabry-Perot interferometer for ultra-wideband fiber optic acoustic sensing," Opt. Express, vol. 26, no. 16, p. 20758, 2018.

[6] J. Liu et al., "Fiber-optic Fabry–Perot pressure sensor based on low-temperature co-fired ceramic technology for high-temperature applications," Appl. Opt., vol. 57, no. 15, p. 4211, 2018.

[7] B. Liang et al., "Highly Sensitive, Flexible MEMS Based Pressure Sensor with Photoresist Insulation Layer," Small, vol. 13, no. 44, pp. 1–7, 2017.

[8] I. Padron, A. T. Fiory, and N. M. Ravindra, "Modeling and design of an embossed diaphragm fabry-perot pressure Sensor," Mater. Sci. Technol. Conf. Exhib. MS T'08, vol. 2, no. October 2017, pp. 992–997, 2008.

[9] C. Liao et al., "Sub-micron silica diaphragm-based fiber-tip Fabry–Perot interferometer for pressure measurement," Opt. Lett., vol. 39, no. 10, p. 2827, 2014.

[10] Y. Zhang, L. Yuan, X. Lan, A. Kaur, J. Huang, and H. Xiao, "High-temperature fiber-optic Fabry–Perot interferometric pressure sensor fabricated by femtosecond laser," Opt. Lett., vol. 38, no. 22, p. 4609, 2013.

[11] F. Xu et al., "High-sensitivity Fabry–Perot interferometric pressure sensor based on a nanothick silver diaphragm," Opt. Lett., vol. 37, no. 2, p. 133, 2012.

[12] Z. Li et al., "Highly-sensitive gas pressure sensor using twin-core fiber based in-line Mach-Zehnder interferometer," Opt. Express, vol. 23, no. 5, p. 6673, 2015.

[13] S. J. Mihailov, D. Grobnic, C. W. Smelser, P. Lu, R. B. Walker, and H. Ding, "Bragg grating inscription in various optical fibers with femtosecond infrared lasers and a phase mask," Opt. Mater. Express, vol. 1, no. 4, p. 754, 2011.

[14] S. Liu et al., "Nano silica diaphragm in-fiber cavity for gas pressure measurement," Sci. Rep., vol. 7, no. 1, pp. 1–9, 2017.

[15] H. Y. Choi, G. Mudhana, K. S. Park, U.-C. Paek, and B. H. Lee, "Cross-talk free and ultra-compact fiber optic sensor for simultaneous measurement of temperature and refractive index," Opt. Express, vol. 18, no. 1, p. 141, 2010.

[16] M. Deng, T. Zhu, Y. J. Rao, and H. Li, "Miniaturized fiber-optic fabry-perot interferometer for highly sensitive refractive index measurement," 2008 1st

Asia-Pacific Opt. Fiber Sensors Conf. APOS 2008, vol. 16, no. 8, pp. 14123–14128, 2008.

[17] L. Zhang et al., "A diaphragm-free fiber Fabry-Perot gas pressure sensor," Rev. Sci. Instrum., vol. 90, no. 2, 2019.

[18] M. Nespereira, J. M. P. Coelho, and J. M. Rebordão, "A refractive index sensor based on a Fabry-Perot interferometer manufactured by NIR laser microdrilling and electric arc fusion," Photonics, vol. 6, no. 4, 2019.

[19] X. Wang et al., "Non-destructive residual pressure self-measurement method for the sensing chip of optical Fabry-Perot pressure sensor," Opt. Express, vol. 25, no. 25, p. 31937, 2017.

[20] J. Zhu, M. Wang, L. Chen, X. Ni, and H. Ni, "An optical fiber Fabry–Perot pressure sensor using corrugated diaphragm and angle polished fiber," Opt. Fiber Technol., vol. 34, no. 1, pp. 42–46, 2017.

[21] M. Manuvinakurake, U. Gandhi, M. Umapathy, and M. M. Nayak, "Bossed diaphragm coupled fixed guided beam structure for MEMS based piezoresistive pressure sensor," Sens. Rev., vol. 39, no. 4, pp. 586–597, 2019.

[22] X. Wang, B. Li, O. L. Russo, H. T. Roman, K. K. Chin, and K. R. Farmer, "Diaphragm design guidelines and an optical pressure sensor based on MEMS technique," Microelectronics J., vol. 37, no. 1, pp. 50–56, 2006.

[23] S. S. Kumar and B. D. Pant, "Polysilicon thin film piezoresistive pressure microsensor: design, fabrication and characterization," Microsyst. Technol., vol. 21, no. 9, pp. 1949–1958, 2015.

[24] B. Tian et al., "Fabrication and structural design of micro pressure sensors for Tire Pressure Measurement Systems (TPMS)," Sensors, vol. 9, no. 3, pp. 1382–1393, 2009.

[25] Z. Yu, Y. Zhao, L. Sun, B. Tian, and Z. Jiang, "Incorporation of beams into bossed diaphragm for a high sensitivity and overload micro pressure sensor," Rev. Sci. Instrum., vol. 84, no. 1, 2013.

[26] Y. Sun, G. Feng, G. Georgiou, E. Niver, K. Noe, and K. Chin, "Center embossed diaphragm design guidelines and Fabry-Perot diaphragm fiber optic sensor," Microelectronics J., vol. 39, no. 5, pp. 711–716, 2008.

[27] Z. Gong, K. Chen, Y. Yang, X. Zhou, and Q. Yu, "Photoacoustic spectroscopy based multi-gas detection using high-sensitivity fiber-optic low-frequency acoustic sensor," Sensors Actuators, B Chem., vol. 260, pp. 357–363, 2018.

[28] S. E. Hayber, T. E. Tabaru, and O. G. Saracoglu, "A novel approach based on simulation of tunable MEMS diaphragm for extrinsic Fabry–Perot sensors," Opt. Commun., vol. 430, no. August 2018, pp. 14–23, 2019.

[29] D. B. Duraibabu et al., "An optical fibre depth (pressure) sensor for remote operated vehicles in underwater applications," Sensors (Switzerland), vol. 17, no. 2, pp. 1–12, 2017.

[30] Z. Gong, K. Chen, Y. Yang, X. Zhou, W. Peng, and Q. Yu, "High-sensitivity fiber-optic acoustic sensor for photoacoustic spectroscopy based traces gas detection," Sensors Actuators, B Chem., vol. 247, pp. 290–295, 2017.

[31] C. Fu, W. Si, H. Li, D. Li, P. Yuan, and Y. Yu, "A novel high-performance beam-supported membrane structure with enhanced design flexibility for partial discharge detection," Sensors (Switzerland), vol. 17, no. 3, 2017.

[32] W. Ma, Y. Jiang, J. Hu, L. Jiang, and T. Zhang, "Microelectromechanical system-based, high-finesse, optical fiber Fabry–Perot interferometric pressure sensors,"

Sensors Actuators, A Phys., vol. 302, no. September, p. 111795, 2020.

[33] F. Wang, Z. Shao, J. Xie, Z. Hu, H. Luo, and Y. Hu, "Extrinsic fabry-pérot underwater acoustic sensor based on micromachined center-embossed diaphragm," J. Light. Technol., vol. 32, no. 23, pp. 4026–4034, 2014.

[34] Y. Yu et al., "Design of a Collapse-Mode CMUT with an Embossed Membrane for Improving Output Pressure," IEEE Trans. Ultrason. Ferroelectr. Freq. Control, vol. 63, no. 6, pp. 854–863, 2016.

[35] W. Zhang, H. Zhang, F. Du, J. Shi, S. Jin, and Z. Zeng, "Pull-In Analysis of the Flat Circular CMUT Cell Featuring Sealed Cavity," Math. Probl. Eng., vol. 2015, 2015.

[36] M. Chattopadhyay and D. Chowdhury, "Design and performance analysis of MEMS capacitive pressure sensor array for measurement of heart rate," Microsyst. Technol., vol. 23, no. 9, pp. 4203–4209, 2017.

[37] H. Gharaei and J. Koohsorkhi, "Design and characterization of high sensitive MEMS capacitive microphone with fungous coupled diaphragm structure," Microsyst. Technol., vol. 22, no. 2, pp. 401–411, 2016.

[38] J. Baltrušaitis, "Methylated Poly(ethylene)imine Modified Capacitive Micromachined Ultrasonic Transducer for Measurements of CO2 and SO2 in Their Mixtures," Sensors, vol. 19, no. 3236, 2019

[39] J. Ma, Miniature Fiber-Tip Fabry–Perot Interferometric Sensors for Pressure and Acoustic Detection (Doctoral dissertation), The Hong Kong Polytechnic University, 2014. http://hdl.handle.net/10397/7136.

SAKARYA ÜNİVERSİTESİ
FEN BİLİMLERİ ENSTİTÜSÜ DERGİSİ

Sakarya University Journal of Science
SAUJS

e-ISSN 2147-835X | Period Bimonthly | Founded: 1997 | Publisher Sakarya University |
http://www.saujs.sakarya.edu.tr/en/

Title: Turkish Sentiment Analysis on Social Media

Authors: Nazan KEMALOĞLU, Ecir KÜÇÜKSİLLE, Muhammed Emin ÖZGÜNSÜR

Recieved: 2021-02-01 23:00:06

Accepted: 2021-04-01 12:13:10

Article Type: Research Article

Volume: 25
Issue: 3
Month: June
Year: 2021
Pages: 629-638

How to cite
Nazan KEMALOĞLU, Ecir KÜÇÜKSİLLE, Muhammed Emin ÖZGÜNSÜR; (2021), Turkish Sentiment Analysis on Social Media. Sakarya University Journal of Science, 25(3), 629-638, DOI: https://doi.org/10.16984/saufenbilder.872227
Access link
http://www.saujs.sakarya.edu.tr/en/pub/issue/62736/872227

Sakarya University Journal of Science 25(3), 629-638, 2021

Turkish Sentiment Analysis on Social Media

Nazan KEMALOĞLU[*1], Ecir Uğur KÜÇÜKSİLLE[2], Muhammed Emin ÖZGÜNSÜR[3]

Abstract

The number of social media users has increased significantly as internet access and internet usage has grown all over the world. As it is the case in any other field, raw data collected from social media platforms are now being transformed into information. Millions of pieces of content are posted every day on platforms such as Twitter, Facebook, and Instagram. Moreover, the ability to extract meaningful information from such content has become an important field of research. This study reports a system for sentiment analysis, based on the data made available on Facebook, Twitter, Instagram, YouTube along with RSS data. Logistic Regression, Random Forest and deep learning algorithm such as Long Short-Term Memory (LSTM) are used to develop the classification model used in the system built as part of this study. Dataset is a new dataset that included data collected from Twitter, used was created and labeled by us. It was found that LSTM model provided the highest accuracy among the models generated using the training dataset. The final version of the model was tested on five different social media platforms and results are communicated.

Keywords: Artificial Neural Network, Turkish Natural Language Processing, Social Media Analysis, Sentiment Analysis

1. INTRODUCTION

In our modern world, global internet usage has grown rapidly, making it an indispensable part of our daily lives. According to 2018 statistics, 79 of the internet users are also actively using social media [1]. The fact that the number of internet users, and therefore social media users has grown so drastically make it necessary for the academia to conduct sentiment analysis, relationship analysis, etc. on social media. Contents shared on social media platforms, communicating users' ideas and opinions, show distinctive characteristics. Therefore, these contents need to be transformed using natural language processing methods if we want to process them. Literature

[*]Corresponding author: nkemaloglu@mehmetakif.edu.tr
[1]Burdur Mehmet Akif Ersoy University, Department of Information Technology, 15000, Burdur.
E-Mail: nkemaloglu@mehmetakif.edu.tr
ORCID: https://orcid.org/0000-0002-6262-4244
[2]Süleyman Demirel University, Faculty of Engineering, Computer Engineering Department, 32000, Isparta
E-Mail: ecirkucuksille@sdu.edu.tr
ORCID: https://orcid.org/0000-0002-3293-9878
[3] Antalya Metropolitan Municipality, Information Technology Department, 07000, Antalya.
E-Mail: eozgunsur@gmail.com
ORCID: https://orcid.org/0000-0002-0859-5120

review showed that Twitter is the go-to social media platform for social media analysis. Literature review further showed that natural language processing (NLP) is used for analyses performed in order to identify questions [2], to calculate ratings [3], to track stock exchange trends [4], and to define side effects of pharmaceuticals [5]. The main purpose of sentiment analysis is to explore individuals' moods, behaviors and ideas using textual documents [6]. With the increasing number of social media users today, there is an abundance of texts including ideas which calls for studies on sentiment analysis. In [7], used tweets classified under 4 categories. Authors developed separate Word2Vec models using product sum method. In their study, authors first classified 4 categories (Banking, Football, Retail, Telecom) based on their positive and negative characteristics; then, they reclassified the combined data, again based on their positive and negative characteristics. Authors used Random Forest and SVM classification algorithms. The results of the study showed that the classification based on the cumulative dataset offered more accurate results when compared to the results obtained using separate categories. Moreover, it was found that the Word2Vec model with sum symbol offers better results when compared to the Word2Vec model with product symbol. In [8], analyzed the tweets obtained from Twitter API. Authors defined the features based on BoW (Bag of Words) model and N-gram model at the character level from the tweets collected. The features obtained were then reduced using CfsSubset algorithm and the most useful ones were selected. Boolean, TF and TF-IDF were used to define the weights of the features obtained. Among the classification algorithms, SVM, Naive Bayes, KNN (K Nearest Neighbour) and Multinominal Naive Bayes were used. It was found that, among these algorithms, Multinominal Naive Bayes resulted in the highest success rate with 66.06%. It was further found that, in the feature extraction process, N-gram model gives better results when compared to BoW model. In [9], extracted features from the dataset obtained from Twitter API using n-gram model. Author extracted seven different N-gram features at the word level, namely 1-gram and 2-gram, 1-gram and 3-gram, 2-gram and 3- gram, 1-gram - 2-gram - 3-gram, 1-gram, 2-gram, 3-gram. SVM, Naive Bayes and Logistic Regression classification algorithms were used. Assessment of the study results showed that the highest accuracy was obtained from the dataset which combines 1-gram and 2-gram features using Naive Bayes algorithm with a 77.78% success rate. In [10], collected data from the Twitter API for 9 different categories. Authors used word-based method and N-gram model for the feature extraction from the dataset. Firstly, authors classified the dataset for 9 categories based on positive, negative and neutral characteristics and then reclassified the whole dataset based on positive, negative and neutral characteristics. According to the results of the study, the highest success rate, 89.5%, was obtained using Random Forest Algorithm as part of Word-based methods, while the success rate of the n-gram method for field-specific classification using SVM algorithm was found to be 90%. However, the same level of success couldn't be obtained using field independent methods. In [11], explored supervised and unsupervised term weighting methods for tweets posted in Turkish language. Authors weighted the features obtained using n-gram and word-based method with the help of six different weighting equations –which are commonly used in the literature– and the traditional TF and TF-IDF methods. Naive Bayes, SVM, Decision Tree (J48), Random Forest and 1 k-nearest neighbours algorithm were used in the study. Authors observed that supervised term weighting methods consistently yield more successful results. Nevertheless, it was noted that N-gram model is more successful than the word-based method. In [12], developed a system to automatically tag tweets –posted in Turkish– as positive, negative and neutral. Using both the positive and negative words in tweets based on a dictionary generated as part of the study, and based on 2-grams, 3-grams, and 4-grams, authors tested the tagging success rate of the system. Analyses showed that the system yields the highest success rate using the dictionary-based method. Moreover, it was found that, among the n-gram models used, 3-grams yield more accurate results when compared to the others. In [13], explored the political involvement of Twitter users based on tweets posted in Turkish. Focusing

on the tweets posted with regards to 2013 Gezi Park protests, authors first divided the dataset into two, namely objective/nonobjective and neutral; and then divided the objective/non-objective group into pro-protest and anti-protest categories. After creating a tweet-word matrix using the tweet dataset, authors classified the most effective features using chi-square test. According to the results of the study, it was found that SVM had the best performance in the first stage of classification with k=100, while Random Forest algorithm had the best performance in the second stage of classification as k-value did not have a significance in this stage. In [14], collected data from book reviews, movie reviews and shopping reviews posted by Turkish users and analyzed the collected data. Authors developed a multi-classifier system in the classification process. SVM and Naive Bayes algorithms were run with several ensemble methods and it was possible to achieve levels of accuracy up to 86.1 In [15], created a dataset of shopping and film reviews. They studied positive, negative sentiment analysis on this dataset. After preprocessing step, features were extracted from the data set with TF-IDF method and used in Naive Bayes and Logistic Regression Algorithms. In addition to these two machine learning algorithms, a specialized RNN architecture; LSTM, was used. For the LSTM word embedding method used. During the training of the LSTM model, different combinations of learning ratio, loss function, LSTM layer count, LSTM units number, batch size and optimizer parameters were tested. In total, over 10 hours of training, the LSTM model for positive-negative labels achieved success of 83.3% and resulting in a more acceptable result than the LR and NB algorithms. In [16], worked on 6 different datasets. The main aim of the study is to examine the success of different segmentation methods on classification. For this reason, after the data were divided into sentences using Zemberek library, used a total of 13 different segmentation methods on sentences. In the study, it was argued that the areas containing more than one sentence were reduced to a single sentence and that giving one sentence as an introduction to the model was more accurate in terms of emotion analysis. The features, obtained after the applied segmentation process were classified by LSTM. The results show that BPE-5k segmentation method is the most appropriate segmentation method in terms of accuracy and performance. In this study, a model which is able to perform sentiment analysis (positive, negative and neutral) was developed using the data collected from Twitter. This model was then assessed for its performance on Facebook, Twitter, Instagram, YouTube platforms and RSS data. In addition to BagofWords and TF-IDF methods, word indexing method was used in the term weighting process. As an feature extraction method which offered high performance in English [17], but failed to match that performance in Turkish [10,11], word indexing method was used in the system which was developed for Turkish, a language known with its challenging structure. The features extracted using the aforementioned method were then modeled using Logistic Regression, Random Forest and LSTM classification algorithms and the highest success rate was obtained from LSTM model at 84.46%. The data set used in the study; It is a unique data set that contains 3 tags that we label positive, negative and neutral. While using the data collected through Twitter for training the model; The model is used for 5 different social media platforms: Twitter, Instagram, Youtube, RSS and Facebook. Supported with the high success rate obtained in this study, the model was used for sentiment prediction on a large social media analysis interface. Logged into this system, users were able to correct any erroneous tags. After being corrected, these tags were saved on a MySQL database in order to be added to the dataset. The model automatically updated daily with the new data.

2. MATERIAL AND METHODS

2.1. Dataset

Data was collected from five social media platforms using their APIs in order to be used as an input in the system developed. In the first stage, only the data obtained from Twitter was used for the training of the system as the data tagging is a time-consuming process. A total of 28189 data were tagged by the specialist. Dataset included 5712 positive, 11567 negative, and

11247 neutrals tweets. The data set is divided into 30% test and 70% training data.

2.2. Data Pre-Processing

As the data obtained from social media represents an individual idea of a user or a group, such data do not follow a certain pattern or rule. Data obtained from social media include abbreviations (internet slang), emoji's (i.e., pictorial icons that generally display a sentiment) and web links (URL), etc. Thus, a number of data preprocessing steps are used in order to have the social media data ready for processing. In this study, the following data preprocessing steps were taken: – Usernames starting with @ symbol (mention) were removed. – Statements starting with # symbol (hashtag) were removed. – Numerical terms were removed. – Repeated letters were removed. – URLs (https:/, www, etc.) were removed. – Punctuation marks (".", "," ,"""", etc.) were removed. – All the uppercase letters were turned into lowercase letters. Following the preprocessing, all the remaining words were reduced to their root words using Zemberek Library [19]. Finally, data obtained were subjected to numeric vectorization.

2.3. Word Representation

After preprocessing, data need to be transformed into numeric data in order to be processed in the classification stage. Vector representation of words was first used by Bengio et al. [19]. This method allows for integer representation of words and word groups [21]. Literature offers several methods developed for this purpose. Among the methods explored for this study were BagofWords, TF-IDF and Word Indexing.

2.4. Bag of Words (BoW)

A text is represented as the words it includes (n-gram) [20]. N-gram modeling is a segment of the character string which includes n characters [21]. In the BoW model, each word available in a text is considered to be a property, while the frequency of such word is the value of this property. Moreover, it is assumed that the order of words in a text has no statistical significance [23]. According to BoW model, words are represented as unigram and bigram n-gram series. Term weights, on the other hand, were used separately with binary methods. In the binary method, an n-gram takes the value of 1 if it exists in the text, and it takes the value of 0 if it doesn't exist in the text.

2.5. Term Frequency - Inverse Document Frequency (TF-IDF)

TF-IDF is a weighting method based on the term frequency multiplied by inverse document frequency. This value is obtained following Equation (1), as follows:

$$tf * idf = \frac{f_{(t,d)}}{N} * log\ log\ (\frac{N}{1+n_t}) \quad (1)$$

Here; t represents the relevant n-gram term, d represents the relevant text, $f_{(t,d)}$ represents the term frequency of n-grams in the text, N represents the total number of words in the document, n_t represents how many different documents the term t (n-grams) occurs in [21].

2.6. N-Gram Modelling

N-gram modeling is one of the most commonly used methods in document classification. N-gram is a segment of the character string which includes n characters [9]. 1-gram, 2-gram, 3-gram representations at the word level are given below for the sentence, "Bug¨un hava ¸cok g¨uzel" (The weather is very nice today).

– 1-gram model: "Bugün" , "hava", "¸cok" , "güzel".

– 2-gram model: "Bugün hava", "hava ¸cok", "¸cok güzel"

– 3-gram model: "Bugün hava ¸cok", "hava ¸cok güzel"

2.7. Creating a Word-Sentence Matrix Using Indexing Method

A corpus was generated using all the data as part of the word indexing method. In this corpus, each unique word was represented with an integer.

Thus, a wordsentence matrix was created for each tweet. Then, a word-sentence matrix is created for each test data based on the sequence of the words available in the corpus. In the feature extraction stage, a total of 5 datasets were created. These datasets are shown in Table 1.

Table 1 Datasets

Dataset	Method	N-Gram
Dataset 1	TF-IDF	Unigram/bigram(1-2–gram)
Dataset 2	BoW	Unigram/bigram(1-2–gram)
Dataset 3	Word Indexing	Unigram (1-gram)

2.8. The Used Libraries

The software for this study was developed using Python programming language. In the development stage, numpy, pandas, keras and scikit-learn libraries were used in addition to Phyton's built-in libraries.

2.9. Classification

Several methods were used for different vectors of words for classification as part of this study. Logistic Regression and Random Forest algorithms were used for BoW, TF-IDF and Indexing methods, while LSTM (Long Short Term Memory) deep learning algorithms, were also used for Indexing method.

2.10. Multinomial Logistic Regression (MLR)

Multinomial Logistic Regression (MLR) is a machine learning algorithm commonly used for the classification of feature vector belonging to a class among a number of possible classes. A function set is created from the feature vector, and each function stands for the probability of a feature vector to belong to a certain class. Parameters to complete these functions are obtained after the training process using the known class tags and feature vector. When these parameters are compared to a new feature vector similar to those compared in the training, Multinomial Logistic Regression is arrange in a way that the new vector has a high probability of belonging to the same class. Multinomial Logistic Regression converts the binary logistic regression procedure into a multi-class format. Each one of the classes has its own parameter vector which is applied to the feature vector in order to define the probability of feature vector [23]. Multinomial Logistic Regression is explained in Equation (2):

$$P(x_i, w) = \frac{exp\ (w^{(k)} h(x_i))}{\sum_{k=1}^{K} exp\ (w^{(k)} h(x_i))} \quad (2)$$

Here, h(x) is the vector of constant functions of input, $w^{(k)}$ is logistic regression with K-means clustering (aka. feature vector) and $w = [w^{(1)^T}, \dots, w^{(K-1)^T}]^T$. It equals zero w(k) = 0, when the density does not depend on w(k) regressors [24].

2.11. Random Forest Classifier

Random Forest Classifier is one of the most successful crowd learning techniques used in pattern recognition and machine learning, and it is commonly used for large-scale classification and skewness problems. Random Forest Algorithm is a system consisting of multiple decision trees [19]. Among its disadvantages related to the tree classifier is its inherently high variability. In practice, it is common that training dataset would lead to a whole different tree with the smallest of change. The reason behind this is the fact that tree classifiers have a hierarchical background. If an error occurs at a node closer to the root of the tree, then it disperses up to the farthest parts of the leaves. A decision forest methodology was developed with the purpose of stabilizing the tree classification. This methodology was first suggested by Ho [26], Amit & Geman [27] and later on by Breiman [28] in an integrated manner (as "random forest"). In Random Forest, each decision tree makes its own decision and the class with the majority vote in the decision forest is deemed as the decision class [21]. All the new data added to the classification are classified by each tree in the forest. Thus, each tree offers a classification result. As a rule, decision forest would select the classification with the majority vote of the trees in the forest. Random forest methodology includes Breiman's "bagging" idea and random selection of features, introduced first by Ho. Refers to bootstrap aggregation, bagging

is a type of crowd learning which was developed to improve the accuracy of a poor classifier creating a set of classifiers. If the number of samples in a dataset is N, then approx. 2/3 of the original sample size is randomly selected N times using preloading in order to be used in training. Remaining samples, on the other hand, are assessed "out-of-bag." Out-of-bag set consists of observations which are used for testing and those not selected to build the subtrees [29]. A random forest training is performed for each decision tree. Learning system creates a classifier from the sample and it adds all the classifiers obtained from different tests together in order to create the ultimate classifier. In order to classify a sample, each classifier casts a vote for the class that it belongs to and the sample is tagged as the member of the class with majority vote. In case of multiple classes with majority vote, one of them is selected randomly [29].

2.12. Recurrent Neural Networks (RNN)

Recurrent Neural Network (RNN) is an artificial neural network model which can utilize long sequences of inputs which is not possible with any other neural network [17]. RNN is especially preferable in Natural Language Processing (NLP) as it offers sequence processing abilities [32]. Basically, RNN learns also taking old data into account. However, such training is not possible due to gradient loss/exploding gradients during the training which is also considered a long-term dependency [17]. The RNN architecture shown in Figure 1 makes use of basic sequential information. In a classic neural network, all the inputs and outputs are assumed to be independent. The term "recurrent" used in RNN as each member of a sequence performs the same task in accordance with the previous outputs [31].

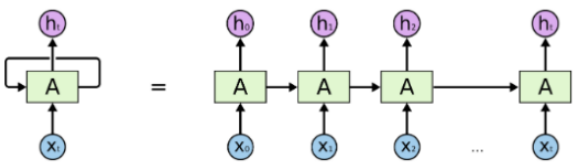

Figure 1 Classic RNN Architecture [22]

2.13. Long Short-Term Memory (LSTM)

LSTM models were developed with the aim to eliminate the exploding gradient issue in RNNs. LSTMs include a 'Forget' layer which is not available in recurrent neural network model [32]. The main idea behind LSTM models is to decide whether or not to store the information in the memory. LSTM have a custom architecture as shown in Figure 2.

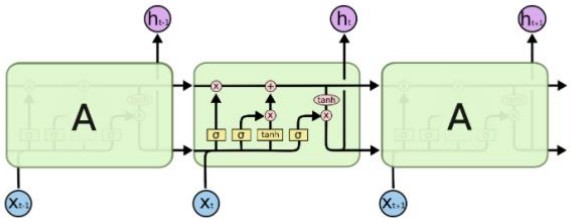

Figure 2 LSTM Model [22]

Memories, aka. cells, available in LSTM decide which information will be stored and which will not be stored. Following this decision, the model combines previous state output, current memory information and current input in a smart way to produce instant state output of the cell [17]. In the developed system, softmax activation function is used in all layers. In the model, "adam" optimization was used and 20 epochs were run.

3. EXPERIMENTAL RESULTS

Dataset obtained for this study was first vectorized separately using BoW, TF-IDF and Word Indexing and then tested using five different classifiers. Table 2 shows the classification success rates.

Table 2 Classification Success Rates

Dataset/Algorithm	Precesion	Recall	F1-Score	Accuracy
Dataset1/ MLR	0.85	0.81	0.82	83.07
Dataset1/ RF	0.86	0.83	0.84	84.24
Dataset2/ MLR	0.82	0.79	0.80	80.91
Dataset2/ RF	0.85	0.83	0.84	83.93
Dataset3 /LSTM	0.84	0.84	0.84	**84.46**

According to Table 2, it is seen that Multinominal Logistic Regression algorithm shows less success on Dataset-1 and Dataset-2 than Random Forest algorithm. In addition, it was observed that the highest success on the created data sets was the LSTM model on the set created with the indexing method. The confusion matrices obtained as a result of the data sets created and the algorithms used are given in Figure 3.

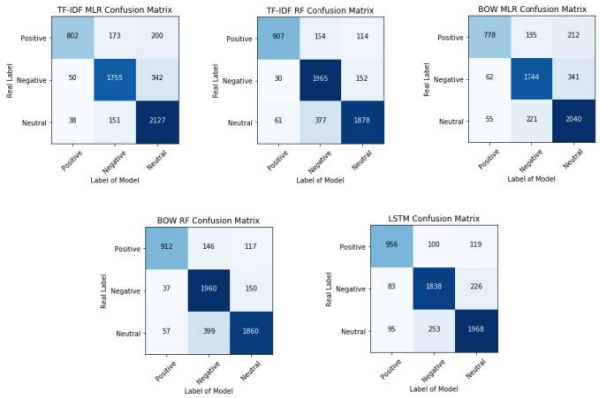

Figure 3 Confusion Matrixes of Models

Analysis results showed that LSTM model which uses indexing method gave the highest accuracy. Following this procedure, the classification model which was trained using Twitter data was tested for Twitter, Instagram, YouTube, Facebook and RSS.

4. SYSTEM

LSTM model trained with Twitter data and the corpus generated with these data were used as output in order to be used for 5 different social media platforms. Figure 4 shows how the model was applied to the system.

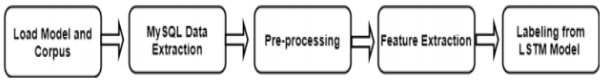

Figure 4 System Model

After the model and the corpus, as output of the previously trained system, were uploaded to the system, data were collected from 5 different tables available in MySQL database. The data were then subjected to the pre-processing steps as defined in Section 2.2. The processed data were digitized using the indexing method as defined in Section 2.3. Finally, digitized data were tested in the model and tags were extracted; then the database was updated using these tags. Figure 5 shows the change in users' moods based on weekly data extracted from YouTube with regards to a selected subject. The graphic shows 6 negative and 1 positive results out of 50 different posts from January 3rd, 2019. Remaining contents were neutral. Neutral contents were not represented in the graphic as they are insignificant for the system. The same applies to Figures 6, 7, 8 and 9.

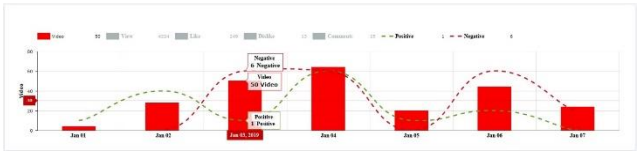

Figure 5 Weekly mood graphic based on a subject selected for YouTube

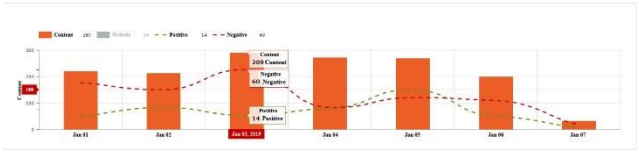

Figure 6 Weekly mood graphic based on a subject selected for RSS

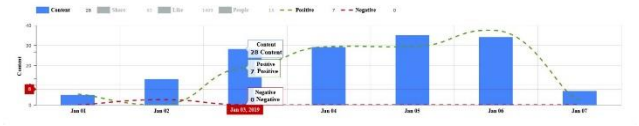

Figure 7 Weekly mood graphic based on a subject selected for Facebook

Figure 8 Weekly mood graphic based on a subject selected for Instagram

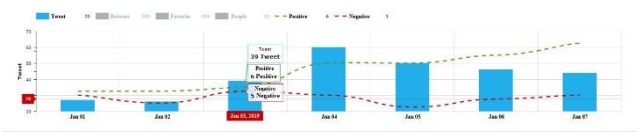

Figure 9 Weekly mood graphic based on a subject selected for Twitter

5. CONCLUSION

Natural language processing in Turkish is considered a challenge given the complex structure of this language. This challenge doubles when the study focuses on a person's or a group's ideas as in sentiment analysis. Nevertheless, the fact that the use of proper language is no longer the main concern, as reported by studies on social media, brings about a number of problems. Complex nature of social media data, irregularities such as the use of abbreviations, emojis, URLs, and adding emphasis with the use of more than necessary letters require the data to be pre-processed. As a result of the analysis, the highest result was obtained from the LSTM model with a success rate of 84.46%. It is seen that the LSTM model chosen to be used for the developed system has achieved a very high rate compared to the studies in the literature. However, among the other algorithms used, it was observed that the Random Forest algorithm on Dataset 1 and Dataset 2 achieved a higher rate than the Multinominal Logistic Regression algorithm. When confusion matrixes (Fig 3) is examined, it is seen that the data with neutral labels are classified more accurately compared to the other two labels. However, positive data could be labeled with less success than the other two labels. The reason for this is thought to be the low rate of positive labeled data in the total dataset. In the following periods, studies will be continued by expanding the dataset. In addition, the same number of data from each label class will be studied so that inconsistencies between data labels do not negatively affect the model. Due to short data processing times and high success rates, LSTM model was selected to be used in combination with the system developed. Users can edit the wrong tags on the interface and save them, with the developed system. After the saved edits, the model is used in the update step. LSTM model is used by retraining with daily data.

Funding

The author (s) has no received any financial support for the research, authorship or publication of this study.

The Declaration of Conflict of Interest/ Common Interest

No conflict of interest or common interest has been declared by the authors.

Authors' Contribution

The authors contributed equally to the study.

The Declaration of Ethics Committee Approval

This study does not require ethics committee permission or any special permission.

The Declaration of Research and Publication Ethics

The authors of the paper declare that they comply with the scientific, ethical and quotation rules of SAUJS in all processes of the paper and that they do not make any falsification on the data collected. In addition, they declare that Sakarya University Journal of Science and its editorial board have no responsibility for any ethical violations that may be encountered, and that this study has not been evaluated in any academic publication environment other than Sakarya University Journal of Science.

REFERENCES

[1] Smartinsigh.com, https://www.smartinsights.com/social-medi-marketing/social-media-strategy/newglobal social-media-research/, Access Date: 21.04.2019.

[2] Ozger, Z.B., Diri, B., "Classification Based Turkish Question Perception", Innovations

and Applications in Smart Systems, ASYU, İzmir, (2014)

[3] Kayahan, D., Sergin, A., Diri, B.," Determination of TV Programme Ratings by Twitter", IEEE 21st Signal Processing and Communication Applications. 1-4, (2013)

[4] Bollen J, Mao H, Zeng X., "Twitter mood predicts the stock market", Journal of Computational Science, 2(1): 1-8, (2011)

[5] Bian, J., Topaloglu, U., Yu, F., "Towards large-scale twitter mining for drug-related adverse events", In Proceedings of the 2012 international workshop on Smart health and wellbeing, 25-32, (2012, October)

[6] Eliaçik, A. B., Erdogan, N., "User Weighted Sentiment Analysis Method for Financial Communities in Twitter", In 11th International Conference on Innovations in Information Technology (IIT), 46-51, (2015)

[7] Ayata, D., Saraçlar, M., Özgür, A.,"Turkish tweet sentiment analysis with word embedding and machine learning", In 2017 25th Signal Processing and Communications Applications Conference, 1-4, (2017, May)

[8] Çoban, Ö., Özyer, B., Özyer, G. T., "Sentiment analysis for Turkish Twitter feeds", In 2015 23nd Signal Processing and Communications Applications Conference, 2388-239, (2015, May)

[9] Onan, A., "Sentiment Analysis On Twitter Messages Based On Machine Learning Methods", Journal of Management Information Systems, 3(2): 1-14 (2017)

[10] Meral, M., Diri, B., "Sentiment analysis for Turkish Twitter feeds", IEEE 22nd Signal Processing and Communication Applications, 23-2, (2014)

[11] Çetin, M., Amasyalı, M. F., "Supervised and Traditional Term Weighting Methods for Sentiment Analysis", In Proceedings of Signal Processing and Communications Applications Conference, 1-4, (2013)

[12] Akgül, E. S., Ertano, C., Diri, B., "Sentiment analysis with Twitter", Pamukkale University Journal of Engineering Sciences, 22(2): 106-110, (2016)

[13] Türkmen, A. C., Cemgil, A. T., "Political interest and tendency prediction from microblog data", In 2014 22nd Signal Processing and Communications Applications Conference (SIU), 1327-1330, (2014, April)

[14] Catal, C., Nangir, M., "A sentiment classification model based on multiple classifiers", Applied Soft Computing, 50: 135-141, (2017)

[15] Ciftci, B., Apaydin, M. S., "A Deep Learning Approach to Sentiment Analysis in Turkish", In 2018 International Conference on Artificial Intelligence and Data Processing (IDAP), 1-5, (2018, September)

[16] Kurt, F., Investigating the Effect of Segmentation Methods on Neural Model based Sentiment Analysis on Informal Short Texts in Turkish, Master's thesis, Middle East Technical University, Ankara, (2018)

[17] Ayata, D., Saraçlar, M., Özgür, A., "Political opinion/sentiment prediction via long short term memory recurrent neural networks on Twitter", In 2017 25th Signal Processing and Communications Applications Conference, 1-4, (2017, May)

[18] Akın, A. A., Akın, M. D., "Zemberek, An Open Source Nlp Framework For Turkic Languages." Structure, 10: 1-5, (2007)

[19] Bengio, Y., Ducharme, R., Vincent, P. , Jauvin, C., "A Neural Probabilistic Language Model", Journal of Machine Learning Research, 1137{1155, (2003)

[20] Şahin, G., "Turkish document classification based on Word2Vec and SVM classifier", In 2017 25th Signal Processing and Communications Applications Conference, 1-4, (2017, May)

[21] Doğan, S., Diri, B., "A new N-gram based classification (Ng-ind) for Turkish documents: author, genre and gender", TBV Journal of Computer Science and Engineering, 3(1): 11- 19, (2010)

[22] GitHub.com, http://colah.github.io/posts/2015-08-Understanding-LSTMs/ Access Date: 21.04.2019.

[23] Kim, T., Wright, S. J., "PMU placement for line outage identification via multinomial logistic regression", IEEE Transactions on Smart Grid, 9(1): 122-131, (2018)

[24] Li, J., Bioucas-Dias, J. M., Plaza, A., "Semisupervised hyperspectral image segmentation using multinomial logistic regression with active learning", IEEE Transactions on Geoscience and Remote Sensing, 48(11): 4085-4098, (2010)

[25] Moraes, R., Valiati, J. F., Neto, W. P. G., "Document-level sentiment classification: An empirical comparison between SVM and ANN", Expert Systems with Applications, 40(2): 621-633, (2013)

[26] Ho, T., "Random decision forest", 3rd International Conf. on Document Analysis and Recognition, August 14{18, Montreal, Canada, 278{282, (1995)

[27] Amit, Y., Geman, D., "Shape quantization and recognition with randomized trees", Neural Comput. 9: 1545{1588, (1997)

[28] Breiman, L., "Random forests", Mach. Learn. 45(1): 5{32, (2001)

[29] Azar, A. T., Elshazly, H. I., Hassanien, A. E., Elkorany, A. M., "A random forest classifier for lymph diseases", Computer methods and programs in biomedicine, 113(2): 465-473, (2014)

[30] Çevik,K.K., Berber, F.S., Küçüksille, E.U., "Mapping location of a suspect by using forensic images taken with their own mobile phone", International Conference on Engineering Technologies (ICENTE'18), 93-96, (2018)

[31] Şeker, A., Diri, B., Balık, H. H., "A Review about Deep Learning Methods and Applications", Gazi Journal of Engineering Sciences (GJES), 3(3): 47-64, (2017)

[32] Kızrak, M. A., Bolat, B., "A Comprehensive Survey of Deep Learning in Crowd Analysis", International Journal of Informatics Technologies, 11(3): 263-286, (2018)

SAKARYA ÜNİVERSİTESİ
FEN BİLİMLERİ ENSTİTÜSÜ DERGİSİ

Sakarya University Journal of Science
SAUJS

e-ISSN 2147-835X | Period Bimonthly | Founded: 1997 | Publisher Sakarya University |
http://www.saujs.sakarya.edu.tr/en/

Title: Sentiment Classification Performance Analysis Based on Glove Word Embedding

Authors: Yasin KIRELLİ, Şebnem ÖZDEMİR

Recieved: 2021-02-25 17:30:10

Accepted: 2021-04-02 09:21:04

Article Type: Research Article

Volume: 25
Issue: 3
Month: June
Year: 2021
Pages: 639-646

How to cite
Yasin KIRELLİ, Şebnem ÖZDEMİR; (2021), Sentiment Classification Performance Analysis Based on Glove Word Embedding. Sakarya University Journal of Science, 25(3), 639-646, DOI: https://doi.org/10.16984/saufenbilder.886583
Access link
http://www.saujs.sakarya.edu.tr/en/pub/issue/62736/886583

Sakarya University Journal of Science 25(3), 639-646, 2021

Sentiment Classification Performance Analysis Based on Glove Word Embedding

Yasin KIRELLİ*[1], Şebnem ÖZDEMİR[1]

Abstract

Representation of words in mathematical expressions is an essential issue in natural language processing. In this study, data sets in different categories are classified as positive or negative according to their content. Using the Glove (Global Vector for Word Representation) method, which is one of the word embedding methods, the effect of the vector set based on the word similarities previously calculated on the classification performance has been analyzed. In this study, the effect of pre-trained, embedded and deterministic word embedding classification performance has analyzed by using Long Short-Term Memory (LSTM). The proposed LSTM based deep learning model has been tested on three different data sets and the results have been evaluated.

Keywords: Sentiment classification, word embedding, word weight, glove word embedding.

1. INTRODUCTION

As a result of the widespread use of digital platforms, users share their feedback and opinions on social platforms, shopping sites, blogs, and many other channels. Sentiment analysis has been a research subject of interest in extracting the outputs produced from texts in this respect not only in data mining but also in natural language processing. The perspective of users can be expressed mathematically by using their own shared words. Those statements can be positive, negative or neutral, and the theme of any outcome can be calculated in this sense [1]. For this reason, sentiment analysis, idea mining and text analysis can often be used interchangeably in this field. The main research subject of sentiment analysis is to make sentiment classification according to the stored text data on the platforms and to discover the idea based information accordingly. Not every comment gives a positive or negative opinion, finding the appropriate data set for better analysis is an important detail at this point. It is crucial to analyze opinions as areas of use: It is frequently preferred in primary sectors such as e-commerce, banking, advertising management [2,3].

In Natural language process research, words are represented vectorially with word embedding [4]. Word embedding allows words with the same meaning to be represented in a similar way. The aim is to create a coordinate system in which the relevant words are shown closer to each other. Word embedding is generally divided into two

*Corresponding author: yasin.kirelli@istinye.edu.tr
[1]İstinye University, Faculty of Economics, Administrative and Social Sciences, Management Information Systems Department, İstanbul.
E-Mail: sebnem.ozdemir@istinye.edu.tr
ORCID: https://orcid.org/0000-0002-3605-8621, https://orcid.org/0000-0001-6668-6285

different groups, frequency-based and prediction-based. It has been observed that probability based methods give more successful results in expressing similar words with close vectors compared to deterministic methods in word vector determination. Glove (Global Vectors for Word Representation) is a predictive word embedding techniques and is an unsupervised learning algorithm applied to obtain vector representations [5]. This technique has been developed by Stanford University. With this method, which consists of the synthesis of matrix factorization and skip-gram methods, a co-occurrence matrix is obtained. This matrix is based on the use of real corpus in subsequent estimates [1,6].

Long Short Term Memory is a deep learning methodology that created idea of having a memory for the learning process. Unlike CNN (Convolutional Neural Network), while extracting only the features in that state, LSTMs also remember previous entries [7,8]. It is a method that makes decisions according to this situation and is therefore more applicable in text processing [9,10]. In this study, LSTM and CNN models have been applied for the extraction of text

features. After the LSTM phase, inputs are provided to the CNN layer for convolution. Thus the emotion classification model has been established with vectorial (Word Frequency Index) and global vector word embedding methods using LSTM. Three different datasets have been used, consisting of movie, restaurant and e-commerce order comments consisting of different categories. Each dataset has 1000 comments. The performance of embedding methods on classification has been evaluated by using three datasets.

2.RELATED WORKS

Extraction of information from text has been an area that has been frequently studied recently. Abel et al. discussed the similarity concept underlying these techniques based on word similarity in word embedding techniques such as Word2Vec or Glove, which are calculated using big data corpora, as a research topic. In a similar study, Mattyws et al. have presented a patent categorization method based on word embedding and LSTM (Long Short-Term Memory) in the process of classifying patents and subgroups of patents [11]. Ashik et al. have discussed the impact results of pre-trained word embedding models in languages other than English [12].

Rafat et al. have discussed skip-gram, continuous bag-of-words (CBOW) and Glove model on 105000 Bengali articles. The effects of embedding models in different languages have been observed [13]. Wang et al. have created a new LSTM model. They have designed a model on Chinese words using the classical frequency-based word embedding technique [14].

3. MATERIAL AND METHOD

3.1. Methodology

In the study, three different experiments have designed. As shown in Figure 1, Glove and Frequency Index techniques, which are the vectors used for the representation of words, have been classified separately with three different datasets and their effect on the classification performance has been observed. In the following chapters, word embedding techniques and LSTM and CNN layers used in our model are explained.

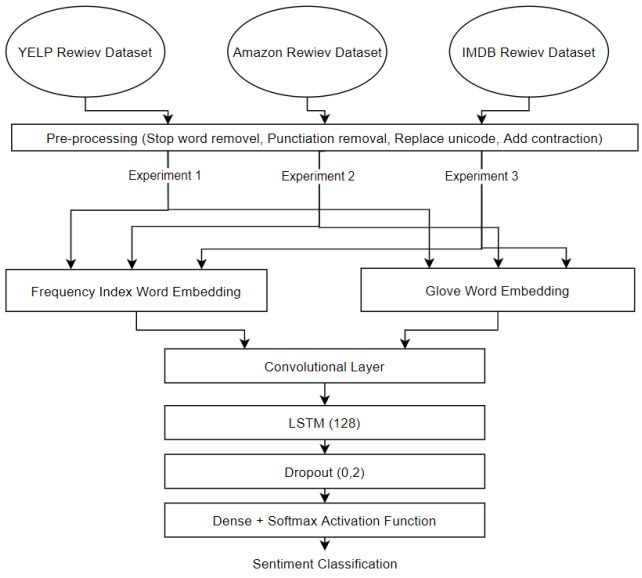

Figure 1 Experiment Model

3.1.1. Data Collecting and Pre-processing

Three different datasets are used for the model. The data have been provided over the data provided in the UCI Machine Learning Repository [15]. The data has been collected from the customer comments made by users on the websites amazon.com, imdb.com and yelp.com, respectively. It consists of positive and negative comments made by users in three different categories as shopping, movie reviews and restaurant reviews. Each dataset consists of 1000 comments and consists of 500 positive and 500 negative comment sentences. Stopwords have removed for 3 different datasets previously, tagged to sentiment labels and word clouds in Table 1 have been obtained by considering the word frequency conditions according to sentiment labels.Pre-processing of the data is a vital step that affects model performance. In the preprocessing process, capital and small letters have been checked respectively and all have been converted to lowercase letters. Punctuations have been deleted and stop words that frequently used in sentences have been removed. Thus, an optimized data set process has been prepared for the model.

Table 1 Wordcloud by sentiment label

Yelp Dataset	Amazon Dataset	IMDB Dataset
		
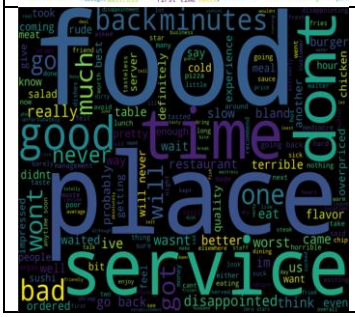	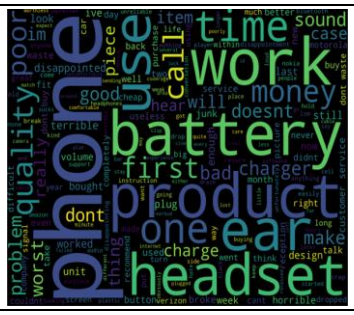	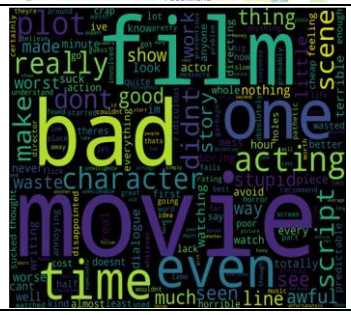

3.2. Word Embedding

With the word embedding step, words are converted to numbers expressed in vectors. In an artificial neural network, the mapping process in the hidden layer is performed for the words and the number representing. With embedding, dimension reduction is performed by using vectors expressing words and at the same time, words with the same meaning similarity are represented by close vectors [16].

3.2.1. Glove (Global Vector) Word Embedding

It is a model proposed by Stanford researchers [5]. According to this model, the vector representation of words is based on the similarity of words. This model has developed based on Skip-Gram and CBOW (Continuous Bag of Words) models. Using these two model approaches, it can be calculated more quickly and is aimed to give accurate results. Unlike the Skip-Gram and CBOW models, it also calculates the usage statistics of words. In this way, semantic relationships are also calculated. A new cost

function is calculated for this problem solution [5].

$$J = \sum_{i,j=1}^{V} f(X_{ij})(w_i^T w_j + b_i + b_j - log\, X_{ij})^2 \quad (1)$$

'Xij' in Formula 1 is the number of occurrences of two words in the corpus. 'V' means our corpus. The weight function 'f (Xij)' must keep the following conditions.

1. When f (0) = 0, terms should not converge to infinity.
2. It should not decrease the weight function F (x) while giving low weight for word pairs that are less common together.
3. For large values of Xij, which is the number of occurrences of two words in the dictionary, the weight function F (x) must be smaller [5].

'X' is expressed word to word co-occurence count matrix. 'Xij' stores the number of occurrences of word j in the context of word 'i'. 'bi' is the bias value added for 'i', symmetrically this case is added for 'j' as 'bj'. It is known that how to calculate according to each word and gradient descent can be applied to minimize the cost function.

3.2.2. Frequency Based Word Embedding

If we consider Corpus (word dictionary) C and each sentence as expression {d1, d2…, dn}, we get N unique words (tokens) extracted from each document. N tokens refer to our dictionary. The dimension of M, which we accept as the Count Vector matrix, appears as DXN. Each row in the M matrix in Figure 2 shows the number of repetitions of each document (Di).

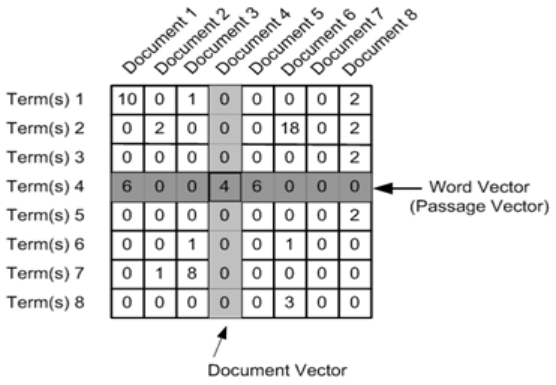

Figure 2 Word vector-matrix reference [17].

3.3. Experiments and Analysis

In this study, the model using three independent datasets, which are also specified in the flow diagram as Figure 1, has been implemented using two different word embedding techniques. All models have word embedding, text feature extraction and emotion extraction main components. In order to build a well organized classification by using LSTM based model, Python 3.8 and Keras deep learning library have been used. Unlike traditional neural networks, LSTM architecture can relate previous data to the existing one. It is a type of RNN (Recurrent Neural Network**)** that can learn long-term addictions and is widely used [18-19]. It has a repetitive neural network loop and each loop allows information to go back into the next neural network.

Table 2 Number of parameters in a model

Word Embedding Method	Glove Word Embedding	
Dataset	Layer (type)	Parameter Count
Yelp	Embedding	196700
	LSTM	80400
	Dense	101
	Total params	277,201
IMDB	Embedding	305300
	LSTM	80400
	Dense	101
	Total params	385,801
Amazon	Embedding	179900
	LSTM	80400
	Dense	101
	Total params	260,401
Word Embedding Method	Frequency Based Word Embedding	
Dataset	Layer (type)	Param

Yelp	Embedding	2000000
	LSTM	80400
	Dense	101
	Total params	2,080,501
IMDB	Embedding	2000000
	LSTM	80400
	Dense	101
	Total params	2,080,501
Amazon	Embedding	2000000
	LSTM	80400
	Dense	101
	Total params	2,080,501

Our model has subjected to a classification process for 10 epochs on 3 different datasets with 1000 pre-determined sentiment classes. Sentiment classification model, %80-%20 test and train set separation process has been performed. In three independent experiments with the Grove word embedding technique, higher accuracy results have obtained compared to the frequency index based word technique. The number of parameters in each model is shown in Table 2. The results showing the effect of the proposed models on accuracy are shown in Table 3. Glove word embedding technique has been observed accuracy results compared to frequency index based word embedding technique in 3 independent experiments. In addition, overfitting problems have been observed at early epoch levels when using frequency index based models. The main reason for this is that in the Gloveword embedding technique, vector representations that take into account more semantic associations are obtained by making use of external and larger datasets in the vector representation of words. On the other hand, the repetition frequency of the words on the dataset studied in frequency based word embedding and the tendency to memorize is higher because vector representations are formed over a narrow dataset.

Table 3 Accuracy Epoch Graphics

Dataset	**Accuracy Epoch Result Graphic Using Glove**	**Accuracy Epoch Result Graphic Using Frequency**
Yelp	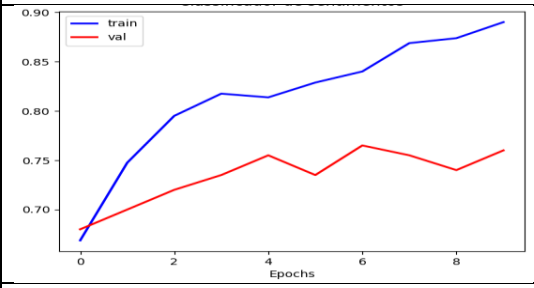	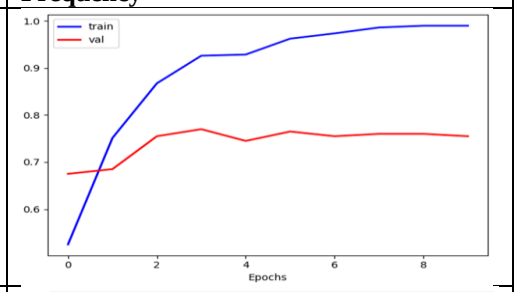
Amazon	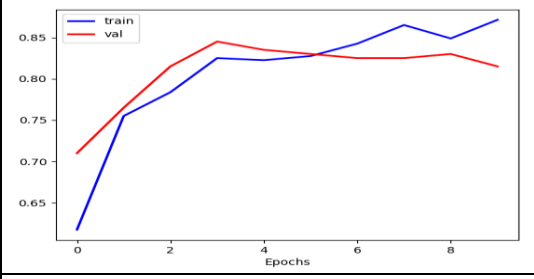	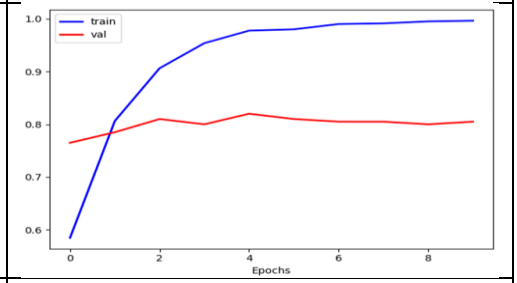
IMDB	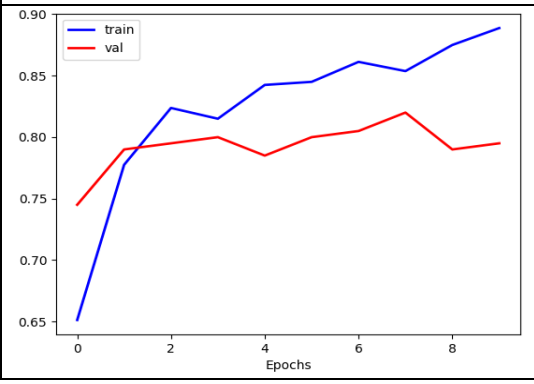	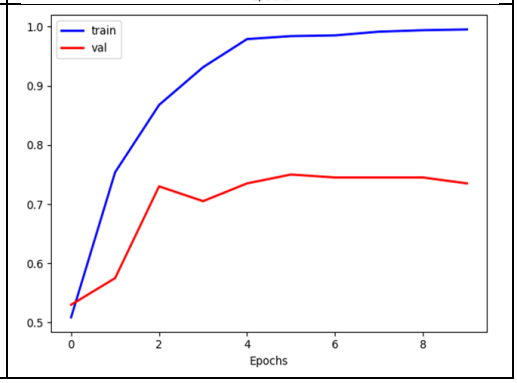

The vector representation of words in Natural Language Processing is an important factor in successful sentiment classification. In our study, the classification success of 2 different word embedding techniques has been observed with the LSTM convulutional model. In all three classification models, a maximum performance difference of 8% has been observed in classification with the proposed model according to the Glove word embedding and Frequency Based Word Embedding technique.

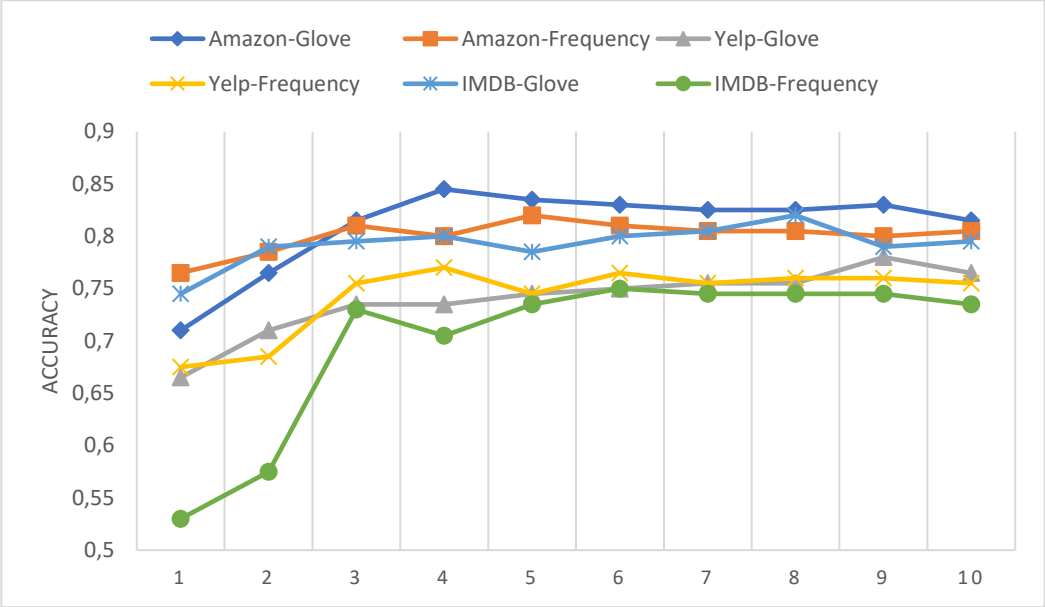

Figure 3 Comparative results by embedding model

In addition, when the Frequency model results have been observed, there is a high tendency to overfitting in the early steps, depending on the dataset and embedding technique. Although close classification rates are observed in Amazon and Yelp datasets as seen in Figure 3, a difference of 8% has observed for imdb dataset and also classification outcomes are as in Table 4.

Table 4 Precision, Recall and F-Score Rates

	Precision	Recall	F-Score
Amazon-Glove	0.8172	0.7917	0.8042
Amazon-Frequency	0.7849	0.7935	0.7892
Yelp-Glove	0.7292	0.7609	0.7447
Yelp-Frequency	0.7813	0.7282	0.7538
Imdb-Glove	0.8681	0.7315	0.794
Imdb-Frequency	0.6703	0.7262	0.6971

4. CONCLUSION

The size and diversity of the corpus with the proposed model affect the classification performance and the pre-trained vectorized techniques that increase the success in classification. For this purpose, the effect of pre-trained and model-dependent train word embedding methods on sentiment analysis has been observed in this study.

Despite the different datasets with high word density, better results have been obtained with the Glove word embedding technique, which

emphasises word similarity. Besides, the model can be trained faster and scalable for the huge corpora. Since it contains a pre-trained vector matrix, it creates a disadvantage with high memory consumption. We are trying to expand our findings in our future work further. In particular, we want to examine the results with different predictive models such as “fastText” and “word2vec”.

Funding

The author has no received any financial support for the research, authorship or publication of this study.

Contribution of the Authors

The authors have contributed equally to the work.

Ethics Committee Approval Notice

This study does not require ethics committee approval or any special permission.

Research and Publication Ethics Statement

In the writing process of this study, international scientific, ethical and citation rules have been followed and no falsification has been made on the collected data. Sakarya University Journal of Science and its editorial board have no responsibility for all ethical violations. All responsibility belongs to the responsible author and this study has not been evaluated in any academic publication environment other than Sakarya University Journal of Science.

REFERENCES

[1] H. Imaduddin, Widyawan and S. Fauziati, "Word Embedding Comparison for Indonesian Language Sentiment Analysis," 2019 International Conference of Artificial Intelligence and Information Technology (ICAIIT), Yogyakarta, Indonesia, 2019, pp. 426-430, doi: 10.1109/ICAIIT.2019.8834536.

[2] Eligüzel, N., Çetinkaya, C., & Dereli, T. (2020). Comparison of different machine learning techniques on location extraction by utilizing geo-tagged tweets: A case study. Advanced Engineering Informatics, 46, 101151. https://doi.org/10.1016/j.aei.2020.101151

[3] Chakraborty, K., Bhatia, S., Bhattacharyya, S., Platos, J., Bag, R., & Hassanien, A. E. (2020). Sentiment Analysis of COVID-19 tweets by Deep Learning Classifiers—A study to show how popularity is affecting accuracy in social media. Applied Soft Computing, 97, 106754. https://doi.org/10.1016/j.asoc.2020.106754

[4] Ayata, Deger & Saraclar, Murat & Ozgur, Arzucan. (2017). Turkish tweet sentiment analysis with word embedding and machine learning. 1-4. 10.1109/SIU.2017.7960195.

[5] Pennington, J., Socher, R., & Manning, C. D. (2014, October). Glove: Global vectors for word representation. In Proceedings of the 2014 conference on empirical methods in natural language processing (EMNLP) (pp. 1532-1543).

[6] Y. Sharma, G. Agrawal, P. Jain and T. Kumar, "Vector representation of words for sentiment analysis using GloVe," 2017 International Conference on Intelligent Communication and Computational Techniques (ICCT), Jaipur, 2017, pp. 279-284, doi: 10.1109/INTELCCT.2017.8324059.

[7] R. Ni and H. Cao, "Sentiment Analysis based on GloVe and LSTM-GRU," 2020 39th Chinese Control Conference (CCC), Shenyang, China, 2020, pp. 7492-7497, doi: 10.23919/CCC50068.2020.9188578.

[8] Li, Dan & Qian, Jiang. (2016). Text sentiment analysis based on long short-term memory. 471-475. 10.1109/CCI.2016.7778967.

[9] Ali, F., Kwak, D., Khan, P., El-Sappagh, S., Ali, A., Ullah, S., Kim, K. H., & Kwak, K.-S. (2019). Transportation sentiment analysis using word embedding and

ontology-based topic modeling. Knowledge-Based Systems, 174, 27–42. https://doi.org/10.1016/j.knosys.2019.02.033

[10] Q. Wang, L. Sun and Z. Chen, "Sentiment Analysis of Reviews Based on Deep Learning Model," 2019 IEEE/ACIS 18th International Conference on Computer and Information Science (ICIS), Beijing, China, 2019, pp. 258-261, doi: 10.1109/ICIS46139.2019.8940267.

[11] M. F. Grawe, C. A. Martins and A. G. Bonfante, "Automated Patent Classification Using Word Embedding," 2017 16th IEEE International Conference on Machine Learning and Applications (ICMLA), Cancun, 2017, pp. 408-411, doi: 10.1109/ICMLA.2017.0-127.

[12] A. A. A. Rafat, M. Salehin, F. R. Khan, S. A. Hossain and S. Abujar, "Vector Representation of Bengali Word Using Various Word Embedding Model," 2019 8th International Conference System Modeling and Advancement in Research Trends (SMART), Moradabad, India, 2019, pp. 27-30, doi: 10.1109/SMART46866.2019.9117386.

[13] A. A. A. Rafat, M. Salehin, F. R. Khan, S. A. Hossain and S. Abujar, "Vector Representation of Bengali Word Using Various Word Embedding Model," 2019 8th International Conference System Modeling and Advancement in Research Trends (SMART), Moradabad, India, 2019, pp. 27-30, doi: 10.1109/SMART46866.2019.9117386.

[14] J. Wang and Z. Cao, "Chinese text sentiment analysis using LSTM network based on L2 and Nadam," *2017 IEEE 17th International Conference on Communication Technology (ICCT)*, Chengdu, China, 2017, pp. 1891-1895, doi: 10.1109/ICCT.2017.8359958.

[15] Dimitrios Kotzias, Misha Denil, Nando de Freitas, and Padhraic Smyth. 2015. From Group to Individual Labels Using Deep Features. In Proceedings of the 21th ACM SIGKDD International Conference on Knowledge Discovery and Data Mining (KDD '15). Association for Computing Machinery, New York, NY, USA, 597–606. DOI:https://doi.org/10.1145/2783258.2783380

[16] Bhoir, Snehal & Ghorpade, Tushar & Mane, Vanita. (2017). Comparative analysis of different word embedding models. 1-4. 10.1109/ICAC3.2017.8318770.

[17] N. (2020, October 19). An Intuitive Understanding of Word Embeddings: From Count Vectors to Word2Vec. Analytics Vidhya. https://www.analyticsvidhya.com/blog/2017/06/word-embeddings-count-word2veec/

[18] K. Zhang, W. Song, L. Liu, X. Zhao and C. Du, "Bidirectional Long Short-Term Memory for Sentiment Analysis of Chinese Product Reviews," 2019 IEEE 9th International Conference on Electronics Information and Emergency Communication (ICEIEC), Beijing, China, 2019, pp. 1-4, doi: 10.1109/ICEIEC.2019.8784560.

[19] Chen, Nan & Wang, Peikang. (2018). Advanced Combined LSTM-CNN Model for Twitter Sentiment Analysis. 684-687. 10.1109/CCIS.2018.8691381.

SAKARYA ÜNİVERSİTESİ
FEN BİLİMLERİ ENSTİTÜSÜ DERGİSİ

Sakarya University Journal of Science
SAUJS

e-ISSN 2147-835X | Period Bimonthly | Founded: 1997 | Publisher Sakarya University |
http://www.saujs.sakarya.edu.tr/en/

Title: Determination of Phenolic Compounds, Organic Volatile Molecules and Anti-Cancer Properties in Inula Viscosa L., Viscum Album L. and Raphanus Sativus L.

Authors: Hafize DİLEK TEPE, Aslı UĞURLU, İdris YAZGAN

Recieved: 2020-06-08 13:30:08

Accepted: 2021-04-05 14:12:59

Article Type: Research Article

Volume: 25
Issue: 3
Month: June
Year: 2021
Pages: 647-662

How to cite
Hafize DİLEK TEPE, Aslı UĞURLU, İdris YAZGAN; (2021), Determination of Phenolic Compounds, Organic Volatile Molecules and Anti-Cancer Properties in Inula Viscosa L., Viscum Album L. and Raphanus Sativus L.. Sakarya University Journal of Science, 25(3), 647-662, DOI: https://doi.org/10.16984/saufenbilder.742432
Access link
http://www.saujs.sakarya.edu.tr/en/pub/issue/62736/742432

Sakarya University Journal of Science 25(3), 647-662, 2021

Determination of Phenolic Compounds, Organic Volatile Molecules and Anti-Cancer Properties in *Inula Viscosa* L., *Viscum Album* L. and *Raphanus Sativus* L.

Hafize DİLEK TEPE*[1], Aslı UĞURLU[2], İdris YAZGAN[2]

Abstract

The plants elecampane (*Inula Viscosa* L.), mistel (*Viscum album* L.) and black radish seed (*Raphanus Sativus* L.) have been used in the treatment of common diseases worldwide as part of traditional medicine for many years. Especially in Turkey, elecampane plant is commonly used as remedy of cancer. In this study, phytochemical components of these three plants were analyzed using liquid chromatography-mass spectrometer/mass spectrometer and gas chromatography-mass spectrometer techniques. Antioxidant activity of the characterized extracts were evaluated using DPPH assay, followed by biological properties were studied using MDA-MB-231 breast cancer line. Differences in the chemical compositions of the extracts resulted in alteration in antioxidant potentials, where elecampane gave the highest antioxidant activity while black radish seed extracts did not provide any meaningful results within the test period. Cytotoxicity studies showed that chemical composition is of the most prominent factor that defined the IC_{50} value of each extract, where pro-oxidant and antioxidant affects were observed in relation to presence of flavonoids. Mistel extract was further tested for wound healing and apoptosis tests, and the extract was obtained as a trigger for both apoptosis and wound-healing. The findings can be a basis for refinement as fractionation of the mistel and elecampane extracts so as to obtain the best mixture that can serve as strong anticancer agent mixture.

Keywords: Elecampene, mistel, phenolic compounds, LC-MS/MS, GC-MS, anticancer.

*Corresponding author: hafize.dilek@hotmail.com
[1] Manisa Celal Bayar University, Applied Science and Research Center (ASRC/DEFAM), Manisa.
ORCID: https://orcid.org/0000-0002-6035-6901
[2] Kastamonu University, Department of Biology, Kastamonu.
E-Mail: a.z.ugurlu@gmail.com; idrisyazgan@gmail.com.
ORCID: https://orcid.org/ 0000-0003-2131-2823; https://orcid.org/ 0000-0002-0264-1253.

1. INTRODUCTION

Cancer is a multifactorial and genetically complex disease. Biological mechanisms such as genetic/epigenetic mutations, continuous proliferative signals, overexpression of oncogenes, inactivation of tumor suppressor genes, inhibition of apoptosis, increased angiogenesis, and metastasis cause cancer development and progression [1]. Among the cancer types, breast cancer is one of the most common types of cancer that affects more than 1 million women worldwide. Breast cancer includes a heterogeneous population of cells. Based on histological and molecular analyzes, five different breast cancer subtypes have been identified as Luminal A (estrogen receptor ER+, progesterone receptor PR+, human epidermal growth factor receptor 2 Her2-), Luminal B (ER+, PR+, HER2+), TNBC (ER-, PR-, HER2-), Her2+ (ER-, PR-, Her2+) and normal breast-like [2]. These different subtypes of breast cancer respond differently to treatment. Nowadays, surgery, chemotherapy, targeted chemotherapy, hormonal therapy and radiotherapy are used in breast cancer treatment and these treatments provide a significant decrease in mortality rates. However, the heterogeneous nature of breast cancer is an obstacle for the treatment. Furthermore, cancer recurrence, metastasis and drug resistance may develop [3,4]. This reveals the need for more effective treatment strategies with less side effects for breast cancer. Bioactive components isolated from natural sources are capable of inhibiting DNA damage, cell proliferation, angiogenesis and metastasis, and stimulating apoptosis and autophagy [5]. Some preclinical studies showed that natural components increase the susceptibility of resistant cancers to existing chemotherapy drugs [6]. In addition, existing chemotherapy drugs usually have a single target effect, while natural components can target many signaling pathways altered in cancer cells [7]. Natural compounds are of great interest because they are less toxic than synthetic drugs and can also affect cancer stem cells. *In vitro* and in vivo studies have shown that a large number of plants and their bioactive compounds exert an inhibitory effect on breast cancer by reducing estrogen receptor expression, inhibiting cell cycle and proliferation, stimulating caspase-mediated apoptosis, reducing anti-apoptotic factors, inhibiting angiogenesis and metastasis [2], [8-13].

The genus *Inula* (Elecampane) belongs to the chamomile family and has different species (*Inula viscosa* L., *I. racemosa, I. helenium* L., *and I. Britannica* L.*)* with very high medicinal value. *Inula* grows in Africa, Asia and Europe, especially in the Mediterranean region. Traditional uses of *Inula* plant species were first used in Roman and Greek medicine. It is also used in traditional Chinese medicine in Ayurveda and Tibetan medicine to treat various diseases such as bronchitis, diabetes, fever, hypertension and inflammation [14]. In Turkey, flowers, leaves and roots of *I. viscosa* are consumed as food raw or cooked [15]. *I. viscosa* has attracted great interest in recent years as a natural source of bioactive compounds in its structure. The anti-inflammatory [16], anti-cancer [17] and antimicrobial [18] studies of this plant have been conducted. Due to the polyphenols in the structure has been shown to have strong antioxidant properties [19]. A complex mixture of secondary metabolites was already identified in *I. viscosa*, as flavonoids, sesquiterpenes lactones and acids, phenolic acids derivatives, glycolipids and triterpenoids [16], [20-23].

Viscum album L. is generally known as mistel and grows as a semi-parasite plant on different host trees in Europe and Asia. Mistel, with the help of the fringe roots, is coniferous like fir, pine, spruce; apple, plum, apricot, cherry-like fruit and poplar, chestnut, alder, oak, willow shed leaves in winter grows as semi-parasites on trees or shrubs [24]. Mistel is used in many different diseases in traditional medicine. These are cardiac diseases, hemorrhoid, diabetes, anxiety, headache, epilepsy, hyperactivity in children, anticancer, toothache, tonsillitis and throat ache, headache, asthma, prostatitis, hypercholesterolemia, hypertension, tachycardia, bronchitis, ulcer, gastritis, cough, hypercholesterolemia, atherosclerosis, splenopancreases diseases, sterility (woman) and brain tumor. *V. album* has remarkable popular usage in Turkish folk medicine as a remedy for cardiac diseases [25-

35]. To date, numerous studies have been carried out to determine the biological potential of the plant [36-38]. Various clinical studies reported the improvement in survival and quality of life, after using mistel extracts, underling the ability of the plant to support the conventional medicine [39]. It has been shown that the mistel extracts reduce the harmful and mutagenic effects of free oxygen radicals produced during radio and chemotherapy [40,41]. Extracts from subspecies have been shown to contain viscotoxins [42], phenylpropanoids [43] and flavonoids [44] in different concentrations depending on the subspecies.

Raphanus sativus L. (Brassicaceae), commonly known as radish, is used in the world as a vegetable or spice in human nutrition [45]. The roots, seeds and leaves of the radish plant show a variety of medicinal properties. In traditional Korean medicine, the seeds are used as degassing, diuretic, expectorant, laxative, stomach-strengthening anti-cancer and anti-inflammatory agents [46,47]. Radish has anti-carcinogenic activity because it contains phytochemicals, glucosinolates (GLS), phenolics, vitamins and their metabolites. In addition, vitamin C, a powerful antioxidant in its structure, prevents DNA and tissue damage caused by free radicals [48,49]. Many studies have been made in different species of radish. However, there are not many publications related to black radish seeds.

These three plant species mentioned above are used in similar diseases in Turkish and world traditional medicine. Therefore, in these three plants volatile biological molecules were scanned with gas chromatography- mass spectrometer (GC-MS) and 32 phenolic compounds were screened with liquid chromatography- mass spectrometer / mass spectrometer (LC-MS/MS) in this study. These scans were identified as some plant-specific phyto-component molecules. Thus, the antioxidant and anti-cancer properties of these three plants could be compared with each other.

2. MATERIAL AND METHODS

2.1. Extraction Process

Before the extraction process, elecampane (1), mistel (2), and black radish seeds (3) samples were washed in pure water and dried in an oven at 80 °C. For analysis, dried samples were pulverized in high-speed plant mill and prepared for extraction. 2 g of powdered plant samples were extracted in 40 mL of 80% methanol and ethanol in ultrasonic bath for 30 min then left at room temperature. The final extraction concentrate was then adjusted to 50 mg / mL.

2.2. Determination of volatile organic molecules by GC-MS

Volatile molecules in the extract were qualitatively analyzed in electron ionization (EI) mode with Agilent Technology 7890A Gas Chromatography (GC) Mass spectrometer (MS). Chromatographic column Agilent HP-5MS, capillary column (30 m* 0.25 mm, film thickness of 0.25 mm). The furnace temperature was started at 40 ^{0}C, followed by standing for 5 min, then at 5 ^{0}C. min^{-1} at 280 ^{0}C. and held for 5 min. Helium gas (99.999%) was used as the carrier gas. The constant flow rate was 1.5 mL min^{-1} and the injector temperature was 250 ^{0}C. The extract was injected in splitless mode with 1 mL. Interpretation of the mass spectrum was performed according to the National Institute of Standards and Technology (NIST) database.

2.3. Determination of phenolic compounds by LC-MS/MS

Determination of phenolic profiles of plants, high performance liquid chromatography mass spectrometer - mass spectrometer (Agilent 1260 Triple Quadrupole MSMS) was used. Each analysis was performed with 3 replications. HPLC column C18 ODS used in the analyzes (25 x 4.6 mm x 5µ) was used. Injection amount for analysis: 2 µL. Water / 0.1% formic acid (A), methyl alcohol (B) was used as carrier phase. The gradient method as follows: 3 min 2% B, 6 min 25% B, 10 min 50% B, 14 min 95% B, 17.5 min 2% B. Flow rate: 0.4 mL / min. In the identification of compounds was performed in positive and negative modes [50]. The chromatogram peaks of the standards and sample were shown in figure 1.

2.4. Antioxidant Test

DPPH (2,2-diphenyl-1-picryl-hydrazyl-hydrate) assay is based on electron-transfer from anti-oxidant molecule to the free radical DPPH molecule that produces a violet solution in ethanol, whose intensity is monitored optically [51], [52]. 0.1, 0.5,1.0 and 5.0 mg/mL DPPH solutions in ethanol, and 1.0, 5.0 and 10.0 mg/mL ascorbic acid prepared in ethanol were used to draw standard graphic. All the tested extracts were used as 1/10th and 1/100th dilutions of the stock to reveal antioxidant capability.

2.5. Cell Culture and Cell Viability Assay

Triple negative MDA-MB-231 breast cancer cells were grown in Dulbecco's Modified Eagle's Medium (DMEM) containing 10% fetal bovine serum (FBS), 1% non-essential amino acid (NEAA), 0.1% penicillin/streptomycin, and 0.01 mg/mL human insulin. The cells were incubated at 37°C in a humidified 5% CO_2 incubator. The 3-(4,5-dimethylthiazol-2-yl)-2,5-diphenyl tetrazolium bromide (MTT) assay was performed to analyze cytotoxic effects of the extracts. 10^4 MDA-MB-231 cells/well were seeded in 96-well plates and grown for 24 h. The cells were exposed to each test extract at different concentrations (0.25, 0.5, 1, 2.5, 6.25, 12.5, 25 mg/mL) and incubated for 24 h. After extract treatment, 0.5% FBS and 0.5 mg/mL MTT containing DMEM was added and incubated for 4 h at 37°C. Formazan crystals were dissolved in 40 mM HCl/isopropanol and 3% SDS, and the optical density was measured at 570 nm using Multiskan Go (Thermo Scientific). IC_{50} values were calculated using GraphPad Prism software.

2.6. Gene Expression Analysis

Subconfluent MDA-MB-231 cells were treated with Mistel extract at doses of IC_{50} values for 24 h. GeneJET RNA Purification Kit (Thermo Scientific) was used for RNA isolation and DNase treatment was performed for 30 min at 37°C. RevertAid First Strand cDNA synthesis kit (Thermo Scientific) was used to convert total RNA (2 µg) into cDNA according to instructions. qPCR reaction mixture was prepared with 10 µL of SYBR Green (Biorad), 1 µL of forward and reverse primer (5 µM), 1 µL of cDNA and 7 µL of dH2O were. Primer sequences were as follows: human Bax: forward 5'-CCCGAGAGGTCTTTTTCCGAG-3', reverse 5'-CCAGCCCATGATGGTTCTGAT-3', human Bcl-2: forward 5'-GGTGGGGTCATGTGTGTGG-3', reverse 5'-CGGTTCAGGTACTCAGTCATCC-3', human GAPDH (internal reference gene): forward 5'-GGAAGGTGAAGGTCGGAGTC-3'; reverse 5'-AACATGTAAACCATGTAGTTGAGGT-3'. Amplifications were carried out in Rotor Gene-Q (Qiagen) with denaturation at 95°C for 5 min and 40 cycles of denaturation at 95°C for 10 sec, annealing and elongation at 57°C for 30 sec. Relative transcript levels were analyzed using ΔΔCt method.

2.7. Wound Healing Assay

$2.5x10^5$ MDA-MB-231 cells were seeded into 6-well plates and grown until confluency. The next day, the cells were treated with 10 µg/mL mitomycin for 2 h to inhibit cell proliferation and then a wound was formed with a 200 µL pipette tip on the monolayer. The cells were treated with Mistel extract at IC_{50} value. The images of the wound were obtained after 24 h and 48 h incubation periods using an inverted microscope (Leica). Wound width was measured for analysis.

Statistical analysis

Data were subjected to Analysis of Two-way ANOVA using GarphPad Prism. Means were separated from each other by Bonferroni post-tests ($p<0.05$). The analysis was performed in triplicate.

3. RESULTS AND DISCUSSION

Table 1 GC-MS characterization of the extracts. Molecules given in the table were chosen based on 90% or higher similarity.

Extract	Identified molecule (similarity%)
Elecampane	1-Dodecene (97); ylangene (98); Copaene (98); Caryophyllene (99); Neoisolongifolene (95); 2(4H)-Benzofuranone, 5,6,7,7a-tetrahydro-4,4,7a-trimethyl- (98); trans-Caryophyllene (95); Hexadecane (96); 1-Hexacosene (95); Squalene (99); 3-Hexenoic acid, (E)- (91); Nerolidol 2 (91); Caryophyllene oxide (91); Selina-6-en-4-ol (91); Cycloheptane,4-methylene-1-methyl-2-(2-methyl-1-propen-1-yl)-1-vinyl (91); 11,11-Dimethyl-spiro[2,9]dodeca-3,7-dien (90); 4',5-Dihydroxy-7-methoxyflavanone (91)
Mistel	*1-Dodecene* (96); methyl linoleate (99); alpha-linolenic acid (95); 9-Tricosene, (Z)- (96); Heptadecane (97); 9-Octadecenamide, (Z)- (98); Eicosane (96); Pentacosane (96); Octadecane (96); Octacosane (98); Nonacosane (99); Vitamin E (99); Beta.-Sitosterol (96); 1-Di(t-butyl)silyloxypropane (90); 1-(2-hydroxy-4,6-dimethoxyphenyl)ethanone (90); 3,5,7-Trimethyl [1,2,4] triazolo [1,5-a]pyrimidinium-2-thiolate (90); Phytol (91); 3,10,10-trimethyl-6-methyliden-1-oxa-spiro(4.5)dec-3-ene (91); 6-fluoro-4,6-cholestadien-3-ol (91);
Black Radish Seeds	*1-Dodecene* (98); 1-Hexadecene (95); Oleic Acid (95); 2(1H)-Naphthalenone, octahydro-4a- (95); Squalene (98); Gamma-Tocopherol (95); Gamma-Sitosterol (97); 2,6-dimethyl-3-(methoxymethyl)-p-benzoquinone (90); Dimethyl-(1,2,3,4,5,6,7,8-octahydro-carbazol-9-yl)-amine (90); 1-Oxaspiro[2.5]octane, 5,5-dimethyl-4-(3-methyl-1,3-butadienyl)- (93); 1,2-Longidione (91); Diepicedrene-1-oxide (91); Lup-20(29)-en-3-ol, acetate, (3.beta.) (91); Pyridine-3-carboxamide, oxime, N-(2-trifluoromethylphenyl) (90); Campesterol (91)

3.1. Phytochemical profile (Volatile compounds content)

GC-MS results revealed that all three extracts do not have many molecules in common while characteristic molecules for each extract were more common. Elecampane extract gave sesquiterpenoids and furanone that show strong biological activities. For example, copaene shows strong anti-oxidant and anti-genotoxic effect [52] while caryophyllene can alter PI3K/Akt/mTOR/S6K1 and STAT3 to inhibit cancer growth and increase apoptosis in different cancers [53]. Similarly, presence of squalene, ylangene, β-caryophyllene oxide and trans-nerolidol are strong resource for antioxidant [54] and anti-cancer source [55] including breast cancer [56]. Besides, presence of benzofuranone derivatives [57] gave strong anticancer capability of elecampane extract. A similar chemical content from guava leaves extract showed regulatory effect on AKT/mTOR/ribosomal p70 S6 kinase (S6K1) and MAPK to suppress cancer growth for prostate cancer [58]. Extracts containing 4',5-Dihydroxy-7-methoxyflavanone gave potent anti-proliferation activity for human breast, colon and melanoma cell lines [59].

3.2. Phenolic Compouns Content

According to the data obtained from the determination of phenolic compounds, chloregic acid, hyperoside and protocathuic acid were found high in elecampene and mistel plants. In

addition, quercetin ratio (125.73 µg/g DW) in elecampene plant was higher than mistel plant and black radish seed. The reason why quercetin has various biological activities is that it has antioxidant properties [60]. With the depletion of this molecule, a link has been found between reducing the risk of cancer and cardiovascular diseases. These findings indicate that this phenolic compound can be used as a protective nutraceutical compound [61]. The amount of sinapic acid (43.70 µg/g DW) in black radish seed is higher than elecampene and mistel (Table 2).

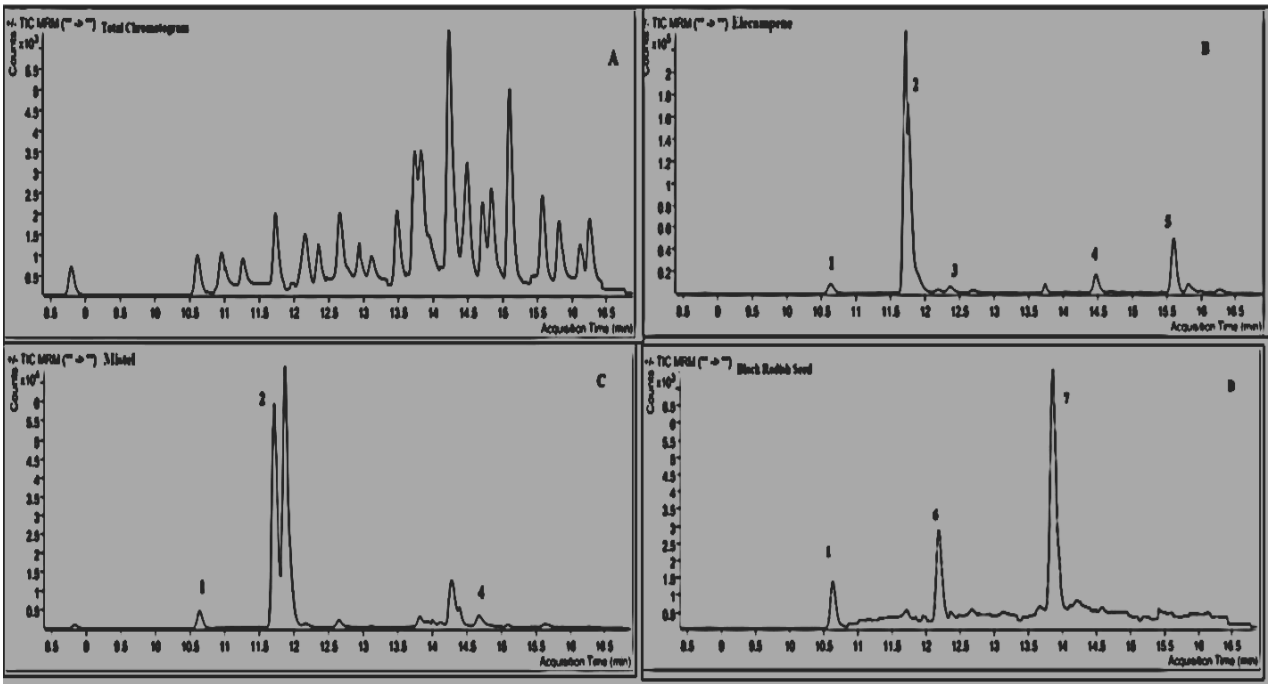

Figure 1 LC-MS/MS chromatograms of phenolic compounds. A: Total chromatogram, B: Elecampene, C: Mistel, D: Black radish seed. Chromatogram peaks:1:Protocathuic acid, 2:Chlorogenic acid, 3:2,5 Dihydroxybenzoic acid, 4: Hyperoside, 5: Quercetin, 6: 4-Hydroxybenzoic acid, 7: Sinapic acid.

Table 2 Phenolic compound content of Elecampane, Mistel and Black Radish Seed
Data represents the means ± SE, *, $p < 0.05$, nd:not detected., Rt: retention time of phenolic compounds, DW: Dry weight

Phenolic compound	**Elecampene**		**Mistel**		**Black Radish Seed**	
	Rt	**µg/g DW**	**Rt**	**µg/g DW**	**RT**	**µg/g DW**
Gallic acid	8.816	1.23±0.08	8.833	7.29±0.18*	8.825	0.12±0.00
Protocatechuic acid	10.643	46.21±1.18**	10.643	22.45±0.38**	10,634	9.24±0.50*
3,4-Dihydroxyphenylacetic acid	10.981	0.54±0.03	10.981	0.32±0.03	10.914	0.07±0.05
Pyrocatechol	11,124	0.27±0.03	11.074	0.23±0.06	11.049	0.22±0.01
(+)-Catechin	11.286	0.06±0.02	11.444	0.23±0.02	11.319	0.27±0.02
Chlorogenic acid	11.735	844.82±15***	11.727	173.79±7.11***	11.727	1.05±0.01
4-Hydroxybenzoic acid	12.198	13.86±0.06*	12.181	4.12±0.08	12.189	17.53±0.25**
2,5-Dihydroxybenzoic acid	12.366	64.11±0.6***	12.391	1.34±0.12	11.954	0.36±0.03
(-)-Epicatechin	12.428	0.02±0.01	12.512	0.03±0.00	12.369	1.08±0.07
Vanillic acid	12.608	4.48±.0.09	12.583	2.58±0.08	12.617	1.23±0.11
Caffeic acid	12.699	9.90±0.20*	12,658	5.56±0.25*	12.683	0.68±0.06
Syringic acid	12.806	0.84±0.01	12.790	2.51±0.05	12.748	0.20±0.01
3-Hydroxybenzoic acid	12.97	0.24±0.01	12.97	0.14±0.02	12.962	0.15±0.00
Vanillin	13.148	0.25±0.02	13.131	1.33±0.02	13.148	1.26±0.17
Verbascoside	13.492	0.07±0.00	13.492	0.07±0.00	13.459	0.04±0.00
Taxifolin	13.745	7.80±0.18*	13.745	0.04±0.01	13.628	nd
p-Coumaric acid	13.859	0.14±0.02	13.834	7.00±0.30*	13.859	12.49±0.6**
Ferulic acid	13.998	0.21±0.01	13.958	3.15±0.11	13.973	3.65±0.12*
Sinapic acid	14.039	0.07±0.00	13.873	0.31±0.02	13.881	43.70±08**
Luteolin 7-glucoside	14.247	0.27±0.06	14.23	0.12±0.02	14.304	nd
Hesperidin	14.452	21.97±0.18**	14.411	23.23±0.42**	14.444	0.22±0.01
Hyperoside	14.487	59.49±3.20***	14.687	20.73±0.38**	14.512	0.07±0.00
Rosmarinic acid	14.498	2.12±0.05	14.632	0.42±0.03	14.514	0.11±0.00
Apigenin 7-glucoside	14.705	4.67±0.15	14,81	0.15±0.00	14.738	0.16±0.00
Pinoresinol	15.001	1.24±0.02	14.984	6.28±0.40*	14.825	0.44±0.02
Eriodictyol	15.127	1.05±0.11	15,103	0.72±±0.01	15.12	0.01±0.00
2-Hydroxycinnamic acid	15.171	0.06±0.02	14.76	0.06±0.00	15.222	0.09±0.01
Quercetin	15.611	125.73±6.00***	15.635	3.26±0.02	15.603	0.23±0.01
Luteolin	15.825	29.43±0.33**	15.816	0.41±0.03	15.833	nd
Kaempferol1	16.138	6.54±0.30*	16.155	0.10±0.01	16.138	0.46±0.03
Kaempferol	16.138	15.90±0.09**	16.262	nd	16.138	nd
Apigenin	16.251	4.50±0.09	16,276	0.40±0.02	16.276	nd

The great interest in phenolic compounds has been rapidly grown in recent years, due to the increased evidence of their attractive nutritional properties on human health. Phenolic compounds have high antioxidant activity, and the consumption of food with abundant phenolic compounds might reduce the risk of coronary heart disease, certain types of cardiovascular disease and cancer [62].

3.3. Antioxidant Test Results

Ascorbic acid (AA) at 10 mg/mL concentrations were used as a reference reducing agent in DPPH assay as described elsewhere [63]. Antioxidant activity of the extracts were calculated as percentage decrease in DPPH absorbance (Equation 1).

$$\%\ Reduction = [\frac{(Abs0-Absi)}{Abs0}]X100 \qquad (1)$$

where Abs0 refers to the absorbance of DPPH at 0 µM vitamin C concentration and Absi is the absorbance of remaining DPPH (unreduced) absorbance at the tested vitamin C concentration.

Elacampane extract revealed the highest antioxidant activity as 0.5 mg/mL extract reduced DPPH that is equivalent to 1 mg/mL AA mediated DPPH reduction. Mistel extract at 10 mg/mL reduced DPPH that is equivalent to 1 mg/mL AA mediated DPPH reduction while black radish seed extract at 10 mg/mL did not provide a meaningful reduction of DPPH within 3-min assay period.

3.4. Cell Viability

MTT analysis was performed in order to determine the cytotoxic effects of elecampane, mistel and black radish seed extracts on MDA-MB-231 cells. There was an inverse correlation between elecampane concentration and cytotoxic effect on MDA-MB-231 cells. The highest cytotoxic activity of elecampane extract was observed at the lowest tested concentration (Figure 2). For detailed analysis of elecampane extract, 0.25, 0,5 and 1 mg/mL concentrations were also evaluated with MTT analysis. The highest cytotoxic activity of elecampane extract was detected at 1 mg/mL concentration. The cytotoxic activity has decreased whether the elecampane concentration is lower or higher than 1mg/mL (Figure 3). This trend has been overwhelmingly reported for flavonoid extracts, where they behave as antioxidants and pro-oxidants depending on the concentration and physiological conditions [64]. It is possible that the elecampane extract behaved like flavanoids. Mistel extract showed the highest reduction in MDA-MB-231 cell viability (92%) at 12.5 mg/mL concentration (Figure 2). IC_{50} values of mistel treatment were calculated as 4.84 mg/m L for 24 h and 3.5 mg/mL for 48 h. Mistel extracts had higher amount of fatty acid and fatty acid esters as shown in Table 1. Methyl linoleate and 9-octadecenamide were reported as antioxidants [65,66]. Beta-sitosterol has anticancer properties against wide range of cancers such as breast cancer, prostate cancer, colon cancer, lung cancer, stomach cancer, ovarian cancer, and leukemia [67]. Vitamin E has also anticarcinogenic activities [68]. These compounds present in mistel extract might synergistically reduce MDA-BM-231 cell viability. Radish extract did not have cytotoxic effect against MDA-MB-231 cells (Figure 2).

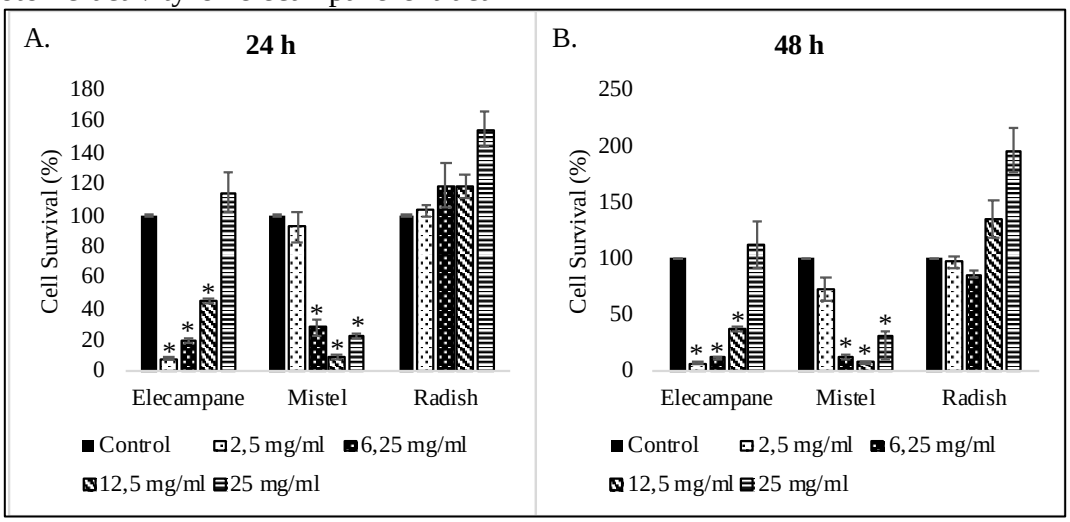

Figure 2 MTT results. MDA-MB-231 cells were treated with extracts at different concentrations for 24 h (A) and 48 h (B). Data represents the means ± SE, *, $p < 0.05$.

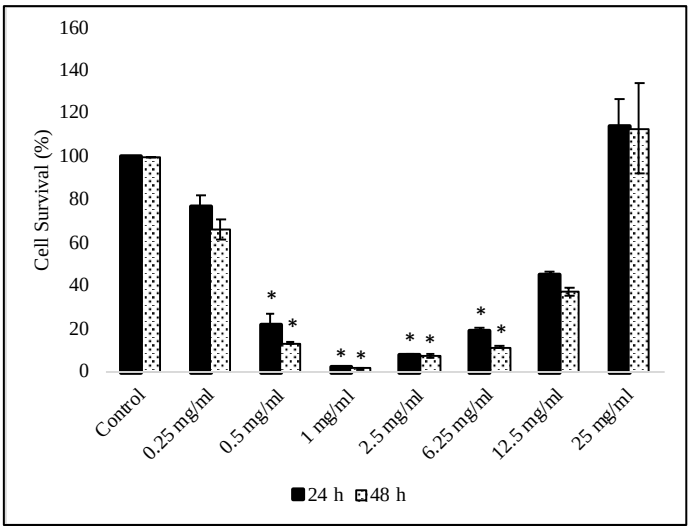

Figure 3 Concentration dependent cytotoxicity of Elacampane extract on MDA-MB-231 cells. The cells were treated with Elecampane extracts at different concentrations for 24 h and 48 h. Data represents the means ± SE, *, $p < 0.05$.

3.5. Apoptotic Marker Gene Expression

Apoptosis is a programmed cell death mechanism that eliminate dysfunctional cells. Evasion of apoptosis is one of the hallmarks of cancer cells [1]. Apoptosis can be triggered by various intracellular and extracellular stimuli, and many anticancer drugs target apoptosis. In mammals, there are two main apoptosis pathways, mitochondria-mediated (intrinsic) and death receptor-mediated (extrinsic). DNA damage, oxygen deficiency, and oxidative stress stimulate the initiation of the intrinsic pathway. When the intrinsic pathway is activated, the permeability of the mitochondria is increased and cytochrome-c is released into the cytoplasm. This pathway is regulated by B-cell lymphoma 2 (Bcl-2) family proteins. Bcl-2 family proteins are divided into two groups; pro-apoptotic and anti-apoptotic proteins. Pro-apoptotic proteins initiate apoptosis by inducing cytochrome-c release while anti-apoptotic proteins inhibit cytochrome-c release [69].

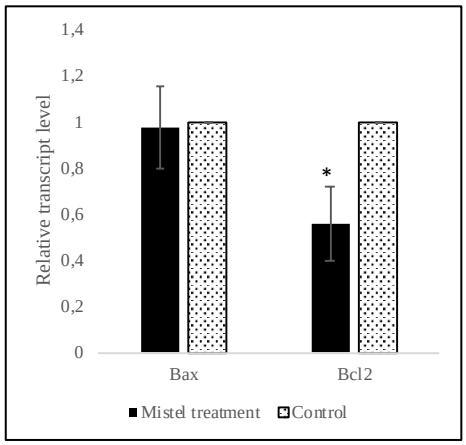

Figure 4 Apoptotic markers. MDA-MB-231 cells were treated with Mistel extract at IC_{50} concentration (3.5 mg/mL) for 48 h. Marker gene expressions were analyzed by qPCR. *, $p < 0.05$.

In order to analyze whether mistel extract treatment induce apoptosis on MDA-MB-231 cells, pro-apoptotic marker gene (Bax) and anti-apoptotic marker gene (Bcl-2) levels were analyzed by qPCR. Bax levels were not changed, however, there was a significant decrease in Bcl-2 level (45%) with mistel extract treatment (Figure 4). Increased Bax/Bcl-2 ratio (1.76) has demonstrated that apoptosis of MDA-MB-231 is stimulated with mistel extract treatment. Compounds found in mistel extract beta-sitosterol and vitamin E has been associated with apoptosis induction in several studies. Beta-sitosterol has been shown to inhibit proliferation and stimulate

apoptosis of MCF-7 and MDA-MB-231 breast cancer cells [67,70,71]. *In vitro* and *in vivo* studies have proven the pro-apoptotic effect of T3, a compound from vitamin E family, on several cancer types as breast, prostate, lung, bladder, liver, colorectal and pancreas [72,73]. The apoptosis induction observed with mistel extract treatment on MDA-MB-231 cells might be due to combined pro-apoptotic effect of beta-sitosterol and vitamin E.

3.6. Wound Healing Assay

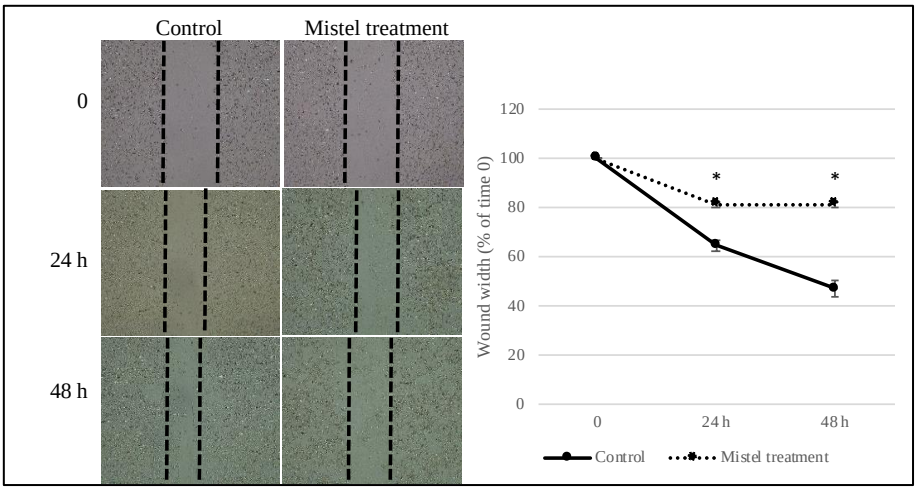

Figure 5 Effect of Mistel extract treatment on cell migration. MDA-MB-231 cells were treated with Mistel extract at IC_{50} concentration for 48 h. The images were obtained with inverted microscope. Cell migration was quantified according to relative distance in each wound.

Cancer cell migration is necessary for development of malignancies. Metastasis begins when cancer cells in the primary tumor site cross the extracellular matrix and join the blood vessels and lymph system and spreads out to the body. Wound healing assay was performed to analyze whether mistel extract treatment can inhibit MDA-MB-231 cell migration. For the control group, approximately 40% and 60% of wound closure was achieved after 24 h and 48 h respectively. Migration capacity of the MDA-MB-231 cells were decreased with mistel extract treatment compared to control group for both time points (Figure 5). Several studies have demonstrated that vitamin E family derivatives inhibit cancer cell migration. T3 has been reported to reduce migration of non-small-cell lung carcinoma cells and gastric cancer cells based on wound healing assay [73,74]. γ-Tocotrienol has significantly reduced migration and invasion of mammary cancer cells by inhibiting Rac1/WAVE2 signaling pathway [75]. It is suggested that vitamin E found in mistel extract might be responsible for the inhibition of MDA-MB-231 cell migration.

4. CONCLUSION

Natural compounds exert anticancer effect by regulating cell cycle, triggering apoptosis, and stimulating various signaling pathways. Current chemotherapy agents target both cancer and normal cells. Plant-derived natural compounds reduce the side effects of cancer treatment. In this study, we identified biochemical components of elecampane, mistel and black radish seed and investigated the anticancer activity of these extracts on MDA-MB-231 breast cancer cells. Mistel and elecampane extracts decreased the percentage of viable MDA-MB-231 cells. The increased Bax / Bcl2 ratio after mistel treatment has indicated that MDA-MB-231 cell death is induced by apoptosis. Besides, mistel extract treatment inhibit the MDA-MB- 231 cell migration. The observed anticarcinogenic

properties might be due to the presence of bioactive compounds such as methyl linoleate and 9-octadecenamide, beta-sitosterol and Vitamin E.

Acknowledgement

The authors would like to thank Manisa Celal Bayar University (Turkey), Applied Science and Research Center (ASRC/DEFAM) for their support in this study.

Funding

The authors has no received any financial support for the research, authorship or publication of this study.

The Declaration of Conflict of Interest/ Common Interest

No conflict of interest or common interest has been declared by the authors.

Authors' Contribution

The design and organization of this study and the characterization of the samples were done by Hafize DİLEK TEPE, cell culture experiments were carried out by Aslı UĞURLU and antioxidant activity measurements were carried out by İdris YAZGAN. In addition, all authors greatly supported the writing of the study.

The Declaration of Ethics Committee Approval

The authors declare that this document does not require an ethics committee approval or any special permission.

The Declaration of Research and Publication Ethics

The authors of the paper declare that they comply with the scientific, ethical and quotation rules of SAUJS in all processes of the article and that they do not make any falsification on the data collected. In addition, they declare that Sakarya University Journal of Science and its editorial board have no responsibility for any ethical violations that may be encountered, and that this study has not been evaluated in any academic publication environment other than Sakarya University Journal of Science.

These findings have suggested a new biological activity for mistel extracts.

REFERENCES

[1] D. Hanahan and R. A. Weinberg, “Review Hallmarks of Cancer : The Next Generation,” Cell, vol. 144, no. 5, pp. 646–674, 2011.

[2] X. Dai et al., “Breast cancer intrinsic subtype classification , clinical use and future trends,” no. May 2016, 2015.

[3] M. Cazzaniga and B. Bonanni, “Breast Cancer Chemoprevention : Old and New Approaches,” vol. 2012, 2012.

[4] C. Desantis, J. Ma, L. Bryan, and A. Jemal, “Breast Cancer Statistics, 2013,” 2014.

[5] S. Goyal, N. Gupta, S. Chatterjee, and S. Nimesh, “Natural Plant Extracts as Potential Therapeutic Agents for the Treatment of Cancer,” Current Topics in Medicinal Chemistry, vol. 17, no. 2, pp. 96–106, 2016.

[6] A. Ranjan, N. M. Fofaria, S. Kim, and S. K. Srivastava, “Modulation of signal transduction pathways by natural compounds in cancer,” Chinese Journal of Natural Medicines, vol. 13, no. 10, pp. 730–742, 2015.

[7] F. M. Millimouno, J. Dong, L. Yang, J. Li, and X. Li, “Targeting Apoptosis Pathways in Cancer and Perspectives with Natural Compounds from Mother Nature,” pp. 1081–1108, 2014.

[8] J. Iqbal et al., “Potential phytocompounds for developing breast cancer therapeutics : Nature’s healing touch,” vol. 827, no. December 2017, pp. 125–148, 2018.

[9] D. Bonofigilo, C. Giordano, F. De Amicis, M. Lanzino, and S. Ando, “Natural Products as Promising Antitumoral Agents

in Breast Cancer: Mechanisms of Action and Molecular Targets.," Mini-Reviews in Medicinal Chemistry, vol. 16, no. 8, pp. 596–604, 2016.

[10] R. Singh Thakur and B. Ahirwar, "Natural Compounds A Weapon to Ameliorate Breast Cancer Cells: A Review," Anti-Cancer Agents in Medicinal Chemistry (Formerly Current Medicinal Chemistry - Anti-Cancer Agents), vol. 17, no. 3, pp. 374–384, 2017.

[11] S. Uysal et al., "Novel in vitro and in silico insights of the multi-biological activities and chemical composition of Bidens tripartita L.," Food and Chemical Toxicology, vol. 111, no. November 2017, pp. 525–536, 2018.

[12] G. Zengin et al., "Journal of Pharmaceutical and Biomedical Analysis Chemical fingerprints , antioxidant , enzyme inhibitory , and cell assays of three extracts obtained from Sideritis ozturkii Aytac An endemic plant from Turkey," vol. 171, pp. 118–125, 2019.

[13] M. Fawzi, S. Yerlikaya, E. J. Llorent-martínez, and A. Uğurlu, "Pharmacological and polyphenolic profiles of Phyllanthus phillyreifolius var. commersonii Müll. Arg : An unexplored endemic species from Mauritius," Food Research International, vol. 115, no. October 2018, pp. 425–438, 2019.

[14] A. M. L. Seca, A. Grigore, D. C. G. A. Pinto, and A. M. S. Silva, "The genus Inula and their metabolites: From ethnopharmacological to medicinal uses," Journal of Ethnopharmacology, vol. 154, no. 2, pp. 286–310, 2014.

[15] F. Ertuğ, "Etnobotanik. Illustrated Flora of Turkey," 2014.

[16] V. Hernández, M. C. Recio, S. Máñez, R. M. Giner, and J. L. Ríos, "Effects of naturally occurring dihydroflavonols from Inula viscosa on inflammation and enzymes involved in the arachidonic acid metabolism," Life Sciences, 2007.

[17] S. Rozenblat, S. Grossman, M. Bergman, H. Gottlieb, Y. Cohen, and S. Dovrat, "Induction of G2/M arrest and apoptosis by sesquiterpene lactones in human melanoma cell lines," Biochemical Pharmacology, 2008.

[18] M. Maoz and I. Neeman, "Effect of Inula viscosa extract on chitin synthesis in dermatophytes and Candida albicans," Journal of Ethnopharmacology, 2000.

[19] G. R. Schinella, H. A. Tournier, J. M. Prieto, P. Mordujovich De Buschiazzo, and J. L. Ríos, "Antioxidant activity of anti-inflammatory plant extracts," Life Sciences, 2002.

[20] O. Danino, H. E. Gottlieb, S. Grossman, and M. Bergman, "Antioxidant activity of 1,3-dicaffeoylquinic acid isolated from Inula viscosa," Food Research International, 2009.

[21] G. Fontana, S. La Rocca, S. Passannanti, and M. P. Paternostro, "Sesquiterpene compounds from Inula viscosa," Natural Product Research, vol. 21, no. 9, pp. 324–327, 2007.

[22] N. Zeggwagh, M. Ouahidi, A. Lemhadri, and M. Eddouks, "Study of hypoglycaemic and hypolipidemic effects of Inula viscosa L. aqueous extract in normal and diabetic rats," Journal of Ethnopharmacolgy, vol. 108, no. 2, pp. 223–7, 2006.

[23] S. Máñez et al., "A glycosyl analogue of diacylglycerol and other antiinflammatory constituents from Inula viscosa," Journal of Natural Products, vol. 62, no. 4, pp. 601–604, 1999.

[24] T. Baytop, Türkiye'de Bitkiler ile Tedavi (Geçmişte ve Bugün) Türkiye'de Kullanılan Tıbbi Bitkiler, 40th ed. İstanbul: İ.Ü.Eczacılık Fak., 1984.

[25] G. Ecevit Genç and N. Özhatay, "An ethnobotanical study in Çatalca (European part of Istanbul) II," Turkish Journal of Pharmaceutical Sciences, vol. 3, no. 2, pp. 73–89, 2006.

[26] Ş. Kültür, "Medicinal plants used in Kırklareli Province (Turkey)," Journal of Ethnopharmacology, vol. 111, no. 2, pp. 341–364, 2007.

[27] Ç. Kizilarslan and N. Özhatay, "Wild plants used as medicinal purpose in the south part of İzmit (Northwest Turkey)," Turkish Journal of Pharmaceutical Sciences, vol. 9, no. 2, pp. 199–218, 2012.

[28] D. U. Saraç, Z. C. Özkan, and S. Akbulut, "Ethnobotanic features of Rize/Turkey province Diren," Biological Diversity and Conservation, vol. 6, no. 3, pp. 57–66, 2013.

[29] S. A. Sargin, E. Akçicek, and S. Selvi, "An ethnobotanical study of medicinal plants used by the local people of Alaşehir (Manisa) in Turkey," Journal of Ethnopharmacology, 2013.

[30] S. Karaman and Y.Z. Kocabas, "Traditional Medicinal Plants of K. Maras (Turkey)," The Sciences, vol. 1, no. 3. pp. 125–128, 2001.

[31] A. Pieroni, H. Muenz, M. Akbulut, K. H. C. Başer, and C. Durmuşkahya, "Traditional phytotherapy and trans-cultural pharmacy among Turkish migrants living in Cologne, Germany," Journal of Ethnopharmacology, 2005.

[32] H. Jalali, A.S. Mozaffari Nejad, A.G. Ebadi, and G. Laey, "Ethnobotany and folk pharmaceutical properties of major trees or shrubs in northeast of Iran," Asian Journal of Chemistry, vol. 21, no. 7, pp. 5632–5638, 2009.

[33] S. Mehmet, D. Serap, and T. Sezen, "Medicinal plants used in Dalaman (Muğla), Turkey," Journal of Medicinal Plants Research, vol. 7, no. 28, pp. 2053–2066, 2013.

[34] G. Bulut, M. Zahid Bozkurt, and E. Tuzlacı, "The preliminary ethnobotanical study of medicinal plants in uşak (Turkey)," Marmara Pharmaceutical Journal, vol. 21, no. 2, pp. 305–310, 2017.

[35] S. A. Sargin, S. Selvi, and V. López, "Ethnomedicinal plants of Sarigöl district (Manisa), Turkey," Journal of Ethnopharmacology, 2015.

[36] O. Adaramoye, M. Amanlou, M. Habibi-Rezaei, P. Pasalar, and M.M. Ali, "Methanolic extract of African mistletoe (Viscum album) improves carbohydrate metabolism and hyperlipidemia in streptozotocin-induced diabetic rats," Asian Pacific Journal of Tropical Medicine, vol. 5, no. 6, pp. 427–433, 2012.

[37] D. D. Orhan, F. S. Senol, S. Hosbas, and I. E. Orhan, "Assessment of cholinesterase and tyrosinase inhibitory and antioxidant properties of Viscum album L. samples collected from different host plants and its two principal substances," Industrial Crops and Products, 2014.

[38] Y. Li, Y. L. Zhao, Y. P. Yang, and X. L. Li, "Chemical constituents of Viscum album var. meridianum," Biochemical Systematics and Ecology, 2011.

[39] S. Loizou, I. Lekakis, G. P. Chrousos, and P. Moutsatsou, "β-Sitosterol exhibits anti-inflammatory activity in human aortic endothelial cells," Molecular Nutrition and Food Research, vol. 54, no. 4, pp. 551–558, 2010.

[40] E. Kovacs, "The in vitro effect of Viscum album (VA) extract on DNA repair of peripheral blood mononuclear cells (PBMC) in cancer patients," Phytotherapy Research, vol. 16, no. 2, pp. 143–147, 2002.

[41] E. Önay-Uçar, A. Karagöz, and N. Arda,

"Antioxidant activity of Viscum album ssp. album," Fitoterapia, vol. 77, no. 7–8, pp. 556–560, 2006.

[42] G. Schaller, K. Urech, G. Grazi, and M. Giannattasio, "Viscotoxin composition of the three European subspecies of Viscum album," Planta Medica, vol. 64, no. 7, pp. 677–678, 1998.

[43] D. Deliorman, I. Çalış, and F. Ergun, "A new acyclic monoterpene glucoside from Viscum album ssp. album," Fitoterapia, 2001.

[44] E. Lorch, "New Investigations on Flavonoids from Viscum album L. ssp. abietis, album and austriacum," Z. Naturforsch, vol. 48, no. c, pp. 105–107, 1993.

[45] L. X. Duan et al., "Thioglucosides from the seeds of Raphanus sativus L.," Helvetica Chimica Acta, vol. 89, no. 12, pp. 2953–2957, 2006.

[46] W. Vent, "Duke, J. A., and Ayensu, E. S., Medicinal Plants of China. 2 Vols. 705 S., 1300 Strichzeichnungen. Reference Publ., Inc. Algonac. Michigan, 1985. ISBN 0-917266-20-4.," Feddes Repertorium, vol. 98, no. 7–8, pp. 398–398, Apr. 1985.

[47] R. N. Chopra, S. L. Nayar, and I. . Chopra, "Glossary of Indian Medicinal Plants (Including the Supplement)." Council of Scientific and Industrial Research, New Delhi, 1986.

[48] R.M.P. Gutiérrez and R.L. Perez, "Raphanus sativus (Radish): their chemistry and biology.," TheScientificWorldJournal, vol. 4, no. 16, pp. 811–837, 2004.

[49] A. Lugasi, A. Blázovics, K. Hagymási, I. Kocsis, and Á. Kéry, "Antioxidant effect of squeezed juice from black radish (Raphanus sativus L. var niger) in alimentary hyperlipidaemia in rats," Phytotherapy Research, vol. 19, no. 7, pp. 587–591, 2005.

[50] A. C. Gören, S. Çikrikçi, M. Çergel, and G. Bilsel, "Rapid quantitation of curcumin in turmeric via NMR and LC-tandem mass spectrometry," Food Chemistry, vol. 113, no. 4, pp. 1239–1242, Apr. 2009.

[51] E. J. Garcia, S. M. De Alencar, A. Reis, A. D. Loguercio, R. Helena, and M. Grande, "Antioxidant Activity by DPPH Assay of Potential Solutions to be Applied on Bleached Teeth," Brazilian Dental Journal, vol. 23, pp. 22–27, 2012.

[52] S. B. Kedare and R. P. Singh, "Genesis and development of DPPH method of antioxidant assay," Journal of Food Science and Technology, vol. 48, no. 4, pp. 412–422, 2011.

[53] K. Fidyt, A. Fiedorowicz, L. Strządała, and A. Szumny, "B-Caryophyllene and B-Caryophyllene Oxide—Natural Compounds of Anticancer and Analgesic Properties," Cancer Medicine, vol. 5, no. 10, pp. 3007–3017, 2016.

[54] F. E. Güneş, "Medical use of squalene as a natural antioxidant," Journal of Marmara University Institute of Health Sciences, vol. 3, no. 4, p. 1, 2013.

[55] Y.J. Xio, J. H. Su, B. W. Chen, Y. J. Tseng, Y. C. Wu, and J. H. Sheu, "Oxygenated ylangene-derived sesquiterpenoids from the soft coral lemnalia Philippinensis," Marine Drugs, vol. 11, no. 10, pp. 3735–3741, 2013.

[56] V. Hanušová et al., "The effects of β-caryophyllene oxide and trans-nerolidol on the efficacy of doxorubicin in breast cancer cells and breast tumor-bearing mice," Biomedicine and Pharmacotherapy, vol. 95, no. July, pp. 828–836, 2017.

[57] Z. Zerenler Çalışkan and E.N. Ay, "Synthesis of Dihydrobenzofuranone Derivatives with Biotechnological Methods," Journal of the Turkish Chemical

Society, Section A: Chemistry, vol. 5, no. 3, pp. 1221–1232, 2018.

[58] N.H. Ryu et al., "A hexane fraction of guava leaves (Psidium guajava L.) induces anticancer activity by suppressing AKT/mammalian target of rapamycin/ribosomal p70 S6 kinase in human prostate cancer cells," Journal of Medicinal Food, vol. 15, no. 3, pp. 231–241, 2012.

[59] J.D. Lambert et al., "Cytotoxic lignans from Larrea tridentata," Phytochemistry, vol. 66, no. 7, pp. 811–815, 2005.

[60] P. Iacopini, M. Baldi, P. Storchi, and L. Sebastiani, "Catechin, epicatechin, quercetin, rutin and resveratrol in red grape: Content, in vitro antioxidant activity and interactions," Journal of Food Composition and Analysis, 2008.

[61] G.S. Kelly, "Quercetin," Alternative Medicine Review, vol. 16, no. 2, pp. 172–194, 2011.

[62] L. Bravo, "Polyphenols: Chemistry, Dietary Sources, Metabolism, and Nutritional Significance," Nutrition Reviews, vol. 56, no. 11, pp. 317–333, Apr. 2009.

[63] F. BAKAR et al., "Synthesis and Characterization of Pollen Extract Mediated Gold Nanostructures," Türk Doğa ve Fen Dergisi, vol. 9, no. 2, pp. 1–8, Nov. 2020.

[64] D. Procházková, I. Boušová, and N. Wilhelmová, "Antioxidant and prooxidant properties of flavonoids," Fitoterapia, vol. 82, no. 4, pp. 513–523, 2011.

[65] M.E.A. Pinto et al., "Antifungal and antioxidant activity of fatty acid methyl esters from vegetable oils," Anais da Academia Brasileira de Ciencias, vol. 89, no. 3, pp. 1671–1681, 2017.

[66] Y. Sugita, K. Takao, Y. Uesawa, and H. Sakagami, "Search for New Type of Anticancer Drugs with High Tumor Specificity and Less Keratinocyte Toxicity," Anticancer Research, vol. 37, no. 11, pp. 5919–5924, 2017.

[67] M. S. Bin Sayeed and S. S. Ameen, "Beta-Sitosterol: A Promising but Orphan Nutraceutical to Fight Against Cancer," Nutrition and Cancer, vol. 67, no. 8, pp. 1214–1220, 2015.

[68] C. Constantinou, A. Papas, and A.I. Constantinou, "Vitamin E and cancer: An insight into the anticancer activities of vitamin E isomers and analogs," International Journal of Cancer, vol. 123, no. 4, pp. 739–752, 2008.

[69] D. R. Green and J. E. Chipuk, "NIH Public Access," no. November, 2008.

[70] M.C. Pagliacci, M. Smacchia, G. Migliorati, F. Grignani, C. Riccardi, and I. Nicoletti, "Growth-inhibitory effects of the natural phyto-oestrogen genistein in MCF-7 human breast cancer cells," European Journal of Cancer, vol. 30, no. 11, pp. 1675–1682, Jan. 1994.

[71] A.B. Awad, R. Rajat, and C. S. Fink, "β-sitosterol, a plant sterol, induces apoptosis and activates key caspases in MDA-MB-231 human breast cancer cells," Oncology Reports, vol. 10, no. 2, pp. 497–500, 2003.

[72] B. B. Aggarwal, C. Sundaram, S. Prasad, and R. Kannappan, "Tocotrienols , the vitamin E of the 21st century : Its potential against cancer and other chronic diseases," Biochemical Pharmacology, vol. 80, no. 11, pp. 1613–1631, 2010.

[73] L.S. De Silva, L. H. Chuah, P. Meganathan, and J.-Y. Fu, "Tocotrienol and cancer metastasis," Biofactors, vol. 42, no. 2, pp. 149–152, 2016.

[74] H. Liu et al., "Inhibitory effects of γ -tocotrienol on invasion and metastasis of human gastric," The Journal of Nutritional

Biochemistry, vol. 21, no. 3, pp. 206–213, 2010.

[75] I. G. Algayadh, V. Dronamraju, and P. W. Sylvester, “Role of Rac1/WAVE2 signaling in mediating the inhibitory effects of γ-tocotrienol on mammary cancer cell migration and invasion,” Biological and Pharmaceutical Bulletin, vol. 39, no. 12, pp. 1974–1982, 2016.

SAKARYA ÜNİVERSİTESİ
FEN BİLİMLERİ ENSTİTÜSÜ DERGİSİ

Sakarya University Journal of Science
SAUJS

e-ISSN 2147-835X | Period Bimonthly | Founded: 1997 | Publisher Sakarya University |
http://www.saujs.sakarya.edu.tr/en/

Title: Effects of Climate Change on Distribution Areas of Formerly Endemic Plant Species Campanula lyrata Lam.

Authors: Behlül GÜLER

Recieved: 2021-02-10 08:14:48

Accepted: 2021-04-06 13:49:17

Article Type: Research Article

Volume: 25
Issue: 3
Month: June
Year: 2021
Pages: 663-672

How to cite
Behlül GÜLER; (2021), Effects of Climate Change on Distribution Areas of Formerly Endemic Plant Species Campanula lyrata Lam.. Sakarya University Journal of Science, 25(3), 663-672, DOI: https://doi.org/10.16984/saufenbilder.877932
Access link
http://www.saujs.sakarya.edu.tr/en/pub/issue/62736/877932

Sakarya University Journal of Science 25(3), 663-672, 2021

Effects of Climate Change on Distribution Areas of Formerly Endemic Plant Species *Campanula lyrata* Lam.

Behlül GÜLER*[1]

Abstract

Species distribution models (SDMs) are useful tools for future potential distribution patterns of species in the face of climate change. Turkey is expected to be affected considerably from climatic change i.e., up to 6°C increase in temperature and 50% decrease in precipitation by 2070. Therefore, there is an urgent need for conservation and management practices for future patterns of species. It is aimed current and future (using CMIP5 projected to 2070) potential distribution areas of *Campanula lyrata* Lam., which is formerly an endemic species. To do this, presence-only data was used, which is obtained from the Global Biodiversity Information Facility (GBIF). Bioclimatic data from was downloaded from WorldClim dataset with 10 km^2 resolution. Species distribution modelling was performed using R program. Two regression techniques and two machine learning techniques namely Generalized Linear Models (GLMs), Generalized Additive Models (GAMs), Support Vector Machine (SVM) and Random Forest (RF), were used, respectively. The bootstrapping method as partitioning resampling was also used for all analysis. Considerably high model performances as well as AUC values for all possible models were found. Significant range shifts between current and future climatic conditions were found. The most relevant relative importance variables were precipitation seasonality and precipitation of the wettest month. This study reveals the importance of the future distributional areas of species.

Keywords: Biology, Botany, Vascular plant, Species distribution models.

1. INTRODUCTION

Climatic change is one of the most important environmental issues in the world. Future projections for climatic events reveal that considerable increase in global temperature, decrease in precipitation and a rise in extreme weather events is expected. [1]. Therefore, distribution patterns of the biological organisms are also expected to change [2]. Biodiversity loss may occur [3] and therefore ecosystem functions might be affected [4]. Projections for distribution areas based on changing global environmental conditions clearly contribute to conservation strategies for the biological organisms [5]. According to projections Turkey is expected to be significantly affected by climate change [6]. It is expected that precipitation will be decreased by

* Corresponding author: behlul.guler@deu.edu.tr
[1] Dokuz Eylul University, Biology Education, Buca, 35350, İzmir, Turkey.
ORCID: https://orcid.org/0000-0003-2638-4340

up to 50% by 2070 projections. Temperatures will also increase by up to 6°C according to the 2070 projections based on HadGEM2-ES/RCP 8.5 scenario [6, 7]. The future trend towards 2100 continues up to 5°C based on ICTP-RegCM3 climate projections [8].

Species distribution models (SDMs) are based on statistical inferences and powerful tools for investigating potential distribution patterns of current and future times [9]. In general presence-only data, presence-absence and abundance data are used for SDMs as species patterns data, while a line of environmental data is used as explanatory data [10]. A number of machine learning methods such as MAXENT, Artificial Neural Networks (ANN), Genetic Algorithm for Rule set production (GARP), Boosted Regression Trees (BRT), Gradient Boosting Machines (GBM), Random Forest (RF) and Support Vector Machines (SVM), and regression methods such as Generalized Linear Models (GLMs), Generalized Additive Models (GAMs) and Multivariate Adaptive Regression Splines (MARS) are used in SDMs statistical inference. These methods could be performed using the *sdm* [11], MaxEnt [12], DOMAIN [13], BIOCLIM [14].

Biological organisms are considerably affected by climate change. In particular, plants and plant communities are significantly affected by changing weather events. These effects strongly depend on the type of climatic event climatic event type and its magnitude [15]. The effects of climate can be as follows: negative effects on community stability [16], extinction of species and plant communities [17], permanent changes on community [18], effects on individuals [16], shifts on ecotones [19], negative effects on amount of photosynthesis, productivity, carbon uptake, biotic interactions such as fine scale community assembly and functionality [20].

Vascular plant diversity in Turkey is quite rich in terms of richness for taxa [21]. Geological and topographical diversity have resulted in a diverse ecosystem for vascular plants. In addition to this Turkey has considerable mountainous regions, and therefore it results in unique habitats for endemic species richness [21-23]. At the same time, Turkey is dramatically affected from the climate change [8]. However, future response of the species and communities in Turkey still remain unclear. Since there may be numerous responses of the species, it should be taken into account to get more information about future responses of species as well as communities.

Campanula lyrata, which I investigated to species distribution modelling in this study, belongs to the Campanulaceae family. It is a hemicriptophyte herbaceous vascular plant species, which mostly grows in stony places, cliffs, river banks. It is a biennial or perennial species and flowering period is between April and July. It could grow up to 50 cm tall and up to 1700 m elevation. *Campanula lyrata* is formerly an endemic species as reported in Flora of Turkey [24, 25, 26] as *Campanula lyrata* subsp. *lyrata*. It distributes across most sub-regions of Western Turkey. However, it is no longer endemic in the current Plant List of Turkey [21]. Therefore, I aimed to reveal current and future potential distribution areas of *Campanula lyrata*, which is projected to 2070 in this study.

2. MATERIALS AND METHODS

2.1. Data compilation

I searched for occurrence data of *Campanula lyrata* from the Global Biodiversity Information Facility (GBIF, https://www.gbif.org/, accessed on February 2021). It resulted in 283 records in GBIF. The basis of the records was fossil specimen 1, human observation 29, living specimen 3, preserved specimen 247 and 3 unknown. I extracted geolocated occurrences, which was finally resulted in 127 occurrences. I performed further analysis using geolocated occurrences.

I downloaded 19 bioclimatic variables from WorldClim database [27-28] with 10 km^2 spatial resolution. These variables were: bio1, Annual Mean Temperature; bio2, Mean Diurnal Range (Mean of monthly (max temp - min temp)); bio3, Isothermality (bio2/bio7) (×100); bio4, Temperature Seasonality (standard deviation ×100); bio5, Max Temperature of Warmest Month; bio6, Min Temperature of Coldest Month; bio7, Temperature Annual Range (bio5-bio6);

bio8, Mean Temperature of Wettest Quarter; bio9, Mean Temperature of Driest Quarter; bio10, Mean Temperature of Warmest Quarter; bio11, Mean Temperature of Coldest Quarter; bio12, Annual Precipitation; bio13, Precipitation of Wettest Month; bio14, Precipitation of Driest Month; bio15, Precipitation Seasonality (Coefficient of Variation); bio16, Precipitation of Wettest Quarter; bio17, Precipitation of Driest Quarter; bio18, Precipitation of Warmest Quarter; bio19, Precipitation of Coldest Quarter.

2.2. Data analysis

Before starting the distribution modelling, I performed multicollinearity analysis among bioclimatic variables. I detected multicollinearity using Variance Inflation Factor [29] through a stepwise procedure. I limited the current distribution range including European terrestrial zone by cropping the map and therefore limiting the area (as same range in Fig. 2a) to be able to obtain more effective collinearity results. Multicollinearity analysis showed that 12 variables from the 19 input variables had collinearity problem. Therefore, VIFs of the remaining variables were without collinearity: bio2, 3.81; bio4, 2.01; bio8, 1.41; bio9, 4.91; bio14, 4.42; bio15, 2.54; bio19, 2.95.

Before fitting the model, I created pseudo-absences on the data. To do this I created 1000 geographically random selected pseudo-absences. Thus, I turned data into presence-background data then presence-only data. Regarding species distribution modelling, I fitted four methods namely Generalized Linear Models (GLMs), Generalized Additive Models (GAMs), Support Vector Machine (SVM) and Random Forest (RF). Each model was evaluated using 10 runs of bootstrapping replications taking 30 percent as a testing data in terms of partitioning methods.

Regarding prediction I fitted both current and future projected analysis. I fitted current potential distribution with ensemble using weighted averaging based on TSS statistic and set optimum threshold criterion as 2 optimization thresholds. For the future projection I used bioclimatic (CMIP5) for the year of 2070 as a resolution of 10 km^2. I ensembled this data as the same method with current data. Further, I revealed distributional change between current and future model based on probability of occurrence. I obtained mean variable importance (and confidence interval) for multiple models based on training dataset. Furthermore, I evaluated the results of each fitted model using accuracy and thresholds. I used the mean values of the thresholds as a parameter to determine extinction, persistence and colonization. I performed the analysis using R program [30]. I used reproducible and extensible *sdm* method [11] for species distribution modelling.

Receiver operating characteristic (ROC) curve is used for evaluation the performance of the models using area under the curve. This is calculated from the specificity (false-positive error) rate and the sensitivity (true positive rate) on the x and y axis, respectively [31]. The AUC values are important to understand model performances. In general, high performance models have >0.9 AUC, moderate performance models have 0.7–0.9 AUC and poor models 0.5–0.7 AUC values [31]. However, 0.8 AUC value is a critical threshold for a model, which could be considered a necessary value [32].

3. RESULTS

All four models result in high accuracy values, which range from 0.98 to 0.99 (Table 1). The results show four models successfully processed and provide considerable patterns. The correlation of the models ranges from 0.91 to 0.95, while TSS values from 0.95 to 0.98. GLMs, GAMs and RF models have higher accuracy values than SVM model. ROC-AUC curves using specificity and sensitivity values of four models is presented in Figure 1. These curves show that all models have quite high AUC values in terms of both training and testing data. Training AUC values is always higher than testing AUC as expected. However, the difference between training and testing data is slightly higher in GLMs, GAMs and SVM than RF. Since I used 30% as a bootstrapping partition testing data is almost predicted in RF as much as training data. This pattern is clearly an effect of model

performance. Predictions for current time and the future time as for the year 2070 is presented Figure 2a, b. Projected distributions of *Campanula lyrata* differs from current distribution especially across the Europe as well as in West America. The change of distribution, which is presented Figure 3, clearly shows that the species have potential to distribute not only in Europe and the America's but also Africa and on Asian continents. Figure 4 presents the potential areas of colonization and extinction for *Campanula lyrata* based on mean values of thresholds. Relative Variable Importance (RVI) of four models in terms of bioclimatic variables are presented in Figure 5. However, these variables are used after the multicollinearity check for the analysis.

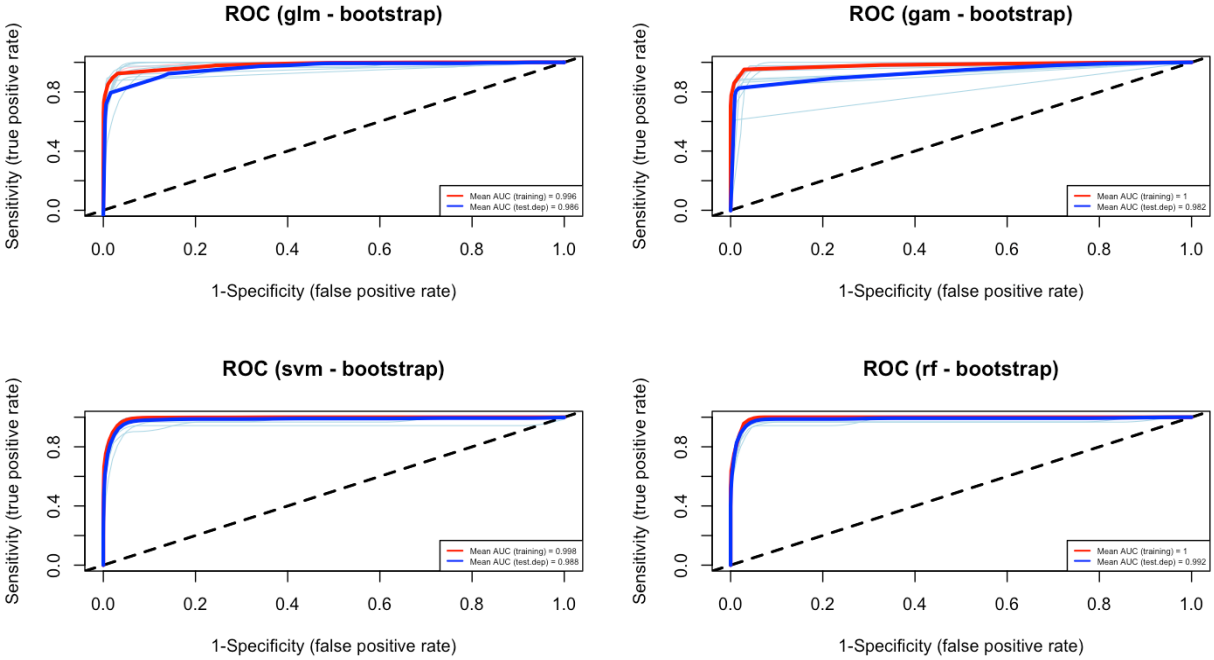

Figure 1 ROC-AUC curves of four models which bootstrapping method is used. The models are Generalized Linear Models (GLMs), Generalized Additive Models (GAMs), Support Vector Machine (SVM) and Random Forest (RF).

Table 1 Mean performance of the fitted models using bootstrap partitioning (Generalized Linear Models (GLMs), Generalized Additive Models (GAMs), Support Vector Machine (SVM) and Random Forest (RF)).

Methods	AUC	COR	TSS	Deviance
GLMs	0.99	0.91	0.95	0.29
GAMs	0.98	0.91	0.96	0.82
SVM	0.99	0.92	0.96	0.11
RF	0.99	0.95	0.98	0.06

4. DISCUSSION

Four models in my analysis have quite high AUC values. GAMs model has slightly lower performance than GLMs, SVM and RF. However, correlation of RF was the highest while deviance is the lowest.

Current potential distribution of *Campanula lyrata* is mostly in the Mediterranean climate zone in Anatolia. It has slightly greater distribution in Aegean region than along the Mediterranean seashore. There is also some distributional range from southeast Anatolia to Mesopotamia. For the future time distributional patterns are rather similar to those along the Mediterranean seashore and to Mesopotamia. However, it considerably increases in mid and north Aegean parts and the Marmara region. This shows a clear increase in south Turkey to north Turkey. With regard to Europe, a strong increase of distribution potential is in West Spain. Following this pattern distribution areas increase in Greece, Italy and Croatia as well as partly rise across Europe. In addition, few areas appear for potential distribution in the west part of the Caspian Sea. Regarding global scale distribution areas

considerably increase in west America as well as India and mid Africa. No significant pattern appears except from this area across five continents. Regarding colonization potential of *Campanula lyrata.* It occurs in the areas ranged from west America to Asia including Australia. However, extinction appears in the region of northern pole and especially Greenland.

Regarding relative importance variables GLMs model result with annual mean temperature, minimum temperature of coldest month, mean temperature of warmest quarter, mean temperature of coldest quarter, precipitation of wettest quarter performed best. GAMs result with the best variables are temperature seasonality, mean temperature of warmest quarter, mean temperature of coldest quarter, precipitation of wettest quarter, temperature annual range. SVM model shows precipitation seasonality is significantly important than other variables. Following this, mean diurnal range, precipitation of wettest month, precipitation of coldest quarter and precipitation of warmest quarter are also important bioclimatic variables. According to RF precipitation of wettest month performed the best. Variables of precipitation of coldest quarter, precipitation seasonality, precipitation of wettest quarter and precipitation of warmest quarter also more important than other variables. Obviously, precipitation seasonality and precipitation of wettest month performed quite high performance than others in terms of overall variable importance results.

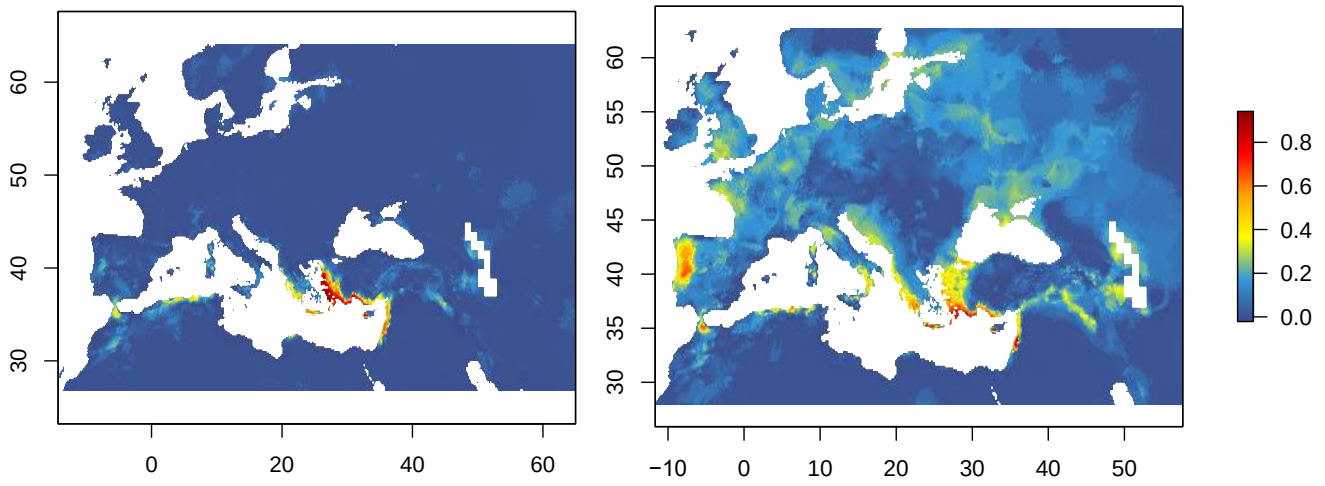

Figure 2a Potential distribution of *Campanula lyrata* for the current time on the left side and for the future (projected as 2070) time on the right side across Turkey and Europe.

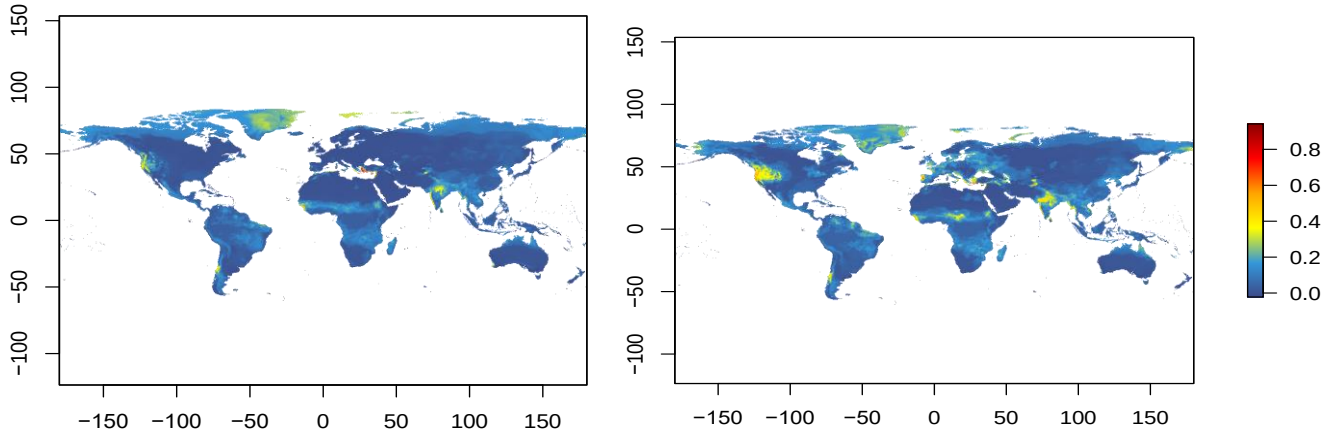

Figure 2b Potential distribution of *Campanula lyrata* for the current time on the left side and for the future (projected as 2070) time on the right side across the world.

For species distribution modelling topographic and biotic variables as well as geologic data are significantly important in addition to bioclimatic variables. Especially biotic relations such as plant-plant interactions and species coexistence patterns constantly affect distribution modelling [33] as well as AUC values of the models [34]. During the modelling process it is important to select highly relevant variables by performing multicollinearity analysis. It might sometimes differ when modelling species is endemic because endemic species could have specific habitat requirements. Therefore, such an important predictor for an endemic species could be eliminated in multicollinearity analysis. This point needs to be considered during variable selection.

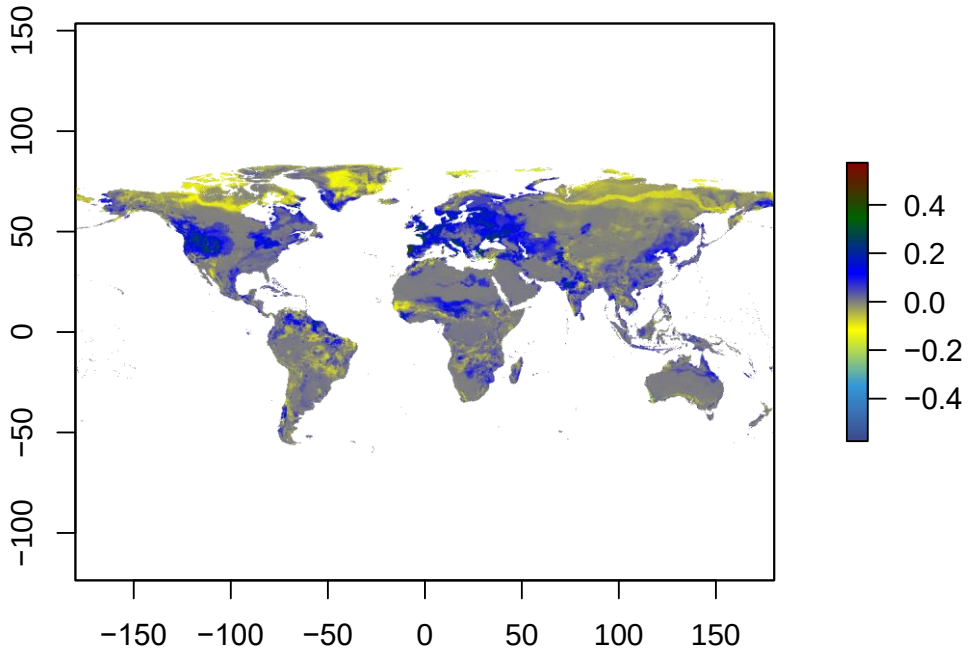

Figure 3 Change of distribution between current and future (projected to 2070) time.

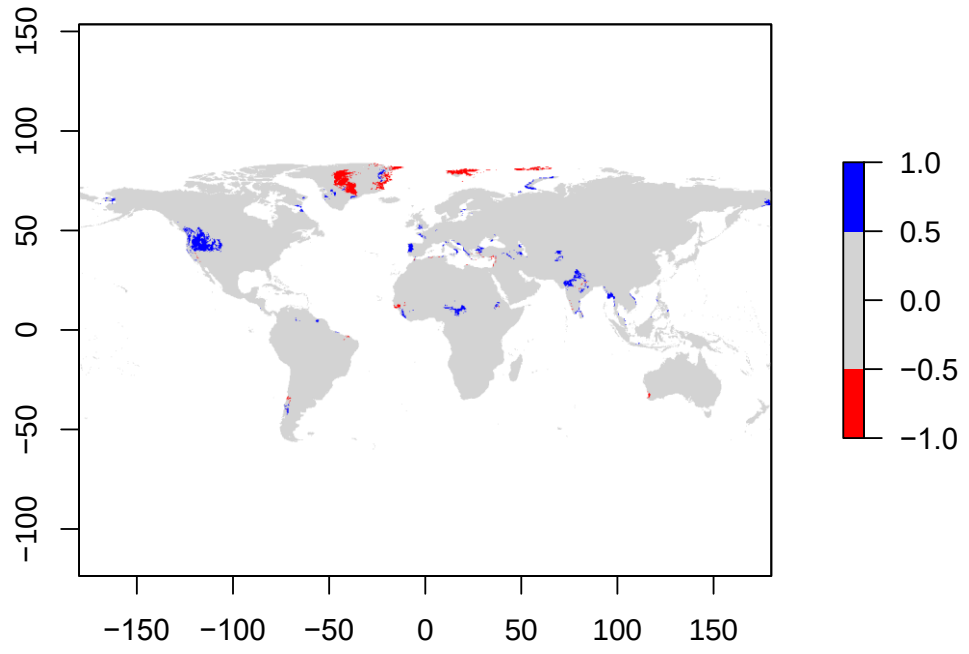

Figure 4 Potential areas of colonisation (blue) and extinction (red) of *Campanula lyrata*.

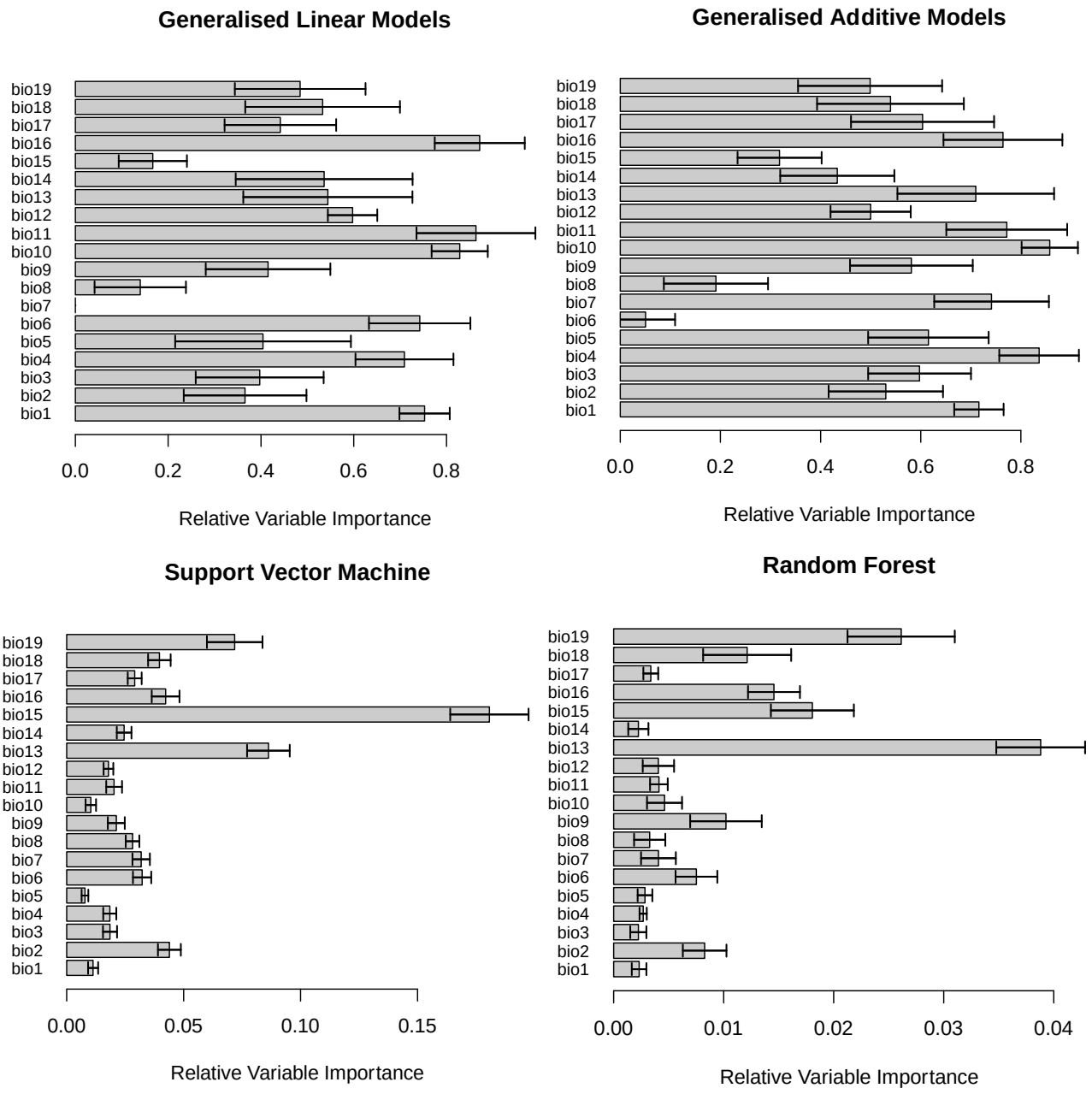

Figure 5 Relative Variable Importances (RVI) of four models in terms of bioclimatic variables.

In conclusion, I found that potential distribution area of *Campanula lyrata* is expected to be increase in Turkey in the future. Climate change would likely affect distribution of the species. However, regarding global scale significant increase does not occur. Instead, potential distribution areas shift from North pole to lower latitudes. Regarding bioclimatic variables precipitation related predictors play an important role for the distribution. Species distribution modelling for *Campanula lyrata* has revealed valuable information about distributional patterns. The method should be performed for various endemic species for Turkey, where the rate of endemic richness is quite high [21].

Acknowledgments

I wish to thank the editor and reviewers for their thoughtful and valuable comments on the manuscript. I thank Nadine Kemp for linguistic control of the manuscript.

Funding

The author has no received any financial support for the research, authorship or publication of this study.

The Declaration of Conflict of Interest/ Common Interest

No conflict of interest or common interest has been declared by the author.

The Declaration of Research and Publication Ethics

The author of the paper declare that he complies with the scientific, ethical and quotation rules of SAUJS in all processes of the paper and that he does not make any falsification on the data collected. In addition, they declare that Sakarya University Journal of Science and its editorial board have no responsibility for any ethical violations that may be encountered, and that this study has not been evaluated in any academic publication environment other than Sakarya University Journal of Science.

REFERENCES

[1] A. Jentsch, J. Kreyling, and C. Beierkuhnlein, "A new generation of climate-change experiments: events, not trends", Frontiers in Ecology and the Environment, vol. 5, no. 7, pp. 365-374, 2007.

[2] C. Parmesan, "Ecological and evolutionary responses to recent climate change", Annual Review of Ecology, Evolution, and Systematics, vol. 37, pp. 637-669, 2006.

[3] SHM. Butchart, M. Walpole, B. Collen, A. van Strien, JPW. Scharlemann, REA. Almond, et al., "Global biodiversity: indicators of recent declines", Science, vol. 328, pp. 1164–1168, 2010.

[4] BJ. Cardinale, JE. Duffy, A. Gonzalez, DU. Hooper, C. Perrings, P. Venail, et al., "Biodiversity loss and its impact on humanity", Nature, vol. 486, pp. 59–67, 2012.

[5] A. Guisan, and W. Thuiller, "Predicting species distribution: offering more than simple habitat models", Ecology letters, vol. 8, no. 9, pp. 993-1009, 2005.

[6] M. Demircan, H. Gürkan, O. Eskioğlu, H. Arabacı, and M. Coşkun, "Climate change projections for Turkey: three models and two scenarios", Türkiye Su Bilimleri ve Yönetimi Dergisi, vol. 1, no.1, pp. 22-43, 2017.

[7] A. Akçakaya, O. Eskioğlu, H. Atay, and O. Demir, "Yeni senaryolar ile Türkiye için iklim değişikliği projeksiyonları. – Meteoroloji Genel Müdürlüğü Matbaası, Turkey", 2013.

[8] B. Önol, and YS. Ünal, "Assessment of climate change simulations over climate zones of Turkey", Regional Environmental Change, vol. 14, no.5, pp. 1921-1935, 2014.

[9] NE. Zimmermann, JrTC. Edwards, CH. Graham, PB. Pearman, and JC. Svenning, "New trends in species distribution modelling", Ecography, vol. 33, no.6, pp. 985-989, 2010.

[10] H. Yilmaz, OY. Yilmaz, and YF. Akyüz, "Determining the factors affecting the distribution of *Muscari latifolium*, an endemic plant of Turkey, and a mapping species distribution model", Ecology and Evolution, vol. 7, no.4, pp. 1112-1124, 2017.

[11] B. Naimi, and MB. Araújo, "sdm: a reproducible and extensible R platform for species distribution modelling", Ecography, vol. 39, no.4, pp. 368-375, 2016.

[12] SJ. Phillips, RP. Anderson, and RE. Schapire, "Maximum entropy modeling of species geographic distributions", Ecological Modelling, vol. 190, pp. 231–259, 2006.

[13] G. Carpenter, AN. Gillison, and J. Winter, "DOMAIN: A flexible modelling procedure for mapping potential distributions of plants and animals", Biodiversity Conservation, vol. 2, pp. 667–680, 1993.

[14] HA. Nix, "A biogeographic analysis of Australian elapid snakes", In R. Longmore (Ed., pp. Atlas of elapid snakes of Australia, Australian flora and fauna series, Canberra, ACT: Australian Government Publishing Service, no. 7, pp. 4–15, 1986.

[15] A. Herrero, and R. Zamora, "Plant responses to extreme climatic events: a field test of resilience capacity at the southern range edge", Plos one, vol. 9, no. 1, pp. 1-12, 2011.

[16] A. Jentsch, J. Kreyling, M. Elmer, E. Gellesch, B. Glaser, K. Grant, … C. Beierkuhnlein, "Climate extremes initiate ecosystem-regulating functions while maintaining productivity", Journal of Ecology, vol. 99, no. 3, pp. 689-702, 2011.

[17] JE. Weaver, "Prairie Plants and Their Environment, A Fifty-five Year Study in the Midwest", University of Nebraska Press, Lincoln, NE, 1968.

[18] CW. MacGillivray, JP. Grime, and The Integrated Screening Programme (ISP) Team, "Testing predictions of the resistance and resilience of vegetation subjected to extreme events", Functional Ecology, pp. 640-649, 1995.

[19] CD. Allen, and DD. Breshears, "Drought-induced shift of a forest–woodland ecotone: rapid landscape response to climate variation", Proceedings of the National Academy of Sciences, vol. 95, no. 25, pp. 14839-14842, 1998.

[20] Z. Wu, P. Dijkstra, GW. Koch, J. Peñuelas, and BA. Hungate, "Responses of terrestrial ecosystems to temperature and precipitation change: A meta-analysis of experimental manipulation", Global Change Biology, vol. 17, no. 2, pp. 927-942, 2011.

[21] A. Güner, S. Aslan, T. Ekim, M. Vural, and MT. Babaç, "Plant List of Turkey: Vascular Plants", Nezahat Gökyiğit Botanical Garden Press, ANG Foundation, İstanbul, 2012.

[22] J. Noroozi, G. Zare, M. Sherafati, M. Mahmoodi, D. Moser, Z. Asgarpour, and GM. Schneeweiss, "Patterns of endemism in Turkey, the meeting point of three global biodiversity hotspots, based on three diverse families of vascular plants", Frontiers in Ecology and Evolution, vol. 7, no.159, 2019.

[23] Ç. Şenkul, and K. Seda, "Türkiye endemik bitkilerinin coğrafi dağılışı", Türk Coğrafya Dergisi, no. 69, pp. 109-120, 2017.

[24] PH. Davis, "Flora of Turkey and the East Aegean Islands", Edinburgh University Press, Edinburgh, vol 1-9, 1965-1985.

[25] PH. Davis, RR. Mill, and K. Tan, "Flora of Turkey and the East Aegean Islands", Edinburgh University Press, Edinburgh, vol 10, 1965-1985.

[26] A. Güner, N. Özhatay, T. Ekim, and KHC. Baser, "Flora of Turkey and the East Aegean Islands", Edinburgh University Press, Edinburgh Herbaceous plants, vol. 11, 2000.

[27] RJ. Hijmans, SE. Cameron, JL. Parra, PG. Jones, and A. Jarvis, "Very high-resolution interpolated climate surfaces for global land areas", International Journal of Climatology: A Journal of the Royal Meteorological Society, vol. 25, no. 15, pp. 1965-1978, 2005.

[28] SE. Fick, and RJ. Hijmans, "WorldClim 2: new 1-km spatial resolution climate surfaces for global land areas", International journal of climatology, vol. 37, no. 12, pp. 4302-4315, 2017.

[29] ER. Mansfield, and BP. Helms, "Detecting multicollinearity. The American

Statistician", vol. 36, no. 3a, pp. 158-160, 1982.

[30] RC. Team, "R: A language and environment for statistical computing", Vienna, Austria.

[31] J. Franklin, "Mapping species distributions: Spatial inference and prediction", Cambridge: Cambridge University Press, 2009.

[32] FEJr. Harrell, "Regression modeling strategies: With applications to linear models, logistic regression, and survival analysis", New York, NY: Springer, 2001.

[33] E. Meineri, O. Skarpaas, and V. Vandvik, "Modeling alpine plant distributions at the landscape scale: Do biotic interactions matter?", Ecological Modeling, no. 231, pp. 1–10, 2012.

[34] L. Pellissier, K. Anne Bråthen, J. Pottier, CF. Randin, P. Vittoz, A. Dubuis, ... A. Guisan, "Species distribution models reveal apparent competitive and facilitative effects of a dominant species on the distribution of tundra plants", Ecography, vol. 33, pp. 1004–1014, 2010.

SAKARYA ÜNİVERSİTESİ
FEN BİLİMLERİ ENSTİTÜSÜ DERGİSİ

Sakarya University Journal of Science
SAUJS

e-ISSN 2147-835X | Period Bimonthly | Founded: 1997 | Publisher Sakarya University |
http://www.saujs.sakarya.edu.tr/en/

Title: An Adaptive Ant Colony System Memorizing Better Solutions (aACS-MBS) For Traveling Salesman Problem

Authors: Dursun EKMEKÇİ

Recieved: 2020-11-06 18:32:56

Accepted: 2021-04-07 22:33:18

Article Type: Research Article

Volume: 25
Issue: 3
Month: June
Year: 2021
Pages: 673-689

How to cite
Dursun EKMEKÇİ; (2021), An Adaptive Ant Colony System Memorizing Better Solutions (aACS-MBS) For Traveling Salesman Problem. Sakarya University Journal of Science, 25(3), 673-689, DOI: https://doi.org/10.16984/saufenbilder.822646
Access link
http://www.saujs.sakarya.edu.tr/en/pub/issue/62736/822646

Sakarya University Journal of Science 25(3), 673-689, 2021

An Adaptive Ant Colony System Memorizing Better Solutions (aACS-MBS) For Traveling Salesman Problem

Dursun EKMEKCİ*[1]

Abstract

Choosing the optimal one among the many alternatives that meet the criteria is one of the problems that occupy life. This kind of problem frequently encountered by commercial companies in daily life is one of the issues that operators focus on with care. Many techniques have been developed that can provide acceptable solutions in a reasonable time. However, one of the biggest problems with these techniques is that the appropriate values can be assigned to the algorithm parameters. Because one of the most important issues determining algorithm performance is the values to be assigned to its parameters. The Ant Colony System (ACS) is a metaheuristic method that produces successful solutions, especially in combinatorial optimization problems (COP). The Ant Colony System Memorizing Better Solutions (ACS-MBS) algorithm is an ACS version developed to associate the pheromone value more with the solution success. In this study, an Adaptive ACS-MBS (aACS-MBS) method is presented that updates the *q0* parameter dynamically, which balances the exploitation and exploration activities of the ACS-MBS. The method has been tested on the traveling salesman problem (TSP) of different sizes, and the obtained results are evaluated together with the change in the q0 parameter, and the solution search strategy of the algorithm is analyzed. With the pheromone maps formed as a result of the search, the effect of transfer functions was evaluated. Results obtained with aACS-MBS were compared with different ant colony optimization (ACO) algorithms. The aACS-MBS fell behind the most successful solution found in the literature, by up to 3.83%, in large-scale TSP benchmarks. As a result, it has been seen that the method can be successfully applied to the COP.

Keywords: ant colony optimization, ant colony system, ant colony system memorizing better solutions, adaptive ant colony system memorizing better solutions

*Corresponding author: dekmekci@karabuk.edu.tr
[1] Karabuk University, Faculty of Engineering, Computer Engineering Department, 78050, Karabük.
ORCID: https://orcid.org/0000-0002-9830-7793

1. INTRODUCTION

One of the main factors that determine the performance of swarm intelligence-based optimization algorithms, which are generally designed inspired by nature, is the model that the algorithm imitates. In this context, the most similar simulation of the problem characteristic should be preferred in the selection of the algorithm. While the model in nature is designed as a computer algorithm, the behaviors of the model are determined as procedures, and the components that affect these behaviors are determined as algorithm parameters. If the model whose algorithm is designed is a swarm that living as a colony, in general, the individual activities of the colony members determine the exploration ability of the algorithm, while collective activities affect the exploitation ability [1]. Another factor affecting the success of the algorithm is the appropriateness of the values assigned for the algorithm parameters. Researchers focusing on metaheuristic methods in the field of operational research have recently developed online and offline techniques that determine the appropriate values for the control parameters of these algorithms.

Ant Colony Optimization (ACO) is a swarm intelligence-based metaheuristic method that imitates the adventure of an ant colony in foraging and determining the shortest path between the food and the nest [2]. In real life, when ants, who leave the nest in search of food, come across a food source, they try to find the shortest path to move the food from that source to their nest. Ants emit an evaporating secretion called pheromone in the process of carrying food between the source and the nest, and the other ants following them continue their journey by following the more intense secretion. In this way, the shortest path is determined after a few tours. Even if the path used is no longer the shortest path due to different factors, this approach makes it easy for ants to find the shortest path. The shortest path determination behavior of the colony members participating in the food collection is illustrated in Figure 1.

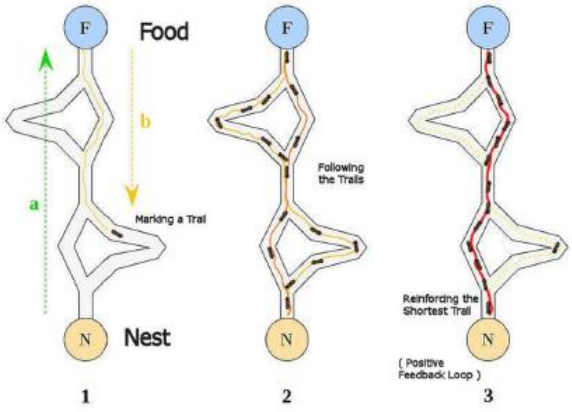

Figure 1 The shortest path finding prototype of artificial ants

The synergy, based on this collective behavior of the ant colony, inspired the development of ACO algorithms with strong exploitation ability, which is especially successful in solving the combinatorial optimization problem (COP) [3]. Although different ACO algorithms, versions, and extensions have been developed concerning this approach, the pheromone chemical is the basic component for all methods [4]. An effective metaheuristic algorithm should provide an appropriate balance between maximum utilization of the search experience so far, and the exploration of relatively unexplored search regions. The variation in ACO algorithms is based on differences in the approach in managing the pheromone trail to reach this targeted balance. The pheromone level induces a probability distribution in the search space and determines which regions of the field are sampled effectively, in other words, in which parts of the field the solutions constructed are concentrated. In this regard, the most successful performing ACO algorithms use strategies where the best solutions found during the search strongly contribute to pheromone updating [3]. In line with this understanding, the Ant Colony Optimization Memorizing Better Solutions (ACO-MBS) which uses "Edge Matrix" to directly correlate the correlation between solution components with solution success, was developed [5]. In the literature, suggestions for pheromone control [6] focus more on determining the evaporation rate [7], assigning pheromone value [8], and limiting the pheromone level [9].

After analyzing the correlations between solution components correctly, it can be said that the second important issue affecting the algorithm performance is the determination of the pheromone trail. Because ants will continue their journey by considering the pheromone density in the environment. Within the scope of the algorithm, turning to the components where the pheromone secretion is most intense increases the exploitation capability of the algorithm while decreasing the exploration capability. In Ant System (AS) [10], which is the first ACO algorithm, the roulette wheel approach based on pheromone concentrations is applied for the node selection, while in Ant Colony System (ACS) [11], the *q0* parameter is added to the algorithm. (These methods are explained in detail in the next section.) Although many metaheuristic methods use different operators for exploitation and exploration conformance, the ACS combines this balance in only one parameter. In the study, the Adaptive Ant Colony System Memorizing Better Solutions (aACS-MBS) method, which dynamically controlled the *q0* parameter of the ACS-MBS, which is improved to associate the pheromone value of the ACS with the solution success more, is proposed. The method has been tested on the traveling salesman problem (TSP), which is one of the popular examples of combinatorial optimization problems (COP), and the results obtained proved that the proposed method increases the exploratory ability of the ACS.

The remainder of the article is designed as follows: Section 2 describes ACO with its general features, the AS and the ACS. Next, the ACS-MBS, an improved version of ACS, is explained. In the section, finally, the proposed method is introduced. In Section 3, TSP, and selected TSP benchmarks are explained. In Section 4, the results obtained with the proposed method and different versions of the ACO are presented. In Section 5, the study has been concluded in all aspects.

2. BACKGROUND OF THE PROPOSED METHOD

In this section, the AS algorithm that applies the ACO approach in its basic form, and the ACS, developed with the updates in the algorithm, are explained in detail. Later, the ACS-MBS, which was developed to reflect the solution success directly to the correlation between the components, and the proposed aACS-MBS method is introduced to update the search orientation of the method in the study process.

2.1. Ant System (AS)

The first ACO algorithm developed inspired by the real ant colony is the AS algorithm. The main steps of the algorithm, the first versions of which are tested on TSP, are shown in Figure 2.

Algorithm 1 General Structure of ACO

```
Set parameters
Initialize pheromone trails
While termination conditions not met do
  for i = 0 to m do
      Construct an artificial ant solution (Si)
  end for
  Daemon actions (optional)
  Update pheromones
End while
Output : The best so far solution
```

Figure 2 General steps of ACO

As seen in Figure 2, in the first step, values for the AS parameters, and the initial pheromone levels are determined. For the initial solutions, to equalizing the selection probabilities of all components, initial pheromone values should be kept as low as 0.1 as possible [7].

While solutions are constructing with *m* determined artificial ants, the first item of the next solution is the node selected randomly. The solution array is then expanded by adding a node from the set of possible neighbors. This process continues until the solution is constructed. The node to be added to the solution array is determined by a probability calculation. In a problem that has *V* nodes, for the ant *k* which

coming to node *i*, the selection probability (p_{ij}^k) of node *j* is determined by (1).

$$p_{ij}^k = \frac{(\tau_{ij})^{\alpha}(\eta_{ij})^{\beta}}{\sum_{u \in V_i^k}(\tau_{iu})^{\alpha}(\eta_{iu})^{\beta}} \quad (1)$$

In (1), τ_{ij} represents the pheromone level between *i-j*, and V_i^k represents the possible nodes that ant k can visit after node *i*. δ_{ij} is the distance between *i-j* and η_{ij} is the inverse of this distance ($1/\delta_{ij}$). α and β are the heuristic parameters of the algorithm.

After solutions are constructed, some problem-specific calculations may be required before pheromone updates. These operations, called *"daemon actions"* are operations that facilitate local search. In the pheromone updating process, firstly the pheromone levels between the components are evaporated at the set ratio, and then the pheromone is added between the components in proportion to the solution success the ants obtain [12]. For these operations, (2) is used.

$$\tau_{ij} \leftarrow (1-\rho).\tau_{ij} + \sum_{k=1}^{m} \Delta\tau_{ij}^k \quad (2)$$

In (2), ρ is the evaporation rate assigned in the range of (0, 1], and $\Delta\tau_{ij}^k$ is the amount of pheromone to be added between *i-j* in proportion to the solution cost (L_k) of the ant *k*. The amount of this pheromone to be added is calculated by (3).

$$\Delta\tau_{ij}^k = \begin{cases} \frac{1}{L_k} \; if \; ant \; k \; used \; edge \; (i-j) \\ 0 \qquad\qquad\qquad otherwise \end{cases} \quad (3)$$

2.2. Ant Colony System (ACS)

The ACS includes the updates made for the AS algorithm to be greedier in generating new solutions. In this context, the updates are based on increasing the amount of pheromone between the components that make up the more successful solution and taking more consideration of the pheromone level in constructing solutions.

Two alternative methods are applied in deriving new solutions in ACS. If the value of *q* randomly selected in the range of [0,1] is bigger than *q0*, the node *j* after *i* is determined by (1). Otherwise, the node who has the highest pheromone concentration between node *i* is selected.

Pheromone updating process in ACS is divided into two categories: The operations in (2) and (3) are defined as *"local pheromone update"* and are applied for all ants in each iteration. *"Global pheromone update"* is applied with (4) for the most successful ant route in the iteration.

$$\tau_{ij} \leftarrow (1-\rho).\tau_{ij} + \rho.\Delta\tau_{ij}^{best} \quad (4)$$

2.3. Ant Colony System Memorizing Better Solutions (ACS-MBS)

The ACS-MBS is one of the ACO versions that developed to reflect the solution success directly among the components that make up the relevant solution array and thus establish the correlation between the components more accurately. While the algorithm takes advantage of the ACS transition rules, it uses transfer functions in pheromone updating. Compared to other popular algorithms of ACO for TSP, the method produced more successful solutions than many of the algorithms [5].

In the ACS-MBS, apart from the pheromone matrix (PM), an edge matrix (EM) is used. In each cycle, after the solutions are constructed by artificial ants, the values in the cells corresponding to the solution components in the EM are compared with the cost of the new solution. If a lower cost solution (S_m) is constructed by using any edge, the cell ($EM_{S_{mi}S_{mj}}$) corresponding to this edge in EM is updated as the new solution cost. Then the relevant update is reflected in the PM. If the solution obtained is the best one so far *"global update"* is applied, if not *"local update"*. In local updating, firstly, the normalization value in the range (0.1 - 1) of the solution cost is calculated with (5).

$$normal_{S_m} = 1 - \frac{[cost(S_m) - \min(EM)] * 0.9}{[max(EM) - \min(EM)]} \quad (5)$$

The pheromone level of the relevant edge is calculated with the specified transfer function for the normalization value obtained by (5). The

pheromone update process in the ACS-MBS is illustrated in Figure 3.

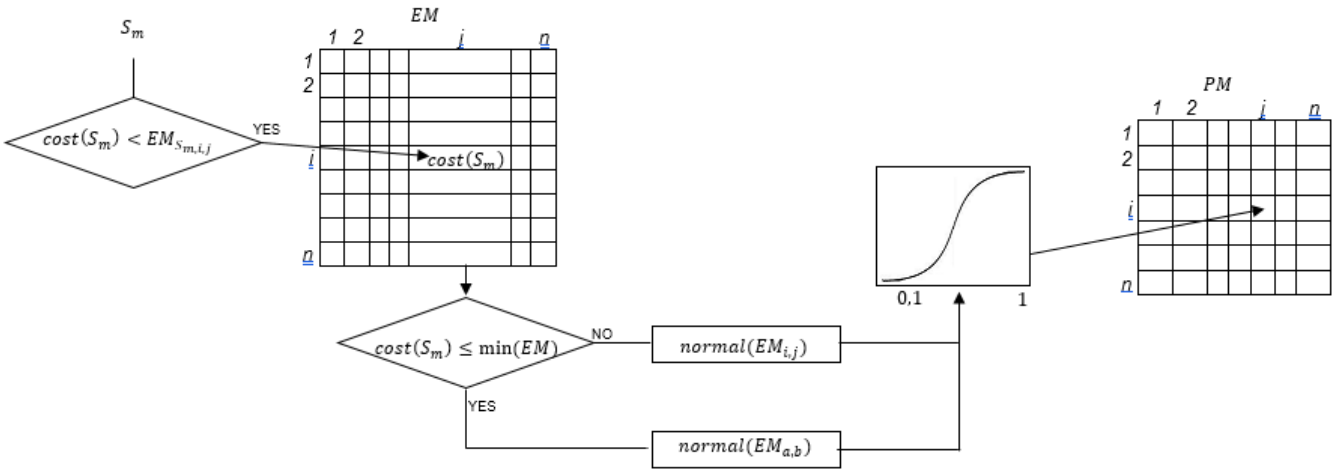

Figure 3 Pheromone updating process in ACS-MBS

Within the scope of the algorithm, different types of transfer functions can be used for the pheromone update, depending on the problem's estimated solution space, problem complexity, and parameter characteristics.

2.4. Proposed Method: Adaptive Ant Colony System Memorizing Better Solutions (aACS-MBS)

In AS and ACS, the amount of pheromone accumulated at the edges can reach values greater than 1, depending on the use of the relevant edge. In the ACS-MBS, the values in PM are limited to 0-1. Therefore, the change in PM in each cycle contains more objective information about the searching of the algorithm. With the proposed method, exploitation/exploration mobility of ACS-MBS is followed over the change in PM, and the value of *q0* is dynamically assigned for the balance between these two.

Firstly, the total amount of *change* in pheromone levels retained in PM in each cycle is calculated with (6).

$$change = \sum_{i=1}^{D}\sum_{j=1}^{D} |old(PM_{i,j}) - new(PM_{i,j})| \quad (6)$$

Then (7) is used to determine the value to be assigned to the *q0* parameter.

$$q0 = 0.8 + change * Dimension \quad (7)$$

Equation (7) is formed by considering the results of the experiments obtained with different parameter values. Experiments have shown that when values less than 0.8 are assigned for the *q0* parameter, the algorithm fails to produce good results, and when bigger values are assigned, the algorithm loses its exploration ability. For the algorithm not to lose its exploitation ability, the minimum value assigns to *q0* is set as 0.8. As seen in (7), the value to be assigned to *q0* is calculated by considering the amount of change in PM. The value calculated by (6) is multiplied by the number of dimensions (nodes) in the problem and added to 0.8.

In this context, the aABC-MBS algorithm is shown in Figure 4 with its main steps.

Algorithm: aACS-MBS

```
Set parameters {α, β, Transfer Function}
// Initialization phase
For i=1 To m
  Construct solution Si randomly
End For
Set EMi,j=max(S)
Set PMi,j=0
// Update EM
For i=1 To m
  For j=1 To n
    If (Si < EMSi,Sj)
      EMSi,Sj=Si
    End If
  End For
End For
// Update PM
For i=1 To n
  normalSn=1-(cost(Sn)-min(EM))*0.9/(max(EM)-min(EM))
  For j=1 To n
    // Calculate f(normalSn) according to the transfer function
    If (f(normalSn) > PMi,j)
      PMi,j=normalSn
    End If
  End For
End For
While termination conditions not met do
  For k=1 To m
    Select node i randomly   i={1, 2, 3, …, n}
    While solution Sk not completed
      Select q randomly
      If (q ≤ q0)
        Next node=max(τi,j)
      Else
        Select next node according to Eq. (1)
      End If
      // Update EM
      For i=1 To m
        For j=1 To n
          If (Si<EMSi,Sj)
            EMSi,Sj=Si
          End If
        End For
      End For
      // Update PM and calculate the change value
      change=0
      For i=1 To n
        normalSn=1-(cost(Sn)-min(EM))*0.9/(max(EM)-min(EM))
        For j=1 To n
          // Calculate f(normalSn) according to the transfer function
          If (f(normalSn)>PMi,j)
            change =abs(PMi,j - normalSn)
            PMi,j=normalSn
          End If
        End For
      End For
      q0=0.8+change * n
    End While
End While
Output: best(S)
```

Figure 4 The aACS-MBS algorithm

3. TSP

As one of the most popular examples of COP, TSP is one of the first benchmarks in which the methods developed by operations researchers were tested. The basic principle in the problem, the first examples of which were put forward in the 1800s, is to try to obtain a closed graph with the shortest length. In a network model with *n* nodes to visit, the salesman starts its travel from any node and returns to the starting node, provided they visit all nodes [13]. Solution cost is directly dependent on route distance. Since the shortest Hamilton tour is searched in *G(V, E)* closed graph, where *V* is the set of nodes, and *E* is the set of edges between these nodes, the problem is in the NP-hard class [14]. The distance matrix (*D*) is associated with *V*, and in many instances of TSP the distances between nodes are symmetrical (d_{ij}=d_{ji}). The Euclidean formula is usually used to calculate distances. In this context, the total route cost is calculated with equation (8).

$$f(x) = \left(\sum_{i=1}^{n-1} d_{ij}\right) + d_{n1} \quad (8)$$

4. EXPERIMENTAL STUDY

The proposed method was run on the .net platform, coded with C # programming language, and on a machine with i7-5600U CPU 2.60 processor, 8 GB RAM, and 64-bit Windows 8 Operating System. The performance of the aACS-MBS algorithm and its searching strategy has been tested on different sizes of TSP benchmarks. In this section, the results obtained with the algorithm are presented, and the analyzes are discussed.

4.1. TSP Benchmarks

The application has been tested on TSP samples taken from the TSPLIB library (http://elib.zib.de/pub/mp-testdata/tsp/tsplib/tsp/index.html). Selected benchmarks are eil51, kroA100, kroA150, kroA200, pr299 and pr439. The numbers of nodes in the problems and the best results known to date [15] [16] are presented in Table 1.

Table 1
Selected TSP benchmarks

Name	Number of Nodes	Best Result
eil51	51	417
kroA100	100	21282
kroA150	150	26524
kroA200	200	29368
pr299	299	48191
pr439	439	107217

4.2. Parameter Settings

The AS, ACS, ACS-MBS, and aACS-MBS algorithms have been run independently 30 times with a maximum cycle number (MCN) is 1000 for the selected test problems. For parameter settings, parameter analysis for the ACS-MBS was considered. In this context, the values in [5] have been assigned to the algorithm parameters. The parameter values assigned for the algorithms are shown in Table 2.

Table 2
Algorithm parameters

	AS	ACS	ACS-MBS	aACS-MBS
Colony Size	20	20	20	20
α	1	1	1	1
β	5	5	5	5
ρ	0.1	0.1	-	-
q0	0.95	0.95	0.95	-
Transfer Function	-	-	linear	linear

In order to analyze the searching strategy and convergence performance of the aACS-MBS in detail, the algorithm was also run by using the *"linear"*, *"sigmoid"* (9), and *"v-shaped"* (10) transfer functions. Transfer functions are drawn in Figure 5. Algorithm was run independently 30 times with these transfer functions, and MCN was 1000 in all experiments.

$$sigmoid = f(x) = \frac{1}{1+e^{-10*(normal_{S_i}-0.5)}} \quad (9)$$

$$v-shaped = f(x) = \begin{cases} 1 & if(x \leq 0.1) \\ x^3 & otherwise \end{cases} \quad (10)$$

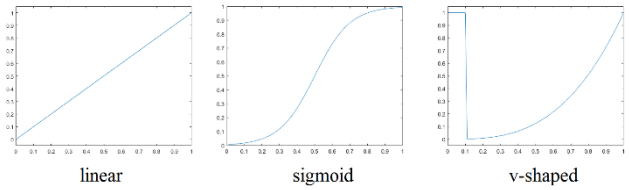

Figure 5 Transfer Functions

4.3. Results

The results obtained by the algorithm are presented in two categories. In the first category, the effect of transfer functions on the algorithm is analyzed. In the second category, aACS-MBS results are compared with solutions obtained with other ACO versions.

4.3.1. Searching Strategy Analysis of aACS-MBS

For the best solutions obtained by aACS-MBS with different transfer functions, the results in each iteration and the current *q0* values are shared in graphics (Figures 6-23). The figures also show the pheromone map that was obtained at the end of the searching process.

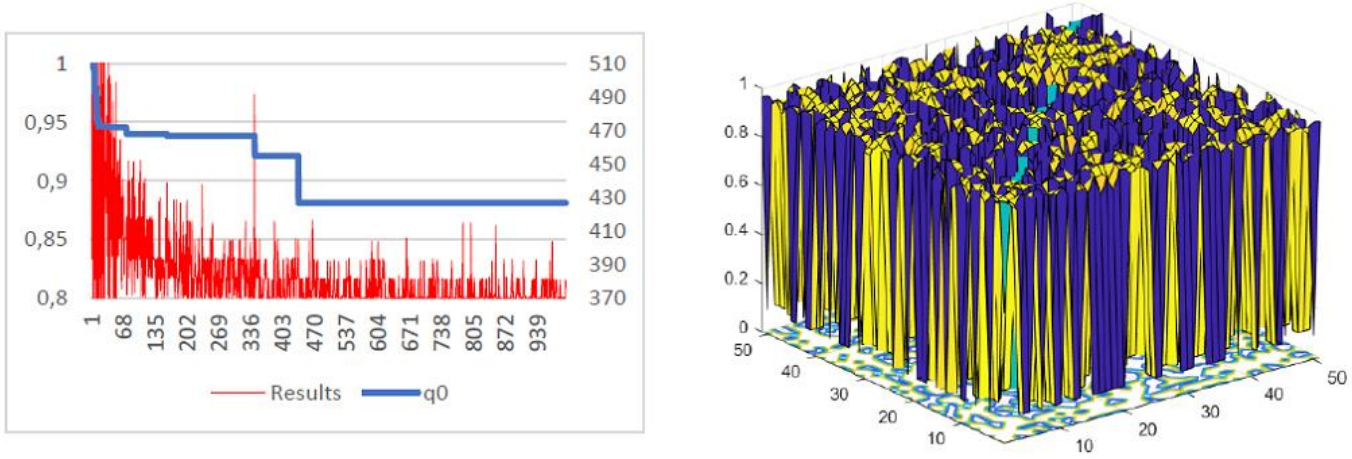

Figure 6 Results, change of q0, and pheromone map obtained in eil51 solution with linear transfer function

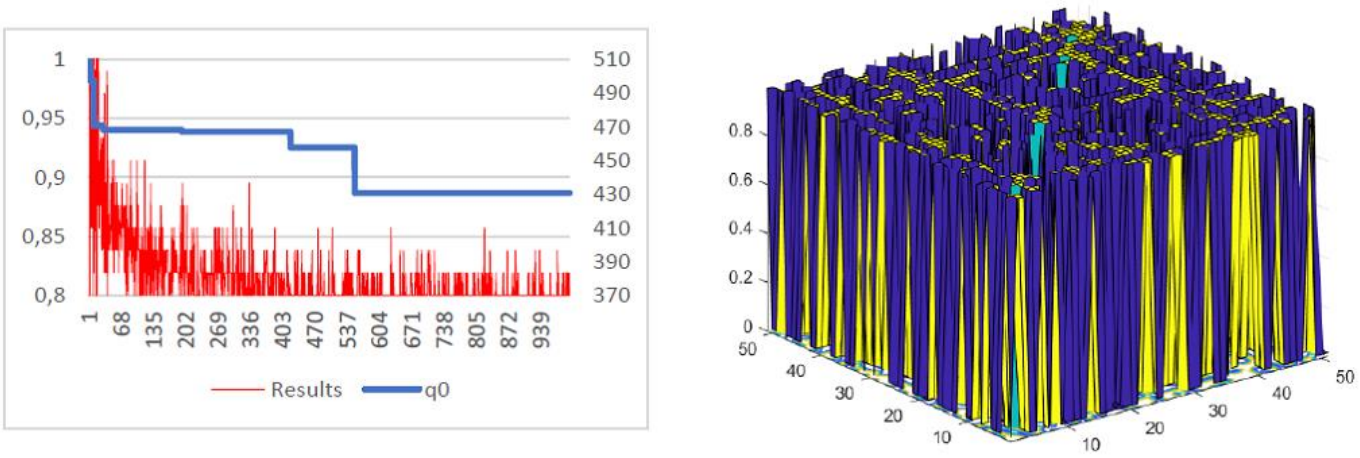

Figure 7 Results, change of q0, and pheromone map obtained in eil51 solution with sigmoid transfer function

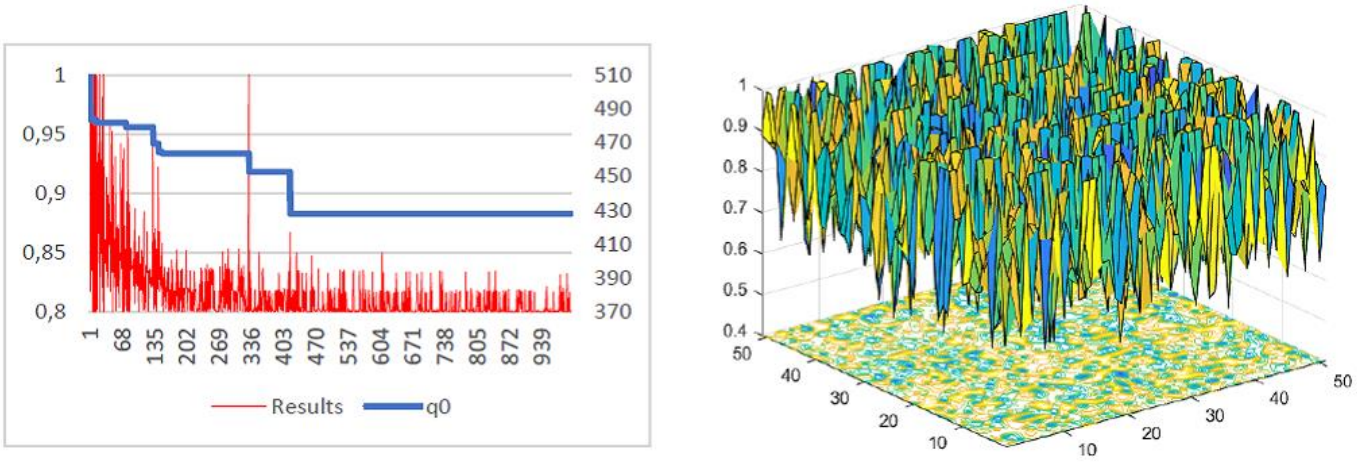

Figure 8 Results, change of q0, and pheromone map obtained in eil51 solution with v-shaped transfer function

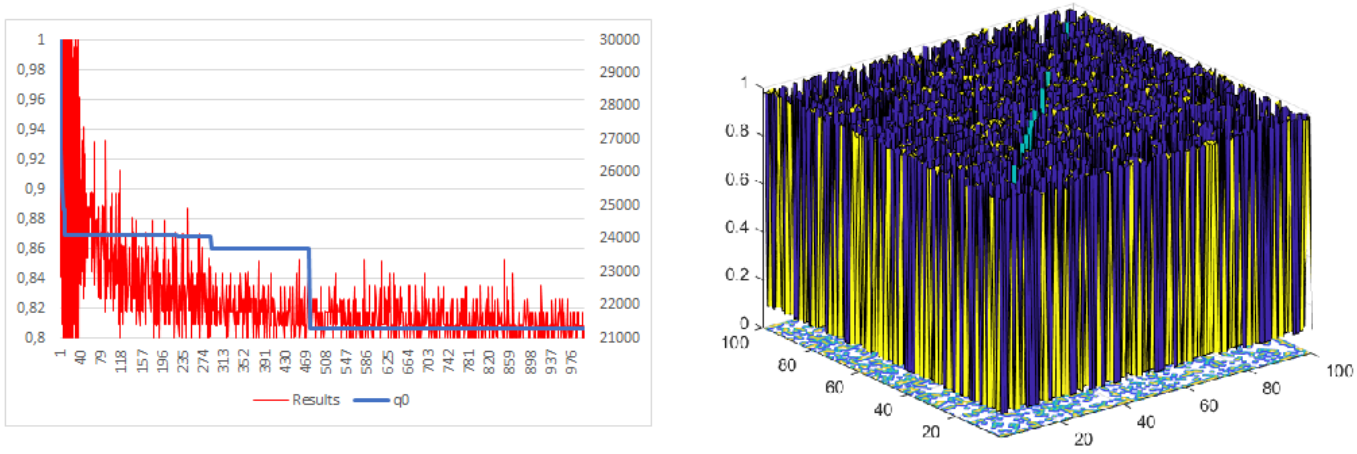

Figure 9 Results, change of q0, and pheromone map obtained in kroA100 solution with linear transfer function

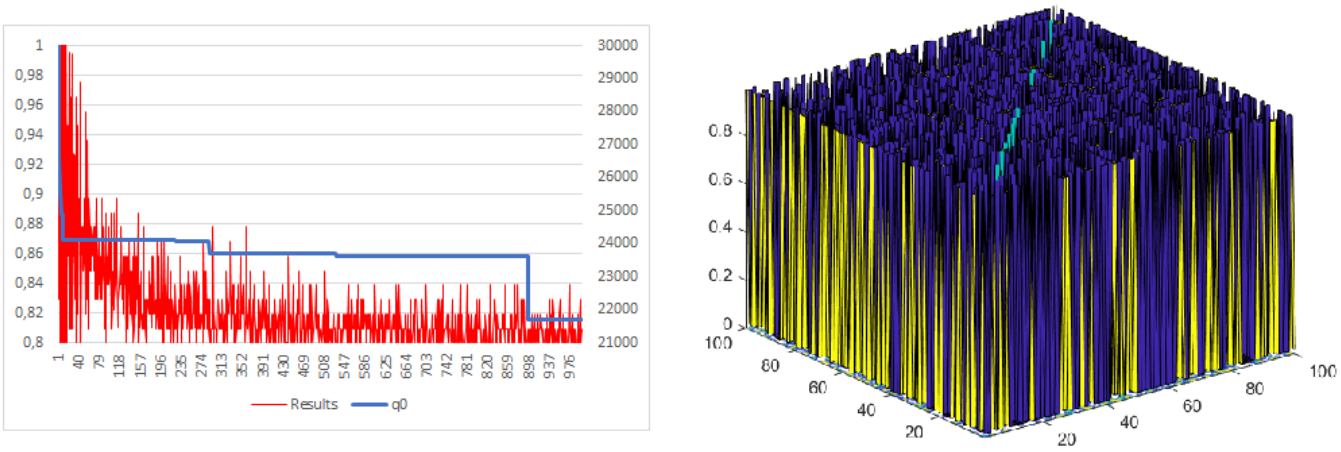

Figure 10 Results, change of q0, and pheromone map obtained in kroA100 solution with sigmoid transfer function

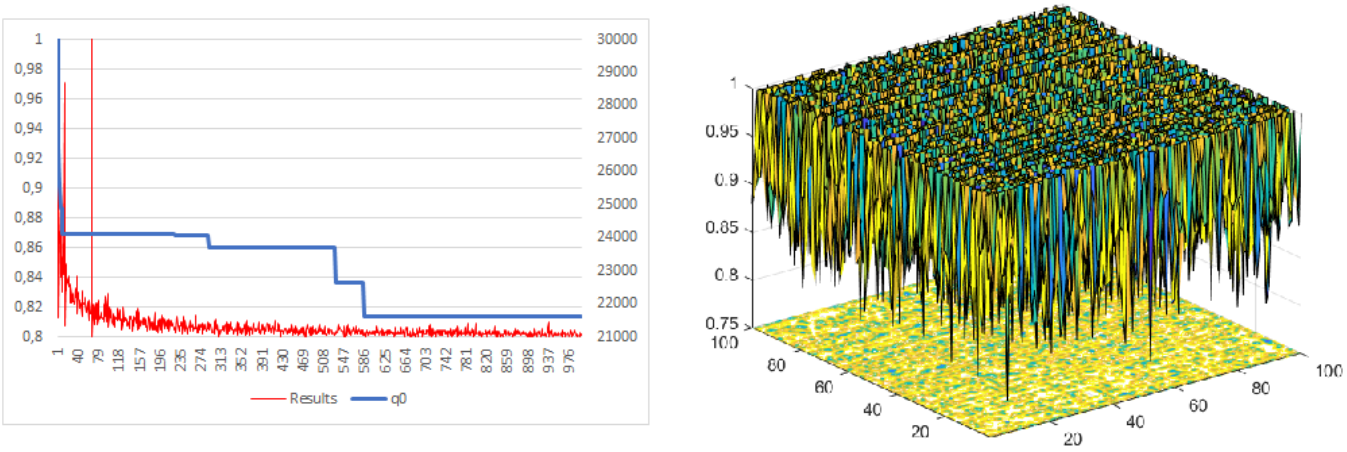

Figure 11 Results, change of q0, and pheromone map obtained in kroA100 solution with v-shaped transfer function

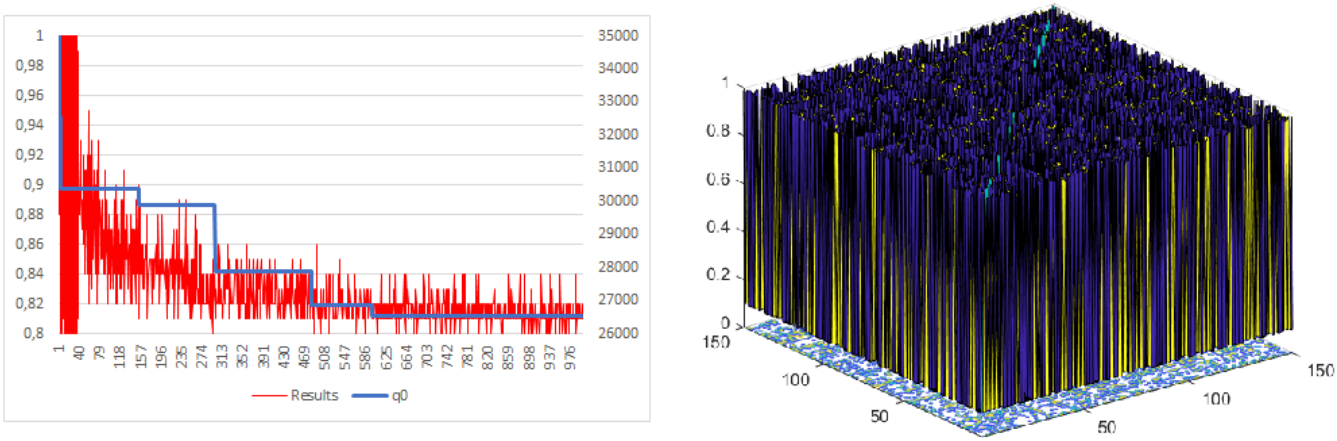

Figure 12 Results, change of q0, and pheromone map obtained in kroA150 solution with linear transfer function

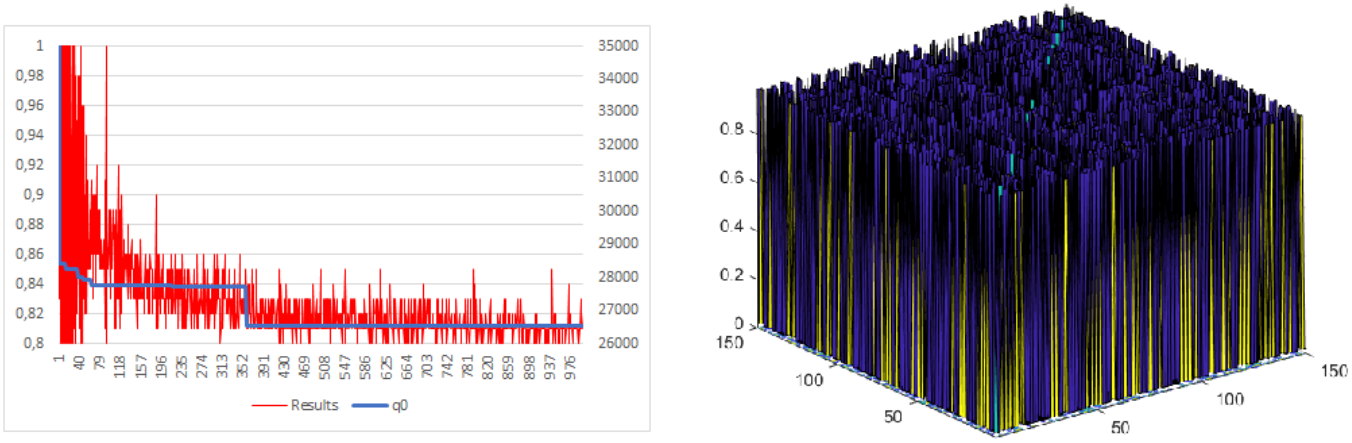

Figure 13 Results, change of q0, and pheromone map obtained in kroA150 solution with sigmoid transfer function

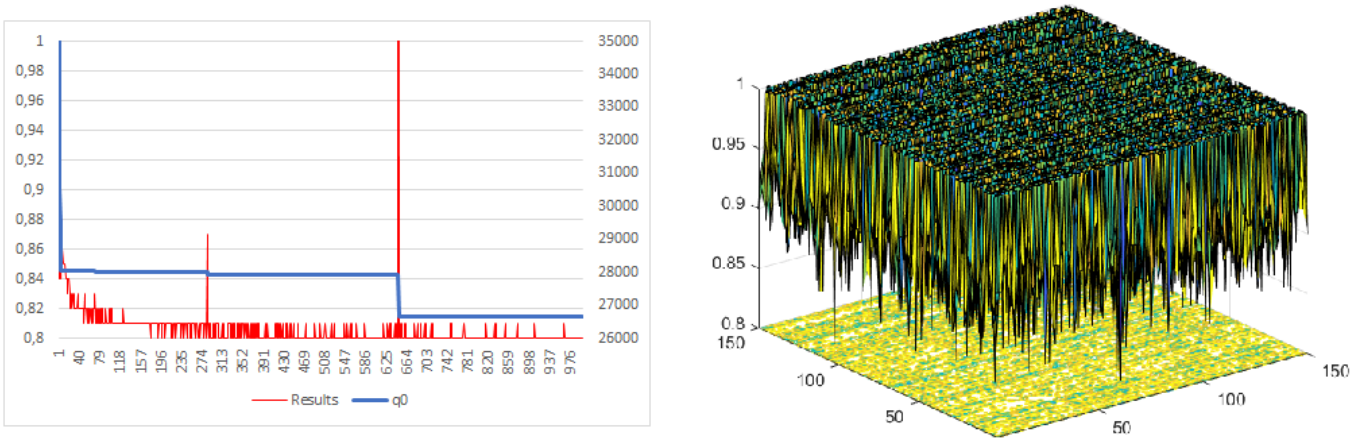

Figure 14 Results, change of q0, and pheromone map obtained in kroA150 solution with v-shaped transfer function

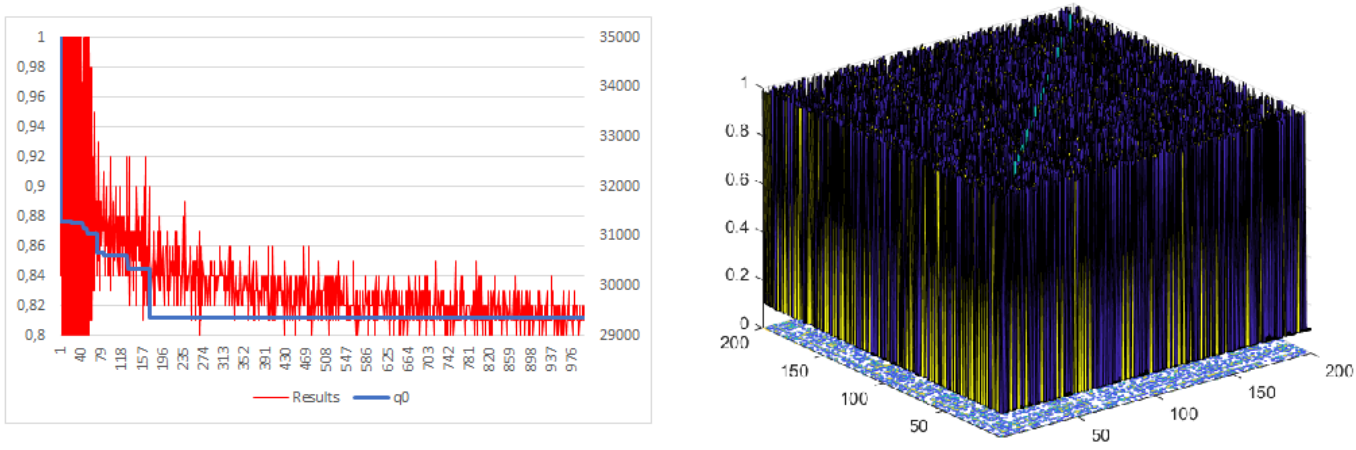

Figure 15 Results, change of q0, and pheromone map obtained in kroA200 solution with linear transfer function

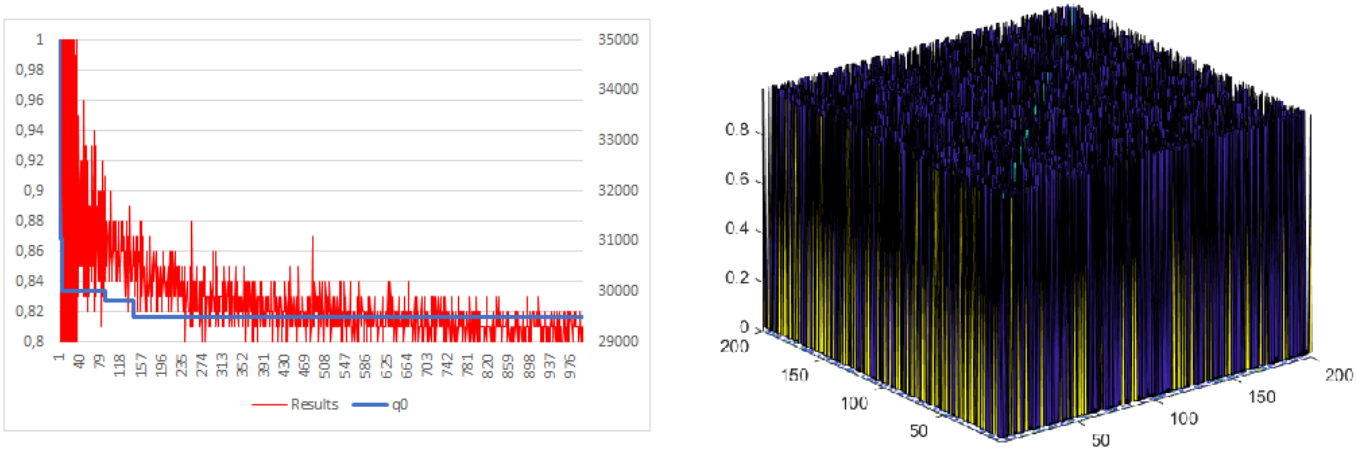

Figure 16 Results, change of q0, and pheromone map obtained in kroA200 solution with sigmoid transfer function

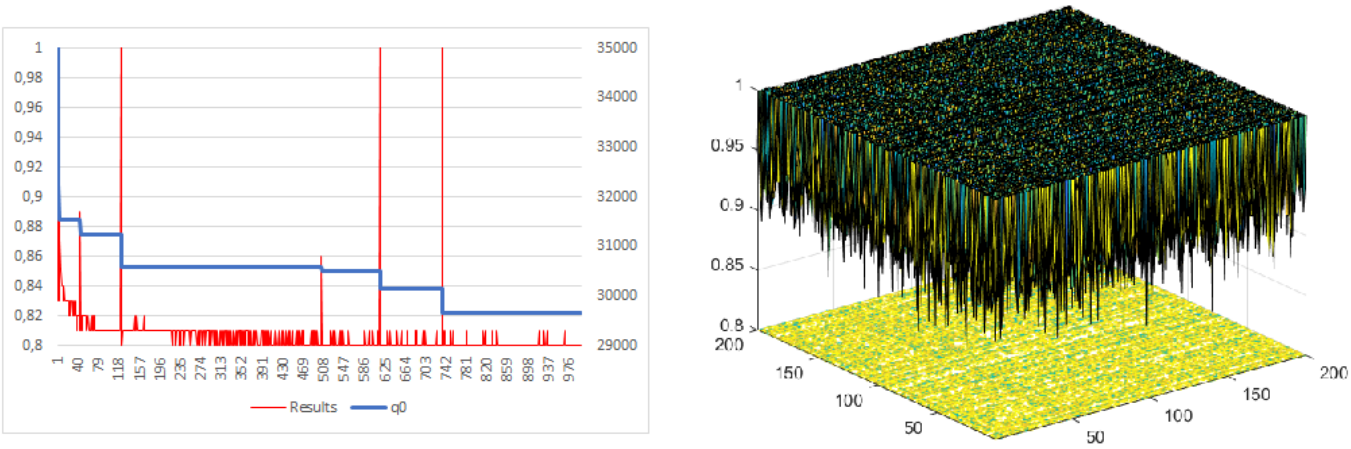

Figure 17 Results, change of q0, and pheromone map obtained in kroA200 solution with v-shaped transfer function

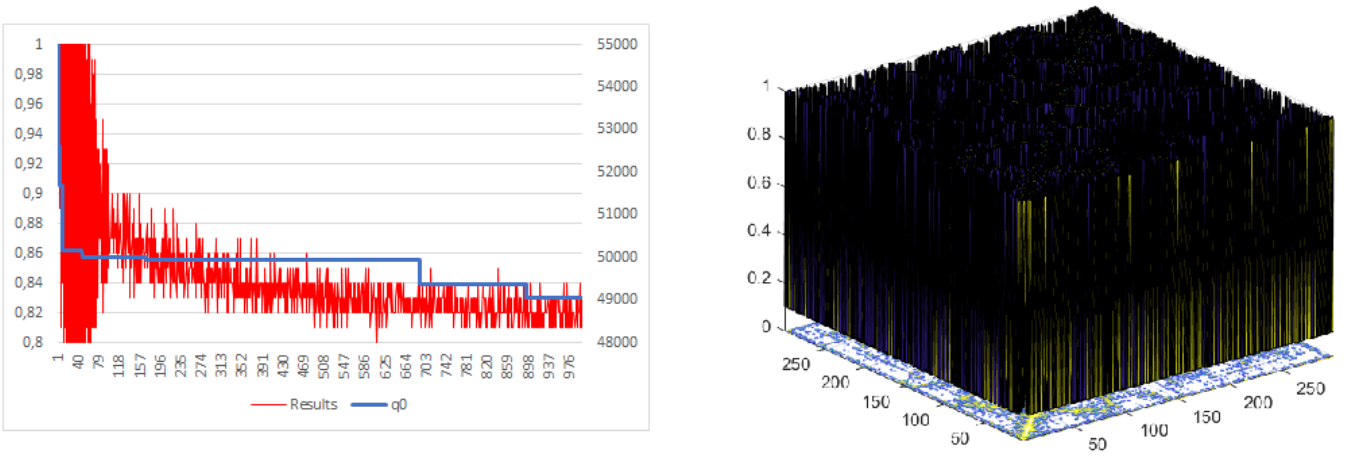

Figure 18 Results, change of q0, and pheromone map obtained in pr299 solution with linear transfer function

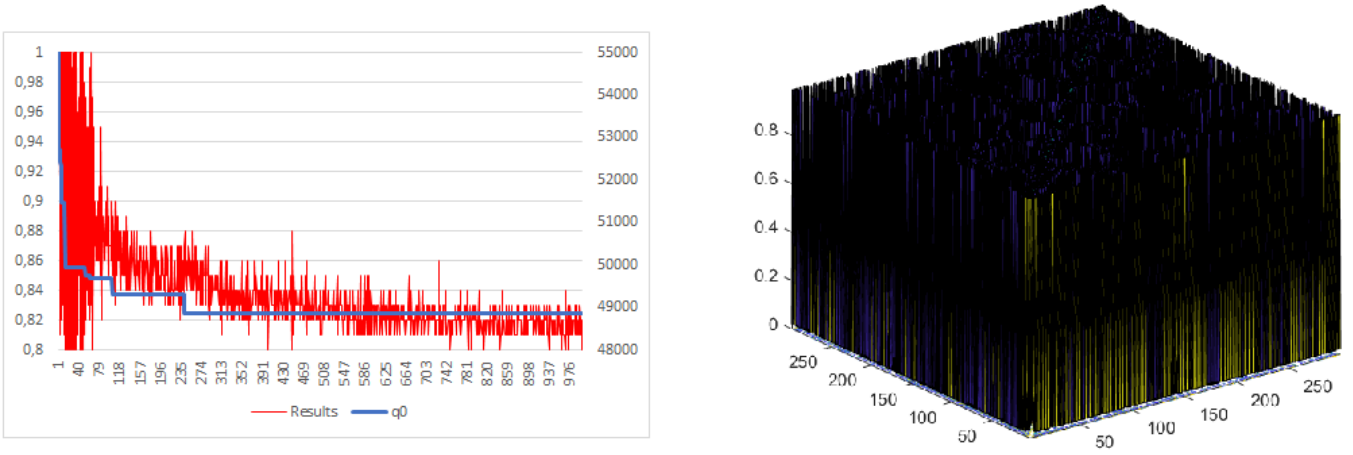

Figure 19 Results, change of q0, and pheromone map obtained in pr299 solution with sigmoid transfer function

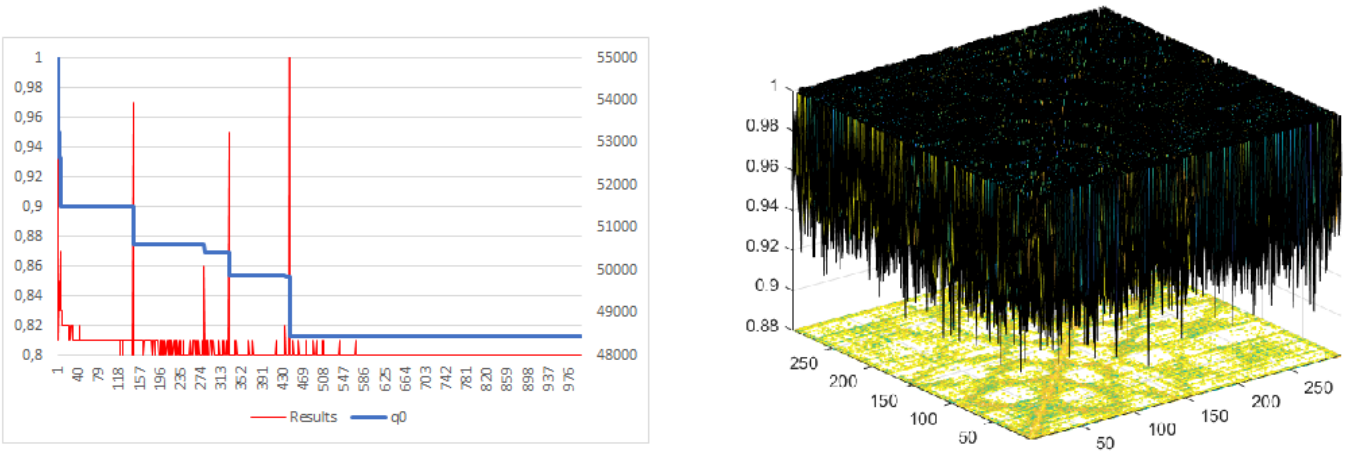

Figure 20 Results, change of q0, and pheromone map obtained in pr299 solution with v-shaped transfer function

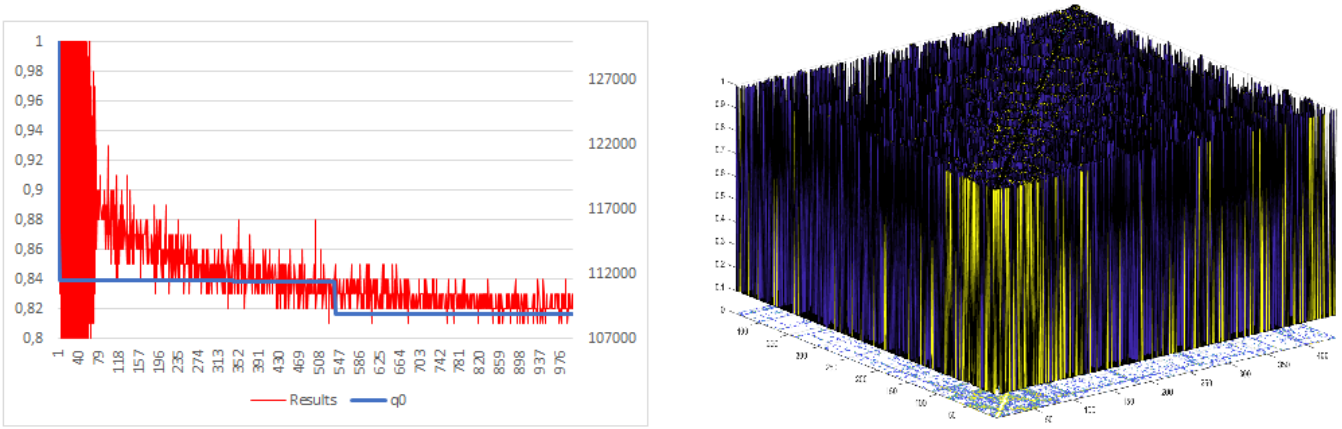

Figure 21 Results, change of q0, and pheromone map obtained in pr439 solution with v-shaped transfer function

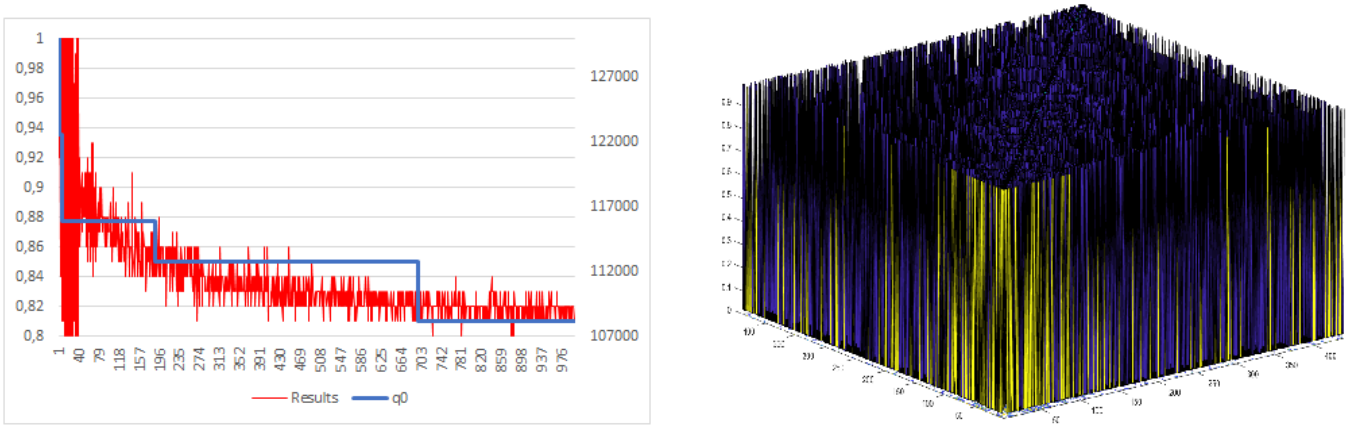

Figure 22 Results, change of q0, and pheromone map obtained in pr439 solution with v-shaped transfer function

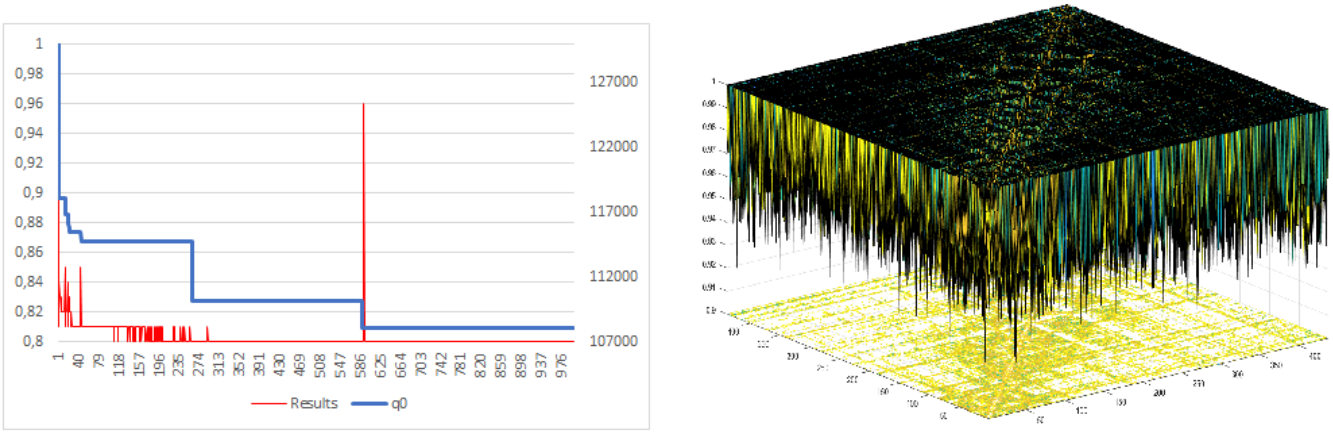

Figure 23 Results, change of q0, and pheromone map obtained in pr439 solution with v-shaped transfer function

4.3.2. Comparisons

The *best* and *worst* results obtained by the algorithms for test problems, the *means* and standard deviation (*SD*) values of the results obtained in 30 trials are presented in Table 3. Table 3 also includes the average CPU time as second, and the ratio of the best results to the best-known (*GAP*) calculated by (11).

$$GAP = \frac{100 * the\ best - known}{the\ best(S)} \quad (11)$$

The results produced by the algorithms were evaluated with statistical analysis. In this context, the Wilcoxon signed-rank method was selected to determine whether the difference is statistically significant. The value used is 0.05. The symbols "+", "=" and "-" indicate that the aACS-MBS performance is significantly “better”, “equal”, or “worse” than the compared algorithm, respectively. Notice that aACS-MBS is the control algorithm.

Table 3
Results of the algorithms for TSP benchmarks

		AS	ACS	ACS-MBS	aACS-MBS
	Best	457	444	431	426
	GAP (%)	91.25	93.92	96.75	97.89
	Worst	499	475	452	434
eil51	**Mean**	477.1	461.05	440.65	430.68
	SD	13.56	9.36	6.35	2.4
	p	0.0034(+)	0.0066(+)	0.0087(+)	
	Time	6.90	7.2	7.38	7.23
	Best	23055	21846	21282	21282
	GAP (%)	92.31	97.42	100	100
	Worst	25275	23251	21287	21695
kroA100	**Mean**	24313.18	22634.46	21773.73	21492.69
	SD	686.98	422.34	302.46	140.82
	p	0.16354(=)	0.05155(=)	0.03836(+)	
	Time	26.02	26.47	26.27	27.56
	Best	30222	28936	26530	27212
	GAP (%)	87.76	91.66	99.98	97.47
	Worst	33088	30842	27798	27746
kroA150	**Mean**	31610.54	29736.15	27044.14	27486.39
	SD	816.96	544.06	394.9	172.42
	p	0.00001(+)	0.00084(+)	0.22363(=)	
	Time	72.41	76.07	71.19	68.57
	Best	31844	30137	29377	29532
	GAP (%)	92.22	97.45	99.97	99.44
	Worst	34859	32060	30758	29967
kroA200	**Mean**	33543.95	31109.64	30108.25	29760.11
	SD	943.53	570.55	405.26	151.17
	p	0.02169(+)	0.11507(=)	0.30153(=)	
	Time	121.56	125.41	120.53	119.17
	Best	53761	54001	51242	50112
	GAP (%)	89.64	89.24	94.05	96.17
	Worst	58677	57359	53598	51073
pr299	**Mean**	55639.12	55497.73	52481.16	50614.59
	SD	1552.51	1038.08	683.69	284.02
	p	0.41294(=)	0.08851(=)	0.05592(=)	
	Time	361.86	365.79	357.11	353.91
	Best	119388	121460	113690	110961
	GAP (%)	89.81	88.27	94.31	96.63
	Worst	130285	129728	119029	114112
pr439	**Mean**	124467.36	125753.55	115943.09	113121.85
	SD	3163.9	2557	1732.17	669.84
	p	0.00001(+)	0.00001(+)	0.00006(+)	
	Time	1051.44	1100.56	1035.79	1047.81

4.4. Discussing

When the results obtained by the aACS-MBS algorithm (Figures 6-23) are examined, it is seen that the fluctuation in the *q0* value decreases as the problem size increases. For linear and sigmoid transfer functions, it can be said that the change in *q0* has similar fluctuation as the results. When a better solution is constructed, the variation in PM increases and this is reflected in the *q0* parameter. When the v-shaped transfer function is used, this fluctuation produces an impulse for *q0*. After

iterations obtaining a better solution, the *q0* value can be reduced to its previous level.

When pheromone maps are examined, it is seen that with the v-shaped transfer function, a more homogeneous pheromone distribution is formed compared to other transfer functions. When using the v-shaped transfer function, levels of pheromone trails at the edges are almost limited in the range of 0.8-1. Therefore, it can be considered that the algorithm constructs solutions using all edges in the searching process.

Examining Table 3, aACS-MBS produced better solutions compared to other ACO variants in 4 out of 6 benchmarks. The algorithm has the best mean value in 5 out of 6 problems. aABC-MBS achieved a statistically significant difference in 4 problems from AS, in 3 problems from ACS, and in 3 problems from ACS-MBS, however, it was not significantly behind in any problem. aACS-MBS also reached the best solution in 2 problems. aACS-MBS has produced solutions closer to the best solutions in the literature, falling behind these results by up to 3.83%.

Since TSP instances are NP-hard class problems, the larger the size of the problem, the more difficult it is to interpret the correlation between nodes. Given that the pheromone approach collects agents around good solutions, it can be more clearly understood that ACO algorithms are insufficient for exploration. Thus, the aACS-MBS is mostly failed to obtain the best solutions for large-scale problems. In this context, different transfer functions that make the exploitation-exploration balance more effective, or different dynamic approaches that determine *q0* can be developed. However, the fact that the algorithm results have lower mean and SD values prove that the algorithm can consistently generate successful solutions, not accidentally.

5. CONCLUSION

The pheromone approach, which can successfully analyze the correlations between solution components, provides an advantage to ACO algorithms, especially in COP solutions. Developing a more successful ACO version depends on a more accurate assignment of the pheromone trail and more accurate interpreting. Developed in parallel with this thought, ACS-MBS makes use of transfer functions to determine the pheromone value. Thus, the amount of pheromone is limited to 0-1. In this study, a solution proposal that dynamically updates the exploitation exploration balance of ACS-MBS using the *q0* parameter was introduced. The method has been tested on different sizes of TSP samples and has proven its applicability for COP solutions.

Acknowledgments

The author wants to thank the reviewers for all useful and instructive comments on the manuscript.

Funding

The author received no financial support for the research, authorship, and/or publication of this paper.

The Declaration of Conflict of Interest/ Common Interest

No conflict of interest or common interest has been declared by the author.

The Declaration of Ethics Committee Approval

The author declare that this document does not require an ethics committee approval or any special permission.

The Declaration of Research and Publication Ethics

The author of the paper declares that he complies with the scientific, ethical, and quotation rules of SAUJS in all processes of the paper and that he does not make any falsification on the data collected. In addition, he declares that Sakarya University Journal of Science and its editorial board have no responsibility for any ethical violations that may be encountered and that this study has not been evaluated in any academic

publication environment other than Sakarya University Journal of Science.

REFERENCES

[1] D. EKMEKCİ, "Optimizasyon Problemleri İçin Geliştirilmiş Feromonal Yapay Arı Koloni (gfYAK) Algoritması," *Eur. J. Sci. Technol.*, no. August, pp. 442–450, Aug. 2020.

[2] M. Dorigo, V. Maniezzo, and A. Colorni, "Positive feedback as a search strategy," Milano, Italy, 1991.

[3] M. Dorigo and T. Stützle, "Ant Colony Optimization: Overview and Recent Advances," in *International Series in Operations Research and Management Science*, vol. 272, 2019, pp. 311–351.

[4] B. Chandra Mohan and R. Baskaran, "A survey: Ant Colony Optimization based recent research and implementation on several engineering domain," *Expert Syst. Appl.*, vol. 39, no. 4, pp. 4618–4627, Mar. 2012.

[5] D. Ekmekci, "An Ant Colony Optimization Memorizing Better Solutions (ACO-MBS) for Traveling Salesman Problem," in *2019 3rd International Symposium on Multidisciplinary Studies and Innovative Technologies (ISMSIT)*, 2019, pp. 1–5.

[6] Kwang Mong Sim and Weng Hong Sun, "Ant colony optimization for routing and load-balancing: survey and new directions," *IEEE Trans. Syst. Man, Cybern. - Part A Syst. Humans*, vol. 33, no. 5, pp. 560–572, Sep. 2003.

[7] M. Dorigo and G. Di Caro, "Ant colony optimization: a new meta-heuristic," in *Proceedings of the 1999 Congress on Evolutionary Computation-CEC99 (Cat. No. 99TH8406)*, 1999, vol. 2, pp. 1470–1477.

[8] D. Zhao, L. Luo, and K. Zhang, "An improved ant colony optimization for the communication network routing problem," *Math. Comput. Model.*, vol. 52, no. 11–12, pp. 1976–1981, Dec. 2010.

[9] Z. Zhang and Z. Feng, "A novel Max-Min ant system algorithm for traveling salesman problem," in *2009 IEEE International Conference on Intelligent Computing and Intelligent Systems*, 2009, vol. 1, no. 60875043, pp. 508–511.

[10] M. Dorigo, V. Maniezzo, and A. Colorni, "Ant system: optimization by a colony of cooperating agents," *IEEE Trans. Syst. Man Cybern. Part B*, vol. 26, no. 1, pp. 29–41, 1996.

[11] M. Dorigo and L. M. Gambardella, "Ant colony system: a cooperative learning approach to the traveling salesman problem," *IEEE Trans. Evol. Comput.*, vol. 1, no. 1, pp. 53–66, Apr. 1997.

[12] M. Dorigo and T. Stützle, "The Ant Colony Optimization Metaheuristic: Algorithms, Applications, and Advances," in *Journal of the Operational Research Society*, vol. 60, no. 7, 2003, pp. 250–285.

[13] E. Ateş, "Gezgin Satıcı Probleminin Çözümü Ve 3 Boyutlu Benzetimi," 2012.

[14] L. Gilbert, "The Traveling Salesman Problem: An overview of exact and approximate algorithms," *Eur. J. Oper. Res.*, vol. 59, pp. 231–247, 1992.

[15] M. A. Tawhid and P. Savsani, "Discrete Sine-Cosine Algorithm (DSCA) with Local Search for Solving Traveling Salesman Problem," *Arab. J. Sci. Eng.*, vol. 44, no. 4, pp. 3669–3679, Apr. 2019.

[16] S. Rana and S. Ranjan Srivastava, "Solving Travelling Salesman Problem Using Improved Genetic Algorithm," *Indian J. Sci. Technol.*, vol. 10, no. 30, pp. 1–6, Sep. 2017.

SAKARYA ÜNİVERSİTESİ
FEN BİLİMLERİ ENSTİTÜSÜ DERGİSİ

Sakarya University Journal of Science
SAUJS

e-ISSN 2147-835X | Period Bimonthly | Founded: 1997 | Publisher Sakarya University |
http://www.saujs.sakarya.edu.tr/en/

Title: CFD Investigation of Different Flow Field Designs for Efficient PEMFC Performance

Authors: Safiye Nur ÖZDEMİR, İmdat TAYMAZ

Recieved: 2021-03-22 15:24:53

Accepted: 2021-04-11 15:07:09

Article Type: Research Article

Volume: 25
Issue: 3
Month: June
Year: 2021
Pages: 690-698

How to cite
Safiye Nur ÖZDEMİR, İmdat TAYMAZ; (2021), CFD Investigation of Different Flow Field Designs for Efficient PEMFC Performance. Sakarya University Journal of Science, 25(3), 690-698, DOI: https://doi.org/10.16984/saufenbilder.901153
Access link
http://www.saujs.sakarya.edu.tr/en/pub/issue/62736/901153

Sakarya University Journal of Science 25(3), 690-698, 2021

CFD Investigation of Different Flow Field Designs for Efficient PEMFC Performance

Safiye Nur ÖZDEMİR[1], İmdat TAYMAZ*[1],

Abstract

Proton exchange membrane (PEM) fuel cell performance depends substantially on the geometry, configuration of the flow channels, and size. A right gas flow field pattern requires a homogeneous reactant distribution, low-pressure drop, and good water management. This paper outlines a numerical study, investigated the influence of the U-type, Z-type, and serpentine flow field configuration on the steady-state cell performance using the CFD technique ANSYS FLUENT PEMFC module. The main goal of this study focuses on a novel perspective for enhancing the design of the PEMFC resulting in better performance. The results indicate that the PEMFC with serpentine flow field configuration yields a significantly higher power density compared to the other designs.

Keywords: CFD, PEM Fuel Cell, Flow Field Design, Cell Performance, MPPT

1. INTRODUCTION

High efficiency, high power density, non-high operating temperatures, and environmental adaptability advantages significantly increase PEMFC's usability in the automotive industry compared to other fuel cells. Toyota Mirai, Honda Clarity, MAN Siemens, GM Opel, and Hyundai Nexo produce electric vehicles that run on fuel cell systems in the automotive industry, are a few of them [1]. However, some events such as reactant distributions, heat and mass transfer, and water flooding, which are directly related to the gas channel design, create problems in PEMFC [2]. Fuel cell flow field, is a main component of the fuel cell, which is of vital importance in the distribution of fuel gas and air, thermal management, and removal of the water formed as a result of the electrochemical reaction from the fuel cell stack, shows diversity in the literature such as parallel, zigzag, pin type, serpentine and interdigitated design [3,4]. Figure 1 shows the schematic representation of the various flow patterns. There are lots of experimental and numerical studies on flow field design in the literature. Many studies focus on the improvement of reactant transport [5-7], cross-sectional geometry and dimensions of the channel [8,9], the number and geometry of the blockages located in the flow channel [10-12]. In recent years, there have been many studies based on flow field design. Yoon, Y.G. et al. examined four different rib widths of the flow field structures by keeping the channel width constant to get optimal

*Corresponding author: taymaz@sakarya.edu.tr
[1]Sakarya University, Faculty of Engineering, Mechanical Engineering Department, Sakarya.
E-Mail: safiyeozdemir@sakarya.edu.tr
ORCID: https://orcid.org/0000-0001-5025-5480; https://orcid.org/0000-0003-1337-7299

cell performance based on experimental work. Increasing the flow field width results in higher current density regardless of full or less humidification. As a result of a conclusion drawn from this study, the best performance was achieved at a rib width is 0.5 mm, as narrow rib widths offer a wider gas flow area [13]. At first, a 3D PEMFC model based on a steady-state regime was developed, investigating the effect of the blockage rate of the baffle plate located in the center of the cathode gas channel on the cell performance. It was found that the power density obtained from baffle plate with a blockage ratio of 1 raised by 5.54 % percent compared to the straight flow field. In the second stage, the number of baffle plates is 1, 3, 5, and 7, respectively, and the effect of the baffle plate number on the power output has been examined in all cases the blockage rate keeping constant at 0.8. The peak performance was achieved when the number of the baffle plates was 5. The net power increase was measured as 9.39 % compared to the flow field without baffle plate [14]. Limjeerajarus and Charoen-amornkitt simulated 3-D, non-isothermal PEMFC models with six different flow field designs based on ANSYS FLUENT PEMFC module to evaluate the cell performance and transport phenomena. Optimal performance was obtained in the single serpentine flow area while the worst performance was obtained in the parallel flow area. However, the most important defection of the single serpentine flow field design was that the power needed to meet for the pressure-drop is nearly ten times greater than the 3PIS (three-channel parallel in series) and 3S (three-channel serpentine) flow field designs and nearly twenty times greater than the 5PIS and 5S flow fields [15]. Shen et al. developed PEMFC with three different flow field structures (parallel, pressurized parallel, and single-serpentine) to explain that flow field design is a backbone that affects the fuel cell efficiency. Numerical simulations were carried out for three different flow fields at 338 K operating temperature and 1 atm operating pressure. The ratio of the Sherwood number, which expresses mass transfer, and the Euler number that describe the pressure drop, is a key factor in determining the fuel cell efficiency. In this study, the most suitable flow field design was found using this factor. Although the cathode gas flow channel of the serpentine flow field design has a large pressure loss, better performance was achieved compared to the parallel flow field [16]. Shimpalee et al. tested the different number of gas flow channels on non-isothermal PEMFC with 200 cm² active area to investigate the reactant distribution and cell performance. Numerical simulations were realized using a commercial solver STAR-CD to specify and compare the current density distribution, membrane water content, and temperature distributions. It was recorded that the multi-channel PEMFC offers the most homogeneous current distribution [17]. Zhu and Zheng proposed a novel flow field configuration good at low-pressure drop, high power output, and much better water management compared to traditional gas flow field patterns. Rib width, channel depth, and channel width were analyzed numerically for the novel flow field design. It was discovered that the effect of the channel depth on cell performance compared to other parameters was not important. It was concluded that the radial gas flow field was more functional for maximum cell performance than parallel and serpentine flow field patterns [18].

Lots of studies based on flow field structure and optimization have been conducted in the literature. There are many numerical studies about the single-channel structure, but in reality, the PEMFC has many gas flow channels. There are few numerical publications available regarding different patterns in the bipolar plate with square geometry. In this study, a PEMFC model with different flow field designs was developed, and then the best flow field design that gives the highest cell performance using maximum power point tracking (MPPT) was determined and investigated.

2. MATERIALS AND METHODS

2.1. Model Description and Assumptions

In this study, numerical models of the PEMFC with 4.41 cm² active area for three different flow configurations were generated using a CAD software SolidWorks program. The numerical models consist of 10 number of flow channels in

both the cathode and anode. Figure 2 shows the flow directions of the fluid supplied to the cathode and anode channels of the PEMFC. The total length of the gas flow channels is 210 mm. The fluid and solid domains of the three different geometries were defined in ANSYS Design Modeler. Table 1 shows the geometric dimensions of the three different designs.

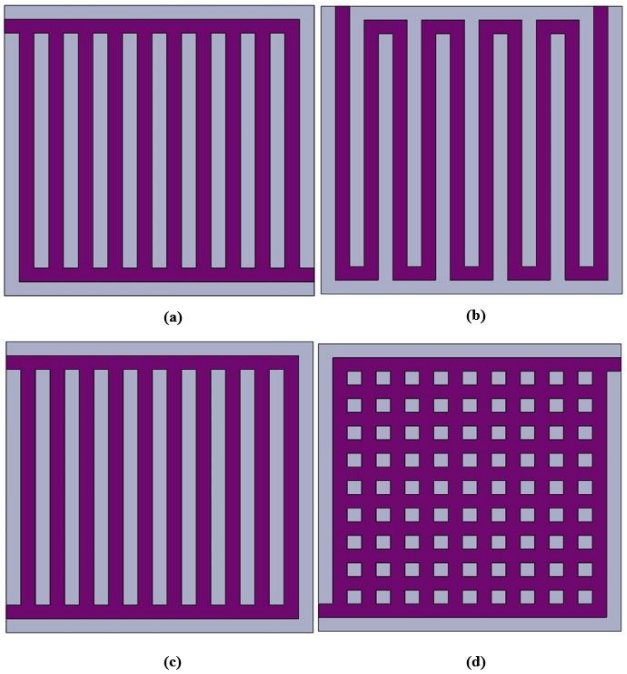

Figure 1 Schematic representation of different flow field designs (a) Z-type, (b) serpentine, (c) U-type, (d) pin-type

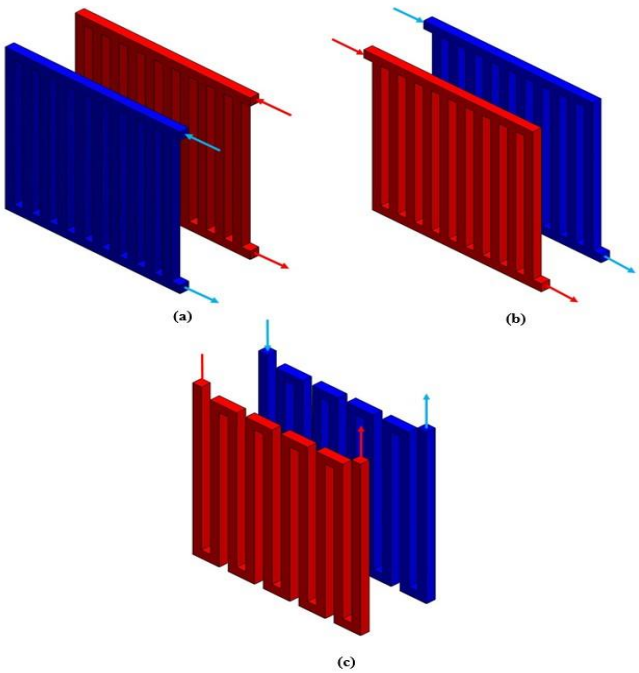

Figure 2 Flow directions in anode and cathode gas flow fields for (a) U-type (b) serpentine (c) Z-type

Table 1 Geometric dimensions

Parameters	Values	Units
Channel width	1	mm
Channel height	1	mm
Rib width	1	mm
Electrode width	21	mm
Electrode length	21	mm
Active area	4.41	cm^2
Gas diffusion layer thickness	0.37	mm
Catalyst layer thickness	0.02	mm
Membrane thickness	0.178	mm

Mesh structures of the models were created in ANSYS Meshing 19.2. The most precise numerical solution is obtained from improved grid structure. The computation time is increased when the mesh is divided into very small elements. Therefore, mesh independence work has been carried out in numerical models. The most crucial requirement to obtain an accurate numerical solution in PEMFC is to construct the hexahedral mesh structure which is generated after mesh independence work. Three different geometries were discretized into 6 million cells and then, numerically solved. Figure 3 shows the grid structure of the numerical model with a serpentine flow field.

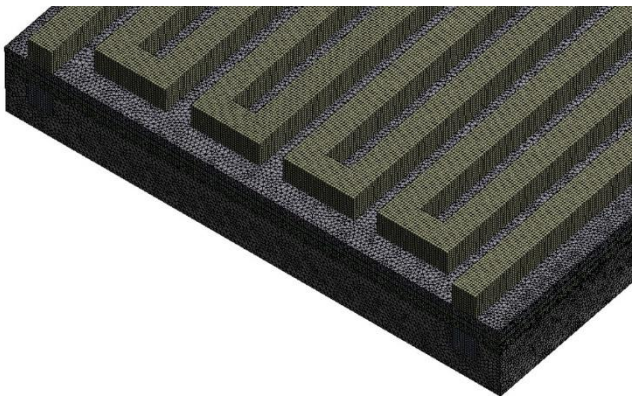

Figure 3 Mesh structure

Iteration independence study was carried out, and then, a convergent solution was obtained as a result of 500 iterations.

2.2. Boundary Conditions

After constructing the PEMFC geometry and mesh, boundary conditions should be defined for

each of the model domains. The input velocity of the hydrogen supplied to the anode channel, the input velocity of the air supplied to the cathode channel, and the mass fractions of the chemical species were calculated and defined in the FLUENT software. The hydrogen velocity entering the anode gas flow field is obtained as the following equation,

$$u_{a,in} = \zeta_a \frac{I}{2F} A_{MEA} \frac{1}{X_{H_2,in}} \frac{RT_{a,in}}{P_{a,in}} \frac{1}{A_{ch}} \quad (1)$$

The air velocity entering the cathode gas flow field is obtained as the following equation,

$$u_{c,in} = \zeta_c \frac{I}{4F} A_{MEA} \frac{1}{X_{O_2,in}} \frac{RT_{c,in}}{P_{c,in}} \frac{1}{A_{ch}} \quad (2)$$

where A_{MEA} is the active area of the membrane electrode assembly, I is the mean current density, ζ is the stoichiometric flow rate and X is the molar fraction of hydrogen/oxygen. The outlet boundary condition of the anode and cathode flow fields typically was assigned as pressure. Since the outlet surfaces of the gas flow fields are exposed to the atmospheric pressure, they are assigned 1 atm. The operating pressure was selected as 303.975 kPa. The cathode terminal plate of the PEMFC is the surface on which current density values are obtained. The boundary conditions defined for the numerical solution are as in Table 2.

Table 2 Boundary conditions

Zone	Type	Unit	Value
Anode Inlet	Inlet velocity	m/s	Calculated
	Stoichiometry	-	2
	Temperature	K	343
	H_2 mass fraction	-	0.495
	H_2O mass fraction	-	0.505
	Relative humidity	-	100%
Cathode Inlet	Inlet velocity	m/s	Calculated
	Stoichiometry	-	2
	Temperature	K	343
	O_2 mass fraction	-	0.217
	H_2O mass fraction	-	0.0664
	Relative humidity	-	100%
Outer Face	Electric potential (anode)	V	0
	Electric potential (cathode)	V	Cell potential
All Zones	Operating pressure	kPa	303.975

2.3. Solution Process

Numerical simulations were realized using ANSYS FLUENT 19.2 PEMFC add-on module to evaluate the performance. In order to find the answer to which gas flow channel design will result in the best performance, the same boundary conditions are defined for three different designs. For numerical solutions, three-dimensional, parallel processing, and double-precision were chosen. Biconjugate gradient stabilization (BCGSTAB) method and F-cycle were used for the solution of the consecutive governing equations system. Relaxation parameters were entered into the program as 0.95, 0.95, 0.7, and 0.3 for protonic potential, water content, pressure, and momentum, respectively to avoid the unstable numerical solution. Numerical simulations were performed on Intel(R) Core(TM) i7-7700HQ CPU (2.80 GHz, 16 GB RAM).

3. RESULTS AND DISCUSSION

In the present work, three different flow field configurations were analyzed numerically based on computational fluid dynamics (CFD) code. Overall assumptions and boundary conditions were the same to reveal the optimal flow area design. Reactants were fully humidified, CFD simulations were actualized at a constant temperature of 343 K. More precise results were obtained using a very small grid size. A numerical model was verified with experimental results of Wang et al. [19] with a straight flow field available in the literature. Figure 4 shows the numerical results are in good harmony with the experimental results. It has been observed that the current densities obtained at low cell potentials are higher than the experimental results. Water flooding, which significantly limits oxygen transport, will occur especially at high current densities, and since this situation is not taken into account in single-phase modeling, it is common to have inconsistencies at this point between the experimental results [20].

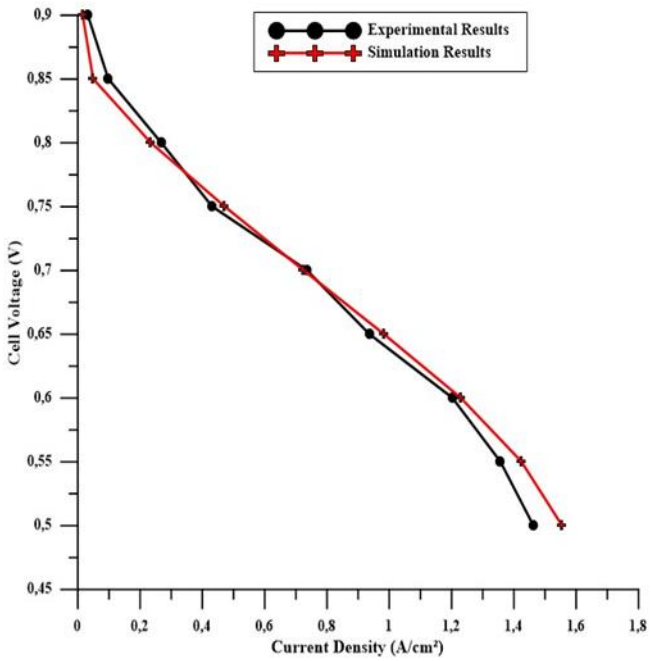

Figure 4 Experimental validation of the numerical results

Three different designs were compared on polarization and power curves. According to the polarization and power curves, the top performance was obtained from the serpentine flow field pattern, and the worst performance was obtained from the U-type flow field pattern. After the required boundary conditions of the PEMFC were defined, the program was run numerically for all three various flow field patterns. The open-circuit voltage is 1.1 V, starting from 0.45 V to be less than this value, the cell potentials have been assigned to the program with 0.05 increments up to 0.90 V. The current density values obtained for each cell potential defined on the cathode current collector plate wall were recorded. The current density-based cell potential (I-V) polarization curve and current density-based power density (I-P) power curve were shown in Figure 5. Numerical results show that the highest power density was obtained as 7772 W/m^2 at 0.55 V cell voltage for serpentine flow field configuration. The maximum current densities are 9964 A/m², 13811 A/m^{2,} and 16071 A/m² for the U-type, Z-type, and serpentine designs at 0.45 V operating voltage.

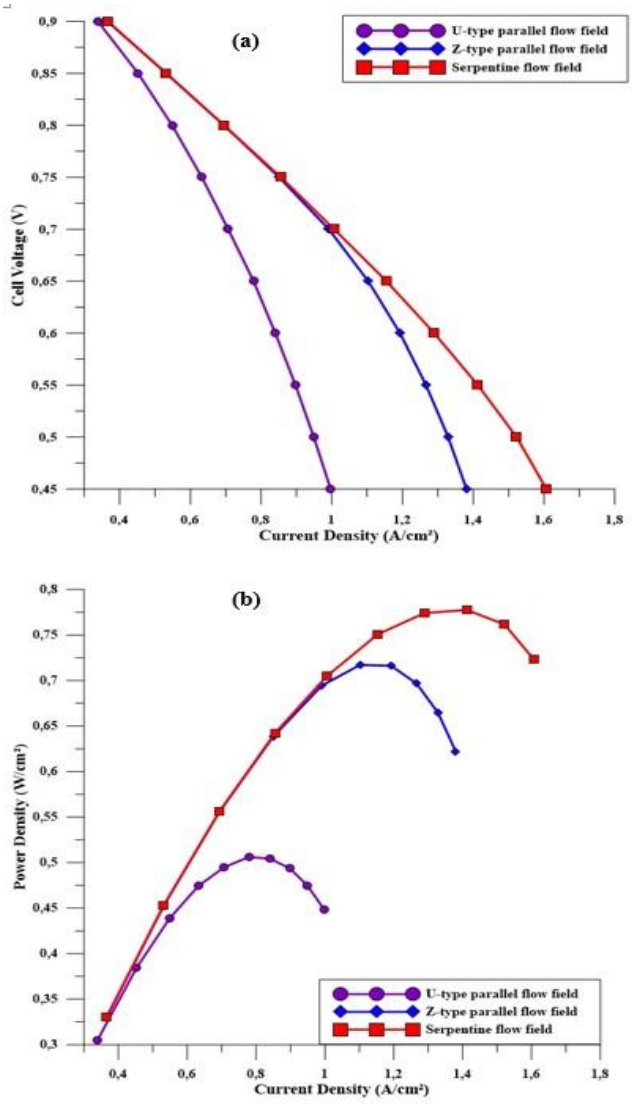

Figure 5 Polarization curve for (a) and power curve for (b) of the three different simulated arrangements (T=343 K, ε=0.8)

Figure 6 shows the oxygen concentration distribution at the interface of the GDL/CL (catalyst/gas diffusion layer) on the cathode side at operating voltage and operating temperature 0.65 V and 343 K, respectively. The oxygen mass fraction is high at the inlet of the cathode gas channel, decreasing gradually towards the channel outlet. The contours show that the most uniform oxygen distribution among the three designs is in the serpentine flow field. It results in the highest power income for the serpentine flow pattern compared to the other patterns. Maldistribution of the oxygen fraction negatively affected the performance of the U-type flow field. The reduction of the oxygen in the cathode gas

flow field is due to its consumption in the electrochemical reaction.

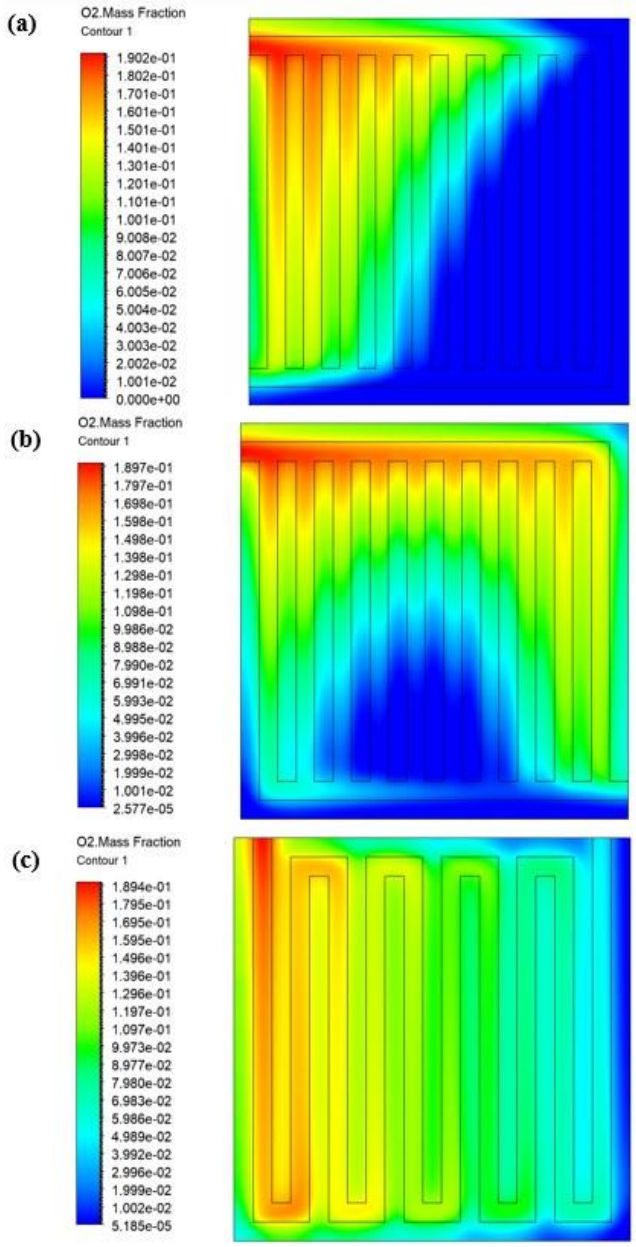

Figure 6 Oxygen concentration distribution at the interface of the GDL/CL on the cathode side at 0.65 V for (a) U-type, (b) Z-type, and (c) serpentine

Figure 7 shows the temperature distribution of the serpentine flow field configuration at the interface of the GDL/CL on the cathode side. The contours illustrate that as the cell potential decreases, current densities will increase, which will cause an increase in temperature. The non-uniform temperature distribution in the active area is observed more clearly at low cell potentials. It was discovered that the temperature gradually decreased from the PEMFC's inlet section to the outlet section because of the water accumulation.

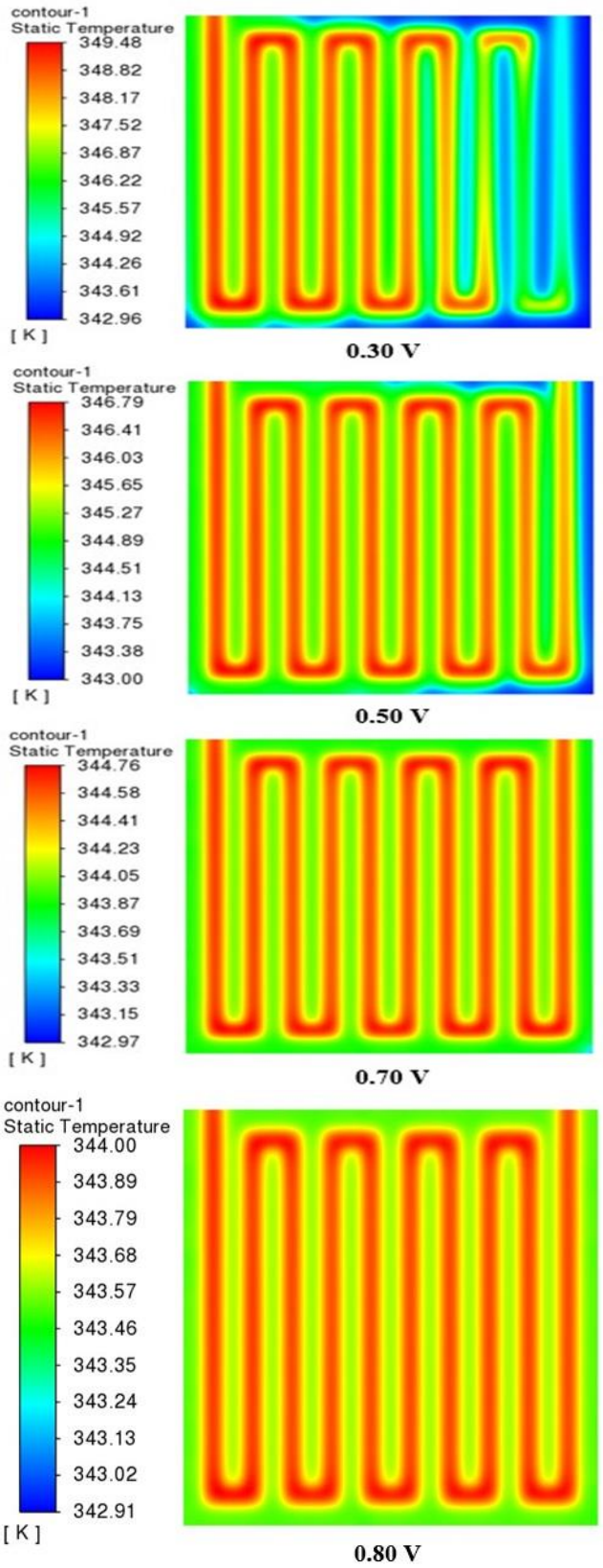

Figure 7 Temperature distribution for various operating voltages

It is concluded that the maximum temperature differences are 6.52 K, 3.79 K, 1.79 K, and 1.09 K at 0.30 V, 0.50 V, 0.70 V, and 0.80 V cell voltages, respectively. Figure 8 shows the water concentration distribution at the interface of the GDL/CL layer on the cathode side at operating voltage and operating temperature 0.65 V and 343 K, respectively. The water mass fraction increased towards the cathode gas flow field outlet section because of the oxygen reduction reaction. A certain level of humidification is essential for the fuel cell to operate at optimum performance. Water accumulation will adversely affect the power output if not kept at a certain level. The water produced from the channel inlet to the outlet section has increased. The most important criterion to be considered in the PEMFC gas flow field is the pressure drop. Pressure loss in the gas flow channel can be compensated by the use of a compressor. The pressure loss, which tends to decrease towards the gas flow channel outlet, is the highest in the inlet section of the gas channel. The difference between the outlet and inlet sections of the cathode gas channel gives the pressure drop. Average flow velocity is increased with increasing pressure drop. Peak levels of pressure drop in U-type, Z-type, and serpentine flow fields are 25.81 kPa, 0.060 kPa, and 0.405 kPa, respectively. The main cause of pressure loss in gas flow channels is friction, however, it is caused by the places where the flow maneuvers.

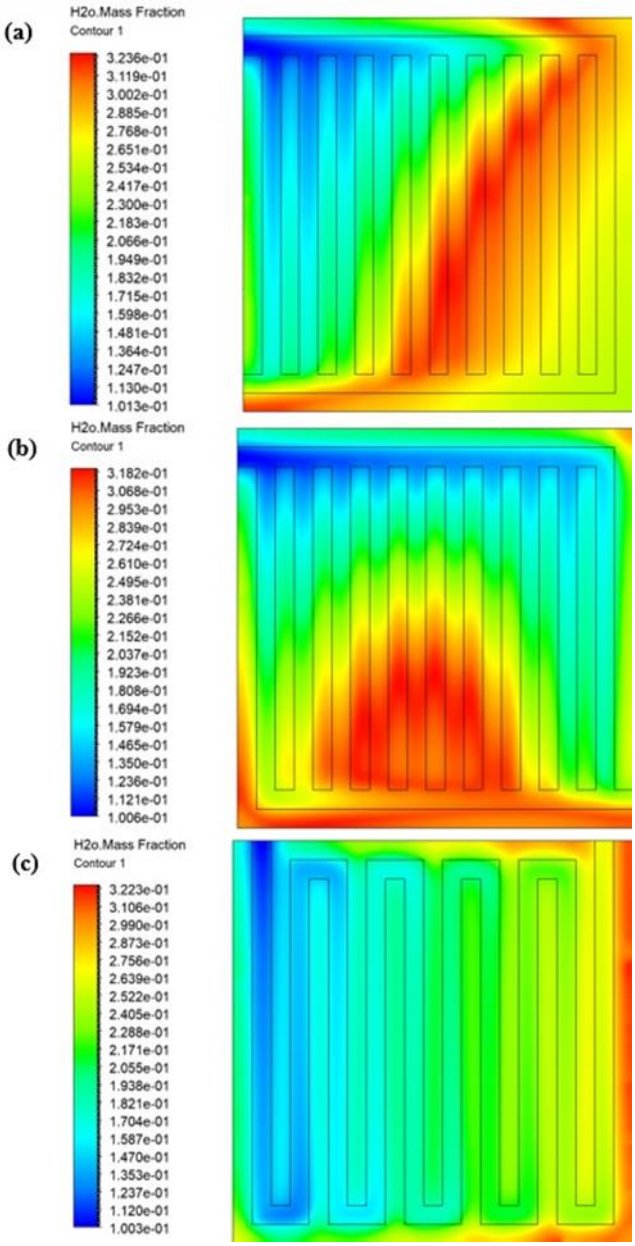

Figure 8 Water concentration distribution at the interface of the GDL/CL on the cathode side at 0.65 V for (a) U-type, (b) Z-type, and (c) serpentine

4. CONCLUSION

A full three-dimensional PEMFC with an active area of 4.41 cm² (2.1 cm × 2.1 cm) was generated. Numerical work was carried out to investigate the impact of U-type, Z-type, and serpentine flow field configurations on cell performance. Model validation was performed for a PEMFC with a single straight flow field, and it was found that the simulation results and experimental data were matched with each other. When the cell potential is 0.70 V or above, the gas

flow field design is Z-type or serpentine, as can be seen from the polarization and power curves, it is observed that it creates any change in its effect on cell performance. When the cell potential was less than 0.70 V, Z-type and serpentine flow field designs substantially affected the cell performance. On the other hand, the worst cell performance was obtained in the U-type flow field pattern. In this study, the model that gives the superior cell performance among three different numerical models developed numerically was determined. This work can guide fuel cell stack manufacturers in terms of optimum flow field configuration. Design, operating parameters can be examined in detail for the best geometry in future work.

Funding

The authors have no received any financial support for the research, authorship or publication of this study.

The Declaration of Conflict of Interest/ Common Interest

No conflict of interest or common interest has been declared by the authors.

Authors' Contribution

The authors contributed equally to the study.

The Declaration of Ethics Committee Approval

This study does not require ethics committee permission or any special permission.

The Declaration of Research and Publication Ethics

The authors of the paper declare that they comply with the scientific, ethical and quotation rules of SAUJS in all processes of the paper and that they do not make any falsification on the data collected. In addition, they declare that Sakarya University Journal of Science and its editorial board have no responsibility for any ethical violations that may be encountered, and that this study has not been evaluated in any academic publication environment other than Sakarya University Journal of Science.

REFERENCES

[1] Wang, Y. et al. (2020) 'Fundamentals, materials, and machine learning of polymer electrolyte membrane fuel cell technology', Energy and AI. Elsevier Ltd, 1, p. 100014.

[2] Pei, P. et al. (2016) 'A review on water fault diagnosis of PEMFC associated with the pressure drop Fourier transform', Applied Energy. Elsevier Ltd, 173, pp. 366–385.

[3] Wilberforce et al. (2019) 'A comprehensive study of the effect of bipolar plate (BP) geometry design on the performance of proton exchange membrane (PEM) fuel cells', Renewable and Sustainable Energy Reviews. Elsevier Ltd, 111(April), pp. 236–260.

[4] Kahraman, H. and Orhan, M. F. (2017) 'Flow field bipolar plates in a proton exchange membrane fuel cell: Analysis & modeling', Energy Conversion and Management. Elsevier Ltd, 133, pp. 363–384.

[5] Perng, S. W. and Wu, H. W. (2015) 'A three-dimensional numerical investigation of trapezoid baffles effect on non-isothermal reactant transport and cell net power in a PEMFC', Applied Energy. Elsevier Ltd, 143, pp.81–95.

[6] Liu, C. et al. (2006) 'Reactant gas transport and cell performance of proton exchange membrane fuel cells with tapered flow field design', Journal of Power Sources 158, pp. 78–87.

[7] Yan, W. M. et al. (2008) 'Effects of serpentine flow field with outlet channel contraction on cell performance of proton exchange membrane fuel cells', Journal of Power Sources, 178(1), pp. 174–180.

[8] Obayopo, S. O., Bello-Ochende, T. and Meyer (2011) 'Performance enhancement of a PEM fuel cell through reactant gas channel and gas diffusion layer optimisation', Africa, (November).

[9] Ahmed, D. H. and Sung, H. J. (2006) 'Effects of channel geometrical configuration and shoulder width on PEMFC performance at high current density', Journal of Power Sources, 162(1), pp. 327–339.

[10] Ozdemir and Taymaz (2021) 'Numerical investigation of the effect of blocked gas flow field on PEM fuel cell performance', International Journal of Environmental Science and Technology. Springer Berlin Heidelberg.

[11] Shen et al. (2018) 'Performance investigation of PEMFC with rectangle blockages in Gas Channel based on field synergy principle', Heat and Mass Transfer/Waerme- und Stoffuebertragung. Heat and Mass Transfer.

[12] Kuo, J. K., Yen, T. S. and Chen, C. K. (2008) 'Improvement of performance of gas flow channel in PEM fuel cells', Energy Conversion and Management, 49(10), pp. 2776–2787.

[13] Yoon, Y. G. et al. (2004) 'Effects of channel configurations of flow field plates on the performance of a PEMFC', Electrochimica Acta, 50(2–3 SPEC. ISS.), pp. 709–712.

[14] Yin, Y. et al. (2018) 'Numerical investigation on the characteristics of mass transport and performance of PEMFC with baffle plates installed in the flow channel', International Journal of Hydrogen Energy. Elsevier Ltd, 43(16), pp. 8048–8062.

[15] Limjeerajarus, N. and Charoen-amornkitt, P. (2015) 'Effect of different flow field designs and number of channels on performance of a small PEFC', International Journal of Hydrogen Energy. Elsevier Ltd, 40(22), pp. 7144–7158.

[16] Shen, J., Tu, Z. and Chan, S. H. (2020) 'Evaluation criterion of different flow field patterns in a proton exchange membrane fuel cell', Energy Conversion and Management. Elsevier, 213(April), p. 112841.

[17] Shimpalee, S., Greenway, S. and Zee, J. W. Van (2006) 'The impact of channel path length on PEMFC flow-field design', 160(January), pp. 398–406.

[18] Zhu, W. and Zheng, M. (2019) 'Radial flow field of circular bipolar plate for proton exchange membrane fuel cells', International Journal of Heat and Technology, 37(3), pp. 733–740.

[19] Wang, L. et al. (2003) 'A parametric study of PEM fuel cell performances', International Journal of Hydrogen Energy, 28(11), pp. 1263–1272.

[20] Nguyen, P. T., Berning, T. and Djilali, N. (2004) 'Computational model of a PEM fuel cell with serpentine gas flow channels', 130, pp.149–157.

SAKARYA ÜNİVERSİTESİ
FEN BİLİMLERİ ENSTİTÜSÜ DERGİSİ

Sakarya University Journal of Science
SAUJS

e-ISSN 2147-835X | Period Bimonthly | Founded: 1997 | Publisher Sakarya University |
http://www.saujs.sakarya.edu.tr/en/

Title: Inoculation of Capsicum annuum L. and Lactuca sativa L. Plants with Local Bacillus Species for Evaluating the Protein Amount

Authors: Büşra ÇİĞDEM, Semih YİLMAZ, Aysun ÇETİN

Recieved: 2021-01-28 16:30:15

Accepted: 2021-04-13 13:20:12

Article Type: Research Article

Volume: 25
Issue: 3
Month: June
Year: 2021
Pages: 699-704

How to cite
Büşra ÇİĞDEM, Semih YİLMAZ, Aysun ÇETİN; (2021), Inoculation of Capsicum annuum L. and Lactuca sativa L. Plants with Local Bacillus Species for Evaluating the Protein Amount. Sakarya University Journal of Science, 25(3), 699-704, DOI: https://doi.org/10.16984/saufenbilder.870099
Access link
http://www.saujs.sakarya.edu.tr/en/pub/issue/62736/870099

Sakarya University Journal of Science 25(3), 699-704, 2021

Inoculation of *Capsicum annuum* L. and *Lactuca sativa* L. Plants with Local Bacillus Species for Evaluating the Protein Amount

Büşra ÇİĞDEM[1], Semih YİLMAZ*[2], Aysun ÇETİN[3]

Abstract

Bacteria with plant growth promoting activity can produce metabolites for facilitating nutrient availability and uptake in plants. *Bacillus* species can colonize in root regions and form symbiotic relationships. They provide benefits as binding free nitrogen, dissolving phosphorus, and producing hormones for growth promotion. Local isolates of *Bacillus thuringiensis*, *B. subtilis*, *B. niratireducens* and *B. paramycoides* were coated to seeds of pepper and lettuce plants in greenhouse conditions according to randomized complete block experimental design with five replications in pots with five kg soil. Bacteria were incubated overnight in Luria Bertani medium at 37° C at 180 rpm until reaching $1x10^8$ CFU/ml. Subsequently, coated to surface sterilized seeds through incubating at 100 rpm for 30-45 min. The plants were harvested and kept at 65-70 °C until drying. Samples were pulverized for determining the amount of N using the Kjeldahl method. The amount of total protein content was also estimated by proportioning the amount of N. The N% in the roots of pepper was found to be 5.00 in control group, while the respective values were 6.14 and 6.04 in *Bt* SY49.1 and *Bs* PSY1 treated groups with considerable increase. Likewise, while the N % in shoot samples of pepper was 5.34% in control, it was 6.26 % in *Bt* SY49.1, 6.29 % in *Bn* PSY1, and 8.26 % in *Bp PSY1* treated groups. For root samples of lettuce, the amount was 6.64% in control, however, in *Bt* PSY1 and *Bs* PSY1 treated groups the results were around 8.00%. In lettuce shoot samples, N% was 12.42 in control, and 13.17, 12.87, and 13.12 % in groups treated with *Bn* PSY1, *Bt* PSY1, *Bs* PSY1, respectively. It is known that, nearly all N incorporate into protein structure in food, and can be deduced that the applied bacterial species cause considerable increase in protein amounts in plants.

Keywords: *Bacillus thuringiensis*, *Bacillus subtilis*, *Bacillus paramycoides*, *B. nitratireducens*, Nitrogen

* Corresponding author: ylmazsemh@yahoo.com
[2] Erciyes University, Kayseri, Turkey.
ORCID: https://orcid.org/0000-0003-4835-1494
[1] Erciyes University, Instıtute of Natural Science, Kayseri, Turkey.
E-Mail: busra-cigdem@hotmail.com
ORCID: https://orcid.org/0000-0003-1999-9873
[3] Erciyes University, Faculty of Medicine, Kayseri, Turkey.
E-Mail: aysuncetin@yahoo.com
ORCID: https://orcid.org/0000-0003-4959-7955

1. INTRODUCTION

In recent years, the interest in sustainable agriculture has increased thanks to the realization that all kinds of resources, including soil, used in nourishing living things, are not endless and inexhaustible, and thus, residue-free production is aimed. PGPR bacteria, which is the abbreviation of 'Plant Growth Promoting Rhizobacteria', is important for sustainable agriculture in terms of promoting plant growth or being used as a biocontrol agent [1].

Bacteria that colonize the roots of plants and increase plant growth after inoculation into the seed are called 'rhizobacteria promoting plant growth' (PGPR) [2]. These bacteria include the species in *Bacillus, Lactobacillus, Paenibacillus, Arthobacter, Streptomyces, Pseudomonas, Burkholderia, Comamonas, Hydrogenophaga, Agrobacterium, Alcaligenes, Enterobacter, Pantoae, Enterobacter, Xanthomonas, Serratia, Rhizotobium, Bradyrbium bacterium, Azizobium* genera [3]. Among these, the most important bacterial groups are included in Pseudomonas, Bacillus, Enterobacter and Erwinia [2].

Plant pathogens originating from fungi or bacteria exist in the rhizosphere and can cause various plant diseases by obtaining nitrogen, which is essential for their survival, from the plant. PGPR bacteria mostly colonize in plant roots [3]. These bacteria live on the root surface and in the rhizosphere, stimulating plant growth directly or indirectly. They benefit the plants directly with their properties like nitrogen fixation, plant hormone production (Gibberellin and Cytokinin), reducing the effect of ethylene hormone, increasing phosphate solubility, increasing iron intake by binding iron to the plant root and indirectly benefit the plants through reducing the effect of harmful microorganisms [4]. In addition, Indoleacetic Acid (IAA) produced by bacteria can increase the effects of plant auxin and directly affect root growth by stimulating the plant's cell division and elongation [2].

It is known that Bacillus species constitute the majority of bacteria in the rhizosphere. İmriz et al. [5] reported in a study that the first commercial preparation was produced from the strain of *Bacillus subtilis* A-13 in the USA in 1985 as a biological control agent. Bacillus type of bacteria show antagonistic effect against plant pathogens as well as stimulating plant growth [6].

One of the crucial nutritional elements that plants need is nitrogen, as it is included in the building units of proteins. It is also found in enzymes, chlorophyll and vitamins. Although nitrogen is the main component of the atmosphere, plants can directly use very few of it. In order for living beings to use nitrogen; it must reduce the triple bond in the nitrogen molecule to the double bond and the nitrogen must combine with oxygen and hydrogen. This phenomenon is called nitrogen fixation. Only bacteria, blue-green algae and some fungi can directly use nitrogen in nature. Bacillus type of bacteria are among such kind of organisms [7].

Within the scope of this study, it was aimed to examine the effect of local Bacillus species on the uptake and utilization efficiency of N in root and shoot samples of Lettuce and Pepper plants. Also correspondingly estimating the protein contents in those samples.

2. MATERIALS AND METHODS

Pepper (*Capsicum annuum* L.) (BATEM Özge Hibrit Sivri Biber) and lettuce (*Lactuca sativa* L.) (Yedikule M5701 variety) seeds were used as experimental material. Local isolates of *Bacillus thuringiensis, Bacillus subtilis* and *Bacillus paramycoides* species were used to determine their effects on these plants.

2.1. Activation of bacteria from stock culture

B. nitratireducens PSY1, *B. thurungiensis* PSY1, *B. subtilis* PSY1 and *B. paramycoides* PSY1 isolates were activated from the stock culture by incubating them in LB agar medium for overnight at 37 ° C at 180 rpm. Then they were transferred to LB medium and incubated

overnight at the same conditions till obtaining $1x10^8$ CFU / ml.

2.2. Surface sterilization and inoculation of seeds

For coating trials, Pepper and Lettuce seeds were surface sterilized with 70% ethanol and 1% sodium hypochlorite. After drying, the seeds were kept at 100 rpm in a shaking incubator for 30-45 minutes in a bacterial solution containing 0.1% sucrose. Seeds were dried on a blotter paper in laminar flow for 1 hour and planted in pots.

2.3. Trial pattern

The trials were carried out under greenhouse conditions in 5 replicates for *B. thuringiensis* SY49.1, *B. nitratireducens* PSY1, *B. thuringiensis* PSY1, B. *subtilis* PSY1, and *B. paramycoides* PSY1 and control group. The experimental soil was composed of 1/2 garden soil, ¼ peat and ¼ pumice (sandy-loam; pH 7.83, 1: 2.5v / v; organic matter 1.86; lime 1.59%; P2O5 kgP2O5 / da EC 0.104). The experiments were carried out under greenhouse conditions. Plants were watered periodically as needed. To the plants in each pot 6 g of 15-15-15 composite and 4 g of ammonium nitrate were applied. Lettuce and pepper samples were harvested when they reached a certain volume. The roots and stems of the harvested samples were separated and dried in the oven at 65-70 °C. The dried samples were ground and powdered for protein determination. Photos of the trials are given in figure 1 below.

Figure 1 Growing plants in greenhouse conditions

C: Transplanting seeds into pots

D: Pepper in pots

F: Lettuce in pots

2.4. Total protein determination with Kjeldahl method

Three basic steps are applied in the Kjeldahl method [8].

1. Incineration
2. Distillation
3. Titration

1g of sample was weighed into the incinerator tubes of the Kjeldahl device. 20 ml of sulfuric acid was added to kjeldahl tablet and burned in the device until there was no turbidity and particles for 1 hour. The incinerator tubes were then removed and cooled. After adding 50 ml of distilled water on it, the distillation phase was started. Nearly 70 ml NaOH solution is taken into incinerator tubes during distillation stage. Then, for the titration stage, 60 ml of 3% boric acid with (pH, 4.65) was added into 100 ml beakers. Subsequently the whole amount of distilled solution was added onto the boric acid in the beaker. In the titration stage, the mixture in the beaker was titrated with 0.1 M sulfuric acid till the pH comes to 4.65. During this process the amount of sulfuric acid used for titration stage was recorded. The amount of nitrogen percentage was calculated according to the following equation, and subsequently multiplied by the pre-determined factor 6.25 for estimating the percentage of protein amount in samples [3].

$$\% N = \frac{(V1 - V0) \times N \times 0.014}{m} \times 100$$

$$\% \boldsymbol{Protein} = \% \boldsymbol{N} \times \boldsymbol{F}$$

V1: The amount of sulfuric acid consumed in titration
V0: The amount of sulfuric acid spent in blank trial titration
N: The normality of sulfuric acid solution used in titration
m:The amount of food sample taken (g)
F: General protein coefficient of foods (6.25)

2.5. Statistical analysis

Analysis of variance (ANOVA) for the data were conducted using SPSS 13.0 (SPSS inc, 2001). Post-hoc analyses were performed with Duncan and Dunnett's T3 tests. P<0.05 was considered as significant [9].

3. RESULTS AND DISCUSSION

The Kjeldahl method is a well-known procedure for estimating the amount of nitrogen in the samples. Since almost all of the nitrogen in foods is added to the protein structure, the percentage of nitrogen is considered to be equivalent to the protein amount [8]. The protein amounts of the dried and ground pepper and lettuce samples estimated by the Kjeldahl method in the root and stem parts are given in Table 1.

Table 1 Percentage of protein content in root and shoot samples of pepper and lettuce

Bacillus spp. isolates	Pepper (protein%)		Lettuce (protein%)	
	Root	Stem	Root	Stem
Control	5±0,06^{a*}	5±0,34^{a}	6±0,64^{b}	12±0,42^{bc}
B. thuringiensis SY49.1	6±0,14^{b}	6±0,26^{b}	4±0,59^{a}	7±1,33^{a}
B. nitratireducens PSY1	5±0,58^{a}	6±0,29^{b}	5±0,36^{ab}	13±0,17^{c}
B. thuringiensis PSY1	3±0,45^{-}	6±0,34^{b}	8±0,32^{c}	12±0,87^{bc}
B. subtilis PSY1	6±0,04^{ab}	5±0,14^{a}	8±0,23^{c}	13±0,12^{c}
B. paramycoides PSY1	5±0,49^{a}	8±0,26^{c}	6±0,95^{b}	9±0,45^{ab}

*Values indicated by different letters in the same column are statistically different.

As seen in Table 1, the protein content of root samples of pepper treated with *B. thuringiensis* SY49.1 (P=0.038) and *B. subtilis* PSY1 (P=0.043) was considerably high compared to the control group. In the samples treated with *B. nitratireducens* PSY1, and *B. paramycoides* PSY1, there was no difference compared to the control. *B. thuringiensis* SY49.1 (P=0.031), *B. nitratireducens* PSY1 (P=0.030), *B. thuringiensis* PSY1 (P=0.031), *B. paramycoides* PSY1 (P=0.00) caused remarkable increase in N amount in stem samples compared with control. There was no significant difference in *B. subtilis* PSY1 treated samples compared to the control group.

In root samples of lettuce, it was clear that, *B. thuringiensis* PSY1 (P=0.029), and *B. subtilis* PSY1 (P=0029) isolates caused an increase in percentage of N and consequently the protein amount compared to control group.

In stem samples of the same plant *B. nitratireducens* PSY1 (P=0.26), and *B. subtilis* PSY1 (P=0.26) isolates resulted in higher N content compared to control. PGPR is known to increase enzyme and hormone levels in plants. Thus, the increase in protein amount is related with enzyme and hormone production. In present study, it was clear that the corresponding increases in N and protein amounts were directly related with the PGPR activity of bacterial species. The differences in nitrogen content in root and stem samples is the indication of high protein synthesis in vegetative parts and thus growth promotion.

The protein contents of sources from vegetables were specified and indicated that green leafy vegetables contain high amount of protein [10]. Li et all. [11] stated that the protein content of lettuce samples was between 18-26% of dry weigh. In another study Yardım [12] reported that the amount of nitrogen in soil and plant samples were around 3.06% in tomato leaf and 2.92% in peach leaf. In a study carried out with *Tribulus terestris L.*, the total amount of protein was estimated as 14.48% using the Kjeldhal method. For producing bacterial cellulose from the peels of various fruits and vegetables, it was reported that cucumber, melon, kiwi, tomato, apple, quince, and pomegranate contained 21.25, 4.93, 10.14, 13.46, 2.43, 3.12, 4.18% protein,

determined with Kjeldhal method, respectively [13].

Breedt et al. [14] examined the yield improvement efficiency of five different bacterial isolates in corn plant in different soil types and reported that nitrogen fixation and consequently the yield was improved [14]. When the corn plants under salinity stress and normal conditions were treated with *Serratia liquefaciens* KM4, total free amino acids, soluble proteins and proline amounts were significantly increased [15]. In another study, cyanobacteria and PGPR were applied to rice in field conditions and caused 73% increase in N content. In the same study, *Providencia sp.* PW5 caused 25% increase in N content in wheat [16].

In conclusion, the local bacterial isolates harboring the genes for plant growth promoting activity can be used for developing new formulations after testing in field conditions and on other plant species.

Funding

The authors has not received any financial support for the research, authorship, or publication of this study.

Author contribution

The authors contributed equally to the study.

Ethics Committee Approval Notice

This study does not require ethics committee approval or any special permission.

The Declaration of Ethics Committee Approval

This study does not require ethics committee permission or any special permission.

The Declaration of Research and Publication Ethics

The authors of the paper declare that they comply with the scientific, ethical and quotation rules of SAUJS in all processes of the paper and that they do not make any falsification on the data collected. In addition, they declare that Sakarya University Journal of Science and its editorial board have no responsibility for any ethical violations that may be encountered, and that this study has not been evaluated in any academic publication environment other than Sakarya University Journal of Science."

REFERENCES

[1] B.S. Bahadır, Ö. Güvenenler, and R. Eltem, "Bitki Gelişimini Teşvik Eden Rizobakterilere Ait Patentlerin İncelenmesi," Marmara Fen Bilimleri Dergisi vol. 1, pp. 1-19, 2017.

[2] A. Grobelak, A. Napora, and M. Kacprzak, "Using plant growth-promoting rhizobacteria (PGPR) to improve plant growth," Ecological Engineering, vol. 84, pp. 22–28, 2015.

[3] AOAC, Official Methods of Analysis, Association of Official Analytical Chemists, 17th Ed., A.H. Washington and J. Kloepper, (2001). Plant Growht Promoting Rhizobacteria (PGPR), Copyright 2001 Academic Press, p.1447.

[4] A.A.J. Jawad, "PGPR ile Farklı Dozlarda Biyokömür Uygulamalarının Mısır Bitkisinin Verimine, Besin Elementi Alımına Ve Kuraklık Toleransına Etkisi". Doktora Tezi, Tez Merkezi. 602881, 2019.

[5] G. İmriz, F. Özdemir, İ. Topal, B. Ercan, M.N. Taş, E. Yakışır, and O. Okur, "Bitkisel Üretimde Bitki Gelişimini Teşvik Eden Rizobakteri (PGPR)'ler ve Etki Mekanizmaları".Elektronik Mikrobiyoloji Dergisi, vol.12, no. 2, pp. 1-19, 2014.

[6] M. Çelikten and A. Bozkurt, "Buğday Kök Bölgesinden İzole Edilen Bakterilerin Buğday Gelişimine Olan Etkilerinin Belirlenmesi," Mustafa Kemal Üniversitesi Ziraat Fakültesi Dergisi, vol. 23, no. 1, pp. 33-48, 2018.

[7] M. Uyanık, K.A.P. Rezaeieh, Y. Delen, B. Gürbüz, "Baklagillerde Bakteri Aşılaması ve Azot Fiksasyonu," Ziraat Mühendisliği Dergisi, vol. 357, 2011.

[8] J. Kjeldahl, "Neue Methode zur Bestimmung des Stickstoffs in organischen Körpern. Fresenius," J. Anal. Chem. Vol. 22, pp. 366–382, 1883. doi: 10.1007/BF01338151.

[9] SPSS, Version 10.0, SPSS Inc, Illinois, Chicago, 2001, 233 S. Wacker Drive.

[10] M. Çetiner, S.E. Bilek, "Bitkisel Protein Kaynakları," Çukurova J. Agric. Food Sci. Vol. 33, no. 2, pp. 111-126, 2018.

[11] Y. Li, H. Liu, K. Xiao, X. Liu, H. Hu, X. Li, and H. Yao, "Correlations between the physicochemical properties of hydrochar and specific components of waste lettuce: Influence of moisture, carbohydrates, proteins and lipids", Bioresource Technology, vol. 272, pp. 482-488, 2019.

[12] P. Yardım, "Toprak Ve Bitki Örneklerinde Toplam Azot Belirlenmesinde Kjeldahl Ve Mikrodalga Yaş Yakma Yöntemlerinin Karşilaştirilmasi," Çukurova Üniversitesi, Fen Bilimleri Enstitüsü (Yüksek Lisans Tezi), Tez Merkezi. 244281, 2009.

[13] M. Güzel and Ö. Akpınar, "Preparation and characterization of bacterial cellulose produced from fruit and vegetable peels by Komagataeibacter hansenii GA2016," International Journal of Biological Macromolecules, vol. 162, pp.1597-1604, 2020.

[14] G. Breedt, N. Labuschagne, and T.A. Coutinho, "Seed treatment with selected plant growth- promoting rhizobacteria increases maize yield in the field," Annals of Applied Biology, vol. 171, no. 2, pp. 229-236, 2017.

[15] M. El-Esawi, I. Alaraidh, A. Alsahli, S. Alzahrani, H. Ali, A. Alayafi, and M. Ahmad, "Serratia liquefaciens KM4 improves salt stress tolerance in maize by regulating redox potential, ion homeostasis, leaf gas exchange and stress-related gene expression," International Journal of Molecular Sciences, vol. 19, no. 11, pp. 3310, 2018. doi:10.3390/ijms19113310.

[16] A. Rana, S.R. Kabi, S. Verma, A. Adak, M. Pal, Y.S. Shivay, R. Prasanna, and L. Nain, "Prospecting plant growth promoting bacteria and cyanobacte-ria as options for enrichment of macro-and micronutrients in grains in rice–wheat cropping sequence," Cogent Food & Agriculture, vol. 1, no. 1, 2015. DOI: 10.1080/23311932.2015.1037379.

SAKARYA ÜNİVERSİTESİ
FEN BİLİMLERİ ENSTİTÜSÜ DERGİSİ

Sakarya University Journal of Science
SAUJS

e-ISSN 2147-835X | Period Bimonthly | Founded: 1997 | Publisher Sakarya University |
http://www.saujs.sakarya.edu.tr/en/

Title: The Essential Oils of Laurus nobilis L. and Molecular-Spectroscopic Analysis for 1,8-Cineole

Authors: Ömer ELKIRAN, Mustafa KARAKAYA

Recieved: 2021-01-25 14:27:32

Accepted: 2021-04-16 18:49:48

Article Type: Research Article

Volume: 25
Issue: 3
Month: June
Year: 2021
Pages: 705-713

How to cite
Ömer ELKIRAN, Mustafa KARAKAYA; (2021), The Essential Oils of Laurus nobilis L. and Molecular-Spectroscopic Analysis for 1,8-Cineole. Sakarya University Journal of Science, 25(3), 705-713, DOI: https://doi.org/10.16984/saufenbilder.867968
Access link
http://www.saujs.sakarya.edu.tr/en/pub/issue/62736/867968

Sakarya University Journal of Science 25(3), 705-713, 2021

The Essential Oils of *Laurus nobilis* L. and Molecular-Spectroscopic Analysis for 1,8-Cineole

Omer ELKIRAN*[1], Mustafa KARAKAYA[2]

Abstract

In the present study, the chemical composition of the essential oils obtained from leaves of *Laurus nobilis* naturally grown in Turkey were evaluated using by GC and GC-MS and chemical differences were depated in means of chemotaxonomy. The leaves of the plant samples were hydro-distilled. Twenty components were identified representing 99.3% of the oils, The main compounds in the essential oils were; 1,8-cineole (%48.47), β-pinene (%14.45), linalool (%8.15) and α-pinene (%5.97). In addition, the complexation energies, chemical shifts of the carbon and hydrogen atoms in the 1,8-cineole structures were calculated by ab initio theoretical approaches. The performances of the B3LYP and M06 functionals were tested on carbon and hydrogen complexation energies of the investigated compound. The electronegativity effect of oxygen and solvent effect on complexation energy of the carbons and hydrogens were evaluated with the results obtained.

Keywords: *Laurus nobilis*, Essential oils, 1,8-cineole, GC-MS, Complexation energy, Density functional theory

1. INTRODUCTION

Essential oils are one of the important work areas of the pharmaceutical and cosmetic industry [1]. The *L. nobilis* is also plant that has cineolic essential oils content. 1,8-cineole is the chemical components present in high proportions in the essential oil content of this plant. The other names of the 1,8-cineole molecule are eucalyptol or 1,8-epoxy-*p*-menthane in literature [2]. This compound is used as food flavoring because it has a sharp aroma and as pharmaceutical chemical [3-6].

As a result of our detailed literature search, the following areas have been carried out in on the quantum computations of this molecule. The molecular orbital's, eigenvalues and symmetry for each orbital [7], vibration frequencies [8,9] have been reported for the 1,8-cineole by density functional theory (DFT) calculations. Molecular docking and binding energies have been computed β-cyclodextrin inclusion complex with five essential oil compounds (linalool, eugenol,

*Corresponding author: omer_elkiran@hotmail.com
[1]Sinop University, Vocational School of Health Services, Environmental Health Programme, 57000, Sinop.
ORCID: https://orcid.org/0000-0003-1933-4003
[2]Sinop University, E-Mail: mkarakayafizik@hotmail.com
ORCID: https://orcid.org/0000-0001-6663-9008

methyl eugenol, estragole, and eucalyptol) modeled by DFT both in the gas phase and in the aqueous phase using polarizable continuum methods [10].

Theoretical IR Frequencies, shifting of bands, second order perturbation energies of hydrogen bonds and interactions for 1,8-cineole + o-, m- and p-cresol binary mixtures at 298.15 K analyzed by using (DFT) with B3LYP hybrid functional [11]. In addition, DFT and experimental studies on cycloaddition reactions of C.N-disubstituted nitrones [12], 2, 4, 6-trimethyl phenol [13] and nickel (II) complexes [14] are recently available in the literature. We wish to investigate the complexation energies, chemical shifts of the carbon and hydrogen_atoms in the 1, 8-cineole structures and to comment the results from approximation methods in this study. According to the literature, leaves of *L. nobilis* have not been the subject of any investigation for this region and this paper is the first such phytochemical study on this plant of Central Black Sea region.

2. EXPERIMENTAL

2.1. Plant materials

L. nobilis specimens were collected in June 2016 from Sinop. The specimens were studied Sinop University, SUBITAM, Sinop, Turkey.

2.2. Isolation of the essential oils

The leaves (100g) were subjected to hydro distillation using a Clevenger-type apparatus for 3 h to yield essential oil.

2.3. Gas chromatography (GC) analysis

The essential oil was analyzed using HP 6890 GC equipped with a FID detector and an HP-5 MS column (30m×0.25mm i.d., film thickness 0.25 μm) and the capillary column were used. The column and analysis conditions were the same as in GC-MS. The percentage composition of the essential oils was computed from GC–FID peak areas without correction factors.

2.4. Gas chromatography/mass spectrometry (GC-MS) analysis

The oil samples were analyzed by GC-MS, using a Hewlett Packard system. HP-Agilent 5973N GC-MS system with 6890 GC. HP-5 MS column (30m×0.25mmi. d., film thickness 0.25 μm) was used with helium as the carrier gas. Injector temperature was 250 ^{0}C, split flow was 1ml/min. The GC oven temperature was kept at 70^{0}C for 2 min and programmed to 150 ^{0}C at a rate of 10 ^{0}C / min and then kept constant at 150^{0}C for 15 min to 240 ^{0}C at a rate of 5 ^{0}C/min. Alkanes were used as reference points in the calculation of relative retention indices (RRI). MS were taken at 70 EV and at a mass range of 35–425. Component identification was carried out using spectrometries electronic libraries (WILEY, NIST). The components of the essential oils were in Table 1 and the chromatograms were shown in Figure 1.

2.5. Computational details

Quantum calculations on the structural optimizations, the complexation energies and chemical shifts were performed using DFT [15], Becke's three-parameter (B3) exchange function [16] along with Lee-Yang-Parr correlational functional (LYP) [17] and M06-2X empirical exchange correlation functionals [18]. M05 and M06 functionals are taken into account for medium-range electron correlation, indirectly, to describe the dispersion interactions [19,20]. "6-311G" was selected as the basis set level with "*d,p*" polarization functions and "++" diffuse functions [21]. Inputs on the atomic coordinates of the 1,8-cineole compound were created by Gauss View program [22] and optimizations and the complexation energies and chemical shift data were obtained by using Gaussian 09W software database [23]. The complexation energies were computed by basis set superposition error (BSSE) and counterpoise (CP) corrections [24]. The water as a solvent, and polarizable continuum model (PCM) were selected for the calculations of solvent effects in CP approach. NMR chemical shifts computings were completed by the Gauge independent atomic orbitals (GIAO) method [25] with the chloroform solvent. Tetramethylsilane

(TMS) was used as a reference molecule in computing of the ^{1}H and ^{13}C isotropic magnetic shielding (IMS) of carbon or hydrogen atoms.

3. RESULTS and DISCUSSION

3.1. Essential Oil Composition

In this study, the chemical composition of the volatile metabolites of *L. nobilis* collected during the flowering period of Turkey. Essential oil of dried aerial parts of *L. nobilis* were evaluated by GC and GC-MS. The analysis results of essential oils of *L. nobilis* are shown in Table 1 and in Figure 1. 21 compounds were identified, representing 99.3% of the *L. nobilis*, essential oil (Figure 1.). At the end 1,8-cineole (48.47%), β-pinene (%14.45), linalool (%8.15) and α-pinene (%5.97) were also determined as the major compounds (Table 1).

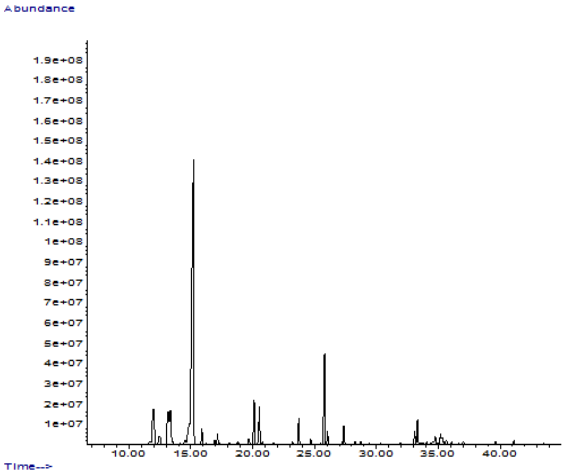

Figure 1 GC chromatogram of essentials oil of *L. nobilis*

Table 1 Chemical composition of essential oil of *L. nobilis*

	RT (min)	RRI	RRI*	Compounds	Peak area (%)
1	11.979	1112	1114[a]	α-Pinene	5.97
2	12.470	1123	1122-1169[b]	3-Carene	1.35
3	13.167	1138	1147[a] 1085-1130[b]	β-Pinene	14.45
4	14.531	1168	1154-1195[b] 1188[c]	α-Terpinene	0.61
5	15.207	1183	1186-1231[b]	1,8-Cineole	48.47
6	15.890	1198	1261-1300[b]	Terpinolene	1.25
7	17.156	1226	1148[d] 1302[a]	Linalool	0.66
8	20.115	1291	1209[d]	4-Terpineol	3.81
9	20.538	1300	1215[e]	α-Terpineol	3.31
10	23.721	1370	1259-1284[b]	Bornyl acetate	1.97
11	24.677	1391	1391[c]	(Z)-3-Hexenol	0.41
12	25.802	1416	1329-1358[b]	α-Terpinyl acetate	8.15
13	26.049	1421	1411-1465[b]	1-Octen-3-ol	1.06
14	27.365	1450	1394-1410[b]	Methyl eugenol	1.44
15	33.093	1576	1562-1590[b]	Spathulenol	1.22
16	33.322	1581	1563-1595[b]	Caryophyllene oxide	2.06
17	34.054	1597	1532-1643[b]	β-Guaiene, trans-	0.3
18	34.757	1613	1584[e]	Ledene oxide	1.14
19	35.181	1622	1611-1655[b]	β-Eudesmol	1.07
20	39.652	1720	1740[f]	Cycloisolongifolene, 8,9-dehydro-9-formyl-	0.6
	Oxygenated monoterpenes 72.10				
	Sesquiterpenes hydrocarbons 20.81				
	Oxygenated sesquiterpenes 6.39				
	Total identified 99.30				

RT: Retention time, RRI: Relative retention index, RRI*: RRI from literature (a (26); b (27); c (28) d (29); e (30); f (31))

In the literature as 1.8-cineole, terpineol, β-pinene, α-pinene, p-cymene, β-caryophyllene as the main constituents of the essential oil of *L. nobilis* leaves are referred to. The acyclic monoterpenes (linalool and myrcenol) may also be present, as well as, dimethyl styrene, eugenol, methyl eugenol and carvacrol [32-36]. In our study, the first major compound is 1,8-cineole similar to other studies in Karadeniz region and different countries [37-40]. Also, another studies using *L. nobilis* essential oils from Brazil isoeugenol (53.5-57.0%) as first major

compounds [32, 41]. In addition, our study major compounds of *L. nobilis* essential oils are show similarity and diversity with other studies. There are lots of factors affecting the production of secondary metabolites in plants. It can be explained as an environmental, geographical, physiological, genetic, political and social factors [37, 42].

3.2. Density Functional Theory Analysis

We have optimized the 1,8-cineole molecule with B3LYP hybrid functional, M06 functional approaches and Møller–Plesset second-order perturbation theory (MP2) to reveal the minimum energy structure. Optimized structure of the 1,8-cineole and relative energy diagram between the ab initio theoretical approaches is given in Figure 2. Total SCF energy is equal –467.263 a.u. in DFT/ restricted-B3LYP calculation method, 6-311++G (d,p) level. Relative energy of M06-2X functional approach (5.78 eV) is fairly smaller than MP2 method (38.49 eV). We are focused on the complexation energy calculation (for the carbons and hydrogens) between the B3LYP and M06-2X functional approaches. 1,8-cineole has cyclohexyl ring. The direction, position and dipole interaction of the dipole moment for the 1,8-cineole with Cs symmetry are reported in a previous DFT study [8]. We have calculated the dipole moment (field-independent basis) with the values of 1.5520 (RB3LYP), 1.5448 (RM06-2X), 2.3382 (RM06-2X solvent=water), 1.6882 Debye (RMP2-FC) by the 6-311++G (d,p) basis set.

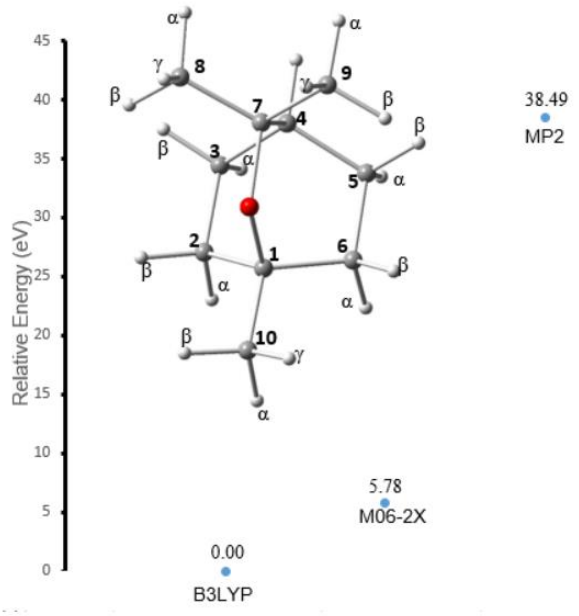

Figure 2 Optimized structure of the 1,8-cineole and relative energy diagram between the ab initio theoretical approaches

Table 2 shows to us the raw and corrected complexation energies with the BSSE energies of the total carbon and hydrogen atoms. The performances of the B3LYP and M06 functionals are tested in Table 2 for the carbon and hydrogen complexation energies of the investigated compound. Uncorrected and CP corrected energy are lower in the calculations of the B3LYP hybrid functional. However, the complexation energies of the total carbon and hydrogen are also lower at M06 functionals. When comparing the complexation energies of hydrogen and carbons in the same methods and basis sets, the hydrogens have of course weaker complexation energies. The atomic radius of hydrogen is much smaller. Because of the electronegativity effect of oxygen, the complexation energies of the carbons bonded to oxygen can be stronger than the others. The complexation energy (corrected) of the carbons are − 1996.94 (in gas phase) and − 1996.71 kcal/mol (in water solvent using PCM method) at M06-2X approach, B3LYP/6-311G (d, p) levels. The corrected complexation energy of the hydrogens are −1906.90 (in gas phase) and − 1906.13 kcal/mol (in water solvent using PCM method) at M06-2X approach, B3LYP/6-311G

(d, p) levels. It can be said that the solvent effect weakens the binding energy of the carbons and hydrogens and intramolecular interaction. Binding energies of inclusion complexes with eucalyptol are − 2.86 (in water using PCM methods,−2.01 (as corrected in gas phase) and − 5.45 kcal/mol (as uncorrected in gas phase) at DFT/B3LYP/6-31G (d) levels in another study [11].

Table 2 Energy values of the 1,8-cineole by ab initio calculations and 6-311++G(d,p) level

	Total carbon atoms		Total hydrogen atoms	
Energies	B3LYP	M06-2X	B3LYP	M06-2X
Uncorrected energy (a.u)	-467.2629	-467.0505	-467.2629	-467.0505
CP corrected energy (a.u.)	-467.2489	-467.0323	-467.2510	-467.0334
BSSE energy (a.u)	0.0141	0.0182	0.0120	0.0172
Raw complexation energy (kcal/mol)	-1884.77	-2008.39	-1801.62	-1917.68
Corrected complexation energy (kcal/mol)	-1875.94	-1996.94	-1794.12	-1906.90

The computed ^{1}H and ^{13}C NMR chemical shifts of 1,8-cineole are listed in Table 3. The computed data are compared with the experimental ones [43] obtained from the literature. Mean absolute errors (MAE) are narrow and indicate that the calculations are consistent with the experimental results. The carbon and hydrogen atoms in the table are numbered and symbolized according to the model in Figure 2. The chemical shifts of the carbons are calculated to be 76.735 ppm (B3LYP), 72.618 ppm (M062X) in **1** and 81.141 ppm (B3LYP), 76.903 ppm (M062X) in **7**. When compared to the others, these values are the highest values. The chemical shifts are also lowest in **3** and **5**. There is a deshielding effect of oxygen due to electronegativity. Due to the electronegative effect, carbons close to the oxygen atom have higher chemical shifts. We can conclude that the deshielding effect is higher on the carbon **1** and **7**. The previous studies have emphasized that the electron-withdrawing groups made smaller the shielding [44, 45].

Table 3 Computed ^{13}C and ^{1}H NMR Chemical Shifts (δ) of 1,8-cineole by ab initio calculations

Labeled Atoms	δ*$_{calculated}$ (ppm) (B3LYP approach)	δ*$_{calculated}$ (ppm) (M06-2X approach)	δ**$_{experimental}$ (ppm)
C1	76.735	72.618	73.62
C2	35.937	35.662	31.57
C3	28.711	28.052	22.90
C4	38.407	34.916	33.00
C5	28.714	28.037	22.90
C6	35.937	35.685	31.57
C7	81.141	76.903	69.77
C8	30.544	33.203	28.92
C9	30.544	33.226	28.92
C10	30.167	33.575	27.61
H2(α)	1.555	1.4255	1.50
H2(β)	1.605	1.6303	1.661
H3(α)	1.493	1.5396	1.50
H3(β)	2.066	2.0485	2.022
H4	1.302	1.0695	1.41
H5(α)	1.492	1.5394	1.50
H5(β)	2.066	2.0484	2.022
H6(α)	1.555	1.4292	1.500
H6(β)	1.605	1.6302	1.661
H8(α)	0.944	0.9411	1.239
H8(β)	1.505	1.4163	1.239
H8(γ)	1.154	1.1994	1.239
H9(α)	0.944	0.943	1.239
H9(β)	1.506	1.4157	1.239
H9(γ)	1.154	1.2004	1.239
H10(α)	0.859	0.8823	1.050
H10(β)	1.056	1.1848	1.050
H10(γ)	1.056	1.1829	1.050
MAE	*1.71378571*	*1.615775*	

*solvent=chloroform and Polarizable Continuum Model.

**Taken from Ref. [23]

4. CONCLUSION

The findings showed that the *L. nobilis* had a low-level variation in essential oil composition and this study demonstrates the occurrence of 1,8-cineole (eucalyptol) chemotype of *L. nobilis* in Central Black Sea region of Turkey. In general, the essential oil composition of *L. nobilis* patterns from the different region showed that, the species

has sabinene, myrcene, camphene were the major and predominant compounds.

The complexation energies, chemical shifts of the carbon and hydrogen_atoms in the 1,8-cineole structures are computed by B3LYP hybrid functional and M06 functional approaches in our theoretical work. The calculations by M062X functional approach have provided the effective results to us for the raw and corrected complexation energies. The solvent effect weakens the complexation energy of the carbons and hydrogens and intramolecular interaction. The complexation energies of the carbons bonded to oxygen are strong due to the electronegativity effect of oxygen. The calculated ^{1}H and ^{13}C NMR chemical shifts of 1,8-cineole are consistent with the experimental results. Due to the electronegative effect, carbons close to the oxygen atom have higher chemical shifts.

Funding

This work was supported by Sinop University Scientific Research Coordination Unit. Project Number: 1901. 14-05, 2015.

The Declaration of Conflict of Interest/ Common Interest

No conflict of interest or common interest has been declared by the authors.

Authors' Contribution

All authors have contributed in experimental study and writing of the manuscript equally.

The Declaration of Ethics Committee Approval

The author declares that this document does not require an ethics committee approval or any special permission.

The Declaration of Research and Publication Ethics

The authors of the paper declare that they comply with the scientific, ethical and quotation rules of SAUJS in all processes of the paper and that they do not make any falsification on the data collected. In addition, they declare that Sakarya University Journal of Science and its editorial board have no responsibility for any ethical violations that may be encountered, and that this study has not been evaluated in any academic publication environment other than Sakarya University Journal of Science.

REFERENCES

[1] F. Comelli, S. Ottani, R. Francesconi, and C. Castellari, "Densities, viscosities, and refractive indices of binary mixtures containing n-hexane+ components of pine resins and essential oils at 298.15 K," Journal of Chemical & Engineering Data, vol. 47, pp. 93-97, 2002.

[2] E. J. L. Lana, K. A. da Silva Rocha, I. V. Kozhevnikov, and E. V. Gusevskaya, "Synthesis of 1, 8-cineole and 1, 4-cineole by isomerization of α-terpineol catalyzed by heteropoly acid," Journal of Molecular Catalysis A: Chemical, vol. 259, pp. 99-102, 2006.

[3] S. Pattnaik, V. R. Subramanyam, M. Bapaji, and C. R. Kole, "Antibacterial and antifungal activity of aromatic constituents of essential oils", Microbios, vol. 89, pp. 39, 1997.

[4] E. A. Laude, A. H. Morice, and T. J. Grattan, "The antitussive effects of menthol, camphor and cineole in conscious guinea-pigs. Pulmonary pharmacology," vol. 7, pp. 179-184, 1994.

[5] S. Gao, and J. Singh, "In vitro percutaneous absorption enhancement of a lipophilic drug tamoxifen by terpenes," Journal of controlled release, vol. 51, pp. 193-199, 1998.

[6] H. Moteki, H. Hibasami, Y. Yamada, H. Katsuzaki, K. Imai, and T. Komiya, "Specific induction of apoptosis by 1, 8-cineole in two human leukemia cell lines, but not a in human stomach cancer cell line," Oncology reports, vol. 9, pp. 757-760, 2002.

[7] S. Aparicio, R. Alcalde, M. J. Dávila, B. García, and J. M. Leal, "Properties of 1, 8-cineole: a thermophysical and theoretical study," The Journal of Physical Chemistry B, vol. 111, pp. 3167-3177, 2007.

[8] M. Baranska, H. Schulz, S. Reitzenstein, U. Uhlemann, M. A. Strehle, H. Krüger, ... and J. Popp, "Vibrational spectroscopic studies to acquire a quality control method of Eucalyptus essential oils," Biopolymers: Original Research on Biomolecules, vol. 78, pp. 237-248, 2005.

[9] K. R. Strehle, P. Rösch, D. Berg, H. Schulz, and J. Popp, "Quality control of commercially available essential oils by means of Raman spectroscopy," Journal of agricultural and food chemistry, vol. 54, pp. 7020-7026, 2006.

[10] L. Lawtrakul, K. Inthajak, and P. Toochinda, "Molecular calculations on β-cyclodextrin inclusion complexes with five essential oil compounds from *Ocimum basilicum* (sweet basil)," Science Asia, vol. 40, pp. 145-151, 2014.

[11] P. Patel, J. Bhalodia, S. S. Sharma, and P. C. Jha, "Refractive index, speed of sound, FT-IR and computational study of intermolecular interaction between binary mixtures of 1, 8-cineole with o-, m-and p-cresol at 303.15, 308.15 and 313.15 K," Journal of Molecular Liquids, vol. 222, pp. 1192-1211, 2016.

[12] S. Mandal, K. K. Maiti, A. Banerji, T. Prange, A. Neuman, and N. Acharjee, "Experimental and DFT studies for substituent effects on cycloadditions of C, N-disubstituted nitrones to cinnamoyl piperidine," 2018.

[13] S. Prabhakaran, and M. Jaffar, "Vibrational analysis, ab initio HF and DFT studies of 2, 4, 6-trimethyl phenol," Indian Journal of Pure & Applied Physics, vol. 56, pp. 119-127, 2018.

[14] R.N. Patel, "Crystal structure, configurational and DFT study of nickel (II) complexes with N 2 O-donor type Schiff base ligand," Indian Journal of Chemistry-Section A (IJCA), vol. 57, pp. 44-51, 2020.

[15] J. Andzelm, and E. Wimmer, "Density functional Gaussian-type-orbital approach to molecular geometries, vibrations, and reaction energies," The Journal of chemical physics, vol. 96, pp. 1280-1303, 1992.

[16] A.D. Becke, "Density-functional exchange-energy approximation with correct asymptotic behavior," Physical Review, vol. 38, pp. 3098. 1988.

[17] C. Lee, W. Yang, and R. G. Parr, "Development of the Colle-Salvetti correlation-energy formula into a functional of the electron density," Physical review B, vol. 37, pp. 785, 1988.

[18] Y. Zhao, and D. G. Truhlar, "A new local density functional for main-group thermochemistry, transition metal bonding, thermochemical kinetics, and noncovalent interactions," The Journal of chemical physics, vol. 125, pp. 194101, 2006.

[19] Y. Zhao, and D. G. Truhlar, "The M06 suite of density functionals for main group thermochemistry, thermochemical kinetics, noncovalent interactions, excited states, and transition elements: two new functionals and systematic testing of four M06-class functionals and 12 other functionals," Theoretical Chemistry Accounts, vol. 120, pp. 215-241, 2008.

[20] E. G. Hohenstein, S. T. Chill, and Sherrill, C. D., "Assessment of the performance of the M05− 2X and M06− 2X exchange-correlation functionals for noncovalent interactions in biomolecules," Journal of Chemical Theory and Computation, vol. 4, pp. 1996-2000, 2008.

[21] A. D. McLean, and G. S. Chandler, "Contracted Gaussian basis sets for molecular calculations. I. Second row

atoms, Z= 11–18," The Journal of Chemical Physics, vol. 72, 5639-5648, 1980.

[22] R. Dennington, T. Keith, and J. Millam, "GaussView, Version 5.0.9, Semichem Inc. ," Shawnee Mission, KS, 2009.

[23] M. J. Frischa, G. W. Trucks, H. P. Schlegel, G. E. Scuseria, M. A. Robb, and J. R. "Cheesman, Gaussian'09, Gaussian. Inc.," Wallingford CT, 2009.

[24] S. F. Boys, and F. J. M. P. Bernardi, "The calculation of small molecular interactions by the differences of separate total energies. Some procedures with reduced errors," Molecular Physics, vol. 19, pp. 553-566, 1970.

[25] C. M. Rohlfing, L. C. Allen, and R. Ditchfield, "Proton and carbon-13 chemical shifts: comparison between theory and experiment," Chemical physics, vol. 87, pp. 9-15, 1984.

[26] O. Elkiran, and C. Avşar, ''Chemical composition and biological activities of the essential oil from the leaves of *Vaccinium myrtillus* L.,'' Bangladesh Journal of Botany, vol. 49, pp. 91-96, 2020.

[27] V. I. Babushok, P. J. Linstrom, and I. G. Zenkevich, ''Retention indices for frequently reported compounds of plant essential oils,'' Journal of Physical and Chemical Reference Data, vol. 40, 043101-47, 2011.

[28] M. Kürkçüoglu, A. Abdel-Megeed, and K. H. C. Başer, ''The composition of *Taif rose* oil,'' Journal of Essential Oil Research, vol. 25, pp. 364-367, 2013.

[29] O. Elkiran, E. Akbaba, and E. Bagci, ''Constituents of essential oils from leaves and seeds of *Laurus nobilis* L.: a chemotaxonomic approach,'' Bangladesh Journal of Botany, vol. 47, pp. 893-901, 2018.

[30] E. Bagci, O. Elkiran, and H. Evren, ''Constituents of the essential oils of *Helichrysum graveolens* (Bieb.) Sweet from Turkey,'' Asian Journal of Chemistry, vol. 25, pp. 7254-7256, 2013.

[31] S. Jena, A. Ray, A. Sahoo, B. Kar, P. C. Panda, and S. Nayak, ''Chemical constituents of leaf essential oil of *Curcuma angustifolia* Roxb. growing in eastern India,'' Journal of Essential Oil Bearing Plants, vol. 19, pp. 1527-1531, 2016.

[32] L. S. Pinheiro, A. A. de Oliveira Filho, and F. Q. S. Guerra, "Antifungal activity of the essential oil isolated from *Laurus nobilis* L. against *Cryptococcus neoformans* strains," Journal of Applied Pharmaceutical Science, vol. 7, pp. 115-118, 2017.

[33] M. Riaz, C. M. Ashraf, and F. M. Chaudhary, "Studies on the essential oil of the Pakistani *Laurus nobilis* Linn. in different seasons," Pakistan Journal of Scientific and Industrial Research, vol. 32, pp. 33-35, 1989.

[34] R. M. Verdian, "Phenological variation of *Laurus nobilis* L. essential oil from Iran," Electronic Journal of Environmental, Agricultural and Food Chemistry, vol. 7, pp. 3321-3325, 2008.

[35] H. Marzouki, A. Piras, B. Marongiu, A. Rosa, and M. A. Dessì, "Extraction and separation of volatile and fixed oils from berries of *Laurus nobilis* L. by supercritical CO2," Molecules, vol. 13, pp. 1702-1711, 2008.

[36] H. Yalçın, M. Anık, M. A. Şanda, and A. Çakır, "Gas chromatography/mass spectrometry analysis of *Laurus nobilis* essential oil composition of northern Cyprus," Journal of medicinal food, vol. 10, pp. 715-719, 2007.

[37] B. Yılmaz, and İ. Deniz, "The Effects of cultivation area and altitude variation on the composition of essential oil of *Laurus nobilis* L. grown in eastern, Western and

Central Karadeniz Region," International Journal of Secondary Metabolite, vol. 4, pp. 187-194, 2017.

[38] L. Caputo, F. Nazzaro, L. F. Souza, L. Aliberti, L. De Martino, F. Fratianni,... and V. De Feo, "*Laurus nobilis*: Composition of essential oil and its biological activities," Molecules, vol. 22, pp. 930, 2017.

[39] C. Ramos, B. Teixeira, I. Batista, O. Matos, C. Serrano, N. R. Neng, J.M.F. Nogueira, M.L. Nunesand and A. Marques, "Antioxidant and antibacterial activity of essential oil and extracts of bay laurel *Laurus nobilis* Linnaeus (Lauraceae) from Portugal," Natural Product Research, vol. 26, pp. 518-529, 2012.

[40] K. K. Chahal, M. Kaur, U. Bhardwaj, N. Singla and A. Kaur, "A review on chemistry and biological activities of *Laurus nobilis* L. essential oil, " Journal of Pharmacognosy and Phytochemistry, vol. 6, pp. 1153-1161, 2017.

[41] L. R. Peixoto, P. L. Rosalen, G. L. S. Ferreira, I. A. Freires, F. G. de Carvalho, L. R. Castellano, and R. D. de Castro, "Antifungal activity, mode of action and anti-biofilm effects of *Laurus nobilis* Linnaeus essential oil against Candida spp," Archives of oral biology, vol. 73, pp. 179-185, 2017.

[42] A. C. Figueredo, J. G. Barroso, L. G. Pedro, and J. J. C. Scheffer, "Factors affecting secondary metabolite production in plants: volatile and essential oils," Flavour and Fragrance Journal, vol. 23, pp. 213-226, 2008.

[43] https://sdbs.db.aist.go.jp/sdbs/cgi-bin/cre_index.cgi

[44] T. Sivaranjini, S. Periandy, M. Govindarajan, M. Karabacak, and A. M. Asiri, "Spectroscopic (FT-IR, FT-Raman and NMR) and computational studies on 3-methoxyaniline," Journal of Molecular Structure, vol. 1056, pp. 176-188, 2014.

[45] M. Karakaya, and F. Ucun, "H2-Anion Interactions and Energy Calculations for Imidazolium-based Ionic Liquids as Hydrogen Storage Materials," International Journal of Engineering Technologies, vol. 2, pp. 1-7, 2016.

SAKARYA ÜNİVERSİTESİ
FEN BİLİMLERİ ENSTİTÜSÜ DERGİSİ

Sakarya University Journal of Science
SAUJS

e-ISSN 2147-835X | Period Bimonthly | Founded: 1997 | Publisher Sakarya University |
http://www.saujs.sakarya.edu.tr/en/

Title: An Efficient Synthetic Approach for The Transition Metal-Free Preparation of 2-Bromo-3-(Bromomethyl)Naphthalene from Naphthalene

Authors: Musa ERDOĞAN

Recieved: 2021-04-03 16:23:19

Accepted: 2021-04-19 14:34:50

Article Type: Research Article

Volume: 25
Issue: 3
Month: June
Year: 2021
Pages: 714-722

How to cite
Musa ERDOĞAN; (2021), An Efficient Synthetic Approach for The Transition Metal-Free Preparation of 2-Bromo-3-(Bromomethyl)Naphthalene from Naphthalene. Sakarya University Journal of Science, 25(3), 714-722, DOI: https://doi.org/10.16984/saufenbilder.909041
Access link
http://www.saujs.sakarya.edu.tr/en/pub/issue/62736/909041

Sakarya University Journal of Science 25(3), 714-722, 2021

An Efficient Synthetic Approach for The Transition Metal-Free Preparation of 2-Bromo-3-(Bromomethyl)Naphthalene from Naphthalene

Musa Erdoğan*[1]

Abstract

Herein, a new efficient method for the synthesis of 2-bromo-3-(bromomethyl)naphthalene is reported. The synthesis is based on (1) preparation of 1,4-dihydronaphthalene via Birch reduction with mild conditions from the reaction of naphthalene, and (2) the reaction between 1,4-dihydronaphthalene and dichlorocarbene formed *in situ* from chloroform and potassium *tert*-butoxide (*t*-BuOK), and (3) access to the key intermediate 1*H*-cyclopropa[*b*]naphthalene from the reaction of 1,1-dichloro-1a,2,7,7a-tetrahydro-1*H*-cyclopropa[*b*]naphthalene with *t*-BuOK, followed by ring-opening of the cyclopropane via bromination with molecular bromine (Br_2). This synthetic sequence allows simple preparation of 2-bromo-3-(bromomethyl)naphthalene in higher yields compared to the two previously reported syntheses. The synthetic approach is modular, low cost, and rapid, and can be utilized to synthesize building blocks of naphthalene derivatives.

Keywords: Metal-free synthesis, Easy synthesis, Naphthalene, Naphthocyclopropane, 2-Bromo-3-(bromomethyl)naphthalene

1. INTRODUCTION

Naphthalene and its derivatives are some of the most functional polycyclic aromatic compounds (PAHs) made up of a large number of aromatic rings [1]. Due to its excellent physicochemical and spectroscopic properties, naphthalene scaffolds found application in various fields of scientific chemistry fields, such as synthetic, materials, medicinal, structural, macromolecular, supramolecular, and fluorescence chemistry; and as backbones or functional devices [1-5]. They have found widespread use as sensors and a marker chromophore unit in biological systems. [6]. Additionally, these materials are an important chemical building block in materials science, as their load-bearing properties and stability make them unique in the fields of organic optoelectronics. [7]. It is also very important that halogenated naphthalene derivatives are synthesized by efficient means. The halogenated naphthalenes are important synthetic derivatives

*Corresponding author: musaerdogan0@gmail.com
[1]Kafkas University, Faculty of Engineering and Architecture, Department of Food Engineering, 36100, Kars, Turkey.
ORCID: https://orcid.org/0000-0001-6097-2862

because the existence of a halogen affords an opportunity for further derivatization. They have established agents for a variety of bond-forming reactions and also serve as a key starting material for synthetic chemistry. The high utility of halogenated organic scaffold has led to the improvement of numerous transformations that place the carbon-halogen motif [8]. Naphthalene derivative **4** has significant synthetic potential, and has been used as a key building block or starting material for the synthesis of the important skeletons such as complex molecules [9], benzolactams with various Pd-catalyzed coupling reactions [10], functionalized chalcogen isochromene-fused chalcogenophene derivatives [11], hydroacenes [12], pharmaceuticals and bioactive products [13], chiral polyaryl cyclophanes [14], and fluorescent π-expanded oxepins [15]. These are just a few examples of their reported synthetic application. In 1986, Smith and his research group reported for the first time the synthesis of 2-bromo-3-(bromomethyl)naphthalene (**4**) [16]. For this, 2-bromo-3-methylnaphthalene (**3**) was synthesized by bromination of the commercially available cyclopentadiene derivate **5** adduct of 2-methylnaphthalene (**6**) (Figure 1) [16]. In the next step, the synthesis of the product **4** was obtained via radical bromination with NBS of the product **3**.

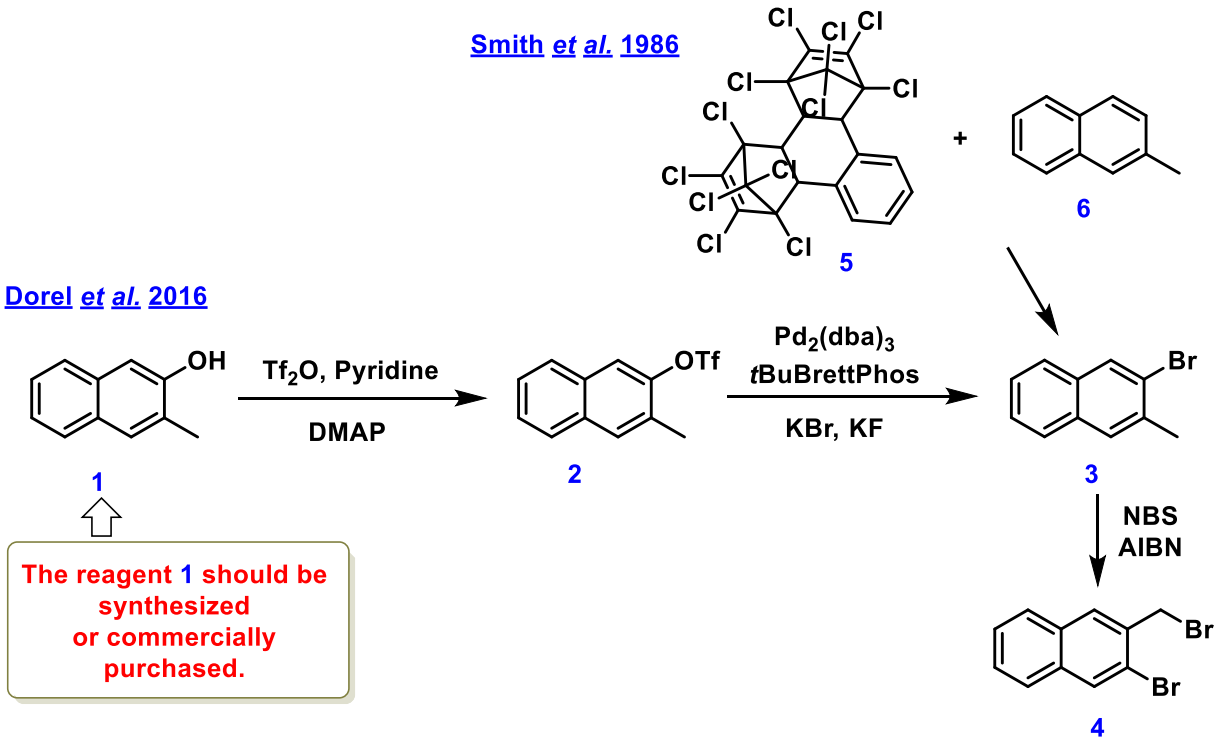

Figure 1 Reported synthesis methods of naphthalene derivative **4**

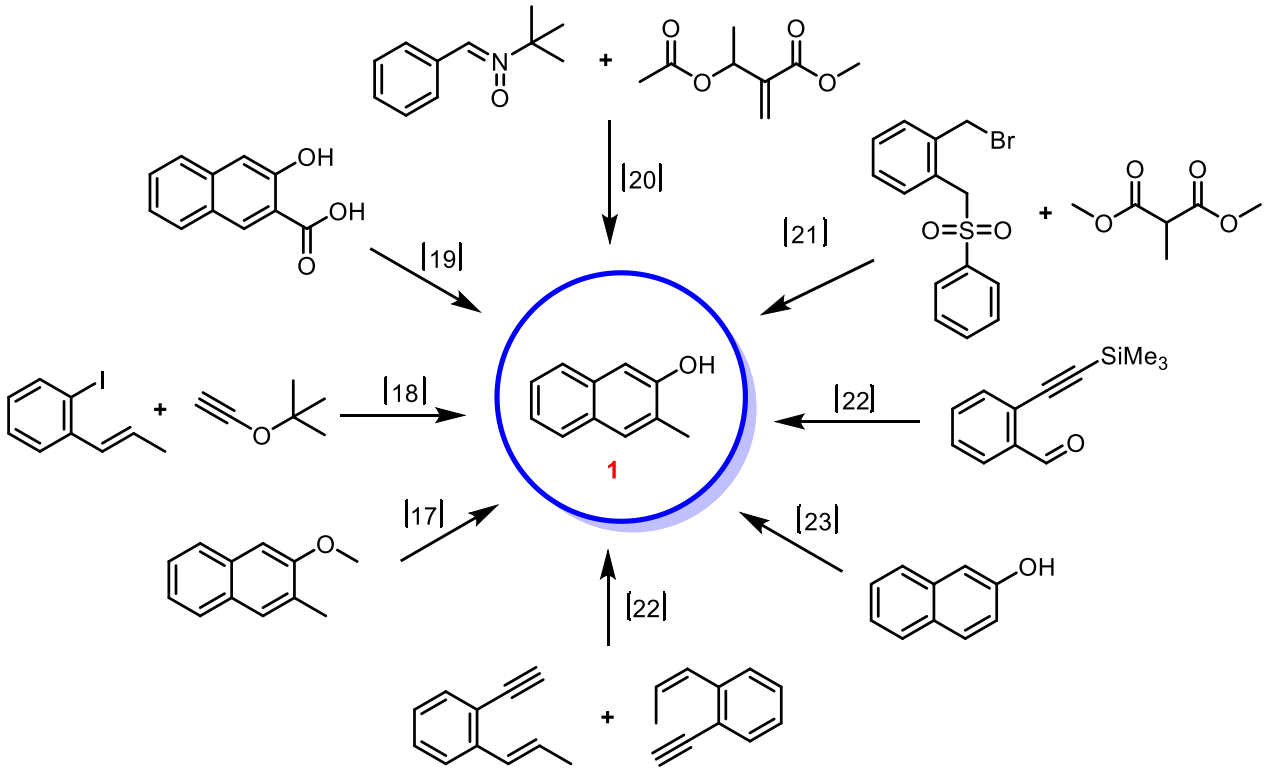

Figure 2 Some reported approaches for preparing 3-methylnaphthalen-2-ol (**1**)

In 2016, Dorel and co-workers reported the synthesis of 2-bromo-3-(bromomethyl)naphthalene (**4**) in three steps (Figure 1) [12]. According to Dorel's approach, starting material 3-methylnaphthalen-2-ol (**1**) should be purchased commercially or obtained by the synthetic methods given in Figure 2 [17-23]. The development of impressive synthetic approaches to obtaining substituted naphthalene and anthracene remains an attractive goal in organic chemistry. To the best of our knowledge, other than these two methods [12,16], no other synthesis method of naphthalene derivative **4** has been reported. These approaches several have certain handicaps including harsh reaction conditions, low reaction yield, and the necessity of using excess and expensive catalysts and ligands. Therefore, it is important to develop new method metal-free and an inexpensive methods.
Herein, an useful transition metal-free and inexpensive method for the preparation of naphthalene derivative **4** starting from naphthalene (**1**) has been developed, and reported.

2. MATERIALS AND METHODS

2.1. Materials

The reactions were accomplished under N_2 gas atmosphere and followed by thin-layer chromatography (TLC). All reagents were used as purchased and used without further purification unless otherwise stated. Column chromatography was achieved with silica gel (60 mesh, Merck) or on neutral alumina. TLC was carried out on silica gel 60 HF254 aluminum plates (Fluka). The ^{1}H and ^{13}C NMR spectra were recorded on a Varian-400 or a Bruker-400 spectrometer in $CDCl_3$ using TMS as the internal reference. All spectra were measured at 25 °C and coupling constants (*J* values) are given in Hz. Chemical shifts are given in parts per million (ppm).

2.2. Experimental procedure

2.2.1. Synthesis

Dihydronaphthalene **8** [31], the product **9** [29], and the product **10** [30] were synthesized according to a previously reported method. The spectral data are identical with those reported in the literature.

1,4-Dihydronaphthalene (**8**): ^{1}H NMR (400 MHz, $CDCl_3$) δ 7.33-6.96 (m, 4H), 5.92-5.87 (m, 2H), 3.39-3.35 (m, 4H).

1,1-Dichloro-1a,2,7,7a-tetrahydro-1H-cyclopropa[b]naphthalene (**9**): ^{1}H NMR (400 MHz, $CDCl_3$) δ 7.10 (s, 4H), 3.22 (ddd, J = 17.0, 5.4, 2.7 Hz, 2H), 2.80 (d, J = 17.0 Hz, 2H), 2.14-1.97 (m, 2H). ^{13}C NMR (100 MHz, $CDCl_3$) δ 133.77, 128.50, 126.12, 66.27, 27.25, 24.77.

1H-cyclopropa[b]naphthalene (**10**): ^{1}H NMR (400 MHz, $CDCl_3$) δ 7.93-7.86 (m, 2H), 7.53-7.41 (s, 2H), 7.46 (m, 2H), 3.53 (s, 2H).

2.2.2. Synthesis of 2-bromo-3-(bromomethyl)naphthalene (4)

To a stirred solution of 1*H*-cyclopropa[*b*]naphthalene (**10**) (0.25 g, 1.78 mmol) in dry CCl_4 (15 mL) under N_2 atmosphere was added dropwise Br_2 (0.314 g, 0.10 mL, 1.96 mmol) in the CCl_4 (10 mL). The reaction mixture was refluxed for 1 h, and then cooled to rt. After evaporation of the solvent, the solid product was recrystallized from CH_2Cl_2 to give the 2-bromo-3-(bromomethyl)naphthalene (**4**) as white crystals. Yield 0.52 g (97%). The spectroscopic data were consistent with those previously reported [12].

2-Bromo-3-(bromomethyl)naphthalene (**4**): ^{1}H NMR (400 MHz, $CDCl_3$) δ 8.10 (s, 1H), 7.95 (s, 1H), 7.84-7.77 (m, 1H), 7.7.76-7.67 (m, 1H), 7.59-7.42 (m, 2H), 4.78 (s, 2H).

3. RESULTS AND DISCUSSION

The chemistry of benzocyclopropenes dates back to ancient times [24]. Nowadays, the science of chemistry owes its development and finding different applications to these ancient synthetic approaches. However, synthetic chemistry has begun to give way to applied chemistry, and interest in compounds with high synthetic potential has decreased. Naphthocyclopropenes's chemistry is interesting chemistry for synthetic applications and may be useful in the synthesis of crucial skeletons to applied chemistry [25,26]. There are a limited number of studies on benzo- or naphthocyclopropenes and its derivatives in the literature [25-27].

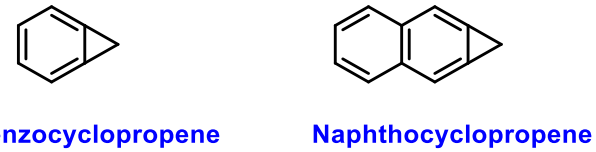

Figure 3 The chemical structure of benzocyclopropenes and naphthocyclopropene

The easy cleavage of the three-member benzocyclopropene ring by electrophiles such as bromine, iodine, HCl, and $AgNO_3$ in the presence of ethanol and aniline previously reported, is of interest both in mechanism and synthesis [26].

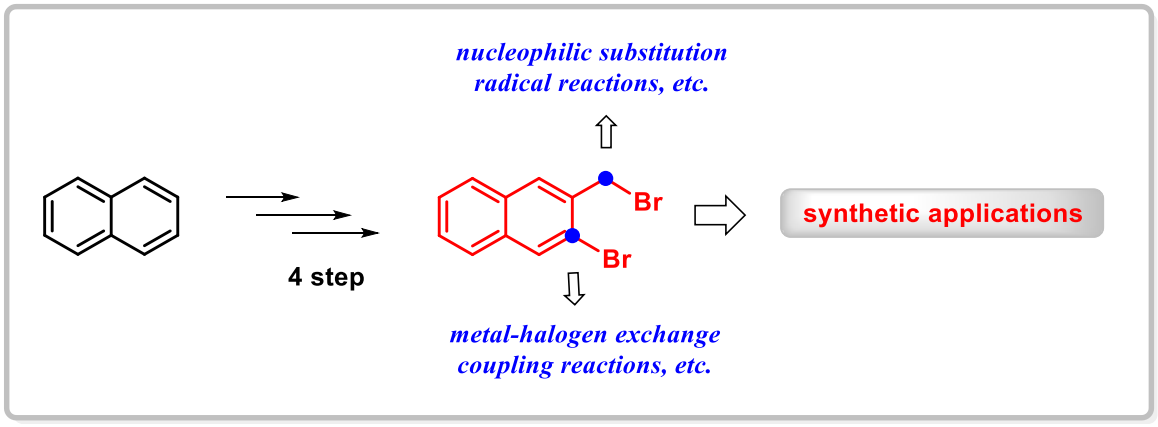

Figure 4 General reactivity of 2-bromo-3-(bromomethyl)naphthalene (**4**)

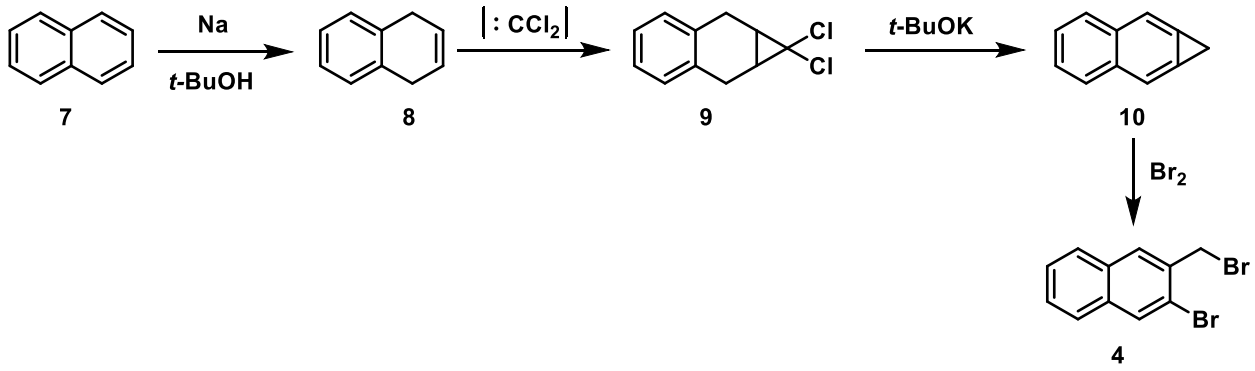

Figure 5 Four-step efficient synthesis of 2-bromo-3-(bromomethyl)naphthalene (**4**)

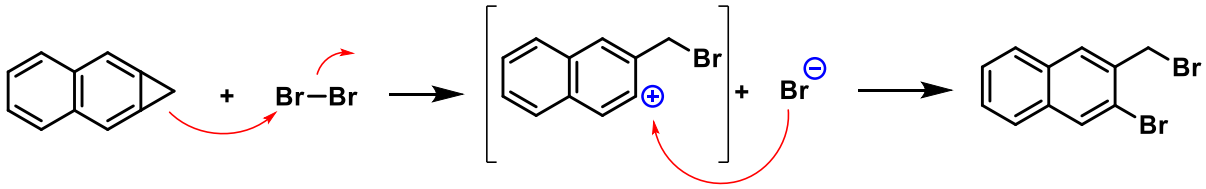

Figure 6 A plausible mechanism for the synthesis of naphthalene derivative **4**

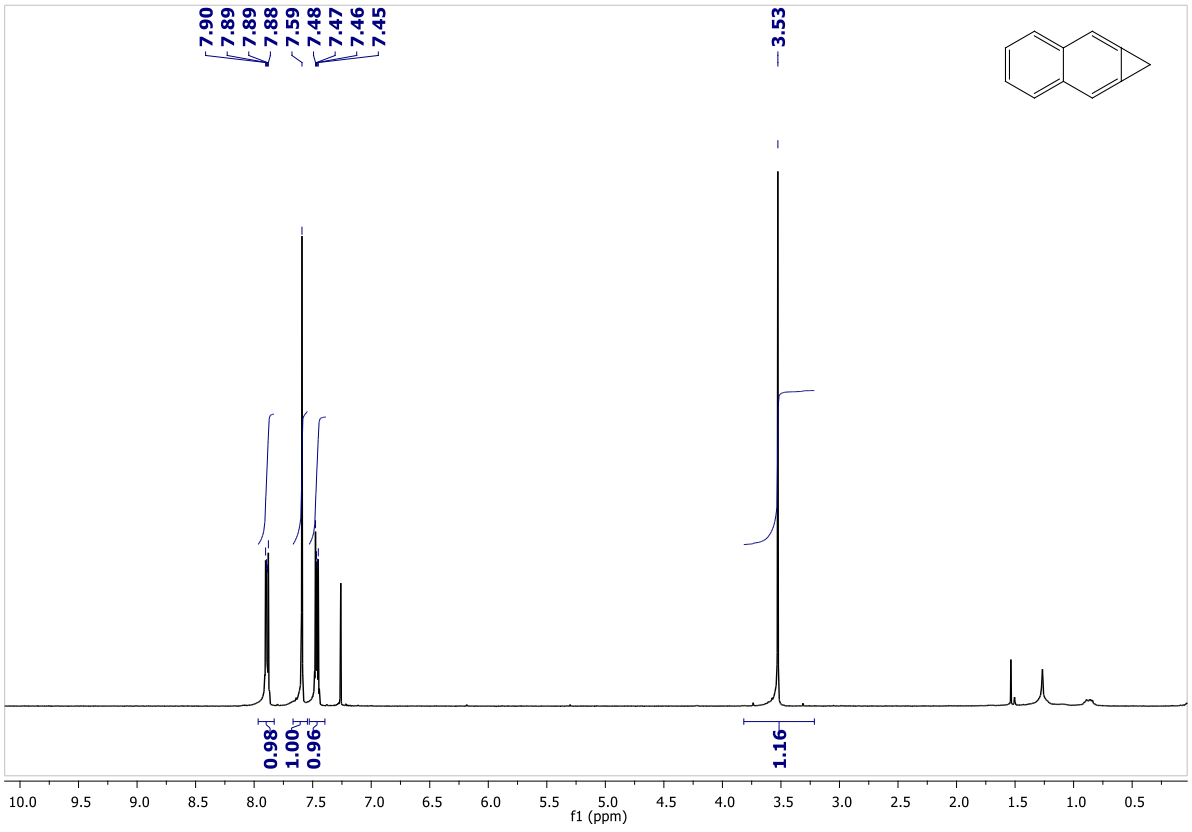

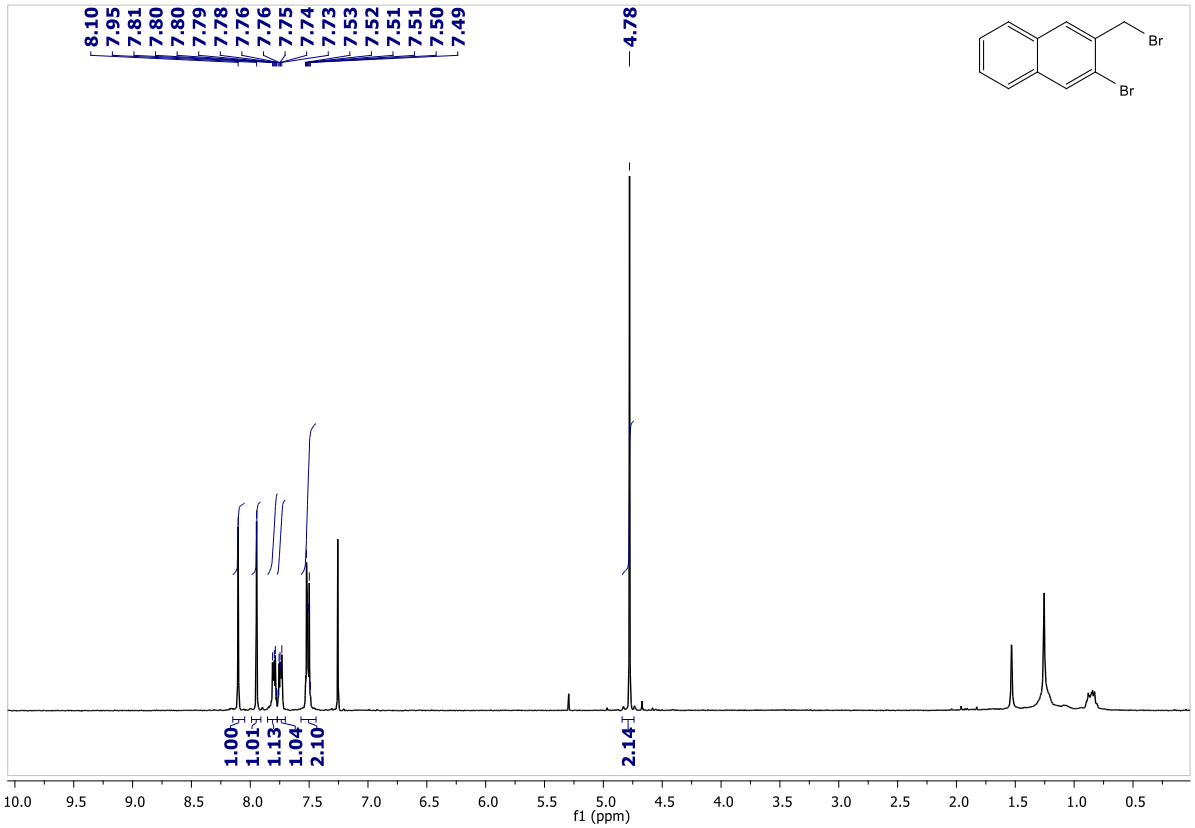

Figure 7 ^{1}H-NMR (400 MHz, $CDCl_3$) spectrum of **4**

However, presumable and selective activation and derivatization of naphthalene derivative **4** can be achieved under different conditions. This fact gives naphthalene derivative **4**, which contains the carbon-halogen bond (C-X), important tasks in synthetic organic chemistry. The naphthalene scaffold **4** has particularly significant potential for coupling and substitution reactions (Figure 4).

In the current study an easy, economical, four-step protocol for synthesis of the product **4** is announced (Figure 5). Firstly, 1,4-dihydronaphthalene (**8**) was obtained via Birch reduction with mild conditions starting from naphthalene which is selectively reduced from the 1,4 positions, according to a method previously reported in the literature [28]. In the next step, the reaction between 1,4-dihydronaphthalene (**8**) and dichlorocarbene which generated *in situ* from $CHCl_3$ and *t*-BuOK gave the previously reported the dichlorocyclopropane derivate **9** [29]. Then, treatment of the dichlorocyclopropane derivate **9** with *t*-BuOK gave the naphthocyclopropene **10** [29]. The naphthocyclopropene **10** became the starting material that allowed us to prepare 2-bromo-3-(bromomethyl)naphthalene (**4**) with ring-opening of the three-membered cyclopropane by bromination. The product **4** was obtained by treatment with Br_2 under refluxing dry CCl_4 for 1 h in excellent yield (97%) (Figure 5). Figure 6 shows the possible reaction mechanism for synthesis of the product **4**.

This synthetic approach allows simple preparation of the product **4** in higher yields compared to the two previously reported syntheses [12,16]. Consequently, the preparation of 2-bromo-3-(bromomethyl)naphthalene (**4**) by the method described herein is experimentally easy and effective. The simplicity, rapidity, and low cost of this procedure make it useful for the synthetic organic chemistry community. The chemical structures of synthesized compounds in this study were determined only by NMR analysis since there are previously reported compounds. (Figure 7). The spectroscopic data were consistent with those previously reported (see experimental section).

4. CONCLUSION

As a result of an economical and practical point of view, an efficient and easy-to-handle metal-free procedure was developed using inexpensive starting material such as naphthalene. The aimed product was synthesized in four steps with high yields. A synthetic sequence to the 2-bromo-3-(bromomethyl)naphthalene core has been developed, which could be approved for the synthesis of variously substituted naphthalene derivatives with this skeleton. The synthesis represents a new approach to the 2-bromo-3-(bromomethyl)naphthalene nucleus and particularly presented an approach for the easy preparation of differently substituted naphthalene derivatives.

Funding

The author has no received any financial support for the research, authorship or publication of this study.

Acknowledgements

The authors declare no conflict of interest. The author is greatly indebted to Prof. Dr. Arif DAŞTAN for providing use of all of his laboratory facilities throughout conducting the research.

The Declaration of Conflict of Interest/ Common Interest

No conflict of interest or common interest has been declared by the author.

Authors' Contribution

ME: This paper is a single-author study. Everything was done by the author.The Declaration of Ethics Committee Approval

The author declares that this document does not require an ethics committee approval or any special permission.

The Declaration of Research and Publication Ethics

The author of the paper declares that they comply with the scientific, ethical and quotation rules of SAUJS in all processes of the paper and that they do not make any falsification on the data collected. In addition, they declare that Sakarya University Journal of Science and its editorial board have no responsibility for any ethical violations that may be encountered, and that this study has not been evaluated in any academic publication environment other than Sakarya University Journal of Science.

REFERENCES

[1] E. T. Akin, M. Erdogan, A. Dastan, and N. Saracoglu, “Access to polysubstituted naphthalenes and anthracenes via a retro-Diels–Alder reaction,” Tetrahedron, vol. 73, no. 37, pp. 5537-5546, 2017.

[2] K. Ohta, T. Goto, and Y. Endo, “1, 2-Dicarba-c loso-dodecaboran-1-yl Naphthalene Derivatives,” Inorganic Chemistry, vol. 44, no. 23, pp. 8569-8573, 2005.

[3] W. Mahabusarakam, C. Hemtasin, S. Chakthong, S. P. Voravuthikunchai, and I. B. Olawumi, “Naphthoquinones, anthraquinones and naphthalene derivatives from the bulbs of Eleutherine americana,” Planta Medica, vol. 76, no. 04, pp. 345-349, 2010.

[4] G. L. Cantrell, and R. Filler, “Synthesis of 1, 2, 3, 4-tetrafluoro-and 1, 2, 3, 4, 5, 6, 7, 8-octafluoroanthracenes via cycloaddition-reversion,” Journal of Fluorine Chemistry, vol. 29, no. 4, pp. 417-424, 1985.

[5] A. L. Fernandez, M. Granda, J. Bermejo, and R. Menendez, “Catalytic polymerization of anthracene oil with aluminium trichloride,” Carbon, vol. 37, no. 8, pp. 1247-1255, 1999.

[6] N. Saino, T. Kawaji, T. Ito, Y. Matsushita, and S. Okamoto, “Synthesis of substituted

anthracenes, pentaphenes and trinaphthylenes via alkyne-cyclotrimerization reaction," Tetrahedron Letters, vol. 51, no. 9, pp. 1313-1316, 2010.

[7] P. T. Lynett, and K. E. Maly, "Synthesis of substituted trinaphthylenes via aryne cyclotrimerization," Organic Letters, vol. 11, no. 16, pp. 3726-3729, 2009.

[8] D. A. Petrone, J. Ye, and M. Lautens, "Modern transition-metal-catalyzed carbon–halogen bond formation," Chemical Reviews, vol. 116, no. 14, pp. 8003-8104, 2016.

[9] D. Hoshino, and K. Mori, "Rapid access to 3-indolyl-1-trifluoromethyl-isobenzofurans by hybrid use of Lewis/Brønsted acid catalysts," Organic & Biomolecular Chemistry, vol. 18, no. 34, pp. 6602-6606, 2020.

[10] H. Taneda, K. Inamoto, and Y. Kondo, "Palladium-Catalyzed Highly Chemoselective Intramolecular C–H Aminocarbonylation of Phenethylamines to Six-Membered Benzolactams," Organic Letters, vol. 18, no. 11, pp. 2712-2715, 2016.

[11] R. do Carmo Pinheiro, D. F. Back, and G. Zeni, "Iron (III) Chloride/Dialkyl Diselenides-Promoted Cascade Cyclization of ortho-Diynyl Benzyl Chalcogenides," Advanced Synthesis & Catalysis, vol. 361, no. 8, pp. 1866-1873, 2019.

[12] R. Dorel, P. R. McGonigal, and A. M. Echavarren, "Hydroacenes made easy by gold (I) catalysis," Angewandte Chemie, vol. 128, no. 37, pp. 11286-11289, 2016.

[13] B. Cui, J. Shan, C. Yuan, W. Han, N. Wan, and Y. Chen, "Synthesis of 2, 3′-spirobi [indolin]-2-ones enabled by a tandem nucleophilic benzylation/C (sp 2)–N cross-coupling reaction sequence," Organic & Biomolecular Chemistry, vol. 15, no. 28, pp. 5887-5892, 2017.

[14] R. A. Pascal Jr, A. Dudnikov, L. A. Love, X. Geng, K. J. Dougherty, J. T. Mague, and N. Byrne, "Chiral Polyaryl Cyclophanes," European Journal of Organic Chemistry, vol. 28, pp. 4194-4200, 2017.

[15] R. Kotani, L. Liu, P. Kumar, H. Kuramochi, T. Tahara, P. Liu, and S. Saito, "Controlling the S1 Energy Profile by Tuning Excited-State Aromaticity," Journal of the American Chemical Society, vol. 142, no. 35, pp. 14985-14992, 2020.

[16] J. G. Smith, P. W. Dibble, and R. E. Sandborn, "The preparation and reactions of naphtho [1, 2-c] furan and naphtho [2, 3-c] furan," Journal of Organic Chemistry, vol. 51, no. 20, pp. 3762-3768, 1986.

[17] L. P. Mangin, and D. Zargarian, "C–H Nickelation of Naphthyl Phosphinites: Electronic and Steric Limitations, Regioselectivity, and Tandem C–P Functionalization," Organometallics, vol. 38, no. 24, pp. 4687-4700, 2019.

[18] W. Zhang, and J. M. Ready, "The Ketene-Surrogate Coupling: Catalytic Conversion of Aryl Iodides into Aryl Ketenes through Ynol Ethers," Angewandte Chemie, vol. 126, no. 34, pp. 9126-9130, 2014.

[19] S. Kancherla, and K. B. Jørgensen, "Synthesis of Phenacene–Helicene Hybrids by Directed Remote Metalation," Journal of Organic Chemistry, vol. 85, no. 17, pp. 11140-11153, 2020.

[20] S. H. Han, A. K. Pandey, H. Lee, S. Kim, D. Kang, Y. H. Jung, and I. S. Kim, "One-pot synthesis of 2-naphthols from nitrones and MBH adducts via decarboxylative N–O bond cleavage," Organic Chemistry Frontiers, vol. 5, no. 22, pp. 3210-3218, 2018.

[21] E. Ghera, and Y. Ben-David, "Annulation reactions leading to naphthalene derivatives. New syntheses of natural 1, 2- and 1, 4-naphthoquinones," Journal of

Organic Chemistry, vol. 50, no. 18, pp. 3355-3359, 1985.

[22] M. G. Rong, T. Z. Qin, X. R. Liu, H. F. Wang, and W. Zi, "De Novo Synthesis of Phenols and Naphthols through Oxidative Cycloaromatization of Dienynes," Organic Letters, vol. 20, no. 19, pp. 6289-6293, 2018.

[23] L. P. Mangin, and D. Zargarian, "C–H Nickelation of Naphthyl Phosphinites: Electronic and Steric Limitations, Regioselectivity, and Tandem C–P Functionalization," Organometallics, vol. 38, no. 24, pp. 4687-4700, 2019.

[24] D. Davalian, P. J. Garratt, W. Koller, M. M. Mansuri, "Strained aromatic systems. Synthesis of cyclopropabenzocyclobutenes, cyclopropanaphthocylobutenes, and related compounds," Journal of Organic Chemistry, vol. 45, no. 21, pp. 4183-4193, 1980.

[25] R. Okazaki, M. Ooka, N. Tokitoh, and N. Inamoto, "Synthesis and reactions of 1, 6-dithiocyanato-and 1, 6-diiodo-1, 3, 5-cycloheptatrienes," Journal of Organic Chemistry, vol. 50 no. 2, pp. 180-185, 1985.

[26] W. E. Billups, and W. A. Rodin, "Regioselective ring opening in annelated benzocyclopropenes," Journal of Organic Chemistry, vol. 53, no. 6, pp. 1312-1314, 1988.

[27] B, Halton, C. S. Jones, A. J. Kay, D. Margetic, and S. Sretenovic, "Studies in the cycloproparene series: chemistry of 1H-cyclopropa [b] naphthalene-3, 6-dione and its transformation into 1 H-cyclopropa [b] anthracene-3, 8-dione 1," Journal of the Chemical Society, Perkin Transactions, vol. 1 no. 14, pp. 2205-2210, 2000.

[28] A. Menzek, A. Altundas, and D. Gueltekin, "A new, safe and convenient procedure for reduction of naphthalene and anthracene: synthesis of tetralin in a one-pot reaction," Journal of Chemical Research, vol. 2003, no. 11, pp. 752-753, 2003.

[29] D. P. Kelly, M. G. Banwell, N. K. Ireland, and A. L. Noel, "Proton-carbon-13 coupling constants in carbocations. 6. Generation and trapping of the (1a. alpha., 7a. alpha.)-1a, 2, 7, 7a-tetrahydro-1H-cyclopropa [b] naphthalen-2-yl cation," Journal of Organic Chemistry, vol. 56, no. 6, pp. 2040-2045, 1991.

[30] W. E. Billups, and W. Y. Chow, "Naphtho [b] cyclopropene," Journal of the American Chemical Society, vol. 95, no. 12, pp. 4099-4100, 1973.

[31] F. Niedermair, S. M. Borisov, G. Zenkl, O. T. Hofmann, H. Weber, R. Saf, and I. Klimant, "Tunable phosphorescent NIR oxygen indicators based on mixed benzo- and naphthoporphyrin complexes," Inorganic Chemistry, vol. 49, no. 20, pp. 9333-9342, 2010.

SAKARYA ÜNİVERSİTESİ
FEN BİLİMLERİ ENSTİTÜSÜ DERGİSİ

Sakarya University Journal of Science
SAUJS

e-ISSN 2147-835X | Period Bimonthly | Founded: 1997 | Publisher Sakarya University |
http://www.saujs.sakarya.edu.tr/en/

Title: Developing A Process Parameter Based Performance Monitoring and Evaluation System for Power Plant

Authors: Mehmet BULUT

Recieved: 2020-11-03 23:48:50

Accepted: 2021-04-20 14:59:19

Article Type: Research Article

Volume: 25
Issue: 3
Month: June
Year: 2021
Pages: 723-734

How to cite
Mehmet BULUT; (2021), Developing A Process Parameter Based Performance Monitoring and Evaluation System for Power Plant. Sakarya University Journal of Science, 25(3), 723-734, DOI: https://doi.org/10.16984/saufenbilder.820735
Access link
http://www.saujs.sakarya.edu.tr/en/pub/issue/62736/820735

Sakarya University Journal of Science 25(3), 723-734, 2021

Developing A Process Parameter Based Performance Monitoring and Evaluation System for Power Plant

Mehmet BULUT*[1]

Abstract

Today, there are many electricity production methods. Thermal power plants are still widely used for electricity production from hydrocarbon sources as one of the electricity generation options. Due to their complex structure, thermal power plants are composed of sections that interact with each other, and they are called units. A change in the performance of any unit or equipment affects the operation of the entire plant positively or negatively. Therefore, performance monitoring and evaluation systems are designed to support the measurement and monitoring of the performance of plant and equipment. In order to increase the availability of the plant, equipment-based maintenance plans should be prepared according to the maintenance needs of the equipment. In this study, a power plant performance monitoring and evaluation system has been developed and designed using process parameters approach for the parameters affecting the performance of plant. In order to monitor and evaluate the performance of thermal power plants, the requirements of the system were revealed and the efficiency and performance increases to be achieved by designing and using this system specific to a natural gas power plant were examined and results are given.

Keywords: Performance monitoring, Electricity, Power generation, Evaluation, Thermal power generation

1. INTRODUCTION

It is of utmost importance that electrical energy is obtained continuously and efficiently under the most optimum conditions. Power plants are facilities consisting of equipment combined to convert other forms of energy (thermal, nuclear, hydropower, geothermal, solar, wind, tidal, etc.) into electrical energy. Electricity generating hydraulic and thermal power plants consist of many large industrial equipment. Regardless of the type, most of power plants basically has a moving device, an alternator and a conversion station. The electrical energy obtained in thermal power plants based on hydrocarbon sources is more than half of all electrical energy produced in the world. Power plants based on thermal energy currently meet 65% of global electricity, and in some countries, electricity generation is provided by thermal power plants with higher electricity percentage. In 2018, 38% of the electricity produced in the world was obtained from coal, 23% from natural gas and 4% from oil [1].

*Corresponding author: mehmetbulut06@gmail.com
[1]Electricity Generation Co. Inc., Headquarter of General Management, Ankara, Turkey
ORCID: https://orcid.org/0000-0003-3998-1785

Monitoring performances of thermal power plants, which have a very important place in the production of electrical energy, evaluating the performance by monitoring the efficiency in the power plants, and determining the reasons that lead to inefficiency and how to increase the capacity is much important. There are many parameters which have an impact on the performance of each of plant elements that need to be found out. For maximum power uptake from the plant, the interaction between the plant equipment should be monitored and their negative impact on each other should be minimized. For example, a problem that may occur in the air filters of a natural gas-fired combined cycle power plant does not only affect the compressor, but also changes in the performance of all elements up to the cooling tower and leads to losses in power generation.

In power plants, instantaneous values are taken and transmitted to the control room by data collection systems like supervisory control and data acquisition (SCADA) and distributed control system (DCS) for control purposes. However, when we look at the combined cycle power plant, it is seen that there are much parameters that should be followed for even only a single unit. Automation systems are geared towards power plant operation and aim to facilitate the operation, especially to reduce the workload of the operator and to minimize the human factor. However, by measuring and monitoring the performance of the plant elements and equipment, it is possible to support the preparation of maintenance programs according to the maintenance needs of the equipment and thus to perform the maintenance on-site and on time and increase the availability [2,3]. For this purpose, performance monitoring and evaluation systems are designed. These systems continuously monitor and evaluate the data obtained during operation of the plant, calculate the required performance parameters for the units and equipment and compare them with their actual values[4,5].

There have been several previous studies to analyze the behavior of thermal power plant (TPP) using optimization techniques. Konrad Swirski proposed using statistical data analysis to improve the features of existing performance monitoring systems in their study [6]. Process performance monitoring and evaluation; It is a process that needs to be done to measure, maintain and improve the thermal efficiency, maintenance planning of the power plant [7]. In the study of Özdemir et al., the performance of the plant was examined in four main parameters as thermal efficiency, pipe efficiency, turbine efficiency and boiler efficiency in the light of the data received from the thermal power plant. In the five-year period of a system operating under high temperature and pressure, contamination, wear, fatigue, etc. that occur in the system elements. performance changes due to reasons have been identified [8]. For the variation of each of the operational parameters in a thermal power plant, performance calculations are made to configure the energy variation database. These can then be used as assessment criteria based on detecting deviations from a reference system updated during plant performance tests. Balaram et al, they aimed to identify the operational gaps associated with the operation of operational parameters in the power plant process [9].

It is of great importance to define the operational gaps associated with the operational parameters in the power plant process [10] and calculate key performance indicators for the management of power plants [11]. Blanco in their study, aims to identify and monitor the semi-stable conditions associated with measurements in the time series of the power plant process [12]. The models are then used for performance monitoring by comparing the calculated measured value with the reference value. The data-based migration plant system modeling method ensures that the model, which can provide a higher accuracy in performance monitoring, is constantly updated. By using the real-time operating data of the plant, the system monitoring study can be done by creating the mathematical models of the plant components [13]. The maintenance priorities [14] required for the power plant can be made by performing performance modeling [15] of a thermal power plant or by using the simulation and parametric optimization of thermal power [16]. Similarly, it can be evaluated as a decision

support system [17] about the plant as a tool for safer operation in the plant. In recent years, many studies have been done in the literature to improve both the operating conditions of thermal power plants and to reveal their performances. In this sense, the approach proposal for temperature distribution control in thermal power plant boilers [18], using of modern information technologies to increase energy efficiency of thermal power plant operation [19], quality assessment of fuel preparation production process in thermal power plants [20] and fault detection and diagnosis in power plants methods in Indian electricity generation sector [21] studies were conducted.

Most facility performance evaluation systems monitor the data obtained during the operation of the facility and evaluate the data obtained according to the design model during the first installation of the facilities. However, due to the aging of the equipment over the years, etc., the capacity decrease is considered normal. In this study, the performance of the facility, the current operating curves of the enterprise are extracted and a performance evaluation is made according to the parameter changes that occur accordingly. In other words, the model curves for the unit and equipment are extracted and compared with the real performance by calculating the new data according to the changing conditions, not the performance parameters that should be in the first installation.

In this study, it is aimed to continuously monitor the current performances and performance losses of units and equipment in order to determine operational problems of power plant operators and managers, to improve unit performance, to accomplish maintenance plans and to make economic decisions in all these studies by developing system-specific performance monitoring and evaluation system. In order for a performance monitoring and evaluation system to be successful and efficient, it should indicate the amount of change in unit and equipment performances and the share of equipment in total performance loss. In this way, power plant operators can estimate the amount, location and economic losses resulting from this loss. In addition to providing an economic enterprise with continuous monitoring of performance, it will also improve future operational conditions and increase safety via helping to predict future problems.

2. PERFORMANCE MONITORING SYSTEMS

One of the most important factors affecting efficiency in thermal power plants is the issue of maintenance and revisions. If a modern monitoring system is used in a plant, maintenance and revision costs and times will be reduced since the plant will be kept under nominal operating conditions and the equipment forming the system will be operated without difficulty, so the effects of improvements in control systems on efficiency can be clearly monitored. The heat cycle should be kept under constant control in the thermal power plants. The correct operation of all measurement and control systems and measuring instruments, their correct value, and the healthy operation of automation systems are vital for power plant efficiency as well as the safety of the power plant.

Steam and water losses in the cycle should be eliminated as soon as possible, the boiler and steam turbine should be operated at nominal loads, keeping the temperature, pressure, flow, level and other measurements and percentage rates as close as possible to the operating conditions in which the unit's efficiency tests are performed. There are many difficulties in determining the most appropriate one from the existing performance monitoring and evaluation systems of which with different aims and abilities, to the needs of the plants. The practices show that these generic software programs do not provide the expected benefits in general. Therefore, designing performance monitoring and evaluation systems according to the structure and needs of the plants will provide much more benefits than using a package program.

As mentioned earlier, coal, natural gas and oil are mostly used as fuel in thermal power plants. In many thermal power plants for electricity generation, there is no Plant performance monitoring system for monitoring and evaluating

the performance as a complete system, on the basis of the unit or on the equipment forming the units, but only some parameters (temperature, flow, pressure, etc.) is measured. These parameters, measured by the plant control system, can be used to determine the performance of a part of the plant and its elements, but they do not represent the current situation. In thermal based power generation plants that have only control system and do not have performance monitoring system, the change and decrease in the performance of the facilities and units in the power plant are evaluated by the power plant operators and plant operation personnel. Even if they are very experienced, it is very difficult for the operators to fully evaluate the performance results due to the excess of parameters in the power plant and its elements and the lack of reference performance values in different operational and environmental conditions. However, due to the changing power demands and falls of the turbine and other plants in the power plant, power plants should always operate under non-design or partial load conditions, which in time leads to a loss of performance of the equipment [22].

The fact that each plant has a separate design and technology makes it difficult to make human-based assessments healthy. Aside from the personnel knowledge and experience, an additional system that can evaluate the power plant performance is needed. Therefore, performance monitoring and evaluation systems that compare the actual value with the reference performance value and determine the economic size of it contribute to achieving healthier results for the power plants.

Thermal power plants should be operated at maximum efficiency and profitability due to their high production income and economic size. In this sense, great importance is given to performance monitoring systems and studies show that these systems increase energy efficiency. Depending on the development of automation and computer systems and the increasing importance of efficiency as much as production with energy crises in the world, it has come to the fore that the operation of the power plants is not sufficient and the performance should be monitored also. Therefore, plant equipment manufacturers have developed plant monitoring systems with or after the plant. Diagnosis procedures are often tested on data obtained through simulators [23,24].

A schematic diagram of a plant efficiency under different operating conditions can be shown as in the figure 1. The graph reveals the efficiency of the facility in terms of the combination of uncontrollable and controllable losses depending on time. The upper curve shows the achievable efficiency of a power plant in design values before aging or deterioration occurs. The lower curve shows its true efficiency due to the degradation and aging of materials in a power plant. The status of the plant at a specific point in the lower curve can be captured by performance testing or monitoring. To move from a point in the real efficiency curve to a point in the achievable efficiency curve with the same working condition, uncontrollable losses can be avoided by changing or maintaining the components [25,26].

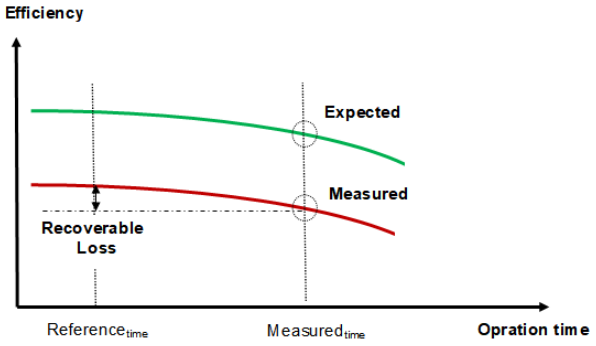

Figure 1 A schematic diagram of a plant efficiency under different operating conditions

2.1. Establishing a Data Management System

The Plant Information (PI) system was established to form the infrastructure of the evaluation and monitoring system in the a combined cycle power plant. PI is used to describe all the information (data) generated by a process consisting of electrical or mechanical equipment. In general, the PI system is used to collect, save and manage data in a process or business. The PI system is capable of gathering processes and enterprises from multiple points

(established in different geographical locations) in one place. In this way, all systems can be observed in one place and all data required for analysis can be collected. The operation of the system is simply as follows: Data received from a data source comes to the PI system via an interface, which can be reported by the user in any desired format [27].

The information generated by the PI system for an industrial enterprise can be low in availability and large in capacity. For this reason, there are several commercial programs called “PI Management Systems" which are developed to make this information usable and meaningful, and to convert it into data that can be saved and stored. The PI system is basically a computer-based system and is capable of communicating with the interfaces of open platform communication (OPC) with other industrial devices that collect sensor data and status messages from intelligent machines is shown in Figure 2.

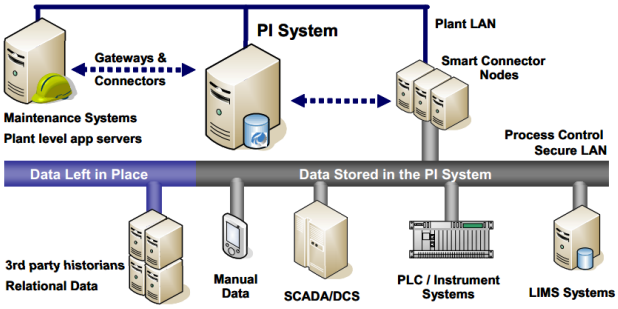

Figure 2 Typical PI system network connection and basic structure (OSIsoft)

2.2. Data Processing and Filtering

The PI system is capable of receiving all parameter data from the OPC machine at regular intervals. Raw state of these data may be too bulk for a healthy observation of the process. It is also possible that unnecessary data is saved and stored for years. In order to prevent this, some of the observed data in the PI system can be compressed with the name Exception and archived data with the name Compression. In this way, unnecessary data is not stored and system performance can be kept high, resources can be used more efficiently. In PI data processing stage; All data from the OPC server connected to the SCADA system is observed and recorded depending on a particular algorithm to be meaningful and give an idea. The collected parameters are stored in archive files, all data between each start and end time.

3. DETERMINATION OF POWER PLANT PERFORMANCE PARAMETERS

Dynamic behavior of power plants is predominantly; it depends on inlet and outlet distortions and changes in set points. This is especially the case in large coal-fired power plants. It is expected from the power plant to keep up with fast operating conditions in case of sudden and sudden load changes, switching in and out. In terms of control engineering, it is very difficult to control a switchboard representing a time-varying and non-linear multivariable process or a system with multiple inputs / outputs (MIMO, multi input multi output).

Increasing competition and fuel costs in the electricity generation sector have led power plant operators to focus on efficiency, availability and reliability. For this purpose, power plant managers should be able to assess the status of their power plants. As a result of these evaluations, it is necessary to understand how much of the targeted performance is realized in the plant operation. For this purpose, long-term monitoring of all the values obtained during the operation of a power plant, performance analysis and comparison with past performance values is very important in detecting the degradation of the unit or equipment. All these reasons reveal the need for performance monitoring and evaluation systems. There are many novel on-line monitoring performance methods of thermal power unit [28-30].

However, since performance losses due to operating and environmental conditions are not within the scope of degradation, the calculation should not take this into account. In order to make the necessary comparisons in order to evaluate the actual performance, the design and off-design performance values of the unit where the performance monitoring and evaluation system will be installed are needed. Design and off-design values are often used in acceptance tests of

the unit and are therefore given to managers by manufacturers. However, in cases where these curves cannot be obtained from manufacturers, design and off-design performance values that can be obtained through performance analysis with appropriate physical modeling software are used in performance monitoring and evaluation systems. In many of the SCADA or other monitoring systems used in today's power plants, especially in Turkey, performance analysis either cannot be accomplished or intended to. Therefore, it is difficult to interpret the changes in the performance of the units in a power plant where measurements are made only for control purposes.

In this study, it is aimed to design and implement a thermal power plant performance monitoring and evaluation system that will monitor and measure the parameters affecting the power plant's performance. With this system to be installed, the operator can be informed about the performance levels of the equipment.

Table 1 Parameters and performance indicators affecting the performance of the plant

Model Name	Parameter Affecting Performance	Performance Outputs
Gas Turbine	Outdoor Temperature Air pressure Relative humidity GT Filter Pressure Loss GT Drop Pressure Loss IGV Angle Fuel Lower Heating Value	Net Power Heat Rate GT Exhaust Flow GT Exhaust Temperature
HRSG	GT Exhaust Flow GT Exhaust Temperature	HP Steam Flow HP Steam Temperature LP Steam Flow LP Steam Temperature
Steam Turbine and Water Cycle	HP Steam Flow HP Steam Temperatu re LP Steam Flow LP Steam Temperature Coolant (Water) Temperature	Net Power Condenser Pressure
All Cycle	Outdoor Temperature Coolant(Water) Temperature	Net Power Heat Rate

GT : Gas turbine
IGV : Inlet guide vane
HRSG : Head Recovery Steam Generator
LP : Low pressure
HP : High pressure

In addition, by providing the operator with flexibility of movement to determine the parameters that cause performance failure and to identify and solve the problem, to contribute to the solution of the problem quickly, easily and as independently of the human factor as possible. Within the scope of the study, natural gas combined cycle power plant (CCPP) was selected as the application area of the project. When monitoring the performance of a unit, the performance degradation of both the unit and the equipment must be determined separately. Total degradation indicates the current state of the unit, while equipment degradation indicates where the total degradation stems from. Once the equipment-based degradations are identified, it is also possible to plan the work required for performance recovery [31]. Therefore, first of all, CCPP Power Plant was divided into 3 main sections and the parameters and performance indicators affecting the performance of these sections were determined in Table 1.

In general, there are two different methods used to evaluate the performance parameters determined by the performance monitoring system and to reveal the performance status of the plant. These methods are;

1- Curve-based method (Performance and correction curves method)
2- Model based method

The curve-based method used to determine the level of performance uses correction factors derived from correction curves prepared by the manufacturer for parameters affecting performance or made as a result of simulations and analyzes. The expected power calculation for the gas turbine made using correction factors is given in (1) as an example. Another method is the model based method. In this method, computer simulation including physical models of the equipment is operated with data measured from the plant and expected performance values are obtained.

$$N_{expected} = N_{measured} \prod_{i=0}^{n} DF_i \quad (1)$$

The curve based method was used in the application to be made at selected a CCPP Plant. For this reason, performance curves supplied by the producer at the plant were investigated and correction curves were obtained with the help of the curves found. However, as a result of the

evaluations, it was seen that the number of performance curves obtained from the units of selected CCPP Plant was insufficient to calculate many of the performance indicators.

For this reason, in order to obtain the required performance curves, the three main sections forming the power plant were simulated with the GateCycle ™ program and performance curves were obtained and the results obtained were reported in the relevant sections of the report. In addition, the simulation model of the whole cycle was created by combining these sections validated with the design values, and the effects of the parameters affecting the whole cycle were examined and the results were presented. With the GateCycle ™ program, the heat-equilibrium and mass-equilibrium equations of the equipment that can be found in the thermal power plant can be established. The configuration of a steam power plant on Gate Cycle is shown in Figure 3.

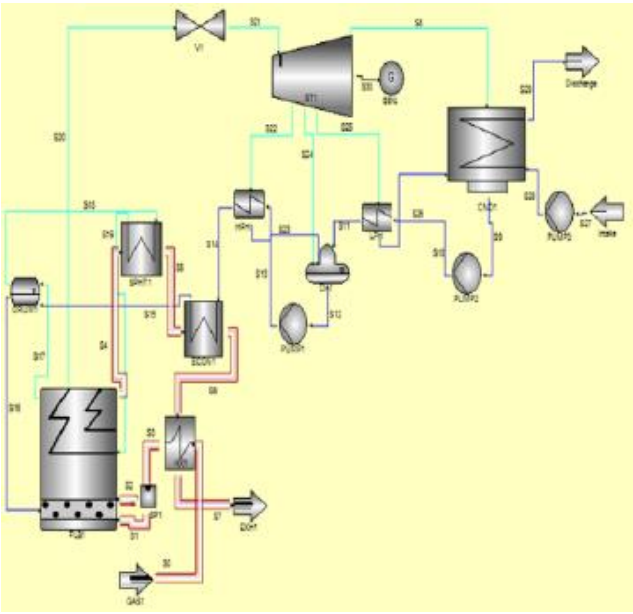

Figure 3 The configuration of a steam power plant on Gate Cycle [32]

Off design simulation models are used to examine the operation of the equipment that is dimensioned according to design values with the design mode under different operating conditions. Thus, with the parametric studies, the effects of various operating values on power plant performance can be seen. It is possible to obtain designs close to the actual design by entering the known design information into the program in the current system. In addition, the obtained design sizes can be verified by comparing them with the actual design information. In addition, the effect of equipment-based degradation on the power plant can be examined in the prepared models. In the studies, it is determined that some additional measurements are needed besides the measured data in the plant to calculate the performance indicators of selected CCPP.

4. COMBINED CYCLE POWER PLANT PERFORMANCE ANALYSIS

Performance parameters on the basis of unit and equipment, degradation, degradation costs and trends in a given time period will be followed and an important historical database will be created for the plant in the future. Necessary measurements and performance parameters of the power plant have been determined on the basis of equipment and total power in order to perform performance calculations. The PI system, which forms the infrastructure of the evaluation and monitoring system, was established at the power plant where the project will be implemented.

Thirdly, the necessary measurements and performance parameters of the plant for performance calculation are determined on the basis of equipment and total plant. In order to calculate the determined performance parameters, the necessary additional measurements (pressure, temperature, flow rate, etc.) and measurement locations were determined by the project and power plant team. Fourthly, the actual working situation is simulated in computer environment and the design working conditions are verified and correction curves are obtained for the equipment (pump, gas turbine, waste heat boiler, etc.).

While the plant was simulated, it was examined as 3 main sections, and finally the entire cycle was simulated by combining these 3 main sections and parametric analyzes were completed. After this process, parametric analyzes were performed on verified simulation models, and performance correction curves were obtained on the basis of equipment. The three main sections that make up

the CCPP cycle are: gas turbine, waste heat boiler and steam turbine and water cycle. Parametric analyzes for the gas turbine group are listed below:

- Change in GT net power according to outdoor temperature
- Change in GT net power according to outdoor air pressure
- Change in GT net power relative to relative humidity
- Change of GT net power according to GT inlet filter pressure loss
- Change in GT net power according to GT output pressure loss
- Change in GT net power according to natural gas lower heat value
- Change in GT net power relative to change in Inlet Guide Vane (IGV) angle

The parameters affecting the gas turbine performance are the parameters affecting the compressor inlet air and the values (pressure, temperature and flow) affecting these weather conditions and fuel properties (LHV- lower heating value). According to the changes in these parameters, the efficiency of the gas turbine (power, outlet temperature and pressure) varies. The parametric analyzes were performed to verify the off-design simulation model and the results are as example in Figure 3.

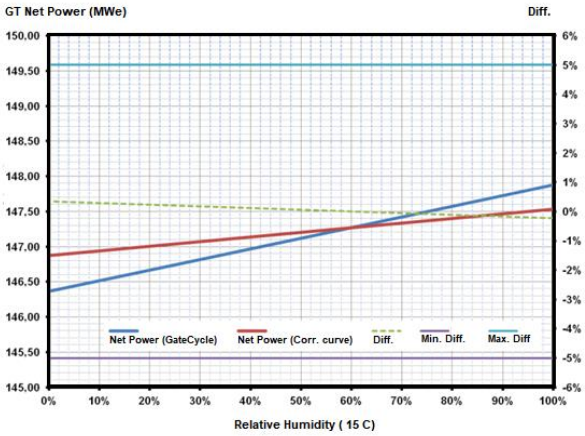

(a) change in relative humidity (15 ° C)

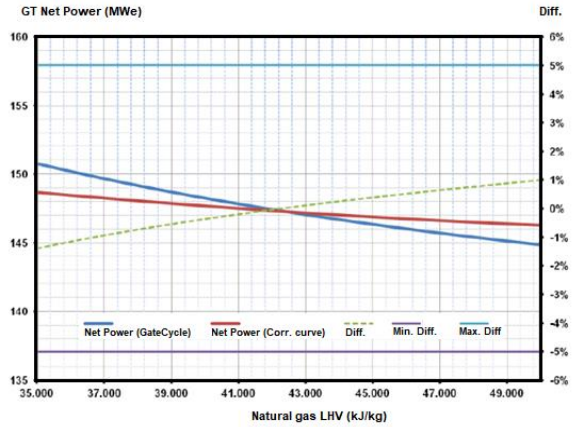

(b) change in natural gas lower heat value (LHV)

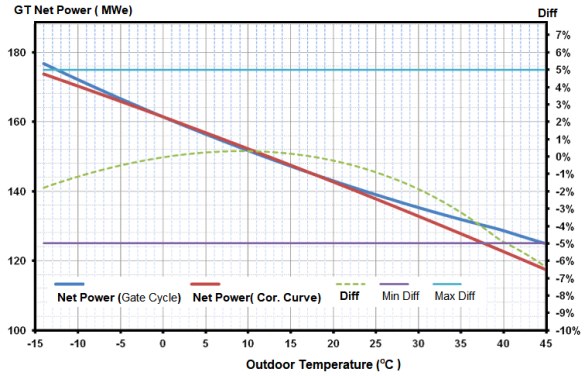

(c) change outdoor temperature

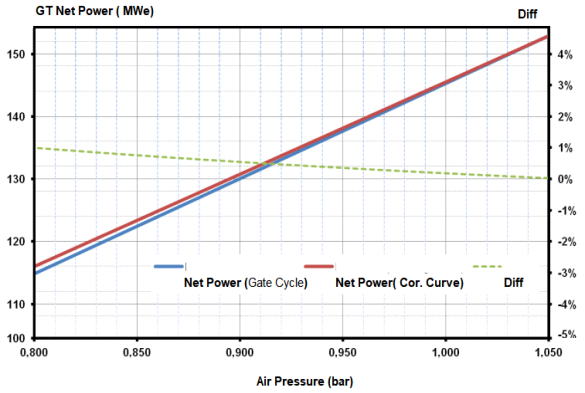

(d) change in air pressure

Figure 3 Change in GT net power relative to a) change in relative humidity (15 ° C), b) change in natural gas lower heat value (LHV) c) change outdoor temperature and d) change in air pressure

By using the correction factors obtained from the correction curves obtained from the measurements based on the parameters determined in the power plant, the status of the total unit and equipment (pump, gas turbine, waste heat boiler, steam turbine etc.) can be monitored. For selected Natural Gas Combined

Cycle Power Plant, a special software has been developed that includes performance parameters of the unit and equipment, degradations, the share of equipment in total degradation, hourly cost of equipment degradation and impact and solution analysis.

When graphs in Figure 3 are examined, the highest difference between the power calculated according to the reference correction curves and the simulation model was calculated as -6% in the outdoor temperature change curve. This difference occurs in sections where the outdoor temperature is 45 ° C. The difference between -15 ° C and 30 ° C is the highest -2%, which is within the acceptable limits for simulation studies. Considering the weather conditions in Istanbul, it is a very rare event that the air temperature reaches 45 ° C. Therefore, the simulations made were verified by comparison with the design and non-design values taken from the plant.

5. CONCLUSION

In order to increase the performance of thermal power plants, this system has been designed to design and implement a power plant performance monitoring and evaluation system that will measure all the parameters affecting the performance by measuring them on a unit basis and compare them with the required reference performances. Outputs targeted from the performance monitoring and evaluation system; It is aimed to monitor the performance of the plant with easy-to-understand graphics depending on time, to provide the operator with the opportunity to monitor performance on the basis of units and equipment, to compare the performances of the equipment with the current performance values, to diagnose the problem before the problem occurs, and to provide solutions to the root of the problem and to provide solutions. All modules (performance indicators, distortions, decay costs, trends, etc.) in the software were followed for a certain period of time and the detected errors were corrected. With this software, performance parameters, distortions, decay costs and trends in a certain period of time can be tracked on a unit and equipment basis, and an important historical database for the plant can be created in the future. In addition, these data will assist the switchboard team both in operating the switchboard well and in predictive maintenance of the switchboard. Thus, the condition of the units and equipment in the power plant can be evaluated more efficiently and possible performance losses can be minimized.

Acknowledgements
I would like to thank TUBITAK for its invaluable support.

Funding
Research supported by TUBITAK within the scope of the project titled “Thermal power plant performance monitoring and evaluation system design and implementation” with 110G092 project number.

The Declaration of Conflict of Interest/ Common Interest
No conflict of interest or common interest has been declared by the authors.

Authors' Contribution

M.B. 1- Organized the data collection/processing, analysis and interpretation. 2- Supported conceptual approach and design of the study. 3- Made conceptual arrangements during preparation. 4-prepared content of the article draft. 5- Wrote the manuscript.

The Declaration of Ethics Committee Approval
The authors declare that this document does not require an ethics committee approval or any special permission.

The Declaration of Research and Publication Ethics

The authors of the paper declare that they comply with the scientific, ethical and quotation rules of SAUJS in all processes of the paper and that they do not make any falsification on the data collected. In addition, they declare that Sakarya University Journal of Science and its editorial board have no responsibility for any ethical violations that may be encountered, and that this study has not been evaluated in any academic

publication environment other than Sakarya University Journal of Science.

REFERENCES

[1] World Bank Group, "Electricity production from oil, gas and coal sources", 2020. https://data.worldbank.org/indicator/ Accesed 25 Sep 2020.

[2] K. Kawai, Y. Takizawa, S. Watanabe, "Advanced automation for power-generation plants - past, present and future," Control Engineering Practice 7, 1405-1411, 1999.

[3] S. Cafaro, L. Napoli, A. Traverso, A.F. Massardo, "Monitoring of the thermoeconomic performance in an actual combined cycle power plant bottoming cycle," Energy, 35, 902–910, 2010.

[4] J. Cai, X. Ma, Q. Li, "On-line monitoring the performance of coal-fired power unit: A method based on support vector machine," Applied Thermal Engineering, 29, 2308–2319, 2009.

[5] A. Valero, MA Lozano, JL Bartolome, "On-line monitoring of power-plant performance, using exergetic cost techniques," Appl Therm Eng, 16:933–48, 1996.

[6] K. Swirski_, Power Plant Performance Monitoring Using Statistical Methodology Approach, Journal of Power Technologies, 91(2) pp. 63–76, 2011.

[7] L. Li, "Process Performance Monitoring and Degradation Analysis, In Thermal Power Plants," Ed. Mohammad Rasul, IntechOpen, 2012. Doi: 10.5772/27335

[8] M.B. Özdemir, T. Menlik, H.İ Variyenli, and L. Sevi, "Performance analysis and rehabilitation methods of a thermal power plant", J. of Polytechnic , 20 (4): 971-978, 2017.

[9] B. Saha, V. Patel and K. Chaterjee, "Assessment of process parameter to improving power plant performance," 2014 Innovative Applications of Computational Intelligence on Power, Energy and Controls with their impact on Humanity (CIPECH), Ghaziabad, pp. 441-446, 2014. doi: 10.1109/CIPECH.2014.7019125.

[10] T. Sudhakar, B. Anjaneya Prasad, K. Prahlada Rao, "Analysis of Process Parameters to Improve Power Plant Efficiency," Journal of Mechanical and Civil Engineering (IOSR-JMCE), Volume 14, Issue 1 Ver. II, pp. 57-64, 2017.

[11] S. Vasilica Oprea and A. Bâra, "Key Technical Performance Indicators for Power Plants," In Recent Improvements of Power Plants Management and Technology, Ed. Aleksandar B. Nikolic and Zarko S. Janda, IntechOpen, 2017. DOI: 10.5772/67858.

[12] J. M. Blanco, L. Vazquez, F. Peña, "Investigation on a new methodology for thermal power plant assessment through live diagnosis monitoring of selected process parameters; application to a case study," Energy, Elsevier, vol. 42(1), pp. 170-180, 2012.

[13] Z. Guo, S. Gu, P. Liu, Z. Li, "Operation dota based modelling and performance monitoring of steam turbine regenerative system under full working conditions," Chemical Engineering Transactions, 61, 127-132, 2017. DOI:10.3303/CET1761019

[14] S. Malik, P.C. Tewari, "Performance modeling and maintenance priorities decision for the water flow system of a coal-based thermal power plant", Int. J. Quality Reliab. Management, 35(4), pp. 996-1010, 2018.

[15] R. Kumar, A.K. Sharma , P.C. Tewari, "Performance modeling of furnace draft air cycle in a thermal power plant", Int. J. Eng. Sci. Technol., 3 (8), pp. 6792-6798, 2011.

[16] P.R. Kumar, V.R. Raju, N.R. Kumar, "Simulation and parametric optimization of thermal power plant cycles", Perspect. Sci., 8, pp. 304-306, 2016.

[17] R. Kumar, "Performance evaluation and decision support system of the water circulation system of a steam thermal power plant", Elixir Mech. Eng., 44, pp. 7551-7557, 2012.

[18] A. Marjanović, Sanja Vujnović, Željko Đurović, "One approach to temperature distribution control in thermal power plant boilers," Automatika, 61:2, 273-283, 2020.

[19] E.K. Arakelyan, A.V. Andryushin, V.R. Sabanin, S.V. Mezin, F.F.Pashchenko "Use of Modern Information Technologies to Improve Energy Efficiency of Thermal Power Plant Operation", 2017 J. Phys.: Conf. Ser. 891-012286, 2017.

[20] R. Patel Himanshukumar, Vipul A. Shah, "Fault Detection And Diagnosis Methods In Power Generation Plants - The Indian Power Generation Sector Perspective: An Introductory Review," PDPU Journal of Energy & Management, pp. 31-49, 2018.

[21] Ya A Tynchenko and I V Kovalev, "Quality assessment of the fuel preparation production process at thermal power plants", J. Phys.: Conf. Ser. 1515-052067, 2020.

[22] S. M. Kim, Y. Jin Joo, Implementation of on-line performance monitoring system at Seoincheon and Sinincheon combined cycle power plant, Energy, 30, 2383–2401, 2005.

[23] V. Verda, R. Borchiellini, "Exergy method for the diagnosis of energy systems using measured data", Energy, Vol.32, pp.490-498., 2007.

[24] A. S. Karakurt, Ü. Güneş, Performance Analysis Of A Steam Turbine Power Plant At Part Load Conditions , Journal of Thermal Engineering, Vol. 3, No. 2, pp. 1121-1128, 2017.

[25] H. Kim, M. Gyun Na, G. Heo, "Application Of Monitoring, Diagnosis, And Prognosis", In Thermal Performance Analysis For Nuclear Power Plants, Nuclear Engineering And Technology, Vol. 46, Issue 6, pp. 737-752, 2014.

[26] M. Bulut, "Designing Performance Monitoring And Evaluation System Of A Thermal Power Plant Using Process Parameters", In Engineering And Architecture Sciences Theory, Current Researches And New Trends, Cetinje, Montenegro: Ivpe Int. Publishing, pp. 160-185, 2020. Doi.10.5281/Zenodo.4101427

[27] H. Hong, W.G. Yang, L. Zhong-Da, "PI database system and its application in power plant SIS", Electric Power Automation Equipment, 11, 2004.

[28] J. Cai, X. Ma, Q. Li, "Online monitoring the performance of coal-fired power unit: A method based on support vector machine", Applied Thermal Engineering, Vol.29, pp.2308-2319, 2009.

[29] L. Pan, D. Flynn, M. Cregan, "Statistical model for power plant performance monitoring and analysis", Universities Power Engineering Conference, UPEC 2007. Vol.4, Issue 6, pp.121-126, 2007.

[30] H.A. Silva Mattos, C. Bringhent, D. F. Cavalca, O.F. Reis Silva, G.B. Campos, J. T. Tomita, "Combined Cycle Performance Evaluation and Dynamic Response Simulation", Journal of Aerospace Techn. and Management. vol.8 no.4, 2016.

[31] Project Report, "Thermal power plant performance monitoring and evaluation system design and implementation", TUBITAK Project No. 110G092, 2013.

[32] F. Vidian, Tomi, "Simulation of 25 MWe Steam Power Plants Using Gate Cycle, Int.

Journal of Engineering and Advanced Technology (IJEAT), Vol. 8 Issue 6, 2019.

SAKARYA ÜNİVERSİTESİ
FEN BİLİMLERİ ENSTİTÜSÜ DERGİSİ

Sakarya University Journal of Science
SAUJS

e-ISSN 2147-835X | Period Bimonthly | Founded: 1997 | Publisher Sakarya University |
http://www.saujs.sakarya.edu.tr/en/

Title: Microstructures and Phase Transformations of Melt-Spun Ti-V-Al high Temperature Shape Memory Alloys with Addition of Zr

Authors: Öznur BAĞ, Fikret YILMAZ, Uğur KÖLEMEN, Semra ERGEN

Recieved: 2020-09-21 16:21:45

Accepted: 2021-04-23 11:17:32

Article Type: Research Article

Volume: 25
Issue: 3
Month: June
Year: 2021
Pages: 735-740

How to cite
Öznur BAĞ, Fikret YILMAZ, Uğur KÖLEMEN, Semra ERGEN; (2021), Microstructures and Phase Transformations of Melt-Spun Ti-V-Al high Temperature Shape Memory Alloys with Addition of Zr. Sakarya University Journal of Science, 25(3), 735-740, DOI: https://doi.org/10.16984/saufenbilder.797337
Access link
http://www.saujs.sakarya.edu.tr/en/pub/issue/62736/797337

Sakarya University Journal of Science 25(3), 735-740, 2021

Microstructures and Phase Transformations of Melt-Spun Ti-V-Al high Temperature Shape Memory Alloys with Addition of Zr

Öznur BAĞ*[1], Fikret YILMAZ[1], Uğur KÖLEMEN[2], Semra ERGEN[1]

Abstract

In this study, the effects of Zr addition on phase transformation temperatures, microstructure of Ti-12V-4Al (wt. %) high temperature shape memory alloys (HTSMAs) manufactured using melt-spinning technique were investigated. During heating, differential scanning calorimetry (DSC) curves showed that austenite transformation temperature of Ti-12V-4Al (wt. %) melt-spun ribbon was single-stage transformation and Ti-12V-4Al-0.5Zr (wt. %) melt-spun ribbon was two-stage transformation. In the scanning electron microscopy (SEM) and X-ray diffraction (XRD) analyzes, unveiled that the melt-spun ribbons consisted of martensite, austenite and R phases. Transmission electron microscopy (TEM) analysis showed that the thickness of martensite plates in ribbons was thinned by the addition of Zr.

Keywords: High temperature, shape memory alloys, phase transition

1. INTRODUCTION

Shape memory alloys (SMAs) can recover their deformed shape are smart materials. The driving forces of this reversible deformation are; there may be load, temperature and magnetic effect. The reason for this feature, which is not seen in traditional metals and alloys, is the solid-solid phase transformations, which are defined as thermo-elastic martensitic phase transformation [1]. Thanks to these reversible phase transformations, shape memory alloys can regain their original state after being deformed. Furthermore, shape memory alloys show superelastic properties and are highly they can remain elastic under stresses. Shape memory alloys are materials that can be used in many fields such as vibration damping, noise reduction, sensors, building, biomedical due to their shape memory and superelasticity properties. NiTi alloys come into prominence due to their good functional and mechanical properties such as ductility, fatigue strength and deformation rate. However, as the transformation temperatures of NiTi alloys are below 100 ^{o}C, high temperatures such as aerospace, automobile and oil industry its use is limited in areas that require [2]. Therefore, researchers are working to develop materials with transformation temperatures above 100 ^{o}C.

As a result of the researches, many high temperature shape memory alloys have been

*Corresponding author: oznurbag@gmail.com
[1]Gaziosmanpaşa University, Faculty of Arts and Science, Department of Physics, 60240,Tokat.
E-mail: oznurbag@gmail.com; fikretyilmaz79@gmail.com; semraergengop@gmail.com
ORCID: https://orcid.org/0000-0002-9944-8221; https://orcid.org/0000-0002-1835-4961; https://orcid.org/0000-0002-5515-0933
[2]Yozgat Bozok University, Faculty of Arts and Science, Department of Physics, 66100, Yozgat.
E-mail: ugur.kolemen@bozok.edu.tr
ORCID: https://orcid.org/0000-0001-9858-8823

found by adding the third element to the binary alloys.

Ti-based alloys are one of the best examples for high temperature shape memory alloys (HTSMAs). Ti-V-Al alloys, which are Ti-based alloys, have low density and have high heat resistance, strength, flexibility, toughness, processability, weldability, corrosion resistance and biocompatibility. Therefore, it is advantageous for use in many high temperature applications, especially in aviation applications. Among the alloying elements added to titanium, the most well-known elements such as Al, Sn, Ga and Zr perform well at high temperatures.

The Zr element, which is generally considered to be a neutral element and compatible with the Ti group, is often added to improve mechanical and shape memory properties [3, 4, 5, 6].

Melt-spinning is the most adopted technique among rapid solidification techniques owing to its high cooling rate (10^5–10^7 °C/s) and simple application. This technique is typically used to create thin metal or alloy ribbons of a certain atomic structure. The melt spinning technique produces a fine-grained microstructure, increasing the solubility of alloying elements and reducing levels of dissociation [7, 8]. These effects can lead to advancements in shape memory alloy systems in terms of shape memory capabilities and superelasticity [9].

In this study, Zr was added to Ti-12V-4Al (wt. %) alloy for the first time and Ti-12V-4Al-0.5Zr (wt. %) ribbon alloy was produced by melt spinning technique. The aim of this work is to investigate the effect of Zr addition on the microstructural evolution and phase transformation temperature of Ti-12V-4Al (wt. %) high temperature shape memory alloy. The microstructure, phase formation, chemical composition and transformation temperatures were examined by using differential scanning calorimetry (DSC), X-ray diffraction (XRD), optic microscope (OM), scanning electron microscopy (SEM) and transmission electron microscopy (TEM).

2. MATERIAL AND METHODS

Firstly, elemental Ti (99.9 % purity), V (99.999 % purity), Al (99.9 %) and Zr (99.9 %) were used to prepare the alloy of nominal composition Ti-12V-4Al and Ti-12V-4Al-0.5Zr. In this study, all percentages are wt. % unless otherwise stated. The alloys were first melted under an argon atmosphere by an arc-melter system. In order to ensure homogenization, the alloys were repeatedly melted three times and then annealed at a temperature of 950 °C for 6 h in vacuum-sealed quartz crucibles. And then was quenched in ice water by breaking the crucible. Afterward, the master alloys were cut into small pieces for rapid solidification by melt-spinning. Then rapidly solidified counter part of the master alloys were prepared using an Edmund Buhler SC melt-spinner. For the melt-spinning process, Ti-12V-4Al (wt. %) and Ti-12V-4Al-0.5Zr (wt. %) master alloys with a weight of about 3 g were prepared and the alloys were placed in the quartz crucible. Then, the quartz crucible, including the master alloys, was mounted in the chamber surrounded by spiral springs inside the glass-covered chamber. The distance between the wheel and the nozzle was adjusted to be 0.2 mm and the lid of the chamber was closed. Before pouring the melt on the disc, after the chamber containing the disc and crucible was vacuumed up to about $4x10^{-2}$ bar, the chamber was filled with argon gas and the disc velocity was set to 25 m/s. The master alloys were then melted and sprayed onto the copper disc with a pressure of about 300 mbar and ribbon alloys were obtained. As-received melt-spun ribbons were 6–10 mm in width and 40–60 μm in thickness.

The crystallization behaviors and the corresponding dynamics of the as-received Ti-12V-4Al (wt. %) and Ti-12V-4Al-0.5Zr (wt. %) melt-spun ribbons were examined by differential scanning calorimetry (Seteram, DSC 131) with the different heating and cooling rate in the temperature range of 50-530 ^{o}C. The crystallization state and phase constituents were identified by the X-ray diffraction (Pixcel3D) using CuKα radiation. Microstructures of ribbon samples were observed on optical microscope (Simadzu DUH-W201S). Samples for OM

observation were prepared by etching with a mixed solution of 10 ml HF, 20 ml HNO_3 and 40 ml H_2O after mechanical grinding and polishing. The surfaces of the melt-spun ribbons were observed by means of a scanning electron microscope (Quanta 200 FEG). The microstructural characterizations were carried out by transmission electron microscopy (JEM100SX) operating at an accelerating voltage of 200 kV. The samples for TEM observation were prepared by twin-jet electro-polishing in an electrolyte of 6 % perchloric acid, 60 % methyl alcohol and 34 % n-butyl alcohol by volume at about −30°C.

3. RESULTS AND DISCUSSION

Figure 1 shows DSC curves of the Ti-12V-4Al (wt. %) and Ti-12V-4Al-0,5Zr (wt. %) melt-spun ribbons at the temperature range 50–530 °C. DSC curves of the at heating / cooling rates of 30 °C / min are displayed in Figure 1.

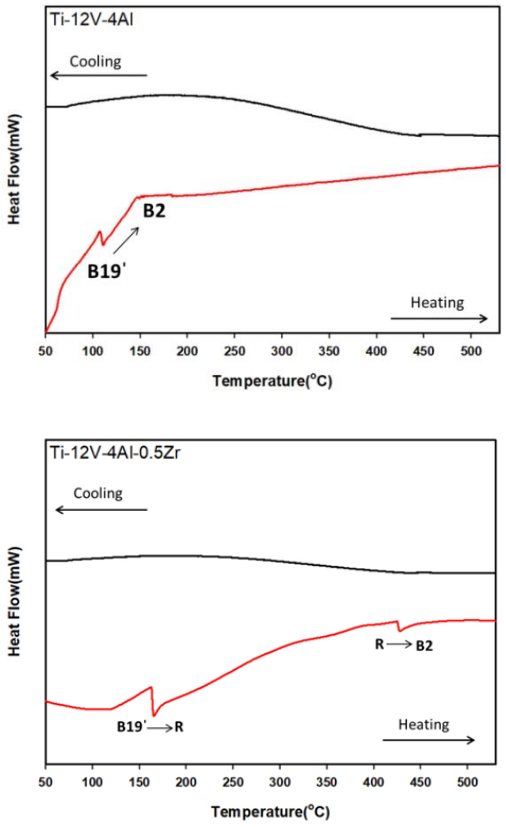

Figure 1 The DSC curves of Ti-12V-4Al (wt. %) and Ti-12V-4Al-0.5Z (wt. %) melt-spun ribbons

In Figure 1, Ti-12V-4Al (wt. %) ribbon shows single-stage transformation. The martensite phase of the Ti-12V-4Al (wt. %) ribbon directly converts to austenite during heating (B19' martensite → B2 austenite). The endothermic peak is clearly visible at about 127 °C upon heating, which ends at 158 °C for Ti-12V-4Al (wt. %) ribbon. The DSC curve of Ti-12V-4Al-0.5Zr (wt. %) ribbon exhibits two endothermic peaks in heating, indicative of two-stage transformation (B19' martensite → R-phase → B2 austenite). Some Zr added alloys (such as Ti-Ni-Zr) [10] also show typical reversible phase transformation behavior of HTSMAs on heating or cooling, where the martensite phase transformation from B19' martensite to B2 austenite occurs in a two-stage process. The first stage is attributed to the B19' martensite → R-phase and the second stage is for the R-phase → B2 austenite transformation [11]. Furthermore, the high cooling rate leads to high solid solubility and grain orientation preference in the suction-cast alloy during rapid solidification. It is believed that the Zr addition on quaternary HTSMAs results in the change of structural features and lattice distortion during martensitic transformation, which has an important role to play in terms of controlling the transformation temperature and phase transition behavior during the temperature change [12]. Its origin cannot be identified by DSC alone. To explain the phenomena mentioned above, in situ XRD was applied to Ti-12V-4Al (wt. %) and Ti-12V-4Al-0.5Zr (wt. %) ribbons at room temperature, and the results are shown in Figure 2.

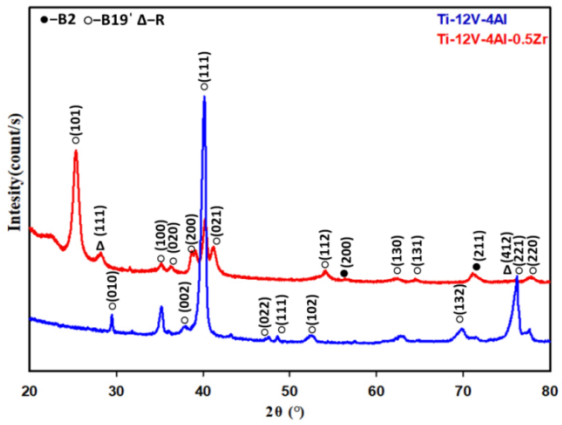

Figure 2 The XRD pattern of Ti–12V-4Al (wt. %) and Ti-12V-4Al-0.5Zr (wt. %) melt-spun ribbons

The Ti-12V-4Al (wt. %) and Ti-12V-4Al-0.5Zr (wt. %) ribbons are mainly at martensite state with B19' structure. The Ti-12V-4Al (wt. %) ribbon has a martensite phase indexed by (111) with a very strong peak at 39.89 degree and the Ti-12V-4Al-0.5Zr (wt. %) sample has a martensite phase indexed by (101) at 26.18 degree. In Ti-12V-4Al-0.5Zr (wt. %) ribbon, it can be seen that the intensity of B2 austenite peaks at diffraction angle of 56.12 and 73.56 degreeses become. As seen in the graphic, R phases appeared at 27.84 and 46.34 degrees in the Ti-12V-4Al-0.5Zr (wt. %) ribbon. This is compatible with the phase transformations occurring in the DSC analysis and helps explain.

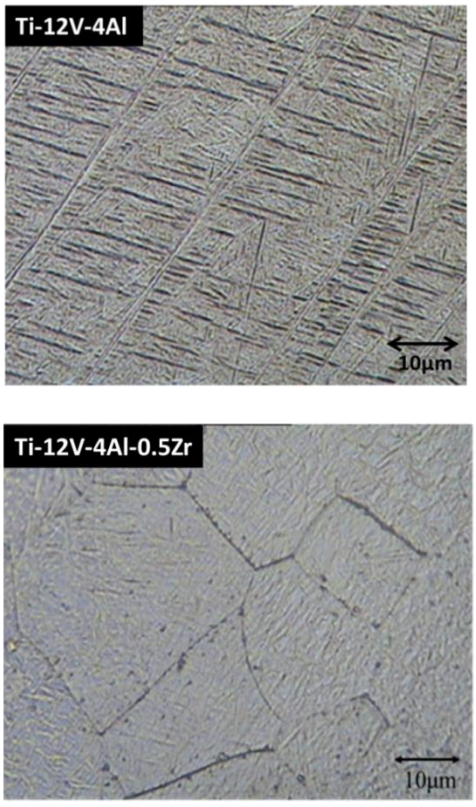

Figure 3 Optical images of Ti-12V-4Al (wt. %) and Ti-12V-4Al-0.5Zr (wt. %) melt-spun ribbons

Figure 3 shows the typical optical morphologies of the Ti-12V-4Al and Ti-12V-4Al-0.5Zr ribbons. Although Ti-12V-4Al ribbon is more pronounced in both samples, typical lath-shaped or thin acicular martensite phases are seen. The orientations of these martensite phases formed in the Ti-12V-4Al-0.5Zr ribbon differ in each grain. Compared to the Ti-12V-4Al ribbon produced, these phases are stacked finer, softer and more dispersed in the Ti-12V-4Al-0.5Zr ribbon. In addition, it is seen that the grain boundaries of Ti-12V-4Al-0.5Zr ribbon emerge more clearly.

Figure 4 shows the SEM images taken at 10000 magnification of the ribbons. It is seen that the microstructures of the ribbons consist dominant martensite phases. A small amount of austenite phases are seen in the Ti-12V-4Al-0.5Zr (wt. %) ribbon. It is estimated that Zr element accumulates in grain boundaries in Ti-12V-4Al-0.5Zr (wt. %) ribbon. The XRD result of Ti-12V-4Al (wt. %) ribbon reveals only B19' martensite phase and no additional peak corresponding to was observed. In addition, in Ti-12V-4Al-0.5Zr (wt. %) ribbon, B2 phase is clearly seen and these results are considered to be compatible with XRD analysis.

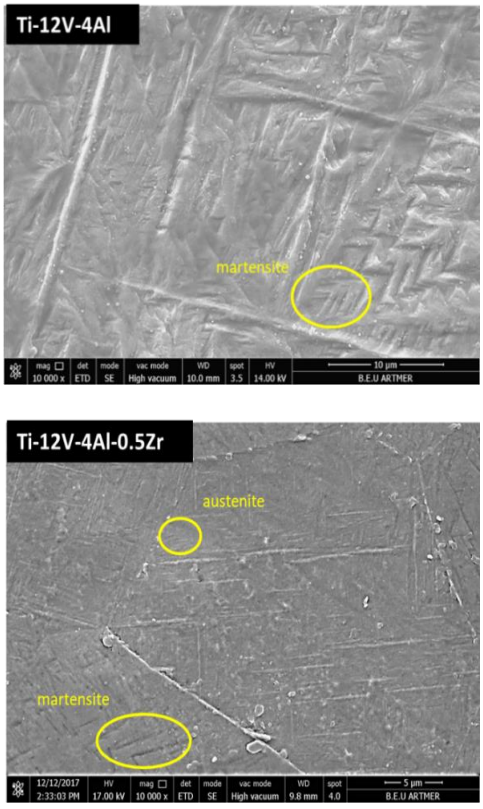

Figure 4 SEM images of the Ti-12V-4Al (wt. %) and Ti-12V-4Al-0.5Zr (wt. %) melt-spun ribbons

TEM images of melt-spun ribbons are depicted in Figure 5. The microstructure is featured with the parallel martensite plates with the width of 100-300 nm in Figure 5a. And various martensite variants distribute in mutually intersecting directions. In Figure 5b, the thickness of the martensite plates is slimmed and become obscure

with Zr amount in the ribbon, which can be ascribed to a decrease in the grain size [13, 14].

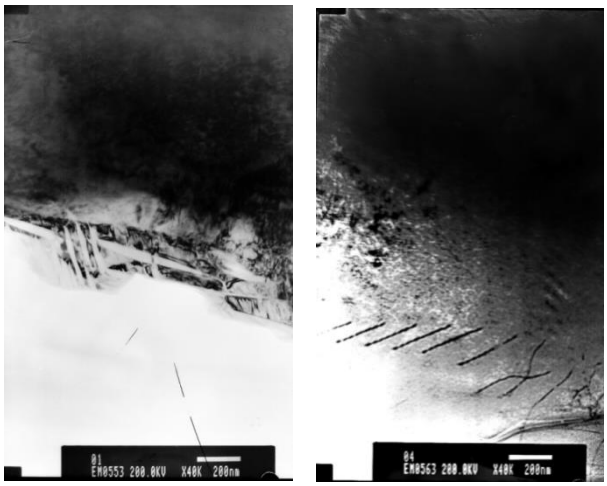

(a) Ti-12V-4Al (b) Ti-12V-4Al-0.5Zr

Figure 5 TEM images for (a) Ti-12V-4Al (wt. %) and (b) Ti-12V-4Al-0.5Zr (wt. %) melt-spun ribbons

4. CONCLUSION

In this research, we have examined the effects of Zr addition on the microstructure and shape memory properties Ti-12V-4Al and Ti-12V-4Al-0.5Zr melt-spun ribbons. The obtained results were as follows:

DSC results show that there is a two-stage B19' martensite → R-phase → B2 austenite transformation in Ti-12V-4Al-0.5Zr ribbon, while a single-stage B19' martensite → B2 austenite transformation occurred in the Ti-12V-4Al ribbon.

In the optical microscope results, it was observed that the microstructure of the melt-spun ribbons contained martensite structures with a lath-shape, grain boundaries were clearly observed in the Ti-12V-4Al-0.5Zr ribbon.

SEM and XRD analyses confirmed that while the Ti-12V-4Al-0.5Zr ribbon consisted of B19' martensite B2 austenite and R phases, the Ti-12V-4Al was composed solely of a B19' martensite phase.

It was found from TEM observations that the size of martensite plates decreased with an increasing Zr amount.

Acknowledgements

The authors would like to thank the Gaziosmanpaşa University Scientific Research Projects Unit (BAP) for contributing to the financial portion of the project.

Funding

This project studies were supported by Gaziosmanpaşa University Scientific Research Projects Unit. Project numbers were 2017 / 95.

The Declaration of Conflict of Interest/ Common Interest

No conflict of interest or common interest has been declared by the authors.

Authors' Contribution

This study is the doctoral thesis of ÖZNUR BAĞ and the supervisior is UĞUR KÖLEMEN. UĞUR KÖLEMEN had a great contribution in providing support for the study, interpreting the findings. FİKRET YILMAZ contributed to resources, validation, device prototype and data analyses. SEMRA ERGEN helped to investigation, writing-review and visualization.

The Declaration of Ethics Committee Approval

The authors declare that this document does not require an ethics committee approval or any special permission.

The Declaration of Research and Publication Ethics

The authors of the paper declare that they comply with the scientific, ethical and quotation rules of SAUJS in all processes of the article and that they do not make any falsification on the data collected. In addition, they declare that Sakarya University Journal of Science and its editorial board have no responsibility for any ethical violations that may be encountered, and that this study has not been evaluated in any academic publication environment other than Sakarya University Journal of Science.

REFERENCES

[1] C. M. Wayman, K. Otsuka, "Shape Memory Materials," Cambridge University Press, 1998.

[2] R. D. Noebe, T. Biles, S. A. Padula, "NiTi-based high temperature shape-memory alloys: properties, prospects, and potential applications, in 'Advanced structural materials: properties, design optimization, and applications," (ed. W. O. Soboyejo and T. S. Srivatsan); New York, Taylor & Francis Group, 2007.

[3] Q. Li, J. Li, G. Ma, X. Liu, D. Pana, "Influence of ω phase precipitation on mechanical performance and corrosion resistance of Ti–Nb–Zr alloy," Material and Design, 11C, pp. 421-428, 2016.

[4] J. Wang, Q. Li, C. Xiong, Y. Li, B. Sun, "Effect of Zr on the martensitic transformation and the shape memory effect in Ti-Zr-Nb-Ta high-temperature shape memory alloys," Journal of Alloys and Compounds, 737, pp. 672-677, 2018.

[5] X. Yi, Y. Wang, B. Sun, B. Cui, J. Liu, X. Meng, Z. Gao, W. Cai, L. Zhao, "Crystallization process and microstructural evolution of as-spun Ti-Ni-Zr alloy ribbon," Journal of Alloys and Compounds, 762, pp. 62-66, 2018.

[6] C. Xiong, L. Yaoa, B. Yuan, W. Qu,, Y. Li, "Strain induced martensite stabilization and shape memory effect of Ti-20Zr–10Nb–4Ta alloy," Materials Science&Engineering A, 658, pp. 28–32, 2016.

[7] O. Uzun, T. Karaaslan, M. Keskin, "Production and structure of rapidly solidified Al–Si alloys," Turk J. Phys., 25:455–66, 2001.

[8] O. Uzun, T. Karaaslan, M. Göğebakan, M. Keskin, "Hardness and microstructural characteristics of rapidly solidified Al–8–16 wt. % Si Alloys," J. Alloys Compd., 376:149–57, 2004.

[9] Y. Kim, Y. Yun, T. Nam, "The effect of the melt spinning processing parameters on the solidification structures in Ti–30 at.% Ni–20 at.% Cu shape memory alloys," Mater Sci Eng A., 438–440:545–8, 2006.

[10] H.Y. Kim, M. Mizutani, S. Miyazaki, "Crystallization process and shape memory properties of TieNieZr thin films," Acta Mater., 57, 1920-1930, 2009.

[11] Y. Motemani, P. J. McCluskey, C. W. Zhao, M. J. Tan, "Analysis of Ti-Ni- Hf shape memory alloys by combinatorial nanocalorimetry," Acta Mater. 59, 7602-7614, 2011.

[12] Y. Y. Li, S. S. Cao, X. Ma, C. B. Ke, X. P. Zhang, "Influence of strongly textured microstructure on the all-round shape memory effect of rapidly solidified Ni51Ti49 alloy," Materials Science & Engineering A., 705, 273–281, 2017.

[13] S. Ergen, O. Uzun, F. Yılmaz, F. Kiliçaslan, "Shape memory properties and microstructural evolution of rapidly solidified CuAlBe alloys," Materials Characterization, 80, pp. 92-97, 2013.

[14] Ö. Bağ, F. Yılmaz, U. Kölemen, S. Ergen, C. Temiz and O. Uzun, "Transformational, microstructural and superelasticity characteristics of Ti–V–Al high temperature shape memory alloys with Zr addition," Physica Scripta, Vol. 96, 8, 2021.

SAKARYA ÜNİVERSİTESİ
FEN BİLİMLERİ ENSTİTÜSÜ DERGİSİ

Sakarya University Journal of Science
SAUJS

e-ISSN 2147-835X | Period Bimonthly | Founded: 1997 | Publisher Sakarya University |
http://www.saujs.sakarya.edu.tr/en/

Title: Comparison of Statistical Methods for Obtaining Image from Video Frames Based on Development of Quality Metric

Authors: Murat Alparslan GÜNGÖR

Recieved: 2020-06-30 15:08:30

Accepted: 2021-04-24 16:17:09

Article Type: Research Article

Volume: 25
Issue: 3
Month: June
Year: 2021
Pages: 741-750

How to cite
Murat Alparslan GÜNGÖR; (2021), Comparison of Statistical Methods for Obtaining Image from Video Frames Based on Development of Quality Metric. Sakarya University Journal of Science, 25(3), 741-750, DOI: https://doi.org/10.16984/saufenbilder.760892
Access link
http://www.saujs.sakarya.edu.tr/en/pub/issue/62736/760892

Sakarya University Journal of Science 25(3), 741-750, 2021

Comparison of Statistical Methods for Obtaining Image from Video Frames Based on Development of Quality Metric

Murat Alparslan GUNGOR[*1]

Abstract

Digital images obtained from the video frames have an important role in different areas. Many image processing techniques have been applied to digital images for different purposes such as edge detection. For a better image processing application, it is very important to obtain images with less oscillation from the video. However, the factors such as camera and environment cause differences among the consecutive frames. These differences cause images with oscillation. Statistical methods can be used to obtain images with less oscillation from multiple frames. In this paper, we developed a quality metric to compare the frames or images in accordance with the quantity of oscillation. A comparative study of statistical methods used to obtain the images with less oscillation from the video frames was presented. Images were obtained by using four statistical methods for the different numbers of frames. This study also focuses on evaluating how the statistical method choice affects the oscillation of images using the proposed quality metric and comparing the processing times of the methods.

Keywords: Video frame, statistics, image quality assessment

1. INTRODUCTION

Today, many researchers are analyzing videos for their researches [1]. Video is considered as the collection of frames. Digital images obtained from the video frames are used for many applications. However, such encountered factors as the environment, transmission channels and imperfections in the video acquisition system – especially due to cheap cameras– cause a decrease in image quality [2, 3]. To date, many techniques have been developed to improve video quality. The techniques proposed by Jasmine and Annadurai [4] introduced the particle optimization with adaptive cumulative distribution based on histogram enhancement technique (PACDHE); Okuhata et al. [5] proposed a novel adaptive real-time video image enhancement based on a variational model of the Retinex theory; Tan et al. [6] improved the denoising capability of pixel similarity weighted frame averaging (PSWFA); Anbarjafari et al. [7] proposed a new video resolution enhancement

[*] Corresponding Author: alparslangungor@hitit.edu.tr
[1] Hitit University, Faculty of Engineering, Department of Electrical and Electronics Engineering, Corum, Turkey
ORCID: https://orcid.org/0000-0001-7446-7808

technique using wavelet transform and an illumination compensation technique; Singh et al. [8] introduced a novel framework for speckle noise removal and contrast enhancement of real ultrasound videos. These are some of the techniques used to improve the video quality. Each technique has its own feature to improve the video images.

The performance of a technique is evaluated by using the quality metrics. In this paper, we proposed a quality metric to measure the differences between consecutive frames of the same scene without movement because the above-mentioned problems also cause differences between consecutive frames. Measuring these differences is very important for image processing applications. The images with less oscillation give better results for image processing applications. For instance, a researcher uses the edge detection algorithm to find the differences between two objects. The researcher obtains the images of the first and second objects respectively. If one of the above-mentioned problems is encountered, i.e., if there are differences between consecutive frames of the same scene without movement, the fake differences can be seen between the images of objects after the edge detection algorithm. Thus, the accuracy of the algorithm is reduced. In the light of this example, less oscillation between frames means a better edge detection algorithm.

As mentioned above, some factors cause differences between consecutive frames. In this paper, the effect of light on the image was analyzed with the proposed metric. Different statistical methods were used to reduce the differences between the images obtained from the consecutive frames. Four statistical methods were applied to obtain images with less oscillation from the frames. The developed quality metric was used to measure the oscillation between the obtained images. The effects of the light, frame number and method on the oscillation between the images were analyzed. Then, the effect of image complexity on oscillation was studied. Finally, the processing times of the methods were compared.

This paper is organized as follows. In Section 2, an overview of the statistical methods is given. The developed quality metric is explained in Section 3 and its performance is discussed in Section 4. Finally, the conclusions are presented in Section 5.

2. STATISTICAL METHODS

We used four statistical methods: arithmetic mean [9], geometric mean [10], harmonic mean [11], and median [10]. These methods are very popular in many image and video processing applications such as denoising [12], text detection in video frames [13, 14], coding and transmission for conversational HD video service [15]. In this paper, we used these methods to obtain images with less oscillation from the video frames.

The arithmetic mean method determines the value of a pixel in the obtained image as follows:

$$O(x,y) = \frac{\sum_{i=1}^{k} f_i(x,y)}{k} \quad (1)$$

where (x, y) represents the coordinates of the pixel, k is the number of frames, O (x, y) and f (x, y) are the pixel values at the (x, y) coordinates of the obtained image and frame, respectively. Equation (1) is repeated to determine the values of all pixels in the obtained image.

For other methods, the same procedure is repeated except Equation (1). Instead of Equation (1), Equation (2), Equation (3) and Equation (4) are used in geometric mean, harmonic mean and median methods, respectively.

$$O(x,y) = (f_1(x,y) f_2(x,y) f_3(x,y) \dots f_k(x,y))^{\frac{1}{k}} \quad (2)$$

$$O(x,y) = \frac{k}{\sum_{i=1}^{k} \frac{1}{f_i(x,y)}} \quad (3)$$

$$O(x,y) = \text{median}\{f_1(x,y), f_2(x,y), f_3(x,y), \dots f_k(x,y)\} \quad (4)$$

While these methods are applied to a group of pixels on an image for conventional image processing applications such as noise reduction, in this paper we applied these methods to pixels that have the same coordinates in different frames.

3. DEVELOPED QUALITY METRIC

In this study, we developed a quality metric to compare the frames or images according to the amount of oscillation. The more above-mentioned problems are encountered, the greater the difference between the consecutive frames of the same scene without movement will be. As a result, more oscillation between the digital images obtained from these frames is created. The aim is to obtain images with less oscillation. The developed metric, Oscillation Assessment Index between Images or Frames (OAIBIF), uses the variance between the images or frames because the maximum oscillation occurs in the maximum variance. OAIBIF metric is defined as follows:

$$\text{OAIBIF} = \left(\frac{\text{mean variance}}{\text{maximum variance}}\right).\text{SP} \quad (5)$$

where SP is defined as the sensitivity parameter. This parameter is determined by the user to achieve the most sensitive results. To calculate the OAIBIF metric for the images or frames of sizes of m * n, first, the variances between pixels with the same coordinates in different images or frames are calculated. Thus, for the images or frames of sizes of m*n, m*n variances are obtained. Equation (6) is used to calculate the mean variance in Equation (5).

$$\text{mean variance} = \frac{[\text{variance }(1,1)+\text{variance }(1,2)+\cdots+\text{variance }(2,1)+\text{variance }(2,2)+\cdots+\text{variance }(m,n)]}{m*n} \quad (6)$$

where variance (1,1), variance (1,2) … and variance (m, n) are defined as variances between the pixels whose coordinates are (1,1), (1,2) … and (m, n), respectively.

The maximum variance in Equation (5) for the different number of images or frames is shown in Table 1.

Table 1
The maximum variance for different number of images or frames

Number of images or frames	The maximum variance
3	21675
4	21675
5	19507.5
6	19507.5
7	18578.57143
8	18578.57143
9	18062.5
10	18062.5
11	17734.09091
12	17734.09091
13	17506.73077
14	17506.73077
15	17340

The minimum and maximum values of the pixel are considered to calculate the maximum variance. For example, for seven images, the maximum variance value is calculated for four 0 and three 255 pixel values.

Larger OAIBIF indicates the images or frames with more oscillation. If OAIBIF is equal to zero, this means that there is no difference between consecutive images or frames, the camera has excellent performance and the above-mentioned problems do not affect the images or frames. If the mean variance is equal to maximum variance, then there is too much difference between consecutive images or frames of the same scene without movement.

4. RESULTS AND DISCUSSION

We used the experimental setup shown in Figure 1 to obtain the consecutive frames.

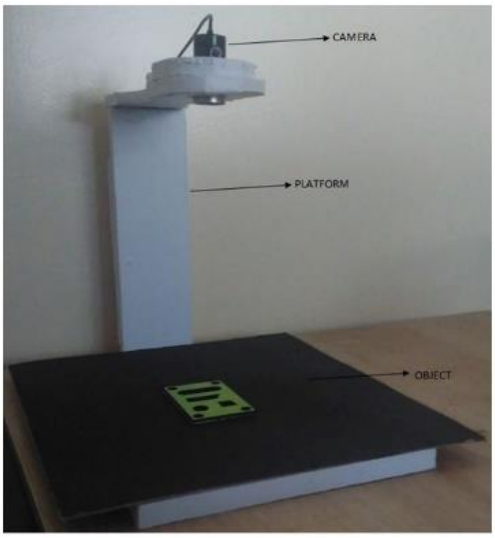

Figure 1 The experimental setup used in the study

Our experimental setup has three parts: a camera, platform, and object. The images of the object were obtained from the camera with the Matlab program and the program is shown in Figure 2.

Figure 2 Screenshot of image obtainment with the camera

We obtained one hundred and fifty frames for each application. These frames were divided into groups of fifteen. One or more frames in each group were used to form an image. To obtain the frames, “Take Frames” button shown in Figure 2 is used. When the "Take Frames" button is clicked, the processing time is very short. This means that the time duration from acquiring the first frame of the first image to the last frame of the last image is short. The aim is to ensure that there is no difference between the frames by keeping the time duration very short; but the above-mentioned problems affect the frames. The calculated OAIBIF values between the frames for an application are shown in Table 2.

Table 2
OAIBIF values between the frames for each image

	OAIBIF
for image 1	3.589054258
for image 2	3.569613997
for image 3	3.461656048
for image 4	3.550260042
for image 5	3.473456519
for image 6	3.511795775
for image 7	3.564171021
for image 8	3.518609685
for image 9	3.504872528
for image 10	3.55007135

Table 2 shows OAIBIF values between the fifteen frames for each image. In this study, the value of SP shown in Equation (5) was selected as 10000. For excellent performance, the value of OAIBIF is desired to be zero. If Table 2 is analyzed, it can be seen that the values of OAIBIF between the frames are about 3.5; meaning that the above-mentioned problems affect the frames.

Digital images are obtained from the video frames. This process is random. In this paper, instead of performing a random process, a group of fifteen frames was created for each image. When an image was to be obtained using a single frame from each group, the first frame in each group was selected. Thus, 10 images for 10 groups were obtained. Then, images were obtained using the different number of frames -k=3,7,11,15- and four statistical methods -arithmetic mean, geometric mean, harmonic mean and median- to reduce the oscillation between images. For example, if an image is obtained from three frames using the arithmetic mean method, the first three frames in the group are taken into account. Ten images were obtained for each number of frame and statistical method. Table 3 shows OAIBIF values between the images

obtained by using the different number of frames and methods.

Table 3
OAIBIF values between the images for different number of frames and methods

Number of Frames and Method	OAIBIF
k=1	3.525118949
k=3, arithmetic mean method	1.318378861
k=3, geometric mean method	1.326692989
k=3, harmonic mean method	1.345553437
k=3, median method	1.315705976
k=7, arithmetic mean method	0.667631561
k=7, geometric mean method	0.674031323
k=7, harmonic mean method	0.690851358
k=7, median method	0.699185843
k=11, arithmetic mean method	0.456831202
k=11, geometric mean method	0.462280189
k=11, harmonic mean method	0.475101222
k=11, median method	0.489580957
k=15, arithmetic mean method	0.352821858
k=15, geometric mean method	0.357759934
k=15, harmonic mean method	0.367979849
k=15, median method	0.382907986

As shown in Table 3, the value of OAIBIF between ten images obtained for k = 1 is 3.525. The different number of frames and statistical methods were used to reduce this value. When Table 3 is analyzed, it is observed that the OAIBIF value decreases as the frame number increases. While the result obtained from the median method is slightly better than the result obtained from the arithmetic mean method for k=3, the arithmetic mean method gives the best results for higher values of k for the first application.

The OAIBIF values between the images shown in Table 3 depend on the OAIBIF values between the frames shown in Table 2. Using the same camera, platform and object, we performed another application. The results of the second application are shown in Table 4 and Table 5.

Table 4
For the second application, OAIBIF values between the frames for each image

	OAIBIF
for image 1	3.190312897
for image 2	3.186761742
for image 3	3.200678401
for image 4	3.20506631
for image 5	3.184293296
for image 6	3.169900469
for image 7	3.166245347
for image 8	3.177909462
for image 9	3.17651831
for image 10	3.172085197

Table 5
For the second application, OAIBIF values between the images for different number of frames and methods

Number of Frames and Method	OAIBIF
k=3, arithmetic mean method	1.088438566
k=3, geometric mean method	1.092957229
k=3, harmonic mean method	1.105049987
k=3, median method	1.081353732
k=7, arithmetic mean method	0.509540425
k=7, geometric mean method	0.512815249
k=7, harmonic mean method	0.523121221
k=7, median method	0.533838721
k=11, arithmetic mean method	0.351981108
k=11, geometric mean method	0.354413779
k=11, harmonic mean method	0.362532798
k=11, median method	0.378225662
k=15, arithmetic mean method	0.277658029
k=15, geometric mean method	0.279574858
k=15, harmonic mean method	0.2860909
k=15, median method	0.302458874

Comparing Table 2 and Table 4, the amount of oscillation between the frames obtained in the second application is less than the amount of oscillation between the frames obtained in the first application. As a result, Table 3 and Table 5 are compared, it is shown that the images obtained

in the second application have less oscillation than the images obtained in the first application. Table 5 shows that while the very close results of the arithmetic mean and median methods are the best results for k=3, the arithmetic mean method is the best method among the four methods to reduce the oscillation between the images for higher values of k, as in the first application.

One of the problems affecting the oscillation between the images is the effect of light. In this study, we performed three applications -third, fourth and fifth applications- to analyze the effect of light on oscillation. In these applications, the fifth application has the brightest environment, while the third application has the least bright environment. OAIBIF values between the frames for the third, fourth and fifth applications are shown in Table 6.

Table 6
For the third, fourth and fifth applications, OAIBIF values between the frames for each image

	OAIBIF for		
	the third application	the fourth application	the fifth application
for image 1	0.531858708	2.261232577	3.025993026
for image 2	0.528763299	2.268105204	3.014552717
for image 3	0.525337575	2.13092498	3.014812282
for image 4	0.527548782	2.187285716	3.027073588
for image 5	0.527707412	2.18979657	3.023207776
for image 6	0.529436853	2.130556246	3.015490315
for image 7	0.526602452	2.141309735	3.022219283
for image 8	0.54445621	2.192560209	3.018972695
for image 9	0.525800341	2.185371059	3.01752655
for image 10	0.526528894	2.129599413	3.014587508

Table 6 shows that more bright environment causes a greater amount of oscillation between the frames. While OAIBIF values are about 0.5 for the third application with the least bright environment, OAIBIF values are about 3 for the fifth application with the brightest environment. The images with the highest oscillation are obtained from the fifth application as shown in Table 7.

Table 7
For the third, fourth and fifth applications, OAIBIF values between the images for different number of frames and methods

	OAIBIF for		
Number of Frames and Method	the third application	the fourth application	the fifth application
k=3, arithmetic mean method	0.20789316	0.765139939	1.011931214
k=3, geometric mean method	0.21333897	0.763563836	1.013906202
k=3, harmonic mean method	0.220275313	0.769359909	1.018262637
k=3, median method	0.242142202	0.948115851	0.961466518
k=7, arithmetic mean method	0.114512857	0.359958343	0.465117995
k=7, geometric mean method	0.120120805	0.360405159	0.466137095
k=7, harmonic mean method	0.127880561	0.36461776	0.469996057
k=7, median method	0.133036902	0.478495225	0.459825836
k=11, arithmetic mean method	0.085669837	0.268136341	0.315076324
k=11, geometric mean method	0.09262416	0.268963015	0.315831138
k=11, harmonic mean method	0.095315794	0.272629301	0.318677491
k=11, median method	0.098329569	0.35570909	0.318922497
k=15, arithmetic mean method	0.071289613	0.207260595	0.244772046
k=15, geometric mean method	0.078451364	0.208771333	0.245430966
k=15, harmonic mean method	0.081223405	0.211895532	0.247664665
k=15, median method	0.080994457	0.276369585	0.251377186

Table 7 shows that the arithmetic mean method is the best method for the third application with low oscillation frames. For the brighter environment, while the arithmetic mean method is less effective for the smaller number of frames, this method is the best method among methods mentioned in this paper as the number of frames increases. For more bright environments and a smaller number of frames, the median method can be used to have images with low oscillation as shown in the fifth application.

The main scope of this paper is to develop a quality metric to measure the oscillation between the images or frames without movement. After analyzing the effect of light on oscillation, we analyzed the effect of image complexity on oscillation using OAIBIF. To make this analysis, we used two images; basic image and complex image, shown in Figure 3.

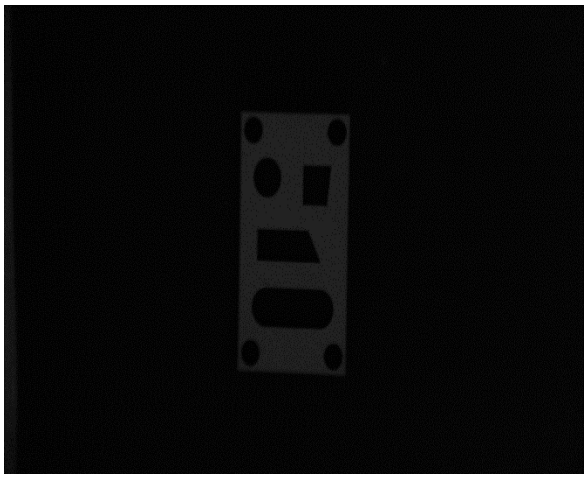

(a)

(b)

Figure 3 (a) Basic image (b) Complex image

As shown in Figure 3, the complex image has more objects than the basic image. OABIF values between the frames for the basic and complex images are shown in Table 8.

Table 8
OAIBIF values between the frames for the basic and complex images shown in Figure 3

	OAIBIF for	
	the basic image	the complex image
for image 1	0.264177891	0.610616396
for image 2	0.273002471	0.606499729
for image 3	0.275166205	0.593290857
for image 4	0.281117924	0.570233579
for image 5	0.2536753	0.603319578
for image 6	0.280907443	0.621834299
for image 7	0.278978147	0.623157961
for image 8	0.284807853	0.618820925
for image 9	0.262726809	0.631207604
for image 10	0.287779072	0.592809232

While OAIBIF values between the frames are about 0.6 for the complex image, these values are about 0.27 for the basic image. Table 8 indicates that more image complexity causes higher oscillation between the frames as expected. When the basic and complex images obtained from the frames with the different methods are compared, it is seen that the complex images have higher oscillation than the basic images for all methods as shown in Table 9. Comparing the methods, the arithmetic mean method gives the best results for both the basic and complex images as in previous applications.

Table 9
For the basic and complex images shown in Figure 3, OAIBIF values for different number of frames and methods

	OAIBIF for	
Number of Frames and Method	the basic image	the complex image
k=3, arithmetic mean method	0.137656504	0.227283693
k=3, geometric mean method	0.139932036	0.231430786
k=3, harmonic mean method	0.142562325	0.238988103
k=3, median method	0.149680735	0.272631404
k=7, arithmetic mean method	0.081331162	0.126619403
k=7, geometric mean method	0.082615391	0.130542197
k=7, harmonic mean method	0.085034682	0.136442148
k=7, median method	0.08954046	0.155499102
k=11, arithmetic mean method	0.056900569	0.09681204
k=11, geometric mean method	0.057782053	0.100964218
k=11, harmonic mean method	0.059020403	0.105030167
k=11, median method	0.063103314	0.118166461
k=15, arithmetic mean method	0.049324521	0.08145526
k=15, geometric mean method	0.049868557	0.08530483
k=15, harmonic mean method	0.050267312	0.088548303
k=15, median method	0.05413561	0.098442251

Finally, we compared the processing times of the methods shown in Table 10.

Table 10
The processing time of the methods for different number of frames

	Processing time (sec)			
	arithmetic mean method	geometric mean method	harmonic mean method	median method
k=3	0.600838	0.653749	0.62164	7.22081
k=7	1.398986	1.529841	1.426312	8.40238
k=11	2.33623	2.53114	2.395979	9.400916
k=15	3.339206	3.555974	3.3489842	10.62196

We obtained Table 10 using 480 images. We used 30 images and averaged the sum of the acquisition time of each image for each k and method. Among these methods, while the shortest processing time belongs to the arithmetic mean method, the median method has the longest processing time. As the number of frames increases, processing time increases as expected.

5. CONCLUSIONS

Video is considered as the collection of frames and digital images obtained from the video frames are used for many applications. The differences between the consecutive frames of the same scene without movement affect the accuracy of the applications such as edge detection. Using the developed metric, OAIBIF, the oscillation between the frames or images can be assessed. In this paper, we obtained frames from different bright environments and compared the oscillation between the frames using OAIBIF. Higher oscillation between the frames means higher oscillation between the images. We used multiple frames with different statistical methods to obtain images with less oscillation. Using OAIBIF, we analyzed the oscillation between the obtained images. Significant results are attained from the analysis providing valuable information to obtain the images with the least oscillation. The arithmetic mean method gives the best results for the less bright environments and this method performs in the shortest time among the methods mentioned in this study. Although the processing time of the harmonic mean method is close to the processing time of the arithmetic mean method,

the images with less oscillation are obtained with the arithmetic mean method. The geometric mean method gives less favorable results than the arithmetic mean method, both in terms of the processing time and in the performance of reducing oscillation between images. Although the median method reduces oscillation between images more than the arithmetic mean method for the brighter environment and the smaller number of frames, the processing time of the median method is much greater than the arithmetic mean method. As the number of frames increases, problems such as storage may occur. Therefore, if the processing time is not taken into account, the median method can be used for brighter environments and the small number of frames to obtain images with less oscillation. Considering both oscillation reduction performance and the processing time, while the arithmetic mean method is less effective for the smaller number of frames and the brighter environments, this method is the best method among the methods mentioned in this paper as the number of frames increases.

After the effect of light on oscillation, the effect of image complexity on oscillation was analyzed by using OAIBIF. The results show that more image complexity causes a higher oscillation between the frames. As in previous applications, the arithmetic mean method gave the best results for both the basic and complex images presented in this study.

The developed metric, OAIBIF, is used to assess the oscillation between the frames or images. The closer this metric to zero means the frames or images with less oscillation are obtained. Although we analyzed the effects of the light, frame number and method, this metric can be used to analyze the effect of any factor on the oscillation between the frames or images.

Funding

The author has no received any financial support for the research, authorship or publication of this study.

The Declaration of Conflict of Interest/ Common Interest

No conflict of interest or common interest has been declared by the authors.

The Declaration of Ethics Committee Approval

This study does not require ethics committee permission or any special permission.

The Declaration of Research and Publication Ethics

The authors of the paper declare that they comply with the scientific, ethical and quotation rules of SAUJS in all processes of the paper and that they do not make any falsification on the data collected. In addition, they declare that Sakarya University Journal of Science and its editorial board have no responsibility for any ethical violations that may be encountered, and that this study has not been evaluated in any academic publication environment other than Sakarya University Journal of Science.

REFERENCES

[1] E. S. Gupta, and Y. Kaur, “Review of different histogram equalization based contrast enhancement techniques,” International Journal of Advanced Research in Computer and Communication Engineering, vol. 3, no. 7, 2014

[2] C. H. Hsia, T. C. Wu, and J. S. Chiang, “A new method of moving object detection using adaptive filter,” Journal of Real-Time Image Processing, vol. 13, no. 2, pp. 311-325, 2017.

[3] M. Szczepanski, “Fast spatio-temporal digital paths video filter,” Journal of Real-Time Image Processing, vol. 16, no. 2, pp. 477-489, 2019.

[4] J. Jasmine, and S. Annadurai, “Real time video image enhancement approach using particle swarm optimization technique with adaptive cumulative distribution function

based histogram equalization," Measurement, vol. 145, pp. 833-840, 2019.

[5] H. Okuhata, K. Takahashi, Y. Nozato, T. Onoye, and I. Shirakawa, "Video image enhancement scheme for high resolution consumer devices," In 2008 3rd International Symposium on Communications, Control and Signal Processing, pp. 639-644, Mar. 2008.

[6] X. Tan, Y. Liu, C. Zuo, and M. Zhang, "A real-time video denoising algorithm with FPGA implementation for Poisson–Gaussian noise," Journal of Real-Time Image Processing, vol. 13, no. 2, pp. 327-343, 2017.

[7] G. Anbarjafari, S. Izadpanahi, and H. Demirel, "Video resolution enhancement by using discrete and stationary wavelet transforms with illumination compensation," Signal, Image and Video Processing, vol. 9, no. 1, pp. 87-92, 2015.

[8] P. Singh, R. Mukundan, and R. De Ryke, "Feature Enhancement in Medical Ultrasound Videos Using Contrast-Limited Adaptive Histogram Equalization," Journal of Digital Imaging, pp. 1-13, 2019.

[9] P. S. Altares, A. R. I. Copo, Y. A. Gabuyo, A. T. Laddaran, L. D. P. Mejia, I. A. Policapio, E. A. G. Sy, H. D. Tizon, and A. M. S. D. Yao, "Elementary statistics: a modern approach," Rex Bookstore Inc., Manila, Philippines, 2003.

[10] C. F. Lee, J. C. Lee, and A. C. Lee, "Statistics for business and financial economics," Singapore: World Scientific, 2000.

[11] N. Bajpai, "Business statistics," Pearson Education India, 2009.

[12] P. Singh, and R. Shree, "A comparative study to noise models and image restoration techniques," Int. J. Comput. Appl., vol. 149, no. 1, pp. 18-27, 2016.

[13] P. Shivakumara, W. Huang, and C. L. Tan, "An efficient edge based technique for text detection in video frames," The Eighth IAPR International Workshop on Document Analysis Systems, pp. 307-314, Sept. 2008.

[14] P. Shivakumara, W. Huang, T. Q. Phan, and C. L. Tan, "Accurate video text detection through classification of low and high contrast images," Pattern Recognition, vol. 43, no. 6, pp. 2165-2185, 2010.

[15] H. Li, W. Lei, W. Zhang, and Y. Guan, "A joint optimization method of coding and transmission for conversational HD video service," Computer Communications, vol. 145, pp. 243-262, 2019.

SAKARYA ÜNİVERSİTESİ
FEN BİLİMLERİ ENSTİTÜSÜ DERGİSİ

Sakarya University Journal of Science
SAUJS

e-ISSN 2147-835X | Period Bimonthly | Founded: 1997 | Publisher Sakarya University |
http://www.saujs.sakarya.edu.tr/en/

Title: Comparison of Object Detection and Classification Methods For Mobile Robots

Authors: Önder ALPARSLAN, Ömer ÇETİN

Recieved: 2020-11-20 17:56:44

Accepted: 2021-04-26 13:29:55

Article Type: Research Article

Volume: 25
Issue: 3
Month: June
Year: 2021
Pages: 751-765

How to cite
Önder ALPARSLAN, Ömer ÇETİN; (2021), Comparison of Object Detection and Classification Methods For Mobile Robots. Sakarya University Journal of Science, 25(3), 751-765, DOI: https://doi.org/10.16984/saufenbilder.828841
Access link
http://www.saujs.sakarya.edu.tr/en/pub/issue/62736/828841

Sakarya University Journal of Science 25(3), 751-765, 2021

Comparison of Object Detection and Classification Methods For Mobile Robots

Önder ALPARSLAN*[1], Ömer ÇETİN[2]

Abstract

As one of today's popular research field, mobile robots, are widely used in entertainment, search and rescue, health, military, agriculture and many other fields with the advantages of technological developments. Object detection is one of the methods used for mobile robots to gather and report information about its environment during these tasks. With the ability to detect and classify objects, a robot can determine the type and number of objects around it and use this knowledge in its movement and path planning or reporting the objects with the desired features. Considering the dimensions of mobile robots and weight constraints of flying robots, the use of these algorithms is more limited. While the size and weight of mobile devices should be kept relatively small, successful object classification algorithms require processors with high computational power. In this study, to be able to use object detection information for mapping and path planning, object detection and classification methods were examined, and for the usage in low weight and low energy consuming platforms through developer boards, detection algorithms were compared to each other.

Keywords: Object Detection and Classification, Mobile Robots, Convolutional Neural Network, Deep Learning.

1. INTRODUCTION

An autonomous mobile robot is a kind of robot which is not bounded to a physical location and has the ability to move around. The travel of the vehicle can be provided by the help of guidance devices which allow the robots to go through pre-defined trajectory or the robot itself has the capability to understand its environment and move around the obstacles and plan a route to the target. This route can be updated in every step by controlling the robot's position and surrounding objects.

Creating a robust mobile robot depends on a reliable and effective path planning strategy [1]. This problem was solved by the algorithms which take the robot to the target in secure with the help

*Corresponding author: oalparslan@hho.edu.tr
[1] National Defence University, Hezârfen Aeronautics and Space Technologies Institute, 34049, Istanbul.
ORCID: https://orcid.org/0000-0001-8803-1597
[2]National Defence University, Air NCO Higher Vocational School, 35410, Izmir.
E-Mail: oalparslan@hho.edu.tr; omer_cetin@outlook.com.tr
ORCID: https://orcid.org/0000-0001-5176-6338

of a well-known pre-defined map [2-4]. A wheeled robot can follow a trajectory with an odometer and internal/external sensors [5]. Nevertheless, these methods are only available when there is a pre-defined map. If the robot is to go into an obscure vicinity, it needs to determine its position and be aware of its surroundings by itself. For these kinds of cases various mapping and path planning algorithms have been proposed also [6].

The problem of understanding the surrounding environment and robot's current position is figured out with SLAM (Simultaneous Localization and Mapping). SLAM is a method that builds up a consistent map and locates the robot on the created map [7,8]. While SLAM or the other known methods are used effectively for robot navigation, these methods are not interested in what are the surrounding objects and obstacles. An object can be classified as an obstacle or as a crossing way and both classifications may be used in path planning. If a robot is to use some specific crossing points or some objects as a temporary target, there is a need for another mapping algorithm including the capability of defining objects. This competence can be provided by object detection algorithms with the help of computer vision technologies.

Object detection and classification is a technology consisting of image processing and computer vision. The main purpose is to identify the objects in an image by associating them with a dataset. The recent methods have additionally started to look for semantic information to understand the scene. One of the biggest challenges for computer vision was processing time. Developers had to whether work on archived data and wait for the results for a while or use supercomputers for real-time application. For this problem, researchers have started to use data preprocessing and some useful methods to shorten processing time. The most notable contributions came from the convolutional neural networks (CNN) and GPU based computing power. Since convolutional neural networks produce very accurate results for detecting and classifying objects, it has become reliable. Moreover, parallel graphic processors work together to run neural network faster, so it is possible to use applications in real world even on developing boards. Besides, researchers have started to seek new mechanisms which speed up the CNN to work with less memory and fewer computational resources, such as compression and quantization of the networks [9].

A mobile robot which requires to determine its route in an unknown environment by using the particular objects nearby needs to have an object detection integrated SLAM method. This has not been used in any research according to the recent inquires. But it would be very useful for certain tasks such as creating a path using doors, windows, or stairs.

In this study, for mobile robot navigation in an unknown environment, to be able to use the object classification with SLAM, the usage of object detection algorithms has been inquired. As it can be seen from various studies, today's object detection and classification methods can be implemented in robots for real-time tasks. It is considered by detecting the crossing points indoor environment, a better understanding of the environment can be provided and robot's navigation can be planned with this information. By means of using object classification in navigation, a new contribution to path planning algorithms is targeted. However, running both algorithms simultaneously demands huge processing power which is not so easy to have in an indoor aircraft or a small mobile device. For this, it is crucial to find an accurate and fast method to perform in this limited capacity. Having knowledge of the advantages, drawbacks and limits of the detection algorithms, one can choose a proper method for new research. The solutions for robot positioning indoor, development of object detection and convolutional neural networks are reviewed in section two. In section three, the criteria to measure object detection algorithms' accuracy is explained and the best-known detection methods are compared to each other for their speed, processing power needs and detection accuracy considering implementing them on small developer boards. Detection algorithms' accuracy with the well-known datasets, their advantages and drawbacks are evaluated in the following

section. It is explained what has been learned, acquired and what is to be done in future works in the last section.

2. LITERATURE REVIEW

The appreciation of robots across the world and the latest research in robotics have started to make robots more apparent in daily life. Among the different types of modern robots, industrial robots and service robots promise a brighter future for now. One of the most basic and important skills for robots that we will see frequently in our near future, self-driving cars [10] and cleaning robots [11], is path planning and autonomous routing. The way the moving robots move from their current position to the target position with their own sensors and decision-making mechanisms has been tried in many different areas with different studies. It has been investigated how the robot can move on different types of surfaces like ground vehicles [12,13], underwater robots [14,15], wall-climbing robot [16] and aircrafts [17,18].

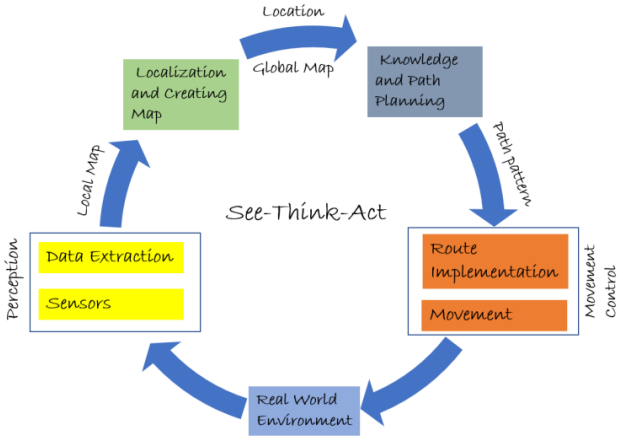

Figure 1 Autonomous robot's life cycle

Mobile robots usually have a similar life cycle which starts with taking data from the sensors (LIDAR, camera, IMU, etc.), extracting meaningful information from these data which results in having a local map. Next, it starts to model the unknown environment fostered with more sensor data which makes it possible to locate itself on the global map. Subsequently, it starts to draw a pathway to the target and sends commands to the moving parts of the robot to go further. This cycle keeps going until the robot's ultimate position. When the robot realizes that there is another obstacle or crossing point, it requires to update its route.

For robot navigation, many various methods have been proposed until. Patle et al. classified path planning algorithms into two categories [6]. The traditional methods comprised of Cell Decomposition [19], Roadmap Approach [20] and Artificial Potential Fields [21] and on the other hand, reactive methods consist of Genetic Algorithms, Fuzzy Logic [22], Neural Networks [23], Particle Swarm Optimization [24], Ant Colony algorithm [25] and the other biological modeling algorithms. In recent years, due to the capacity of exploring the environment, efficient calculation, rapid reaction, resiliency in the operation and capability to decide by itself, reactive methods are generally preferred [6].

While it is very possible to locate a robot by Global Positioning System, it is not robust in the buildings. An autonomous mobile robot in a building needs to obtain its position, map the environment, update it simultaneously to ensure loop closures and abstain from wasting time. In an unknown environment, the problem of building up a map and localization simultaneously with the help of sensors is known as SLAM [7,8]. Modern SLAM approaches' architecture can be seen in Figure 2. Following the sensor data was fused and processed, the graph structure is constructed. After the controlling of data connections and loop closures, the graph optimization is made, and metric and topologic maps are built up. In the closed areas, LIDAR has been the primary sensor for SLAM and robot navigation [26]. Besides, low-cost mono and stereo optic cameras have also been preferred for SLAM under the name of VSLAM [27,28].

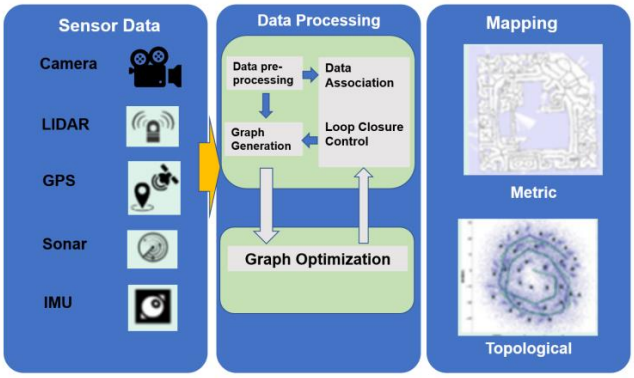

Figure 2 A typical SLAM architecture for generating metric or topologic maps

Apart from SLAM, detection, and classification of objects through images, videos and live cameras have been attracting so much interest in recent years thanks to its increasing success rate and practical applications. The methods and algorithms are in the scope of research fields in academic communities and companies working with computer vision related technologies. There have been many technological developments in the last decade for this common interest and making it very effectively usable in real world applications. Without a doubt, robotic researchers benefit from the advantages of computer vision and object detection. The latest developments made it possible to use them for security applications, robotic vision, analysis of territories, medical diagnoses and many independent categories including even for finding the rotten potato in a factory.

The first steps of computer vision came up with the projects in the 1960s which tried to mimic human visual using artificial intelligence [29]. Studies in the 1970s included current methods such as extraction of edges, motion prediction and optical flow [29]. As a major successful work, Fischler [30] achieved to detect roughly certain shapes such as faces with template matching in the 80s. Following researches generally had used geometric representations for object detection until the 1990s [31], which later evolved into statistical methods (Artificial Neural Networks [32], SVM [33], Adaboost [34]). This period is to be considered until 2012 when convolutional deep neural networks were successfully implemented [35].

A Convolutional Neural Network (CNN or ConvNet) is a class of deep neural networks, most commonly applied to analyzing visual imagery [36]. Convolutional Neural Network (CNN) was first proposed for image recognition in computer vision by LeCun et al. [37] in 1989 to recognize handwritten postal codes and later used widely in image recognition and classification tasks. There is also an important study of Kunihiko who used a similar model with a different name in 1980 [38]. Later, CNN has been used in classifying handwritten numbers [39], recognizing address numbers [40], determining traffic signs [41] and in various other studies. However, the high computational cost and memory consumption of deep neural networks prevented its use in small memory devices and latency sensitive applications. Especially the emergence of SVM and Bayesian models and the fact that they can work with smaller data sets (MNIST, Caltech-101) with fewer parameters has reduced the use of CNN. With the use of much larger data sets after the 2000s, the use of deep networks has become feasible.

The great success of Krizhevsky et al. [35] for object classification in ILSVRC 2012, has been another milestone. The success of Krizhevsky's classification by labeling 1.2 million images in the Imagenet dataset with the benefit of data augmentation techniques led to the wide use of CNN. Realizing the potential of CNN in image classification, many researchers have studied to understand CNN and apply it to traditional computer vision tasks. The achievements and lessons learned in these studies have contributed to CNN and computer vision science.

Many models have been proposed with the use of convolutional neural networks for object recognition and classification. R-CNN [42-44], one of the two-level algorithms, divides the image into regions by means of the features in the image and performs the object classification and bounding process on these regions. Mask R-CNN [45] is a convolutional network model reinforcing R-CNN. There are other studies to enhance the performance of R-CNN such as the Faster R-CNN [44] which increases the number of frames per second (fps) to be processed. However, although

these two-level models have a good detection success, the detection speed is relatively low and the memory consumption is high. This fact makes two-level detection algorithms almost impossible to use in mobile robots considering the existing processor technologies especially on small platforms that can carry very limited load.

To have a lower computation cost and faster results, one level models have been proposed. Compared to the two-level models, YOLO [46-48], SSD [49], DSSD [50] and RetinaNet [51] algorithms appear to be able to detect objects much faster. This relatively high speed comes from the simpler and shorter algorithms.

While conventional convolutional networks have N connections for each N layer, the network of DenseNet has N(N+1)/2 direct connections. The former layers' feature maps are used as inputs for subsequent layers. In this way, it considerably reduces the number of parameters and provides higher performance results. [52]. SSD model is quite simple compared to methods that need object proposals, since it completely eliminates the proposal stage, feature resampling phase and covers all computations in a single network. This model ensures to be easy for training and compatible with detection systems [49]. RetinaNet is comprised of two task-specific subnetworks and one backbone network which are united in a single network. Backbone network computes feature maps for input image while subnet networks are responsible for classifying objects and bounding with a box. It provides a simple, one-stage model detection [51]. YOLO ignores the wide pipeline which optimizes individual components. It focuses on directly being faster without giving up detection accuracy and it succeeds to be fast by its structure [53]. The simple network provides 45 frames per second, while the fast version can reach more than 150 fps. YOLO takes the input image as a whole both in training and test and thereby it figures out contextual information about categories. As it is said highly generalizable [53], when applied to new domains or unexpected inputs, it is still successful.

These new methods use CNN architectures as the network backbone which determines the depth of the network, the number of layers and parametric values of the network structure. Although the depth of the network directly affects the calculation performance, it seems the trend in recent years is on deepening the network. While AlexNet [35] has 8 layers, GoogleNet [54] announced in 2015, has 22 layers, ResNet and DenseNet [57,52] are over 100 layers. Another popular network Darknet, which is frequently engaged with YOLO, has two versions with 19 and 53 layers [47,48].

Open source deep learning tools such as Caffe [58], TensorFlow (from Google) [59], CNTK (from Microsoft) [60], Torch [61] have also been offered for CNN, which are successfully used today in topics such as object recognition [54], image classification [35,56], motion detection [55] and natural language processing [62,63].

Looking to the usage of computer vision for mobile robots' navigation, in numerous works, visionary data has been used for path planning. Moghadam et al. [64], combined the 2-dimensional laser data with stereo camera data. In this way, they succeeded to perceive 3-dimensional buildings. Sabe et al. [65], benefited from the stereo camera to avoid obstacles and move around on different surfaces. However, to be successful, it must have sufficient texture knowledge. The biggest disadvantage of using the camera as a sensor is there may be deviations in distance data on homogeneous environments such as a flat wall and in low light environments. In such cases, texture validation and surface validation techniques are applied [66]. Pomerleau handled path tracking as a classification problem and succeeded in detecting the deviation of the vehicle from the road line with the system he trained with artificial neural networks [67]. Ran et al. trained the images using CNN which are gathered with a spherical camera and they ensured that the robot turned to the correct route by determining how many degrees it was traveled from the desired direction [68]. Hadsell and his friends labeled the environment by dividing it into 5 classes in order to provide a pathway on off roads [69]. Surfaces such as trees and buildings are classified as obstacle or super obstacle, surfaces such as soil and asphalt as ground or

super-ground, and navigation is planned on the land where the robot can go between obstacles. In [70], a digital surface model is created using the images taken by an unmanned aerial vehicle to identify the vine rows and inter-row terrain. This model is then used to generate a path plan for unmanned ground vehicle Many other methods also successfully classified the environment as obstacles, targets or corridors, yet they didn't look for what exactly is the surrounding objects. Understanding what the crossing point is and moving to that point in accordance with this information may be helpful for the robot's navigation.

3. COMPARISION OF OBJECT DETECTION METHODS

In the context of the study, the most popular object detection methods are inquired and compared for their success, performance and working principles. To be able to compare successfully, there is a need to use standard datasets and measuring tools which are also defined below.

3.1. How to measure accuracy and error

One of the most important steps in designing artificial neural networks is to evaluate the performance of the system or in other words to measure errors to be able to minimize them. The final goal of all detection algorithms is reducing the loss. The loss value has to be calculated before various strategies are implemented to diminish it. A basic loss function (Mean Absolute Error) in a classification or regression operation can be calculated using Eq.1 when the loss function of a single training data is *l* and the dataset is x.

$$L(x, W) = \frac{1}{N}\sum_{i=1}^{N} \mathrm{l}(x_i, \mathrm{W}) \qquad (1)$$

Mean squared error as one of the most known methods to measure the error calculates the sum of the differences between expected output and actual output as seen in Eq.2.

$$L = \frac{1}{N}\sum_{i=1}^{N} ||o_i - y_i||^2 \qquad (2)$$

Softmax. is a method that is usually used for multiclass problems and frequently preferred in image classification. It receives input data from the preceding fully connected layer and uses it to classify. It takes probabilistic input data and determines belonging value to a certain class [71]. Below loss function calculates the cross- entropy of softmax with the output of the neural network where y_j is output and p_j is the estimated probability vector:

$$L = -\sum_j \; y_j - logp_j \qquad (3)$$

The success of object recognition and classification algorithms is measured with their accuracy and speed. However, there is more than one metric used for the concept of accuracy. These metrics are important for a proper understanding of the success to be considered separately. TP (True Positive), truely located targets; FP (False Positive), mistakenly detected objects; FN (False Negative), undetected objects; β (threshold), the probability of the prediction; Recall, the proportion of correctly found objects to all real objects; Precision refers to the sensitivity of the true detections in total predictions. To calculate Precision and Recall Eq.4 can be used as shown below.

$$Precision = \frac{\mathrm{TP}}{\mathrm{TP+FP}},\ Recall = \frac{\mathrm{TP}}{\mathrm{TP+FN}} \qquad (4)$$

The proportion of overlapping predicted bounding box with the actual minimum bounding box gives IOU (Intersection Over Unit) value and can be obtained for the predicted bounding box b and the expected box b_g by the Eq.5:

$$\mathrm{IOU}(b, b^{\mathrm{g}}) = \frac{\mathrm{area}(b \cap b^{\mathrm{g}})}{\mathrm{area}(b \cup b^{\mathrm{g}})} \qquad (5)$$

For object recognition algorithms, TP, FP and FN values are determined according to the IOU value. According to the threshold value of the datasets or the one determined by the researcher, when the IOU value is higher than the given threshold the case is accepted as a TP. Average Precision (AP), calls for the use of Precision and Recall together for a category, whereas mean Average Precision (mAP) refers to the accuracy value for all categories. FPS, which is the number of frames that can be processed per second, is also used as

an important metric for real time detection algorithms.

3.2. The Role of Datasets

In research of object detection, datasets played a vital role. They helped to solve both the complex problems and measuring and comparing the different detection algorithms' performances. Looking the datasets used for detection methods, 4 significant datasets outshine: PASCAL VOC (proposed by Everingham et al. in 2010 and upgraded in 2015 [72,73]), MS COCO [74], ImageNet [75] and Open Images [76]. In Table 1, it is possible to see the main features of these datasets and highlights. Moreover, many other studies have played an important role in the object detection field, such as Caltech [77] and KITTI [78].

PASCAL VOC dataset has the most faced 20 categories of daily life. The number of image counts for every class is high and possible to use it in real-life applications. It contains more than one object with different features in an image and also uncommon examples. ImageNet outshines with the high number of categories and images. MS COCO is developed for real life applications and has more categories and images than VOC. In every image, there are many images and it is available for segmentation which is not comprised in ImageNet. Lastly, Open Images dataset released in 2017 and it supports big scale object detection, object extrication and visual correlation.

Table 1
The comparison of well-known datasets

Dataset	Number of Input Data	Number of Category	Object number in each image	Image Size	Release Date
PASCAL VOC (2012)	11540	20	2.4	470×380	2005
ImageNet	More than 14 million	21841	1.5	500×400	2009
MS COCO	328000+	91	7.3	640x480	2014
Open Images	More than 9 million	6000++	8.3	Various	2017

3.3. The Comparison of Methods for Using in Robot Navigation

Considering mentioned criteria for mobile robots and calculations of the object detection algorithms, when the most known object detection algorithms have been compared, the results in Table 2 have been acquired.

From numerous detection algorithms, R-CNN[42] is the first one in which CNN was integrated into RP (Region Proposal) methods and it came up with considerably better results. However, calculation cost is high, training and test time are long. SPPNet [79], is the first usage of SPP (Spatial Pyramid Pooling) in CNN and it provided speeding up of R-CNN. Nevertheless, it has similar drawbacks with R-CNN. The first method training the network end-to-end without region proposal is Fast R-CNN [43] in which one pooling layer is suggested. By the way like its name it is much faster than SPPNET and quite successful. However, external RP calculation creates a bottleneck and it is still too slow for real-time applications.

With Faster R-CNN [44], the RPN (Region Proposal Network) was suggested instead of selection sort to create high quality and zero cost RPs. Convolution layers were shared and RPN and Fast R-CNN were merged in a single network. It showed a processing speed of 5 FPS with VGG16 network model. Speaking of disadvantages, the training process is quite difficult and it doesn't have enough speed for real time applications.

Authors use an insignificant region generation scheme, constant for each image in R-CNN-R [80] method. Combined with SPP, this provides a fast detector that does not require processing an image with algorithms other than the CNN itself. It showed the community that it is possible to use simple and fast algorithms with CNN. However, its detection speed is lower than 5 FPS and it is still inadequate for real-time applications and it sometimes has unsatisfactory detection results owing to the failure of detecting regions. RFCN [81] used a fully connected convolutional neural network. Without sacrificing detection accuracy,

detection speed is raised (~10 FPS). Its shortcomings are training process is long and difficult and yet not satisfactory for real-time applications. Mask RCNN [45] is announced as a simple, resilient and efficient object segmentation. The common usage of bounding box was attached with object mask by upgrading Faster RCNN. Anyway, its detection speed was around 5 FPS which is not suitable for real-time applications.

YOLO [46] is the first efficient single layer object detection algorithm. It totally abolishes the RP process which results in high speed and makes it possible to use it in real-time applications. Its biggest disadvantages are the detection accuracy which is lower than modern detection methods and being unsuccessful for small object detection. With YOLOv2 [47], A faster background structure, DarkNet19, was suggested which provided a more accurate and fast detection. Nonetheless similar to its preceding it is unsuccessful for detecting small objects.

Table 2
The comparison of popular detection algorithms

Detection Method	Backbone Structure	Size of Input Image	Results with Different Datasets		FPS
RCNN (2014) [42]	AlexNet	Constant	58.5 (PASCAL VOC07)	53.3 (PASCAL VOC12)	<0.1
SPPNet (2014) [79]	ZFNet	Optional	60.9 (PASCAL VOC07)		<1
Fast RCNN (2015) [43]	AlexNet VGGM VGG16	Optional	70.0 (PASCAL VOC07)	68.4(PASCAL VOC12)	<1
Faster RCNN (2015) [44]	ZFnet VGG	Optional	73.2 (PASCAL VOC07)	70.4 (PASCAL VOC12)	<5
RCNN⊖R (2015) [80]	ZFNet +SPP	Optional	59.7(PASCAL VOC07)		<5
RFCN (2016) [81]	ResNet101	Optional	80.5 (07+12) 83.6 (07+12+CO)	77.6 (07++12) 82.0 (07++12+CO)	<10
Mask RCNN (2017) [45]	ResNet101 ResNeXt101	Optional	50.3 (ResNeXt101) (COCO Dataset)		<5
YOLO (2016) [46]	GoogleNet	Constant	66.4 (PASCAL VOC07)	57.9 (PASCAL VOC12)	<25
YOLOv2 (2017) [47]	DarkNet	Constant	78.6 (PASCAL VOC07)	73.5 (PASCAL VOC12)	<50
SSD (2016) [49]	VGG16	Constant	76.8 (PASCAL VOC07)	74.9 (PASCAL VOC12)	<60
YOLOv3(2018) [48]	DarkNet	Variable	79.26 (PASCAL VOC07)	57,9 (MS COCO)	<155 (Fast YOLO)
YOLOv4(2020) [82]	CSPDarknet 53	Variable	65,7 (MS COCO)		<120

SSD [49] is a single layer successful detection method. It is both benefited from the ideas of YOLO and region proposal methods. By the way, multi-scale convolutional layers are extracted. It is faster (around 60 FPS, while it is lower than 50 FPS in YOLOv2) and more accurate than YOLOv2. It is used in many studies and researches and obtained successful results. Yet, it is not proper to say it is successful for small objects.

YOLOv3 [48], is quite faster than SSD (claimed to be 155 FPS) and lessened the weakness of YOLOv2 for detecting small objects. Even though approaching the claimed speed means sacrificing detection accuracy, it is quite accurate and fast compared to other single level models. The tests with the same datasets in the same processors produce highly superior results.

In 2020, YOLOv4 [82] has been announced. The usage of CSPDarknet53 improved the learning

capability of the network. A spatial pyramid pooling block was added to CSPDarknet53 to enhance the perceiving of the area and extract the best context features. Instead of the Feature Pyramid Networks (FPN) used in YOLOv3 for detecting objects, PANet is used in various detection levels as adding parameters method. It is possible to see that YOLOv4, drives YOLOv3's success up especially in the field of detection rate.

4. EVALUATION

The object detection methods are scrutinized to be able to understand which one is more suitable to use in a small mobile robot particularly a flying one. Since one of the constraints of mobile robots is carriage limits, it is substantially important to use a smaller developer board for determining surrounding objects. Although parallel graphic processors help to have a better computing ability, it is crucial to limit the demands from the developer board. Therefore, when looking over to methods one of the biggest criteria is the speed of the algorithm which slows down with the limited computing capabilities. The other criterion, of course, is how accurate it is over well-known datasets. Lastly, another important figure is input size which is to be bigger if it is needed to detect small objects. While it costs more computing power, for a route searching robot the far distant objects might be crucial.

For object classification, region proposal methods have offered the most accurate results and two-stage models have shown promising outcomes. However, in small mobile robots such as UAVs and rovers, it seems quite impossible to use them due to their detection speed. In a mobile robot, the algorithm needs to work in real-time with successful classifications. The very first attempts of one stage models were promising with detection speed but not satisfactory for their detection accuracy. However, in recent years it seems one stage models like YOLO, SSD and RetinaNet have made the detection and classification possible to use in mobile robots. These methods and variations did have nearly %80 detection accuracy with MS COCO and PASCAL VOC datasets. Even if this is not satisfying for critical decisions for a single image, it could be plausible for using real-time vision on a mobile robot.

A mobile robot equipped with a camera sensor displays the environment lively. When the robot is navigating, it approaches the objects from different angles and sometimes under various lightings. This is helpful to object detection if the method can't classify or falsely detects the object in the first frame. One of the disadvantages of recent fast algorithms, they have difficulties in detecting small-sized objects. Whereas it is quite advantageous making the neural network simpler and smaller, it is difficult to cope with small sized objects in the images. It is recommended to use a slower method or increase the input image size manually if sacrificing detection speed is possible.

Having a good detection rate by using only one convolutional network, YOLO appears to be the fastest algorithm among the current detection algorithms. As stated by Bochkovskiy et al. [82], when YOLOv4 is compared to its peers, it does not fall short in detection success while showing a clear better performance in object detection speed.

5. CONCLUSION

In this study, it is aimed to research object detection algorithms to be able to use for mobile robot navigation. Even if various computer vision methods have been used for robot navigation, there is no certain work on using the classification data in path planning as a crossing point. This is not so easy particularly with the limited computing capacity of small developer boards on mobile robots. To find a robust solution, it is needed to dig into detection methods for their computing power requirements, real-time detection speed and detection accuracy as well.

CNN and modified network models are popularly used by robotic researchers so as to determine what is surrounding the robot. These methods have been examined and their accuracy, speed and computational requirements have been compared in the context of the study. It can be inferred from the results that the latest algorithms show

dominance over older methods by detection speed. Among the contemporary methods, there are many superiorities, but the best method mostly depends on users' expectations.

For mobile robot navigation in an unknown environment, an algorithm running real-time on a developer board, though, it does not have the most precise detection rate, classifying various categories with a limited accuracy is satisfactory for using object detection in path planning. In the study, the results of methods have been obtained with standard datasets. It is a good way to compare algorithms, yet it cannot guarantee that one can take the exact same results in different environments. For this research, it was tried to specialize in the comparison of their usage in small mobile robots. Consequently, it is thought that the most appropriate method is YOLOv4 which demands small computational power but easily classifies crossing points like windows, doors and ladders.

It is probable that newer algorithms have already been proposed for object detection. Hopefully, they will produce more accurate results with less computational needs. While this superfast development is still in progress, it is planned to experience the latest algorithms in our flying robot during its journey for navigation according to detection information and it is quite possible to compare the methods after having experimental results.

Funding

The authors has no received any financial support for the research, authorship or publication of this study.

The Declaration of Conflict of Interest/ Common Interest

No conflict of interest or common interest has been declared by the authors.

Authors' Contribution

The authors (a PhD candidate and thesis advisor) contributed equally to the study in the context of thesis- "Mapping and Path Planning of an autonomous flying robot in unknown closed environment with object classification".

The Declaration of Ethics Committee Approval

This study does not require ethics committee permission or any special permission.

The Declaration of Research and Publication Ethics

The authors of the paper declare that they comply with the scientific, ethical and quotation rules of SAUJS in all processes of the paper and that they do not make any falsification on the data collected. In addition, they declare that Sakarya University Journal of Science and its editorial board have no responsibility for any ethical violations that may be encountered, and that this study has not been evaluated in any academic publication environment other than Sakarya University Journal of Science.

REFERENCES

[1] Hassani, Imen, Imen Maalej, and Chokri Rekik. "Robot path planning with avoiding obstacles in known environment using free segments and turning points algorithm." Mathematical Problems in Engineering 2018 (2018).

[2] O. Khatib, "Real-Time Obstacle Avoidance for Manipulators and Mobile Robots", International Journal of Robotics Research, 5(1):90-98, 1986.

[3] J.F.Canny and J.H. Reif, "New Lower Bound Techniques for Robot Motion Planning Problems", Proceedings of the 28th IEEE Symposium on Foundations of Computer Science, pp. 49-60, Los Angeles, CA, 1987.

[4] R. A. Jarvis, "Distance Transform Based Collision-Free Path Planning for Robot", Advanced Mobile Robots, World Scientific Publishing, pp.3-31, 1994.

[5] Ganganath, Nuwan, and Henry Leung. "Mobile robot localization using odometry and kinect sensor." 2012 IEEE International Conference on Emerging Signal Processing Applications. IEEE, 2012.

[6] Patle, B. K., et al. "A review: On path planning strategies for navigation of mobile robot." Defence Technology (2019).

[7] J. Leonard and H. Durrant-Whyte, "Simultaneous map building and localization for an autonomous mobile robot," Proceedings IROS '91:IEEE/RSJ International Workshop on Intelligent Robots and Systems '91, no. 91, pp. 1442–1447, 1991.

[8] C. Cadena, L. Carlone, H. Carrillo, Y. Latif, D. Scaramuzza, J. Neira, I. Reid, and J. Leonard, "Past, Present, and Future of Simultaneous Localization and Mapping: Toward the Robust-Perception Age," IEEE Transactions on Robotics, vol. 32, no. 6, pp. 1309–1332, 2016.

[9] Cruz, Nicolás, Kenzo Lobos-Tsunekawa, and Javier Ruiz-del-Solar. "Using convolutional neural networks in robots with limited computational resources: detecting NAO robots while playing soccer." Robot World Cup. Springer, Cham, 2017.

[10] Badue, Claudine, et al. "Self-driving cars: A survey." Expert Systems with Applications (2020): 113816.

[11] Seo, T., Jeon, Y., Park, C., & Kim, J. (2019). Survey on Glass And Façade-Cleaning Robots: Climbing Mechanisms, Cleaning Methods, and Applications. International Journal of Precision Engineering and Manufacturing-Green Technology, 6(2), 367-376.

[12] Jaradat, Mohammad Abdel Kareem, Mohammad H. Garibeh, and Eyad A. Feilat. "Autonomous mobile robot dynamic motion planning using hybrid fuzzy potential field." Soft Computing 16.1 (2012): 153-164.

[13] Rus, Daniela, Bruce Donald, and Jim Jennings. "Moving furniture with teams of autonomous robots." Proceedings 1995 IEEE/RSJ International Conference on Intelligent Robots and Systems. Human Robot Interaction and Cooperative Robots. Vol. 1. IEEE, 1995.

[14] Yao, P., Zhao, Z., & Zhu, Q. (2019). Path planning for autonomous underwater vehicles with simultaneous arrival in ocean environment. IEEE Systems Journal, 14(3), 3185-3193.

[15] M. P. Aghababa, "3D path planning for underwater vehicles using five evolutionary optimization algorithms avoiding static and energetic obstacles," Applied Ocean Research, vol. 38, pp. 48–62, 2012.

[16] R. Yue, J. Xiao, S. L. Joseph, and S. Wang, "Modeling and path planning of the city-climber robot part II: 3D path planning using mixed integer linear programming," in Proceedings of the IEEE International Conference on Robotics and Biomimetics (ROBIO '09), vol. 6, pp. 2391–2396, Guilin, China, December 2009.

[17] Shiri, H., Park, J., & Bennis, M. (2019, December). Massive autonomous UAV path planning: A neural network based mean-field game theoretic approach. In 2019 IEEE Global Communications Conference (GLOBECOM) (pp. 1-6). IEEE.

[18] Ropero, F., Muñoz, P., & R-Moreno, M. D. (2019). TERRA: A path planning algorithm for cooperative UGV–UAV exploration. Engineering Applications of Artificial Intelligence, 78, 260-272.

[19] Tunggal, Tatiya Padang, et al. "Pursuit algorithm for robot trash can based on fuzzy-cell decomposition."International Journal of Electrical and Computer Engineering 6.6 (2016): 2863.

[20] Ma, Xiaozhi, et al. "Conceptual framework and roadmap approach for integrating BIM into lifecycle project management."Journal of Management in Engineering 34.6 (2018): 05018011.

[21] J. Sun, J. Tang and S. Lao, "Collision Avoidance for Cooperative UAVs With Optimized Artificial Potential Field Algorithm," *IEEE Access*, vol. 5, pp. 18382-18390, 2017.

[22] Azzeddine Bakdi, Abdelfetah Hentout, Hakim Boutami, Abderraouf Maoudj, Ouarda Hachour, Brahim Bouzouia, Optimal path planning and execution for mobile robots using genetic algorithm and adaptive fuzzy-logic control, Robotics and Autonomous Systems, Volume 89, pp. 95-109, 2017.

[23] Aleksandr I. Panov, Konstantin S. Yakovlev, Roman Suvorov, Grid Path Planning with Deep Reinforcement Learning: Preliminary Results, Procedia Computer Science, Volume 123, pp. 347-353, 2018.

[24] Manh Duong Phung, Cong Hoang Quach, Tran Hiep Dinh, Quang Ha, Enhanced discrete particle swarm optimization path planning for UAV vision-based surface inspection, Automation in Construction, Volume 81, Pages 25-33, 2017.

[25] Liu, J., Yang, J., Liu, H. et al. An improved ant colony algorithm for robot path planning. Soft Comput 21, 5829–5839 (2017).

[26] Filipenko, Maksim, and Ilya Afanasyev. "Comparison of various slam systems for mobile robot in an indoor environment." 2018 International Conference on Intelligent Systems (IS). IEEE, 2018.

[27] C. Tao, Z. Gao, J. Yan, C. Li and G. Cui, "Indoor 3D Semantic Robot VSLAM Based on Mask Regional Convolutional Neural Network," in IEEE Access, vol. 8, pp. 52906-52916, 2020.

[28] Chen, L.; Jin, S.; Xia, Z. Towards a Robust Visual Place Recognition in Large-Scale vSLAM Scenarios Based on a Deep Distance Learning. Sensors, 2021.

[29] Szeliski, Richard. Computer vision: algorithms and applications. Springer Science & Business Media, 2010.

[30] Fischler, M., & Elschlager, R. (1973). The representation and matching of pictorial structures. IEEE Transactions on Computers, 100(1), 67–92.

[31] Mundy, J. (2006). Object recognition in the geometric era: A retrospective. In J. Ponce, M. Hebert, C. Schmid, & A. Zisserman (Eds.), Book toward category level object recognition (pp. 3–28). Berlin: Springer.

[32] Rowley, H., Baluja, S., & Kanade, T. (1998). Neural network based face detection. IEEE TPAMI, 20(1), 23–38.

[33] Osuna, E., Freund, R., & Girosit, F. (1997). Training support vector machines: An application to face detection. In CVPR (pp. 130–136).

[34] Viola, P., Jones, M. Rapid, "Object detection using a boosted cascade of simple features." CVPR, 1, 1–8, 2001.

[35] A. Krizhevsky, I. Sutskever, and G. E. Hinton. Imagenet classification with deep convolutional neural networks. Advances in neural information processing systems, pp. 1097–1105, 2012.

[36] Valueva, M.V.; Nagornov, N.N.; Lyakhov, P.A.; Valuev, G.V.; Chervyakov, N.I. (2020). "Application of the residue number system to reduce hardware costs of the convolutional neural network implementation". Mathematics and Computers in Simulation. Elsevier BV. 177: 232–243.

[37] Y. LeCun, B. Boser, J. S. Denker, D. Henderson, R. E.Howard, W. Hubbard, and L. D. Jackel. Backpropagation applied to

handwritten zip code recognition. Neural computation, 1(4):541–551, 1989.

[38] K. Fukushima. Neocognitron: A self-organizing neural network model for a mechanism of pattern recognition unaffected by shift in position. Biological Cybernetics, 36(4): 93-202, 1980.

[39] Y. LeCun, L. Bottou, Y. Bengio, and P. Haffner. Gradientbased learning applied to document recognition. Proceedings of the IEEE, 86(11):2278–2324, 1998.

[40] P. Sermanet, S. Chintala, and Y. LeCun. Convolutional neural networks applied to house numbers digit classification. In Pattern Recognition (ICPR), 2012 21st International Conference on, pages 3288–3291. IEEE, 2012.

[41] P. Sermanet and Y. LeCun. Traffic sign recognition with multi-scale convolutional networks. In Neural Networks (IJCNN), The 2011 International Joint Conference on, pages 2809–2813. IEEE, 2011.

[42] R. Girshick, J. Donahue, T. Darrell, J. Malik, "Rich Feature Hierarchies for Accurate Object Detection and Semantic Segmentation", 2014 IEEE Conference on Computer Vision and Pattern Recognition, pp. 580-587, 2014.

[43] R. Girshick, "Fast R-CNN IEEE International Conference on Computer Vision", IEEE, vol. 2015, pp. 1440-1448.

[44] S. Ren, K. He, R. Girshick, J. Sun, "Faster R-CNN: Towards Real-Time Object Detection with Region Proposal Networks", IEEE Transactions on Pattern Analysis and Machine Intelligence, vol. 39, no. 6, pp. 1137-1149, June 2017.

[45] K. He, G. Gkioxari, P. Dollár, R. Girshick, "Mask R-CNN", 2017 IEEE International Conference on Computer Vision (ICCV), pp. 2980-2988, 2017.

[46] J. Redmon, S. Divvala, R. Girshick, A. Farhadi, "You Only Look Once: Unified Real-Time Object Detection", 2016 IEEE Conference on Computer Vision and Pattern Recognition (CVPR), pp. 779-788, 2016.

[47] J. Redmon, A. Farhadi, "YOLO9000: Better Faster Stronger", 2017 IEEE Conference on Computer Vision and Pattern Recognition (CVPR), pp. 6517-6525, 2017.

[48] J Redmon, A. Farhadi, YOLOv3: An Incremental Improvement, 2018.

[49] W Liu, D Anguelov, D Erhan et al., SSD: Single Shot MultiBox Detector, pp. 21-37, 2015.

[50] C Y Fu, W Liu, A Ranga et al., DSSD: Deconvolutional Single Shot Detector, 2017.

[51] T Y Lin, P Goyal, R Girshick et al., "Focal Loss for Dense Object Detection", IEEE Transactions on Pattern Analysis & Machine Intelligence, no. 99, pp. 2999-3007, 2017.

[52] Huang, G., Liu, Z., Weinberger, K. Q., & van der Maaten, L. (2017a). Densely connected convolutional networks. In CVPR.

[53] Redmon, J., Divvala, S., Girshick, R., & Farhadi, A. (2016). You only look once: Unified, real time object detection. In CVPR (pp. 779–788).

[54] P. Sermanet, D. Eigen, X. Zhang, M. Mathieu, R. Fergus, and Y. LeCun. Overfeat: Integrated recognition, localization and detection using convolutional networks. arXiv preprint arXiv:1312.6229, 2013.

[55] Salman, Ahmad, et al. "Automatic fish detection in underwater videos by a deep neural network-based hybrid motion learning system." ICES Journal of Marine Science, 2020, pp. 1295-1307.

[56] Szegedy, C., Liu, W., Jia, Y., Sermanet, P., Reed, S., Anguelov, D., Erhan, D., Vanhoucke, V., & Rabinovich, A. (2015). Going deeper with convolutions. In CVPR (pp. 1–9).

[57] He, K., Zhang, X., Ren, S., & Sun, J. (2016). Deep residual learning for image recognition. In CVPR (pp. 770–778).

[58] Y. Jia, E. Shelhamer, J. Donahue, S. Karayev, J. Long, R. Girshick, S. Guadarrama, and T. Darrell. Caffe: Convolutional architecture for fast feature embedding. arXiv preprint arXiv:1408.5093, 2014.

[59] M. Abadi, A. Agarwal, P. Barham, E. Brevdo, Z. Chen, C. Citro, G. S. Corrado, A. Davis, J. Dean, M. Devin et al., "Tensorflow: Largescale machine learning on heterogeneous systems, 2015," Software available from tensorflow. org, vol. 1, 2015.

[60] D. Yu, A. Eversole, M. Seltzer, K. Yao, Z. Huang, B. Guenter, O. Kuchaiev, Y. Zhang, F. Seide, H. Wang et al., "An introduction to computational networks and the computational network toolkit," Technical report, Tech. Rep. MSR, Microsoft Research, 2014, 2014. research. microsoft. com/apps/pubs, Tech. Rep., 2014.

[61] R. Collobert, K. Kavukcuoglu, and C. Farabet, "Torch7: A matlablike environment for machine learning," in BigLearn, NIPS Workshop, no. EPFL-CONF-192376, 2011.

[62] O. Vinyals, A. Toshev, S. Bengio, and D. Erhan. Show and tell: A neural image caption generator. arXiv preprint arXiv:1411.4555, 2014.

[63] A. Karpathy and L. Fei-Fei. Deep visual-semantic alignments for generating image descriptions. arXiv preprint arXiv:1412.2306, 2014.

[64] Moghadam, Peyman, Wijerupage Sardha Wijesoma, and Dong Jun Feng. "Improving path planning and mapping based on stereo vision and lidar." 2008 10th International Conference on Control, Automation, Robotics and Vision. IEEE, 2008.

[65] Sabe, Kohtaro, et al. "Obstacle avoidance and path planning for humanoid robots using stereo vision." IEEE International Conference on Robotics and Automation, 2004. Proceedings. ICRA'04. 2004. Vol. 1. IEEE, 2004.

[66] PTGrey, 2004. Point grey research inc. http://www.ptgrey.com/

[67] Pomerleau, Dean A. "Efficient training of artificial neural networks for autonomous navigation." Neural computation 3.1 (1991): 88-97.

[68] Ran, Lingyan, et al. "Convolutional neural network-based robot navigation using uncalibrated spherical images." Sensors 17.6 (2017): 1341.

[69] Hadsell, R.; Sermanet, P.; Ben, J.; Erkan, A.; Scoffier, M.; Kavukcuoglu, K.; Muller, U.; LeCun, Y. Learning long-range vision for autonomous off-road driving. J. Field Robot. 2009, 26, 120–144.

[70] Zoto, J., Musci, M. A., Khaliq, A., Chiaberge, M., & Aicardi, I. (2019, June). Automatic path planning for unmanned ground vehicle using uav imagery. In International Conference on Robotics in Alpe-Adria Danube Region (pp. 223-230). Springer, Cham.

[71] Tang, Y. "Deep Learning using Linear Support Vector Machines." arXiv: Learning (2013):

[72] Everingham, M., Gool, L. V., Williams, C., Winn, J., & Zisserman, A. (2010). The pascal visual object classes (VOC) challenge. IJCV, 88(2), 303–338.

[73] Everingham, M., Eslami, S., Gool, L. V., Williams, C., Winn, J., & Zisserman, A. (2015). The pascal visual object classes

challenge: A retrospective. IJCV, 111(1), 98–136.

[74] Lin, T., Maire, M., Belongie, S., Hays, J., Perona, P., Ramanan, D., Dollár, P., & Zitnick, L. (2014). Microsoft COCO: Common objects in context. In ECCV (pp. 740–755).

[75] Deng, J., Dong, W., Socher, R., Li, L., Li, K., & Li, F. (2009). ImageNet: A large scale hierarchical image database. In CVPR (pp. 248–255).

[76] Kuznetsova, Alina, et al. "The open images dataset v4." International Journal of Computer Vision (2020): 1-26.

[77] Fei-Fei, Li, Rob Fergus, and Pietro Perona. "Learning generative visual models from few training examples: An incremental bayesian approach tested on 101 object categories." 2004 conference on computer vision and pattern recognition workshop. IEEE, 2004.

[78] Geiger, Andreas, Philip Lenz, and Raquel Urtasun. "Are we ready for autonomous driving? the kitti vision benchmark suite." 2012 IEEE Conference on Computer Vision and Pattern Recognition. IEEE, 2012.

[79] He, K., Zhang, X., Ren, S., & Sun, J. (2014). Spatial pyramid pooling in deep convolutional networks for visual recognition. In ECCV (pp. 346–361).

[80] Lenc, K., & Vedaldi, A. (2015). R-CNN minus R. In BMVC15.

[81] Dai, J., Li, Y., He, K., & Sun, J. (2016c). RFCN: Object detection via region based fully convolutional networks. In NIPS (pp. 379–387).

[82] Bochkovskiy, Alexey, Chien-Yao Wang, and Hong-Yuan Mark Liao. "YOLOv4: Optimal Speed and Accuracy of Object Detection." arXiv preprint arXiv:2004.10934 (2020).

SAKARYA ÜNİVERSİTESİ
FEN BİLİMLERİ ENSTİTÜSÜ DERGİSİ

Sakarya University Journal of Science
SAUJS

e-ISSN 2147-835X | Period Bimonthly | Founded: 1997 | Publisher Sakarya University |
http://www.saujs.sakarya.edu.tr/en/

Title: Using Physical Parameters for Phase Prediction of Multi-Component Alloys by the Help of TensorFlow Machine Learning with Limited Data

Authors: Kağan ŞARLAR

Recieved: 2020-12-14 15:57:44

Accepted: 2021-04-28 14:07:42

Article Type: Research Article

Volume: 25
Issue: 3
Month: June
Year: 2021
Pages: 766-773

How to cite
Kağan ŞARLAR; (2021), Using Physical Parameters for Phase Prediction of Multi-Component Alloys by the Help of TensorFlow Machine Learning with Limited Data. Sakarya University Journal of Science, 25(3), 766-773, DOI: https://doi.org/10.16984/saufenbilder.840548
Access link
http://www.saujs.sakarya.edu.tr/en/pub/issue/62736/840548

Sakarya University Journal of Science 25(3), 766-773, 2021

Using Physical Parameters for Phase Prediction of Multi-Component Alloys by the Help of TensorFlow Machine Learning with Limited Data

Kağan ŞARLAR*[1]

Abstract

In recent years developing new material and compounds have become more important because of the community's needs. Material scientist and physicist great effort make significant changes in daily life. But nowadays it is important to make these changes in a short time. In this point of view, artificial intelligence and machine learning gives the scientist a great opportunity to predict the properties of new compounds before produced in the laboratory. In this study, the valence electron concentration (VEC), atomic size difference (δ), enthalpy of mixing (ΔH_{mix}), the entropy of mixing (ΔS_{mix}) and electronegativity difference ($\Delta\chi$) values are calculated for each alloy and a dataset has been created. We use gradient boosted trees machine learning method with TensorFlow artificial intelligence program to explore phase selection using an experimental dataset consisting of 118 multi-component alloy system. We divide the whole dataset into two portions with training and evaluate dataset. The training dataset contains 73 and evaluate dataset contains 45 multi-component alloy systems. We also show three of the predicted multi-component alloy system to examine which physical values are used predominantly during prediction. We look at the Receiver Operating Characteristic (ROC) of the results, which will give us a better idea of the tradeoff between the true positive rate and false positive rate. It has been observed that this learning method predicts the structure correctly in 95% of the results with limited data.

Keywords: Multicomponent alloy, Machine learning, TensorFlow, Artificial intelligence.

*Corresponding author: kagansarlar@kmu.edu.tr
[1]Physics Department, Kamil Ozdag Faculty of Sciences, Karamanoglu Mehmetbey University, Yunus Emre Campus, 70100 Karaman,Turkey
Email:kagansarlar@kmu.edu.tr
ORCID: https://orcid.org/0000-0002-8871-2357

1. INTRODUCTION

Since ancient times, humanity has discovered and developed new materials for the development of society [1]. In recent years, these materials cannot meet the needs of developing technology. Therefore, the development of new generation materials is of great importance for industrial and technological applications [2,3]. Multi-component alloys offer a wide range of functional materials to be produced [4]. But scientists have to struggle with the rapid change of needs and long laboratory studies. Today, machine learning is used extensively in many other areas such as fraud prevention, risk analysis, better customer insight, and more complex solutions such as improving medical science [5]. Artificial Intelligence is the general name of the technology that tries to imitate human intelligence. Machine learning is also the application of computational methods that support this technology [6]. While machine learning imitates human intelligence, unlike other applications, it is a set of algorithms which do not need rules that we will interpret and define [7,8]. If we explain how to learn machine learning by comparing it with human learning, when a person learns new information, he/she does not need someone else to load this information into his/her brain. Similarly, in machine learning, the rules are not given beforehand (loading information to the brain), only information-containing datasets are given, and machine learning performs the desired task by understanding these datasets. [6]. TensorFlow is a free and open-source software library for data flow and differentiable programming in a variety of tasks [9]. It is a symbolic math library and is also used for machine learning applications such as neural networks. It is used for both research and production at Google. TensorFlow has been developed by the Google Brain team for internal Google use. It was released for free as open-source under the Apache License 2.0 on November 9, 2015.

Density functional theory (DFT) calculations are a technique used to predict the phase for multi-component alloys. However, to simulate the DFT method, computers must operate for a very long time and have large simulation cells for each alloy. Also, the uncertainties in treating the d orbitals of transition-metal atoms that are often components of multi-component alloys make DFT calculations impractical [10].

Parametric approaches are widely used to predict the phase of multi-component alloys. Guo et al. proposed that the phase selection of multi-component is determined by parameters such as the valence electron concentration (VEC), structure factor (δ), enthalpy of mixing (ΔH_{mix}), the entropy of mixing (ΔS_{mix}) and electronegativity difference ($\Delta\chi$). Unlike the parametric approaches, machine learning (ML) provides a significant tool that offers insight from given data of relevant properties of alloys. Machine learning models, which give fast and accurate results, have been used increasingly in material design in recent years [11-14].

In this study, the valence electron concentration (VEC), structure factor (δ), enthalpy of mixing (ΔH_{mix}), the entropy of mixing (ΔS_{mix}) and electronegativity difference ($\Delta\chi$) values are calculated for each alloy and a dataset has been created. This dataset was trained by machine learning with Gradient Boosted Trees and it was predicted which amorphous or solid solution phase structure would be formed. Data collection is a long process. In this study, it was also aimed to make better estimation with fewer data by using the TensorFlow library with Gradient boosted trees method.

2. METHODS

2.1. Data collection and analysis

We used the data from Guo's phase estimation article [15]. The given dataset contains 118 entries. However, it should not be forgotten that we aim to make a phase estimation with a small amount of data. In Guo's study different physical parameters are used for predicting the alloys' phase amorphous or not. In this study phase estimation was made based on the five physical properties given below as input. Guo et al. [16-18] have used three parameters which are atomic size difference (δ), mixing enthalpy (ΔH_{mix}) and

mixing entropy (ΔS_{mix}). The δ, ΔH_{mix} and ΔS_{mix} which are defined as follows:

$$\delta = 100\sqrt{\sum_{i=1}^{N} c_i(1-r_i/\bar{r})^2} \quad (1)$$

$$\Delta H_{mix} = \sum_{i=1, i\neq j}^{n} \Omega_{ij} c_i c_j \quad (2)$$

$$\Delta S_{mix} = -R\sum_{i=1}^{N} c_i \ln c_i \quad (3)$$

where *N* is the number of components of the alloy, c_i is the atomic percentage of element *i* in the alloy. $\bar{r}(=\sum_{i=1}^{n} c_i r_i)$, is the average atomic radius. r_i is the atomic radius which found for all elements in ref [15]. $\Omega_{ij}(=\Delta H^{mix}{}_{AB})$ is the regular melt-inter action parameter between i^{th} and j^{th} elements, $\Delta H^{mix}{}_{AB}$ is the heat of mixing [19], and *R* is the gas constant.

Besides these values, valence electron concentration and electronegativity difference were added to the data to diversify learning. Electronegativity difference is defined as follows:

$$\Delta\chi = \sqrt{\sum_{i=1}^{n} C_i(\chi_i - \bar{\chi})^2} \quad (4)$$

where $\bar{\chi} = \sum_{i=1}^{n} C_i \chi_i$, χ_i is the Pauling electronegativity for the *i*th element.

Valance electron concentration (VEC) is calculated by

$$VEC = \sum_{i=1}^{n} C_i (VEC)_i \quad (5)$$

where $(VEC)_i$ is the VEC for the *i*th element.

Before transferring the data of 118 multi-component alloy to machine learning, we divide the whole dataset into two portions with training and evaluate dataset. The training dataset contains 73 and evaluate dataset contains 45 multi-component alloy systems. And statistical data analysis Pearson correlation coefficients were performed overall 118 multi-component alloy system. Pearson's correlation was calculated for each pair of features. It has been observed that there is no strong correlation (P~1.0) between any two features. As a result, we suggest that these five features can be used in machine learning. The data in this work can also be found at https://github.com/kaansarlar/Gradientboostedtrees-article-data.

2.2. Gradient Boosted Trees

Gradient Boosted Trees is a machine learning technique, for regression and classification problems [20]. Boosting is a method of transforming a weak learner into a strong learner [21]. It does this gradually with iterations. Gradient Boosted Trees are calculated in four steps. First, the loss function is defined as $L(y_i, F(x))$. y_i is observed value and $F(x)$ is the predicted value. The loss function is a measure of how well the coefficients of the model fit the underlying data. In step two, the constant variable is determined. $F_0(x) = \arg\min_{\gamma} \sum_{i=1}^{n} L(y_i, \gamma)$ In the formula, the value in sigma is the loss function. γ is the predicted value. The loss function will be summed up for all observations and the minimum state of its value will be found. For this, the loss function is derivatized, the values added up and set to zero. As a result, there is the initial leaf. This value is equal to the average of all values in the target variable. Step three takes place in 4 stages and is a cycle that will be applied to all trees. Errors are calculated based on the previous estimate.

$$r_{im} = -\left[\frac{\partial L(y_i, F(x_i))}{\partial F(x_i)}\right]_{F(x)=F_{m-1}(x)} \quad i = 1,.....,n$$ In the formula, r means residual. i observation number, m denotes the number of the established tree. It is a parenthetically differentiated loss function. When looked outside the parentheses, it is seen that the value of F (x) represents the output of the previous tree. With this formula, residues are calculated for all observations. Step four, a

decision tree is created for residuals and the value of each leaf is found. $\gamma_{jm} = \arg\min_{\gamma} \sum_{x_i \in R_{ij}} L(y_i, F_{m-1}(x_i) + \gamma) \; j = 1 \ldots J_m$. The formula minimizes the error for each leaf. In the same way, the derivation of the loss function is taken and the values are summed and equalled to the class. The number that comes out is the value of the leaf. Estimates are made for each observation. $F_m(x) = F_{m-1}(x) + \nu \sum_{j=1}^{J_m} \gamma_{jm} I(x \in R_{jm})$ when the formula is examined, it is seen that F (x) = results of the previous tree + learning rate * new tree. The cycle will continue like this. The flow chart of gradient boosted trees is shown in Figure 1.

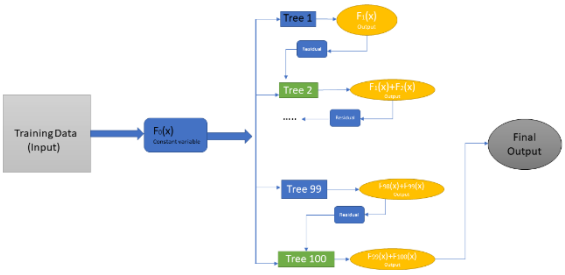

Figure 1 Flow chart of the gradient boosted trees

3. RESULTS AND DISCUSSION

All code is written in python and TensorFlow's estimator is used. First, the data is divided into two parts. Firstly, 73 data were taught to the model as train data. The model was trained on the train data set. Then, the trained model was shown in the Evaluate data set with 45 data, and it was asked to predict whether the alloys were amorphous or solid solutions.

Table 1 Results of the model after processing the trained data series.

auc	0.951428
auc_precision_recall	0.987701
average_loss	0.377974
label/mean	0.777778
loss	0.377974
precision	0.968750
prediction/mean	0.691700
recall	0.885714
global_step	100.000000

Table 1 shows the models' result after training. Here auc is the percentage of correct number of classifications, auc_precision_recall is the percentage of relevant instances, among the retrieved instances, that have been retrieved over the total amount of relevant instances, average_loss is the average value of loss function given the current batches, the label/mean is the mean of the value labels, the loss is current value of the loss, precision is how many of the values we guess as positive are actually positive, prediction/mean is the value of the corresponding predictions. (two classes could give you a value between 0 and 1), recall computes the recall of the predictions with respect to the labels, global_step is the number of iterations. The models' prediction accuracy is 95 %. In figure 2. we examined which physical values are used predominantly during the prediction of the alloy $Al_{0.8}CrCu_{1.5}FeMnNi$ in solid solution form. Here, alloy $Al_{0.8}CrCu_{1.5}FeMnNi$ is chosen at random. The prediction of our model for this alloy is 97%

for the solid solution and 3% for amorphous structure. To avoid any errors in the program, the d symbol is used instead of the Δ symbol. As seen in this prediction, the entropy of mixing and enthalpy of mixing contributed more than other physical parameters.

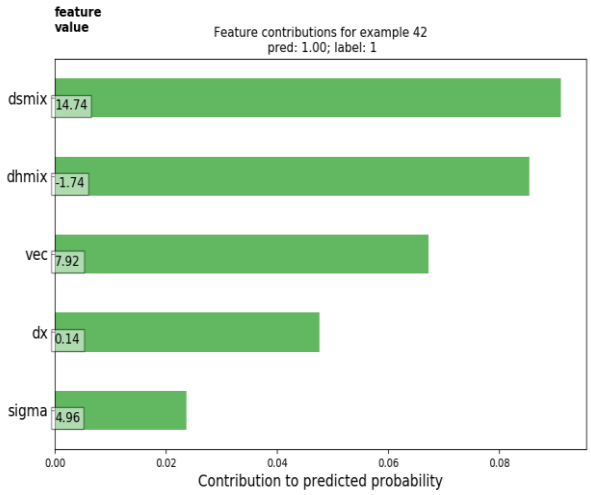

Figure 2 Contribution of physical parameters in the prediction of the phase structure of $Al_{0.8}CrCu_{1.5}FeMnNi$.

Figure 3 shows the prediction results of the alloy $Zr_{41.2}Ti_{13.8}Cu_{12.5}Ni_{10}Be_{22.5}$ using the gradient boosted trees model. The prediction of our model for this alloy is 2% for the solid solution and 98% for amorphous structure.

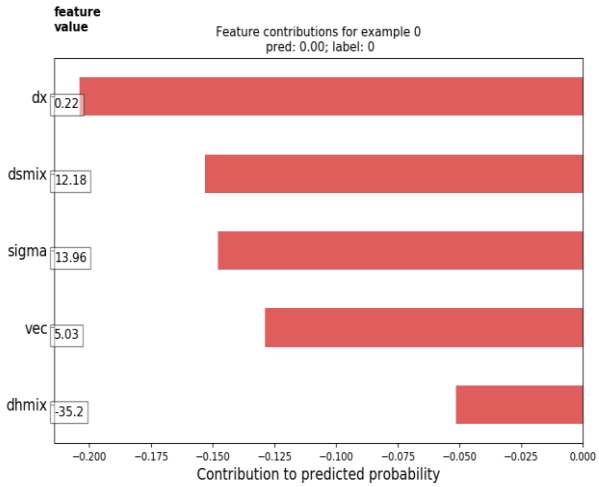

Figure 3 Contribution of physical parameters in the prediction of the phase structure of $Zr_{41.2}Ti_{13.8}Cu_{12.5}Ni_{10}Be_{22.5}$.

As seen in this prediction, electronegativity difference and entropy of mixing contributed more than other physical parameters. When Figure 2 and Figure 3 were compared, the model perceived positive contributions of physical properties as the solid solution and negative contributions as the amorphous phase. Not all predictions we make for multi-alloy systems have such high predictions. Figures 4 shows an example for the amorphous phase.

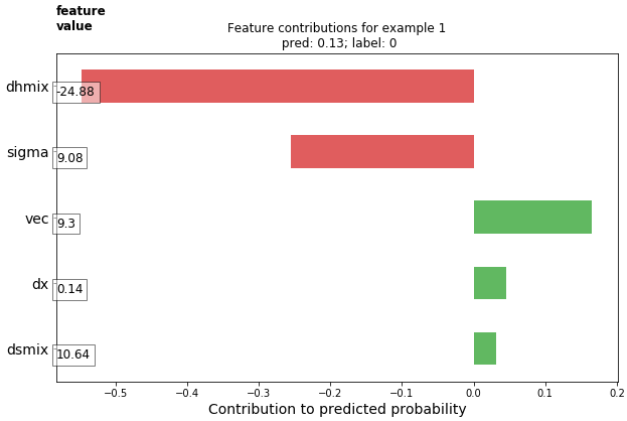

Figure 4 Contribution of physical parameters in the prediction of the phase structure of $Pd_{40}Cu_{30}Ni_{10}P_{20}$.

In Figure 4 the calculated probabilities for the $Pd_{40}Cu_{30}Ni_{10}P_{20}$. alloy is 87% for the amorphous phase and 13% for the solid solution, respectively.

The accuracy of the phase estimation results of the $Al_{0.8}CrCu_{1.5}FeMnNi$, $Zr_{41.2}Ti_{13.8}Cu_{12.5}Ni_{10}Be_{22.5}$, $Pd_{40}Cu_{30}Ni_{10}P_{20}$ alloy systems shown as an example out of 45 samples. In Table-2, the experimental results of these analysed alloy systems and machine learning phase predictions are compared.

Table 2 Comparison of machine learning results with experimental results.

Alloy System	**Experimental Phase**	**Machine Learning estimation (Solid-State Phase)**	**Machine Learning estimation (Amorphous Phase)**	**References**

$Al_{0.8}CrCu_{1.5}FeMnNi$	Solid-State	97 %	3 %	[15]
$Zr_{41.2}Ti_{13.8}Cu_{12.5}Ni_{10}Be_{22.5}$	Amorphous Phase	2 %	98 %	[15]
$Pd_{40}Cu_{30}Ni_{10}P_{20}$	Amorphous Phase	13 %	87 %	[15]

The Receiver Operating Characteristic (ROC) curve arises from the ratio of sensitivity to precision in cases where the discrimination threshold differs in binary classification systems. ROC can be simply expressed as the fraction of true positives versus false positives. As with any classification process, the methods strive to strike the balance between precision (the ability to eliminate false positives) and sensitivity (the ability to detect correct positives). In figure 5 we can also look at the ROC of the results, which will give us a better idea of the tradeoff between the true positive rate and false-positive rate.

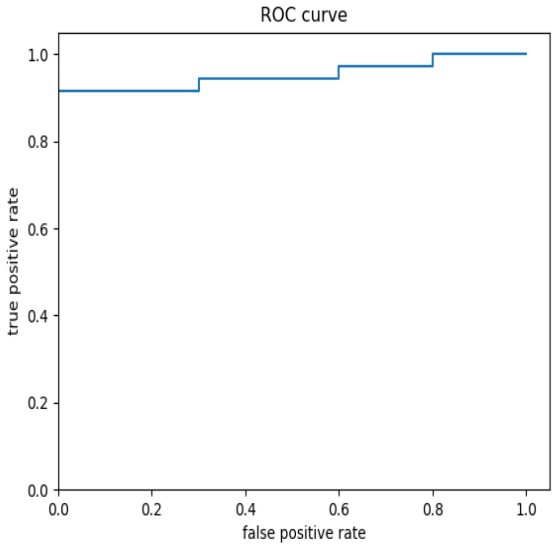

Figure 5 Receiver Operating Characteristic curve

4. CONCLUSION

In this study, the phase prediction of multi-component alloys has been tried to be made with limited data. The machine learning method chosen for prediction is Gradient boosted trees. The accuracy of the method is 95%. When the contribution of each physical property is examined, it is seen that the additive amounts for each alloy are different. With this method, it can be predicted in which phase group the alloy to be produced will be, before starting the experimental work, with a highly accurate prediction. Thus, a preliminary study can be done before the experiment is carried out. We expect this work to guide the design and phase prediction of new multi-component alloys.

Acknowledgments

The author would like to thank the SAUJS editors and reviewers who reviewed the study.

Funding

The author received no financial support for the research, authorship, and/or publication of this paper.

The Declaration of Conflict of Interest/ Common Interest

No conflict of interest or common interest has been declared by the author.

The Declaration of Ethics Committee Approval

This study does not require ethics committee permission or any special permission.

The Declaration of Research and Publication Ethics

The authors of the paper declare that they comply with the scientific, ethical and quotation rules of SAUJS in all processes of the paper and that they do not make any falsification on the data collected. In addition, they declare that Sakarya University Journal of Science and its editorial board have no responsibility for any ethical violations that may be encountered, and that this study has not been evaluated in any academic publication environment other than Sakarya University Journal of Science.

REFERENCES

[1] P. F. Pagoria, G. S. Lee, A. R. Mitchell, and R. D. Schmidt, 'A review of energetic materials synthesis', *Thermochim. Acta*, vol. 384, no. 1–2, pp. 187–204, 2002.

[2] M. H. Phan and S. C. Yu, 'Review of the magnetocaloric effect in manganite materials', *J. Magn. Magn. Mater.*, vol. 308, no. 2, pp. 325–340, 2007.

[3] M. N. Gueye, A. Carella, J. Faure-Vincent, R. Demadrille, and J. P. Simonato, 'Progress in understanding structure and transport properties of PEDOT-based materials: A critical review', *Prog. Mater. Sci.*, vol. 108, no. November 2019, p. 100616, 2020.

[4] R. Shan, J. Han, J. Gu, H. Yuan, B. Luo, and Y. Chen, 'A review of recent developments in catalytic applications of biochar-based materials', *Resour. Conserv. Recycl.*, vol. 162, no. June, p. 105036, 2020.

[5] E. Glikson and A. W. Woolley, 'Human trust in artificial intelligence: Review of empirical research', *Acad. Manag. Ann.*, vol. 14, no. 2, pp. 627–660, 2020.

[6] C. Chen, Y. Zuo, W. Ye, X. Li, Z. Deng, and S. P. Ong, 'A Critical Review of Machine Learning of Energy Materials', *Adv. Energy Mater.*, vol. 10, no. 8, pp. 1–36, 2020.

[7] S. Lalmuanawma, J. Hussain, and L. Chhakchhuak, 'Applications of machine learning and artificial intelligence for Covid-19 (SARS-CoV-2) pandemic: A review', *Chaos, Solitons and Fractals*, vol. 139, p. 110059, 2020.

[8] I. Z. A. D. P. No and W. Naudé, 'DISCUSSION PAPER SERIES Artificial Intelligence against COVID-19 : An Early Review Artificial Intelligence against COVID-19 : An Early Review', no. 13110, 2020.

[9] 'Abadi, Mart'in, Barham, P., Chen, J., Chen, Z., Davis, A., Dean, J, "Tensorflow: A system for large-scale machine learning." In 12th $USENIX$ Symposium on Operating Systems Design and Implementation ($OSDI$ 16) pp. 265–283, 2016

[10] R. Feng, P. K. Liaw, M. C. Gao, and M. Widom, 'First-principles prediction of high-entropy-alloy stability', *npj Comput. Mater.*, vol. 3, no. 1, p. 50, Dec. 2017.

[11] M. Rupp, A. Tkatchenko, K. R. Müller, and O. A. Von Lilienfeld, 'Fast and accurate modeling of molecular atomization energies with machine learning', *Phys. Rev. Lett.*, vol. 108, no. 5, pp. 1–5, 2012.

[12] Y. M. Zhang, S. Yang, and J. R. G. Evans, 'Revisiting Hume-Rothery's Rules with artificial neural networks', *Acta Mater.*, vol. 56, no. 5, pp. 1094–1105, 2008.

[13] L. Ward, A. Agrawal, A. Choudhary, and C. Wolverton, 'A general-purpose machine learning framework for predicting properties of inorganic materials', *npj Comput. Mater.*, vol. 2, no. July, pp. 1–7, 2016.

[14] B. Meredig and C. Wolverton, 'A hybrid computational-experimental approach for automated crystal structure solution', *Nat. Mater.*, vol. 12, no. 2, pp. 123–127, 2013.

[15] S. Guo and C. T. Liu, 'Phase stability in high entropy alloys: Formation of solid-solution phase or amorphous phase', *Prog. Nat. Sci. Mater. Int.*, vol. 21, no. 6, pp. 433–446, 2011.

[16] S. Guo, C. Ng, J. Lu, and C. T. Liu, 'Effect of valence electron concentration on stability of fcc or bcc phase in high entropy alloys', *J. Appl. Phys.*, vol. 109, no. 10, 2011.

[17] S. Guo, 'Phase selection rules for cast high entropy alloys: an overview', *Mater. Sci. Technol.*, vol. 31, no. 10, pp. 1223–1230,

2015.

[18] Z. Wang, S. Guo, and C. T. Liu, 'Phase Selection in High-Entropy Alloys: From Nonequilibrium to Equilibrium', *JOM*, vol. 66, no. 10, pp. 1966–1972, Oct. 2014.

[19] A. Takeuchi and A. Inoue, 'Classification of Bulk Metallic Glasses by Atomic Size Difference, Heat of Mixing and Period of Constituent Elements and Its Application to Characterization of the Main Alloying Element', *Mater. Trans.*, vol. 46, no. 12, pp. 2817–2829, 2006.

[20] G. Ke *et al.*, 'LightGBM: A highly efficient gradient boosting decision tree', *Adv. Neural Inf. Process. Syst.*, vol. 2017-Decem, no. Nips, pp. 3147–3155, 2017.

[21] A. J. Ferreira and M. A. T. Figueiredo, 'Boosting Algorithms: A Review of Methods, Theory, and Applications', in *Ensemble Machine Learning: Methods and Applications*, C. Zhang and Y. Ma, Eds. Boston, MA: Springer US, 2012, pp. 35–85.

SAKARYA ÜNİVERSİTESİ
FEN BİLİMLERİ ENSTİTÜSÜ DERGİSİ

Sakarya University Journal of Science
SAUJS

e-ISSN 2147-835X | Period Bimonthly | Founded: 1997 | Publisher Sakarya University |
http://www.saujs.sakarya.edu.tr/en/

Title: Optimization of the Green Synthesis of Silver Nanoparticle with Box-Behnken Design: Using Aloe Vera Plant Extract as a Reduction Agent

Authors: Nazan GÖKŞEN TOSUN, Özlem KAPLAN

Recieved: 2020-10-08 13:17:34

Accepted: 2021-05-02 13:35:56

Article Type: Research Article

Volume: 25
Issue: 3
Month: June
Year: 2021
Pages: 774-787

How to cite
Nazan GÖKŞEN TOSUN, Özlem KAPLAN; (2021), Optimization of the Green Synthesis of Silver Nanoparticle with Box-Behnken Design: Using Aloe Vera Plant Extract as a Reduction Agent. Sakarya University Journal of Science, 25(3), 774-787, DOI: https://doi.org/10.16984/saufenbilder.806916
Access link
http://www.saujs.sakarya.edu.tr/en/pub/issue/62736/806916

Sakarya University Journal of Science 25(3), 774-787, 2021

Optimization of the Green Synthesis of Silver Nanoparticle with Box-Behnken Design: Using Aloe Vera Plant Extract as a Reduction Agent

Nazan GÖKŞEN TOSUN*[1] Özlem KAPLAN[2]

Abstract

Nowadays, many of plants are used as a reduction agent in biosynthesis of silver nanoparticles. In this study, green synthesis of silver nanoparticles (AgNPs) was aimed to optimize with Box-Behnken design (BBD). *Aloe vera* plant extract was utilized as a reduction agent as it is the famous natural product in field of cosmetic and skin health care. The synthesized AgNPs using *Aloe vera* plant extract solution was optimized by Box-Behnken design using the influence of different factors such as microwave power, time, $AgNO_3$ concentration, and ratio of volume of *Aloe vera* plant extract solution to volume of $AgNO_3$ and the percentage yield of particle formation as a response. Quadratic polynomial model was used to carry out mathematical modelling and response surface analysis was performed to determine the independent variable-response relationship. The optimized silver nanoparticles were characterized using FTIR spectroscopy and UV-VIS spectrophotometry. The antibacterial activity of optimized AgNPs was determined by testing against Gram positive (*Staphylococcus aureus*, *Enterococcus faecalis*) and Gram negative (*Pseudomonas aeruginosa and Klebsiella pneumoniae*) bacteria. Briefly, the trials interpreted successful synthesis of the AgNPs along with comprehension of the related factors affecting their quality characteristics and remarkably developed antibacterial activity as helpful impact.

Keywords: silver nanoparticles, Box-Behnken design, *Aloe vera* plant

1. INTRODUCTION

Recently, nanoparticle-based studies are sustained widely due to their potential applications, especially in the interdisciplinary sciences and nanotechnology field [1]. The synthesis of nanoparticles can be performed by physical, chemical and biological methods. All these methods have advantages and disadvantages. For example, chemical methods are expensive because of using special chemical agents and very toxic [2]. The physical methods could be required high temperature or pressure.

On the other hand, plant extracts used in biological methods have low toxicity or no and the reaction can realize at room temperature. Therefore, the biological methods can be applied in microbiology because the plant extracts are safe, eco-friendly and cheap [3]. In this respect,

*Corresponding author: nazan_goksen@hotmail.com
[1]Gaziosmapasa University, Department of Biomaterial and Tissue Engineering, Tokat, Turkey.
ORCID: https://orcid.org/0000-0001-5269-1067
[2]İstanbul University, Department of Molecular Biology and Genetics İstanbul, Turkey.
E-Mail: ozlem.kaplan@istanbul.edu.tr
ORCID: https://orcid.org/ 0000-0002-3052-4556

numerous plant extracts have been utilized as a biological reduction agent in the synthesis of nanoparticles [4–7]. As an antimicrobial agent, the AgNPs are utilized important applications like in cosmetics, water purification, and medical diagnostic and textile [8]. The AgNPs are significant biomaterials due to their antimicrobial activities because they can help overcome antimicrobial resistance [9].

Aloe vera is botanically known as *Aloe barbadense miller* and it has been frequently used in cosmetic as a natural product for years [10]. *Aloe vera* plant was studied also wound healing and burn healing and health of skin[11–13]. Like many of other plants, *Aloe vera* has been utilized in the green synthesis of AgNPs as biological reagent because of its antimicrobial activity [14,15].

In this research, optimizing of green synthesis of AgNPs using *Aloe vera* plant extract solution was aimed. These nanoparticles are known to have been synthesized from literature before, but the synthesis procedure has not been optimized using any program. In the literature, some researchers have reported using the BBD to optimize the synthesis of AgNPs [16]. The BBD has been widely used in many sciences of fields like formulation development and analytical chemistry [17–20]. We decided to optimize the synthesis of AgNPs utilizing BBD. Therefore, in this experimental study, effective parameters for optimization of AgNPs using *Aloe vera* extract solution were identified and AgNPs were optimized, then the results of AgNPs were comprehensively given to support the theory of the study based on the green synthesis of AgNPs.

2. METHODS

2.1. Materials

Aloe vera plant was obtained from Gaziosmanpasa University Faculty of Agriculture (Tokat, Turkey). Silver nitrate ($AgNO_3$) (Carlo Erbaa), sodium hydroxide (NaOH), the filter discs and nutrient agar were purchased from Sigma Aldrich Chemicals (Istanbul, Turkey). Deionized water was used in all stages from the synthesis of the nanoparticle to its purification. The sterilized water was used for antimicrobial studies.

2.2. Preparation of *Aloe vera* Extract

Aloe vera plant was washed with deionized water and a certain amount (5 g) of washed *Aloe vera* were boiled in 50 mL of distilled water for 20 minutes at 60 °C. After that the extract was filtered to remove leaves and the filtrate was stored at 4 °C.

2.3. Optimization of the AgNPs

The optimization of AgNPs was realized via BBD by using Design Expert® ver. 12.0 software. Four effective factors including power of microwave, time, $AgNO_3$ concentration and ratio of volume of *Aloe vera* leaves extract solution to volume of $AgNO_3$ were chosen as independent factors for optimization at three different levels which were changed dependent of the factors. A total of 29 experiments calculated by the design were recommended as shown in Table 1. Synthesized AgNPs of absorbance value were calculated as % yield at range of 350-450 nm and these values were placed in BBD as responses. After placing the data in the BBD, mathematical modeling was created to evaluate the results. Quadratic model was determined by ANOVA along with other parameters such as correlation coefficient (r2), adjusted r2, predicted r2, and predicted residual squares. Ideal circumstances for synthesis of AgNPs have been optimized by numerical desirability function and graphical optimization techniques.

2.4. Synthesis of AgNPs using *Aloe vera* plant extract

For the synthesis of AgNPs, a certain volume of $AgNO_3$ (5-10 mM) solution was added to a certain volume of plant extract so that the $AgNO_3$ ratio of the plant extract was within a certain range (0.1 - 0.5) and the solution was stirred with the help of a magnetic stirrer. Finally, the solution was diluted with 0.1 M NaOH solution to adjust the pH of the medium to 7.5. The solution was heated by microwave for certain seconds (10-60) and in the certain power range of 150 -800 watts.

Table 1 The Box-Behnken Design of matrix illustrating trial runs carried out for optimization of synthesized AgNPs using *Aloe vera* plant extract solution.

Run	Concentration of $AgNO_3$ (mM)	Volume of extract / Volume of $AgNO_3$	Power of microwave (Watt)	Time (sec.)	%Yield
1	7.5	0.3	800	60	38.7661
2	10	0.3	800	35	40.5157
3	7.5	0.3	800	10	57.2744
4	5	0.3	800	35	47.1455
5	7.5	0.1	150	35	0
6	10	0.5	475	35	69.7974
7	7.5	0.1	800	35	0
8	7.5	0.5	475	10	83.0571
9	7.5	0.3	475	35	90
10	10	0.3	475	10	71.8232
11	7.5	0.5	475	60	57.1823
12	7.5	0.5	150	35	57.1823
13	10	0.1	475	35	0
14	7.5	0.3	475	35	90
15	5	0.3	475	60	52.7624
16	7.5	0.5	800	35	75.6906
17	10	0.3	475	60	47.6059
18	7.5	0.3	475	35	90
19	5	0.1	475	35	0
20	5	0.3	150	35	38.1215
21	7.5	0.3	475	35	90
22	5	0.3	475	10	52.302
23	7.5	0.3	150	10	51.105
24	7.5	0.3	475	35	90
25	7.5	0.1	475	60	0
26	7.5	0.3	150	60	43.6464
27	7.5	0.1	475	10	0
28	10	0.3	150	35	58.7477
29	5	0.5	475	35	71.9153

The reduction process of silver ions was observed by the color change from yellowish to brown based on the reaction conditions. The synthesized AgNPs were centrifuged at 15000 rpm for 15 minutes and washed twice with deionized water, dried and stored at 4 ° C in the dark.

2.5. Characterization of optimized AgNPs using *Aloe vera* plant extract

AgNPs were characterized by scanning the 200-500 nm range using a Nanodrop DeNoVIX spectrophotometer (Wilmington, USA) for UV-VIS spectrum savingin room conditions. The AgNPs were also analyzed to characterize chemically via FTIR spectroscope (Jasco FT/IR 4700, Germany).

2.6. Antibacterial activity testing of *Aloe vera* extract and silver nanoparticles

The optimized AgNPs were done testing of antibacterial activity using *Enterococcus faecalis (E. faecalis) Staphylococcus aureus (S. aureus), Pseudomonas aeruginosa (P. aeruginosa) and Klebsiella pneumoniae (K. pneumoniae)* strains. The antibacterial activity of produced AgNPs against the strains were tested utilizing disc diffusion method. The strains were seeded in medium and incubated overnight at 210 rpm, 37°C. The cultured bacterial suspension was adjusted to $1x10^8$ CFU / mL and the bacterial suspension was seeded on nutrient agar loaded petri dish and then the sterile blank discs, which are used generally for disc diffusion method, were placed on petri dish. One of the discs was loaded with 20 µL of *Aloe vera* extract and the other was loaded with 20 µL of *Aloe vera*& AgNPs solution then incubated overnight at 37°C. After that, the zones caused by inhibition were measured.

2.7. Minimum inhibitory concentration (MIC) of *Aloe vera* extract and AgNPs

The MIC values were determined using 96-well plates. Firstly, the preparing AgNPs solution (1 mg/ mL) was added to wells then serial dilution was carried out. The bacterial suspension was adjusted to $1x10^8$ CFU / mL and seeded to wells. after that, the plates were incubated overnight at 37°C and MIC values were measured by using Plate Reader.

3. RESULTS AND DISCUSSION

3.1. Synthesis of AgNPs using *Aloe vera* plant extract

In the last few years, many of plants are studied for the green synthesis of AgNPs using by bioreduction method [21–23]. In this study, AgNPs were synthesized using *Aloe vera* plant extract via biological reduction method. *Aloe vera* plant extracts were used as a reduction agent in this synthesis of AgNPs because of its important biological molecules which are treated various diseases [24].

3.2. Optimization of AgNPs

The BBD method of the Design Expert® ver. 9.0 software (Stat-Ease Inc., Minneapolis, USA) was used to optimize the synthesis procedure of AgNPs. These AgNPs of absorbance values were measured to calculate the percentage yield of particle formation by UV-Vis at 350-500 nm and then optimized as responses. Power of microwave, time, $AgNO_3$ concentration, and ratio of volume of *Aloe vera* leaves extract solution to volume of $AgNO_3$ were decided as factors at three different levels which were changed dependent of the factors. A total of 29 experiments calculated by the design were recommended. The acquired data coincided with the quadratic polynomial model and various statistical parameters were used to fit the analysis. After data modeling which is demonstrating the existence of interaction and curvature effect was performed, polynomial equation was generated for response factor. The parameter of coefficient of correlation were calculated as perfectly in the range between 0.9915, along with great values of predicted and adjusted r2, and low values of PRESS. Additionally, model diagnostic graphs for response are shown in Figure 1, showing that the data is parallel to the selected model.

$$\%\text{Yield} = 90.00 + 2.19 * \text{A} + 34.57 * \text{B} + 0.8824 * \text{C} - 6.30 * \text{D} - 0.5295 * \text{AB} - 6.81 * \text{AC} - 6.17 * \text{AD} + 4.63 * \text{BC} - 6.47 *$$

$$BD - 2.76 * CD - 18.43 * A^2 - 35.42 * B^2 - 23.75 * C^2 - 17.84 * D^2 \quad (1)$$

3.3. Factor-response relationship and response surface mapping

Response surface analysis (RSA) was obtained using 3D response surface plots and 2D contour plots, which elucidated the existence of interactions among the factors and their impacts on the response factor. The RSA plots for percent of yields of AgNPs are shown in Fig.2. The relationship between $AgNO_3$ concentration and values of the ratio between volume of *Aloe vera* plant extract solution and $AgNO_3$ volume is shown in Fig. 2(A). In cases where the ratio between extract volume and $AgNO_3$ volume is particularly low at 0.1, the percentage yield of particle formation tends to be minimal even if the $AgNO_3$ concentration is high. However, at the high level of the ratio between extract volume and $AgNO_3$, the increase in $AgNO_3$ concentration showed a curvilinear trend with a first medium level, followed by a sharp rising pattern to high levels. In addition, the effect of the ratio between extract volume and $AgNO_3$ volume on the particle formation efficiency of AgNPs showed an increasingly decreasing trend in the values of particle formation efficiency from nearly 0.2 to 0.5 levels of the factor. The 3D graph and 2D plot of relationship between $AgNO_3$ concentration and microwave power were indicating in Fig 2(B). When the relationship between $AgNO_3$ concentration and microwave power were evaluated both effect on yield of particle formation is lower at low and high levels than middle levels, yield of particle formation tends to increase at middle levels. Moreover, the relationship between $AgNO_3$ concentration and the time is like the relationship between $AgNO_3$ concentration and microwave power and its 3D response surface plots and 2D contour plots are depicted in Fig. 2(C). The relationship between power of microwave and value of the ratio between volume of *Aloe vera* plant extract solution and $AgNO_3$ volume is indicated as a 3D response surface plots and 2D contour plots in Fig 3(A). At the low levels of the ratio between volume of *Aloe vera* plant extract solution and $AgNO_3$ volume, the increase in power of microwave did not cause increase in the yield of particle formation and the particle formation yield percentage tended to remain at very low levels. The yield of particle formation is remained at low levels, even if the $AgNO_3$ concentration increase while the ratio is at low levels.

In addition, the relationship between value of the ratio between volume of *Aloe vera* plant extract solution and $AgNO_3$ volume and the time is like the relationship between power of microwave and value of the ratio between volume of *Aloe vera* plant extract solution and $AgNO_3$ volume. Their graphs are shown in Fig 3(B). The last relationship between time and power of microwave is like the relationship between $AgNO_3$ concentration and the time and their graphs seen into Fig 3(C). At low and high levels of power and time, the percentage of particle formation efficiency tends to remain middle levels. At the middle levels of power and time, percentage of particle formation efficiency indicated an increasing trend. The lowest of percentage of yields were determined at low $AgNO_3$ concentration and power of microwave, low and high time interval, and low value of the ratio between volumes of *Aloe vera* plant extract solution and $AgNO_3$ volume.

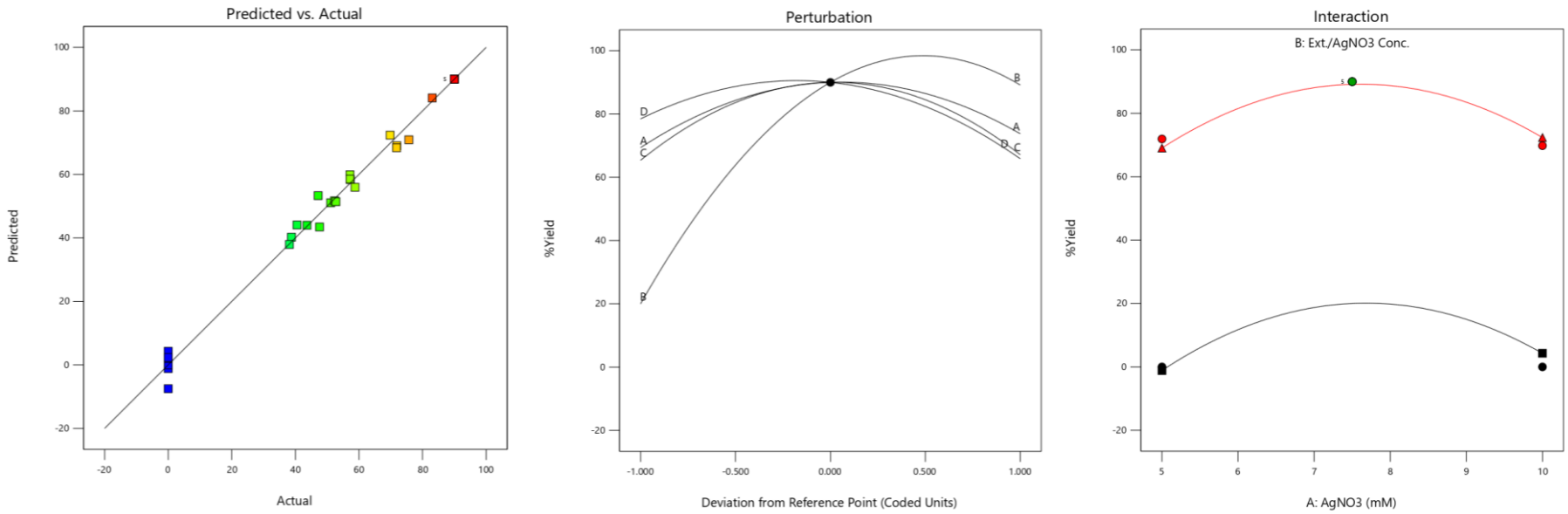

Figure 1 The graphs indicating 'Predicted vs. Actual plot', perturbation chart and interaction plot for response values

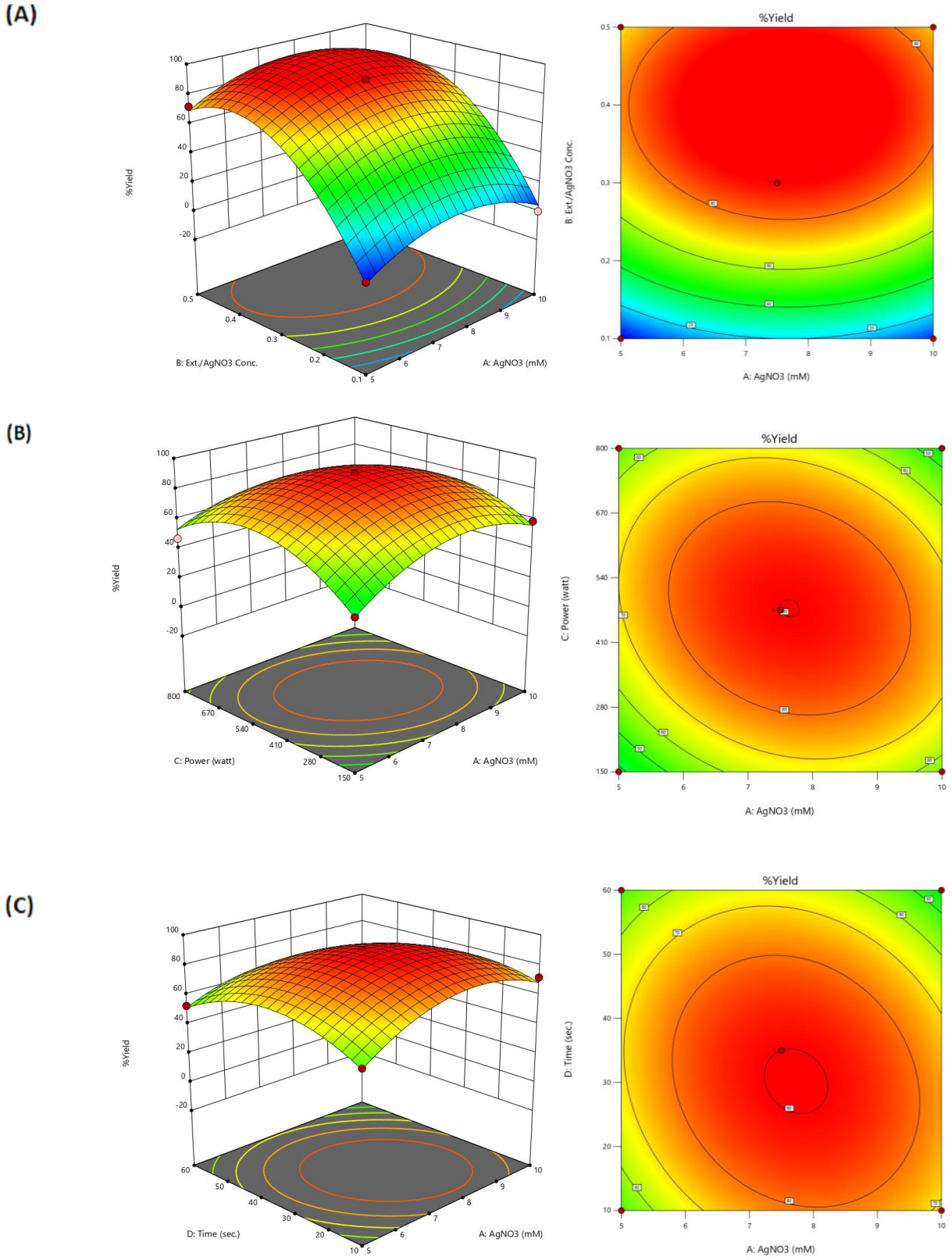

Figure 2 The graphs indicating the impact of factors like A: $AgNO_3$ concentration, B: ratio, C: Power of microwave and D: time volume on percentage of particle formation (%Yield) of synthesized AgNPs using Aloe vera plant extract solution as the response factor.

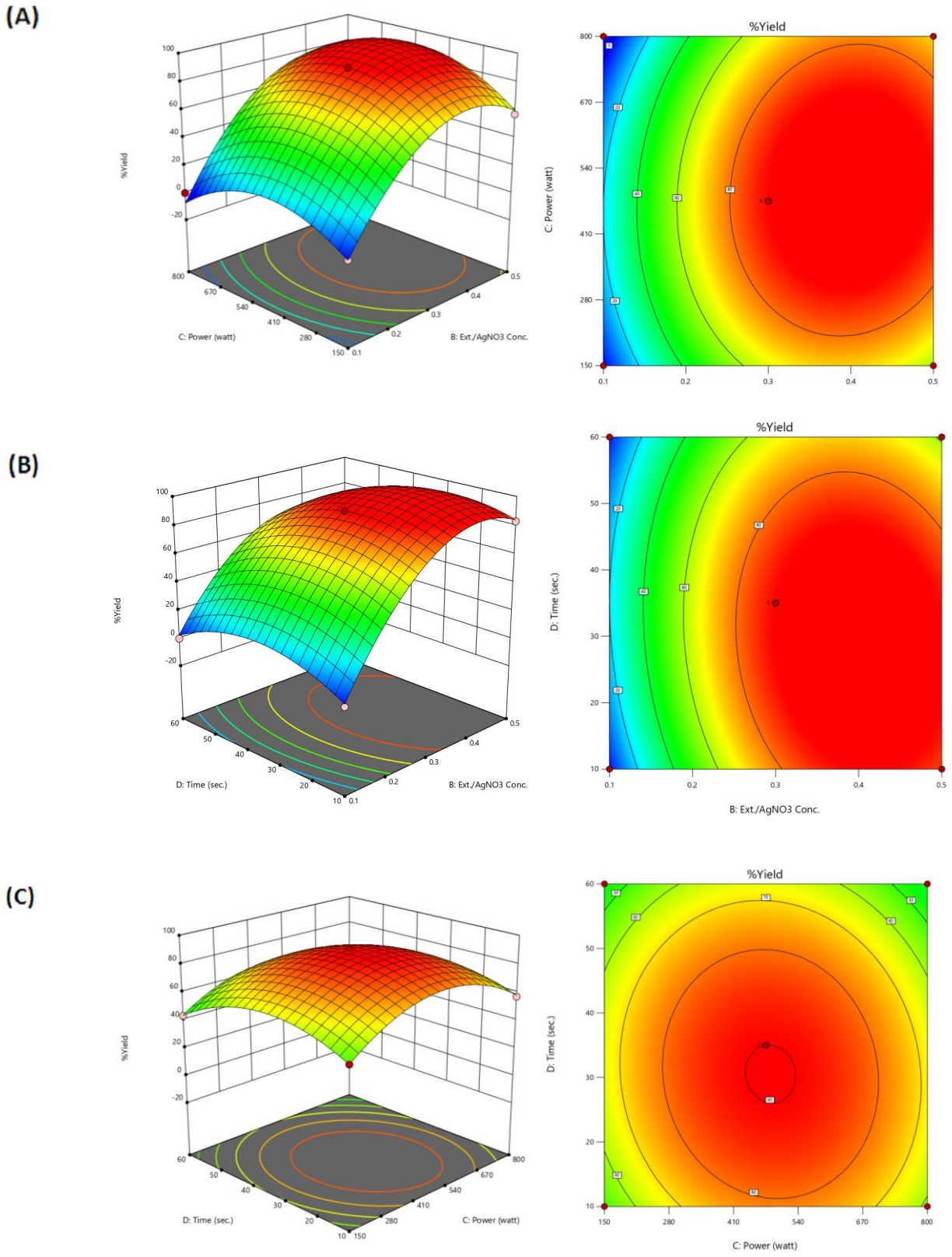

Figure 3 The graphs indicating the impact of factors like B: ratio, C: Power of microwave and D: time volume on percentage of particle formation (%Yield) of synthesized AgNPs using Aloe vera plant extract solution as the response variable.

3.4. Search for the optimized AgNPs

The AgNPs were optimized and then their values were evaluated to identify with numerical optimization. It was seen that the desirability function value was close to 1.0 and the goal for the response variable were achieved. As the optimized AgNPs synthesis setting, the overlay plot showed the yellow color area as the optimized area along with the flagged point displaying 7.5 mM concentration of $AgNO_3$, microwave power at 475-watt, time at 35 seconds and 0.3 of the ratio (Fig.4).

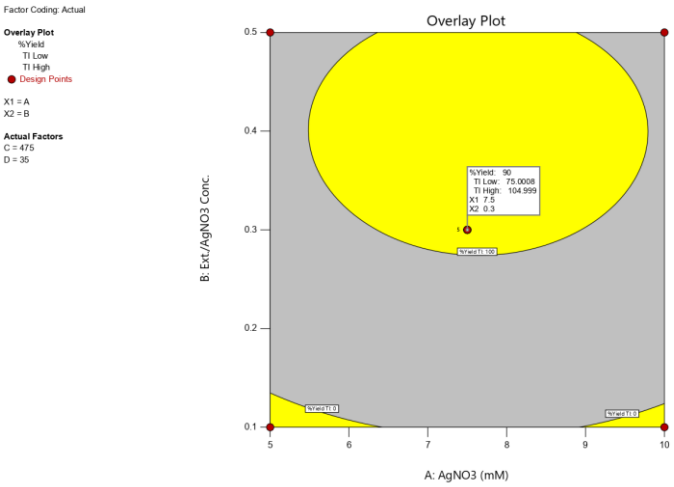

Figure 4 The graphs showing yellow color area as the optimized area and flagged point as the optimized synthesized AgNPs using *Aloe vera* plant extract.

3.5. Characterization of optimized AgNPs using Aloe vera plant extract

3.5.1. UV-VIS spectrophotometry

The AgNPs obtained as a result of optimization were characterized by UV-VIS spectrophotometry producing absorption spectra and the result was shown in Fig.5. Optimized AgNPs were synthesized by adjusting parameters such as microwave power, time, $AgNO_3$ concentration and volume of the *Aloe vera* plant leaf extract solution to optimum values. The spectrum indicating the peak was observed at 478 nm and this result was fitting with brownish color of the nanoparticles.

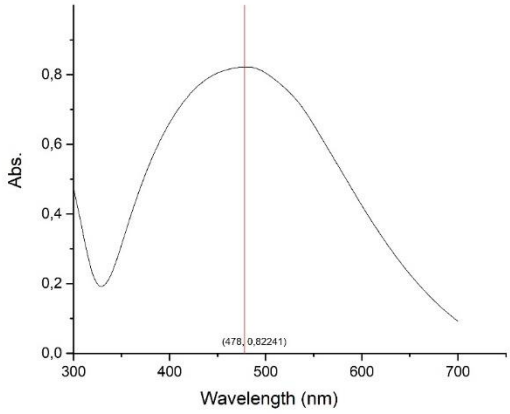

Figure 5 UV-Visible spectra of optimized AgNPs using *Aloe vera* plant extract

At the same time, the study was realized by changing the volume of *Aloe vera* plant extract solution, $AgNO_3$ concentration and microwave power. When ratio of Aloe vera plant leaf extract solution to total solution was 0.1, AgNPs were not produced. It was decided that AgNP synthesis was not carried out in the trials where the ratio of the volume of *Aloe vera* plant leaf extract to the total solution volume was 0.1 value, as there was no peak in the 300-700 nm range. However, when the ratio was higher than 0.3, absorption peaks shift towards the higher wavelength and it was observed that the wavelength range of the peak increased.

3.5.2. FTIR spectroscopy

FTIR spectrum of the optimized AgNPs using *Aloe vera* plant extract was shown in Fig.6. The significant absorption bands for AgNPs were observed at 2903.3, 1633.41 and 1389.46. The optimized AgNPs were exhibited a wide absorption band of –OH groups at 3270.68. The absorption band at 2903.3 was associated with C–H stretching of aliphatic –CH, –CH2 groups. The absorption peaks at 1633 and 1389 was assigned to the asymmetrical and symmetrical –COO stretching of carboxylate compounds in Aloe vera. The absorption peak at 1077 was associated with C–O stretch.

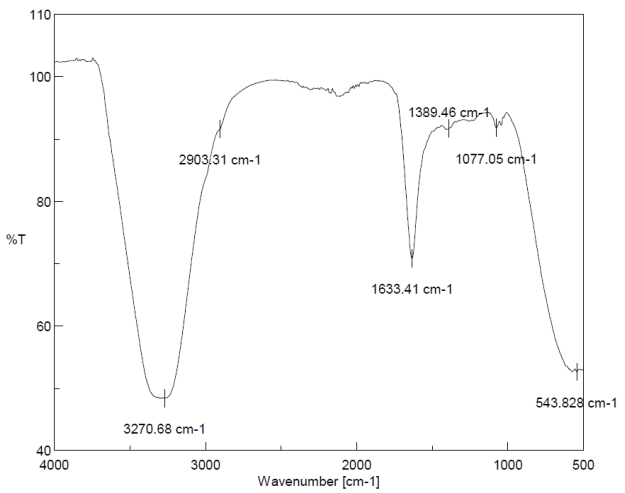

Figure 6 FTIR spectra of optimized AgNPs using *Aloe vera* plant extract

3.6. Antibacterial activity of AgNPs

3.6.1. DISC Diffusion Method

It has been known that the AgNPs have an antibacterial effect. They have effect on both of Gram-positive bacteria and Gram-negative bacteria [25–27]. The antibacterial mechanism of AgNPs has not been clearly explained, but a variety of possible mechanisms have been proposed. AgNPs can completely release Ag + ions and these ions can adhere to the cell wall and damage the cell membrane, as well as increase the permeability of the membrane and free silver ions taken into the cell can damage DNA by inducing reactive oxygen production. For these reasons, they can exhibit antibacterial activity by inhibiting the growth of bacteria[28–30]. *Aloe vera* is used in wound healing treatment or as a cosmetic product [31]. In this study, AgNPs optimized using Aloe *vera* plant were examined antibacterial effect on *S. aureus*, *E. faecalis*, *K. pneumoniae* and *P. aeruginosa* by using Disc Diffusion Method (Fig.7). However, the antibacterial effect of *Aloe vera* plant extract on the same bacteria were studied to compare with the AgNP form and inhibition zones were measured and shown in Table 2.

Table 2 Inhibition zones diameter (mm) AgNPs determined by DISC Method.

Microorganisms	Inhibition zones diameter (mm)
K. pneumoniae	12
P.aeruginosa	11
E. faecalis	13
S. aureus	13

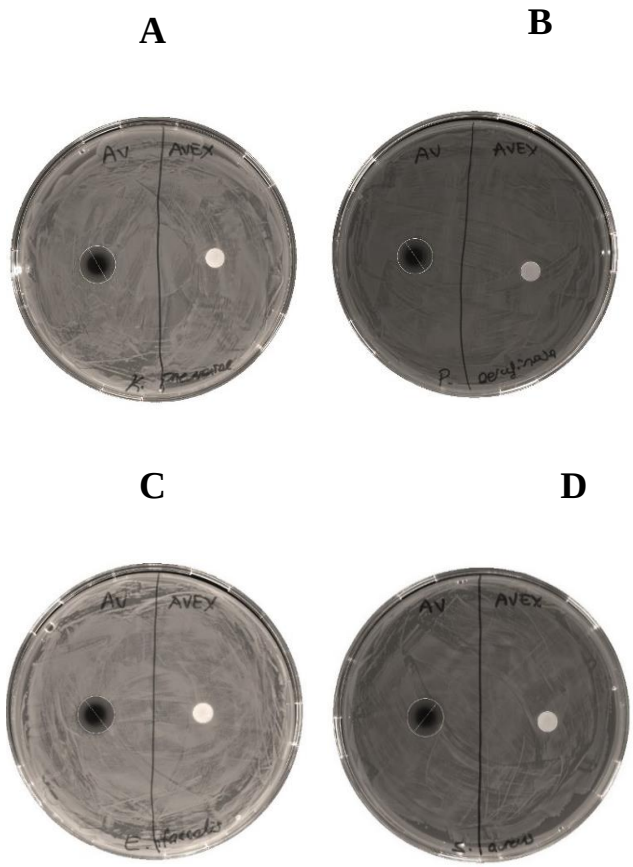

Figure 7 Antibacterial activity assay of *Aloe vera* plant extract and optimized AgNPs using *Aloe vera* plant extract against *K. pneumoniae (A), P. aeruginosa (B), E. faecalis (C), and S. aureus (D).*

Since the standard antimicrobial blank discs have diameter of 6.0 mm, the inhibition zone value should be higher than 6.0 mm to prove the sample has antimicrobial activity. As the results of DISC assay were evaluated while optimized AgNPs using *Aloe vera* plant extract exhibited

antibacterial effect, it was observed that *Aloe vera* plant had no antibacterial effect on the any bacteria.

3.6.2. Minimum inhibitory concentration (MIC) of Aloe vera extract and silver nanoparticles

The MIC method is used to determine the minimum inhibition concentration value of the active component [32]. In this study, MIC values of the AgNPs was measured by Plate Reader and the results were shown in Fig.8. Moreover, the percentage of inhibition curve of optimized AgNPs were seen into Fig. 9 and the inhibition values of *Aloe vera* plant extract solution was tested to determine the AgNPs effectiveness and shown in Fig 10. Both graphs also were plotted by using MIC data.

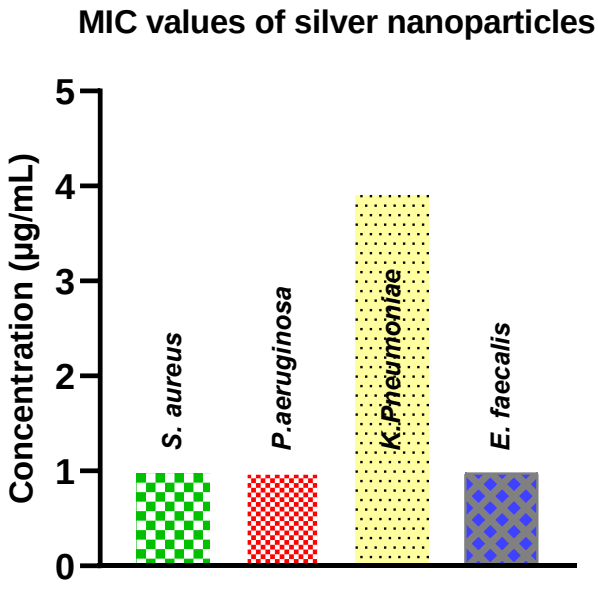

Figure 8 MIC value of optimized AgNPs using *Aloe vera* plant extract

MIC analysis was also analyzed for *Aloe vera* plant extract to determine the minimum inhibitory concentration of only optimized AgNPs. In this study, while optimized AgNPs using *Aloe vera* plant extract exhibited antibacterial effect even at minimum concentration, it was observed that Aloe vera plant extract has no antibacterial effect on any the bacteria even at maximum concentration.

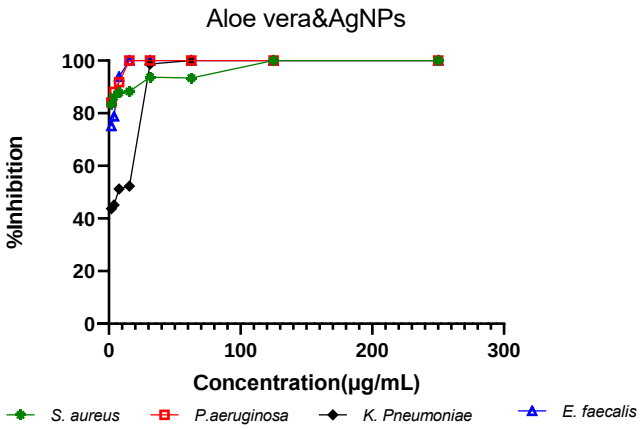

Figure 9 %Inhibition values on the bacteria of synthesized AgNPs using Aloe vera plant extract

The optimized AgNPs at concentration of 125 µg/mL completely inhibited all the bacteria strains (Fig.8). However, *Aloe vera* plant extract at concentration of 500 µg/mL inhibited just 30 % of the *P. aeruginosa* strain, 27.8 % of *S. aureus* strain, 18 % of *K. pneumonia* strain and there was no influence on *E. faecalis* strain (Fig.10).

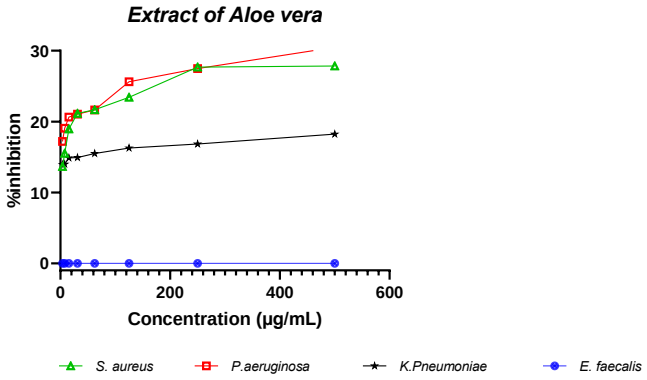

Figure 10 %Inhibition values on the bacteria of *Aloe vera* plant extract

4. CONCLUSION

In summary AgNPs were synthesized by using *Aloe vera* plant extract solution as a biological reduction agent. The synthesized AgNPs were systematically optimized with BBD utilizing by Design Expert® ver. 12.0 software depending on the influence of different factors. The optimized AgNPs and *Aloe vera* plant extract solution were tested against Gram negative and Gram-positive bacteria strains. The optimized AgNPs using *Alo vera* plant have exhibited antibacterial

effectiveness. The results of DISC assay were supported MIC data. As a result, this study tried to optimize the factors affecting the production efficiency of AgNPs synthesized using *Aloe vera* plant, which has the possibility to take place as a prospective antibacterial agent in cosmetic and therapeutic applications.

REFERENCES

[1] T.E. Antoine, S.R. Hadigal, Intravaginal zinc oxide tetrapod nanoparticles as novel immunoprotective agents against genital herpes., Journal of Immunology. 196 (2016) 4566–4575. https://doi.org/doi: 10.4049/jimmunol.1502373.

[2] D. Garibo, H.A. Borbón-Nuñez, J.N.D. de León, E. García Mendoza, I. Estrada, Y. Toledano-Magaña, H. Tiznado, M. Ovalle-Marroquin, A.G. Soto-Ramos, A. Blanco, J.A. Rodríguez, O.A. Romo, L.A. Chávez-Almazán, A. Susarrey-Arce, Green synthesis of silver nanoparticles using Lysiloma acapulcensis exhibit high-antimicrobial activity, Scientific Reports. 10 (2020) 1–11. https://doi.org/10.1038/s41598-020-69606-7.

[3] H. Khadri, M. Alzohairy, A. Janardhan, A.P. Kumar, G. Narasimha, Green Synthesis of Silver Nanoparticles with High Fungicidal Activity from Olive Seed Extract, Advances in Nanoparticles. 2 (2013) 241–246. https://doi.org/http://dx.doi.org/10.4236/anp.2013.23034.

[4] P. Mohanpuria, Æ.N.K. Rana, Biosynthesis of nanoparticles : technological concepts and future applications, (2008) 507–517. https://doi.org/10.1007/s11051-007-9275-x.

[5] H.J. Prabu, I. Johnson, ScienceDirect Plant-mediated biosynthesis and characterization of silver nanoparticles by leaf extracts of Tragia involucrata , Cymbopogon citronella , Solanum verbascifolium and Tylophora ovata, Karbala International Journal of Modern Science. 1 (2015) 237–246. https://doi.org/10.1016/j.kijoms.2015.12.003.

[6] A. Khatoon, F. Khan, N. Ahmad, S. Shaikh, Silver nanoparticles from leaf extract of Mentha piperita : Eco-friendly synthesis and e ff ect on acetylcholinesterase activity, Life Sciences. 209 (2018) 430–434. https://doi.org/10.1016/j.lfs.2018.08.046.

[7] H. Padalia, P. Moteriya, S. Chanda, Green synthesis of silver nanoparticles from marigold flower and its synergistic antimicrobial potential, Arabian Journal of Chemistry. 8 (2015) 732–741. https://doi.org/10.1016/j.arabjc.2014.11.015.

[8] D. Li, B. Mathew, C. Mao, Biotemplated Synthesis of Hollow Double-Layered Core / Shell Titania / Silica Nanotubes under Ambient Conditions, Small. 8 (2012) 3691–3697. https://doi.org/10.1002/smll.201200421.

[9] K. Cho, J. Park, T. Osaka, S. Park, The study of antimicrobial activity and preservative effects of nanosilver ingredient, Electrochimica Acta. 51 (2005) 956–960. https://doi.org/10.1016/j.electacta.2005.04.071.

[10] A. Surjushe, R. Vasani, D.G. Saple, ALOE VERA: A SHORT REVIEW, Indian Journal of Dermatology. 53 (2008) 163–166. https://doi.org/10.4103/0019-5154.44785.

[11] P. Mag, A.W. Khan, S. Kotta, S.H. Ansari, R.K. Sharma, A. Kumar, J. Ali, Formulation development , optimization and evaluation of aloe vera gel for wound healing, 9 (2013) 6–10. https://doi.org/10.4103/0973-1296.117849.

[12] R. Maenthaisong, N. Chaiyakunapruk, S. Niruntraporn, The efficacy of aloe vera used for burn wound healing : A systematic review, 33 (2007) 713–718. https://doi.org/10.1016/j.burns.2006.10.384.

[13] S.M. M, S. Kumar, Aloe vera their chemicals composition and applications : A review Aloe vera their chemicals composition and applications : A review, (2014).

[14] A.O. Dada, A.A. Inyinbor, E.I. Idu, O.M. Bello, A.P. Oluyori, T.A. Adelani-akande, A.A. Okunola, Effect of operational parameters , characterization and antibacterial studies of green synthesis of silver nanoparticles using Tithonia diversifolia, PeerJ. (2018) 1–17. https://doi.org/10.7717/peerj.5865.

[15] K. Logaranjan, A.J. Raiza, S.C.B. Gopinath, Y. Chen, Shape- and Size-Controlled Synthesis of Silver Nanoparticles Using Aloe vera Plant Extract and Their Antimicrobial Activity, Nanoscale Research Letters. (2016). https://doi.org/10.1186/s11671-016-1725-x.

[16] S.P. Sivagnanam, A.T. Getachew, J.H. Choi, Green synthesis of silver nanoparticles from deoiled brown algal extract via Box-Behnken based design and their antimicrobial and sensing properties, Green Process Synth. 6 (2017) 147–160. https://doi.org/10.1515/gps-2016-0052.

[17] A.K. Nayak, M.S. Hasnain, J. Malakar, Development and optimization of hydroxyapatite- ofloxacin implants for possible bone delivery in osteomyelitis treatment, Curr. Drug Deliv. 10 (2013) 241–250. https://doi.org/10.2174/1567201811310020008.

[18] M.S. Hasnain, S. Siddiqui, S. Rao, P. Mohanty, T. Jahan Ara, S. Beg, QbD-Driven Development and Validation of a Bioanalytical LC-MS Method for Quantification of Fluoxetine in Human Plasma, Journal of Chromatographic Science. 54 (2016) 736–743. https://doi.org/10.1093/chromsci/bmv248.

[19] A.K. Nayak, S. Kalia, M.S. Hasnain, Optimization of aceclofenac-loaded pectinatepoly (vinyl pyrrolidone) beads by response surface methodology, Int. J. Biol. Macromol. 62 (2013) 194–202. https://doi.org/https://doi.org/10.1016/j.ijbiomac.2013.08.043.

[20] J. Malakar, K. Das, A.K. uma. Nayak, In situ cross-linked matrix tablets for sustained salbutamol sulfate release - formulation development by statistical optimization, Polimery w Medycynie. 44 (2014) 221–230. https://doi.org/10.3109/10837450.2011.557731.

[21] D. Raghunandan, B. Mahesh, S. Basavaraja, S. Balaji, S. Manjunath, A. Venkataraman, Microwave-assisted rapid extracellular synthesis of stable biofunctionalized silver nanoparticles from guava (Psidium guajava) leaf extract, Nanoparticle J. Res. 13 (2011) 2021–2028. https://doi.org/10.1007/s11051-010-9956-8.

[22] N. Roy, A. Barik, Green Synthesis of Silver Nanoparticles from the Unexploited Weed Resources, International Journal of Nanotechnology and Applications. 4 (2010) 95–101. http://www.ripublication.com/ijna.htm.

[23] L. Lin, W. Wang, J. Huang, Q. Li, D. Sun, X. Yang, H. Wang, Y. N. He, Nature factory of silver nanowires: plant mediated synthesis using broth of Cassia fistula leaf, Chem. Eng. J. 162 (2010) 852–858. https://doi.org/https://doi.org/10.1016/j.cej.2010.06.023.

[24] S.P. Chandran, M. Chaudhary, R. Pasricha, A. Ahmad, M. Sastry, Synthesis of gold nanotriangles and silver nanoparticles

using Aloe vera plant extract, Biotechnology Progress. 22 (2006) 577–583. https://doi.org/10.1021/bp0501423.

[25] B. Das, S.K. Dash, D. Mandal, T. Ghosh, S. Chattopadhyay, S. Tripathy, S. Das, S.K. Dey, D. Das, S. Roy, Green synthesized silver nanoparticles destroy multidrug resistant bacteria via reactive oxygen species mediated membrane damage, Arabian Journal of Chemistry. 10 (2017) 862–876. https://doi.org/10.1016/j.arabjc.2015.08.008.

[26] A. Sharanappa, A.R. Shet, L.R. Patil, V.S. Hombalimath, S. Kadapure, Biosynthesis of silver nanoparticles using citrus sinensis peel extract and their application as antibacterial agent, International Journal of Research in Pharmaceutical Sciences. 11 (2020) 4726–4732. https://doi.org/10.26452/ijrps.v11i3.2762.

[27] D. MubarakAli, N. Thajuddin, K. Jeganathan, M. Gunasekaran, Plant extract mediated synthesis of silver and gold nanoparticles and its antibacterial activity against clinically isolated pathogens, Colloids and Surfaces B: Biointerfaces. 85 (2011) 360–365. https://doi.org/10.1016/j.colsurfb.2011.03.009.

[28] V.S. Ramkumar, A. Pugazhendhi, K. Gopalakrishnan, P. Sivagurunathan, G.D. Saratale, T.N.B. Dung, E. Kannapiran, Biofabrication and characterization of silver nanoparticles using aqueous extract of seaweed Enteromorpha compressa and its biomedical properties, Biotechnology Reports. 14 (2017) 1–7. https://doi.org/10.1016/j.btre.2017.02.001.

[29] N. Durán, G. Nakazato, A.B. Seabra, Antimicrobial activity of biogenic silver nanoparticles, and silver chloride nanoparticles: an overview and comments, Applied Microbiology and Biotechnology. 100 (2016) 6555–6570. https://doi.org/10.1007/s00253-016-7657-7.

[30] R.A. Bapat, T. V. Chaubal, C.P. Joshi, P.R. Bapat, H. Choudhury, M. Pandey, B. Gorain, P. Kesharwani, An overview of application of silver nanoparticles for biomaterials in dentistry, Materials Science and Engineering C. 91 (2018) 881–898. https://doi.org/10.1016/j.msec.2018.05.069.

[31] P.K. Sahu, D.D. Giri, R. Singh, P. Pandey, S. Gupta, A.K. Shrivastava, A. Kumar, K.D. Pandey, Therapeutic and Medicinal Uses of <i>Aloe vera</i>: A Review, Pharmacology & Pharmacy. 04 (2013) 599–610. https://doi.org/10.4236/pp.2013.48086.

[32] H. AKBAŞ, A. YILDIRIM, Ş. MENEVŞE, N. GÖKŞEN, Antiproliferative and Antimicrobial Effects of Tris(2-hydroxyethyl)ammonium-Based Protic Ionic Liquids with Some Fatty Acids, Journal of the Institute of Science and Technology. 10 (2020) 2021–2027. https://doi.org/10.21597/jist.695018.

SAKARYA ÜNİVERSİTESİ
FEN BİLİMLERİ ENSTİTÜSÜ DERGİSİ

Sakarya University Journal of Science
SAUJS

e-ISSN 2147-835X | Period Bimonthly | Founded: 1997 | Publisher Sakarya University |
http://www.saujs.sakarya.edu.tr/en/

Title: Experimental 70% Hepatectomy Model: Apoptotic Index, Proliferative Index and Mitotic Index

Authors: Şamil ÖZTÜRK, Latife Ceyda İRKİN

Recieved: 2021-02-24 18:57:13

Accepted: 2021-05-03 19:19:00

Article Type: Research Article

Volume: 25
Issue: 3
Month: June
Year: 2021
Pages: 788-799

How to cite
Şamil ÖZTÜRK, Latife Ceyda İRKİN; (2021), Experimental 70% Hepatectomy Model: Apoptotic Index, Proliferative Index and Mitotic Index. Sakarya University Journal of Science, 25(3), 788-799, DOI: https://doi.org/10.16984/saufenbilder.886245
Access link
http://www.saujs.sakarya.edu.tr/en/pub/issue/62736/886245

Sakarya University Journal of Science 25(3), 788-799, 2021

Experimental 70% Hepatectomy Model: Apoptotic Index, Proliferative Index and Mitotic Index

Şamil ÖZTÜRK *[1] Latife Ceyda İRKİN[2]

Abstract

Liver regeneration is known to begin after experimentally induced liver resection. At first 24-48 hours, DNA synthesis reaches the maximum level after resection and significantly regeneration known to occur on the first 10 days. In this study, we were examined the regeneration of liver on the 1st and 14th days after the resection.

In experiment 21 Wistar albino male rats were used. The rats were randomly divided into three groups. The first group was the control, the second group was sacrificed one day after hepatectomy, and the third group was sacrificed 14 days after hepatectomy. All experimentally groups realized midline incision with laparotomy for resection of liver. Pedicles of the left lateral and median lobes of the liver were applied 70% hepatectomy by 4/0 silk binding. At the end of 1st and 14th days, liver tissue removed for light misroscobic analysis.

No histopathological findings were found in the control group. The tissue of all experimentally groups were showed some histopatological changes such as sinuzoidal dilatation, vacuolization in the hepatocytes. This histopatological findings were seem to increase at grup II more than group III and group I with routin H&E staining.

Mitotic index, apoptotic index and proliferation index of values at group II was reached the maximum level. Group III dramatically reduced the value of these index and were seem to reach near to values of the control group. Relative liver weight that determined each of experimentally groups were statistically significant differences compared to the control group.

As a result, in this study, liver regeneration was shown in liver transplants without any agent that would contribute to the clinic.

Keywords: Partial hepatectomy, TUNEL, apoptosis, immunohistochemistry, PCNA.

1. INTRODUCTION

The liver is the largest organ of the body that secretes both endocrine and exocrine, plays a major role in regulating metabolic functions, and also weighs approximately 1,5 kg and has the largest gland feature in the body [1]. It has a central role in many fundamental

* Corresponding author: samilozturk16@hotmail.com
[1] Çanakkale Onsekiz Mart University, Vocational School of Health Services, Çanakkale, Turkey.
ORCID: https://orcid.org/0000-0002-9435-8139
[2] Çanakkale School of Applied Sciences, Çanakkale, Turkey.
E-Mail: latifeirkin@gmail.com
ORCID: https://orcid.org/0000-0001-6603-8413

physiological events such as bile acid synthesis and secretion, blood-glucose balance and lipoprotein synthesis, storage of vitamins (A, D, E, K, and B12), biotransformation, detoxification and expression of endogenous and exogenous compounds [2]. A disfunction that may occur in the liver affects all systems of the body. Many factors such as drugs, chemicals, accidents, alcohol, liver tumors, liver diseases of viral origin and surgical interventions (partial hepatectomy) can cause damage in the liver tissue. When the liver is damaged due to various reasons, replication and proliferation may begin to complete its functional mass [3,4]. This feature is extremely important for hepatocytes that normally divide rarely. This proliferative capacity and adaptation ability is maintained against different metabolic conditions. These events reveal the loss and increase of liver tissue [3]. The liver has a tremendous interaction between cells and a complex mediator network that can repair itself in a few weeks in situations such as significant tissue loss, and is the only organ that goes to tissue regeneration quickly after resection or injury [5].

It is one of the most important stages in modern surgery that liver regeneration has become a common and controllable procedure. For cancer treatment or transplantation, 60-70% of the liver volume can be safely removed to be used as a liver donor graft [6]. Today, in studies conducted with methods such as computed tomography, angiography and scintigraphy, it has been shown that the liver reaches its original size in 3-6 months in adults and less than 3 months in children after liver resection. In the presence of cirrhosis, this period can be up to 9-15 months [7,8]. It has been reported that the human liver can tolerate even resections up to 80-85% [9]. Regeneration occurs even if the resection is less than 10% [10]. It has been shown that regeneration in the remaining liver tissue after partial hepatectomy starts from the first day and DNA synthesis reaches its maximum in the first 24-48 hours after hepatectomy [11]. Hepatocytes normally show very rare mitosis activity. However, active cell replication begins within 24 hours after partial hepatectomy and continues until the organ reaches its normal weight. Significant regeneration occurs within the first 10 days and this event is completed in 4-5 weeks. The excised lobes do not take the same shape. Regeneration mostly occurs in the form of new lobules and the growth of residual lobules [12,13]. Endocrine, paracrine and autocrine interactions are required for regeneration and liver restructuring after experimental partial hepatectomy in humans and animals [14,15]. Necessary stimuli for hepatic regeneration are the pancreas, other extrahepatic organs and humoral factors originating from the regenerating liver itself [12,13].

It has been observed that hepatocyte proliferation increases in cases such as surgical removal of a part of the liver lobes or damage of hepatocytes from viruses or chemicals. However, studies have shown that after liver resection, the regenerative activity is increased as a result of giving a more stimulus. In addition, various drug applications are used to heal the medically damaged liver more quickly. However, as with many chemical drug treatments, side effects are inevitable in these studies. Therefore, we conducted this study in order to reveal the regeneration occurring as a result of hepatectomy in the liver tissue without any stimulus or chemical medication on the days of 1 and 14 with immunohistochemical staining and TUNEL method.

2. MATERIAL AND METHOD

This study, 21 adult male Wistar Albino rats in Trakya University Experimental Animal Research Unit, weighing between 250-300 g and having the same biological and physiological characteristics were used. During the duration of the experiment, all our subjects were fed daily drinking water and pelleted feeds (Purina) containing 21% crude protein under optimum laboratory conditions (22 ± 1^0C, 12 hours light/dark cycle). Cage maintenance was done regularly. A total of 3 groups were created in the experiment.

Approval for the study was obtained from Trakya University Ethics Committee on 09.06.2011.

2.1. Hepatic resection method

Ketamine (Ketalar®, 10ml, 50mg/ml, Pfizer, USA) (25mg/kg, intramuscular) 50mg/ kg/ip, xylazine (Rompun® 50ml, 23,32mg / ml, Bayer, Germany) 5mg/kg/General anesthesia was applied with a rope. Before laparotomy in order to prevent bacterial translocation intramuscularly at 25 mg/kg of cefazolin vial (MN Pharmaceutical Inc., Istanbul, Turkey) were performed [16]. Laparotomy was performed with an upper midline incision. The left lateral and median lobe pedicles of the liver were tied with 4/0 silk and 70% hepatectomy was performed as defined by Higgins and Anderson [17]. After the surgical procedure, the fascia was closed with 3/0 vicryl and the skin with 4/0 silk and cleaned with povidone iodine. Oral intake of water and diet was allowed from the 24th post-operative hour [18].

2.2. Experimental design

The rats were divided into 3 groups, one control and two experiment groups, with 7 animals in each group.

Group I: Control group (n=7): The rats were not applied to the hepatectomy.

Group II: Study group (1 day) (n=7): The rats in this group were sacrificed 1 day after hepatectomy.

Group III: Study group (14 days) (n=7): The rats in this group were sacrificed 14 days after hepatectomy.

After resection, the subjects of each group were sacrificed as planned and the livers of the rats were completely removed. Liver samples taken were detected in Bouin fixative (75 cc picric acid + 25 cc formalin + 5 cc Acetic acid) for light microscope and immunohistochemical examination.

2.3. Relative liver weight

The remaining liver weight after partial hepatectomy was subtracted from the liver weight at autopsy and the ratio of this value to the whole liver weight was calculated. The liver regeneration rate was found by multiplying the obtained value by 100 [19]. Whole liver weight was accepted as 3-4% of the rat weight [20]. Results are expressed as per.

Relative liver weight = [liver weight at autopsy- (whole liver weight-resected liver weight)/whole liver weight]×10

2.4. Histopathological parameters

2.4.1. Mitotic index

After fixing in Bouin **fixative** for 4 days, liver tissue was blocked in paraffin after routine tissue follow-up and stained with Hematoxylin-Eosin (H&E) Mitotic index**:** The number of hepatocytes and total hepatocytes showing mitotic activity at 30 high-power fields was calculated and expressed as their ratio per 1000 cells [21].

Mitotic index = (number of mitotic cells)/(total number of cells)×100

2.4.2. Proliferation index

After fixing in Bouin fixator for 4 days, liver tissue was blocked in paraffin after routine tissue follow-up and stained with proliferated cell nuclear antigen (PCNA) from immunohistochemical stains. Proliferation index; PCNA stained cell number and total hepatocyte count at 30 high power fields were calculated. It was then defined as the ratio per 1000 cells [21].

Proliferation index= (number of PCNA stained cells) / (total number of cells)×100

2.4.3. Apoptotic index

After fixing in Bouin fixator for 4 days, liver tissue was blocked in paraffin after routine tissue follow-up and stained with TUNEL kit,

which is an apoptosis marker. Apoptotic index; TUNEL stained cell count and total hepatocyte count were calculated in 30 large magnification fields. It was then defined as the ratio of every 1000 cells (114) [21].

Apoptotic index= (apoptotic cell number) / (total cell number) × 100

2.5. Light microscopic inspection

For this purpose, the liver tissues were fixed in Bouin fixator for 4 days, and then the washing process was started. The tissues were washed in 70% alcohol for 2 days and the dehydration process was started. Tissues were kept for 1 hour in increasing alcohol series (70, 90, 96, 100%). After the dehydration stage, the tissues were treated with toluol for 3 series 15 minutes for the transparency step. Before embedding, the tissues were kept in soft paraffin for 1 night. The next day, liver tissues were removed from soft paraffin and kept in liquid hard paraffin for 1 hour and blocked. 5 μm thick sections were taken from these blocks using a Leica RM-2245 cylinder microtome. The sections taken were stained with H&E (Sigma-Aldrich). in order to reveal the histological structural changes in the liver. Photographs were taken by a light microscope (Olympus CX31-Japan).

2.6. Immunohistochemical analysis

The sections lowered into water were boiled for 20 minutes in the microwave oven in antigen retrival. After allowing to cool for 20 minutes at room temperature, the sections were washed with PBS. After this step, it was treated with 3% hydrogen peroxide (H_2O_2) prepared in methanol (Riedel-de Häen 24229) for 20 minutes to remove the hydrogen peroxidase activity. Sections were washed with phosphate buffer solution (PBS; pH 7.6) by rinsing in distilled water. 1% Preimmune rabbit serum (Ultra V Block, LabVision, TA-015-UB) was applied to sections to block non-specific antibody binding. The sections were then incubated with primary antibody diluted 1/100 in the moist chamber for 1 hour. The antibody used was mouse monoclonal anti-PCNA antibody (MS-106-B, Thermo LabVision, USA). Sections were kept in secondary antibody solution (Biotinylated Goat Anti-Mouse, LabVision, TM-015-BN) for 20 minutes after washing with PBS 3 times. Streptavidin peroxidase solution (Streptavidin Peroxidase, LabVision, TS-015-HR) was applied to the sections washed 3 times in PBS for 20 minutes. After washing the sections 3 times with PBS, 3-amino 9 ethyl carbazole (AEC) chromogen solution (LabVision, TA-002-HAC) was applied for 10 minutes.

Proliferation index; the number of PCNA stained cells in 30 high-power fields and the total number of hepatocytes was calculated and defined as the ratio per 1000 cells (μm^2), and the average number of PCNA positive cells was determined.

2.7. Statistical analysis

All data are expressed as mean (±) standard deviation (SD). The differences in the results between the groups were evaluated by Kruskal-Wallis analysis of variance. For comparisons between groups with significant differences, Mann-Whitney U test was used. If $p < 0.05$, the difference was considered statistically significant. In addition, hepatocyte vacuolization and sinusoidal dilatation numbers were determined semiquantitatively in all groups. Semi-quantitative evaluation was done as follows; none (-), rare (±), low (+), medium (++), too much (+++), too much (++++).

2.8. TUNEL staining

The 5 μm sections taken from the paraffin blocks on the slide were kept in an oven at 37°C for a night, then kept in toluol for 3x5 minutes and then passed through the decreasing alcohol series (100%, 95%, 70%) for 3 minutes and lowered into distilled water. Proteinase K (20 μg/ml, Chemicon, 21627) was applied to the sections kept in distilled water for 5 minutes at room temperature for 15 minutes for antigen recovery. Sections washed with distilled water were kept in 3% H_2O_2 prepared in methanol for 5 minutes to block

endogenous peroxidase. After shaking with distilled water and PBS, the pool around the sections was drawn with hydrophobic pen (Zymed, 00-8899) and a pool was created for 5 minutes at room temperature with equilibration buffer. Then the sections were kept at 37°C in terminal deoxynucleotidyl transferase (TdT) enzyme for a hour, then rinsed with stop/wash buffer for 15 seconds and kept at room temperature for 10 minutes. Conjugate of antidigoxigenin was applied to sections washed in PBS 3 times and kept at room temperature for 30 minutes. After washing the sections 3 times with PBS, diamino benzidine (DAB) chromogen solution (LabVision, TA-002-HAC) was applied for 10 minutes. After washing the sections with distilled water, contrast staining was done by applying methyl green for 10 minutes. Sections rapidly passed through distilled water were also rapidly passed through 100% N-Butanol. After dehydrated sections were kept in toluol for 3x2 minutes, the closure solution was placed and closed with coverslip and evaluated under a light microscope.

3. RESULTS AND DISCUSSION

3.1. Relative liver weight results

The remaining liver weight after partial hepatectomy was subtracted from the liver weight at autopsy and the ratio of this value to the whole liver weight was calculated. The liver regeneration rate was found by multiplying the obtained value by 100. Whole liver weight was accepted as 3.4% of the rat weight.

When the relative liver weights determined in the all groups were compared, a statistically significant difference according to $p < 0.05$. When the groups II and III were compared (11.46 ± 2.21, 38.45 ± 7.11), a statistically significant difference was found as $p < 0.001$ (Figure 1).

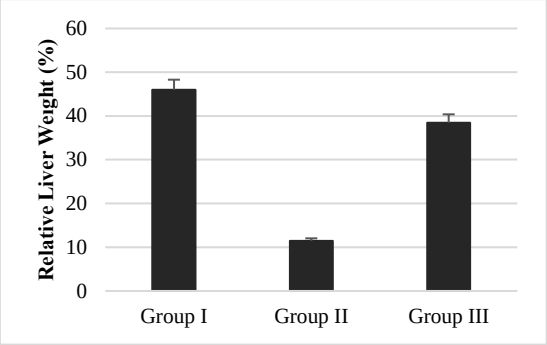

Figure 1 Relative liver weight values of experimental groups

Groups	Group I (control)	Group II (1st day)	Group III (14th day)
Hepatocyte vacuolization	-	++++	+
Sinusoidal dilatation	-	+++	±

Table 1 Semi-quantitative evaluation of hepatocyte vacuolization and sinusoidal dilatation in experimental groups

PV: Portal ven, long arrow: hepatocyte vacuolization, short arrow: sinusoidal dilatation

3.2. Light microscopic results

When the H&E stained liver sections of the rats in the control group were examined under a light microscope. It was observed that the liver sections were in normal histological appearance. It was observed that hepatocytes, which are liver parenchymal cells, were placed regularly around the central veins to form hepatocyte cords. Branch of the portal vein, hepatic arteriole and bile duct were observed in the portal areas around the hepatic lobules. In the sinusoid wall, endothelial cells were distinguished by the flat-shaped and dark staining of their nuclei, while Kupffer cells were distinguished by their nuclei larger than the endothelial cell nuclei, oval or triangular shapes. Hepatocyte nuclei were one or two large and round in shape, and their cytoplasm showed eosinophilia.

In all groups, hepatocyte vacuolization and sinusoidal dilatation counts were determined semiquantitatively. It was observed that the hepatocytes in the liver sections of animals

belonging to groups II**,** and III had common mitosis at various stages and was noticeable in hepatocytes vacuolization and sinusoidal dilatation. In group II hepatocyte vacuolization and sinusoidal dilatation were noticeable too much (++++) (Figure 2b-c, Table 1). In the sections belonging to the group III, it was observed that hepatocyte vacuolization decreased very much and became similar to the control group, decreasing in less (+) and sinusoidal dilatation as rare (±) (Table 1). When the sections belonging to all groups were evaluated, it was observed that the classical liver lobule structure was preserved (Figure 2). MI value of the group I, group II and group III were evaluated. The statistically significant difference between the groups were evaluated according to $p<0.05$. Statistically significant difference was observed between the control group and the other experimental groups. When the group I and II were compared, a statistically significant difference was found at the $p<0.001$ level. When the group I and III were compared, a statistically significant difference was found in $p<0.01$ (Figure 5).

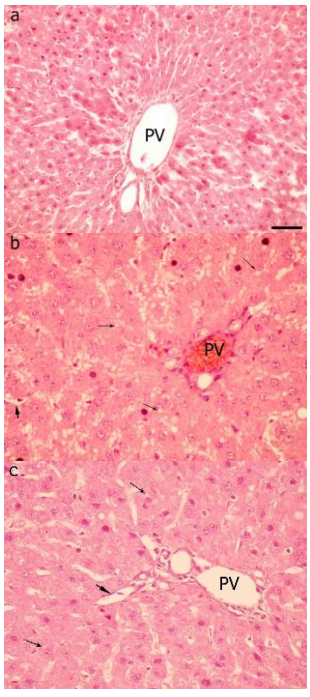

Figure 2 a) Normal histological appearance of the liver (group I), b) the liver section after 1 day of resection-intense vacuolization is seen around the portal areas (group II), c) the liver section after 14 day of resection-vacuolization is seen around the portal areas (group III) (X400), H&E staining.

3.3. Immunohistochemical results

PCNA immunostaining of group I liver section was weak, group II (1 day after resection) PCNA positive cell density was strong, group III PCNA positive cell was weak immunoreactivity (Figure 3). When the PCNA values detected into all groups were compared, a statistically significant difference was found between the group I and in all study groups (Figure 5). PI value of group I, group II and group III were evaluated. When the group II and group I were compared, statistically significant differences was found ($p<0.0001$). When the control and group III were compared, the statistically significant difference was low ($p<0.05$) (Figure 5).

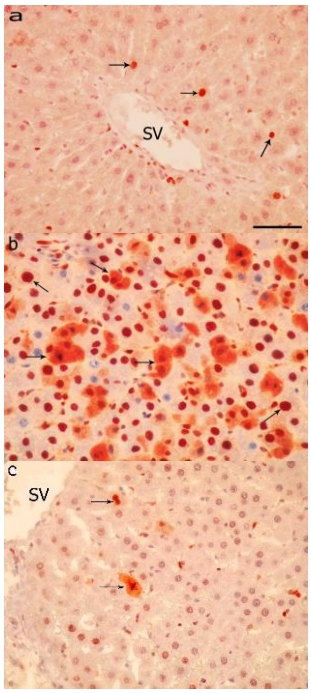

SV: Central ven, arrow: PCNA positive cells

Figure 3 a) PCNA immunostaining of (group I) liver section, b) PCNA immunostaining of the (1 day after resection)-PCNA positive cell density is seen (group II), c) PCNA immunostaining of the (14 days after resection)-PCNA positive cell density is seen (group III).

3.4. TUNEL results

A statistically significant difference was found between group I and experimental groups (group II, III) when the apoptotic index (AI) values obtained as a result of the evaluation of cells whose apoptotic nuclei were stained as a result of TUNEL staining performed into all groups (Figure 4). AI value of the group I, group II and group III were evaluated. The statistically significant difference between the groups were evaluated according to $p<0.05$. When the group II and group I were compared, a statistically significant difference was found ($p<0.001$). When the group I and group III were compared, the statistically significant difference was found low ($p<0.05$, Figure 5).

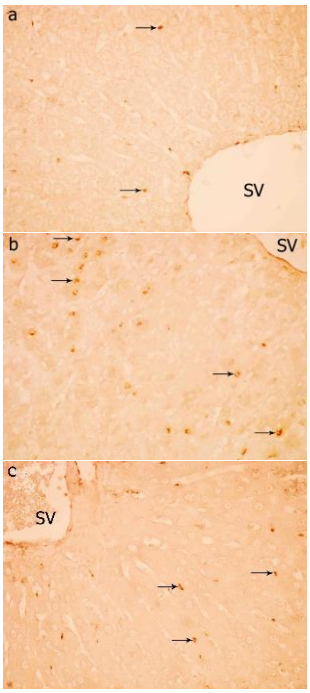

SV: Central ven, arrow: TUNEL positive cells

Figure 4 a) The liver section of group I, b) TUNEL positive cell high density was seen in group II, c) TUNEL positive cell low density was seen in group III (X400), TUNEL staining

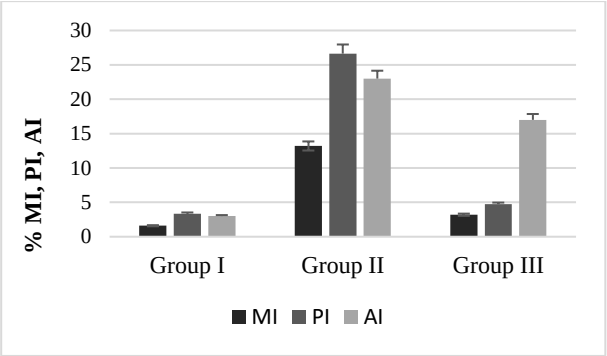

Figure 5 Mitotic, proliferative and apoptotic index values of control and experimental groups

3.5. Discussion

The liver exhibits a distinct feature from other organs with its regeneration capacity. The liver regulates many basic mechanisms such as biotransformation, regulation of metabolic functions and immunological events. However, it has many functions that have not been fully illuminated yet [22,23].

The existence of the ability to replenish the tissue mass after the loss or damage of an organ is defined as regeneration [3]. Regeneration is a complex process in which cytokines, hormones, transcription factors and oxidative stress products play a role [5]. Studies have shown that the liver has the ability to repair itself in significant tissue losses, thanks to intercellular interaction and a complex mediator network [24, 25]. Most studies on liver regeneration have been studied on the pre-existing damaged liver in experimental animals, or liver damage has been caused by using chemicals or a partial hepatectomy [26]. Palmes and Spiegel [26] described the model used in partial hepatectomy studies by stating the ratio of each liver lobe to the total mass of all liver lobes in rats. According to the total liver mass, the right lobe contains 38%, the left lobe is 30%, the tail lobe is 8%, and the quadrat (quadrilateral) lobe, which is two-part, contains 10%. It has been stated that the most suitable model for partial hepatectomy studies in rats is resection of 68-70% of the liver [24].

Partial hepatectomy is one of the most frequently used surgical procedures today and

is an inevitable surgical treatment option in primary liver tumors, trauma, liver metastases of gastrointestinal tumors and liver transplantations [5, 25]. Liver resection has become safer with the development of diagnostic methods, improvement and improvement in surgical techniques, and improvement in postoperative care, especially in the last 25 years [27]. Postoperative mortality and morbidity in liver resection are directly related to preoperative liver function and the functional and regenerative capacity of the remaining liver after postoperative resection. It is a very important support mechanism for replacing the functional hepatic mass in a short time after regeneration of liver tissue with normal parenchyma, tissue injuries and hepatocellular necrosis. Active cell replication starts within 24 hours after partial hepatectomy and this replication continues until the organ reaches its first weight [8].

We do not know exactly the regulatory mechanisms, changes that occur in liver regeneration and their interrelationships. What we know for sure is that the liver knows when to start regeneration and when to stop [3]. Loss of liver tissue initiates regeneration [10]. The sensitive point that allows regeneration to stop is the relationship between body mass and liver mass. When the liver reaches the size to meet the functional needs of the body and carry out metabolism, regeneration stops [28-30]. Interestingly, when a large liver tissue transplant is performed after transplantation relative to the recipient, liver mass decreases until the optimal liver to body mass ratio is achieved [23].

Liver regeneration rates can be calculated by evaluating the liver mass taken in damages caused by partial hepatectomy and the masses of the whole liver taken after a certain time after hepatectomy. They reported that the remaining liver weight doubled 48 hours after 2/3 partial hepatectomy in rats and reached full weight within 7-10 days. In our study, it was found that the liver weights regenerated after 72 hours after partial hepatectomy nearly doubled in the partial hepatectomy groups [14, 31].

In some studies, liver age weights and their amounts of 68% and 32% were used to determine the regeneration rate by placing it in the Child's formula [14, 31]. In our study, the relative liver weight defined by Fishback [19]. The remaining liver weight after partial hepatectomy was subtracted from the liver weight at autopsy and the ratio of this value to the whole liver weight was calculated. The liver regeneration rate was found by multiplying the obtained value by 100 [20]. In the values we obtained, after 70% partial hepatectomy, relative liver weight increased significantly in all study groups starting from the group II.

Partial hepatectomy was performed in this study. Determination of mitotic index and more importantly PCNA index has been used frequently in studies on liver regeneration and played an important role in interpretation of regeneration [32, 33-35]. Hou et al. [25] Mitotic index and PCNA index data were also used to determine the effects of an organic compound named FR167653 on liver regeneration in rats with partial hepatectomy. In their study, they determined that the mitotic index that they determined simultaneously from the liver sections of the control group rats they underwent partial hepatectomy was higher than the PCNA index. The mitotic index and PCNA index data were in parallel with each other. According to the mitotic index and PCNA index results, group II and group III was high. Both mitotic index and PCNA indexes were found to be higher on 1st day compared to 14th day. By decreasing mitotic and PCNA index values in the group III approached to the control group. When the PCNA index results were evaluated in this study, results was in parallel with the previous studies. Proliferation index values between the groups were found to be statistically significant. Studies have shown that the mitotic activity peaks in the resected liver tissue and the tissue has an intense proliferating activity. It was determined in this study and previous studies that the

proliferation activity depends on the time after resection.

Akcan [36] reported that one of the opposite mechanisms seen after hepatectomy is apoptosis and that cell apoptosis begins when regeneration reaches its peak. In addition, it showed that apoptosis accompanies cell proliferation, overgrown cells are eliminated and new tissue formation is successfully completed. Sowa et al. [37] showed that the TUNEL index increased significantly after resection. Although apoptosis decreased over time, the TUNEL index continued to increase compared to control groups. Thus, these data showed that in 70% hepatectomy first apoptosis and correspondingly regeneration occurs. In addition, it has been shown that more tissue damage in the early postoperative phase increases the number of apoptotic cells. In contrast, a slight increase in the TUNEL index was observed at the beginning of 90% hepatectomy. However, 1 day after the operation, apoptosis was observed to increase strongly, which means that the regeneration in tissue damage was highest after 14 days. The TUNEL index supports the results. In this study, it was observed that apoptosis was at the maximum level in the group II, and apoptosis gradually decreased in the group III in the following days.

4. CONCLUSION

In this study, we planned the histological examination of liver regeneration after liver resection. It was observed that regeneration due to the relative weight of the liver increased significantly over time. In histopathological examination performed with light microscopy, it was observed that vacuolization of hepatocytes and dilatation in sinusoids occurred first after partial hepatectomy, and increased mitotic activity, which is an indicator of regeneration increase, in the following days.

Vacuolization, sinusoidal dilatation, apoptosis and mitosis activities were at the highest levels in hepatocytes in group II. In Group III, it was observed that these values reached values close to Group I. It was observed that the mitotic index reached the highest value in group II, and decreased in time in group III. In immunohistochemical staining of liver tissue, it was observed that PCNA positive cells were concentrated in group II and the number of positive cells in group III decreased. It was observed that the time spent in resection directly affected the proliferative process.

Apoptotic cells were observed as positive in staining with the TUNEL method. It was observed that the apoptotic index values reached the maximum level after 24 hours (group II). It was observed that TUNEL positive cells decreased in group III and positivity close to group I.

We think that the data obtained from our study will constitute a very important reference for liver transplantation. Because transplants are inevitable in organ failure and transplant failures pose an important problem. The data we have obtained is of a nature to shed light on the clinic, and transplants can be made according to the course of both mitotic activity and apoptotic activity.

Funding

"This study is supported by Trakya University Scientific Research Projects Coordination Unit. Project Number: 2011-125."

The Declaration of Conflict of Interest/ Common Interest

No conflict of interest or common interest has been declared by the authors.

Authors' Contribution

In the study, the first author contributed 60% and the second author contributed 40%.

The Declaration of Ethics Committee Approval

Approval for the study was obtained from Trakya University Ethics Committee on 09.06.2011.

The Declaration of Research and Publication Ethics

The authors of the paper declare that they comply with the scientific, ethical and quotation rules of SAUJS in all processes of the article and that they do not make any falsification on the data collected. In addition, they declare that Sakarya University Journal of Science and its editorial board have no responsibility for any ethical violations that may be encountered, and that this study has not been evaluated in any academic publication environment other than Sakarya University Journal of Science.

REFERENCES

[1] Aktümsek, "Anatomi ve fizyoloji insan biyolojisi," Nobel Yayınları, Ankara, 3th edt, pp. 366-367, 2006.

[2] T. E. Andreoli, "Liver," In M. B. Fallon, B. M. McGuire, G. A. Abrams, M. R. Arguedas (ed), Cecil essentials of medicine, 5th edt. WB Saunders Company, Philadelpia, pp. 365-398, 2001.

[3] N. Fausto, "Liver regeneration," *Journal of Hepatol*, vol. 32, pp. 19-31, 2000.

[4] M. Basoglu, A. A. Balık, R. Kavak, C. Gundogdu, Z. Erman, R. Yıldırgan, D. Oren, "Effects of growth hormone on hepatic regeneration," *Turk J Med Sci.*, vol. 30, pp. 529-534, 2000.

[5] Z. G. Ren, J. D. Zhao, K. Gu, J. Wang, G. L. Jiang, "Hepatic proliferation after partial liver irradiation in Sprague-Dawley rats," *Mol. Biol. Rep.*, vol. 39, pp. 3829-3836, 2012.

[6] E. A. Pomfret, J. J. Pomposelli, F. D. Gordon, N. Erbay, L. Lyn, W. D. Lewis, "Liver regeneration and surgical outcome in donors of right-lobe liver grafts," *Transplantation*, vol. 76, pp. 5-10, 2003.

[7] T. Nakamura, S. Mizuno, "The discovery of hepatocyte growth factor (HGF) and its significance for cell biology, life sciences and clinical medicine," *Proc Jpn Acad Ser B Phys Biol Sci*., vol. 86, no:6, pp. 588-610, 2010.

[8] S. Perek, S. Kapan, "Cerrahi Gastroenteroloji," In U. Değerli, Y. Bozfakıoğlu (ed), İstanbul, Nobel Tıp Kitabevleri, vol. 5, pp. 194-208, 2000.

[9] G. Garcea, G. J. Maddern, "Liver failure after major hepatic resection," *J Hepatobiliary Pancreat Surg*., vol. 16, pp. 145-155, 2009.

[10] G. K. Michalopoulos, M. C. DeFrances, "Liver regeneration", *Science*, vol. 296, pp. 60-66, 1996.

[11] L. Chen, H. L. Sun, L. Yang, H. J. Du, W. An, "Transfection of human hepatic stimulator substance gene could protect BEL-7402 cells against hepatotoxins," *Zhonghua Gan Zang Bing Za Zhi.*, vol. 12, no:2, pp. 99-101, 2004.

[12] H. Y. Hsu, M. C. Yu, C. W. Lee, "RAM score is an effective predictor for early mortality and recurrence after hepatectomy for hepatocellular carcinoma," *BMC Cancer*, vol. 17, no:1, pp. 742, 2017.

[13] S. Iwatsuki, B. W. Shaw, T. E. Jr Starzi, "Experience with 150 liver resections," *Ann Surg.*, vol. 197, pp. 247-252, 1983.

[14] M. Canbek, M. Uyanoglu, S. Canbek, E. Ceyhan, A. Ozen, B. Durmus, O Turgak, "The effect of geraniol on liver regeneration after hepatectomy in rats," *In Vivo*, vol. 31, no: 2, pp. 209-213, 2017.

[15] M. Bouattour, E. Raymond, S. Qin, A. L. Cheng, U. Stammberger, G. Locatelli, S. Faivre, "Recent developments of c-Met as a therapeutic target in hepatocellular carcinoma," *Hepatology*, vol. 67, no: 3, pp. 1132-1149, 2018.

[16] M. J. Xu, D. Feng, H. Wu, H. Wang, Y. Chan, J. Kolls, N. Borregaard, B. Porse, T. Berger, T. W. Mak, J. B. Cowland, X. Kong, B Gao, "Liver is the major source of elevated serum lipocalin-2 levels after bacterial infection or partial hepatectomy: a critical role for IL-6/STAT3," *Hepatology*, vol. 61, no: 2, pp. 692-702, 2015.

[17] R. Bönninghoff, K. Schwenke, M. Keese, R. Magdeburg, H. Bitter-Suermann, M. Otto, T. Hasenberg, S. Post, J. Sturm, "Effect of different liver resection methods on liver damage and regeneration factors VEGF and FGF-2 in mice," *Can J Surg.*, vol. 55, no: 6, pp. 389-393, 2012.

[18] R. Yang, T. Uchiyama, S. K. Watkins, X. Han, M. P. Fink, "Ethyl pyruvate reduces liver injury in a murine model of extrahepatic cholestasis," *Shock*, vol. 22, pp. 369-375, 2004.

[19] N. Ekici Günay, S. Muhtaroğlu, A. Bedirli, "Administration of Ginkgo biloba extract (egb761) alone and in combination with fk506 promotes liver regeneration in a rat model of partial hepatectomy," *Balkan Med J.*, vol. 35, no: 2, pp. 174-180, 2018.

[20] K. Kagure, Y. Q. Zhang, H. Shibata, I. Kojima, "Immediate onset of DNA synthesis in remnant rat liver after %90 hepatectomy by an administration of follistatin," *J Hepatol*., vol. 28, no: 3, pp. 977-984, 1998.

[21] M. Selzner, P.A. Clavien, "Failure of regeneration of the steatotic rat liver: Disruption at two different levels in the regeneration pathway," *Hepatology*, vol. 31, pp. 35-42, 2000.

[22] R. G. Kilbourn, D. L. Traber, C. Szabo, "Nitrik oxide and shock," Dis Mon., vol. 47, no: 5, pp. 277-348, 1997.

[23] H. Hayashi, M. Nagaki, M. Imose, Y. Osawa, K. Kimura, S. Takai, M. Imao, T. Naiki, T. Kato, H. Moriwaki, "Normal liver regeneration and liver cell apoptosis after partial hepatectomy in tumor necrosis factor-alpha-deficient mice," *Liver Int.*, vol. 25, no: 1, pp. 162-170, 2005.

[24] J. A. Ebrenfried, T. C. Ko, E. A. Thompson, B. M. Evers, "Cell cycle-mediated regulation of hepatic regeneration," *Surgery*, vol. 122, no: 5, pp. 927-935, 1997.

[25] R. Veteläinen, A. K. van Vliet, T. M. van Gulik, "Severe steatosis increases hepatocellular injury and impairs liver regeneration in a rat model of partial hepatectomy," *Ann Surg.*, vol. 245, pp. 44-50, 2007.

[26] D. Palmes, H. U. Spiegel, "Animal models of liver regeneration," *Biomaterials*, vol. 25, no: 9, pp.1601-1611, 2004.

[27] W. C. Meyers, R. S. Jones, "Anatomy," In W. C. Meyers, R. S. Jones (eds), Textbook of liver and biliary surgery, Press: JB Lippincott Company, Philadelphia, pp. 18-38, 1990.

[28] F. G. Court, S. A. Wemyss-Holden, R. A. Dennison, G. J. Maddern, "The mystery of liver regeneration," *Br J Surg.*, vol. 89, pp. 1089-1095, 2002.

[29] J. Kountouras, P. Boura, N. J. Lygidakis, "Liver regeneration after hepatectomy," *Hepatogastroenterology*, vol. 48, no: 38, pp. 556-562, 2001.

[30] N. Fausto, "Hepatic regeneration," D. Zakim, T. D. Boyer Eds., Press: Hepatology WB Saunders, Philadelphia, pp. 32-58, 1998.

[31] S. T. Fan, C. M. Lo, C. L. Liu, C. M. Lam, "Hepatectomy for hepatocellular

carcinoma toward zero hospital deaths," *Ann Surg.,* vol. 229, pp. 322-330, 1999.

[32] N. Assy, G. Y. Minuk, "Liver regeneration: methods for monitoring and their applications," *J Hepatol.,* vol. 26, pp. 945-952, 1997.

[33] Picard, L. Lambotte, P. Starkel, C. Sempoux, A. Saliez, V. V. D. Berge, "Steatosis is not sufficient to cause an impaired regenerative response after partial hepatectomy in rats," *J Hepatol., vol.*32, pp. 645-652, 2002.

[34] J. O. Castro-e-Silva, S. Zucoloto, F. S. Ramalho, L. N. Z. Ramalho, J. M. C. Reis, A. A. C. Bastos, M. V. H. Brito, "Antiproliferative activity of *Copaifera duckei* oleoresin on liver regeneration in rats," *Phytother Res.,* vol. 18, pp. 92-94, 2004.

[35] E. Kamer, A. Çöker, A. R. Sevinç, E. Özkara, E. Özer, T. Özzeybek, "Effect of intraperitoneal dministration of gemcitabine and paclitaxel on hepatic regeneration in rats," *Turk J Gastroenterol.,* vol. 14, no: 1, pp. 1-6, 2003.

[36] Akcan, "The effect of amrinone on liver regeneration in experimental hepatic resection model," *J Surg Res.,* vol. 130, pp. 66-72, 2006.

[37] J. P. Sowa, J. Best, T. Benko, M. Bockhorn, Y. Gu, E. M. Niehues, "Extent of liver resection modulates the activation of transcription factors and the production of cytokines involved in liver regeneration," *World J Gastroenterol.,* vol. 14, no: 46, pp. 7093-8100, 2008.

SAKARYA ÜNİVERSİTESİ
FEN BİLİMLERİ ENSTİTÜSÜ DERGİSİ

Sakarya University Journal of Science
SAUJS

e-ISSN 2147-835X | Period Bimonthly | Founded: 1997 | Publisher Sakarya University |
http://www.saujs.sakarya.edu.tr/en/

Title: Detection of Covid-19 from Chest CT Images Using Xception Architecture: A Deep Transfer Learning Based Approach

Authors: Özlem POLAT

Recieved: 2021-04-01 14:11:06

Accepted: 2021-05-05 13:21:05

Article Type: Research Article

Volume: 25
Issue: 3
Month: June
Year: 2021
Pages: 800-810

How to cite
Özlem POLAT; (2021), Detection of Covid-19 from Chest CT Images Using Xception Architecture: A Deep Transfer Learning Based Approach. Sakarya University Journal of Science, 25(3), 800-810, DOI:
https://doi.org/10.16984/saufenbilder.903886
Access link
http://www.saujs.sakarya.edu.tr/en/pub/issue/62736/903886

Sakarya University Journal of Science 25(3), 800-810, 2021

Detection of Covid-19 from Chest CT Images Using Xception Architecture: A Deep Transfer Learning Based Approach

Özlem POLAT*[1]

Abstract

Covid-19 infection, which first appeared in Wuhan, China in December 2019, affected the whole world in a short time like three months. The disease caused by the virus called SARS-CoV-2 affects many organs, especially the lungs, brain, liver and kidney, and causes a large number of deaths. Early detection of Covid-19 using computer-aided methods will ensure that the patient reaches the right treatment without wasting time, and the spread of the disease will be controlled. This study proposes a solution for detecting Covid-19 using chest computed tomography (CT) scan images. Firstly, features are extracted by Xception network, convolutional neural network (CNN) based transfer learning method, then classification process is performed with a fully connected neural network (FCNN) added at the end of this architecture. The classification model was tested ten times on the accessible SARS-CoV-2-CT-scan dataset containing 2482 CT images labelled as covid and non-covid. The precision, recall, f1-score and accuracy metrics were used as performance measures; and ROC curve related to the model was drawn. While obtaining an average of 98.89% accuracy, in the best case, 99.59% classification performance was achieved. Xception outperforms other methods in the literature. The results promise that the proposed method can be evaluated as a clinical option helping experts in the detection of Covid-19 from CT images.

Keywords: Covid-19, Classification, Deep learning, Xception

1. INTRODUCTION

The infection epidemic caused by the SARS-CoV-2 virus was named Coronavirus Disease 2019, shortly Covid-19, by the World Health Organization (WHO). Covid-19 spread rapidly to many countries and was officially announced as a pandemic by WHO on March 11, 2020, with the death of more than 4000 people [1]. Covid-19 is a respiratory disease, and adversely affects many organs, especially the lungs. The disease is highly contagious and has many different symptoms, mainly fever, dry cough and tiredness. Since the first Covid-19 case was detected in China, the disease spread first to other provinces of China and then to all over the world [2]. Due to the sudden emergence of Covid-19 and its spread all over the world, different research centers immediately started working for the detection, prevention and treatment of the disease [3]. Studies are not only conducted in the field of medicine and biotechnology; In addition, researchers from different fields are working on

*Corresponding author: ozlem.polat@cumhuriyet.edu.tr
[1] Sivas Cumhuriyet University, Faculty of Technology, Department of Mechatronics Engineering, Sivas, Turkey. ORCID: https://orcid.org/0000-0002-9395-4465

the diagnosis and prevention of the disease with the help of computer-aided systems.

In some cases, if there is no vaccine or drug for Covid-19, it is compulsory to detect the disease in a short time and isolate the infected person from healthy people for controlling the spread of the disease. With the onset of the Covid-19 pandemic, the reverse transcription polymerase chain reaction (RT-PCR) test developed by Corman et al. [4] has begun to be used for the definitive diagnosis of the disease. It is presented that the overall positive RT-PCR rate initially was in the range of approximately 30-60% for swab samples taken from the throat [5]. The sensitivity of the RT-PCR test in the first days of the Covid-19 is low. Therefore, the problem arises that people with Covid-19 cannot be diagnosed and cannot receive the appropriate treatment for them. In addition, patients who have not been diagnosed with Covid-19 infect more people because of the contagious nature of the virus. Lung CT is both easy to use and can give results in a short time for the determination the presence of Covid-19. According to the results of recent research, Covid-19 disease shows the same or very similar radiological features in almost all patients [6]. Radiological features of Covid-19 were seen in people with negative RT-PCR tests but with symptoms of the disease. Therefore, it is beneficial to use lung CT to determine whether the patient is infected with Covid-19 [7].

As soon as medical images were scanned and uploaded to a computer, researchers started processing it automatically. In recent years, computer technologies and machine learning techniques have begun to be preferred in medical sciences in order to diagnose some diseases or lesions in the body [8]. Panwar et al. [9] proposed a CNN-based model called nCOVnet for detecting Covid-19 from lung X-ray images. nCOVnet consists of 24 layers, and 18 of which are part of VGG16 model. They used a dataset of 337 chest X-ray images in total, including Covid-19 positive and negative; and revealed an accuracy of 88.10%. Apostolopoulos and Mpesiana [10] applied different transfer learning networks for solving Covid-19 detection problem; and used publicly available two datasets including 1427 and 1442 X-ray images. VGG19 provided the best classification results with 98.75%.

The study by Li et al. [11] offered COVNet using ResNet50 deep learning architecture as the backbone. They trained and tested the model on 4352 CT images of 3322 cases. As a result of the experiments, they obtained the values of 90%, 96% and 0.96 for sensitivity specificity and AUC, respectively. In the study explored by Jain et al. [12], ResNet101 deep learning model was attempted to distinguish Covid-19 and viral pneumonia from x-ray images. The dataset, originally containing 1215 X-ray images, was increased by data augmentation to 1832; and, as a result of the tests, 97.77% classification accuracy has been achieved. Harmon et al. [13] applied artificial intelligence based Grad-CAM method on CT images. They achieved up to 90.8% accuracy.

Rahimzadeh and Attar [14] solved the same problem using transfer learning methods on X-ray images. They extracted the features with the use of Xception and ResNet50V2 networks in parallel; and they concatenated the features and classified with FCNN with Softmax activation function. The dataset including normal, pneumoni and Covid-19 classes were augmented and the model tested on 11,302 images. 91.4% overall average accuracy was obtained for all classes. Ozturk et al. [15] used a network of 17 convolution layers in their study; and they applied different filters to each layer. They also preferred the DarkNet model as a classifier; and they achieved 98.08% and 87.02% success in the double and triple classification problem, respectively, in distinguishing Covid-19. In a study which set out to detection of Covid-19,

Wang et al. [16] proposed a deep learning model (Covid-Net), which achieved 92.4% classification performance. Sethy et al. [17] extracted the features related to X-ray images using deep CNN and classified them using Support Vector Machine (SVM) for detection of coronavirus infected patients. The methodology deals with three categories of images, i.e., Covid-19, pneumonia and normal. They achieved 95.33% success with ResNet50+SVM.

Hemdan et al. [18] reported 90% success rate using DenseNet201 and VGG16 in a study investigating Covid-19. Narin et al. [19] performed a series of experiments using five different transfer learning applications on X-ray images. They have implemented three binary classifiers. They had the best performance of 96.1% for covid-19 vs normal with ResNet50 and ResNet101. Ying et al. [20] developed a new deep learning model called DRE-Net built on the ResNet architecture; and detected Covid-19 from CT images with 86% accuracy.

Wang et al. [21] modified the Inception transfer learning network to build the Covid-19 detection algorithm from chest CT images; and they obtained 79.3% classification performance. Wang et al. [22] created a 3D deep neural network called DeCovNet, using 3D CT volumes. First, segmentation was applied using U-Net, and the segmented images were given as input to DeCovNet network. They managed to detect Covid-19 in CT images with 90.8% accuracy. Xu et al. [23] used two CNN 3D classification methods on CT images, and obtained 86.7% accuracy rate for three classes: Covid-19, viral pneumonia and normal. Yoo et al. [24] created deep learning based three binary decision trees and achieved 98%, 80% and 95% classification performance with ResNet18.

Another study was conducted by Albahli [25] using deep learning models. Albahli tried to classify other chest diseases against Covid-19 with the model he used; and achieved a classification accuracy of 87% with ResNet152. Civit-Masot et al. [26] suggested VGG16 model as the solution of Covid-19 detection problem. They trained and tested the model on 396 X-ray images (132 Covid-19, 132 Healthy and 132 Pneumonia); and obtained 86% accuracy rate. Singh et al. [27] evaluated a CNN-based model on CT images to classify patients infected with Covid-19. Ahuja et al. [28] trained transfer learning models on CT images to determine the presence of Covid-19; and with ResNet18 model they achieved 99.4% classification performance.

As seen above, many studies have been conducted using different datasets to detect Covid-19. Apart from these, there is also a SARS-CoV-2-CT-Scan dataset consisting of 2482 CT images labeled as covid and non-covid created by Soares et al. [29]. This dataset was also used in [30-32] for Covid-19 detection. Soares et al. used various machine learning methods, but achieved the best success with eXplainable Deep Learning approach (xDNN). Silva et al. [30] have achieved 98.99% and 87.60% accuracy with the modified EfficientNetB0 using SARS-CoV-2-CT-Scan dataset and another dataset containing 812 CT scan images, respectively. Yazdani et al. [31] proposed to use attentional residual convolutional network, which can better focus on infected lung areas; and they achieved 92% classification performance. Konar et al. [32] used a semi-controlled shallow neural network containing a network they called PQIS-Net to segment the lung CT images and used fully connected layers to determine the class labels of images.

This study aims to detect Covid-19 from CT images, that is, CT images are classified as covid and non-covid. For this purpose, Xception network, one of the deep transfer learning architectures, has been trained and tested on the SARS-CoV-2-CT-Scan dataset. The main contributions of this study are as follows: (1) Covid-19 caused by the SARS-CoV-2 virus is a disease with high contagiousness and causing death. Fast and accurate detection of Covid-19 will enable early treatment and thus reduce the hospitalization rate and mortality rate of patients. (2) The model proposed in this study classifies covid and non-covid cases from chest CT images. (3) With the proposed transfer learning technique, weights related to the network that were previously trained with big data are used. Thus, classification is performed with less computational load and high performance without the need for a very large data set.

2. MATERIALS and METHODS

2.1. SARS-CoV-2-CT-Scan Dataset

In this study, a publicly available dataset consisting of 2482 CT images was used. Images were obtained from a total of 120 patients, 60 female and 60 male, who were infected with the

SARS-CoV-2 virus (covid) and were not infected by this virus but have other pulmonary diseases (non-covid). The distribution of the sexes of the patients is as follows: 32 of 60 patients belonging to the covid class are male and 28 are female. In the non-covid class, the number of male and female patients are equal, that is, 30. The dataset was created from CT images of patients admitted to hospitals in Sao Paulo, Brazil. In the dataset, there are 1252 and 1230 CT images of covid and non-covid classes, respectively. Sample CT images of these classes are shown in Figure 1.

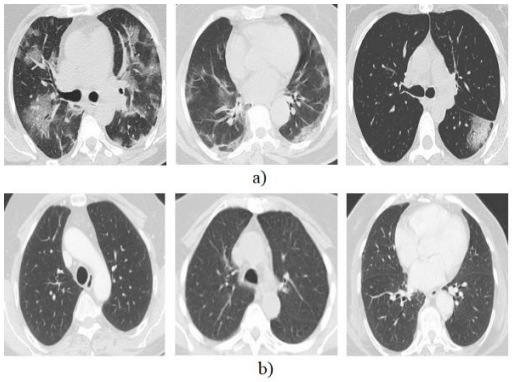

Figure 1 Chest CT images a) covid b) non-covid

In order to train and test Xception architecture, CT images are divided into two groups as 70% and 30%. Thus, 1737 of the images were used for training and 745 for test.

2.2. Convolutional Neural Networks

Convolution was first described by LeCun et al. [33] in 1989. Convolution is simply a mathematical operation in which two matrices are multiplied on an element-by-element basis and then summed [34]. Networks using convolution process are called convolutional neural networks (CNN). CNNs usually consist of five layers:

1) Convolution layer: In this layer, the filter matrix, which will automatically extract the features from the image with the image matrix is subjected to the convolution process. First, the filter is placed in the upper left corner of the image. Here, pixels of the image matrix and filter matrix with the same index are multiplied by each other and all results are summed. This sum is then recorded in the output matrix called the feature map. Then the filter is shifted to the right and the multiplication operations are repeated. At the end of the row, the filter is shifted downwards and the same operations are repeated from left to right. After all rows are scanned from left to right with these operations, an output matrix is created.

2) Non-linearity layer: This layer is used after the convolution layer; and transform the linear output of the previous layer into a nonlinear structure using an activation function. In this way, the learning of the network is accelerated. Rectified Linear Unite (ReLU) [35], which has the ability to pull negative values to zero, is generally preferred as the activation function.

3) Pooling layer: This layer is typically used after non-linearity layer. The main function of this layer is to reduce the dimension of the feature map. With the dimension reduction process, both the computational load is reduced and the system is prevented from overfitting. As in the convolution layer, the filter sizes can be different from each other in this layer. Thanks to these filters, average pooling, where the values in the input matrix are averaged, or maximum pooling, where the maximum is taken, is performed.

4) Flattening layer: This layer transforms the matrix into a vector by successively adding the rows of the output matrix obtained from the previous layer, so that one-dimensional data can be input to fully connected layers.

5) Fully connected layer(s): All neurons in this layer are connected to every neuron of the next layer. By using the softmax activation function in the last layer, the images are labeled and the classes they belong to are determined.

2.3. Xception Architecture

With the spread of CNNs in computer vision, different structured models using CNN have been created. Firstly, the LeNet-style models [36] were introduced in 1995, and then various models were created to be used in classification and recognition problems. One of these models is Inception. The Inception architecture, also known as Inception-v1 [37], was created in 2014 by Szagedy et al. Later it was updated as Inception-

v2, Inception-v3 [38] and Inception-ResNet [39]. The Xception network [40] used in this study can be called an interpretation of the Inception modules. The name Xception also comes from "extreme inception". Therefore, it will help to understand the Xception architecture to talk briefly about Inception first.

The object to be detected in object recognition or image classification may be large in some images and small in some images. In other words, the size of the object can be of different sizes in different images. Different object sizes can make it difficult to determine the filter size for the convolution process. A large filter size should be preferred for the object that looks large in the images, and a small filter size should be preferred for small objects. Inception architecture offers a solution to the problems caused by objects of different sizes by proposing to use more than one filter of different sizes at the entrance. It also suggests sending the output of this module to another inception module again. Figure 2 shows a simplified Inception module.

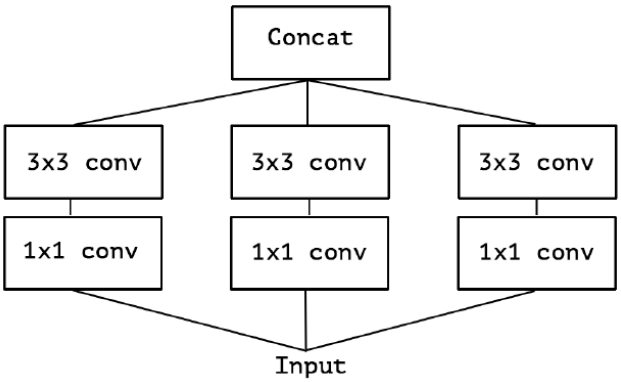

Figure 2 Simplified inception module [40]

In Xception architecture, differently from Inception architecture, a convolution operation almost same with depthwise separable convolution [41] is used. This type of convolution contains a depthwise convolution and a pointwise convolution that follows it. In depthwise convolution each filter independently processes only one channel of the input image; and in pointwise convolution, 1x1 dimensional filter iterates every single point of the input.

The module in Xception architecture uses depthwise separable convolution in different order; in other words, as seen in Figure 3, 1x1 convolution is used first and then channel-wise spatial convolution.

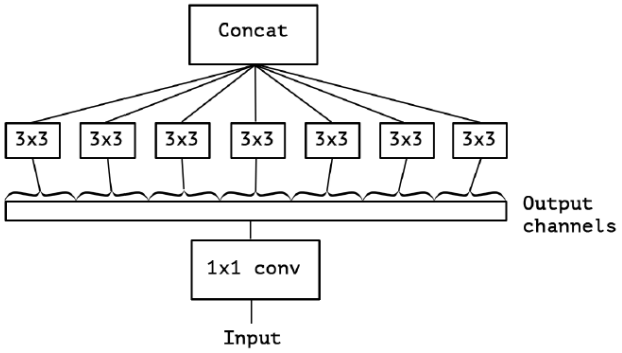

Figure 3 Extreme version of Inception module [40]

Xception architecture consists of three structures: Entry flow, middle flow and exit flow. These three structures consist of 14 modules (4, 8 and 2 modules, respectively) containing 36 convolution layers in total. There are residual connections in modules except the first module of entry flow and the last module of exit flow. The Xception architecture starts with entry flow, which contains 4 modules and each module has two convolution layers. In the first module, convolution is performed with 32 and 64 filters with 3x3 filter size. In the other three modules in this flow, separable convolution is realized with 128, 256 and 728 filters in 3x3 filter size. The entry flow accepts 299x299x3 size images as input and creates a 19x19x728 size feature map at the output. In middle flow, three separable convolution processes with 728 filters in 3x3 size are repeated 8 times. Middle flow creates a 19x19x728 feature map at the output. The feature map, which is the output of middle flow, is given as input to exit flow. Exit flow has two modules. In the first module, separable convolution is performed with 728 and 1024 filters in 3x3 sizes, while in the last module it is performed with 1536 and 2048 filters. Afterwards, the architecture is terminated with the addition of fully connected layers. The flows and modules related to the Xception architecture are shown in the Figure 4.

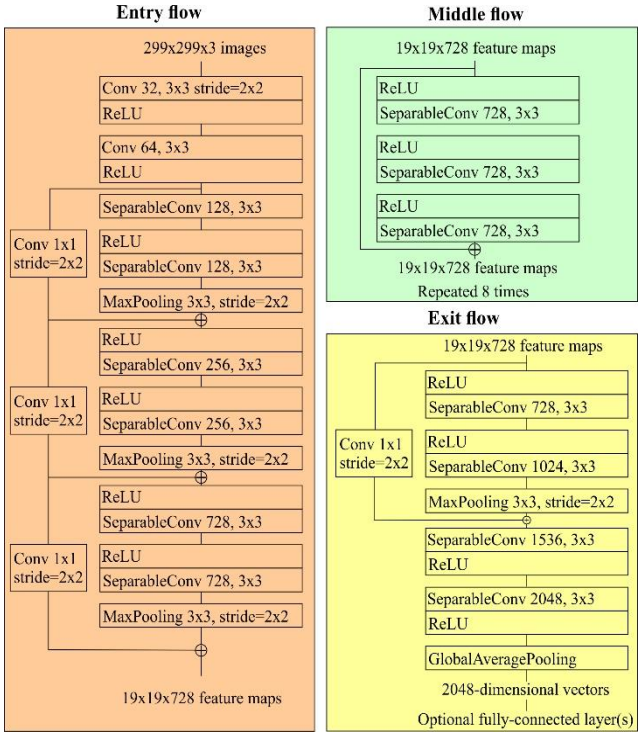

Figure 4 Xception architecture

3. EXPERIMENTAL RESULTS

In this study, chest CT images of cases with and without Covid-19 disease were trained and tested using Xception, ResNet50V2 and VGG16 deep learning architectures. While these models were used to extract features from images, a 2-layer FCNN was used for classification purpose. The first layer of FCNN was formed with 16 neurons; in the last layer where softmax was used, as many neurons are used as the number of classes. Experimental results were compared with the results determined by the experts in terms of precision (1), recall (2), f1-score (3) and accuracy (4) metrics. The mathematical expressions for these metrics are as follows:

$$Precision = \frac{TruePositive}{TruePositive+FalsePositive} \quad (1)$$

$$Recall = \frac{TruePositive}{TruePositive+FalseNegative} \quad (2)$$

$$F1-score = 2 \times \frac{Precision \times Recall}{Precision+Recall} \quad (3)$$

$$Accuracy = \frac{TP+TN}{TP+FP+TN+FN} \times 100 \quad (4)$$

Proposed model was trained and tested on Google Colab using the Keras [42] and Tensorflow [43] libraries. The dataset was split by 70% and 30% as training and test, and has been trained and tested with Xception, ResNet50V2 and VGG16 architectures.

The parameters for experiment, the number of epochs and batch size, were set to 50 and 16, respectively. Adadelta [44], Adam and SGD were chosen as optimizers for Xception, ResNet50V2 and VGG16 transfer learning models, respectively, due to their better performance. Adadelta, Adam, and SGD were used with learning rates of 1.0, 0.0001, and 0.0001, respectively. Experiments related to models were run 10 times. The average accuracy values for, Xception, ResNet50V2 and VGG16 were obtained as 98.89%, 96.95% and 97.72%, respectively. Since Xception gives better results than the other two methods, this study focuses on the Xception model and its results. So the results related to Xception obtained from these 10 experiments are shown in Table 1.

Table 1 Experimental results of Xception network

Exp. No	Precision	Recall	F1-score	Acc. (%)
1	1.00	1.00	0.99	99.19
2	0.99	0.99	0.99	98.79
3	0.99	0.99	0.99	99.33
4	0.99	0.99	0.99	98.93
5	0.99	0.99	0.99	99.06
6	0.98	0.98	0.98	97.72
7	0.98	0.98	0.98	98.26
8	0.99	0.99	0.99	99.46
9	0.98	0.98	0.98	98.66
10	1.00	1.00	1.00	99.59
Ave.	0.99	0.99	0.99	98.89

According to Table 1, covid and non-covid class images are classified with an average accuracy of 98.89%. The best classification performance is obtained from the 10th experiment with an accuracy of 99.56%. The Receiver Operator Characteristic (ROC) curve is an evaluation metric often used in classification problems. It is created by plotting True Positive Rate against False Positive Rate at various threshold values. Area Under Curve (AUC) is a measure of the classifier's ability to distinguish between classes and takes values between 0 and 1. The closer the

AUC value to 1, the better the classifier's performance. The ROC curve for the model with the AUC values can be seen from Figure 5. Confusion matrix and accuracy-loss graphs of the model for experiment 10 are shown in Figures 6 and 7, respectively. As seen from the confusion matrix, 375 of 376 images with covid and 367 of 369 images without covid are classified correctly; that is, the recall values for the covid and non-covid classes are calculated as 0.997 and 0.995, respectively. For this reason, the average recall values of the classes are stated as 1.00 in the Table 1 due to the rounding of the numbers.

In addition, the obtained classification results prove that even with a small number of FCNN layers and a small number of neurons such as 16 used in this layer, covid and non-covid classes are distinguished from each other with high performance.

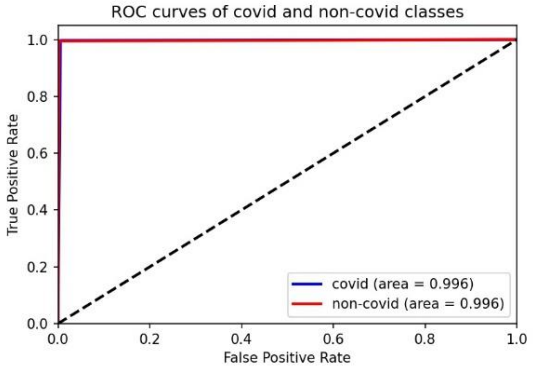

Figure 5 ROC curve for the Xception model

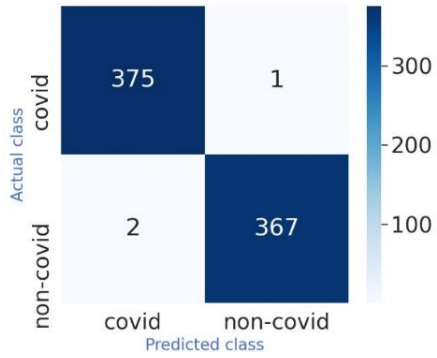

Figure 6 The confusion matrix of the 10th best performing experiment

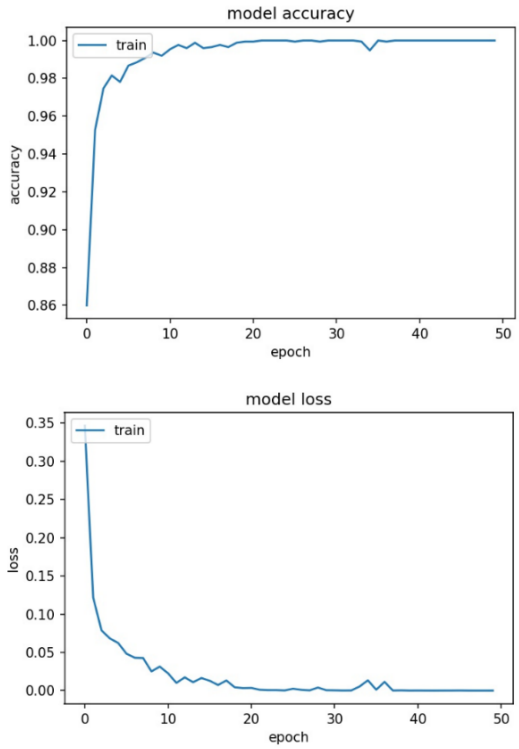

Figure 7 Accuracy and loss graphics of the classifier

Since 2019, many studies have been carried out on different datasets in order to detect Covid-19 from CT images with computer-aided technologies and help experts in the diagnosis of the disease. In these studies, both classical machine learning methods and frequently deep learning techniques were used. Table 2 shows the comparative results related to proposed study and other studies in the literature using the same dataset. As can be seen from Table 2, other studies have also used CNN-based deep learning; and the Xception model outperforms other models using the same dataset.

Table 2 Performance comparison

Authors	Methods	Acc. %)
Soares et al. [29]	xDNN	97.38
Silva et al. [30]	Modified EfficientB0	98.99
Yazdani et al. [31]	Attentional Residual Conv. Network	92.00
Konar et al. [32]	PQIS-Net	93.10
Proposed	Xception	99.59

4. CONCLUSION

With the onset of the Covid-19 epidemic and its globalization, studies in the field of computer technologies have started and continue rapidly, as in other fields. The definitive diagnosis of Covid-19 is possible with the RT-PCR test; however, this test gives results between 4 and 6 hours and this period is not too short. For this reason, computer-aided technologies have begun to be produced that will help experts in the detection of the disease and give results within seconds. There are various transfer learning models in the literature. In this study, Xception, ResNet50V2 and VGG16 models were examined. The models were trained and tested, on a public dataset of 2482 images. As a result, images belonging to the covid and non-covid classes were classified with an average performance of 98.89%, 96.95% and 97.72% for the Xception, ResNet50V2 and VGG16 models, respectively. Because it is more successful than other models, Xception is recommended as a transfer learning method for the detection of Covid-19. In addition, the best 99.59% classification performance was achieved with Xception. The achievements are at a level that can compared with the literature, and the proposed model gives better results than studies using the same dataset. This is promising in that the proposed model will assist experts in medical decision making.

In future study, it is aimed to detect Covid-19 by applying hybrid models consisting CNNs on more data using data augmentation techniques.

Funding

The author has no received any financial support for the research, authorship or publication of this study.

The Declaration of Conflict of Interest/ Common Interest

No conflict of interest or common interest has been declared by the authors.

The Declaration of Ethics Committee Approval

This study does not require ethics committee permission or any special permission.

The Declaration of Research and Publication Ethics

The authors of the paper declare that they comply with the scientific, ethical and quotation rules of SAUJS in all processes of the paper and that they do not make any falsification on the data collected. In addition, they declare that Sakarya University Journal of Science and its editorial board have no responsibility for any ethical violations that may be encountered, and that this study has not been evaluated in any academic publication environment other than Sakarya University Journal of Science.

REFERENCES

[1] S.E. Park, “Epidemiology, virology, and clinical features of severe acute respiratory syndrome – coronavirus-2 (SARS-CoV-2; Coronavirus Disease-19)” Clin Exp Pediatr vol. 63, no. 4, pp. 119-124, 2020. doi:10.3345/cep.2020.00493

[2] C.C. Lai, C.Y. Wang, Y.H. Wang, S.C. Hsueh, W.C. Ko et al., “Global epidemiology of coronavirus disease 2019 (COVID19): disease incidence, daily cumulative index, mortality, and their association with country healthcare resources and economic status” Int J Antimicrob Agents, vol. 55, no. 4, pp. 105946, 2020. doi:10.1016/j.ijantimicag.2020.105946

[3] WHO. Coronavirus disease (covid-2019) r&d. https://www.who.int/blueprint/priority-diseases/key-action/novel-coronavirus/en/ Last access date 02.04.2021.

[4] V.M. Corman, O. Landt, M. Kaiser, R. Molenkamp, A. Meijer et al., “Detection of 2019 novel coronavirus (2019-nCoV) by

real-time RT-PCR", Euro Surveill, vol. 25, no. 3, pp. 2000045, 2020.

[5] Y. Yang, M. Yang, C. Shen, F. Wang, J. Yuan et al. "Evaluating the accuracy of different respiratory specimens in the laboratory diagnosis and monitoring the viral shedding of 2019-nCov infections", medRxiv, 2020. doi:10.1101/2020.02.11.200214

[6] M. Chung, A. Bernheim, X. Mei, N. Zhang, M. Huang et al., "CT imaging features of 2019 novel coronavirus (2019-nCoV)", Radiology, vol. 295, no. 1, pp. 202-207, 2020. doi:10.1148/radiol.2020200230

[7] T. Ai, Z. Yang, H. Hou, C. Zhan, C. Chen et al., "Correlation of chest CT and RT-PCR testing for coronavirus disease 2019 (COVID-19) in China: A report of 1014 cases", Radiology, vol. 296, no. 2, pp. E32-E40, 2020. doi:10.1148/radiol.2020200642

[8] G. Litjens, T. Kooi, B.E. Bejnordi, A.A.A. Setio, F. Ciompi et al., "A survey on deep learning in medical image analysis", Medical Image Analysis, vol. 42, pp. 60-88, 2017. doi:10.1016/j.media.2017.07.005

[9] H. Panwar, P.K. Gupta, M.K. Siddiqui, R. Morales-Mendenez, V. Singh, "Application of deep learning for fast detection of COVID-19 in X-Rays using nCOVnet", Chaos, solitons and fractals, vol. 138, pp. 109944, 2020. doi:10.1016/j.chaos.2020.109944

[10] I.D. Apostolopoulos, T.A. Mpesiana, "Covid-19: automatic detection from x-ray images utilizing transfer learning with convolutional neural networks", Phys Eng Sci Med, vol. 43, pp. 635-640, 2020. doi:10.1007/s13246-020-00865-4

[11] L. Li, L. Qin, Z. Xu, Y. Yin, X. Wang et al., "Using artificial intelligence to detect COVID-19 and community-acquired pneumonia based on pulmonary CT: Evaluation of the diagnostic accuracy", Radiology, vol. 269, no. 2, pp. E65-E72, 2020. doi:10.1148/radiol.2020200905

[12] G. Jain, D. Mittal, D. Thakur, M.K. Mittal, "A deep learning approach to detect Covid-19 coronavirus with X-ray images", Biocybernetics and Biomedical Engineering, vol. 40, no. 1, pp. 1391-1405, 2020. doi:10.1016/j.bbe.2020.08.008

[13] S. A. Harmon, T.H. Sanford, S. Xu, E.B. Turkbey, H. Roth et al., "Artificial intelligence for the detetion of Covid-19 pneumonia on chest CT using multinational datasets", Nat Commun, vol. 11, pp. 4080, 2020. doi:10.1038/s41467-020-17971-2

[14] M. Rahimzadeh and A. Attar, "A modified deep convolutional neural network for detecting Covid-19 and pneumonia from chest x-ray images based on concatenation of Xception and ResNet50V2", Informatics in Medicine Unlocked, vol. 19, pp. 100360, 2020. doi:10.1016/j.imu.2020.100360

[15] T. Ozturk, M. Talo, E.A. Yildirim, U.B. Baloglu, O. Yildirim et al., "Automated detection of Covid-19 cases using deep neural networks with X-ray images", Computers in Biology and Medicine, vol. 121, pp. 103792, 2020. doi:10.1016/j.compbiomed.2020.103792

[16] L. Wang, Z.Q. Lin, A. Wong, "COVID-Net: A tailored deep convolutional neural network design for detection of Covid-19 cases from chest radiography images", arXiv, arXiv:2003.09781, 2020. https://arxiv.org/abs/2003.09871

[17] P.K. Sethy, S.K. Behera, P.K. Ratha, P. Biswas, "Detection of coronavirus disease (Covid-19) based on deep features ansd support vector machine", International Journal of Mathematical, Engineering and Management Sciences, vol. 4, no. 5, pp. 642-651, 2020. doi:10.33889/IJMEMS.2020.5.4.052

[18] E.E.D. Hemdan, M.A. Shouman, M.E. Karar, "COVIDX-Net: A framework of

deep learning classifiers to diagnose Covid-19 in X-ray images", arXiv, arXiv:2003.11055, 2020. https://arxiv.org/abs/2003.11055

[19] A. Narin, C. Kaya, Z. Pamuk, "Automatic detection of coronavirus disease (Covid-19) using x-ray images and deep convolutional neural networks", arXiv, arXiv:2003.10849, 2020. https://arxiv.org/abs/2003.10849

[20] S. Ying, S. Zheng, L. Li, X. Zhang, X. Zhang et al., "Deep learning enables accurate diagnosis of novel coronavirus (Covid 19) with CT images", medRxiv, 2020. doi:10.1101/2020.02.23.20026930

[21] S. Wang, B. Kang, J. Ma, X. Zeng, M. Xiao et al., "A deep learning algorithm using CT images to secreen for coronavirus disease (Covid-19)", medRxiv, 2020. doi:10.1101/2020.02.14.20023028

[22] X. Wang, X. Deng, Q. Fu, Q. Zhou, J. Feng et al., "A weakly-supervised framework for Covid-19 classification and lesion localization from chest CT", IEEE Trans Med Imaging, vol. 39, no. 8, pp. 2615-2625, 2020. doi:10.1109/TMI.2020.2995965

[23] X. Xu, X. Jiang, C. Ma, P. Du, X. Li et al., "Deep learning system to screen coronavirus disease 2019 pneumonia", arXiv, 2002.09334, 2020. https://arxiv.org/abs/2002.09334

[24] S.H. Yoo, H. Geng, T.L. Chiu, S.K. Yu, D.C. Cho et al., "Deep learning-based decision-tree classifier for Covid-19 diagnosis from chest X-ray imaging", Front Med, vol. 7, no. 427, pp. 1-8, 2020. doi: 10.3389/fmed.2020.00427

[25] S. Albahli, "A deep neural network to distinguish covid-19 from other chest diseases using X-ray images", Curr Med Imaging Rev, vol. 16, pp. 1-11, 2020. doi: 10.2174/1573405616666200604163954

[26] J. Civit-Masot, F. Luna-Perejon, M.D. Morales, A. Civit, "Deep learning system for Covid-19 diagnosis aid using X-ray pulmonary images", Appl Sci, vol. 10, no. 13, pp. 4060, 2020. doi:10.3390/app10134640

[27] D. Singh, V. Kumar, K. Vaishali, M. Kaur, "Classification of Covid-19 patients from chest CT images using multi-objective differential evolution-based convolutional neural networks", Eur J Clin Microbiol Infect Dis, vol.39, pp. 1379-1389, 2020. doi: 10.1007/s10096-020-03901-z

[28] S. Ahuja, B.K. Panigrahi, N. Dey, V. Rajinikanth, T.K. Gandhi, "Deep transfer learning-based automated detection of Covid-19 from lung CT scan slices", Appl Intell, pp. 1-15, 2020. doi:10.1007/s10489-020-01826-w

[29] E. Soares, P. Angelov, S. Biaso, M.H. Froes, D.K Abe, "SARS-CoV-2 CT Scan Dataset: A large dataset of real patients CT scans for SARS-CoV-2 identification", MedRxiv, 2020.

[30] P. Silva, E. Luz, G. Silva, G. Moreira, R. Silva, D. Lucio, D. Menotti, "Covid-19 Detection in CT Images with Deep Learning: A Voting-Based Scheme And Cross-Datasets Anaşysis", Informatics in Medicine Unlocked, vol. 20, pp. 100427, 2020.

[31] S. Yazdani, S. Minaee, R. Kafieh, N. Saeedizadeh, M. Sonka, "Covid CT-Net: Predicting Covid-19 from Chest CT Images using Attentional Convolutional Network", arXiv, 2020.

[32] D. Konar, B.K. Panigrahi, S. Bhattacharyya, N. Dey, "Auto-Diagnosis of COVID-19 using lung CT images with semi-supervised shallow learning network", IEEE Access, vol. 9, pp. 28716-28728, 2020. doi: 10.1109/ACCESS.2021.3058854

[33] Y. LeCun, B. Boser, J.S. Denker, D. Henderson, R.E. Howard, W. Hubbard, L.D. Jackel, “Backpropagation applied to handwritten zip code recognition”, Neural Comput, vol. 1, no. 4, pp. 541-551, 1989. doi: 10.1162/neco.1989.1.4.541

[34] I. Goodfellow, Y. Bengio, A. Courville, "Deep Learning", MIT Press, 2016.

[35] V. Nair, G.E. Hinton, "Rectified Linear Units Improve Restricted Boltzmann Machines", In Proc.: 27th International Conference on Machine Learning (ICML'10), June 21-24, Haifa, Israel pp. 807-814, 2010.

[36] Y. LeCun, L. Jackel, L. Bottou, C. Cortes, J.S. Denker, H. Drucker, I. Guyon, U. Muller, E. Sackinger, P. Simard et al., “Learning algorithms for classification: A comparison on handwritten digit recognition”, Neural Networks: The Statistical Mechanics Perspective, pp. 261-276, 1995.

[37] C. Szegedy, W. Liu, Y. Jia, P. Sermanet, S. Reed, D. Anguelov, D. Erhan, V. Vanhoucke, A. Rabinovich, “Going deeper with convolutions”, In: Proceedings of the IEEE conference on computer vision and pattern recognition. arXiv:1409.4842, 2014. https://arxiv.org/abs/1409.4842

[38] C. Szegedy, V. Vanhoucke, S. Ioffe, J. Shlens, Z. Wojna, “Rethinking the inception architecture for computer vision”, arXiv:1512.00567, 2015. https://arxiv.org/abs/1512.00567

[39] C. Szegedy, S. Ioffe, V. Vanhoucke, A. Alemi, “Inception-v4, Inception-ResNet and the impact of residual connections on learning”, arXiv:1602.07261, 2016. https://arxiv.org/abs/1602.07261

[40] F. Chollet, “Xception: Deep learning with depthwise separable convolutions”, arXiv, arXiv:1610.02357v3, 2017. https://arxiv.org/abs/1610.02357

[41] L. Sifre, “Rigid-motion scattering for image classification”, Ph.D. thesis, 2014.

[42] F. Chollet, “Keras”, 2015. https://github.com/fchollet/keras

[43] A. Martin, A. Agarwal, P. Barham, E. Brevdo, Z. Chen et al., "TensorFlow: Large-scale machine learning on heterogeneous systems" (software available from: tensorflow.org), 2015.

[44] M.D. Zeiler, “Adadelta: An adaptive learning rate method”, ArXiv abs/1212.5701, 2012. https://arxiv.org/abs/1212.5701v1

SAKARYA ÜNİVERSİTESİ
FEN BİLİMLERİ ENSTİTÜSÜ DERGİSİ

Sakarya University Journal of Science
SAUJS

e-ISSN 2147-835X | Period Bimonthly | Founded: 1997 | Publisher Sakarya University |
http://www.saujs.sakarya.edu.tr/en/

Title: Determination of Relay Opening Current Information and Coordination of Distribution Network of Sakarya Province, Yazlık Region

Authors: Volkan ULUTAŞ, Uğur ARİFOĞLU, Halime HIZARCI

Recieved: 2020-10-09 12:21:08

Accepted: 2021-05-05 14:22:49

Article Type: Research Article

Volume: 25
Issue: 3
Month: June
Year: 2021
Pages: 811-820

How to cite
Volkan ULUTAŞ, Uğur ARİFOĞLU, Halime HIZARCI; (2021), Determination of Relay Opening Current Information and Coordination of Distribution Network of Sakarya Province, Yazlık Region . Sakarya University Journal of Science, 25(3), 811-820,
DOI: https://doi.org/10.16984/saufenbilder.808190
Access link
http://www.saujs.sakarya.edu.tr/en/pub/issue/62736/808190

Sakarya University Journal of Science 25(3), 811-820, 2021

Determination of Relay Opening Current Information and Coordination of Distribution Network of Sakarya Province, Yazlık Region

Volkan ULUTAŞ*[1] Uğur ARİFOĞLU[1] Halime HIZARCI[1]

Abstract

Electricity is delivered to end users through generation, transmission, and distribution phases. The most important issues during energy journey is to provide selective, rapid, and safe protection to ensure energy continuity. In this context, when the operating conditions defined in the protection systems are exceeded, an effective protection system and coordination are required to provide that as few consumers as possible are affected by the energy outage and reliably isolate the fault. If the short circuit is not separate from the network quickly after a short circuit occurs, network equipment and electrical devices may be damaged because of overcurrent that occurs. In this study, the coordination of overcurrent protection relay at 34.5 kV voltage level of the distribution network in Sakarya Province, Serdivan District, Yazlık region is made and MATLAB/Simulink is used in the modeling of the system. All data of inspected distribution network is embedded to MATLAB/Simulink file and then optimum protection is provided on relay coordination settings by performing power flow analysis and short circuit calculations.

Keywords: Overcurrent, protection relays, circuit modeling, distribution network

1. INTRODUCTION

Dependency on electric energy is increasing in parallel with technological developments in the world day by day. Electric energy generated in power plants is transmitted at voltage level of 380 kV and is generally distributed at voltage level of 34.5 kV, and it is demanded to reach residences at voltage level 380~400 V. While going through whole these processes, it is undoubtedly very important to minimize technical losses, provide clean and reliable energy as well as uninterrupted energy [1]. Though the issues such as using a new equipment in the network, maintenance of the existing ones and wisely selection of the devices that will be used while designing reduce the possibility of fault emerging, they do not completely eliminate it. Circuit breakers are designed to open under load and especially during short circuit. But they cannot break/open by themselves. For this they must be supported with

*Corresponding author: volkanulutas7@gmail.com
[1] Sakarya University, Faculty of Engineering, Department of Electrical and Electronics Engineering, Sakarya, Turkey.
E-Mail: arifoglu@sakarya.edu.tr, hhizarci@sakarya.edu.tr
ORCID: https://orcid.org/0000-0002-5131-4806, https://orcid.org/0000-0001-8082-5448, https://orcid.org/0000-0002-5720-6996

proper relay equipment that will continuously monitor the network and generate break signal when the fault occurs [2].

Relay coordination should be done very well taking into account the principle of selectivity in order to eliminate the fault as quickly as possible and to ensure that the minimum number of subscribers are affected by the interruption, to prevent loss of life/injuries, to avoid the power system equipment from becoming unusable and short service life [3]. The process of delaying relay the opening times of the relays positioned as they move from the short circuit point occurring at a point of the power system to the source supplying this short circuit is called relay coordination [4].

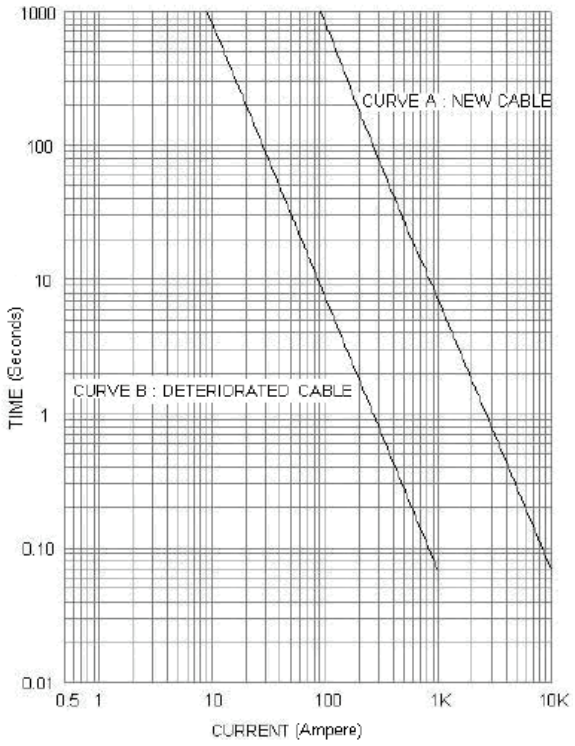

Figure 1 Comparison curves of a new cable and thermally damaged

It is always preferable to use of equipment placed in the network for many years and to have the least possible number of faults. It is essential to keep aging rate at the lowest level to prolong the life of network equipment. For this purpose, as well as maintenance made without delay, it is necessary to prevent the thermal and dynamic effects generated by electrical stresses in the network. Consequently, the life of network equipment can be extended only achieving effective relay coordination. A new cable and damaged cable are compared in Figure 1 [5].

In this study, firstly operation principles of overcurrent relay which are of great importance on power systems protection and how their coordination is achieved of these equipment is dwelled on, then relay coordination of an example electric distribution network at voltage level 34.5 kV is performed for better understanding of the issue. The example distribution network was first modeled in MATLAB/Simulink environment [6], then the power flow and short circuit analysis were realized [7], values related with relay coordination were calculated according to the results obtained from these analyses. As a result, relay coordination is realized to ensure the safest operation of the network without giving an opportunity to occurrence of any risk in the region examined with the outputs of this study.

2. METHOD

Overcurrent relays detect the amplitude of the fault current occurred in the network for any reason and send an opening command to contacts responsible for opening according to the preset current-time characteristic. These relays are divided into two groups as electromechanical and electronic [8]. The operating current that overcurrent relays are set is called starting current and it is indicated by I_s.

Overcurrent relays have definite time and/or inverse time operation characteristics. When fault current (I) exceeds the setting starting current (I_s) in the definite time operating order, the relay contacts change positions after waiting for the set time. On the other hand, in the inverse time operation, time delay of protection relay in the opening process is not fixed and this value changes depending on I/I_s ratio and time factor. Relays are generally arranged to have inverse time operating characteristic in phase-phase and three phase short circuits, and definite time characteristic in phase-earth short circuits [9].

Inverse time relay characteristics according to IEC 60255-3, “Electrical relays-Part3: Single

input energizing quantity measuring relays with dependent or independent time" standard is defined as short time inverse (STI), standard inverse (SI), very inverse (VI), extremely inverse (EI) and longtime inverse (LTI) curve. General equation of opening time for inverse time curve is given in Equation (1).

$$t = \left[\frac{A}{\left(\frac{I}{I_S}\right)^{\alpha} - 1} + B\right] \times TMS \qquad (1)$$

Variables used in Equation (1) listed below:

t: opening time (s)

A ve B: constant for characteristic (s)

I: instantaneous current value (A)

I_s: setting current threshold value (A)

α: constant for characteristic (-)

TMS: time multiplier setting (-)

The values of all constants in Equation (1) are specified in IEC 60255-151 standards. IEC 60255-151 inverse time protection curves when TMS=1 are given in Figure 2. TMS multiplier adjustment range for all curves is (0.025-3.2) [10].

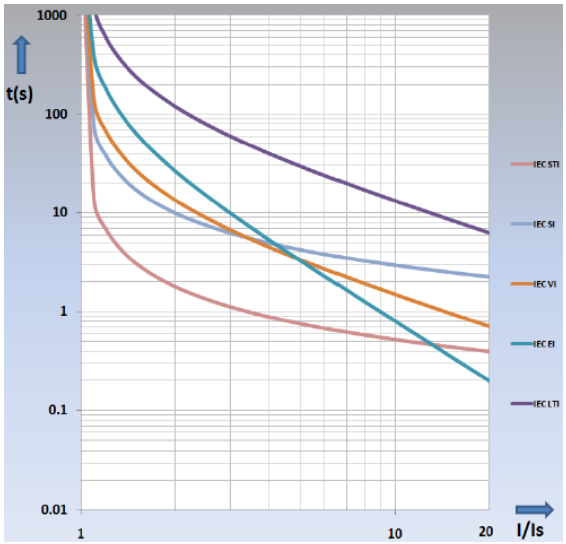

Figure 2 IEC inverse time protection curves when TMS=1

Relay coordination will be done with standard inverse curves in this study. In IEC 60255 standard, Equation (2) is obtained when the values of A=0.14, B=0 and α = 0.02 are replaced in Equation (1).

$$t = \left[\frac{0.14\ s}{\left(\frac{I}{I_S}\right)^{0.02} - 1}\right] \times TMS \qquad (2)$$

The values such as TMS, A, B and α used in inverse time curves are not valid for definite time curves. Graphs related with definite time curves are as in Figure 3 [10].

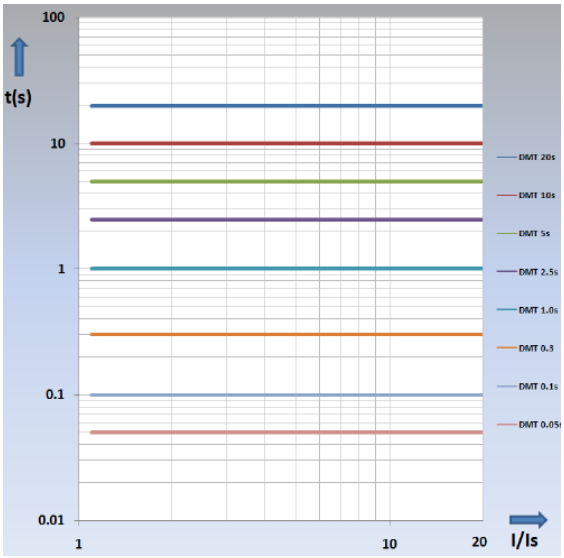

Figure 3 Definite time graphs at various time and current values

Single line diagram of the region in this study is given in Figure 4. A double circuit copper (Cu) XLPE (cross-linked polyethylene) line comes from Sakarya TM to DM1TR1 distribution center, and energy of Yazlık Region to be examined is supplied from Feeder 1 under normal operating conditions. Neutral resistance of Sakarya TM is established as 20 Ω and thus earth fault current is limited to 1000 A.

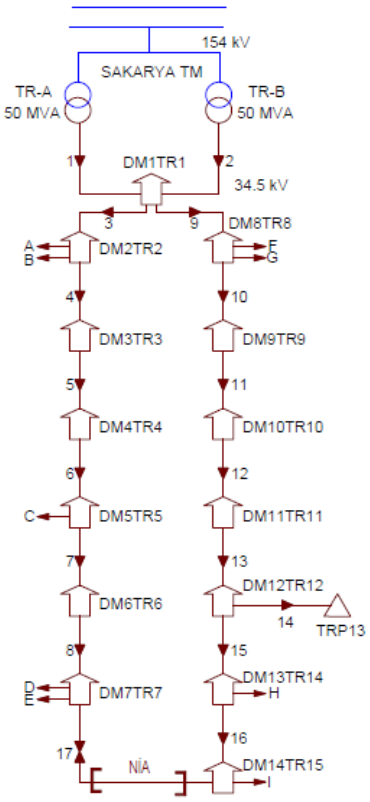

Figure 4 Single line diagram of modeled network

Under normal operating condition, each cabin is connected radially to the grid. In the case of any fault, energy continuity in the region may be maintained by activating ring system. Line data of the network given single line diagram and current transformer (CT) ratio of the breakers protecting this line are given in Table 1.

Table 1 Data of modeled network

Feeder number	**Section**	**Length (m)**	**CT (A)**
1	3(1x240/25 XLPE-Cu)	7582	600/5
2	3(1x240/25 XLPE-Cu)	7556	600/5
3	3(1x240/25 XLPE-Cu)	645	600/5
4	3(1x185/25 XLPE-Al)	707	300/5
5	3(1x185/25 XLPE-Al)	492	300/5
6	3(1x185/25 XLPE-Al)	956	300/5
7	3(1x185/25 XLPE-Al)	508	300/5
8	3(1x185/25 XLPE-Al)	853	300/5
9	3(1x240/25 XLPE-Cu)	1357	600/5
10	3(1x185/25 XLPE-Al)	821	300/5
11	3(1x185/25 XLPE-Al)	718	300/5
12	3(1x185/25 XLPE-Al)	524	300/5
13	3(1x185/25 XLPE-Al)	835	300/5
14	3xSwl	907	100/5
15	3(1x185/25 XLPE-Al)	587	300/5
16	3(1x185/25 XLPE-Al)	850	300/5
17	3(1x185/25 XLPE-Al)	708	300/5

3. SHORT CIRCUIT ANALYSIS

Short circuit analysis results are important in many stages such as establishment and operation of network. Generally, 5% of short circuits occurred in electric distribution network are three phase short circuit, 70% phase to earth short circuit, 15% phase-phase short circuit and 10% two phase-earth short circuit [11].

For the protection relays to open in case of fault, the setting starting current value must be below the value of short circuit current value. Short circuit analysis should be done at the network point that cause maximum current flow through the relay [12]. In the study, line numbers are shown in Figure , and according to the case of short circuit at the end of the line, the current value that will pass through the protection relay of this line is considered in the relay coordination [13].

In this study, MATLAB/Simulink model of the distribution network is given in Figure 5. The model of Adapazarı TM, which is not shown in the single line diagram in Figure 4. Because if the distribution system encounters a network fault, Adapazarı TM can feed the system. So while the system normal working, relay coordination is not necessary from Adapazarı TM. Cabinets, line 1, line 2, transformer centers and measuring blocks were defined as subsystem model and complexities in the modelling file are eliminated. The real data of all the equipment used in the modeling file. Test reports of transformers, disconnectors and breakers were examined and the laboratory results obtained were included in the analysis [14]. Disconnectors and breakers have 16 kA withstand current. The relay current circuit thermal resistance is 4 I_n (20A) (continuous) [10].

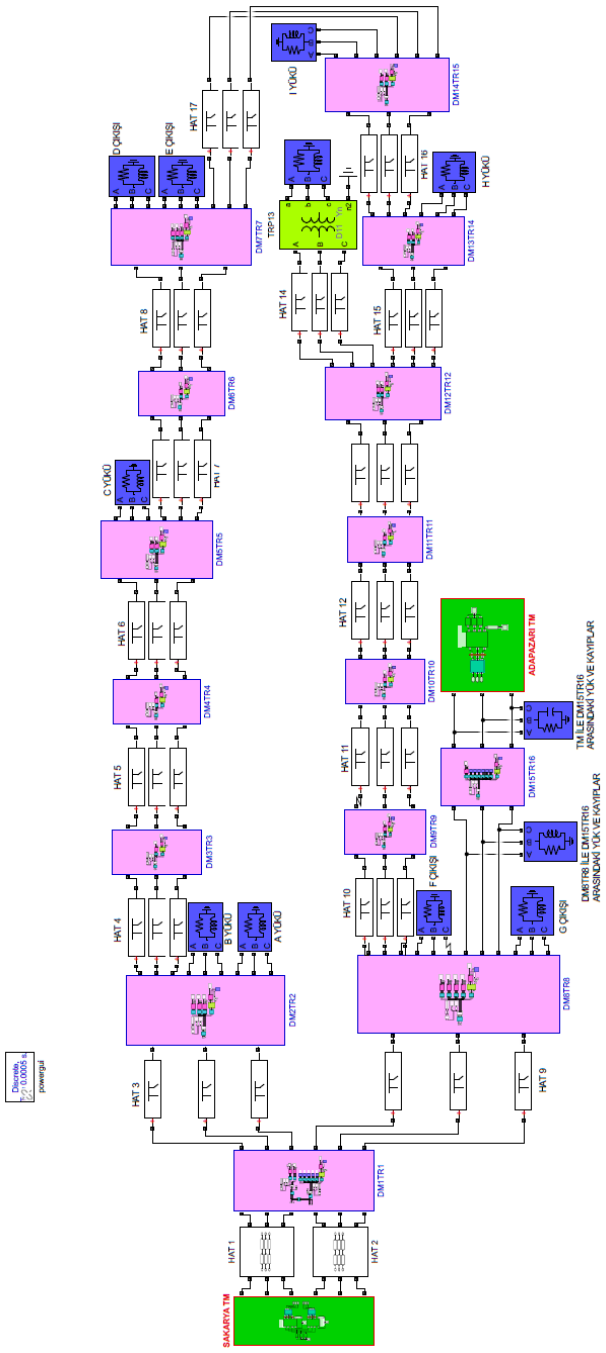

Figure 5 MATLAB/Simulink model of the network

In order to protection relays to open in case of failure, the adjusted starting current value must be below the short circuit current value. Short circuit analysis should be done at network points that cause maximum current flow through the relay [13]. Short circuit currents of system modeled in MATLAB/Simulink program are shown in Table 2.

Table 2 Results of short circuit analysis

Feeder number	Short circuit current (kA)		
	3-Phase	Phase-Phase	Phase-Earth
1	4.87	4.24	0.88
3	4.74	4.13	0.87
4	4.61	4.01	0.87
5	4.53	3.94	0.86
6	4.34	3.78	0.85
7	4.25	3.7	0.85
8	4	3.57	0.84
9	4.66	4.05	0.87
10	4.51	3.92	0.86
11	4.37	3.8	0.86
12	4.28	3.72	0.85
13	4.15	3.61	0.84
15	4.07	3.54	0.84
14	3.368	2.93016	-
16	3.94	3.42	0.83

Power flow analysis is of great importance especially for the actions to be taken in future planning of a system. Power flow solutions play a determinant role in studies to be made for voltage drop, transformer power, line capacity, active-reactive powers and even harmonics [15]. While specifying the current setting value in relay coordination, inrush current value of the system (the highest current drawn at the time of first energizing the system) should also be taken into consideration. In the study, the power flow analysis of the system will be used for determination of the inrush current.

According to IEC SI, the first relay which is in the transformer center, overcurrent relay setting time must be <=0.4e [16].

Inverse time curve will be studied for the first threshold (I>) values of the relays. Inverse time curves are a function of both current and time, the opening times change according to current. There is an inversely proportional relationship between current and time. This allows for large short circuit current to cut the energy instantaneously and not to cut the energy in the short-term inrush current. The first threshold value for the relay at the substation output is determined according to the line capacity value and the TMS factor is set to the range 0.3-0.4 [16]. In this study, the analysis was carried out by decreasing the factor of 0.05 for each cabin. The starting current values are set to 600 A for the transformer station and DM1TR1, and 300 A for afterwards (excluding

the cabin outputs except the ring). Inverse time relay coordination is given in Table 3.

Table 3 First threshold setting of relays

Relay	Is (A)	TMS
Sakarya TM (1)	600	0.35
DM1TR1 (3)	600	0.3
DM2TR2 (A)	100	0.05
DM2TR2 (B)	100	0.05
DM2TR2 (4)	300	0.25
DM3TR3 (5)	300	0.2
DM4TR4 (6)	300	0.15
DM5TR5 (C)	100	0.05
DM5TR5 (7)	300	0.1
DM6TR6 (8)	300	0.05
DM7TR7 (D)	100	0.05
DM7TR7 (E)	100	0.05
DM1TR1 (9)	600	0.3
DM8TR8 (F)	100	0.05
DM8TR8 (G)	100	0.05
DM8TR8 (10)	300	0.25
DM9TR9 (11)	300	0.2
DM10TR10 (12)	300	0.15
DM11TR11 (13)	300	0.1
DM12TR12 (14)	100	0.05
DM12TR12 (15)	300	0.05
DM13TR14(16)	∞	0
DM14TR15 (I)	100	0.05

Graphs of the values in Table 3 are given in Figure 6Figure for Sakarya TM (1) and DM1TR1 (3)(9) and in Figure 7 for other cabins.

Calculations were made with Equations (3) - (6) in order to test the compatibility of the first threshold inverse time coordination setting to the system and to determine how long the relays will send interrupt commands. The short circuit current of 2 kA in Feeder 5 at the DM3TR3 output is taken as reference in these calculations.

DM3TR3 (Feeder 5):

TMS=0.2, I_s=300 A

$$t = \left[\frac{0.14}{\left(\frac{2000}{300}\right)^{0.02}-1}\right] \times 0.2 = 0.724 \text{ s} \quad (3)$$

DM2TR2 (Feeder 4):

TMS=0.25, I_s=300 A

$$t = \left[\frac{0.14}{\left(\frac{2000}{300}\right)^{0.02}-1}\right] \times 0.25 = 0.9051 \text{ s} \quad (4)$$

DM1TR1 (Feeder 3):

TMS=0.3, I_s=600 A

$$t = \left[\frac{0.14}{\left(\frac{2000}{600}\right)^{0.02}-1}\right] \times 0.3 = 1.723 \text{ s} \quad (5)$$

TM Output (Feeder 1):

TMS=0.35, I_s=600 A

$$t = \left[\frac{0.14}{\left(\frac{2000}{600}\right)^{0.02}-1}\right] \times 0.35 = 2.0105\ s \quad (6)$$

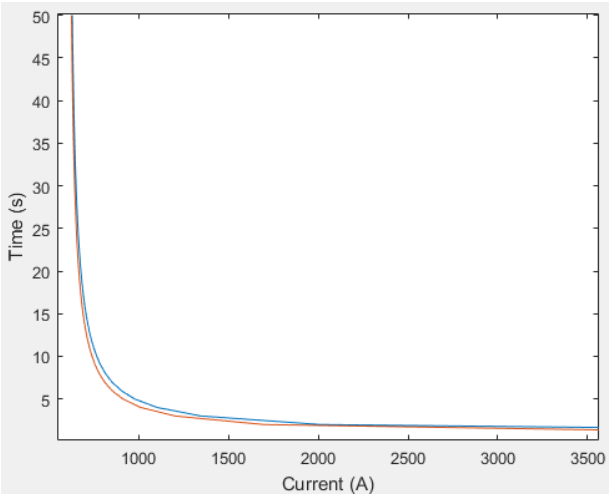

Figure 6 I > inverse time curve for TM output relay and main distribution center (DM1TR1)

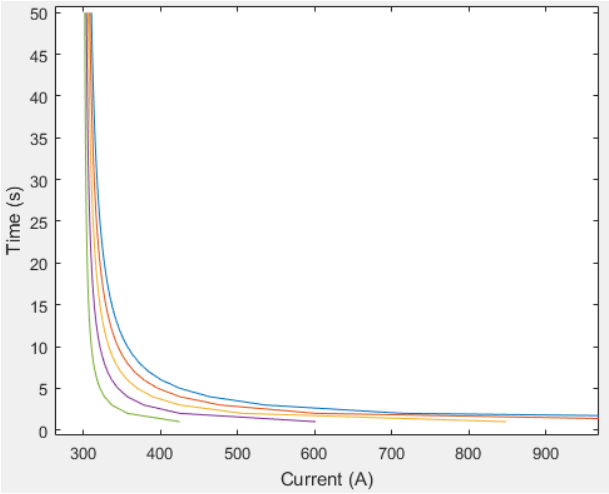

Figure 7 I> inverse time curve for other relays

The definite time curve will be studied for the second threshold values (I >>) of the relays. This setting is taken as 1.1 times the short circuit

current in the second or third cabinet for the relays at the substation outputs and time value is are selected in the range of 0-0.3 s [16]. After this adjustment, time value t=0.15 s was chosen at the DM1TR1 main distribution center which is the first cabin.

Since the next cabins are very close to each other, the short circuit current values obtained at the end of the calculations are very close to each other. Hence, to ensure the most effective relay coordination, the second threshold values of some cabins have been made passive so that the least number consumer are affected by the load density and interruption. It was decided that the relay coordination values for the second threshold should be as in Table 4 in this study.

Table 4
Second threshold setting of relays

Relay	I >> (kA)	t >> (s)
Sakarya TM (1)	4.8	0.3
DM1TR1 (3)	4.8	0.15
DM2TR2 (A)	∞	0
DM2TR2 (B)	∞	0
DM2TR2 (4)	∞	0
DM3TR3 (5)	∞	0
DM4TR4 (6)	3.8	instantaneous
DM5TR5 (C)	∞	0
DM5TR5 (7)	∞	0
DM6TR6 (8)	3.5	instantaneous
DM7TR7 (D)	∞	0
DM7TR7 (E)	∞	0
DM1TR1 (9)	4.8	0.15
DM8TR8 (F)	∞	0
DM8TR8 (G)	∞	0
DM8TR8 (10)	∞	0
DM9TR9 (11)	∞	0
DM10TR10 (12)	3.8	instantaneous
DM11TR11 (13)	∞	0
DM12TR12 (14)	∞	0
DM12TR12 (15)	3.6	instantaneous
DM13TR14(16)	∞	0
DM14TR15 (I)	∞	0

The constant time curve will be studied for the third threshold values (I >>>) of the relays. Due to the first and second threshold values, mostly there is no need to the third threshold. However, in terms of the soundness of the application, the third threshold value was used for the substation and the main distribution center (DM1TR1) in this study. The third threshold value for the relays at the substation output is set as 1.1 times the short circuit current in the first cabinet and the time value has been selected in the range of 0-0.15 s [16]. The third threshold value for the substation output is designed as 5.2 kA instantaneous time and for DM1TR1 as 5 kA instantaneous time.

Table 5 Earth settings of relays

Relay	I_0 > (A)	t (s)
Sakarya TM (1)	60	1.2
DM1TR1 (3)	60	1.05
DM2TR2 (A)	60	0.03
DM2TR2 (B)	60	0.03
DM2TR2 (4)	60	0.9
DM3TR3 (5)	60	0.75
DM4TR4 (6)	60	0.6
DM5TR5 (C)	60	0.03
DM5TR5 (7)	60	0.45
DM6TR6 (8)	60	0.3
DM7TR7 (D)	60	0.03
DM7TR7 (E)	60	0.03
DM1TR1 (9)	60	1.05
DM8TR8 (F)	60	0.03
DM8TR8 (G)	60	0.03
DM8TR8 (10)	60	0.9
DM9TR9 (11)	60	0.75
DM10TR10 (12)	60	0.6
DM11TR11 (13)	60	0.45
DM12TR12 (14)	60	0.03
DM12TR12 (15)	60	0.3
DM13TR14(16)	60	0.15
DM14TR15 (I)	60	0.03

In this study, the definite time curve is used for the relays to protect the network against earth faults. Earth protection setting for the relays at the substation output is set to 30-120 A and <= 1.4 s [16]. In the study, t is 1.2 in the substation, and the time values in relay coordination are adjusted so that they start from the closest cabinet to the point where the fault occurred and decrease towards the last cabinet farthest from the fault. Coordination parameters obtained under these conditions are shown in Table 5, and graphs are given in Figure 8.

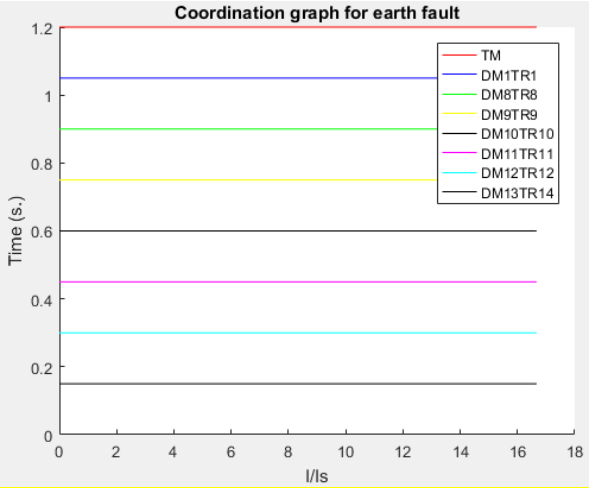

Figure 8 Coordination graph for earth fault

Relay detecting the fault and generating an opening signal and opening the circuit breaker, a time such as 300 ms is required. In this case, one relay should be configured with a time delay of 300 ms in coordination with the other relay behind it. In places where the distance between the two cabinets is very short, such as in the selected region in this thesis, short circuit currents are very close to each other. It is possible to reduce it to 150 ms according to experiences. However, the normally accepted and required time is considered to be 300 ms.

4. CONCLUSIONS

While conducting relay coordination in a power system, analyses are made by considering many factors. Short circuit and power flow analysis are the primary come first among these. In this study, firstly, these two analyses of the investigated network were made with the help of MATLAB/Simulink program, and information about the general condition of the power system was obtained. In the light of this information, starting currents for relay coordination were determined and time factors were calculated. Although the relay coordination has been done virtually, a study has been presented in the network studied so far, blended with the previous experiences. For the coordination of the relays different scenarios can be defined according to the operating scheme of the network. In this study, only the first scenario (between DM7TR7 and DM14TR15 is open in normal operating condition) is studied. If desired, this study can be expanded for new and different scenarios, which also consider factors such as various fault states, load densities and subscriber numbers.

Before implementing a project at the design stage in the field, usage of simulation studies is very important in terms of detecting some mistakes made during the project stage and reaching the correct values. Various projects such as renewal of the network, additional facility work and addition of new loads to the network can be analyzed in a simulation environment and the potential impacts of the project on the field can be examined in a realistic way from various aspects. In this study, the data entry required for the network examined by considering the real operating conditions was provided by using the simulation program.

Acknowledgments

The authors would like to thank to SEDAŞ for providing data of system.

Funding

The authors have not received any financial support for the research, authorship, or publication of this study.

The Declaration of Conflict of Interest/ Common Interest

No conflict of interest or common interest has been declared by the authors.

Authors' Contribution

V.U: Conceptualization, methodology, writing, simulation studies, investigation, original draft.

U.A: Review, editing, supervision.

H.H: Review, editing.

The Declaration of Ethics Committee Approval

This study does not require ethics committee permission or any special permission.

The Declaration of Research and Publication Ethics

The authors of the paper declare that they comply with the scientific, ethical and quotation rules of SAUJS in all processes of the paper and that they do not make any falsification on the data collected. In addition, they declare that Sakarya University Journal of Science and its editorial board have no responsibility for any ethical violations that may be encountered, and that this study has not been evaluated in any academic publication environment other than Sakarya University Journal of Science.

REFERENCES

[1] Akdağ, O. (2018). 154 / 33 , 6 kV Malatya1 Trafo Merkezinde Aşırı Akım Röle Koordinasyonu Benzetimi. DÜMF Mühendislik Dergisi. 9:1. 27–38.

[2] Bajánek, T. Development of overcurrent protection relay model using IEC 61850-9-2 sampled values. FEEC BUT, Doctoral degree programme.

[3] Gürsu, B. (2014). Elektromanyetizm Algoritması İle Radyal Şebekelerde Ters Zamanlı Yönsüz Selektif Aşırı Akım Röle Koordinasyonu. Eleco 2014 Elektrik-Elektronik-Bilgisayar ve Biyomedikal Mühendisliği Sempozyumu. (27–29 Kasım 2014). Bursa

[4] C. Aggarwal, H. A. Mangalvedekar, H. B. Chaudhari (2008). Effect of fault location on optimal coordination of directional over current relay. IEEE Reg. 10 Annu. Int. Conf. Proceedings/TENCON, no. 1. 1–5, 2008.

[5] S. M. Mousavi, H. A. Abyaneh, and M. Mahdavi (2009). Optimum setting and coordination of overcurrent relays considering cable damage curve. 2009 IEEE Bucharest PowerTech Innov. Ideas Towar. Electr. Grid Futur., 1–5.

[6] U. Arifoğlu, Simulink 10.1 ve Uygulamaları, 1st ed. Alfa Yayım Basım Dağıtım, 2020.

[7] U. Arifoğlu, Güç Sistemlerinin Analizi, 2nd ed. Papatya Bilim, 2020.

[8] Akbaba, S. (2008). Harmoıniklerin Dijital Aşırı Akım Röleleri Üzerindeki Etkisi. Yüksek Lisasn Tezi. Yıldız Teknik Üniversitesi Fen Bilimleri Enstitüsü.

[9] Akdağ, O. ve Yeroğlu, C. (2019). Güç Sistemlerinde Aşırı Akım Koruma Koordinasyon Modelinin Oluşturulması, Benzetimi ve Optimizasyonu. Erzincan Üniversitesi Fen Bilim. Enstitüsü Dergisi. 202–214, 2019.

[10] Köseoğlu, A. (2011). CPM 31OG Dijital Aşırı Akım Koruma Rölesi Genel Broşürü. Dema Röle. www.demarole.com.tr/images/uploads/47b02994f92349dabedae72d927d3eb1_5.-cpm-310g-kullanim-kilavuzu.pdf, Erişim Tarihi: 15 Nisan 2021.

[11] S. Küçük, "Elektrik Tesislerinde Arızalar." PapatyaBilim Üniversite Yayınclığı,2018.

[12] A. Shobole, M. Baysal, M. Wadi, and M. R. Tur. (2017). Protection Coordination Practice in Electrical Substation Part-1 Overcurrent and Earth Fault Protection Case Study of Siddik Kardesler Substation (SKS). Gazi Univ. J. Sci., 180–198.

[13] P. Çağdaş Ozan. www.elektrikport.com/teknik kutuphane/ozel-dosyaasiri-akim-role-koordinasyonu-(iec-si-standartina-gore)/7943#ad-image-0. Erişim Tarihi: 02.05.2021

[14] Soysal, S. (2008). Bolu - Düzce Bölgesi 154 kV / 34,5 kV İletim VE Dağıtım Şebekesinin Bilgisayar Ortamında Modellenmesi. Yüksek Lisans Tezi, Sakarya Üniversitesi Fen Bilimleri Enstitüsü.

[15] O. Aliman and I. Musirin (2013).

Overcurrent relays coordination for commercial building. IEEE 7th Int. Power Eng. Optim. Conf. (PEOCO 2013). 608–612.

[16] "Koruma Sistemi Felsefesi", (2019), İşletme ve Bakım Dairesi Başkanlığı, TEİAŞ, Ankara.

SAKARYA ÜNİVERSİTESİ
FEN BİLİMLERİ ENSTİTÜSÜ DERGİSİ

Sakarya University Journal of Science
SAUJS

e-ISSN 2147-835X | Period Bimonthly | Founded: 1997 | Publisher Sakarya University |
http://www.saujs.sakarya.edu.tr/en/

Title: A Study on Analysis of Sinter Microstructure and Phase Morphology

Authors: Ömer Saltuk BÖLÜKBAŞI

Recieved: 2020-05-07 14:32:46

Accepted: 2021-05-05 14:32:35

Article Type: Research Article

Volume: 25
Issue: 3
Month: June
Year: 2021
Pages: 821-833

How to cite
Ömer Saltuk BÖLÜKBAŞI; (2021), A Study on Analysis of Sinter Microstructure and Phase Morphology. Sakarya University Journal of Science, 25(3), 821-833, DOI: https://doi.org/10.16984/saufenbilder.733658
Access link
http://www.saujs.sakarya.edu.tr/en/pub/issue/62736/733658

Sakarya University Journal of Science 25(3), 821-833, 2021

A Study on Analysis of Sinter Microstructure and Phase Morphology

Ömer Saltuk BÖLÜKBAŞI*1

Abstract

Sinter is a blast furnace input material obtained by temperature to 900-1200 ºC without full melting and adhering to each other with superficial melting. It is considered as a multi-phase material with its heterogeneous microstructure. In general, the main mineral phases are hematite, magnetite, silicoferrite of calcium and aluminium (SFCA) and silicates. By determining the SFCA structure in the sinter material, the sintering process will be made more stable and important parameters affecting the quality in the sintering process will be examined. Sinter material consists of iron ore, iron and steel industry by-products and auxiliary materials. The scope of this project is the determination of the amount of SFCA formed by bonding SiO_2, CaO, Fe_2O_3, Al_2O_3 and MgO compounds and monitoring this value as a parameter by sinter manufacturers. Sinter samples having different characteristic features were made ready for X-ray diffraction (XRD) and optical microscopy inspections by polishing, etching and cold mounting in epoxy for mineralogical analyses. Before raw data obtained from the analysis were evaluated at Autoquan, they were converted into Autoquan format and then, read in XRD device and mineralogical composition of the sinter was revealed by XRD analyses. Detailed imaging of mineralogical compounds were made so as to complement scanning electron microscope (SEM) analyses and XRD analyses; elemental composition of the compounds and valence conditions of the elements were determined by energy dispersive spectroscopy (EDS) method. Phase structures such as hematite, magnetite, and calcium ferrite were qualitatively determined by mineralogical investigations on sinter samples. Furthermore, the variations of SFCA phases (SFCA, SFCA-I and SFCA-II) were studied through Rietveld method.

Keywords: Sintering, iron ore, microstructure, mineralogy, SFCA, formation process

1. INTRODUCTION

Sinter is a porous material obtained from partial melting of a mixture of fine iron ore, limestone, dolomite and iron-containing waste materials (flue dust, BOF slag, mill scale, gas cleaning mud). In sinter research; it is important for the technological quality of the sinter to pay attention to the chemical structure, minerology and the distribution of different mineral phase structure forms in the matrix during the sintering process [1]. Sinter production has a dynamic operating parameter and a complex structure. By determining the SFCA structure in the sinter material, the sintering process will be made more

*Corresponding author: osaltuk.bolukbasi@iste.edu.tr
[1]Iskenderun Technical University, Faculty of Engineering and Natural Science, Department of Metallurgical and Materials Engineering, 31200, İskenderun/Hatay.
E-Mail: osaltuk.bolukbasi@iste.edu.tr
ORCIDhttps://orcid.org/0000-0002-8862-009X

stable to examine important parameters affecting the quality during the sintering process. In the production of the sinter, the bonding phase (SFCA) formed through chemical reactions of SiO_2, CaO, Fe_2O_3, Al_2O_3 and MgO requires to be quantified and this value may be considered by the sinter manufacturers as a parameter to ensure high sinter quality [2].

The researchers agree that the sinter quality depends on the SFCA mineral phase formed during the sintering process [2-5]. During studies on the effects of ore mixtures of different compositions on sinter quality, it has been observed that the reducibility and cold strength of the sinter depends on the presence of calcium ferrite in the structure of the sinter [5-7]. These studies explain that the microstructure consisting of hematite cores surrounded by SFCA-I, one of the SFCA types, is the desired structure for high sinter quality [2, 3, 7-9]. SFCA, the main bond phase of the sinter, is defined as a solid solution $CaO.2Fe_2O_3$ accompanied by Al_2O_3 and SiO_2. This phase is considered to be the SFCA quadruple bond phase complex. SFCA phase is series of solid solutions that can contain Fe^{+2} and Mg^{+2}. [9, 11, 12, 13].

Figure 1-a) shows the typical sintering process of iron ore, fluxes and coke breeze. SFCA phases, calcium-rich ferrite structures, calcium silicates and glassy structures are observed within a typical sinter produced with ore grains in the sinter matrix [9, 14-17]. At low temperatures (<1220 °C) in the sinter body, assimilation is expected to be low and contains a significant amount of residual ore resulting in a heterogeneous texture. A more homogeneous structure is formed in the sinter material due to the high degree of overheating and melt mobility, which occurs at high temperatures (>1300 °C) [18-21]. The homogeneous and heterogeneous formation of the sinter is given in the Figure 1-b).

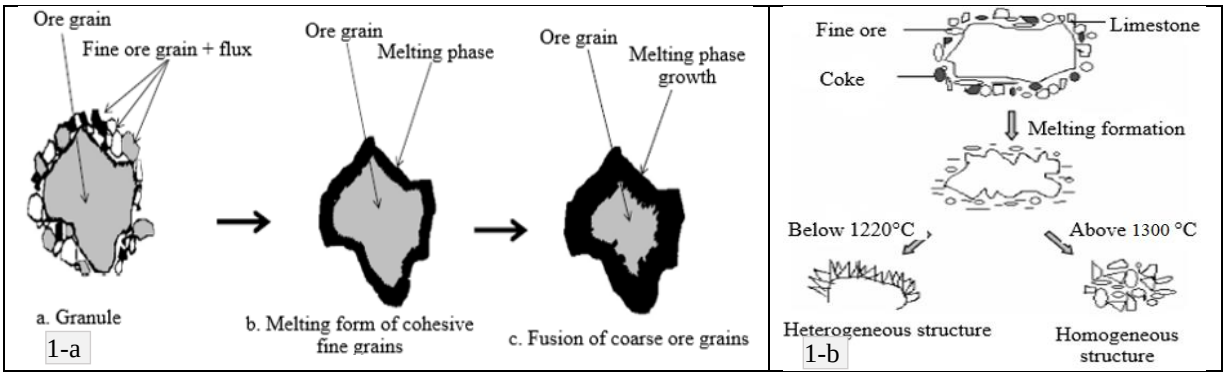

Figure 1-a) Sintering scheme of iron ore, flux and coke breeze [5, 7, 9], b) Homogeneous and heterogeneous formation of sinter [5, 19, 20, 21]

Studies show that the percentage of iron content in raw materials was found to affect the microstructure of the SFCA in the sintering process. While a SFCA form bond structure is obtained in sinter made with iron ore with <62% Fe grade, a form consisting of SFCA and SFCA-I mixture were obtained in the sinter made with 62-65% Fe. SFCA-I was mostly formed in sinter made with 65-68% Fe grade iron ores [14, 22].

In practice, SFCA-I compound structure and SFCA phase structure are seen together. SFCA-I is characterized by a high content of Fe and a low content of Si. The morphology, plate and sections of SFCA-I can be in acicular structures. However, the view of SFCA under the optical microscope is columnar and block-shaped, containing less Fe and it is more stable at high temperature (>1300 ^oC). The third type of SFCA phase, as known SFCA-II, can be observed in scattered appearance dendritic structure [9, 19]. In some studies, a third type of SFCA phase structure observed in dendritic morphology and stated that this structure took shape in very thin SFCA-II form and was the first type of SFCA that took shape during the sintering process [7, 18]. This structure is very thin in the form of SFCA-II and it is called the first type of SFCA species that take shape

during the sintering process [7, 9, 19, 23]. The studies took into account the microstructure of sinter, and its chemical structure, mineralogy, morphology, and the distribution of different mineral phase structures within the sinter matrix during the sintering process [24, 25].

SFCA phase has been the subject matter of many studies due to its effects on the sinter product such as high strength (TI-Tumbler index), high reducibility (RI-Reduction index) and low temperature degradation (RDI-Reduction degradation index) and has been accepted as the main mineralogical bond in the sintering process [2, 23, 26, 27]. This study will provide information on how to use the Rietveld Method to calculate the ratio of the phases in the sinter SFCA, how to determine the percentage of all compounds in the sinter structure, as well as the quantitative content of the existing phase structures.

2. MATERIAL AND METHODS

The chemical reactions between iron ores and fluxes in the sinter process take place at high temperature (900-1200 ^{o}C), and iron ore particles (cores) surrounded with silicoferrite of calcium and aluminium, dicalcium silicate and glassy structure form the basic compound of the sinter cake. Sinter reactions also regulate the volume fraction of different minerals that may affect the quality of the sinter and thus the performance of blast furnace [25].

Sinter matrix structure consists of reactions of flux formers and fine iron ore in the melting phase formation where coarse grains are assimilated and solid-liquid reactions take place. In parallel to preparation of sample in epoxy, sinter samples are powdered through micronizing mill device and before it placed into the device. Iron ores form sinter cake compound in the form of composition consisting of SFCA and dicalcium silicate and glassy structure [28]. Sinter reactions are a special process that continues its activity by controlling the microstructure and concentration of SFCA during the sintering process [15, 29]. A typical industrial scale sinter plant is shown in Figure 2.

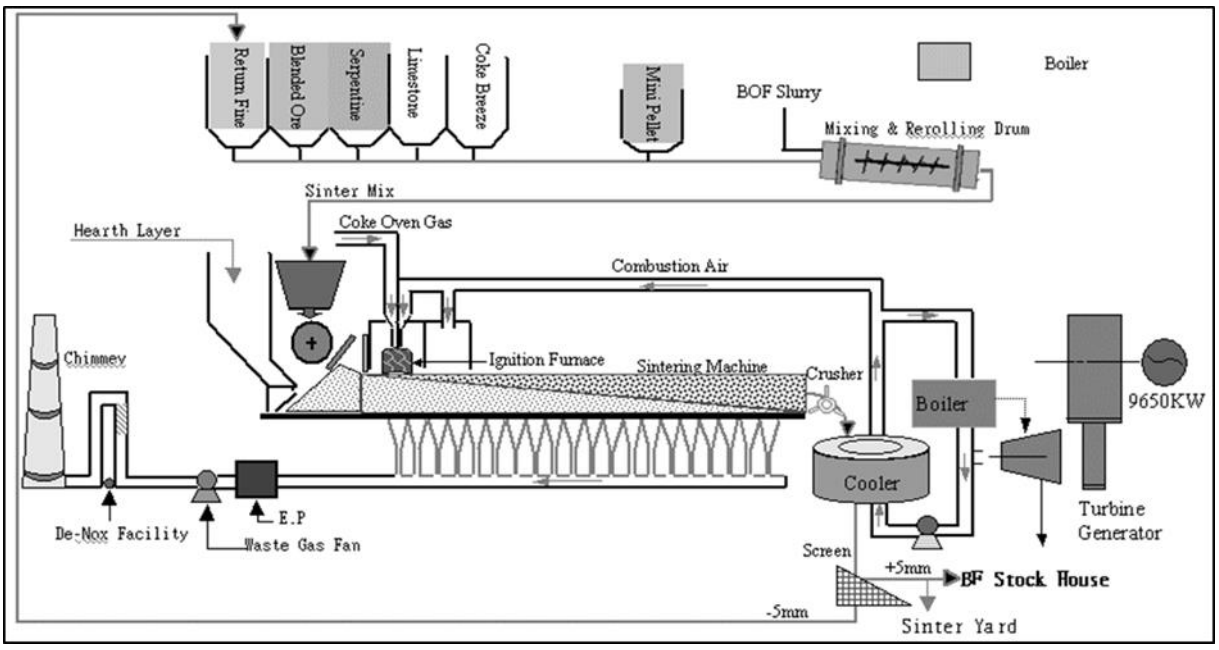

Figure 2 Sinter production flow chart on a typical industrial scale [32].

Sintering parameter: Ignition temperature 1055 °C, sintering time 25 min., pressure drop 1100 (mmH_2O), sintering rate 23 mm/min. Sinter raw material usage values: Domestic iron ore 45%, foreign iron ore 55%, total fuel 72 (kg/t. sinter), Limestone 8.50%, dunite 3.20%, sinter return dust 25.60%, Basicity (CaO/SiO_2) 1.85. Chemical analysis of the sinter is seen in Table 1.

Table 1
Chemical analysis of the sinter (%)

Fe(tot)	FeO	Fe_2O_3	CaO	MgO	SiO_2	Al_2O_3	K_2O+Na_2O	TiO_2	MnO	S	CaO/SiO_2
55.14	7.00	70.94	9.81	1.57	5,63	1.58	0.25	0.11	0.89	0.02	1.74

Sinter is considered as a multi-phase material due to its heterogeneous microstructure. In general, the main mineral phases include hematite, magnetite, SFCA, ferrite structures and silicates. Sinter mineral formation mainly consists of SFCA, SFCA-I and SFCA-II phases. The key binding phases that provide the strength of the material are SFCA and SFCA-I. These structures were examined considering the contents of mineralogical structures and operational practices (used blend, temperature, sintering time, etc.). Rietveld software programs are designed to accurately define peak profiles as much as possible. The rietveld method directly reports the relative weight fractions of all phase crystals included in the model. The system calculates a series of measurement factors that are directly proportional to the relative quantities of the phases using the least squares method. The results of XRD analysis of the sinter material performed using the Autoquan program by the Rietveld method is displayed in Table 2.

Table 2
Phase structures of the sinter using the Autoquan program (Rwp: error in %).

Sinter	Phase composition mass%	Error%
	Grade%	Rwp=2.44%
C_2S-Larnite	5.87	0.58
Hematite_	21.76	0.35
Magnetite	39.34	0.50
SFCA-I	5.95	1.02
SFCA	26.83	1.07
Wuestite	0.25	0.06
	100.00	

Sinter samples having different characteristic feature will be made ready for optical microscopy inspections by polishing, etching and freezing in epoxy for mineralogical researches (indicated in Figure 3). After polishing, the specimen is analyzed by visual examination using an optical microscopy. Resin, hardener were used by 10 ml and 2,6 ml respectively. Sinter samples were made polishing with 9 micron, 3 micron and 1 micron respectively.

Figure 3 Preparation of sinter samples for mineralogical researches.

The six sample was prepared for XRD analysis and given the standard of verify correct quantification by laboratory of Pretoria. In order to ensure that described sample preparation was adequate, XRD were conducted on the sinter samples. In the XRD analysis of sinter samples, an X-Ray tube with Co K-alpha radiation, which makes measurements more precisely than tubes with Cu K-alpha radiation in iron-containing phases, was used. It was then micronized in a micronizing mill, and then prepared for analysis using a back loading preparation method. It was analyzed with using a Panalytical X'Pert Pro powder diffractometer with X'Celerator detector. The data was collected in the angular range $5^o \leq 2\theta \leq 90^o$ with a step size $0{,}008^o$ 2θ and a 13-s scan step time. Phases were identified using X'Pert Highscore plus software and quantification was accomplished with Autoquan/BGMN software. Image of X-ray diffraction instrument was seen in Figure 4.

Figure 4 Sinter sample preparation of X-ray diffraction analysis.

2.1. Sintering reactions and description of bonding phase

When sinter blend consisting of iron ore, limestone, coke breeze and dunite mixture is heated in sinter machine, iron oxide, SFCA and silicate phases are formed in the sinter formation at 1220-1300 ^{o}C. Dicalcium ferrite (C_2F-$2CaO.Fe_2O_3$) is formed between 750 and 780 ^{o}C as the first product. With increased sintering temperature, dicalcium ferrites react with hematite to take the form of calcium ferrite (CF-$CaO.Fe_2O_3$). Quartz begins to react with the SFCA-I and SFCA form at 1050 ^{o}C. SFCA-I breaks down between 1220 ^{o}C and 1240 ^{o}C and takes the form of SFCA [17, 23, 30].

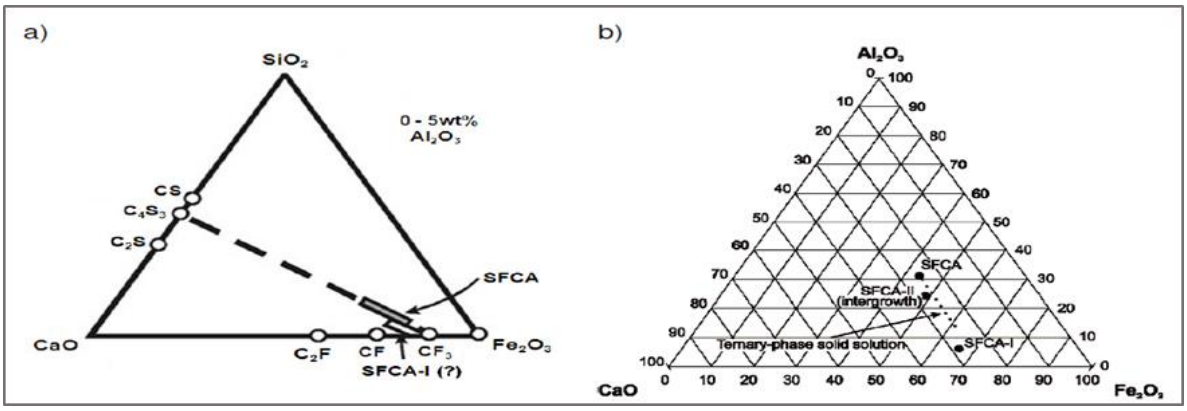

Figure 5-a) Reveals the composition relationship between SFCA and SFCA-I in the quadruple bond system Fe_2O_3-Al_2O_3-CaO-SiO_2. The diagram b) exhibits the formation relationship among SFCA, SFCA-I and SFCA-II [4].

Scientists use the CaO-Fe_2O_3-SiO_2 phase diagram shown in Figure 5 to indicate the mineral compositions of the SFCA phase. The shaded area shown in the Figure 5-a) represents the SFCA composition encountered in the industrial sinters. The SFCA forms shown in the Figure 5-b) are named as SFCA, SFCA-I and SFCA-II (dendritic) solid solution series. In composition, CF_3 ($CaO.3Fe_2O_3$), C_2F ($2CaO.Fe_2O_3$) and C_4S_3 ($4CaO.3SiO_2$) or Fe_2O_3-AI_2O_3-CaO compounds are designed to create a link within a planar structure.

According to many studies, the composition of the phases in the sinter were reported to consist of iron oxides by 40-70%, ferrites by 20-50% (mostly SFCA, silico ferrite of calcium and aluminium), glassy phases by more than 10% and dicalcium silicates by more than 10% [9, 14, 22, 31].

3. RESULTS AND DISCUSSION

The sinter material, its microchemical structure, mineralogy, morphology and the location of different mineral phase structure forms in the matrix during the sintering process have been studied by many scientists [18, 26, 29]. Our study analyses the microstructure of the SFCA phase and the effects of this microstructure on the chemical composition and morphology of the sinter. As a result of the tests, it was found that the SFCA bond structure coexists with the SFCA-I and SFCA-II main phase structures, and the SFCA-I phase structure contains high Fe and low Si. During microscopic examinations, it was observed that the morphology of SFCA-I has a plate-like appearance and its cross sections are acicular (Figure 5-a) and b). It has been determined that SFCA's morphology is columnar and block-shaped, contains less Fe, and it is more stable at higher temperature (>1300 ^oC).

A study by Scarlett et al. [17] suggests that the phase compositions in the sinter matrix structure consist of iron oxide by 35 to 60%, ferrites (mostly SFCA) by 20 to 45%, glassy phases by more than 10% and dicalcium silicates by more than 10%. They emphasize that the bond phase morphology is typically composed of SFCA phase composition as well as iron oxides and silicates, forming the most important bond phase structure since SFCA has a major impact on the quality properties of the sinter [18, 19, 26]. Chemical composition of the sinter phases was given in Table 3.

Table 3
Chemical composition of the sinter phases (%).

Sinter Phases	MgO	Al_2O_3	SiO_2	K_2O	CaO	MnO	Fe_2O_3	TiO_2
Amorphous	0.36	2.17	38.38	0,77	41.32	0.18	16.81	0.00
Larnite	0.31	1.59	38.24	0.65	44.25	0.19	14.78	0.00
Hematite	1.45	0.76	0.08	0.02	1.36	1.99	94.34	0.02

Magnetite	2.41	0.73	0.17	0.01	1.47	1.76	93.45	0.05
SFCA-I	1.58	2.38	4.43	0.05	11.09	0.92	79.56	0.05
SFCA	0.57	3.02	7.99	0.03	15.33	0.49	72.57	0.00
Wuestite	0.00	0.00	0.00	0.00	0.00	0.00	88.13	0.00

In our investigation, it was observed that the quality of the sinter depends on the mineral phase form generated during the sintering process and SFCA is the strongest bond phase that affects the sinter quality. During studies on the effects of ore mixtures of different compositions on sinter quality, it has been observed that the reducibility and cold strength of the sinter depends on the presence of calcium ferrite in the microstructure of the sinter. The literature studies also suggest that the form consisting of hematite cores surrounded by SFCA-I is the desired structure for high sinter quality [7, 18, 19]. During the reduction reactions, the porous structure of the acicular SFCA has been proven to provide a wide surface contact to prevent spread of cracks [10, 30].

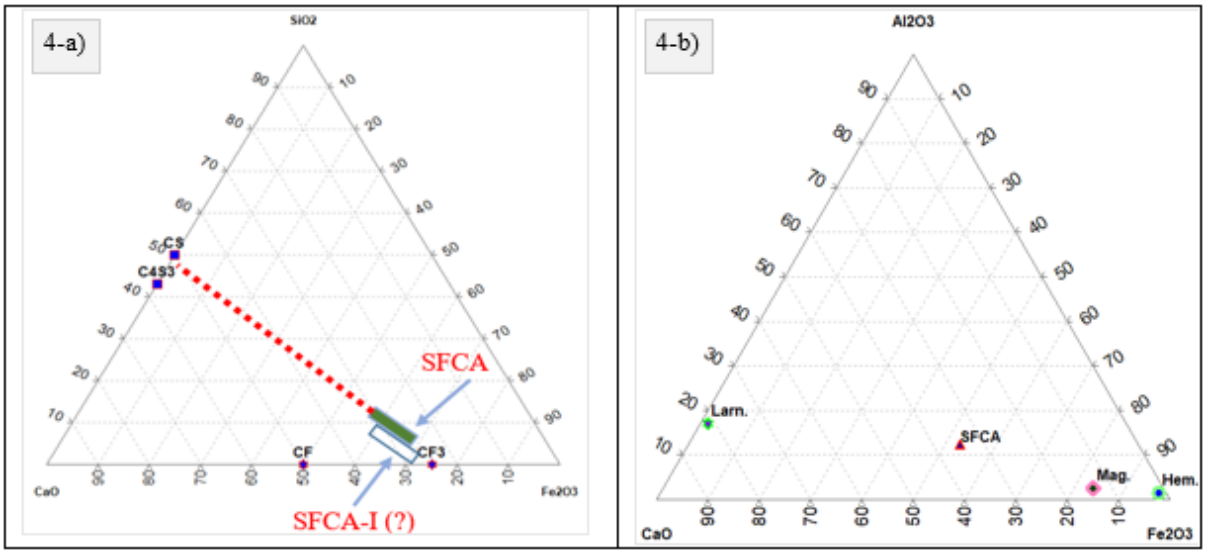

Figure 6-a) exhibits compositional link between SFCA and SFCA-I in the $CaO\text{-}SiO_2\text{-}Fe_2O_3$ triple phase diagram in the sinter, b) indicates compositional relationship among the $CaO\text{-}SiO_2\text{-}Fe_2O_3$ triple phase diagram and hematite, magnetite, larnite and SFCA.

In the examination of the sinter phase structure (shown in Figure 6); it has been observed that start of mineral compositions, CF_3 ($CaO.3Fe_2O_3$), CA_3 ($CaO.3AI_2O_3$) and C_4S_3 ($4CaO.3SiO_2$) or Fe_2O_3-AI_2O_3-CaO compounds can be designed to be able to create a link in a planar structure [13, 18, 19, 30]. In the study, the SFCA composition encountered in the industrial sinter was observed and triple phase diagrams were drawn as SFCA forms, SFCA, SFCA-I and SFCA-II (dendritic) solid solution series [13, 19].

The Figure 7 demonstrates both main SFCA phase structures together. SFCA-I is characterized by a high content of Fe and a low content of Si. As seen in the Figure 7-a), the morphology of SFCA-I can be plate-like and its sections can be acicular. However, as seen in the Figure 7-b), the morphology of SFCA is columnar and block-shaped, containing less Fe and it is more stable at higher temperature (>1300 ^oC). The third type of SFCA phase structure can be observed in dendritic morphology. This structure is very thin, in the form of SFCA-II and is the first type of SFCA that took shape during the sintering process [7, 13, 18- 21]. Figure 7-a) and 7-b) show the typical SFCA and SFCA-I phase structures in the sinter material.

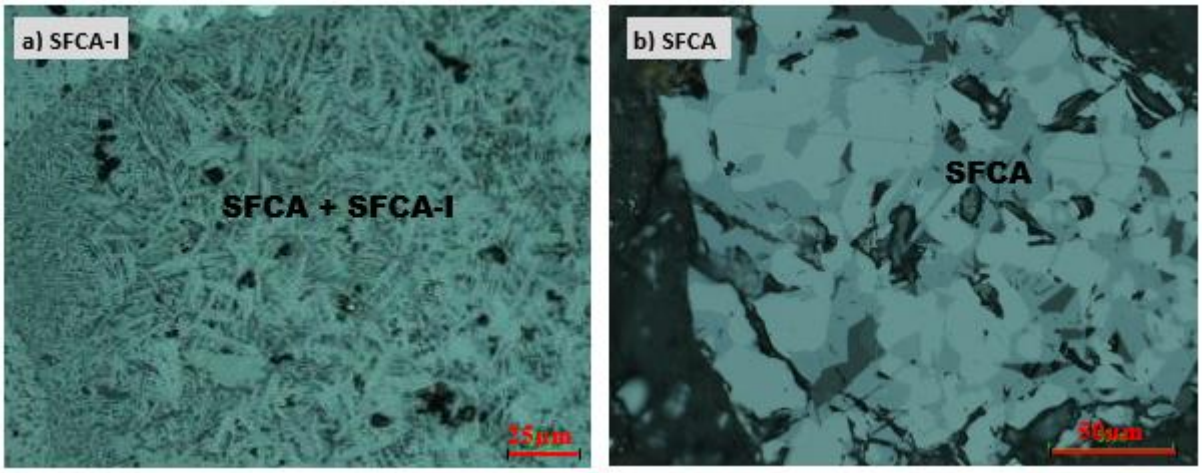

Figure 7-a) and b) show the typical SFCA and SFCA-I phase structures in the sinter material.

Our study also investigated the formation and crystal size of SFCA. Phase structures determined by EDS analysis and the size of each were measured with Image J program. In the examinations, it has been observed that approximately 13% of the structures to be called dendritic crystals are smaller than 4 μm. Where the sintering temperature is 1200-1300 ^{o}C, the crystal structure grows, and such large crystals are called acicular SFCA. It has been determined that the SFCA crystals of approximately 24% of the structures to be called acicular structures are larger than 4 μm (microns) and less than 10 μm. During the heating process of acicular SFCA sinter process, it collapsed in the form of columnar SFCA during the cooling phase upon completion of melting at 1300 ^{o}C. In this formation, crystal structures were larger and approximately 30% were found to be larger than 10 μm.

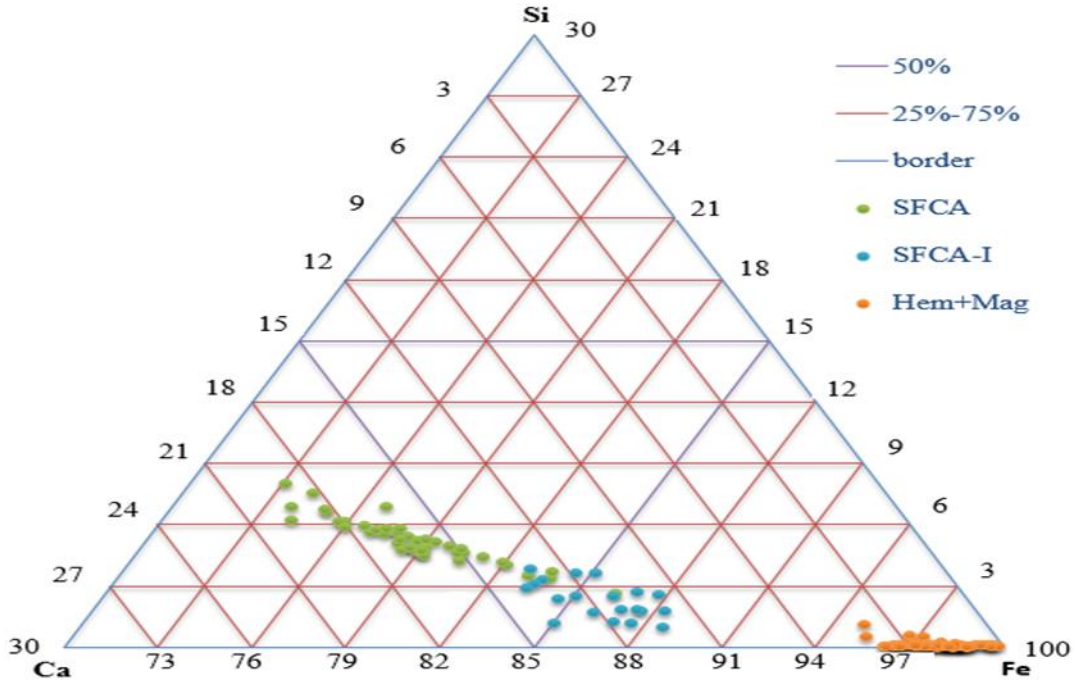

Figure 8 Matrix bond image of hematite, magnetite, SFCA, and SFCA-I phase structures in the sinter structure of the Ca-Si-Fe triple phase diagram.

A ternary phase diagram was obtained with detailed EDS analysis on sinter samples. Sinter types are determined according to the element content of the phase structures according to SEM-EDS analysis. The phase structures of hematite, magnetite and SFCA were characterized with the help of element values (especially Si, Ca, Fe) in sinter. In the Figure 8, the orange colored dots represent hematite and magnetite phase structures, the blue colored dots represent SFCA-I phase structures and the green colored dots clusters represent SFCA phase structures.

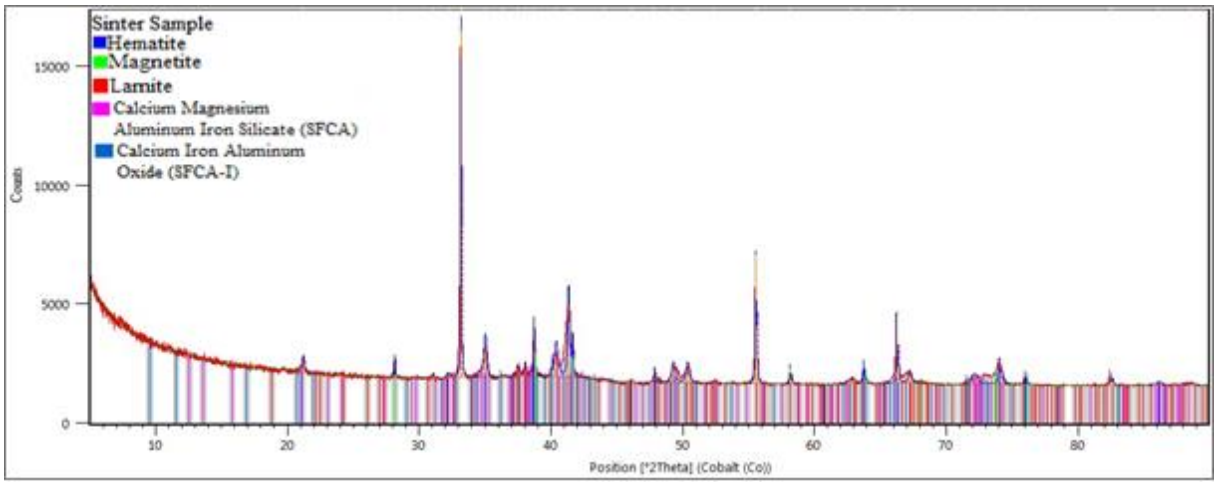

Figure 9 XRD research on Sinter sample with High Score Plus and Rietveld Program.

Figure 9 reveals the Rietveld measurement of the sinter sample. In this study, Autoquan program working with Rietveld method was used to define the phase structures in sinter samples. In this study, the contents of the sinter phase structures were obtained quantitatively (%) by the Autoquan software using the Rietveld method.

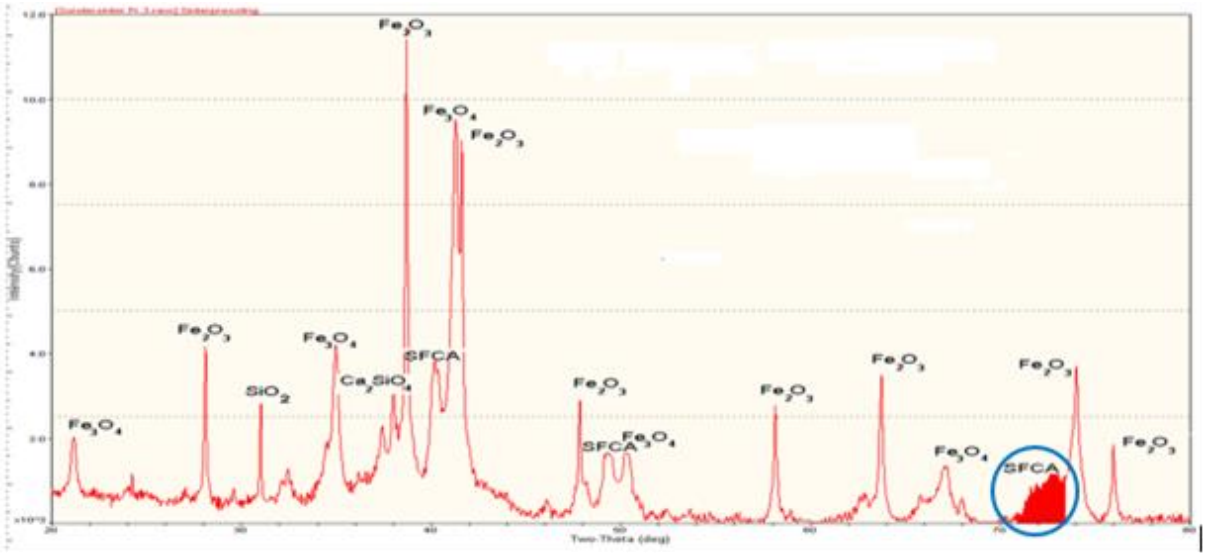

Figure 10 The region where SFCA calculation is made by means of XRD scanning.

Another study we conducted on the determination of the phase structures in the sinter material is given in the Figure 10. In this study, SFCA value is required to be at the rate of 70 %, the area of the region below the angle of 2 Theta between 71°-73°, the region (the red zone in Figure 8) gives

quantitative information about the SFCA phase content. The program calculates the area in this region using the integral. If the value is low (<60%), lime is added to the system. If the value is high (>85%), the lime ratio is reduced. It is ensured that the SFCA value in this region remains between 60-85%. However, in this research; it was determined that magnetite (Fe_3O_4), hematite (Fe_2O_3), larnite (Ca_2SiO_4), quartz (SiO_2) and SFCA phases could not be quantitatively determined but only qualitatively. This method will give more suitable results for sinter plants with stable production of raw material and process parameters. Raw material and process conditions may vary in industrial sinter production. For this reason, each facility has to determine its ideal sinter phase morphology and SFCA operating parameters according to its production conditions.

In our study, we mainly focused on two approaches in determining the phase content of the sinter. In the first one, quantitative results related to SFCA is found by using the method of calculating the areas under the peaks containing the SFCA structure. Detailed phase morphology information could not be obtained about SFCA structures. However, changes that may occur in sinter material morphology or process conditions affect the accuracy of the results with the current calculation method. The present method gives proper results in very variable sinter input and more stable process conditions. This approach demonstrates that the results obtained are not healthy, as a result of absorbing the curves obtained with the tube that radiates Cu-alpha, with fluorescence and absorption effect especially in iron-containing materials. Another method was to calculate the ratios of the phases in SFCA with the rietveld method using the tube that radiates Co-alpha (indicated in Tables 2 and 3). Interpretation of the results with the Rietveld method was only possible with the Autoquan program. In the first method, only the area under the SFCA peaks in the region obtained by XRD scanning is calculated by the software. The SFCA value in this region is required to be 70%. In the second method, all parameters (ferrite structures, SFCA types, Fe_2O_3 etc.) that are important in determining the quality in the sinter process are examined. With this method, results can be obtained quantitatively in percentage [33]. Thanks to this method, all changes that may occur in the sinter structure or process conditions can be examined and the sinter phase structures that are likely to occur can be tracked in a more controlled way.

4. CONCLUSION

By calculating the quantitative values of the phases within the sinter, the monitoring and directing of the sinter quality were made more precise with SFCA. A detailed SFCA value cannot be obtained by calculating the area under the peaks in the sinter structure. With the Rietveld Method, the sinter mineralogical structure was fully controlled by calculating all phases in the sinter. Optimum sintering parameters were controlled by the SFCA was more stable blast furnace charge sintering was provided better process control and cost advantage. In the study, it is important to find an optimum SFCA quantity according to mineral compositions and sinter quality which complies with the generally accepted specifications. Sintering plants in the integrated iron and steel plants was followed quality on the basis of small basicity (CaO/SiO_2) ratio. The effects of ferrite structures, wustite (FeO) and aluminum oxide (Al_2O_3), which are important in determining the quality in sinter production, on sinter quality are not examined. By controlling the SFCA in the sinter structure, this quaternary phase matrix (CaO, Al_2O_3, Fe_2O_3, SiO_2) will be taken under control and all parameters that may affect the quality of the process will be examined. With the detection of SFCA in the sinter internal structure, the control of the sinter mineralogical structure will be ensured, and the sinter quality will be improved. Sinter is an important material that is charged to blast furnaces and affects blast furnace efficiency. Mineralogically more stable sinter will be produced with the control of SFCA within the sinter. In this way, more sinter will be charged to the blast furnaces and the raw material costs of the blast furnace will be reduced. Because, the production cost of sinter material is lower than the pellet material charged to the high furnace. With the control of SFCA, sinter quality parameters

(basicity, RDI, sieve analysis, etc.) will improve and blast furnace production performance will increase.

Acknowledgements

The author would like to thank the 2219-International Postdoctoral Research Fellowship Programme of the Scientific and Technological Research Council of Turkey (TUBITAK). I am thankful to TUBITAK for their support.

Funding

This project studies were supported the Department of Science Fellowships and Grant Programmes (BIDEB). Project number was 1059B191401374

The Declaration of Conflict of Interest/ Common Interest

No conflict of interest or common interest has been declared by the author.

Authors' Contribution

The author solemly performed the computations and wrote the manuscript.

The Declaration of Ethics Committee Approval

The author declare that this document does not require an ethics committee approval or any special permission.

The Declaration of Research and Publication Ethics

The author of the paper declare that they comply with the scientific, ethical and quotation rules of SAUJS in all processes of the article and that they do not make any falsification on the data collected. In addition, they declare that Sakarya University Journal of Science and its editorial board have no responsibility for any ethical violations that may be encountered, and that this study has not been evaluated in any academic publication environment other than Sakarya University Journal of Science.

REFERENCES

[1] R.P. Bhagat, U. Chattoray, and S.K. Sil, "Porosity of sinter and its relation with the sintering indices", ISIJ International, vol. 46, no. 11, p. 1728-1730, 2006.

[2] T. Umadevi, R. Sah, and P. C. Mahapatra, "Influence of sinter basicity (CaO/SiO_2) on low and high alumina iron ore sinter quality", Mineral Processing and Extractive Metallurgy, 123(2), 75-85, 2014.

[3] R. Chaigneau, "Fluxed sinter formation and SFCA reduction under Simulated Conditions", PhD Thesis, Delft University Press, p. 12-28, 1994.

[4] L.H. Hsieh and J.A. Whiteman, "Effect of oxygen potential on mineral formation in lime-fluxed iron ore sinter", ISIJ International, vol. 29, no. 8, p. 625- 634, 1989.

[5] C. E. Loo, R. P. Williams, and L. T. Matthews, "Influence of material properties on high temperature zone reactions in sintering of iron ore", Transactıons of The Institution of Mining And Metallurgy Sectıon C-Mineral Processing and Extractive Metallurgy, vol.101, p. 7-15, 1992.

[6] N. Chakraborti, K. Deb, and A. Jha, "A genetic algorithm based heat transfer analysis of a bloom re-heating furnace", Steel Research, vol. 71, no. 10, p. 396-402, 2000.

[7] N. A. Webster, M. I. Pownceby, I. C. Madsen, and J. A. Kimpton, "Silico-ferrite of calcium and aluminum (SFCA) iron ore sinter bonding phases: new insights into their formation during heating and cooling", Metallurgical and Materials Transactions B, 43(6), 1344-1357, 2012.

[8] N.J. Bristow and A.G. Waters, "Role of SFCA in promoting high-temperature reduction properties of iron ore sinters". Mineral Processing & Extractive

Metallurgy, Section C. vol. 100. p. 1-4, 1991.

[9] S. Nicol, J. Chen, M. I. Pownceby, and N. A. Webster, "A Review of the Chemistry, Structure and Formation Conditions of Silico-Ferrite of Calcium and Aluminum (SFCA) Phases", ISIJ International, 58(12), 2157-2172, 2018.

[10] T. Takayama, R. Murao, and M. Kimura, "Quantitative Analysis of Mineral Phases in Iron-ore Sinter by the Rietveld Method of X-ray Diffraction Patterns", ISIJ International, ISIJINT-2017, 2018.

[11] M. Kama, T. Miyazaki, K. Ito, Y. Hida, and M. Sasaki, "Morphological analysis of calcium ferrite and hematite in sintered ore", Transactions ISIJ. vol. 24, 1984.

[12] W.G. Mumme, "The crystal structure of SFCA-II, $Ca_{5.1}Al_{9.3}Fe^{3+}_{14.30}Fe^{2+}_{0.55}O_{48}$, a homologue of the aenigmatite structure type, and new structure type, and new crystal refinement of SFCA, $Ca_2Al_5Fe_7O_{20}$", Implications for the nature of the ternary-phase solid-solution previously reported in the CaO-Al_2O_3-iron oxide system, Neues Jahrbuch Miner. Abh., vol. 178, no. 3, p.307-335, 2003.

[13] M. I. Pownceby, N. A. S. Webster, J. R. Manuel, and N. Ware, "The influence of ore composition on sinter phase mineralogy and strength", Mineral Processing and Extractive Metallurgy, 125(3), 140-148, 2016.

[14] W.G. Mumme, J.M.F. Clout, and R.W. Gable, "The crystal structure of SFCA-I $Ca_{3.18}Fe^{3+}_{14.66}Al_{1.34}Fe^{2+}_{0.82}O_{28}$, a homologue of the aenigmatite structure type, and new structure type, and new crystal refinements of β-CCF, $Ca_{2.99}Fe^{3+}_{14.30}Fe^{2+}_{0.55}O_{25}$ and Mg-free SFCA, $Ca_{2.45}Fe^{3+}_{9.04}Al_{1.74}Fe^{2+}_{0.16}Si_{0.6}O_{20}$". Neues Jahrbuch Miner. Abh, vol. 173, no. 1, p. 93-117, 1988.

[15] M. I. Pownceby and J.M.F. Clout, "Importance of fine iron ore chemical composition and high temperature phase relations, applications to iron ore sintering and pelletizing", Mineral Processing and Extractive Metallurgy, vol. 112, p. 44-51, 2003.

[16] W. Wang, X. H. Chen, R. S. Xu, J. Li, W. J. Shen, and S. P. Wang, "Research progress on multiscale structural characteristics and characterization methods of iron ore sinter", Journal of Iron and Steel Research International, 1-13, 2020.

[17] R. Mežibrický, M. Fröhlichová, R. Findorák, and V. S. Goettgens, "Ore Assimilation and Secondary Phases by Sintering of Rich and High-Gangue Iron Ores", Minerals, 9(2), 128, 2019.

[18] T. Harvey, "Influence of Mineralogy and Pore Structure on the Reducibility and Strength of Iron Ore Sinter", Doctoral dissertation, University of Pretoria, Republic of South Africa, 2020.

[19] M. A. Nyembwe, "Study of sinter reactions when fine iron ore is replaced with coarse ore, using an infrared furnace and sinter pot tests", Doctoral dissertation, The University of Newcastle, Australia, 2012.

[20] D. Fernández-González, I. Ruiz-Bustinza, J. Mochón, C. González-Gasca, and L. F. Verdeja, "Iron ore sintering: Process". Mineral Processing and Extractive Metallurgy Review, 38(4), 215-227, 2017.

[21] A. Cores, L. F. Verdeja, S. Ferreira, I. Ruiz-Bustinza, and J. Mochon, Editor's Page: "Iron ore sintering. Part 1. Theory and practice of the sintering process", Rev. Avances en Sistemas Informática, 10 (1), 152-171, 2013.

[22] S. Blake, R.G. Launsby, and D. L. Weese, "Experimental design meets the realities of the 1990s", Quality Progress, p.99-101, 1994.

[23] P.R Dawson, J. Ostwald, and K.M. Hayes, "The influence of sintering temperature profile on the mineralogy and properties of iron ore sinters", Proc. Aust. Inst. of Mining and Metallurgy, p. 163-169,1984.

[24] A. Cores, A. Babich, M. Muñiz, S. Ferreira, and J. Mochon, "The influence of different iron ores mixtures composition on the quality of sinter", ISIJ International, vol. 50 , no. 8, p. 1089-1098, 2010.

[25] M.S. De Magalhaes and P.R.G. Brandao, "Microstructures of industrial sinters from Quadrilatero Ferrifero's iron ores", Minerals Engineering, Elsevier, p.1251, 2003.

[26] M. I. Pownceby and T.R.C. Patrick, "Stability of SFC (silico-ferrite of calcium): solid solution limits, thermal stability and selected phase relationships within the Fe_2O_3-$CaO_{Si}O_2$ (FCS) system". European Journal of Mineralogy. vol. 12. p. 455-468, 2000.

[27] N. V. Y. Scarlett, M. I. Pownceby, I. C. Madsen, and A. N. Christensen, "Reaction sequences in the formation of silico-ferrites of calcium and aluminum in iron ore sinter", Metallurgical and materials transactions B, vol. 35B, p. 929- 936, 2004.

[28] Y. Ishikawa, Y. Shimomura, M. Sasaki, and H. Toda, "Improvement of sinter quality based on the mineralogical properties of ores", Ironmaking Proceedings. vol. 42. p. 17-29, 1983.

[29] L. X. Yang and E. Matthews, "Sintering reactions of magnetite concentrates under various atmospheres", ISIJ International, vol. 37, no. 11, p. 1057-1065, 1997.

[30] S. Nicol, E. Jack, and P. C. Hayes, "Controlled Solidification of Liquids within the SFC Primary Phase Field of the Fe_2O_3-CaO-SiO_2 System in Air", Metallurgical and Materials Transactions B, 50(6), 3027-3038, 2019.

[31] N.V.Y. Scarlett, M. I. Pownceby, I. C Madsen, and A. N. Christensen, "In situ X-ray diffraction analysis of iron ore sinter", Journal of Applied crystallography, vol. 37, no. 3, p. 362-368, 2004.

[32] P. Łechtańska and G. Wielgosiński, "The use of ammonium sulfate as an inhibitor of dioxin synthesis in iron ore sintering process", Ecological Chemistry and Engineering, 2014.

[33] R. A. Young, "The Rietveld method, International Union Crystallography", Oxford University Press, Oxford, 298p, 1993.

SAKARYA ÜNİVERSİTESİ
FEN BİLİMLERİ ENSTİTÜSÜ DERGİSİ

Sakarya University Journal of Science
SAUJS

e-ISSN 2147-835X | Period Bimonthly | Founded: 1997 | Publisher Sakarya University |
http://www.saujs.sakarya.edu.tr/en/

Title: Effects of Rotating Frame on a Vector Boson Oscillator

Authors: Abdullah GUVENDİ

Recieved: 2021-04-07 17:07:23

Accepted: 2021-05-07 20:36:07

Article Type: Research Article

Volume: 25
Issue: 3
Month: June
Year: 2021
Pages: 834-840

How to cite
Abdullah GUVENDİ; (2021), Effects of Rotating Frame on a Vector Boson Oscillator. Sakarya University Journal of Science, 25(3), 834-840, DOI: https://doi.org/10.16984/saufenbilder.911340
Access link
http://www.saujs.sakarya.edu.tr/en/pub/issue/62736/911340

Sakarya University Journal of Science 25(3), 834-840, 2021

Effects of Rotating Frame on a Vector Boson Oscillator

Abdullah GUVENDI*[1]

Abstract

We analyze the effects of the spacetime topology and angular velocity of rotating frame on the dynamics of a relativistic vector boson oscillator (VBO). To determine these effects on the energy of the VBO we solve the corresponding vector boson equation in the rotating frame of 2+1 dimensional cosmic string-induced spacetime background. We obtain an exact energy spectrum, which depends on the angular velocity of the rotating frame and angular deficit parameter of the background. We show that the effects of angular deficit parameter on each energy level of the VBO cannot be same and the angular velocity of the rotating frame couples with the spin of the VBO. Furthermore, we have obtained that the angular velocity of rotating frame breaks the symmetry of the positive-negative energy states.

Keywords: Non-inertial effects, quantum fields in curved spaces, topological defects.

1. INTRODUCTION

The relativistic wave equations for spin-1/2, spin-1 and spin-3/2 particles can be derived via canonical quantization of the classical spinning particle with zitterbewegung. These equations can be obtained as possible quantum states from the mentioned classical quantization procedure [1]. After demonstrating that there is a unifying principle for this class of relativistic wave equations [1], it has been shown that the well-known duffin-kemmer-proca equations and the many-body dirac equation (fully-covariant) [1-3] can be derived from similar action. Spin-1 sector of the duffin-kemmer-petiau (DKP) equation has been derived as excited state via the mentioned procedure provided that the spinor is a symmetric spinor of rank-two [1,4,5]. Under this condition, the symmetric spinor can be constructed by kronocker product of two dirac spinors [1,4-6]. However, it is important to underline that this symmetric spinor does not include the spin-0 sector in 2+1 dimensions [7]. The vector boson equation (VBE) corresponds to the spin-1 part of the DKP equation in 2+1 dimensions [1,4-7] and its massless form can also be derived via the same quantization procedure [4]. It has been declared that massless VBE and Maxwell equations are equivalent [4], and moreover it has been clearly shown that the state functions for massless form of the VBE have probability interpretation [4]. A few applications of the VBE can be found in the refs. [5-8]. In this work, we introduce the vector boson oscillator (VBO) and investigate its dynamics in the rotating frame of the 2+1 dimensional cosmic string-generated spacetime.

*Corresponding author: abdullah.guvendi@ksbu.edu.tr
[1]Kutahya Health Sciences University, Faculty of Engineering and Natural Sciences, Department of Basic Sciences, 43100, Kutahya.
E-Mail: abdullah.guvendi@ksbu.edu.tr ORCID: https://orcid.org/ 0000-0003-0564-9899

Cosmic strings are predicted to be linear topological defects that probably occurred in the early stages of the universe [9]. After Cosmic strings were introduced in $2+1$ dimensional spacetime [10], the obtained solution was naturally expanded to $3+1$ dimensions where there is a dynamical symmetry [11]. The spacetime backgrounds of cosmic strings include a conical singularity on the intersection point of the string with the space-like subspace [9-11]. Even though these spacetime backgrounds are locally flat [9-11] out of the intersection point, they are not flat when viewed globally [9-11]. Because of this feature, the cosmic strings can be responsible for several physical events in the universe [12-15]. The spacetime background of the cosmic string is characterized by α parameter, which is angular deficit parameter depending on the linear mass density (μ_s) of the cosmic string [12-15]. The gravitational [9-14] and electrostatic effects [12,15] of these topological defects on the dynamics of physical systems depend on the parameter α. The influences of topological defects on the dynamics of quantum mechanical systems have been widely studied [15-17]. In one of such works, it has been shown that the spin-symmetric [18] quantum state of a positronium system can be used to detect the topological defects [15]. The effects of topological defects on the spectral lines of quantum systems are not same for each spectral line of the quantum systems [19]. This means that the effects of topological defects are distinguishable from the other effects such as doppler effect and redshift [15,19].

On the other hand, the investigations about the effects of rotating frames on the quantum systems have provided very interesting results and accordingly such studies have attracted great attention for a long time [20-22] since these investigations have discovered very important effects [23-29]. The sagnac effect [23], mashhoon effect [24], persistent currents in the quantum ring and the coupling between the angular momentum of the quantum systems with the velocity of uniformly rotating frame [25] can be considered among these effects. One of the interesting results of these investigations is that the non-inertial effects stemming from the rotating frames restrict the physical region of the spacetime backgrounds where the particles can be placed [20-22]. It has been shown that the phase shift in neutron interferometry is due to the coupling of angular velocity of the earth with the angular momentum of the neutron [26]. The effects of rotating frame on the C_{60} molecules were analized [27,28] and the obtained results have indicated that rapidly rotating molecules can acquire a topological phase [27,28].

In this contribution, we investigate the influences of rotating frame on the relativistic dynamics of a VBO in the $2+1$-dimensional cosmic string spacetime. In order to determine the effects of both uniformly rotating frame and spacetime topology on the system in question we solve the corresponding VBE. We obtain an exact energy spectrum depending on the parameters of spacetime background.

2. GENERALIZED FORM OF THE VBE

In this part of the manuscript, we introduce the generalized form of the VBE and arrive at a set of coupled equations for a VBO in the rotating frame of 2+1 dimensional cosmic string-generated spacetime background.The generalized form of the VBE can be written as the following [1-8],

$$\{\beta^{\mu}\left(\partial_{\mu}-\Omega_{\mu}\right)+i\frac{mc}{\hbar}I_4\}\Psi(\mathbf{x})=0,$$
$$\beta^{\mu}=\frac{1}{2}(\gamma^{\mu}\otimes I_2+I_2\otimes\gamma^{\mu}),$$
$$\Omega_{\mu}=\Gamma_{\mu}\otimes I_2+I_2\otimes\Gamma_{\mu}. \qquad (1)$$

In eq. (1), γ^{μ} are the generalized dirac matrices, Γ_{μ} are the spinorial affine connections for spin-1/2 field, m is the rest mass of vector boson, c is the speed of light, $\hbar$ is usual planck constant, the symbol $\otimes$ indicates kronocker product [28], **x** is the spacetime position vector, I_2 and I_4 stand for the $2x2$ and $4x4$ dimensional identity matrices, respectively, and Ψ is the symmetric spinor of rank-two. The $2+1$ dimensional spacetime geometry of the uniformly rotating cosmic string-generated background is represented through the following line element [20-22],

$$ds^2=(1-\varpi^2\alpha^2r^2)c^2dt^2-2\varpi\alpha^2r^2cdtd\phi$$

$$- dr^2 - \alpha^2 r^2 d\phi^2 \,. \qquad (2)$$

In eq. (2), α is the angular deficit parameter, $\alpha = 1 - 4G\mu_s/c^2$, depending on the linear mass density (μ_s) of the cosmic string and newtonian gravitational constant (G) [15]. The azimuthal angle range is $0 \leq \phi < 2\pi$ in this spacetime background. Here, we deal with $\mu_s > 0$ case, since the $\mu_s < 0$ case describes an anti-conical spacetime background with negative curvature [20-22]. Therefore, the $\alpha > 0$ case does not make sense in the general relativity context [20-22]. The eq. (2) describes a flat spacetime background, in terms of polar coordinates, when $\varpi = 0$ and $\alpha = 1$ [15]. In eq. (2), we should notice that the radial coordinate must satisfy $r \ll 1/(\varpi\alpha)$, since this spacetime geometry can be defined for values of the r inside the range: $0 < r < 1/(\varpi\alpha)$. This condition guarantees that the vector boson considered is placed inside of the light-cone and imposes a spatial constraint. That is, the wave function vanishes at $r = 1/(\varpi\alpha)$ [20-22]. At this point, we should underline that the ϖ in eq. (2) is $\frac{\Omega}{c}$ and Ω is the angular velocity (not frequency) of the uniformly rotating frame. Therefore, the Ω rises to a hard-wall confining potential [20-22]. Now, one can obtain the tetrads $e^a_{\ \mu}$ [15],

$$g_{\mu\nu} = e^a_{\ \mu}\, e^b_{\ \nu}\, \eta_{ab}, \qquad e^\mu_{\ a} = g^{\mu\nu} e^b_{\ \nu} \eta_{ab},$$
$$\eta_{ab} = diag(1,-1,-1), \ (\mu,\nu,a,b = 0,1,2.). \qquad (3)$$

In eq. (3), η_{ab} is the flat spacetime metric tensor and hence the indices a, b indicate the local reference frame. The tetrads, which satisfy the following orthonormality conditions,

$$e^\mu_{\ a} e^a_{\ \nu} = \delta^\mu_{\ \nu}, \ \ e^a_{\ \mu} e^\mu_{\ b} = \delta^a_{\ b}, \qquad (4)$$

are obtained as the following,

$$e^\mu_{\ a} = \begin{pmatrix} 1 & 0 & 0 \\ 0 & 1 & 0 \\ -\varpi & 0 & \frac{1}{\alpha r} \end{pmatrix}, e^a_{\ \mu} = \begin{pmatrix} 1 & 0 & 0 \\ 0 & 1 & 0 \\ \varpi\alpha r & 0 & \alpha r \end{pmatrix}.$$

By using the tetrads one can obtain the generalized dirac matrices γ^μ via the relation $\gamma^\mu = e^\mu_{\ a}\, \gamma^a$ where γ^a are the space-independent dirac matrices [15]. According to line element in eq. (2) the space-dependent dirac matrices are obtained,

$$\gamma^t = \gamma^{-0}, \qquad \gamma^r = \gamma^{-1}, \quad \gamma^\phi = -\varpi\gamma^{-0} + \frac{1}{\alpha r}\gamma^{-2}. \qquad (5)$$

The choice of space-independent dirac matrices is not unique and different choices can be preferred, of course. According to signature of eq. (2) the space-independent dirac matrices can be chosen as $\gamma^{-0} = \sigma^z$, $\gamma^{-1} = i\sigma^x$, $\gamma^{-2} = i\sigma^y$ [29-31], in which σ^x, σ^y and σ^z are the pauli spin matrices. Also, we can obtain the spinorial connections for spin-1/2 fields via the following expression [15],

$$\Gamma_\mu = \frac{1}{4}\, g_{\lambda\sigma} = \left(e^a_{\ \nu,\mu}\, e^\sigma_{\ a} - \Gamma^\sigma_{\nu\mu}\right) S^{\lambda\nu},$$
$$(\lambda,\sigma,\mu,\nu,a,b = 0,1,2.), \qquad (6)$$

where $\Gamma^\sigma_{\nu\mu}$ are the christoffel symbols obtained through $\Gamma^\sigma_{\nu\mu} = 1/2\,(\partial_\nu g_{\mu\sigma} + \partial_\mu g_{\sigma\nu} - \partial_\sigma g_{\nu\mu})$ and $S^{\lambda\nu}$ are the spin operators determined by $S^{\lambda\nu} = 1/2\ [\gamma^\lambda, \gamma^\nu]$. Now, one can obtain the spinorial connections (non-vanishing) as the following,

$$\Gamma_t = \frac{i}{2}\varpi\alpha\, \gamma^{-0}, \quad \Gamma_\phi = \frac{i}{2}\alpha\, \gamma^{-0}. \qquad (7)$$

The VBO coupling, describing the interaction of magnetic moment (anomalous) with a linearly varying electric field [3,16,17,21], can be introduced through the following non-minimal substitution,

$$\partial_r \rightarrow \partial_r + \frac{m\omega}{\hbar}(\sigma^z \otimes \sigma^z)r,$$
$$(\sigma^z \otimes \sigma^z) = \text{diag}\,(1,-1,-1,1), \qquad (8)$$

where ω is the oscillator frequency (coupling strength) [3]. Eq. (2) allows to factorization of the spinor as the following,

$$\Psi(t,r,\phi) = e^{-i\frac{E}{\hbar}t} e^{is\phi} \begin{pmatrix} \psi_1(r) \\ \psi_2(r) \\ \psi_3(r) \\ \psi_4(r) \end{pmatrix}, \qquad (9)$$

where E and s are the total energy and spin of the system under consideration.

3. ENERGY SPECTRUM

In this section, we obtain an equation system consisting of three equations for the components of the symmetric spinor and arrive at an exact energy spectrum for the $\mathcal{VBO}$ in question. To end this, we substitute eq. (5), (7), (8) and eq. (9) into the eq. (1) and then we can acquire a set of coupled equations, in the most symmetric form, as the following,

$$\begin{aligned} &W\psi_-(r) - M\psi_+(r) - 2(\partial_r - \kappa r)\,\psi_0(r) = 0,\\ &2M\psi_0(r) - \frac{S}{r}\psi_-(r) + (\partial_r + \kappa r + \frac{1}{r})\,\psi_0(r) = 0,\\ &W\psi_+(r) - B\psi_-(r) - \frac{2S}{r}\psi_0(r) = 0, \end{aligned} \tag{10}$$

here, $\psi_\pm(r) = \psi_1(r) \pm \psi_4(r)$, $\psi_0(r) = \psi_2(r) = \psi_3(r)$ provided that $m \neq 0$ and the abbreviations are given as the following,

$$W = \frac{E}{\hbar c} + \varpi j\,, \quad S = \frac{s}{\alpha}, \quad M = \frac{mc}{\hbar}, \quad \kappa = \frac{m\omega}{\hbar}.$$

By considering a new change of variable, $\xi = \kappa r^2$, we can write the equation system in eq. (10) as the following,

$$\begin{aligned} &W\psi_-(\xi) - M\psi_+(\xi) - \kappa\sqrt{\frac{\xi}{\kappa}}(2\partial_\xi - 1)\,\psi_0(\xi) = 0,\\ &M\psi_0(\xi) + \kappa\sqrt{\frac{\xi}{\kappa}}\left(2\partial_\xi + 1 + \frac{1}{\xi}\right)\psi_+(\xi)\\ &\qquad - \frac{S}{\sqrt{\frac{\xi}{\kappa}}}\psi_-(\xi) = 0,\\ &W\psi_+(\xi) - M\psi_-(\xi) - \frac{S}{\sqrt{\frac{\xi}{\kappa}}}\psi_0(\xi) = 0, \end{aligned} \tag{11}$$

one of which is algebraic. By solving these equations in favor of $\psi_0(\xi)$ we can arrive at a wave equation. Through an ansatz reads as, $\psi_0(\xi) = \frac{\psi(\xi)}{\sqrt{\xi}}$, the wave equation becomes as the following,

$$\begin{aligned} &\xi^2\partial_\xi^2\,\psi(\xi) + \left(\xi A + \frac{1}{4} - G^2 - \frac{\xi^2}{4}\right)\psi(\xi) = 0,\\ &A = -\frac{1}{2} + \frac{M(W^2 - M^2) + 2SW\kappa}{4M\kappa},\ G = \frac{S}{2}.\\ &E_{n,s} = -\Omega\hbar s \mp \omega\hbar\frac{s}{\alpha} \end{aligned} \tag{12}$$

Dividing each term in this equation by ξ^2, the well-known whittaker differential equation is obtained [7]. At any rate, the solution function of eq. (20) is found in terms of the whittaker function $\boldsymbol{W}_{A,G}$ as $\psi(\xi) = N\boldsymbol{W}_{A,G}(\xi)$, where N is an arbitrary constant [7]. The function $\boldsymbol{W}_{A,G}$ can only be polynomial degree of n if the parameters satisfy the termination condition that reads as $\frac{1}{2} + G - A = -n$ [7]. This termination condition gives a condition for the quantization of the energy of system in question and accordingly one can obtain the following non-perturbative energy spectrum,

$$\pm mc^2\sqrt{1 + \frac{4\omega\hbar}{mc^2}\left(n + 1 + \frac{s}{2\alpha}\right) + \frac{s^2\omega^2\hbar^2}{\alpha^2 m^2 c^4}}\,, \tag{13}$$

which can be clarified as,

$$E_{n,0} = \pm mc^2\sqrt{1 + \frac{4\omega\hbar}{mc^2}(n+1)}\,, \tag{14}$$

if $\Omega = 0$ and $s = 0$. The result in eq. (14) is exactly same with the previously announced result for one-dimensional kemmer oscillator [32] and form of the eq. (14) is same with the result of one-dimensional dirac oscillator [33]. In the latest comparison (see eq. (14) and [33]), one can realize that the difference is only mass factor of the particles. Also, it is very interesting that the result in eq. (14) is found to be in a good agreement with the recently announced results for a composite structure consisting of a fermion-antifermion pair interacting via dirac oscillator coupling [3]. Therefore, eq. (13) gives an opportunity to analyze the effects of both uniformly rotating frame and spacetime topology on the energy of the $\mathcal{VBO}$. In eq. (13) we see that the effects of Ω and α on each energy level of the $\mathcal{VBO}$ cannot be same. It is clear that the parameters Ω and α do not any impact on the energy of $\mathcal{VBO}$ when $s = 0$.

4. RESULTS AND DISCUSSIONS

In this contribution, we have investigated the influences of uniformly rotating frame and spacetime topology on a relativistic vector boson oscillator. In order to analyze the effects of angular velocity (Ω) of the rotating frame and angular deficit of the spacetime background on

the energy of the vector boson oscillator (VBO) we have solved the generalized vector boson equation in the rotating frame of a 2+1 dimensional spacetime. The spacetime has been considered as $2+1$-dimensional static cosmic string-induced spacetime [15]. The rotating frame of this background is introduced in eq. (2), which represents to the flat Minkowski spacetime in terms of polar coordinates when angular velocity of the rotating frame and angular deficit of the background vanish. We have performed an exact solution for the system in question and accordingly we have arrived at a spectrum in energy domain. This energy spectrum has given in eq. (13) and it can be reduced in the form of eq. (14) when $\Omega = 0$ and $s = 0$. We have verified that the eq. (14) is exactly same with the previously announced results for one-dimensional kemmer oscillator [32] and form of the eq. (14) is also same with the results obtained for one-dimensional dirac oscillator [33]. Furthermore, eq. (14) has been found to be in a good agreement with the previously published results for a composite structure consisting of a fermion-antifermion pair that they interacts through dirac oscillator coupling [3]. The non-perturbative energy spectrum in eq. (13) includes the effects of spin coupling, uniformly rotating frame, angular deficit parameter of the spacetime background, frequency (coupling strength) of the oscillator and mass of the vector boson. This property of the energy spectrum provides a suitable basis to discuss the effects of both Ω and α on the system under consideration. The results have shown that the parameter Ω of the rotating frame breaks the symmetry (positive-negative) of the energy levels and it is also clear that the effects of Ω and α on each energy level of the system cannot be same. As it can be seen in eq. (2) that the information about the spacetime topology is carried by the angular coordinate and accordingly parameter α of the background alters differently the energy levels corresponding to possible spin eigen-states, $(s = \pm 1,0)$, when $\Omega = 0$. We can also see that such a system does not sense the effects of the parameter α when $\Omega = 0$ and $s = 0$. In this paper, all of the discussions have been made for the parameters defined in the range: $\alpha \in [0,1)$ and $0 < r < 1/(\varpi\alpha)$, where r is the distance between the particle and topological defect. Therefore, one can also conclude that the parameter Ω restricts the relativistic dynamics of the quantum system under consideration whether $\alpha = 1$ or $0 < \alpha < 1$.

Funding

The author has no received any financial support for this research.

The Declaration of Conflict of Interest/ Common Interest

No conflict of interest or common interest has been declared by the author. The author have fully disclosed conflict of interest situations to the journal.

Author' Contribution

This article has been prepared by the author.

The Declaration of Ethics Committee Approval

This study does not require ethics committee permission or any special permission.

The Declaration of Research and Publication Ethics

The author declares that he complies with the scientific, ethical and quotation rules of SAUJS in all processes of the present paper and that he does not make any falsification on the data collected. Also, the author declares that Sakarya University Journal of Science and its editorial board have no responsibility for any ethical violations that may be encountered, and that the present study has not been evaluated in any academic publication environment other than Sakarya University Journal of Science.

REFERENCES

[1] A. O. Barut, “Excited states of zitterbewegung,” Physics Letters B, vol. 237, no. 3, pp. 436-439, 1990.

[2] A. O. Barut and S. Komy, “Derivation of nonperturbative Relativistic Two-Body

Equations from the Action Principle in Quantumelectrodynamics," Fortschritte der Physik/Progress of Physics, vol. 33, no. 6. pp 309-318, 1985.

[3] A. Guvendi, "Relativistic Landau for a fermion-antifermion pair interacting through Dirac oscillator interaction," The European Physical Journal C, vol. 81, no. 2. pp 1-7, 2021.

[4] N. Ünal, "A simple model of the classical zitterbewegung: photon wave function,"Foundations of Physics, vol. 27, no. 5. pp 731-746, 1997.

[5] Y. Sucu and N. Ünal, "Vector bosons in the expanding universe," The European Physical Journal C, vol. 44, no. 2. pp 287-291, 2005.

[6] Y. Sucu and C. Tekincay, "Photon in the Earth-ionosphere cavity: Schumann resonances," Astrophysics and Space Science, vol. 364, no. 4. pp 1-7, 2019.

[7] M. Dernek and S. G. Doğan and Y. Sucu and N. Ünal, "Relativistic quantum mechanical spin-1 wave equation in 2+1 dimensional spacetime," Turkish Journal of Physics, vol. 42, no. 5. pp 509-526, 2018.

[8] G. Gecim and Y. Sucu, "The GUP effect on tunneling of massive vector bosons from the 2+1 dimensional blackhole," Advances in High Energy Physics, vol. 2018, no. 8. pp 1-8, 2018.

[9] A. Vilenkin, "Cosmic strings and domain walls," Physics Reports, vol. 121, no. 5. pp 263-315, 1985.

[10] S. Deser, R. Jackiw and G. Hooft, "Three-dimensional Einstein gravity: dynamics of flat space," Annals of Physics, vol. 152, no. 1. pp 220-235, 1984.

[11] J. R. Gott and M. Alpert, "General relativity in a (2+1)-dimensional space-time," General Relativity and Gravitation, vol. 16, no. 3. pp 243-247, 1984.

[12] B. Linet, "Force on a charge in the space-time of a cosmic string," Physical Review D, vol. 33, no. 6. pp 1833, 1986.

[13] D. D. Harari and V. D. Skarzhinsky, "Pair production in the gravitational field of a cosmic string," Physics Letters B, vol. 240, no. 3-4. pp 322-326, 1990.

[14] L. Parker, "Gravitational particle production in the formation of cosmic strings," Physical Review Letters, vol. 59, no. 12. pp 1369, 1987.

[15] A. Guvendi and Y. Sucu, "An interacting fermion-antifermion pair in the spacetime background generated by static cosmic string," Physics Letters B, vol. 811, no. 135960. pp 135960, 2020.

[16] M. Hosseinpour, H. Hassanabadi and F. M. Andrade,"The DKP oscillator with a linear interaction in the cosmic string space-time," The European Physical Journal C, vol. 78, no. 2. pp 1-7, 2018.

[17] J. Carvalho, C. Furtado and F. Moreas, "Dirac oscillator interacting with a topological defect," Physical Review A, vol. 84, no. 3. pp 032109, 2011.

[18] A. Guvendi, "The lifetimes for each state of $l = 0$ levels of the para-positronium," Eur. Phys. J. Plus, vol. 136, no. 4. pp 1-10, 2021.

[19] G. A. Marques and V. B. Bezerra, "Hydrogen atom in the gravitational fields of topological defects," Physical Review D, vol. 66, no. 10. pp 105011, 2002.

[20] K. Bakke and C. Furtado, "Bound states for neutral particles in a rotating frame in the cosmic string spacetime," Physical Review D, vol. 82, no. 8. pp 084025, 2010.

[21] S. Zare, H. Hassanabadi and M. de Montigny, "Non-inertial effects on a generalized DKP oscillator in a cosmic string space-time," General Relativity and Gravitation, vol. 52, no. 3. pp 1-20, 2020.

[22] L. C. N. Santos and C. C. Barros, "Scalar bosons under the influence of noninertial effects in the cosmic string spacetime," The European Physical Journal C, vol. 77, no. 3. pp 1-7, 2017.

[23] E. J. Post, "Sagnac Effect," Reviews of Modern Physics, vol. 39, no. 2. pp 475-493, 1967.

[24] B. Mashhoon, "Neutron interferometry in a rotating frame of reference," Physical Review Letters, vol. 61, no. 23. pp 2639-2642, 1988.

[25] F. W. Hehl and W. T. Ni, "Inertial effects of a Dirac particle," Physical Review D, vol. 42, no. 6. pp 2045-2048, 1990.

[26] S. A. Werner, J. L. Staudenmann and R. Corella, "Effects of Earth's rotation on the Quantum Mechanical Phase of the Neutron," Physical Review Letters, vol. 42, no. 17. pp 1103-1106, 1979.

[27] J. Q. Shen and S. L. He, "Geometric phases of electrons due to spin-rotation coupling in rotating C_{60} molecules," Physical Review B, vol. 68, no. 19. pp 195421, 2003.

[28] J. Q. Shen, S. L. He and F. Zhuang, "Aharonov-Carmi effect and energy shift of valence electrons in rotating C_{60} molecules," The European Physical Journal D, vol. 33, no. 1. pp 35-38, 2005.

[29] A. Guvendi, R. Sahin and Y. Sucu, "Exact solution of an exciton energy for a monolayer medium," Scientific Reports, vol. 9, no. 1. pp 1-6, 2019.

[30] A. Guvendi, R. Sahin and Y. Sucu, "Binding energy and decaytime of exciton in dielectric medium," The European Physical Journal B, vol. 94, no. 1. pp 1-7, 2021.

[31] A. Guvendi and S. G. Doğan, "Relativistic Dynamics of Oppositely charged Two Fermions Interacting with External Uniform Magnetic Field," Few-Body Systems, vol. 62, no. 1. pp 1-8, 2021.

[32] A. Boumali, "One-dimensional thermal properties of the Kemmer oscillator," Physica Scripta, vol. 76, no. 6. pp 669, 2007.

[33] M. H. Pacheco, R. R. Landim and C. A. S. Almeida, "One-dimensional Dirac oscillator in a thermal bath," Physics Letters A, vol. 311, no. 2-3. pp 93-96, 2003.

SAKARYA ÜNİVERSİTESİ
FEN BİLİMLERİ ENSTİTÜSÜ DERGİSİ

Sakarya University Journal of Science
SAUJS

e-ISSN 2147-835X | Period Bimonthly | Founded: 1997 | Publisher Sakarya University |
http://www.saujs.sakarya.edu.tr/en/

Title: Quantum Irreversibility in a Misaligned Spin System

Authors: Selçuk ÇAKMAK

Recieved: 2020-11-18 21:15:52

Accepted: 2021-05-08 15:53:22

Article Type: Research Article

Volume: 25
Issue: 3
Month: June
Year: 2021
Pages: 841-848

How to cite
Selçuk ÇAKMAK; (2021), Quantum Irreversibility in a Misaligned Spin System. Sakarya University Journal of Science, 25(3), 841-848, DOI: https://doi.org/10.16984/saufenbilder.827989
Access link
http://www.saujs.sakarya.edu.tr/en/pub/issue/62736/827989

Sakarya University Journal of Science 25(3), 841-848, 2021

Quantum Irreversibility in a Misaligned Spin System

Selçuk ÇAKMAK*[1]

Abstract

A single spin that is misaligned with respect to the static external magnetic field is investigated as a toy model to clarify the nature of irreversibility in terms of inner friction and irreversible work. The coherence generation and the effects of unwanted transitions are analyzed in detail. The behavior of inner friction and irreversible work as a function of protocol time are analyzed for a finite-time unitary transformation. The coherence generation is shown to be the common sign for the inner friction and irreversible work. The excess energy sourced by the unwanted transitions for a quasistatic transformation is found to be the only sign for irreversible work. The angle dependencies of the inner friction and irreversible work are also analyzed explicitly. The selected model and the considered realistic parameters are available to be implemented for the finite-time operations on the nuclear magnetic resonance setups.

Keywords: Quantum thermodynamics, Nonequilibrium and irreversible thermodynamics, Irreversible work, Inner friction

1. INTRODUCTION

The fast driving protocols are required for powerful thermal heat engines and refrigerators which are, however, the source of irreversibility [1-21]. In the scales where the quantum fluctuations are also relevant, the two irreversibility measures named recently as the inner friction and irreversible work have been introduced as two distinct irreversibility quantifiers that arise from the fast Hamiltonian driving protocols [14,16]. The inner friction and the irreversible work can be considered as the system response to the external driving techniques. The mechanism of the system response can be explained fully with the quantum mechanical theory. The initial studies on the concept of inner friction and irreversible work are realized on various models [12-19]. The inner friction has been recently investigated in ref [14] considering misalignment and disordered samples. There have been studies that investigate the effects of inner friction on work output and the efficiency of the quantum counterpart of classical Otto and Carnot heat engines [16,19]. The finite-time driven quantum two-level system undergoing the unitary evolution shows that the quantum friction arises in the case of the fast-driven model. The basic reason is explained according to the quantum adiabatic theorem as the system cannot follow its instantaneous eigenstates

* Corresponding author: selcuk.cakmak@samsun.edu.tr
[1] Samsun University, Software Engineering Department, Samsun, Turkey.
ORCID: https://orcid.org/0000-0002-1284-0870

[12,16,17]. On the other hand, the irreversible work and inner friction are investigated analytically considering reversible isothermal and reversible adiabatic conditions [12].

The inner friction or irreversible work can be defined from the comparison of the work done on the system during the actual finite time process with the one obtained along the ideal adiabatic or isothermal process (see Figure 1). The quantum relative entropy, which is one of the basic distance measurement between two quantum states, has been recently connected both to the inner friction and the irreversible work [12]. The connection shows here that the measures treated an equal footing. The reasons for arising entropy in terms of quantum relative entropy during finite-time unitary driving are investigated in detail in ref [18]. The population mismatch and the coherence generation are reported as two basic contributions to entropy production [18].

In this study, we focus on the finite-time unitary-driven of a spin-$1/2$ system that is misaligned with respect to the external static magnetic field. We analyze the energetic deviation from the reversible quantum adiabatic and reversible quantum isothermal transformation under realistic conditions. The role of misalignment and the total protocol time on the inner friction and the irreversible work are investigated in detail. Also, the coherence and the population mismatch effects on the inner friction and irreversible work are explicitly revealed. The obtained results indicate the differences between the inner friction and irreversible work inevitably arises from the population mismatch contribution.

2. THEORY

2.1. Irreversible Work

A thermal equilibrium state with inverse temperature β_i $(1/k_B T_i)$ is defined by Boltzmann-Gibbs distribution [15]. Unitary driving leads to the initial system represented by ρ_0 to out of the equilibrium state, $\rho_0 \rightarrow \rho_\tau$, which causes the energetic deviation from the reversible state (isothermal transformation) which is driven quasi-statically isothermal $(\beta_i = \beta_B)$, $\rho_0 \rightarrow \rho_B$. This energetic deviation indicates dissipated work from the system, known as irreversible work. More precisely, the irreversible work is the difference between the work obtained through unitary transformation and the one through the reversible isothermal process (see Figure 1). The magnitude of the energetic deviation from the reversible state is related to the quantum relative entropy, $D(\rho_\tau||\rho_B) = tr[\rho_\tau(\ln \rho_\tau - \ln \rho_B)]$. Thus, the irreversible work can be given as [12]

$$\langle \omega_{irr} \rangle = \beta^{-1}[D(\rho_\tau||\rho_B)]. \quad (1)$$

The unitary driving protocol is followed by a relaxation process in which the system reaches a thermal equilibrium state via dissipate energy into the heat bath, evolves naturally.

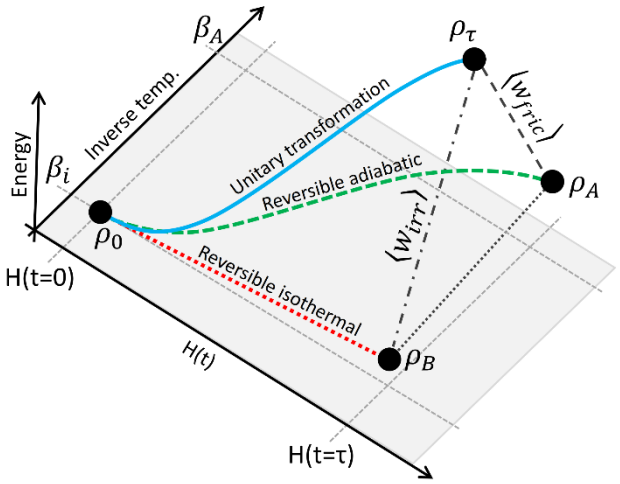

Figure 1 Sketch of the transformations discussed in the text. All the transformations are considered to start with an initial thermal state at inverse temperature β_i. The blue solid line indicates parametric finite time (unitary) transformation of the system Hamiltonian from $H(t=0)$ to $H(t=\tau)$ in a time interval τ. The state ρ_τ defined at the end of the unitary process is a nonequilibrium state due to the inter-level transitions. The green dashed and red dotted lines are the reversible adiabatic and isothermal processes which define effective thermal states corresponding to $H(t=\tau)$ as denoted by ρ_A and ρ_B, respectively. The relative entropy of ρ_τ to ρ_A or to ρ_B gives the inner friction or irreversible work as indicated by black dashed and dash-dotted lines, respectively.

The Eq. 1 enables the exploration of the different contributions on the irreversible work by the separation approach in Ref. [18]. The population

mismatch measured by the difference in populations between ρ_τ and ρ_B, which is caused by unwanted transitions and the coherence generated in the unitary driving operation are two quantitative contributions to irreversible work. The coherence generated in the process can be defined as [18]

$$C(\rho_\tau) = D(\rho_\tau||\Delta[\rho_\tau]) = S(\Delta[\rho_\tau]) - S(\rho_\tau) \quad (2)$$

Where $\Delta[\rho_\tau]$ is the density matrix in the energy basis of system at the end of unitary driving. $S(\Delta[\rho_\tau])$ and $S(\rho_\tau)$ are von Neumann entropy $\big(S(\rho) = -tr(\rho \ln \rho)\big)$. Considering Eq. 2 the irreversible work can be reformed as [18]

$$\langle \omega_{irr} \rangle = \frac{1}{\beta_i}[C(\rho_\tau) + D(\Delta_\tau[\rho_\tau]||\rho_B)]. \quad (3)$$

This equation explains that the finite-time transformations can generate coherence and make an unstable distribution of the populations with respect to ρ_B. These are two measurable indicators for the irreversible work, quantitatively.

2.2. Inner Friction

The difference between the work performed on the system during the actual unitary process and the reversible adiabatic one, however, defines the inner friction (see Figure 1). The reversible adiabatic transformation requires the protection of the population of each energy level. This is possible with infinite time unitary driving ($\tau \to \infty$). At the end of the reversible adiabatic transformation, the system reachs to desired state, ρ_A. Also, the system can follow its instantaneous eigenstates. The reversible adiabatic state, $\rho_A = \sum_n P_n^{(0)} \left|\epsilon_n^{(A)}\right\rangle\left\langle\epsilon_n^{(A)}\right|$ where the $P_n^{(0)}$ is initial population of n^{th} energy level and $\left|\epsilon_n^{(A)}\right\rangle$ is the eigenstate of the H_A. On the other hand, the fast-driving protocols, generally, cause the deviation from the desired state which is obtained by the reversible adiabatic transformation, ρ_A. So, this deviation requires extra work on the system to reach the desired state, ρ_A. The extra work mentioned here is called inner friction. The amount of extra work depend the duration of finite-time transformation, τ. The distance between the desired state and the reached state via finite time driving is a quantitative measurable indicator. The quantum relative entropy is a useful tool to measure the amount of the distance between ρ_τ and ρ_A, $D(\rho_\tau||\rho_A)$. Besides, the system releases the excess energy-sourced by the finite-time transformation, as heat form to the heat bath. The inverse temperature of the heat bath is $\beta_A\ (1/k_B\, T_A)$. Thus the inner friction is defined as below [12]

$$\langle \omega_{fric} \rangle = \beta^{-1}[D(\rho_\tau||\rho_A)] \geq 0. \quad (4)$$

Since the inner friction can be given by the quantum relative entropy a similar contribution separation as given in Eq. 3 can also be done for the inner friction.

3. RESULTS

The considered system Hamiltonian of a two-level single spin interacting to the time-dependent magnetic field along the z-axis and x-axis, could be defined as [14]

$$H(t) = \Omega_0 I_z + \Omega(t)(\cos\theta\, I_z + \sin\theta\, I_x). \quad (5)$$

Where Ω_0 is the static magnetic field along the z-axis, the $\Omega(t)$ is externally controlled time-dependent magnetic field and θ is the misaligned angle of spin with respect to the static magnetic field.

During the finite time transformation, we tune the magnetic field from its initial Ω_i to a final Ω_f value. It changes linearly with time t. The driving function is given as

$$\Omega(t) = \Omega_i\left(1 - \frac{t}{\tau}\right) + \Omega_f\left(\frac{t}{\tau}\right), \quad (6)$$

where $\Omega_f = 2\Omega_i$ and $\Omega_i = \Omega_0$. The τ is the duration of the finite-time transformation. Also, the finiti-time transformation can be described by a unitary evolution of the density matrix expressed by von Neumann equation $\dot{\rho}(t) = -i[H(t), \rho(t)]$. The density matrices of the initial and final states are ρ_0 (where $t = 0$) and ρ_τ (where $t = \tau$), respectively.

For the above discussed driving protocol (Eq. 6), on the considered model (Eq. 5), we now investigate the role of the misalignment and the total time allocated to the protocol on the irreversible work and inner friction given by Eqs. 1 and 4, respectively. To see the possible existence of the irreversibility in a quantum system that can be experimentally achievable, we chose the parameters which are thermodynamically implemented in liquid state nuclear magnetic resonance (NMR), recently [19]. Therefore, we set the bath temperature at $T = 10\ peV/k_B$ and the frequency at $\Omega_0 = 2\pi f$ here $f = 2\ kHz$ with considering the misalignment angles as $\left\{0, \frac{\pi}{5}, \frac{\pi}{4}, \frac{\pi}{3}, \frac{\pi}{2}\right\}$.

We first investigate the inner friction given the Eq. 4 and plot the inner friction versus the total protocol time for different misalignment angles. Please recall here that the density matrix for the reversible adiabatic may be written in the form as $\rho_A = \sum_n P_n^{(0)} \left|\epsilon_n^{(A)}\right\rangle\left\langle\epsilon_n^{(A)}\right|$ which is constructed in terms of initial level populations $P_n^{(0)}$ and the final eigenstates of the Hamiltonian $H(t=\tau)$. The state ρ_A for a qubit is infected an effective thermal state at temperature τ_A, i.e, $\rho_A = e^{-\beta_A H(t=\tau)}/Z_A$, where $Z_A = tr\left[e^{-\beta_A H(t=\tau)}\right]$. The inner friction quantifies how the density matrix defined at the end of the parametric finite-time transformation deviates from the reversible correspondence ρ_A. Figure 2 shows that we obtain zero inner friction at the quasi-static regime $(\tau = 0)$ and without misalignment $(\theta = 0)$. The former is the consequence of the celebrated quantum adiabatic theorem in which the system density matrix follows the instantaneous eigenstates without changing the initial level populations. The latter one is due to the absence of time-ordering in the unitary time evolution in the case of $[H(t = t_1), H(t = t_2)] = 0$ which results also zero inner friction. On the other hand, when the Hamiltonian at different time instants is incompatible, (when $0 < \theta \leq \pi/2$) we obtain non-zero inner friction for a finite-time transformation as shown in Figure 2. The inner friction is high for a fast-transformation (small τ values) which decays almost exponentially as a function of τ. The transformation considered here can be regarded as fast or slow by making interpretation using the energy-time uncertainty relation [22]. If we denote ΔE as the minimum energy gap between the energy levels during the transformation, then one can name the transformation, physically, as fast when $\tau \ll \hbar/\Delta E$ or slow when $\tau \gg \hbar/\Delta E$ [23]. For a given τ, we obtain higher inner friction for a larger misalignment θ since the angle, θ, affects the eigenenergies and leads to higher system energies for a larger θ.

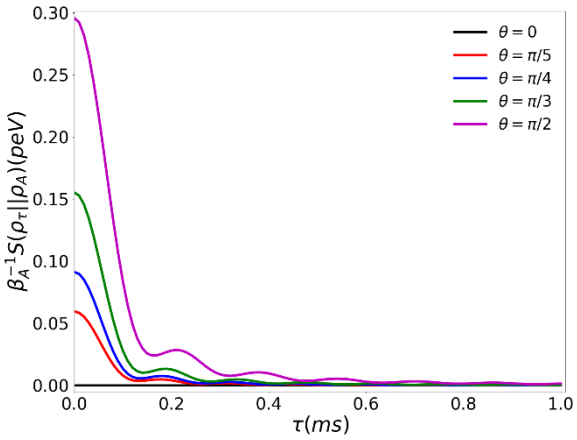

Figure 2 Inner friction arises in unitary transformation as a function of driving time τ for different misalignments θ, at $T_i = 10\ peV/k_B$.

The second considered irreversibility measure is the irreversible work which is defined as the relative entropy of ρ_τ to the state at the end of the reversible isothermal processes, ρ_B. Figure 3 shows the irreversible work as a function of protocol time for different misalignment angles θ. The irreversible work is always non-zero even in the case of zero misalignment $\theta = 0$ and in the quasi-static regime $(\tau \to \infty)$ due to the population mismatch between the final states ρ_τ and ρ_B (which will be discussed later in the text in detail). For non-zero misalignment $(0 < \theta \leq \pi/2)$, we obtain higher irreversible work for the fast transformation which decays to a non-zero stable value as τ increases. In contrast to inner friction as shown in Figure 2, the irreversible work is always greater than zero and approaches to larger non-zero stable values for larger misalignment not only at quasistatic regime but also at a finite-time transformation. This effect is originated from

the population mismatch between the states ρ_τ and ρ_B as we will discuss as a next.

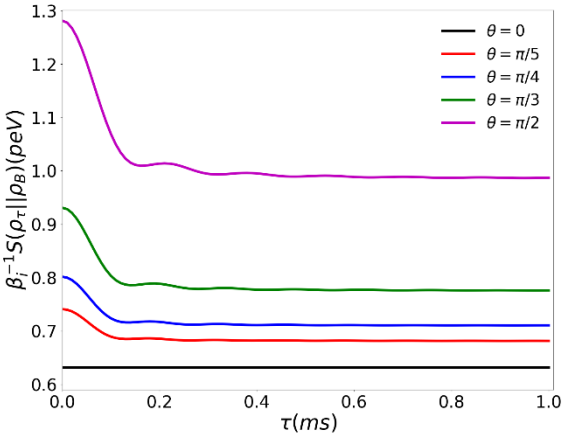

Figure 3 The irreversible work dissipated from the system as a function of the driving time τ for different misalignments θ, at $T_i = 10\ peV/k_B$.

We now investigate the mechanisms that contribute to inner friction and irreversible work. According to Eq. 3, there are two contributions to irreversibility. The first is coming from the coherence generation in τ_A during the finite time parametric transformation and the other one is the population mismatch between the state ρ_τ and the target states defined at the end of reversible transformations (i.e., ρ_A and ρ_B). In Figure 4 (a), we present the contributions on the irreversibility using Eq. 3 as a function of protocol time for the misalignment $\theta = \pi/4$. The coherence generation contribution is shown in Figure 4 (b) is the same for both the inner friction and the irreversible work since $C(\rho_\tau)$ measures the coherence generation in the energy frame during the finite time process. For a fast process, the coherence generation is high which decays and becomes zero at the quasistatic limit as predicted by the quantum adiabatic theorem.

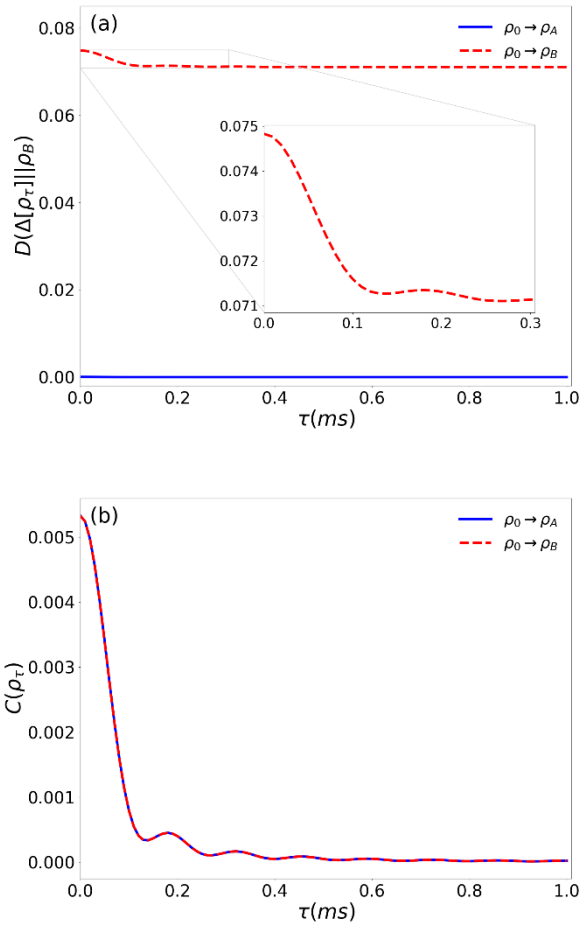

Figure 4 Population mismatch (a) and coherence generation (b) contributions to the irreversible work (dashed-red) and inner friction (solid-blue) as a function of driving time τ. The inset in (a) shows a magnification to the population mismatch effect for irreversible work.

The difference between the inner friction and irreversible work comes from the population mismatch contribution. For a fast transformation, the population mismatch is high for both cases. Since the final state ρ_τ approaches to ρ_A in the quasistatic limit, the population mismatch contribution on the inner friction decays to zero as τ increases. For the irreversible work case, the population mismatch contribution, however, approaches to a non-zero stable value as τ increases. Therefore, we conclude here that this is the population mismatch contribution that leads to differences between the two irreversibility measures and the non-zero stable value for the irreversible work at the quasistatic transformation limit.

4. CONCLUSIONS

We have investigated the concepts of irreversible work and inner friction for a driven single spin misaligned with respect to the external static magnetic field. The relative entropy between the actual state obtained at the end of the parametric finite-time transformation and the state obtained in a reversible adiabatic or a reversible isothermal transformation is a quantitative measure for the inner friction or irreversible work. The irreversibility measures are analyzed as a function of protocol time at different misalignment angles for the eligible parameters for NMR setups. For a finite-time transformation, we found a large deviation from the target states indicating the irreversibility in our setting. The mechanisms that contribute to the irreversibility measures have been also investigated. We emphasize that the coherence generation is the same for both inner friction and irreversible work. The differences between the irreversible work and the inner friction are found to be originated from the population mismatch contribution between the target states and the one obtained at the end of the unitary protocol.

We would like to remark here that the typical energy gaps and the heat source energy $k_B T_i$ a few peVs. Therefore, the irreversible work and the inner friction shown in Figures 2 and 3 are on the same order of magnitude which is also a few peVs for the finite-time transformation. For the considered operation regime, both thermal and quantum fluctuations affect the protocol adopted here. Here we elucidate how the quantum fluctuations associated with the coherence generation in the energy frame due to the fast driving leads to irreversibility from two different perspectives of definitions.

In NMR, the characteristic decoherence times are in order of seconds. On the other hand, the time allocated to the considered unitary driving protocol is in order of milliseconds. We, therefore, conclude here that the results obtained for the irreversible work and friction can be realized by using the NMR techniques [10, 24, 25].

Funding

This work was supported by Research Fund of the Samsun University. Project Number: BAP.MÜF.5501.2020.001

The Declaration of Conflict of Interest/ Common Interest

No conflict of interest or common interest has been declared by the author.

The Declaration of Ethics Committee Approval

The author declares that this document does not require an ethics committee approval or any special permission.

The Declaration of Research and Publication Ethics

The author of the paper declares that he complies with the scientific, ethical and quotation rules of SAUJS in all processes of the paper and that he does not make any falsification on the data collected. In addition, he declares that Sakarya University Journal of Science and its editorial board have no responsibility for any ethical violations that may be encountered, and that this study has not been evaluated in any academic publication environment other than Sakarya University Journal of Science.

REFERENCES

[1] H.T. Quan, Y.X. Liu, C.P. Sun and F. Nori, "Quantum thermodynamic cycles and quantum heat engines," Phys. Rev. E 76, 031105, 2007.

[2] O. Abah, J. Roßnagel, G. Jacob, S. Deffner, F. Schmidt-Kaler, K. Singer and E. Lutz, "Single-ion heat engine at maximum power," Phys. Rev. Lett. 109, 203006, 2012.

[3] F. Altintas, A.Ü.C Hardal and Ö.E Müstacaplıoğlu, "Rabi model as a quantum coherent heat engine: from quantum biology to superconducting circuits," Phys. Rev. A 91, 023816, 2015.

[4] R. Dillenschneider and E. Lutz, “Energetics of quantum correlations,” Europhys. Lett. 8, 50003, 2009.

[5] R. Uzdin, “Coherence-induced reversibility and collective operation of quantum heat machines via coherence recycling,” Rev. Appl. 6, 024004, 2016.

[6] D. Türkpençe, F. Altintas, M. Paternostro and Ö.E. Müstecaplıoglu, “A photonic Carnot engine powered by a spin-star network,” EPL 117, 50002, 2017.

[7] A. del Campo, J. Goold and M. Paternostro, “More bang for your buck: super-adiabatic quantum engines,” Sci. Rep. 4, 6208, 2015.

[8] O. Abah, M. Paternostro and E. Lutz, “Shortcut-to-adiabaticity quantum Otto refrigerator,” Phys. Rev. Research. 2, 023120, 2020.

[9] G. Xiao and J. Gong, “Construction and optimization of a quantum analog of the Carnot cycle,” Phys. Rev. E 92, 012118 2015.

[10] T.B. Batalhão, A.M. Souza, L. Mazzola, R. Auccaise, R.S. Sarthour, I.S. Oliveira, J. Goold, G. De Chiara, M. Paternostro and R.M. Serra, "Experimental reconstruction of work distribution and study of fluctuation relations in a closed quantum system," Phys. Rev. Lett. 113, 140601 2014.

[11] A.E. Allahverdyan, K.V. Hovhannisyan, A.V. Melkikh and S.G. Gevorkian, “Carnot cycle at finite power: attainability of maximal efficiency,” Phys. Rev. Lett. 111, 050601, 2013.

[12] F. Plastina, A. Alecce, T.J.G. Apollaro, G. Falcone, G. Francica, F. Galve, N. Lo Gullo and R. Zambrini, “Irreversible work and inner friction in quantum thermodynamic processes,” Phys. Rev. Lett. 113, 260601, 2014.

[13] G. Thomas and R. S. Johal, “Friction due to inhomogeneous driving of coupled spins in a quantum heat engine,” Eur. Phys. J. B 87, 166, 2014

[14] A. Alecce, F. Galve, N.L. Gullo, L. Dell’Anna, F. Plastina and R. Zambrini, “Quantum Otto cycle with inner friction: finite-time and disorder effects,” New J. Phys. 17, 075007, 2015.

[15] S. Çakmak, F. Altintas, and Ö.E. Müstecaplıoglu, "Irreversibility in a unitary finite-rate protocol: the concept of internal friction," Phys. Scr. 91, 075101, 2016.

[16] S. Çakmak, F. Altintas, A. Gençten and Ö.E. Müstecaplıoglu, "Irreversible work and internal friction in a quantum Otto cycle of a single arbitrary spin," Eur. Phys. J. D. 71, 75, 2017.

[17] P.A. Camati, J.F.G. Santos and R.M. Serra, “Coherence effects in the performance of the quantum Otto heat engine,” Phys. Rev. A 99, 062103, 2019.

[18] G. Francica, J. Goold and F. Plastina, “Role of coherence in the nonequilibrium thermodynamics of quantum systems,” Phys. Rev. E 99, 042105, 2019.

[19] S. Çakmak and F. Altintas, “Quantum Carnot cycle with inner friction,” Quantum Inf. Process. 19, 248, 2020.

[20] A.D. Varizi, A.P. Vieira, C. Cormick, R.C. Drumond and G.T. Landi, “Quantum coherence and criticality in irreversible work,” Phys. Rev. Research. 2, 033279, 2020.

[21] N. Shiraishi and H. Tajima, "Efficiency versus speed in quantum heat engines: rigorous constraint from Lieb-Robinson bound," Phys. Rev. E 96, 022138, 2017.

[22] D. Türkpençe and F. Altintas, “Coupled quantum Otto heat engine and refrigerator with inner friction,” Quantum Inf. Process. 18, 255, 2019.

[23] A.E. Allahverdyan and Th.M. Nieuwenhuizen, “Minimal work principle:

Proof and counterexamples," Phys. Rev. E 71, 046107, 2005.

[24] J.P.S. Peterson, T.B. Batalhão, M. Herrera, A.M. Souza, R.S. Sarthour, I.S. Oliveira and R.M. Serra, "Experimental Characterization of a Spin Quantum Heat Engine," Phys. Rev. Lett. 123, 240601, 2019.

[25] R.J. de Assis, T.M. de Mendonça, C.J. Villas-Boas, A.M. de Souza, R.S. Sarthour, I.S. Oliveira and N.G. de Almeida, "Efficiency of a Quantum Otto Heat Engine Operating under a Reservoir at Effective Negative Temperatures," Phys. Rev. Lett. 122, 240602, 2019.

SAKARYA ÜNİVERSİTESİ
FEN BİLİMLERİ ENSTİTÜSÜ DERGİSİ

Sakarya University Journal of Science
SAUJS

e-ISSN 2147-835X | Period Bimonthly | Founded: 1997 | Publisher Sakarya University |
http://www.saujs.sakarya.edu.tr/en/

Title: Real Time Control Application of the Robotic Arm Using Neural Network Based Inverse Kinematics Solution

Authors: Nurettin Gökhan ADAR

Recieved: 2021-04-04 21:57:17

Accepted: 2021-05-18 12:34:31

Article Type: Research Article

Volume: 25
Issue: 3
Month: June
Year: 2021
Pages: 849-857

How to cite
Nurettin Gökhan ADAR; (2021), Real Time Control Application of the Robotic Arm Using Neural Network Based Inverse Kinematics Solution. Sakarya University Journal of Science, 25(3), 849-857, DOI:
https://doi.org/10.16984/saufenbilder.907312
Access link
http://www.saujs.sakarya.edu.tr/en/pub/issue/62736/907312

Sakarya University Journal of Science 25(3), 849-857, 2021

Real Time Control Application of the Robotic Arm Using Neural Network Based Inverse Kinematics Solution

Nurettin Gökhan ADAR*[1]

Abstract

Robotic arms are widely used in many industrial applications at present. The control of robotic arms involves position coordination Cartesian space by a forward/inverse kinematics solution method. The inverse kinematics is difficult for real-time control applications, computational requirements are intensive and the run-time is high. The traditional solution methods used geometric, algebraic, and numerical iterative techniques are inadequate and slow in the inverse kinematics solution. Recently, alternative solution methods based on artificial intelligence techniques have been developed to solve the inverse kinematics problem. In this study, a multi-layered feed-forward Artificial Neural Network model was developed to solve the inverse kinematics of the 5 degrees of freedom robotic arm. Using the Proportional-Integral control algorithm combined with this Artificial Neural Network model, the real-time position control of the robotic arm was accomplished. The obtained results were compared with the PI control supported by an analytical inverse kinematics solution in real-time. The results showed that the PI control combined with Artificial Neural Network has superior tracking ability, smaller control error, and better absolute fit to the reference.

Keywords: Inverse kinematics, Robotic arm, Artificial neural network, PI control, Real-time

1. INTRODUCTION

Robot manipulators are extensively used in the manufacturing industry and also have many other specialized applications such as health care, agriculture, military. Manipulator applications involve pick and place an object in a specific position, precision grasping, and manipulation of the objects. Motion control of a robot manipulator is a fundamental problem that must be addressed at the design stage. In recent years, researchers have aimed to develop intelligent and learning robots to further accelerate robotic systems by maintaining high precision and accuracy in robot control. Some of these techniques are the artificial neural network imitated the human brain [1-3], particle swarm optimization algorithm inspired by the bird and fish flocking [4,5], firefly algorithm inspired by the social behavior of fireflies in the tropical [6].

*Corresponding author: gokhan.adar@btu.edu.tr
[1] Bursa Technical University Faculty of Engineering and Natural Sciences, Department of Mechatronics Engineering.
ORCID: https://orcid.org/0000-0001-6888-5755

For the motion control of robot manipulators, there is a requirement for the robot kinematics to identify the relationship between Cartesian coordinates in which robot movements are explained and joint parameters in which the control is achieved. Forward kinematics calculate the position, orientation, and velocity of the end effector from the joint displacements and angles. The inverse kinematics, which is the more difficult and complex, calculate the joint displacements and angles from the end effectors position and velocity. In the inverse kinematics solution, traditional methods used geometric, iterative, and algebraic methods are inadequate and slow due to the nonlinear equations and the complexity of the robot manipulator increasing exponentially with the number of joints. For this reason, researchers have proposed alternative solution methods based on artificial intelligence techniques to solve the inverse kinematics problem, as in other problems related to robots. Robot manipulators are widely used in various industrial automation applications and also the other specialized fields as medical, military. Manipulator applications involve pick and place an object in a specific position, precision grasping, and manipulation of the objects. To accomplish these, the end-effector motion which should be efficiently controlled is defined. Robot kinematics defined mapping between joint space and Cartesian space (x, y, z) is needed for the position control of robot manipulators. Forward kinematics and inverse kinematics are used for the kinematic analysis of robot manipulators. Forward kinematics computes the position, orientation, and velocity of the end effector from the joint displacements and angles, whereas inverse kinematics computes the joint displacements and angles from the end effector's position and velocity.

Köker solved the inverse kinematics problem of the six-joint Stanford robot manipulator by combining characteristics of neural networks and genetic algorithms [7]. Karlik and Aydin investigated the best neural-network configurations to solve the inverse kinematics of a six-joint robot manipulator. To find the inverse kinematics solutions, placement and orientation angles of the robot were used [8]. Köker et al. proposed the neural network solution of inverse kinematics by using cubic trajectory planning for a three-joint robotic manipulator [9]. Mayorga and Sanongboon presented a neural network for fast calculation of the inverse kinematics and effective geometrically bounded singularities prevention of redundant manipulators [10]. Daya et al. presented a neural network architecture that consists of 6 sub-neural to control the position of robotic manipulators [11]. Duka used feed-forward neural network computed desired trajectories in the two-dimensional Cartesian coordinate system for the three-link planar manipulator [12]. Zacharie implemented Logistic Belief Neural Network (LBNN) on a mobile robot with two gripped arms. LBNN was designed to control five degrees of freedom robot arm in real-time [13]. El-Sherbiny et al. compared Artificial Neural Network (ANN), adaptive neuro fuzzy inference system (ANFIS), and genetic algorithm techniques used to solve the inverse kinematics problem of the 5-DOF robot arm [14]. Jiang and Ishita presented a control system consisting of a traditional controller and a neural network controller with a parallel structure for trajectory tracking control of industrial robot manipulators. Neural network controller played a major role in the generating of the actuating force/torque required by the dynamic trajectory [15]. Xu et al. suggested a recurrent neural network-based controller for redundant manipulators subject to kinematic uncertainties. The controller can provide robustness and adaptability even under uncertain conditions because it can learn uncertain model parameters online [16]. Sharma used a 2-DOF Proportional Integral Derivative (PID) for trajectory control of a two-joint planar robot arm [17].

The control of robotic manipulators has a wide research area because of difficult manipulation tasks. Even though many robots work with high accuracy, repeatability, and stability, research continues on the improvement of robotic manipulators to upward increase the precision in robot control. Numerous advanced control algorithms have been developed so far, but PID controllers are employed as the first choice in most current robots in industrial operations due to their simplicity and practicability. However, the

linear PID controllers are not adequate for precise control of robot manipulators equipped with direct-drive actuators or perform high-speed motion despite all their advantages. It fails to provide effective control to nonlinear, uncertain, and coupled systems. The capability and utility of the conventional PID controller can be increased to a good extent with hybridization.

This paper describes the implementation of the PI control algorithm combined with ANN for inverse kinematics solving to real-time position control of robot manipulator. Obtained results of the proposed control algorithm are compared with the outcomes of PI control method used for analytical inverse kinematics solving in real-time.

2. KINEMATICS ANALYSIS OF ROBOTIC ARM

5 DOF robotic arm which is similar to human arm structure was studied. A forward and inverse kinematics equation is needed to control the robotic arm in Cartesian space. Forward kinematics equations are derived using the Denavit-Hartenberg (D-H) method. The coordinate systems of the robotic arm are shown in Figure 1 and D-H parameters of the robot arm are given in Table 1 where θ_i represents rotation about the Z-axis, a_i transition along the X-axis, α_i rotation about the X-axis and d_i transition along the Z-axis.

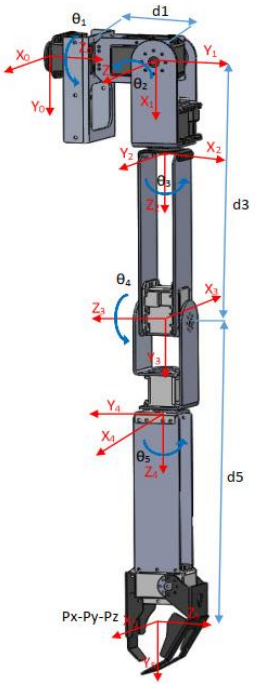

Figure 1 The robotic arm coordinate systems

Table 1
D-H parameters of the robotic arm

	$\mathbf{d_i}$	$\boldsymbol{\alpha_i}$	$\mathbf{a_i}$	$\boldsymbol{\theta_i}$
1	d_1=100	90°	0	θ_1+90°
2	0	90°	0	θ_2+90°
3	d3=250	90°	0	θ_3+90°
4	0	-90°	0	θ_4
5	d_5=100	90°	0	θ_5

Details of the forward kinematics equations of the robotic arm whose x-y-z position coordinates are given below are presented in [18]:

$$P_x = \cos\theta_1(d_3 + d_5\cos\theta_4)\sin\theta_2 - d_5(\cos\theta_1\cos\theta_2\cos\theta_3 + \sin\theta_1\sin\theta_3)\sin\theta_4$$

$$P_y = (d_3 + d_5\cos\theta_4)\sin\theta_1\sin\theta_2 + d_5(-\cos\theta_2\cos\theta_3\sin\theta_1 + \cos\theta_1\sin\theta_3)\sin\theta_4 \quad (1)$$

$$P_z = d_1 - \cos\theta_2(d_3 + d_5\cos\theta_4) - d_5\cos\theta_3\sin\theta_2\sin\theta_4$$

where P_x, P_y, and P_z represent the position of the end-effector according to the base frame respectively.

In this study, the Algebraic method, one of the closed-form methods, was used to obtain the robotic arm inverse kinematics equations. The target homogeneous transformation matrix can be selected as follow:

$$T_{target} = \begin{bmatrix} n_x & o_x & a_x & p_x \\ n_y & o_y & a_y & p_y \\ n_z & o_z & a_z & p_z \\ 0 & 0 & 0 & 1 \end{bmatrix} \quad (2)$$

where p (p_x, p_y, p_z) is the position of the end-effector and n (n_x,n_y,n_z), o(o_x,o_y,o_z) and a (a_x,a_y,a_z) are orthogonal unit vectors that define the orientation of end-effector frame.

Derivation of the inverse kinematics equations of the robotic arm whose θ_1, θ_2, θ_3, θ_4, θ_5 equations are given below is presented in [18]:

$$\theta_1 = atan2(p_x - o_x\, d_5, -o_y\, d_5 + p_y\,)$$

$$\theta_2 = acos(\,(o_z\, d_5 + d_1 - p_z)/d_3)$$

$$\theta_3 = atan2(o_x \cos(\theta_1)\cos(\theta_2) + o_y \cos(\theta_2)\sin(\theta_1) + o_z \sin(\theta_2)\,, o_y \cos(\theta_1) - o_x \sin(\theta_1)) \quad (3)$$

$$\theta_4 = \text{acos}\,(((d_1 - p_z)\cos(\theta_2) + (p_x\, cos(\theta_1) + p_y\, sin(\theta_1))\sin(\theta_2) - d_3)/d_5)$$

$$\theta_5 = atan2(-a_z \cos(\theta_2) + a_x \cos(\theta_1)\ \sin(\theta_2) + a_y \sin(\theta_1)\sin(\theta_2)\,, -n_z \cos(\theta_2) + a_z \cos(\theta_1)\ \sin(\theta_2) + n_z \sin(\theta_1)\sin(\theta_2))$$

where θ_1, θ_2, θ_3, θ_4, and θ_5 are presented joint angles respectively.

3. SOLUTION OF INVERSE KINEMATICS WITH ANN

ANN can be used to overcome the complexity and difficulty of solving robot inverse kinematics equations. The model can be characterized as a fully connected three-input which are the x-y-z Cartesian coordinate of end-effector, fifteen-hidden, five-output which are θ_1, θ_2, θ_3, θ_4 and θ_5 joint angles neural network. Levenberg-Marquardt is selected to implement Multilayer neural networks training and the sigmoid logistics transfer function is used in the output.

There are two main steps to develop ANN: training and testing. For this, a total of 520 data were collected from the experimental setup. 400 of the 520 data were for training while 120 data were for testing. The development of the neural network was carried out in the Matlab/Simulink Neural Network toolbox. Input and output data of the ANN are given in Figure 2.

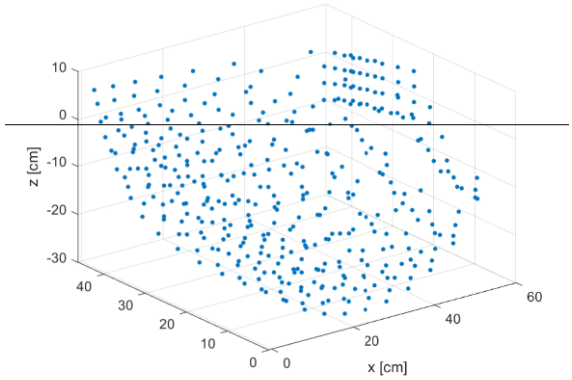

(a)

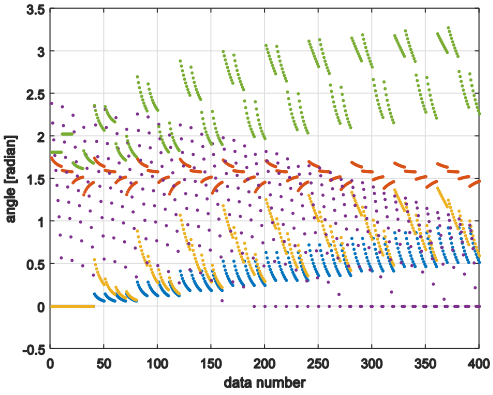

(b)

Figure 2 ANN input and output training data set

4. THE CONTROL OF ROBOTIC ARM

The robotic arm was controlled to compare the performance of ANN and analytical inverse kinematics. PI control algorithm was applied to control the position of the robotic arm for both ANN model and analytical inverse kinematics solution in real-time. The structure of the proposed control system is shown in Figure 3.

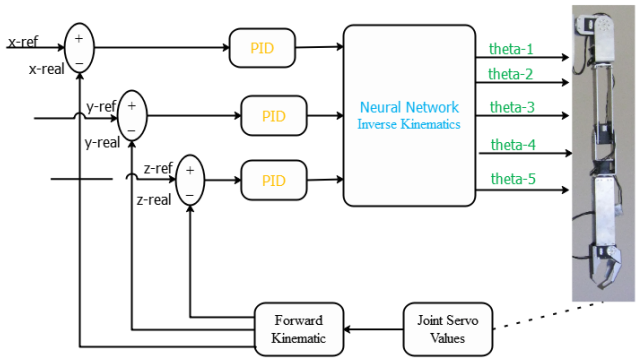

Figure 3 Structure of the proposed control system

General expressions of PI controller are given below:

$$u(t) = K_p\left((r(t) - y(t)) + \frac{1}{T_i}\int_0^t (r(t) - y(t))\,dt\right) \quad (4)$$

where *r(t)*, *y(t)* and *u(t)* are the reference, process output, and control signal, respectively. K_p is the PID gain, T_i is the integral time constants.

The gains of PI controller for 5 DOF robot arm automatically were tuned by MathWorks algorithm to achieve a balance between performance and robustness. K_p and K_i gain values of the PI controllers used for Cartesian coordinates (x, y, z) are tuned as shown in Table 2.

Table 2
The gain values of the PI controllers

PI Controller	K_p	K_i (K_p/T_i)
x-coordinate	0.5	0.1
y-coordinate	0.5	0.2
z-coordinate	0.3	0.15

In this control method, reference x-y-z values are provided externally by the user. Servo motors used in the robotic arm have embedded sensors. Each motor's angular position can be provided feedback in real-time. Forward kinematics is used to compute the actual position of the end effector from the feedback motor's angular position. Error is obtained by comparing the computed actual position (real x-y-z values) and reference x-y-z values. This error is the input of the PI controller to get the control signal. Control signals obtained from the controller are given as input to the ANN or Inverse kinematics to calculate joint angles. Using these joint angle values, it is provided to move to the desired position of the robotic arm with servo motors.

5. IMPLEMENTATION AND RESULTS

Experimental setup is given in Figure 6. A computer, power supply, USB converter, and robotic arm constitute the hardware part of the experimental setup. the robotic arm is driven with Dynamixel servo motors. Each motor communicates with a computer with RS-485 using a USB converter. Figure 4 demonstrates the fundamental configuration of the arm at its home position.

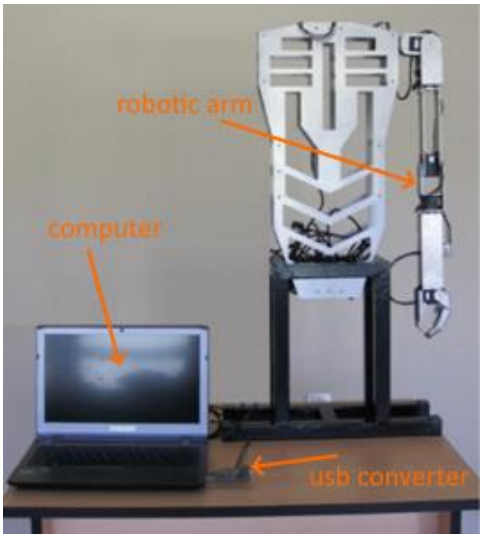

Figure 4 Fundamental configuration of the robotic arm

The algorithm was developed using Matlab-Simulink. Communication between Matlab-Simulink and servo motors is established using the RapidSTM32 library. RapidSTM32 is a Simulink device driver block set and tool suite for the STM32 microcontroller family.

In this study real-time applications of the 5-DOF robotic arm were implemented to compare the performance of ANN and analytical inverse kinematics.

Figure 5 shows the tracking capabilities on the desired trajectory of the robotic arm used different inverse kinematics solution approaches (analytical and ANN). Also, it can be seen how the end-effector tracks the desired position on the x, y, and z coordinates in the Cartesian space.

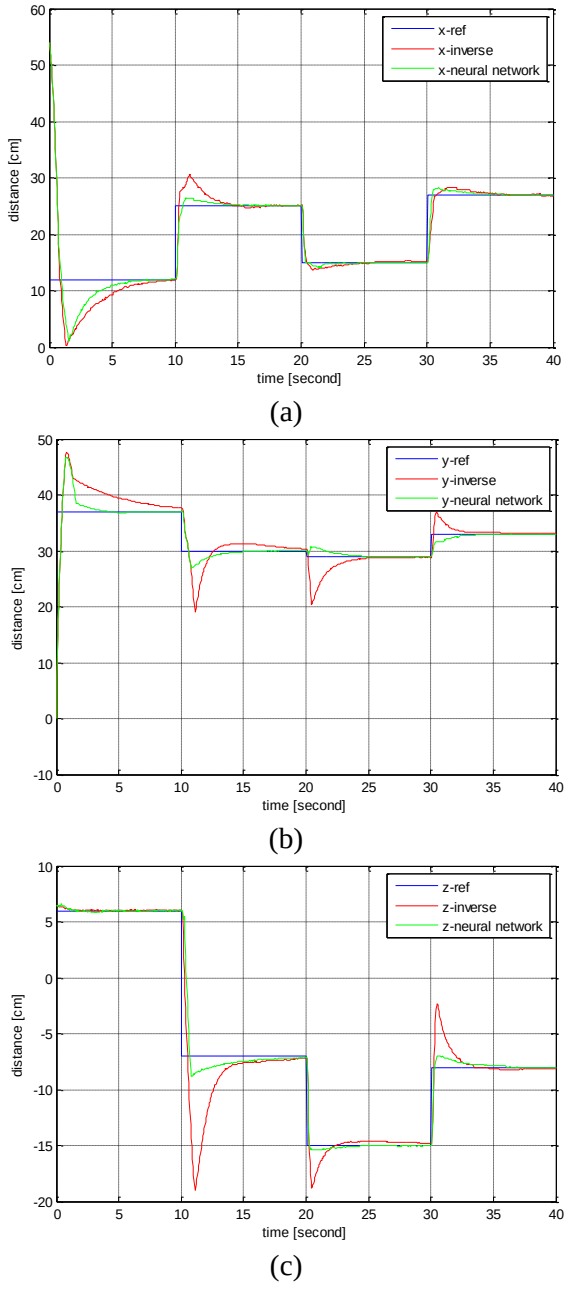

Figure 5 Trajectory tracking capabilities of the analytical and ANN approach for the x coordinate, the y coordinate, the z coordinate.

The reference position was modified at 10, 20, and 30 seconds. PI control system combined with ANN solves responded to the changes in x-y-z coordinates of reference position in less time and with smaller error than the analytical solution. In the PI control with the analytical solution, large overshoot/undershoot are observed at the points of change of the reference position. In initial time (t=0), PI controller combined with ANN has values away from x and y reference positions. This is because the ANN solution initially uses random weights. However, it has faster control response and lower settling time.

The relative errors and Root Mean Square Errors (RMSE) in the x-y-z coordinates for each interval of the reference position are given in Table 3 and Table 4, respectively. Relative Error and RMSE are calculated as follows:

$$Relative\ Error\ (\%) = \frac{Ref.Position - Arm's\ Position\ in\ Real\ Time}{Ref.Position} \times 100$$

$$RMSE = \sqrt{\frac{1}{N}\sum_{k=1}^{N}(Ref.Position - Arm's\ Position\ in\ Real\ Time)^2} \quad (5)$$

Table 3. The relative errors in the x-y-z coordinates of PI control approaches used analytical and ANN-based inverse kinematics.

Coordinate	Time (sec)	Relative Error (%)	
		Analytical Inverse Kinematics	ANN-Based Inverse Kinematics
x	10	1.4655	-0.2799
	20	-0.4980	-0.2088
	30	-0.6612	0.3126
	40	0.5636	0.1269
y	10	-1.8490	-0.0589
	20	1.2316	-0.3517
	30	0.5013	0.1028
	40	0.4398	-0.0665
z	10	-0.3731	0.1854
	20	-2.8472	-1.6168
	30	1.3420	-0.0673
	40	-1.9753	-0.0342

Table 4 RMSE in the x-y-z coordinates of PI control approaches used analytical and ANN-based inverse kinematics.

Coordinate	Time İnterval (sec)	RMSE	
		Analytical Inverse Kinematics	ANN-Based Inverse Kinematics
x	0-10	9.5114	9.0954
	10-20	2.4381	1.7242
	20-30	1.3613	1.2985
	30-40	1.7884	1.5574
y	0-10	5.5952	4.9086
	10-20	2.7881	1.3991
	20-30	2.3009	0.6003
	30-40	1.0700	0.6950
z	0-10	0.1107	0.1350
	10-20	3.9429	2.4764
	20-30	1.2369	0.8968
	30-40	1.5826	0.8437

The PI control method used the ANN-based inverse kinematics solution has achieved smaller relative errors to the reference position. Also, the robotic arm controlled in real-time using ANN-based inverse kinematics has reached close to the reference position with lower RMSE values at all-time intervals, as can be seen from Tables 4. It is seen that the ANN method has also a better absolute fit to the reference.

6. CONCLUSION

This study aims to minimize the PI control error in real-time of the 5 DOF robotic arm by using the ANN model to solve inverse kinematics. For this aim, an ANN model with optimal topology was developed that solves the inverse kinematics problem and predicts joint angles. The training performance of the designed network was evaluated and a high correlation was obtained. Validation results showed that the ANN model solves this problem with high accuracy, provides a strong estimate and good generalization capability.

The position control of the robotic arm was accomplished the PI control algorithm combined with ANN and This proposed approach was compared with the PI control supported by an analytical inverse kinematics solution in real-time.

Tracking ability and control errors in the x-y-z coordinates of the robotic arm, which was controlled by two different methods for 40 seconds in real-time, were examined and the high accuracy of the results obtained from the PI control combined with ANN can be clearly observed.

Funding

The author has no received any financial support for the research, authorship or publication of this study.

The Declaration of Conflict of Interest/ Common Interest

No conflict of interest or common interest has been declared by the authors.

The Declaration of Ethics Committee Approval

This study does not require ethics committee permission or any special permission.

The Declaration of Research and Publication Ethics

The authors of the paper declare that they comply with the scientific, ethical and quotation rules of SAUJS in all processes of the paper and that they do not make any falsification on the data collected. In addition, they declare that Sakarya University Journal of Science and its editorial board have no responsibility for any ethical violations that may be encountered, and that this study has not been evaluated in any academic publication environment other than Sakarya University Journal of Science.

REFERENCES

[1] C. Song, S. Xie, Z. Zhou, and Y. Hu, “Modeling of pneumatic artificial muscle using a hybrid artificial neural network

approach. Mechatronics," vol. 31, pp. 124-131, 2015.

[2] F. Luan, J. Na, Y. Huang, and G. Gao, "Adaptive neural network control for robotic manipulators with guaranteed finite-time convergence," Neurocomputing, vol. 337, pp. 153-164, 2019.

[3] K. Zheng, Q. Zhang, Y. Hu and B. Wu, "Design of fuzzy system-fuzzy neural network-backstepping control for complex robot system," Information Sciences, vol. 546, pp. 1230-1255, 2021.

[4] Y. Wang, Y. Shi, D. Ding and X. Gu, "Double global optimum genetic algorithm–particle swarm optimization-based welding robot path planning," Engineering Optimization, vol. 48, pp. 299-316, 2016

[5] S. Dereli and R. Köker, "IW-PSO Approach to the Inverse Kinematics Problem Solution of a 7-DOF Serial Robot Manipulator," Sigma Journal of Engineering and Natural Sciences, vol. 36, pp. 77-85, 2018

[6] A.K. Sadhu, A. Konar, T. Bhattacharjee and S. Das, "Synergism of Firefly Algorithm and Q-Learning for Robot Arm Path Planning," Swarm and Evolutionary Computation, vol. 43, pp. 50-68, 2018

[7] R. Köker, "A genetic algorithm approach to a neural-network-based inverse kinematics solution of robotic manipulators based on error minimization," Information Sciences, vol. 222, pp. 528-543, 2013.

[8] B. Karlik and S. Aydin, "An improved approach to the solution of inverse kinematics problems for robot manipuşators," Engineering Applications of Artificial Intelligence, vol. 13, pp. 159-164, 2000.

[9] R. Köker, C. Öz, T. Çakar and H. Ekiz, "A study of neural network based inverse kinematics solution for a three-joint robot," Robotics and Autonomous Systems, vol. 49, pp. 227-234, 2004.

[10] R.V. Mayorga and P. Sanongboon, "Inverse kinematics and geometrically bounded singularities prevention of redundant manipulators: An artificial neural network approach," Robotics and Autonomous Systems, vol. 53, pp. 164-176, 2005.

[11] B. Daya, S. Khawandi and M. Akoum, "Applying Neural Network Architecture for Inverse Kinematics Problem in Robotics," J. Software Engineering & Applications, vol. 3, pp. 230-239, 2010.

[12] A.V. Duka, "Neural network based inverse kinematics solution for trajectory tracking of a robotic arm," Procedia Technology, vol. 12, pp. 20-27, 2014.

[13] Zacharie M., "Advanced Logistic Belief Neural Network Algorithm for Robot Arm Control", Journal of Computer Science, vol. 8, no. 6, pp. 965-970, 2012.

[14] A. El-Sherbiny, M.A. Elhosseini and A.Y. Haikal, "A comparative study of soft computing methods to solve inverse kinematics problem," Ain Shams Engineering Journal, vol. 9, no. 4, pp. 2535-2548, 2018.

[15] Z.H. Jiang and T. Ishita, "A Neural Network Controller for Trajectory Control of Industrial Robot Manipulators," vol. 3, no. 8, pp. 1-8, August 2008.

[16] Z. Xu, S. Li, X. Zhou, W. Yan, T. Cheng and D. Huang, "Dynamic neural networks based kinematic control for redundant manipulators with model uncertainties," vol. 329, pp. 255-266, February, 2019.

[17] R. Sharma, P. Gaur and A.P. Mittal, "Performance analysis of two-degree of freedom fractional order PID controllers for robotic manipulator with payload," ISA Transactions, vol. 58, pp. 279-91, 2015.

[18] N. G. Adar, “Desing, Manufacturing and Control of Mobile Robot” Ph.D. dissertation, Dept. Mech. Eng., Sakarya Univ., Sakarya, 2016.

SAKARYA ÜNİVERSİTESİ
FEN BİLİMLERİ ENSTİTÜSÜ DERGİSİ

Sakarya University Journal of Science
SAUJS

e-ISSN 2147-835X | Period Bimonthly | Founded: 1997 | Publisher Sakarya University |
http://www.saujs.sakarya.edu.tr/en/

Title: Vote-Based: Ensemble Approach

Authors: Abdul Ahad ABRO

Recieved: 2021-03-23 18:56:37

Accepted: 2021-05-31 09:24:51

Article Type: Research Article

Volume: 25
Issue: 3
Month: June
Year: 2021
Pages: 858-866

How to cite
Abdul Ahad ABRO; (2021), Vote-Based: Ensemble Approach. Sakarya University Journal of Science, 25(3), 858-866, DOI:
https://doi.org/10.16984/saufenbilder.901960
Access link
http://www.saujs.sakarya.edu.tr/en/pub/issue/62736/901960

Sakarya University Journal of Science 25(3), 858-866, 2021

Vote-Based: Ensemble Approach

Abdul Ahad ABRO*[1]

Abstract

Vote-based is one of the ensembles learning methods in which the individual classifier is situated on numerous weighted categories of the training datasets. In designing a method, training, validation and test sets are applied in terms of an ensemble approach to developing an efficient and robust binary classification model. Similarly, ensemble learning is the most prominent and broad research area of Machine Learning (ML) and image recognition, which assists in enhancing the capability of performance. In most cases, the ensemble learning algorithm yields better performance than ML algorithms. In this regard, numerous approaches had been studied significantly and used to accomplish better yields from the existing literature; however, the outcomes of these methods are inadequate. Unlike existing methods, the proposed technique aggregates an ensemble classifier, known as vote-based, to employ and integrate the advantage of ML classifiers, which are Naive Bayes (NB), Artificial Neural Network (ANN) and Logistic Model Tree (LMT). This paper proposes an ensemble framework that aims to evaluate datasets from the UCI ML repository by adopting performance analysis. The experimental consequences reveal that the intended approach outperforms than the conventional approaches. Furthermore, the experimental outputs indicate that the suggested method provides more accurate results according to the base learner approaches in terms of accuracy rates, an area under the curve (AUC), recall, precision, and F-measure values. This method can be used for binary classification, image recognition and machine learning problems.

Keywords: Machine Learning, Artificial Neural Network (ANN), Ensemble learning, Data Mining, Classification.

1. INTRODUCTION

Machine Learning and Ensemble Learning multiple approaches intend to merge specific decisions by weighted or unweighted vote-based to classify new events as an active research area. These systems are mainly aimed towards achieving efficient results in classification rather than using a single model. Ensemble Learning is an approach of ML, which associates distinct base models to develop a single predictive model [1]. This is one of the sophisticated approaches of data assessment to pact with reflections having several datasets, as automated tools are being applied in it to locate patterns and relationships. Several methods are used in ensemble learning to progress

*Corresponding author: abdulahadabro1@gmail.com
[1]Department of Computer Engineering, Ege University, Turkey.
ORCID: https://orcid.org/0000-0002-3591-9231

prediction models [2]. It is much viable for resolving classification problems due to its robustness, highly concise prediction and measurements of variable significance. Ensemble learning is successfully deployed for its significant performance in numerous aspects, including medical, remote sensing, pattern recognition and sensors (IoT) for its magnificent outputs. NB, introduced by Chen et al. [3], proposed the particular relevant method, which chose some of the attributes to design the NB approach. The outcomes refer to the classification accuracy by maintaining efficiency, time and simplicity. ANN, suggested by Khwaja et al. [3], merged the bagging and boosting to train the model on sampling original training data in bagged-boosted ANNs. The results show the decreased variance compared to single ANN, boosted ANN, bagged ANN.

On the other hand, SVM, proposed by Nieto et al. [4], comprised of statistical learning theory with a latest class model, generates the classification values which possess the well-known accuracy of the multivariate function. SVM is a paradigm that utilizes classification algorithms for two-group challenges. It is accuracy and predictive performance on the survival of traumatic brain injuries performed significantly improved than logistic regression. SVM is a valuable approach for resolving classification and regression challenges. While the LMT [5], the combination of decision tree and logistic regression models give accurate outcomes of these algorithms; whereas, the high computational cost makes it inadmissible. The suggested method LogitBoost, with 14 benchmark datasets, provides the training time decreed while accuracy remains constant in fast incremental learning of logistic model tree. The main idea of this research is summarized in the following manner:

I) Vote-based ensemble learning method improves the binary classification performance accuracy. II) Comparative analysis of three base learners and seven datasets from the UCI ML Repository based on five evaluation criteria; accuracy (Acc), AUC, precision, recall and F-measure.

This research is organized into several sections. In section 2, related works pertain to machine and ensemble learning are presented. In section 3, the methodology is discussed in detail. Section 4, provides experimental design, the definition of the datasets, performance evaluation and results. Finally, the conclusion and future work are suggested in section 5.

2. RELATED WORK

In literature review, each ensemble and ML model has its pros and cons. Generally, its behaviour majorly depends upon the features of various suggested areas. Therefore, the performance evaluation of ensemble and ML models for vote-based assessment is significantly desired, although many assessment assignments have been agreed out by researchers, such as [6,7,8]. There are a wide variety of methods to build ensembles. In this work, we mainly focus on the vote-based ensemble method, which comprises other supervised ML algorithms. In [9], ensemble classifiers have been well researched and utilized to enhance the accuracy in multiple tasks. Many ensemble approaches, including weighted majority voting (WMV), majority voting, max combiner, mean combiner and median combiner, were introduced.

In contrast, specific classifiers can be aggregated utilizing any of these approaches. WMV is most demanding among the other method due to its theoretical usage, sensitivity and efficient results. In [10], naïve Bayes attempts to weigh up the general knowledge of classification in a multi-domain e-commerce platform. This model is designed to the immense computational efficiency of the traditional naïve and has an improved capability of classification for dealing with datasets. It enhances the performance and adaptability of the method. In other studies [11,12], a single layer of neurons was introduced between the input and output layers. The network was trained using epochs and an Adam optimizer with a default learning rate, whereas ANN is one of the methods which perform best in terms of sensitivity, followed by the SVM, decision tree and Logistic regression methods. In [13], the Logistic model tree, Random Forest (RF) and

classification and regression tree (CART) were constructed using training data. As per this detailed study, all three models show valuable performances; the RF model has the maximum analytical ability in comparison to the LMT and CART models. However, there are still few state-of-the-art models, for instance [14,15], CART which has been employed for assessment rarely, and therefore should be more examined and linked in a more advanced manner. The aim of classification is to correctly predict the target class for each case in the data. Whereas in the prototype build training process, a classification algorithm co-ordinate among the principles of the predictors and the standards of the target. Distinct classification algorithms accomplish distinct methods for finding associations. These associations are prototype, which can operate to a distinct dataset in which the class is unidentified.

3. METHODOLOGY

This section provides the analysis of the suggested method, preprocessing of data and classification of algorithms used in detail.

3.1. The Analysis of Proposed Method

This system consists of several stages: datasets, base learners, comparative analysis of results, conclusion and future work shown in Figure 1. In addition, 10-fold cross-validation used for all learners and datasets to obtain generalization performance of the system is shown.

3.2. Preprocessing of Data

The ranges of the values in data preprocessing may be high. In this scenario, classification algorithms could be affected significantly or negatively by some features. Therefore, data values are normalized to [0,1] range using min-max normalization technique [16], in Equation (1)

$$\hat{x}_i = \frac{x_i - \min_{x_i}}{\max_{x_i} - \min_{x_i}} \cdot (\max x_{new} - \min x_{new}) + \min x_{new} \quad (1)$$

For mapping value of a feature xi from the range [min(xi), max(xi)] to a new range [minxnew, maxxnew], the normalized feature x̂i is computed.

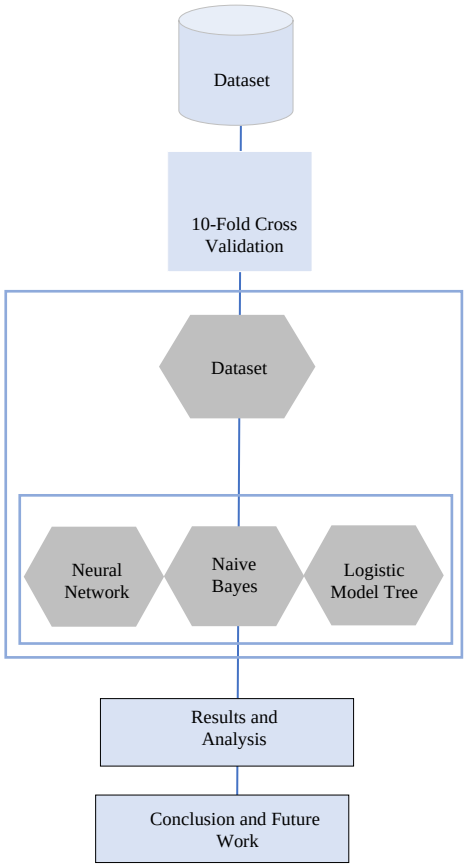

Figure 1 Overview of the proposed system

3.3. Classification of Algorithms

In this paper, a framework has been proposed for an ensemble learning method, including NB, ANN and LMT. Ensemble Learning, such as vote-based, enables one to diminish various influences such as classification error. Furthermore, combinations of many classifiers, particularly in the case of unstable classifiers, which may generate a more reliable classification than a single classifier.

The key concept of this analysis is to establish and provide data comprised of diverse attributes to present new methods related to binary classification. NB is a robust ML algorithm, which is used for predictive modelling [17]. It is an algorithm for classifying binary and multi-class problems. This approach is appropriate for binary or categorical input values. ANN is an information processing paradigm, which is considered as Universal Function Approximators. It is a modest and very influential process. It is considered as the class of feedforward artificial

neural network and composed of a highly interconnected processing model to solve the classification and regression model [18]. Whereas [19], SVM is a robust supervised ML algorithm, which is used for classification and regression challenges. It is a versatile and high-dimensional space-effective algorithm. LMT is defined as a set of logistic regression and decision tree learning. It is creating a more accurate model than C4.5 and CARD in real-world datasets. It is also a well-known enhanced decision tree learner [20].

4. EXPERIMENTAL DESIGN

We describe and present the experimental process, evaluation measures and experimental results for this study in the subsections:

4.1. The Experimental Process

In the experimental process, seven datasets have been used ML Repository for classification schemes [21]. The number of instances, attributes, and classes for each dataset are presented. The specifications of these datasets are demonstrated in Table 1. The performance of our algorithm is being associated to several other state-of-the-art learning schemes on datasets and shows that it produces accurate outcomes.

All experiments are performed on a total of 3 ML classifiers by using WEKA (Waikato Environment for Knowledge Analysis) ML toolkit and JAVA programming language [22]. We utilized default parameter values for all classifiers. We carry out 10-fold cross-validation to all datasets to yield reliable results. This cross-validation is imposed on the actual dataset casually segregated into 10 similar sized sets, one of which is used as test validation, while the remaining sets are used for training operations. The process is repeated 10 times and considered the averages of the results.

Dataset characteristics are evaluated concerning the attributes and the number of instances. These datasets are typically used to solve ML-related concerns. Datasets are chosen according to their distinct parameters from the Repository. It is determined by investigating the appropriate data or datasets which are being utilized in the various research papers related to ML issues. The proposed vote-based ensemble learning technique has been introduced for this process. This method utilized the imbalanced classification problems of binary (two-class) where the positive case, such as (class 1), is taken as an unusual and negative case (class 0) is taken as normal. In this work, three different ML approaches have been carried out along with the ensemble learning method, which is considered appropriate for this mechanism. However, the performance metrics are calculated based on the datasets according to binary classification problems.

Table 1
Datasets Specifications

Datasets	Attributes	Instances	Classes
Audiology	69	226	24
Balance Scale	4	625	3
Credit Approval	15	690	2
Heart (Statlog)	13	270	2
Ionosphere	34	351	2
Sonar	60	208	2
Zoo	17	101	7

4.2. Analysis of Algorithm

The hybrid nature of algorithm produces dynamically efficient outcomes with respect to different ensemble classifiers and target class for each case in the data. The result of vote-based ensemble approach is progressive. This approach provides more beneficial and efficient outputs by using the advantages of these algorithms.

5. MEASURES OF EVALUATION

This section describes the five performance evaluation measures of the suggested method, consisting of accuracy, AUC, precision, recall and F-measure.

Accuracy represents how near a measurement is to an identified or accepted figure. It is further defined in Equation (2).

$$ACC = \frac{TP + TN}{TP + TN + FP + FN} \quad (2)$$

In equation 2, TN, FN, FP and TP show the number of True Negatives, False Negatives, False Positives and True Positives. AUC is the area under the ROC curve for classifier performance. Its value will always be between 0.0 and 1.0. ROC graphs are two-dimensional graphs. In this curve, the TP rate is plotted on the Y-axis and FP rate is plotted on the X-axis [23]. If AUC value is close to 1, the classifier is more reliable and better than a random classifier.

Precision is a positive analytical value [8]. Precision defines how reliable measurements are, although they are farther from the accepted value. The precision is shown in Equation (3).

$$\text{Precision} = \frac{TP}{TP + FP} \tag{3}$$

The recall is the hit rate [24]. The recall is the reverse of precision; it calculates false negatives against true positives. The recall is illustrated in Equation (4).

$$\text{Recall} = \frac{TP}{TP + FN} \tag{4}$$

F-measure can be defined as the weighted average [8] of precision and recall. This rating considers both false positives and false negatives. The F-measure is presented in Equation (5).

$$F - \text{measure} = \frac{2}{1/\text{precision} + 1/\text{recall}} \tag{5}$$

In the weighting operation, these criteria are adjusted by the reference class prevalence proportionally in the data. Tables 2-8 present accuracy, AUC, precision, recall and F-measure individual weighted values for all datasets [25,26].

Table 2
Weighted values for audiology dataset

Audiology (Standardized)					
Methods	Acc(%)	AUC	Precision	Recall	F-Measure
NB	73.4513	0.943	0.750	0.943	0.500
ANN	83.1858	0.978	1.000	0.832	0.857
SVM	81.8584	0.941	1.000	0.819	0.857
LMT	**84.0708**	0.957	1.000	0.841	0.667

Table 3
Weighted values for balance scale dataset

Balance Scale					
Methods	Acc(%)	AUC	Precision	Recall	F-Measure
NB	90.4000	0.971	0.901	0.904	0.938
ANN	**90.7200**	0.977	0.916	0.907	0.911
SVM	87.6800	0.879	0.868	0.877	0.909
LMT	89.7600	0.981	0.859	0.898	0.873

Table 4
Weighted values for credit approval

Credit Approval					
Methods	Acc(%)	AUC	Precision	Recall	F-Measure
NB	77.6812	0.896	0.793	0.777	0.769
ANN	83.6232	0.895	0.836	0.836	0.836
SVM	**84.9275**	0.856	0.861	0.849	0.850
LMT	84.7826	0.920	0.852	0.848	0.848

Table 5
Weighted values for heart (statlog) dataset

Heart (Statlog)					
Methods	Acc(%)	AUC	Precision	Recall	F-Measure
NB	83.7037	0.898	0.837	0.837	0.837
ANN	78.1481	0.839	0.784	0.781	0.782
SVM	**84.0741**	0.837	0.841	0.841	0.840
LMT	83.3333	0.897	0.833	0.833	0.833

Table 6
Weighted values for ionosphere dataset

Ionosphere					
Methods	Acc(%)	AUC	Precision	Recall	F-Measure
NB	82.6211	0.935	0.842	0.826	0.829
ANN	91.1681	0.915	0.918	0.912	0.909
SVM	88.604	0.853	0.891	0.886	0.883
LMT	**93.1624**	0.922	0.934	0.932	0.930

Table 7
Weighted values for sonar dataset

Sonar					
Methods	Acc(%)	AUC	Precision	Recall	F-Measure
NB	67.7885	0.800	0.704	0.678	0.673
ANN	**82.2115**	0.878	0.822	0.822	0.822
SVM	75.9615	0.758	0.759	0.760	0.759
LMT	77.8846	0.846	0.779	0.779	0.779

Table 8
Weighted values for zoo dataset

Zoo					
Methods	Acc(%)	AUC	Precision	Recall	F-Measure
NB	95.0495	1.000	0.963	0.950	0.947
ANN	**96.0396**	0.993	0.960	0.960	0.958
SVM	96.0396	0.984	0.960	0.960	0.958
LMT	94.0594	0.997	0.941	0.941	0.939

Table 9
Our proposed vote-based approach

Proposed Vote-Based Classifier ANN, LMT, NB						
Classifier	Acc (%)	Impr. (%)	AUC	Precision	Recall	F-Measure
Audiology	**85.3982**	**1.3274**	**0.979**	0.914	0.854	**0.922**
Balance Scale	*90.7200	**0.0000**	**0.989**	0.891	*0.907	0.880
Credit Approval	**85.6522**	**0.7247**	0.918	0.857	**0.857**	**0.856**
Heart (Statlog)	**84.8148**	**0.7407**	**0.900**	**0.848**	**0.848**	**0.848**
Ionosphere	**94.5869**	**1.4245**	**0.952**	**0.947**	**0.946**	**0.945**
sonar	**82.6923**	**0.4808**	**0.893**	**0.827**	**0.827**	**0.827**
Zoo	**97.0297**	**0.9901**	0.999	**0.969**	**0.970**	**0.968**

- * Indicates the similar performance results concerning base learner.
- High Acc, AUC, Precision, Recall and F-measure are shown in Bold, while the greyed shows insufficient results.
- Impr. represents improvement according to the best results of Tables 2-8.

6. EXPERIMENTAL RESULTS

To sum up, Tables 2-8, have been designed according to the diverse datasets concerning the numerous approaches of ML in terms of different specifications. In Table 2, LMT has better outcomes, which provides 84.0708% Acc in comparison to others. Likely, in Table 3, ANN indicates 90.7200% Acc adequate consequences. Similarly, in Table 4, the SVM presents 84.9275% Acc effective results. Likewise, in Table 5, the SVM illustrates the 84.0741% Acc productive outcomes. In Table 6, LMT has shown the 93.1624% Acc result. Furthermore, in Table 7, ANN represents the 82.2115% Acc output. However, in the end, ANN shows a 96.0396% Acc result in Table 8. In general, ANN has more successive consequences than SVM; whereas the SVM provides more effective outputs than NB in most of the datasets. On the other hand, LMT has also provided satisfactory results to some extent, which is illustrated in Tables 2 and 8.

In Table 9, the vote-based ensemble learning method has been applied, in which the model is trained with the combined prediction preceding model. The vote-based has been set as a classifier and experienced the diverse datasets with numerous methods like ANN, LMT and NB in the given order. The Audiology, Credit Approval, Heart (Statlog), Ionosphere, Sonar and Zoo datasets have significant outputs regarding the accuracy, recall, precision, AUC and F-measure parameters in Table 9; however, the Balance Scale dataset show a similar outcome for Table 3.

In Table 9 demonstrates the comparison of all dataset results concerning our proposed vote-based meta-ensemble learning method. As it is clearly shown in Table 9, a Meta-ensemble classifier, vote with three base learners (namely, ANN, LMT and NB), provides highly accurate

outcomes in comparison to others. Moreover, it is analyzed that when the vote-based ensemble method combines with ANN, it provides more accurate outcomes than ANN; whereas ANN does not provide better outcomes when applied individually.

7. CONCLUSION AND FUTURE WORK

Based on the numerical and experimental outcomes, the core findings of this research effort can be summarized as follows:

In this paper, the ensemble learning classifier is being widely used due to its effectiveness and high performance in various fields such as ML and pattern recognition. In this study, the vote-based was correlated with the standard implementations of NB, ANN, SVM and LMT. The experimental results with 07 datasets indicate the outperformance of the model among all the four methods by a large margin. It ensured that vote-based has a similar diversity-accuracy pattern to Neural Network but is more accurate and diverse than it. A reasonable performance has been achieved by utilizing our applied ensemble techniques when compared with similar studies in the literature. A marginal improvement has been fetched statistically and shows significant differences in favor of the implemented method. Many machine learning algorithms, on the other hand, are incompetent to deliver good results since they are dependent relative on datasets. The sensitivity of a algorithm can be considerably influenced by the size of the training and test sets. In the future, other hybridization of ensemble learning methods will be utilized for performance improvement.

Acknowledgements

No acknowledgements has been declared by the author.

Funding

The author received no financial support for the research, authorship or publication of this study.

The Declaration Of Conflict Of Interest/ Common Interest

No conflict of interest or common interest has been declared by the author.

The Declaration of Ethics Committee Approval

This work does not require ethics committee permission or any special permission.

The Declaration of Research And Publicatıon Ethics

The author of the paper declares that he complies with the scientific, ethical and quotation rules of SAUJS in all processes of the paper and that he does not make any falsification on the data collected. In addition, she declares that Sakarya University Journal of Science and its editorial board have no responsibility for any ethical violations that may be encountered, and that this study has not been evaluated in any academic publication.

REFERENCES

[1] M. A. Shehab and N. Kahraman, “A weighted voting ensemble of efficient regularized extreme learning machine,” *Comput. Electr. Eng.*, vol. 85, 2020.

[2] J. Cao, S. Kwong, R. Wang, X. Li, K. Li, and X. Kong, “Class-specific soft voting based multiple extreme learning machines ensemble,” *Neurocomputing*, vol. 149, no. Part A, pp. 275–284, 2015.

[3] A. S. Khwaja, A. Anpalagan, M. Naeem, and B. Venkatesh, “Joint bagged-boosted artificial neural networks: Using ensemble machine learning to improve short-term electricity load forecasting,” *Electr. Power Syst. Res.*, vol. 179, no. October 2019, p. 106080, 2020.

[4] P. J. G. Nieto, E. García-gonzalo, and J. C. Á. Antón, “Journal of Computational and Applied A comparison of several machine learning techniques for the centerline

segregation prediction in continuous cast steel slabs and evaluation of its performance," *J. Comput. Appl. Math.*, vol. 330, pp. 877–895, 2018.

[5] S. Lee and C. H. Jun, "Fast incremental learning of logistic model tree using least angle regression," *Expert Syst. Appl.*, vol. 97, pp. 137–145, 2018.

[6] H. Liu and L. Zhang, "Advancing Ensemble Learning Performance through data transformation and classifiers fusion in granular computing context," *Expert Syst. Appl.*, vol. 131, pp. 20–29, 2019.

[7] S. Shen, M. Sadoughi, M. Li, Z. Wang, and C. Hu, "Deep convolutional neural networks with ensemble learning and transfer learning for capacity estimation of lithium-ion batteries," *Appl. Energy*, vol. 260, no. December 2019, p. 114296, 2020.

[8] A. A. ABRO, E. TAŞCI, and A. UGUR, "A Stacking-based Ensemble Learning Method for Outlier Detection," *Balk. J. Electr. Comput. Eng.*, vol. 8, no. 2, pp. 181–185, 2020.

[9] A. A. Aburomman, M. Bin, and I. Reaz, "A novel SVM-kNN-PSO ensemble method for intrusion detection system," vol. 38, pp. 360–372, 2016.

[10] F. Xu, Z. Pan, and R. Xia, "E-commerce product review sentiment classification based on a naïve Bayes continuous learning framework," *Inf. Process. Manag.*, no. February, p. 102221, 2020.

[11] S. S. Panesar, R. N. D. Souza, F. Yeh, and J. C. Fernandez-miranda, "Machine Learning Versus Logistic Regression Methods for 2-Year Mortality Prognostication in a Small, Heterogeneous Glioma Database," *World Neurosurg. X*, vol. 2, p. 100012, 2019.

[12] A. A. Abro, M. Alci, and F. Hassan, "Theoretical Approach of Predictive Analytics on Big Data with Scope of Machine Learning."

[13] W. Chen *et al.*, "A comparative study of logistic model tree, random forest, and classification and regression tree models for spatial prediction of landslide susceptibility," *Catena*, vol. 151, pp. 147–160, 2017.

[14] A. Kumar and A. Halder, "Ensemble-based active learning using fuzzy-rough approach for cancer sample classification," *Eng. Appl. Artif. Intell.*, vol. 91, no. December 2019, p. 103591, 2020.

[15] X. Zheng, W. Chen, Y. You, Y. Jiang, M. Li, and T. Zhang, "Ensemble deep learning for automated visual classification using EEG signals," *Pattern Recognit.*, vol. 102, p. 107147, 2020.

[16] T. Classification and B. K. Singh, "Investigations on Impact of Feature Normalization Techniques on Investigations on Impact of Feature Normalization Techniques on Classifier ' s Performance in Breast Tumor Classification," no. April 2015, pp. 10–15, 2017.

[17] L. Fan, K. L. Poh, and P. Zhou, "A sequential feature extraction approach for naïve bayes classification of microarray data," *Expert Syst. Appl.*, vol. 36, no. 6, pp. 9919–9923, 2009.

[18] E. Lella and G. Vessio, "Ensembling complex network 'perspectives' for mild cognitive impairment detection with artificial neural networks," *Pattern Recognit. Lett.*, vol. 136, pp. 168–174, 2020.

[19] R. Moraes, J. F. Valiati, and W. P. Gavião Neto, "Document-level sentiment classification: An empirical comparison between SVM and ANN," *Expert Syst. Appl.*, vol. 40, no. 2, pp. 621–633, 2013.

[20] N. Landwehr, M. Hall, and E. Frank, "Logistic model trees," *Mach. Learn.*, vol. 59, no. 1–2, pp. 161–205, 2005.

[21] UCI Machine Learning Repository, 2018, https://archive.ics.uci.edu/ml/index.php

[22] E. Frank, M. A. Hall, I. H. Witten, and T. Weka, "Eibe Frank, Mark A. Hall, and Ian H. Witten (2016). The WEKA Workbench. Online Appendix for 'Data Mining: Practical Machine Learning Tools and Techniques', Morgan Kaufmann, Fourth Edition, 2016.," p. 2016, 2016.

[23] T. Fawcett, "An introduction to ROC analysis," *Pattern Recognit. Lett.*, vol. 27, no. 8, pp. 861–874, 2006.

[24] L. A. Bull, K. Worden, R. Fuentes, G. Manson, E. J. Cross, and N. Dervilis, "Outlier ensembles: A robust method for damage detection and unsupervised feature extraction from high-dimensional data," *J. Sound Vib.*, vol. 453, pp. 126–150, 2019.

[25] T. Fawcett, "ROC graphs: Notes and practical considerations for researchers," *Mach. Learn.*, vol. 31, no. 1, pp. 1–38, 2004.

[26] A. A. Abro, M. A. Yimer, and Z. Bhatti, "Identifying the Machine Learning Techniques for Classification of Target Datasets," *Sukkur IBA J. Comput. Math. Sci.*, vol. 4, no. 1, 2020.